istituto nazionale di fisica nucleare
laboratori nazionali di frascati

2012
ANNUAL REPORT

FOREWORD

Laboratori Nazionali di Frascati-Frascati National Laboratories (LNF)
Present and Future

Many important steps have been taken during 2012 that will influence the future of the LNF. The DAFNE collider, running at record luminosities at these center of mass energies, in the second half of the year has been subject to an intensive machine study that will enable, after the long shutdown period during which new detectors will be installed in the KLOE detector, a long period of stable data taking. At the end of the KLOE run it is expected that the SIDDHARTA-2 experiment will take over conducting experiments on kaonic atoms that only the DAFNE kaon beams can enable. DAFNE, besides working as a collider, also brings with it the BTF (Beam Test Facility), a state of the art testing area capable of pretty unconventional beams, and the Synchrotron Beam Lines, that attract users from all over Europe.

A great deal of work has been put on the SuperB flagship project; on one side the experimental groups worked to the preparation of the TDR that is due for summer 2013. On the machine side a complete costing and resource loaded schedule has been prepared by the central team and submitted to the ministerial review. The review committee acknowledged the details presented but unfortunately the project was considered too expensive with respect to the resources that the Italian Research Minister could provide in the expected amount of time and SuperB has been hence terminated. At that point LNF, and INFN at large, are faced to understand in which direction its future will go when DAFNE will have completed its scientific life. On ne hand a luminosity tau-charm factory, still based on the crab-waist scheme and capable of luminosities in excess of 10^{35} $cm^{-2}s^{-1}$ with polarized beams is being studied as a backup for SuperB in order to understand whether, with a dedicated design, the project could fit in the available budget. On the other end a new project, IRIDE (for **I**nterdisciplinary **R**esearch **I**nfrastructure with **D**ual **E**lectron linacs) has been recently proposed; this project, based on the existing know-how in LNF on FEL's and state-of-the-art accelerators, is based on two superconducting linacs, about 1.5 GeV each, working in Continuous Wave mode (thus allowing high beam intensities), that can be coupled in various ways in order to have low energy electron-(electron)positron collisions, to feed a competitive FEL, to interact with high power lasers in order to produce gammas for nuclear photonic studies or for new generation, low emittance, polarized positron sources and to produce intense neutron beam. Also low energy gamma-gamma and electron-gamma experiments are foreseeable. This intriguing project is at this moment being detailed by the interested groups and a White Book with all details of IRIDE is foreseen by

summer 2013. A decision from INFN on which direction to go is hopefully to be expected before the end 2013.

The other on-site facilities, like the SPARC-LAB FEL, the NAUTILUS Gravitational Antenna, the SCF-LAB for space applications and X-LAB for manipulation of X-rays with capillaries lenses, as well as all other collaborations worked at full steam in 2012 albeit suffering, as all other facilities, of the difficult personnel situation that INFN at large, and LNF in particular due to the time profile of its staff, are living: experienced staff retiring represent a loss in competences that is not even numerically compensated by hiring new personnel. This situation is possibly dramatic and represents a real threat to the very existence of LNF as an efficient lab and must be tackled vigorously by INFN management.

Finally 2012 has been the year of the Higgs boson discovery at the LHC collider at Cern and LNF has been a good collaborator in all four major LHC experiments, with contributions that are well recognized also inside these gigantic scientific enterprises: a demonstration of the level of quality of our staff, a resource that our Country MUST defend.

Umberto Dosselli

Director

ATLAS

A. Annovi, M. Antonelli(Resp.), M.M. Beretta, H. Bilokon,
E. Capitolo(Tech.), A. Castegnaro(Laur.), F. Cerutti, V. Chiarella, G. Corradi(Tech.), M. Curatolo,
R. Di Nardo(Ass. Ric.), M. Dreucci, B. Esposito, M. Gatta (Tech.), C. Gatti, P.F. Laurelli,
G. Maccarrone, A. Martini, G. Mancini(laur.), G. Nicoletti, G. Pileggi (Tech.),
B. Ponzio(Tech.), V. Russo(Tech.), A. Sansoni,V. Santini(laur.)
M. Testa, T. Vassilieva (Tech.), E. Vilucchi, G. Volpi.

In collaboration with:
Centro di Calcolo:
M. Pistoni, D. Spigone

1 Introduction

In the 2012 data taking ATLAS collected proton-proton collisions at 8 TeV center of mass energy corresponding to an integrated luminosity of about 20 fb^{-1}. On 4 July, 2012, the LHC experiments reported the evidence of the Higgs boson with a mass of about of 125 GeV. Our group contributed significantly to this discovery with fundamental contributions to the analysis $H \to ZZ \to 4\ell$, and $H \to WW \to 2\ell 2\nu$ as will be described in the following. In both channels we benefit of the matured expertize on performances. Missing Transverse Energy measurement is one of the main object used in the WW channel, and muon reconstruction (efficiency, momentum calibratio, etc) is crucial for the 4 lepton channel. These contributions have been made possible also thanks to the reliability and the innovative tools available on the LNF Tier2 that has been recently approved by the INFN. In parallel with the data taking activity, including shifts and maintenance, we are deeply involved in two upgrade Phase I activities the Fast TracK (FTK) for the upgrade of the trigger system, and the new Small Wheel for the upgrade of the muon system.

2 Reconstruction of the missing transverse energy

The reconstruction and calibration of the missing transverse energy ($\not\!\!E_T$) developed in ATLAS makes use of the full event reconstruction and of a calibration based on reconstructed physics objects (refined calibration) [1)]
Calorimeter cells are associated with a parent reconstructed and identified high-p_{T} object in a chosen order: electrons, photons, hadronically decaying τ-leptons, jets and muons.
Cells belonging to topologically formed clusters (topoclusters) not associated with any such objects are also taken into account in the $\not\!\!E_T$ calculation.
Once the cells are associated with a category of object as described above and calibrated accordingly, $\not\!\!E_T$ is calculated as follows:

$$E_{x(y)}^{\mathrm{miss,calo}} = E_{x(y)}^{\mathrm{miss},e} + E_{x(y)}^{\mathrm{miss},\gamma} + E_{x(y)}^{\mathrm{miss},\tau} + E_{x(y)}^{\mathrm{miss,jets}} + E_{x(y)}^{\mathrm{miss,softjets}} + E_{x(y)}^{\mathrm{miss,calo},\mu} + E_{x(y)}^{\mathrm{miss,CellOut}} \quad (1)$$

where each term is calculated from the negative sum of calibrated cell energies inside the corresponding objects:

- $E_{x(y)}^{\mathrm{miss},e}$, $E_{x(y)}^{\mathrm{miss},\gamma}$, $E_{x(y)}^{\mathrm{miss},\tau}$ are reconstructed from cells in electrons, photons and taus, respectively
- $E_{x(y)}^{\mathrm{miss,jets}}$ is reconstructed from cells in jets with $p_{\mathrm{T}}>$ 20 GeV
- $E_{x(y)}^{\mathrm{miss,softjets}}$ is reconstructed from cells in jets with 7 GeV $<p_{\mathrm{T}}<$ 20 GeV
- $E_{x(y)}^{\mathrm{miss,calo},\mu}$ is the contribution to $\not\!\!E_T$ originating from the energy lost by muons in the calorimeter
- the $E_{x(y)}^{\mathrm{miss,CellOut}}$ term is calculated from the cells in topoclusters which are not included in the reconstructed objects. For the calculation of this term an energy flow algorithm is used.

The final $E_{x(y)}^{\mathrm{miss}}$ is then calculated adding the $E_{x(y)}^{\mathrm{miss},\mu}$ term.
The $\not\!\!E_T$ muon term is calculated from the momenta of muon tracks reconstructed with $|\eta| < 2.7$: $E_{x(y)}^{\mathrm{miss},\mu} = -\sum_{\text{selected muons}} p_{x(y)}^{\mu}$
In the region $|\eta| < 2.5$, only well reconstructed muons in the muon spectrometer with a matched track in the inner detector are considered.

In order to deal appropriately with the energy deposited by the muon in calorimeters, the muon term is calculated differently for isolated and non-isolated muons.
This algorithm, allowing to calibrate cells separately and independently according to the object to which they belong, has the best performances in terms of linearity and resolution of the $\not{E}_T$ for events containing electrons, photons, taus and muons.
The $\not{E}_T$ reconstruction, especially the low-pt contribution $E_{x(y)}^{\mathrm{miss,CellOut}}$ and $E_{x(y)}^{\mathrm{miss,softjets}}$, is strongly affected by the increasing of pile-up. For several analyses involving $\not{E}_T$ measurements is essential a precise modeling of pile-up in simulation. Moreover the systematic uncertainty due to the pile-up is an issue for several important analyses concerning Higgs searches (see Sec. 3.1).
The systematic uncertainty induced by the pileup can be determined in situ by exploiting the

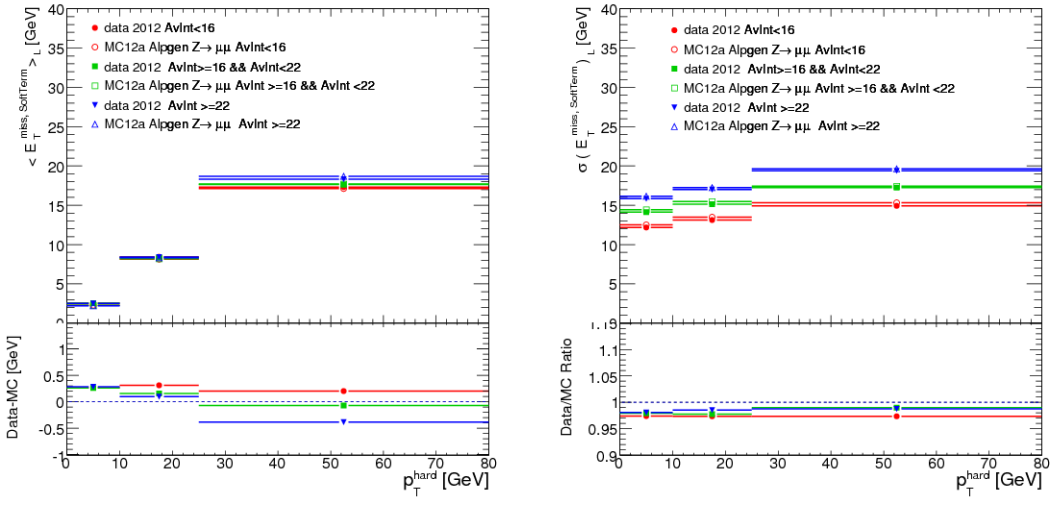

Figure 1: Mean (left) and resolution (right) of the longitudinal component of the soft-terms as a function of the total transverse momentum of the hard objects and the number of average bunch crossing interactions for data and MonteCarlo.

balance between the soft-terms and the total transverse momentum of the hard objects (p_T^{hard}) in $Z/\gamma^* \to \mu^+\mu^-$ events. In figure 1 the mean and the resolution of soft-terms as function of p_T^{hard} and the number of average bunch crossing interactions is shown.

3 PileUp suppression

In 2012, when about 30 mean interaction per bunch crossing are expected, pileup suppression will be an issue especially for the $\not{E}_T$ reconstruction. Degradation of $\not{E}_T$ performances are mostly due to the soft-terms contribution, $E_T^{\mathrm{miss,CellOut}}$ and $E_T^{\mathrm{miss,SoftJets}}$ term. Several techniques have been studied to reduce the impact of pile-up contribution, mainly combining the tracks pointing capability and the calorimeter information. The use of tracks pointing at the primary vertex allow to reduce the dependence on the $\not{E}_T$ performances the number of reconstructed vertices. However the acceptance of ATLAS tracking system is limited by $|\eta| < 2.5$ and further suppression is needed in forward region. Calorimeter clusters are used in the whole eta range to estimate the transverse energy density of the event ρ, following the approach for pile-up suppression in Ref. [2]. The energy density of the event ρ is an estimate of the in time and out of time pile-up activity

and its contribution is subtracted to the $\not\!\!E_T$. The aim of the algorithm should ideally to improve resolution without affecting the linearity of the $\not\!\!E_T$. A trade-off between the two effects should be found. In Fig. 2(right) the $\not\!\!E_T$ resolution as a function of the number of vertices is shown for several methods. In Fig. 2(left) the effect on the calibration in $Z/\gamma^* \to \mu^+\mu^-$ events, is also shown. The best compromise is obtained when both tracks and calorimeter pile-up subtraction are used (green and magenta points). Black points correspond to the uncorrected $\not\!\!E_T$, red point and blue points correspond to algorithm using respectively tracks and clusters information alone.

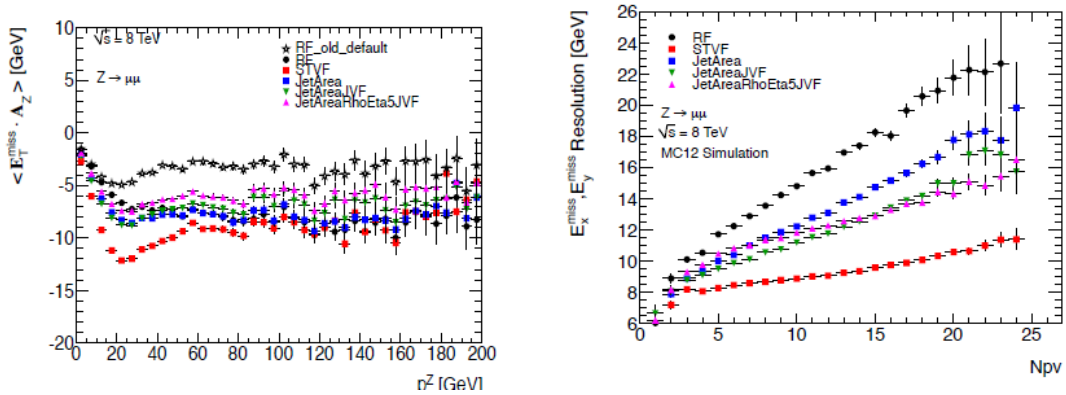

Figure 2: Left:$\not\!\!E_T$projection on the Z-boson p_T direction as a function of the p_T of the Z boson. Right: $\not\!\!E_{Tx}$ resolution as a function of the number of vertices in the event. Black points correspond to the uncorrected $\not\!\!E_T$, other colors correspond to several pile-up suppression algorithms.

3.1 Search for the Higgs boson in the $H \to WW^{(*)} \to l\nu l\nu$ decay channel

For a SM Higgs boson with a mass greater than 135 GeV, the $H \to WW^{(*)}$ is the dominant decay mode and in the region around m_H= 160 GeV the purely leptonic mode $H \to WW^{(*)} \to l\nu l\nu$ is the most sensitive channel. The experimental signature for this channel consists of two opposite sign, isolated and with high transverse momentum leptons (e or μ) and large missing transverse energy, $\not{E}_T$, due to the undetected neutrino. The main backgrounds for this channel, after the two leptons requirement, are the Drell-Yan and $Z + jets$ processes, tt and single top ($tW/tb/tqb$), WW , other diboson processes ($WZ/ZZ/W\gamma$), and $W + jets$ where a jet is misidentified as a lepton. The full 2011 and 2012 data sample have been used for this analysis [3)] corresponding to an integrated luminosity of 4.6 fb^{-1}at a center of mass energy of 7 TeV and 21 fb^{-1}at 8 TeV, respectively. Data are subdivided into $H + 0$-jet, $H + 1$-jet, and $H + 2$-jet channel in order to maximize the sensitivity by applying further selection criteria that depend on the jet multiplicity. The event are selected by using a single lepton trigger requiring a high-p_T electron or muon. The selection criteria for this analysis are the following:

- exactly two isolated opposite-sign leptons (p_T> 25,15 GeV). This requirement reduces mostly the QCD and the $W + jets$ backgrounds.
- large missing energy requirement and Z mass veto cut, used to suppress the Drell-Yan and the $Z + jets$ contamination. In particular the quantity $E^{\text{miss}}_{\text{T,rel}}$ is used in this analysis defined as $E^{\text{miss}}_{\text{T,rel}}$= $\not{E}_T$ sin($\Delta\phi_{min}$) with $\Delta\phi_{min}$ = min ($\Delta\phi, \pi/2$) and $\Delta\phi$ defined as the absolute azimuthal angular difference between the $\not{E}_T$ vector and the nearest candidate lepton or jet with p_T> 25 GeV.
- b-jet veto is used to suppress the tt background.
- topological cuts ($\Delta\phi_{ll}$ <1.8 and m_{ll} <50 GeV) are used to reduce the SM WW contamination exploiting the spin correlations in the $WW^{(*)}$ system arising from the spin-0 nature of the Higgs boson.
- cuts on p^{ll}_T (0-jet channel) or p^{tot}_T [1] (1-jet and 2-jet channel) are used to further suppress Drell-Yan and soft-jets backgrounds.

[1]defined as the magnitude of the vector $\overrightarrow{p^{tot}_T}$ where $\overrightarrow{p^{tot}_T}$ is the vector sum of the transverse

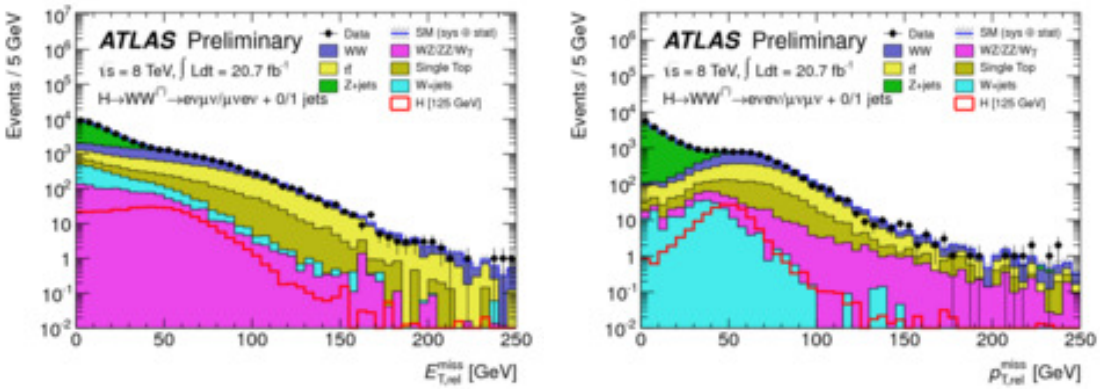

Figure 3: The $E^{\text{miss}}_{\text{T,rel}}$ distribution in the *emumue* channel (right) with the minimum lepton p_T cut applied and the $p^m_T iss$ distribution after the $E^{\text{miss}}_{\text{T,rel}}$ cut. The signal is shown for m_H= 125 GeV.

The crucial aspects for this analysis are

- the understanding of the $\not\!\!E_T$(real or fake). In fact $\not\!\!E_T$ spectrum and resolution are very sensitive to pile-up and with an higher pileup environment an increase of resolution is expected with the results that one have to tighten the cut on $E_{\mathrm{T,rel}}^{\mathrm{miss}}$ with a signal loss. Understanding of sources on data-MC disagreement on $\not\!\!E_T$ distribution (especially with high pileup) and improvements in additional Drell- Yan suppression are fundamental for this channel, in particular for the same-flavour channels. Figure 3(a) shows the $E_{\mathrm{T,rel}}^{\mathrm{miss}}$ distribution of the $e\mu$ and μe channel (left) and μe channel (right) with the minimum lepton p_{T} cut applied. and with the signal that is shown for $\mathrm{m_H}$= 125 GeV. In the same-flavour channels additional variable are used to further reject Drell- Yan background. An alternative measurement of the missing transverse momentum is obtained using inner detector tracks (p_T^{miss}). The resolution of this track-based quantity is less sensitive to pile-up interactions than the calorimeter-based $\not\!\!E_T$. Figure 3(b) shows the p_T^{miss} distribution after the pre-selection and the requirement on $E_{\mathrm{T,rel}}^{\mathrm{miss}}$.
- an excellent understanding of the background in the signal region. Signal free control region are used in data to constrain MC expectations in order to use MC simulation to extrapolate to the signal region. The $W + jets$ background contribution has been estimated using a control sample of events from data where one of the two leptons satisfies the identification and isolation criteria and the other lepton fails these criteria while satisfying a loosened selection. The $Z + jets$ background is normalized using a Z control sample ($|m_{ll} - M_Z| < 15$ GeV) correcting for mismodeling of $\not\!\!E_T$ tails. The top background prediction is normalized to the data using a control sample defined by reversing the b-jet veto and removing the requirements on m_{ll} and $\Delta\phi_{ll}$. The SM WW background, which represent the 65% of the total background, is normalized using an high-m_{ll} control region. The remaining backgrounds from di-bosons are estimated using MC simulation.

The transverse mass variable, m_{T}, is used in this analysis to test for the presence of a signal. This variable is defined as:

$$m_{\mathrm{T}} = \sqrt{(E_{\mathrm{T}}^{\mathrm{ll}} + E_{\mathrm{T}}^{\mathrm{miss}})^2 - |\mathbf{p}_T^{ll} + \mathbf{p}_T^{miss}|} \tag{2}$$

Figure 4 shows the distributions of the transverse mass for events satisfying all criteria in the $H + 0$-jet (left) and $H + 1$-jet (right) analyses at 8 TeV with a superimposed signal shown for $\mathrm{m_H}$= 125 GeV.

Njet	Signal	Total bkg.	Observed
=0	25 ± 5	161 ± 11	154
=1	7 ± 2	47 ± 6	62
>=2	1.2 ± 0.2	4.6 ± 0.7	2

Table 1: Summary table for 7 TeV. The observed numbers of events and the expected number of signal ($m_H = 125$ GeV) and background events are reported. The $e\mu + \mu e$ and $ee\mu\mu$ channels are combined.

Tables 1 and 2 show the expected numbers of signal ($m_H = 125$ GeV) and observed events at 7 TeV and 8 TeV respectively, for the N_{jet}=0, N_{jet}=0 and N_{jet}=2 analyses.
The expected and observed significances, shown in Figure 5a, at $m_H = 125GeV$ are 3.7 s.d.($p_0 = 1 \times 10^{-4}$) and 3.8 (8×10^{-5}) respectively. Figure 5b shows, as a function of $\mathrm{m_H}$, the

momenta of the jet, the two leptons and the $\not\!\!E_T$ vector

Njet	Signal	Total bkg.	Observed
=0	97 ± 20	739 ± 47	831
=1	40 ± 13	261 ± 30	309
>=2	8.7 ± 14	36 ± 4	55

Table 2: Summary table for 8 TeV. The observed numbers of events and the expected number of signal ($m_H = 125$ GeV) and background events are reported. The $e\mu + \mu e$ and $ee\mu\mu$ channels are combined.

observed and expected cross section upper limits at 95% CL, for the combined $H + 0$-jet, $H + 1$-jet and $H + 2$-jet analyses. Observed exclusion is for $m_H > 133$ GeV. The excess of events is quantified by the signal strength, which is defined as the ratio of the observed cross section to the value predicted for a Standard Model Higgs boson . For $m_H = 125$ GeV it is measured to be:

$$\mu = 1.03^{+0.22}_{-0.21}(stat)^{+0.21}_{-0.17}(theo.syst.)^{+0.11}_{-0.10}(expt.syst.)^{+0.05}_{-0.04}(lumi)$$

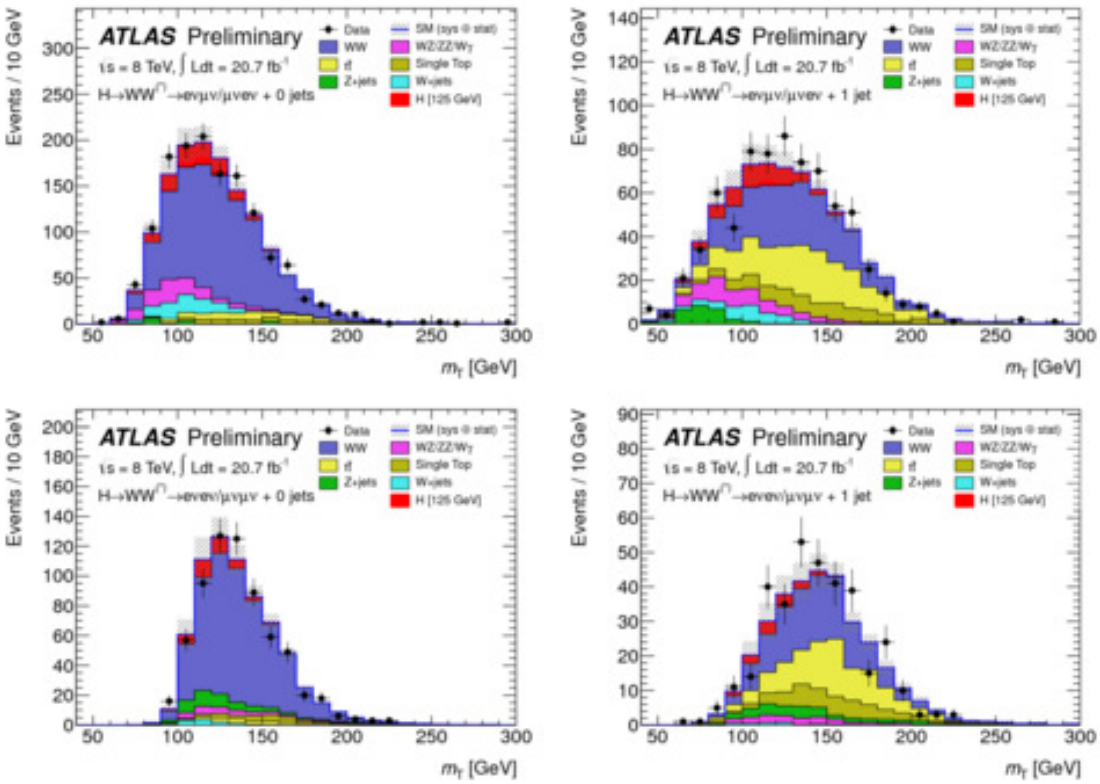

Figure 4: Transverse mass after all selection criteria in the $H + 0 - jet$ (left) and $H + 1 - jet$ (right) analyses at 8 TeV for opposite flavour (top) and same flavour (bottom) final state. The superimposed signal shown is for mH = 125 GeV.

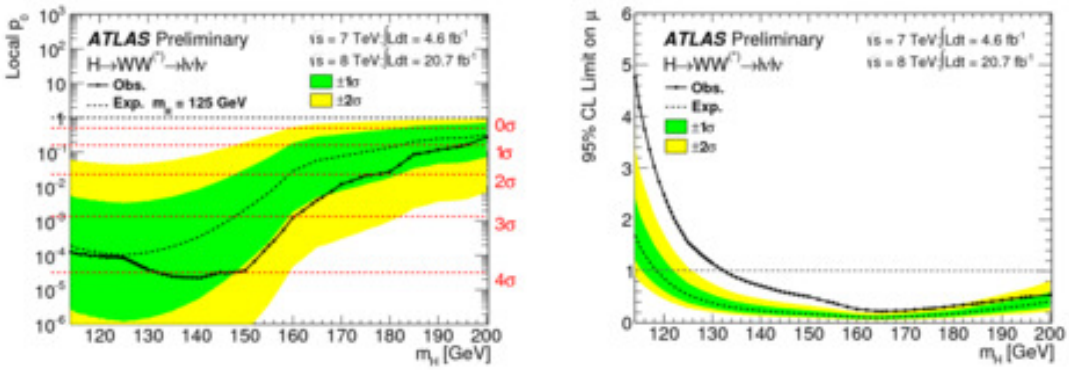

Figure 5: Results of p_0 and 95% C.L. upper limits using combined 7 TeV and 8 TeV data. The p_0 is given probability for the background-only scenario as a function of m_H. The expected 95% CL upper limit is computed in absence of the signal. For both figures, the smaller green bands re[resent $\pm 1\sigma$ uncertainties on the expected values, and the larger yellow badn represent $\pm 2\sigma$ uncertainties.

3.2 Observation of an excess of events in the search for the Standard Model Higgs boson in the $H \to ZZ^{(*)} \to 4l$ channel

The $H \to ZZ^{(*)} \to l^+l^-l'^+l'^-$ with l, l'=e or μ decay channel provide a good sensitivity for the SM Higgs boson search over a wide mass range. The main advantages for this channel are the purity (S/B$\sim$1) and the possibility to fully reconstruct the invariant mass of the Higgs boson. In particular three finale state (4μ, $4e$, $2e2\mu$) are considered. The latest results on this analysis uses all the data collected in 2011 corresponding to an integrated luminosity of 4.8 fb^{-1}at $\sqrt{s} = 7$ TeV and 21 fb^{-1}of data collected in 2012 at $\sqrt{s} = 8$ TeV.
The analysis searches for Higgs boson candidates is performed by selecting two same-avour, opposite-sign lepton pairs in an event. The impact parameter of each lepton along the beam axis is required to be within 10 mm of the reconstructed primary vertex. To reject cosmic rays, muon tracks are required to have a transverse impact parameter less than 1 mm. Each muon (electron) must satisfy $p_{\mathrm{T}} > 6$ GeV ($p_{\mathrm{T}} > 7$ GeV) and be measured in the pseudorapidity range $|\eta| < 2.7$ ($|\eta| < 2.7$). The highest p_{T}lepton in the quadruplet must satisfy $p_{\mathrm{T}} > 20$ GeV, and the second (third) lepton in p_{T}order must satisfy $p_{\mathrm{T}} > 15$ GeV ($p_{\mathrm{T}} > 10$ GeV). The leptons are required to be separated from each other by $\Delta R > 0.1$ if they are of the same avour and $\Delta R > 0.2$ otherwise. Only quadruplets with the same-flavour and opposite-sign lepton pair closest to the Z boson mass are kept. The pair with the mass closest to the Z boson mass is referred to as the leading di-lepton and its invariant mass, m_{12}, is required to be between 50 and 106 GeV. The remaining same-flavour, opposite-sign lepton pair is the sub-leading di-lepton and its invariant mass, m_{34}, is required to be in the range $m_{\mathrm{min}} < m_{34} < 115$ GeV, where m_{min} is 12 GeV for $m_{4\ell} < 140$ GeV and rises linearly to 50 GeV at $m_{4\ell} = 190$ GeV. It stays at 50 GeV for $m_{4\ell} > 190$ GeV. The Z boson corresponding to the leading (sub-leading) di-lepton pair is labelled Z_1 (Z_2).
The Z + jets and $t\bar{t}$ background contributions are further reduced by applying impact parameter as well as track- and calorimeter-based isolation requirements on the leptons.
Main backgrounds to the $H \to ZZ^{(*)} \to 4l$ analysis are: the irreducible ZZ background and the reducible Z + jets and $t\bar{t}$ backgrounds. The former is estimated using MC simulation normalised to the theoretical cross section, while the latters are evaluated using data-driven methods. The composition of the reducible backgrounds depends on the avour of the sub-leading di-lepton and different approaches are taken for the $\ell\ell + \mu\mu$ and the $\ell\ell + ee$ final states. The expected $m_{4\ell}$

distributions for the total background and one signal hypothesis are compared to the combined $\sqrt{s} = 8$ TeV and $\sqrt{s} = 7$ TeV data in Fig. 6(a) for the mass range $80-170$ GeV. Figure 6(b) shows the distribution of the m_{34} versus the m_{12} invariant mass for the selected candidates in the $m_{4\ell}$ range $120 - 130$ GeV. The expected distributions for a SM Higgs boson with $m_H = 125$ GeV (the sizes of the boxes indicate the relative density) and for the total background (the intensity of the shading indicates the relative density) are also shown.

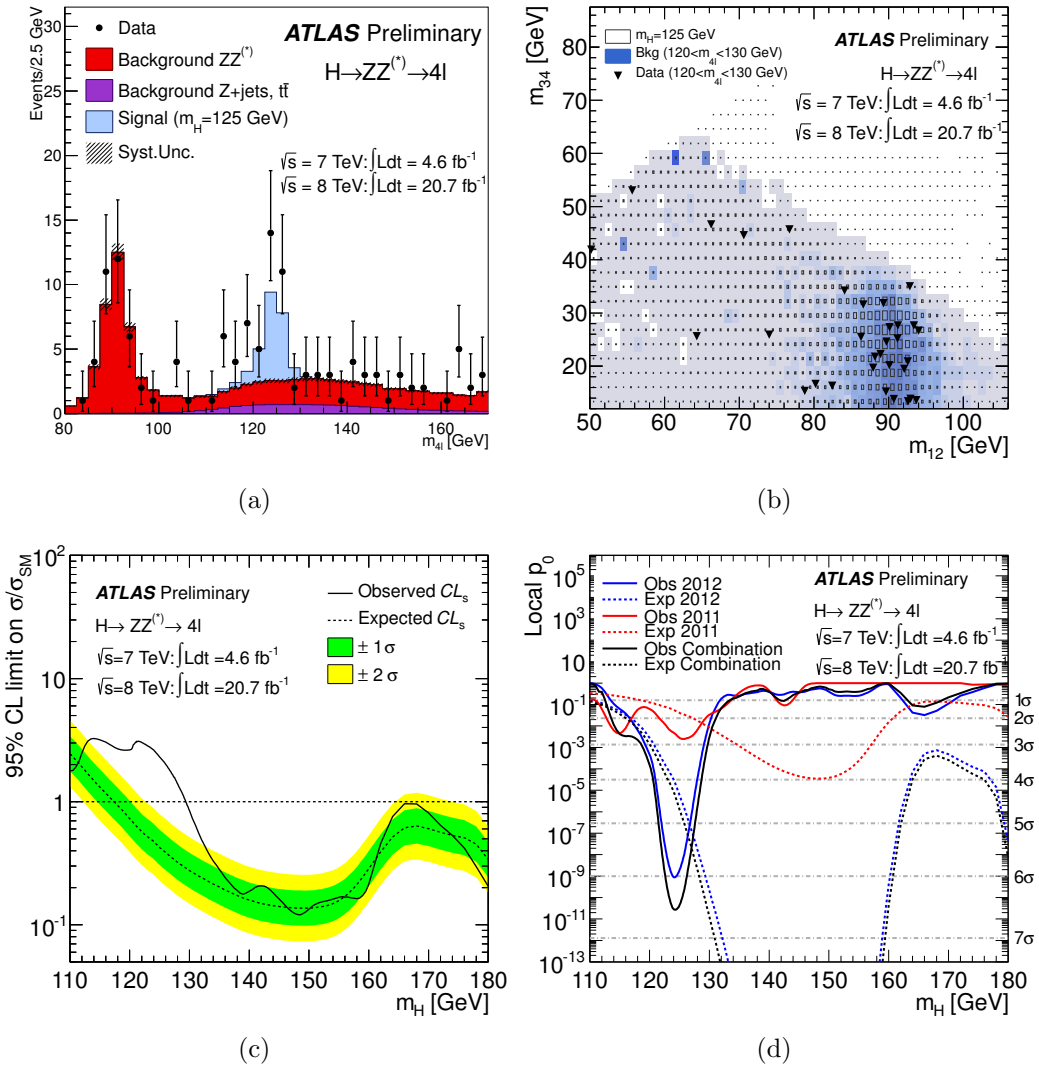

Figure 6: (a) The distribution of the four-lepton invariant mass, $m_{4\ell}$, for the selected candidates compared to the background expectation for the combined $\sqrt{s} = 8$ TeV and $\sqrt{s} = 7$ TeV data sets in the low mass range $80 - 170$ GeV. The signal expectation for the m_H=125 GeV hypothesis is also shown. (b) Distribution of the m_{34} versus the m_{12} invariant mass for the selected candidates in the $m_{4\ell}$ range 120-130 GeV. The expected distributions for a SM Higgs with $m_H = 125$ GeV (the sizes of the boxes indicate the relative density) and for the total background (the intensity of the shading indicates the relative density) are also shown. (c) The expected (dashed) and observed (full line) 95% CL upper limits on the SM Higgs boson production cross section as a function of m_H, divided by the expected SM Higgs boson cross section. The green and yellow bands indicate the expected limits with $\pm$ 1σ and $\pm$ 2σ fluctuations. (d) The observed local p0 for the combination of the 2011 and 2012 data sets (solid black line); the $\sqrt{s} = 7$ TeV and $\sqrt{s} = 8$ TeV data results are shown in solid lines (blue and red). The dashed curves show the expected median local p0 for the signal hypothesis when tested at the corresponding m_H.

Figure 6(c) shows the observed and expected 95% CL cross section upper limits, as a function of

m_H. The observed exclusion starts only at around 130 GeV due the excess at 125 GeV.
The significance of an excess is given by the probability, p_0, that a background-only experiment is more signal-like in terms of the test statistic than the observed data. In Fig. 6(d) the local p_0 is presented as a function of the m_H hypothesis.
The value for the tted mass from the prole likelihood is $mH = 124.3^{+0.6}_{-0.5}$ (stat) $^{+0.5}_{-0.3}$ (syst) GeV, where the systematic uncertainty is dominated by the energy and momentum scale uncertainties. The global signal strength factor μ [2] fitted at the best for m_H (124.3 GeV) is $1.7^{+0.5}_{-0.4}$.

3.3 Measurements of spin-parity properties of the new Higgs-like particle in the $H \to ZZ^{(*)} \to 4l$ decay channel

In order to confirm that the new discovered Higgs-like particle decaying in the $H \to ZZ^{(*)} \to 4l$ channel is the SM Higgs boson, the measurement of its spin and parity is needed since in the Standard Model the J^{CP} of the Higgs boson is predicted to be 0^{++}. The observation of the $\gamma\gamma$ decay of the new particle disfavour the spin 1 state[3]. The data used for this study correspond to 4.6 fb^{-1} at *sqrts* =7 TeV and 21 fb^{-1} at $\sqrt{s}$ =8 TeV using $H \to ZZ^{(*)} \to 4l$ candidates reconstructed in the region 115 GeV $< m_{4l} <$ 130 GeV. For the $X \to ZZ^{(*)} \to 4l$ decays, the sensitive observables to the spin and paity of the X particle are the masses of the two Z bosons and the five angles (a production angle and four decay angles) illustrated in Fig. 7 and defined as:

- $\theta_1(\theta_2)$: angle between the negative final state lepton and the direction of flight of Z_1 (Z_2) in the Z rest frame;
- Φ: angle between the decay planes of the four nal state leptons expressed in the four lepton rest frame;
- Φ_1: angle between the decay plane of the leading lepton pair and a plane dened by the vector of the Z_1 in the four lepton rest frame and the positive direction of the parton axis.
- θ^*: production angle of Z_1 in the 4-lepton rest frame.

These variables are evaluated for candidates passing the $H \to ZZ^{(*)} \to 4l$ selection described in 3.2 Four different spin-parity (J^P) states have been considered: 0^+, 0^-, 1^+, 1^-, 2^+ (equivalent to a Kaluza Klein graviton) , 2^- (pseudo-tensor), The analysis performed treats the spin/parity hypotheses pairwise in order to try to exclude one against the other. The distribution of the discriminating variables comparing 0^+ to 0^- for fully simulated JHU MC events after reconstruction and analysis selection are shown in figure 8. In order to distinguish different pairs of spin-parity, two multivariate approaches have been developed: one uses boosted decision tree (BDT) trained using the discriminating variables of fully simulated signal samples for each spin parity pair; the other uses a matrix element likelihood ratio (MELA) as a discriminant of different spin-parity hypotheses. Figure 9 shows the distributions of BDT and $\mathrm{J^P}-$MELA discriminannts compareing the The statistical test for a pair of J^P hypotheses is given by

$$\mathcal{P}^{ij} = \mu^{\mathrm{sig}} f_i^{\mathrm{sig}} N_{\mathrm{sig}} \left[(1-\varepsilon) \cdot \mathrm{PDF}^{ij}_{\mathrm{H_0}} + \varepsilon \cdot \mathrm{PDF}^{ij}_{\mathrm{H_1}} \right] + \sum_{\mathrm{bkg_k}} f_i^{\mathrm{bkg_k}} N_{\mathrm{bkg_k}} \mathrm{PDF}^{\mathrm{ij}}_{\mathrm{bkg_k}}, \quad (3)$$

[2]The signal strenght μ acts as a scale factor on the total number of events predicted by the Standard Model for each of the Higgs boson signal processes

[3]Landau-Yang theorem

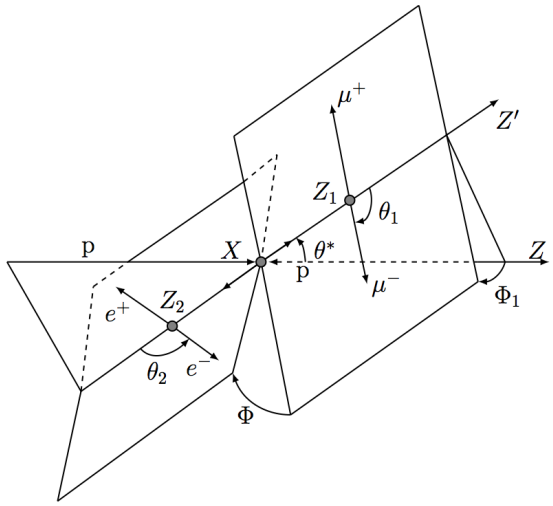

Figure 7: Production and decay angles for a $H \to ZZ^{(*)} \to 4l$ decay.

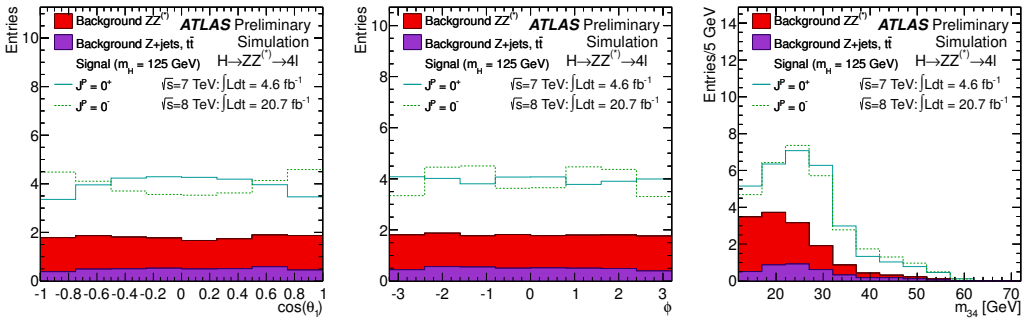

Figure 8: Expected distributions for $\sqrt{s} = 7$ TeV and $\sqrt{s} = 8$ TeV for $m_H = 125$ GeV including backgrounds in the mass range 115 GeV $< m_{4l} <$ 130 GeV comparing 0^+ versus 0^-.From left to right: $cos(\theta_1)$, ϕ, m_{34}.

where $\mu^{\rm sig}$ is the signal strength, $N_{\rm sig}$ is the number of expected SM signal events in the full mass region (115 GeV $< m_{4\ell} <$130 GeV), $f_i^{\rm sig}$ is the signal fraction in the $i^{\rm th}$ S/B mass bin (low and high), and $(1-\varepsilon)$ is the fraction of the $\rm H_0$ signal hypothesis represented by the $\rm PDF^{ij}_{H_0}$ for the $j^{\rm th}$ $\rm J^P$ discriminant. Similarly, $f_i^{\rm bkg_k}$, $N_{\rm bkg_k}$ and $\rm PDF^{ij}_{bkg_k}$ are the bin fraction, total background and PDF for the $k^{\rm th}$ background, respectively. The parameters $N_{\rm sig}$, $N_{\rm bkg_k}$ are nuisance parameters which are constrained by Gaussian terms, and their uncertainties are determined from the nominal analysis. The parameter $\mu^{\rm sig}$ is left free in the fit.
Distributions of the log-likelihood ratio generated with more than 800,000 Monte Carlo pseudo-experiments when assuming the spin 0^+ hypothesis and testing the 0^-, 1+ and 2+ hypotheses for BDT analysis are shown in Fig. 10. The SM spin and parity remain the favoured hypothesis over the 0^-, 1^+ and 2^+ states. The 0^- is excluded at the 97.8% confidence level using $\rm CL_S$ when compared to 0^+ for the BDT analysis.

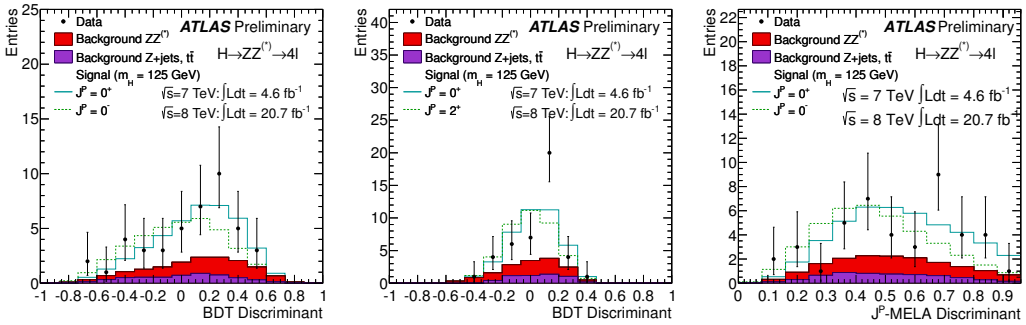

Figure 9: Distributions of the BDT (left and center) and J^P-MELA (right) discriminants for data and MC expectations for the combined $\sqrt{s} = 7$ TeV and $\sqrt{s} = 8$ TeV data sets. For BDT analysis 0^+ vs 0^- and 0^+ vs 2^+ ; for J^P-MELA 0^+ vs 0^- is shown.

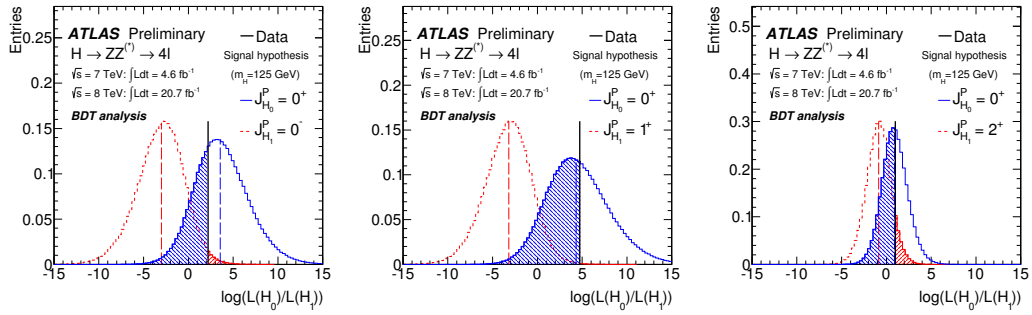

Figure 10: Log-likelihood ratio when assuming the spin 0^+ hypothesis and testing the 0^- (left), 1+ (center) and 2+ (right). The data are indicated by the solid vertical lines, and the median of each of the expected distributions is indicated by a dashed line. The shaded areas correspond to the observed p-values, representing the compatibility with the tested hypothesis H1 (right shaded area) and the assumed hypothesis H0 (left shaded area).

4 Tier-2

During the year 2012 the Frascati's Tier-2 successfully and continuously performed all the typical activities of an ATLAS Tier-2: Monte Carlo production and users and physics groups analysis, [4]. With the exception of the last two weeks of December when the site was shut down for the infrastructure works of the conditioning system, LNF Tier-2 has worked continuously, as we can see from the chart fig.11 left,
which highlights the different activities performed in the Tier-2 in 2012. Moreover, the efficiency of the site was always maintained above 90%, so it received the greatest share of data consistent with its size. Fugure 11 right reports the overall wall clock consumptions of all jobs at Frascati Tier-2, while the number of all jobs run at Frascati Tier-2 is reported in figure 12 left, finally, with the pie chart **??** right we can compare the CPU utilization of all jobs in the Italian ATLAS Tier-2 and see that for Frascati are consistent with the smaller size with respect to the other Tier-2s. Among the most significant activities involving Tier-2's staff, we can mention the operating system upgrade of the entire storage system and the migration of the farm from the gLite middleware to the new European Middleware Interface (EMI). Moreover, Frascati's Tier-2 hosts

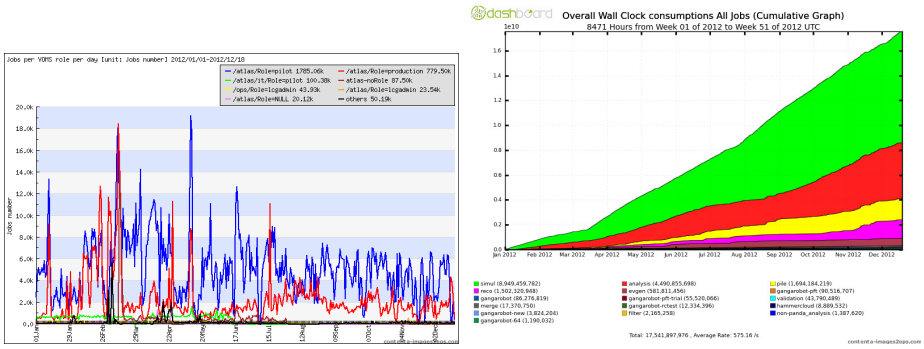

Figure 11: left: Activities performed at LNF tier-2 during year Tier-2; right:Wall clock time of all jobs at Frascati's Tier-2 in 2012

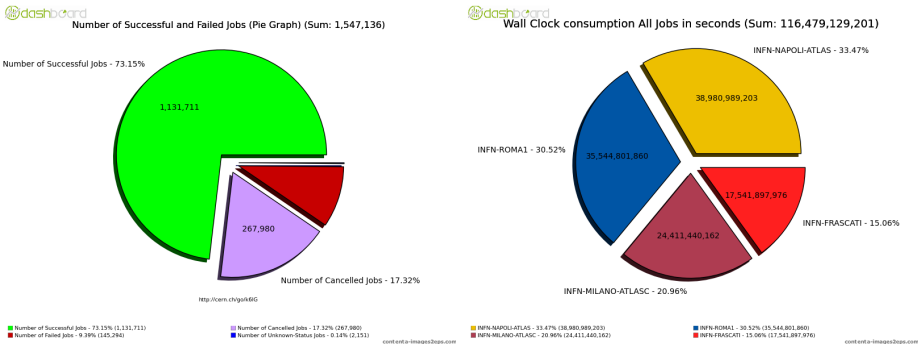

Figure 12: left: Jobs run at Frascati's Tier-2 in 2012; right: Wall clock time of all jobs at Italian Tier-2 in 2012.

a second DPM storage system to test new functionalities before to run them in production. About analysis activity, in collaboration with CERN developers, we promoted the use of Proof on Demand (PoD) [5] for the analysis on ATLAS Tier-2s. PoD is a set of tools designed to interact with any resource management system (RMS) to start the PROOF daemons, then it is able to enable a PROOF cluster on the Tier-2's cluster. In this way any user can quickly setup its own PROOF cluster on the resources, with the RMS taking care of scheduling, priorities and accounting. PoD features an abstract interface to RMSs and provides several plugins for the most common RMSs: we experienced PROOF for data analysis on the on the Italian ATLAS Tier-2s: Frascati, Napoli and Roma1, for our tests we used both the gLite and PBS plug-ins and data were accessed via xrootd. So we provided the Tier-2 SRM, Disk Pool Manager, of xrootd protocol too. Thanks to the xrootd protocol, in the 2013 Frascati's Tier-2 will be part of the new ATLAS storage federation. In 13 left we show the results of submission tests we made on the Frascati Tier-2, where the number of allocated slots are in function of time for each bulk submission. In 13 right we report the results of the readout rate tests made at Roma1, Frascati and Napoli Tier-2's.

5 The Fast TracK Upgrade

The trigger is a fundamental part of any experiment at hadron colliders. It is needed to select on-line the interesting low cross-section physics from the huge QCD background.

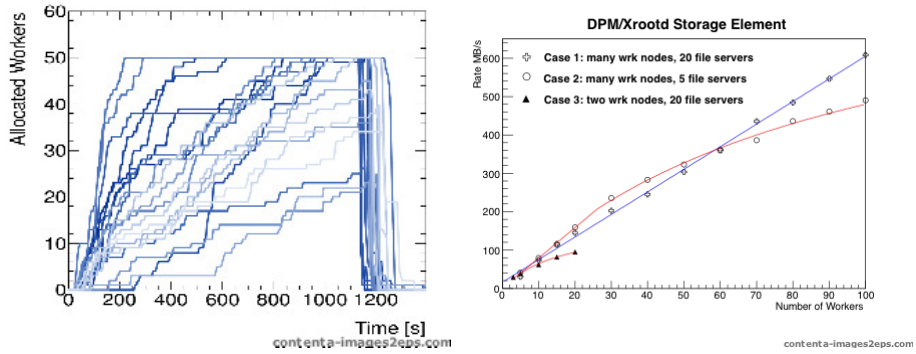

Figure 13: left: Results of the submission tests on the Frascati Tier-2: number of allocated slots as function of time for each bulk submission; right:Results of the readout rate tests at Roma1, Frascati and Napoli Tier-2's

Experience at high luminosity hadron collider experiments shows that controlling trigger rates at high instantaneous luminosity can be extremely challenging. As the luminosity increases, physics goals change in response to new discoveries, and detector aging. It is thus essential that the trigger system be flexible and robust, and redundant and significant operating margin. Providing high quality track reconstruction over the full ATLAS Inner Detector by the start of processing in the level-2 computer farm can be an important element in achieving these goals.
With the goal to improve and make more robust the ATLAS trigger, during summer 2007 the group joined the Fast-Track (FTK) proposal for "A hardware track finder for the ATLAS trigger". This is a proposal to build a hardware track finder as an upgrade to the ATLAS trigger. It will provide global reconstruction of tracks above 1 GeV/c in the silicon detectors, with high quality helix parameters, by the beginning of level-2 trigger processing. FTK can be particularly important for the selection of 3rd-generation fermions (b and τ). These have enormous background from QCD jets, which can be quickly rejected in level-2 if reconstructed tracks are available early. This R&D proposal was completed with the submission of the FTK Technical Proposal that was finally approved by the ATLAS collaboration meeting in June 2011. We are continuing the design and prototyping R&D aiming to prepare the FastTrack Technical Design Report to be submitted in Spring 2013.
The FTK processor performs pattern recognition with a custom device called the Associative Memory (AM). It is an array of VLSI chips that stores pre-calculated trajectories for a ultra-fast comparison with data. The first way to reduce the combinatorial at high luminosity is to work with better resolution in the AM. In order to do that, we will need a new AM chip with a high density of patterns, so that all possible tracks with a thinner resolution can be stored in the AM. Even with better resolution the number of candidate tracks that the AM will find at these high instantaneous luminosities will be very large. For this reason we redesigned the FTK architecture to increase the internal parallelism and data-flow to accommodate a larger flux of data.
For this purpose it was essential a new ideas. The efficiency curves for patterns is slowly increasing for efficiencies above 70%. This is due to the fact that many low probability patterns are needed to gain the missing efficiency. This is a consequence of the fact that the AM performs pattern recognition with a fixed resolution. We developed the idea of variable resolution patterns that increases the equivalent number of pattern per AMchip by a factor 3-5 with a corresponding reduction in hardware size [doi:10.1109/ANIMMA.2011.6172856].
In 2012 we completed the design of the new AMchip04 that for the first time implements the Associative Memory with variable resolution. This is a very challenging task because we need to

increase the pattern per chip with respect to the current AM chip designed for the SVT upgrade at CDF by a factor 30 with similar power consumption running at 100 MHz clock speed instead of 40 MHz. In order to achieve these goals we need several separate improvements: better technology 65 nm instead of 180 nm, design full custom cell that implements the core AM logic, a specific optimization of the global logic, and possibly implement a 3D silicon device to increase the available area. Frascati and Milano worked on the design of the full custom AM cell. This work is the critical element of this project because advanced techniques are required to meet the density and power consumption goals. This element will require intensive simulation to verify functionality under all conditions.

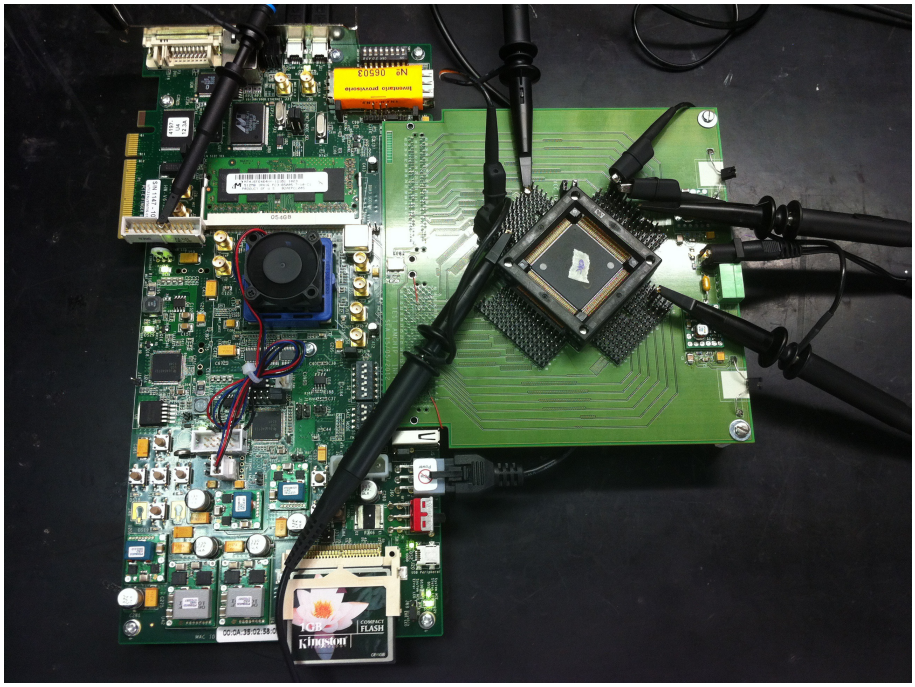

Figure 14: Test system for the AMChip04.

Hundred prototype AMchip04 were produced and delivered at the end of May. Figure 14 shows the test system setup that uses a Xilinx ML605 evaluation board in combination with a PCB that mounts one AMchip04 prototype in a ZIF socket. The Virtex FPGA on the ML605 board is programmed to implement a microblaze processor that runs linux in order to execute the test progam directly on the ML605 board. The test program receives the test vectors via ethernet and send them to the AMchip comparing the output on a clock by clock basis. The AMchip04 prototype perform as expected with a perfect match of predicted output versus expected output. The AMchip04 has been tested up to 100MHz. In particular the full custom AM cell is performing as expected. During the tests we measured the power consumption and found that it was higher than the expected value but still within the worst case expected values. We studied the different contributions to the power consumption that are reported in Table 3.
The estimated power for the full custom AM cell was of 60mA. The measured increased in power consuption is acceptable. The power consumption of other contributions was expected to be significantly smaller. The new version of the device will reduce power consumption by lowering the core voltage to 1.0V using specific cells and exploring the use of low-Vt transitor that allow a reduction of dinamic power consuption in exchange for a higher leakage current.

contributor	current drawn (mA)
leakage	7
clock distribution	30
receiving input	6
data distribution	82
full custom AM cell	70
total	195

Table 3: Core current draw by the AMchip04 split into different contribution. The current is evaluated at 100MHz at the nominal input core voltage of 1.2V.

The Frascati group led the FTK vertical slice integration at CERN. During 2011 a vertical slice has been assebled at CERN. A first setup, see Figure 15 has been assebled in TDAQ lab 32 with a VME crate, an Associative Memory board (AMB), and an EDRO board with one FTK_IM installed. With this setup data flow has been established sending data over SLink using a QUEST card. In September the system has been moved to USA15 cavern where it has been connected to the SCT detector and ATLAS DAQ. During Setember-October the system has been intgrated in the ATLAS DAQ and dataflow was established with level-1 rate up to 70kHz. Work continued to prepare a realist pattern bank to be loaded in the hardware and decoding of input data. New software and firmware has been deployed. The updated system has been commissioned at the begining of 2012. It has been included in the ATLAS data taking for a few days, for Cosmics runs first and then during pp collisions at 2.76 TeV. With collisions data FTK found the first pattern-match. The FTK vertical slice activity will continue during the 2013-2014 shutdown. Since TDAQ lab 32 has been dismissed a new FTK setup is being prepared in TDAQ lab 4 for this purpose.
Guido Volpi coordinated the simulation activity of the Fast-Tracker collaboration. The simulation activity was essential to define the specifications for the AMchip design, including the variable resolution presented at the ANIMMA 2011 conference. It was essential to find an affordable configuration for FTK at high luminosity 3*10^{34} and 10^{35} $cm^{-2}s^{-1}$. The proof-of-principle was then integrated into the current FTKSim package. A new and important branch of activity emerged: the integration of the standalone FTK simulation within the ATLAS software and production frameworks. we worked in close contact with the ATLAS experts at CERN and this new activity is now half completed. This is already beyond the needed schedule because the FTK studies for the Technical Design Report can be completed with the standalone simulation, but it will allow a wider application of the FTK simulation inside the Atlas collaboration.

6 The new Small Wheel upgrade

The upgrade program for LHC is under study with the aim to increase the luminosity by a factor of 10. The present detectors of ATLAS have been designed according to the rates expected at the nominal LHC luminosity. Fig. 1 shows the expected counting rates in the ATLAS Muon chambers. With the luminosity upgrade of LHC, the rate of prompt muons and the background of photons and neutrons will increase proportionally. In these conditions, an upgrade of the present muon chambers in the End-cap inner and middle muon wheels, the latter for rapidity $\eta > 2$, will be needed. For their replacement, muon chambers based on the Micromegas technology that com- bine precision measurement and triggering capability in the same detector have been chosen for precision tracking and eventually for triggering. The final chambers to be used for the upgrade of the ATLAS Muon Spectrometer should be of approximate size 1 m x 2 m, with the following characteristics:

Figure 15: FTK vertical slice in USA15.

- high-rate capability (>5kHz=cm^2);
- spatial resolution ∼100mm for impact angles 45;
- transverse coordinate resolution ∼1 cm;
- time resolution: ∼ 5-10 ns;
- high efficiency >98%;
- level-1 triggering capability;
- radiation hardness and good ageing properties.

The New Small Wheel is a first priority project for the ATLAS experiment to maintain and improve the trigger and the excellent tracking performance of the end cap muon system at the highest energy and lu-minosity expected. Our lab has been chosen as one of the production sites. First assembling tests are ongoing. Extensive tests have been performed on prototypes with cosmics and at test beams.

6.1 Cosmic Ray Stand

The ATLAS cosmic Ray Stand (CRS) is located in the Gran Sasso hall at LNF. It was originally designed for the test of the ATLAS muon chambers (MDT). A recent picture is shown on the left panel of figure 16. A fully instrumented MDT chamber is hooked to a couple of rails that allow it to roll in and out. Plastic scintillators are used for triggering: three pairs are mounted on top of the MDT chamber; three pairs are placed on ground, below 30 cm of iron used for screening from low-momentum muons. The CRS setup has been recently revised in view of the future tests of the MicroMegas chambers. The MDT chamber will be moved to the upper rails and in its place we will put a table where we will lay the chambers under test. The table will be free to roll on the rails to easy the detector posistioning (right panel of figure 16). The trigger scintillators will also be re-arranged.

Figure 16: Left: Recent picture of the ATLAS CRS. The top scintillators used for the trigger are visible, and also two MDT chambers, one of which is fully instrumented. Right: A sketch of the new CRS setup. The instrumented MDT chamber is moved to the upper rails and in its place is a table upon which detectors under test will be placed. The table is able to roll on the rails to easy the positioning of detectors.

In order to test the MicroMegas we will use as a reference tracker the MDT chamber. It is designed to have a position resolution of about 70 μm. During this year we put back to work the trigger, acquisition, and gas systems. Writing of a new reconstruction package is underway. A first example of reconstructed cosmic tracks is shown in figure 17.

7 MicorMegas tests with particle beams

A number of tests on MicroMegas have been carried out at beam test facilities (BTF) at CERN and LNF. Tests at CERN were performed at H2 and H6 beam lines at the Super Proton Synchrotron (SPS), providing 120 GeV/c pion beam with an intensity ranging from 5 to 30 kHz over an area of 2 cm^2. During the H2 test beam data was taken in presence of a magnetic field of intensity up to 0.5 T. Several prototype chambers were tested. These had an active area of about 10×10 cm^2 and strip pitches ranging from 250 to 400 μm. A gas mixture of 93% Ar and 7%CO_2 was used. The chambers were mounted on a frame as shown in figure 18 left. They were free to rotate around the vertical axis allowing the test of the tracking capabilities for non orthogonal tracks (μTPC mode). The readout was performed with an APV25 hybrid chip sampling the integrated charge on the strips every 25 ns. An example of APV25 charge samplings is shown in figure **??** right. Here the spectrum is fit with a function taking into account the charge collection and induction on the strips and the APV25 signal response. Typical duration of the signal is

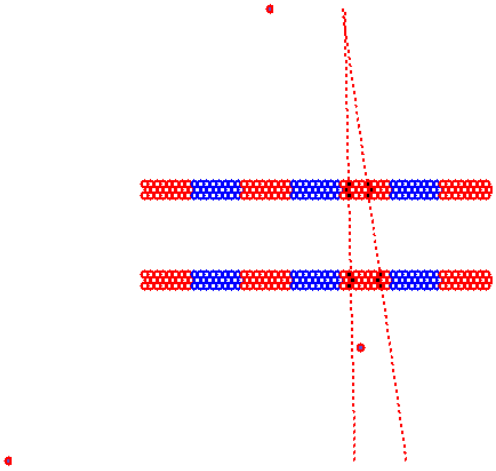

Figure 17: Tracks of two simultaneous cosmic rays reconstructed in the MDT chamber.

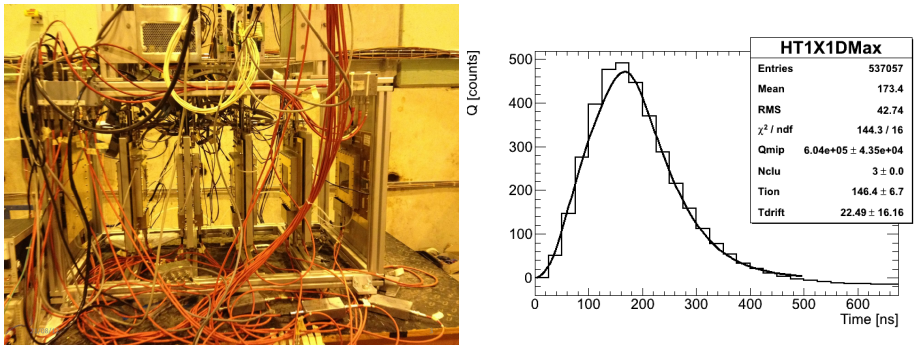

Figure 18: left: picture of the test beam setup at H6 beam line at CERN SPS; right: charge samplings measured from the APV chip.

about 100-200 ns compatible with the ion drift-time. The exponential decay-time of the signal is due to an RC-CR shaper with a 50 ns time-constant. These prototypes showed an efficiency close to 100% and spatial resolution of about 100μm both for orthogonal and diagonal tracks.
Test with electron were performed at the Frascati BTF with momenta of about 500 MeV/c 20 Hz rate over an area of about 2 cm^2. Three 10x10 cm2 MM chambers have been exposed to 0.5 GeV BTF electron beam. The experimental setup is shown in figure 19. Fig 1: Picture of the experimental setup. It consists of 2 scintillator counters providing the trigger, three 10x10 cm2 MM chambers, and a lead-scintillating fibers calorimeter to monitor the spill multiplicity. MMs are filled with a 93% Ar 7% CO2 gas mixture and are operated with a drift field of 0.6KV per cm and a gap of 540 V. Two MMs have been readout with APV25 and one MM has been readout with a low noise current to voltage amplifier prototype. High gain, 220K, has been achieved with 3 stages allowing a good output dynamics (1V) and a small power consumption(75mV). To increase the detector readout area, at the price of an increase of the MM output capacity, four X strips with 125 m pitch have been connected in parallel. Typical signals of 200/300 mV with

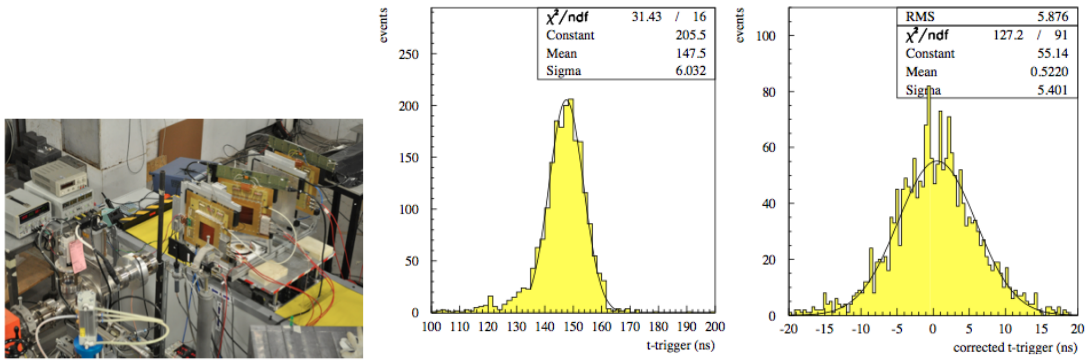

Figure 19: right: experimental setup at BTF; t-trigger distribution:uncorrected (center) and corrected (right) for the collected charge value

about 100 ns width have been observed in coincidence with the trigger. The analogic signal has been discriminated with 75 mV threshold. Time and time over threshold information are provided by a multi-hit TDC. The t-trigger distribution, the difference in time between the discriminated signal and the triggershows a time resolution of about 6 ns. The small tail at low t-trigger values is due to events with low collected charge. Figure **??** right shows the t-trigger distribution after the charge effect correction.

Public presentations:

- SM@LHC2012 10-Apr-12 LHC MPI and underlying event results (ATLAS+CMS)
- Search for the SM Higgs boson in the HWW(*)ll decay channel at LHC, LNF mini-workshop 28th March 2012
- M Antonelli "discovery of a narrow resonance with at 125 GeV at LHC", Los Alamos general Seminar.
- "A Hardware Track Finder for the ATLAS Trigger" presented at Real Time 2012 Conference 13/6/2012
- "A Fast Hardware Tracker for the ATLAS Trigger System" (Poster) presented at Frontier Detector for Frontier Physics 21/6/2012
- "ARAMIS: Advanced Real-time Architectures of Data processing, Pattern Recognition and Data Transmission for Frontier Applications in High Energy Physics, High Reliability Systems and Visual Science" (Poster) presented at Frontier Detector for Frontier Physics 21/6/2012

Publications:

- "Search for the Standard Model Higgs boson in the H-¿WW(*)-¿ lnulnu decay mode with 4.7 fb-1 of ATLAS data at sqrt(s) = 7 TeV" ATLAS-CONF-2012-012, 5 March 2012
- "Search for the Standard Model Higgs boson in the H-¿WW(*)-¿lvlv decay mode using Multivariate Techniques with 4.7 fb-1 of ATLAS data at sqrts=7 TeV" ATLAS-CONF-2012-060, 6 June 2012

- Observation of an Excess of Events in the Search for the Standard Model Higgs Boson in the H -¿ WW -¿ l nu l nu Channel with the ATLAS Detector" ATLAS-CONF-2012-098, 18 July 2012
- "Update of the H -¿ WW(*) -¿ e nu mu nu analysis with 13.0 fb1 of sqrts = 8 TeV data collected with the ATLAS detector" ATLAS-CONF-2012-158, 13 November 2012
- "Measurements of the properties of the Higgs-like boson in the four lepton decay channel with the ATLAS detector using 25 fb-1 of proton-proton collision data", ATLAS-CONF-2013-013
- "Updated results and measurements of properties of the new Higgs-like particle in the four lepton decay channel with the ATLAS detector". ATLAS-CONF-2012-169
- "Observation of an excess of events in the search for the Standard Model Higgs boson in the H-¿ ZZ(*)-¿ 4l channel with the ATLAS detector", ATLAS-CONF-2012-092
- "Observation of a new particle in the search for the Standard Model Higgs boson with the ATLAS detector at the LHC", Phys.Lett. B716 (2012) 1-29
- "Observation of a new particle in the search for the Standard Model Higgs boson in the H ZZ()4 channel and its properties using 4.6 fb1 and 20.7 fb1 of proton-proton collisions at s = 7 TeV and 8 TeV, respectively, recorded with the ATLAS detector.",ATL-COM-PHYS-2013-146
- "Observation of a new particle in the search for the Standard Model Higgs boson in the H ZZ()4 channel : limits on the for VBF and VH production of the new particle and High mass search using 4.6 fb1 and 20.7 fb1 of proton-proton collisions at s = 7 TeV and 8 TeV, respectively, recorded with the ATLAS detector."ATL-COM-PHYS-2013-145
- "Observation of a new particle in the search for the Standard Model Higgs boson in the H ZZ()4 channel : mass and signal strength measurement using 4.6 fb1 and 20.7 fb1 of proton-proton collisions at s = 7 TeV and 8 TeV, respectively, recorded with the ATLAS detector."ATL-COM-PHYS-2013-144
- "Observation of a new particle in the search for the Standard Model Higgs boson in the H ZZ()4 channel and measurements of its properties using 4.6 fb1 and 13.0 fb1 of proton-proton collisions at s = 7 TeV and 8 TeV, respectively, recorded with the ATLAS detector." ATL-COM-PHYS-2012-1483
- "Search for the Standard Model Higgs boson in the decay channel HZZ()4 with 5.8 fb1 of pp collision data at s=8 TeV with ATLAS", ATL-COM-PHYS-2012-835
- R. Di Nardo et al., Enabling data analysis la PROOF on the Italian ATLAS Tier-2s using PoD, J. Phys.: Conf. Ser. 396 (2012) 032043, [http://iopscience.iop.org/1742-6596/396/3/032043/]
- The EDRO board connected to the Associative Memory: a "Baby" FastTracker processor for the ATLAS experiment https://cdsweb.cern.ch/record/1382040/, doi:10.1016/j.phpro.2012.02.502, Physics Procedia, Vol 37, 2012, 1772-1780, ISSN 1875-3892
- The FastTrack Real Time Processor and Its Impact on Muon Isolation, Tau and b-Jet Online Selections at ATLAS, IEEE Trans. Nu cl. Sci. 59, 348. http://dx.doi.org/10.1109/TNS.2011.2179670

- "Associative Memory for L1 Track Triggering in LHC Environment", Real Time Conference (RT), 2012 18th IEEE-NPSS , vol., no., pp.1-6, 9-15 June 2012, doi: 10.1109/RTC.2012.6418193
- The AMchip04 and the processing unit prototype for the FastTracker, 2012 JINST 7 C08007

References

1. ATLAS Collaboration, "Performance of missing transverse momentum reconstruction in proton-proton collisions at 7 TeV with ATLAS", EPJC 72 (2012), arXiv:1108.5602 [hep-ex]
2. M.Cacciari and G.P.Salam, "PileUp subtraction using jet areas",Phys.Lett.B659 (2008) 119-126, arXiv:0707.1378 [hep-ph]
3. ATLAS Collaboration, "Measurements of the properties of the Higgs-like boson in the $W \to l\nu l\nu$ decay channel with the ATLAS detector using 25 fb$^-$1 of proton-proton collision data", ATLAS-CONF-2013-030
4. : D. Barberis et al., "ATLAS computing activities and developments in the Italian Grid Cloud", J. Phys.: Conf. Ser. 396 (2012) 042052
5. : R. Di Nardo et al., Enabling data analysis la PROOF on the Italian ATLAS Tier-2s using PoD, J. Phys.: Conf. Ser. 396 (2012) 032043, [http://iopscience.iop.org/1742-6596/396/3/032043/]

BABAR

A. Calcaterra, R. de Sangro (Resp.), G. Finocchiaro, P. Patteri,
S. Martellotti, I. Peruzzi , M. Piccolo, M. Rama, A. Zallo

1 Introduction

The *BABAR* experiment has been running at the PEP-II asymmetric B factory of the SLAC National Laboratory (Stanford, USA) from 2001 to 2008, collecting a data sample corresponding to approximately $0.5\,\mathrm{ab}^{-1}$. The data were collected mostly at the CM energy corresponding to the $\Upsilon(4S)$ mass; large data sample were also obtained at the CM energy corresponding to the $\Upsilon(2S)$ and $\Upsilon(3S)$ resonances. The experiment has produced a wealth of important physics results, ranging from measurements of all three angles of the Unitarity triangle, to the discovery of the $D-\bar{D}$ mixing, the discovery of the η_b, the discovery of several interesting charm and charmonium states. The study of the ISR events, also pursued at *BABAR* has produced many important results in the energy range down hadron threshold production.

After the end of data taking the complete data set was reprocessed, and large amount of Monte Carlo events were generated and fully reconstructed. During 2012 the intense analysis period has not yet slowed down: this year the number of published paper was similar to that of 2011, while the number of contributed papers to international conferences even exceeded it. To date the *BABAR* analysis effort has resulted in more than 500 publications in Phys. Rev. Lett. or Phys. Rev. D.

The main activity of the LNF group in 2012 has been the pubblication of the paper on the combined final measurement of γ from *BABAR*, the pubblication of the analysis of $B \to D^{*+}D^{*-}$ selected with a partial reconstruction technique, and the start of a new physics analysis for the measurement of the Electric Dipole Moment of the τ lepton, the subject of a doctoral thesis of a new PHD student who joined the group. Members of the group have also been actively involved in the preparation of the *Physics of the B-Factories Book*, in collaboration with the Belle group, to illustrate the analysis strategies and the physics results of the B-factories. The book is now in the final review process internal to the two collaborations. We'll give a brief description of these activities in the next sections.

2 Physics of the B-factories book

Over the last decade BaBar and Belle have studied the physics of bottom and charm mesons, tau leptons, heavy quarkonium states, etc. that were produced at the PEP-II and KEKB e^+e^- storage rings. The two collaborations have developed increasingly sophisticated techniques for extracting the maximum amount of information from data. A project is ongoing to document all these techniques in a book, named *Physics of the B-Factories*. The book will provide descriptions of all of the techniques developed by the experiments and a comprehensive overview of the measurements. The editing of the book is in its final stage and the publication is currently expected to happen in 2013. One member of our group is co-author of the chapter on the measurement of the angle γ of the Unitarity Triangle, while another provided a written contribution to the chapter on the measurement of $\sin(2\beta)$.

3 Combined measurement of the CKM angle γ from $B \to D^{(*)}K^{(*)}$ decays

We have worked on the determination of the Cabibbo-Kobayashi-Maskawa CP-violating angle γ through the combination of various measurements involving $B^{\pm} \to DK^{\pm}$, $B^{\pm} \to D^{*}K^{\pm}$, and $B^{\pm} \to DK^{*\pm}$ decays performed by BaBar. Using up to 474 million $B\bar{B}$ pairs we obtain $\gamma = (69^{+17}_{-16})^{\circ}$ modulo 180°. The total uncertainty is dominated by the statistical component, with the experimental and Dalitz-amplitude-model systematic uncertainties amounting to $\pm 4^{\circ}$. The corresponding two-standard-deviation region is $41^{\circ} < \gamma < 102^{\circ}$. This result is inconsistent with $\gamma = 0$ with a significance of 5.9 standard deviations and it is competitive with the combinations performed by the LHCb and Belle experiments. The article has been accepted by Phys. Rev. D.

4 Measurement of $\sin 2\beta$ with partial reconstruction of B mesons to the $D^{*+}D^{*-}$ decay

In 2012 this analysis has undergone a thorough review process, which resulted in its final publication at the end of the year. The analysis was presented for the first time at the ICHEP 2012 summer conference in Melbourne by a member of our group.

The parameters S, C are extracted from the CP and tag side vertices time difference Δt distribution of events selected using event topology and kinematic cuts. In fig. 1 we show the

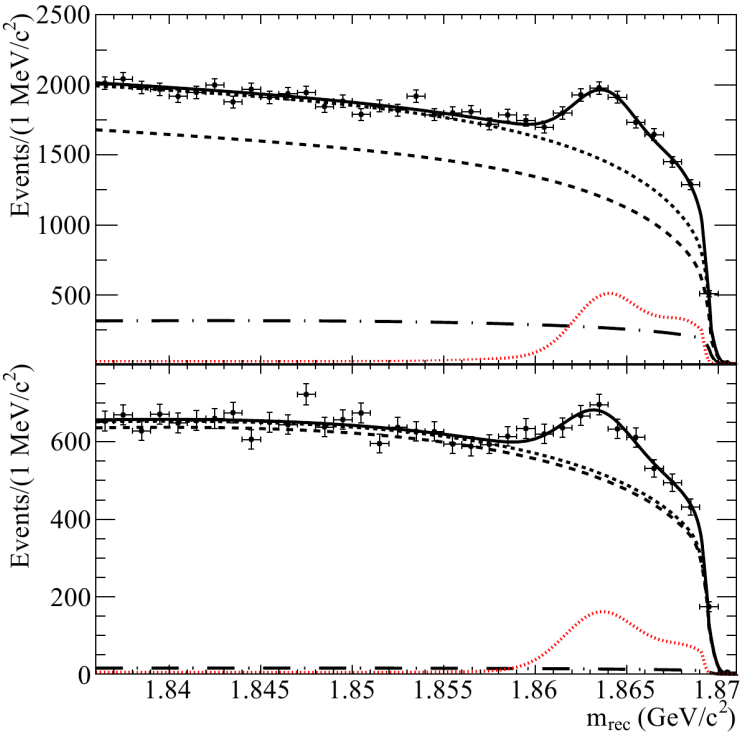

Figure 1: Result of the kinematical fit of kaon (top) and lepton (bottom) tagged data events, with PDF's overlaid: total PDF (solid line), total background ($B\overline{B}$ + continuum, short-dashed line), $B\overline{B}$ combinatorial background (dashed line), continuum u, d, s, c background (dot-dashed line) and signal (dotted red line).

recoil mass distribution of the full *BABAR* dataset (black crosses), corresponding to $\approx 435\ fb^{-1}$ of integrated luminosity. The presence of an excess of events in the signal region is evident.

We fit the data with a PDF (black curve), made of a signal component (red) plus a continuum (green) and $B\bar{B}$ (blue) combinatorial background component. We find a total of 3843 ± 397 (1128 ± 218) events in the kaon (lepton) sample. We fit the time distribution in the data, whose

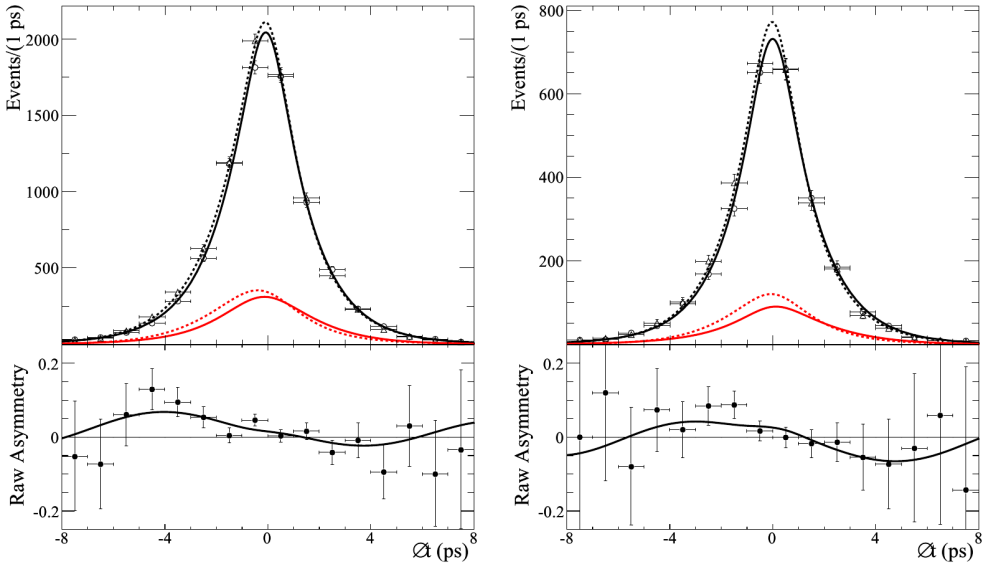

Figure 2: Top: Δt distribution for B^0 (dashed) and $\overline{B}^0$ (solid) for kaon(left plot) and lepton(right plot) tags; the lower curves are the corresponding signal PDFs. Bottom: corresponding raw time-dependent CP asymmetry. Only data in the restricted signal region $m_{\rm rec} > 1.860$ GeV/c^2 are shown.

result we show in fig. 2 where we plot the time difference distribution of data events for the full collected sample, and the corrisponding raw CP asymmetry for the lepton and kaon tag samples. The final result is:

$$\begin{array}{ll} C & = +0.12 \pm 0.11 \\ S & = -0.42 \pm 0.16 \end{array} \qquad \text{kaon tags,}$$

$$\begin{array}{ll} C & = +0.20 \pm 0.15 \\ S & = -0.21 \pm 0.20. \end{array} \qquad \text{lepton tags.}$$

The combined statistical and systematic errors are:

$$C = +0.15 \pm 0.09 \pm 0.05 \quad (1)$$
$$S = -0.34 \pm 0.12 \pm 0.09, \quad (2)$$

This measurement reduces the error of the previous BaBar measurement performed with fully reconstructed $D^{*+}D^{*-}$final states by $\approx 25\%$.

A description of this analysis and its results have been included in the B-Factories legacy book.

5 Measurement of the τ lepton Electric Dipole Moment in the $e^+e^- \to \tau^+\tau^-$ production

The search for a CP violation signature arising from an electric dipole moment (EDM) different from zero of the τ lepton is searched in the $e^+e^- \to \tau^+\tau^-$ reaction with Babar data. This analysis started in 2012 with the study of the τ EDM measurement algorithms and methods on Monte Carlo samples.

The EDM gives a tree level contribution to the τ-pairs production cross section; the corresponding Feynman diagrams are shown Fig.3. Taking into account the EDM contribution in the

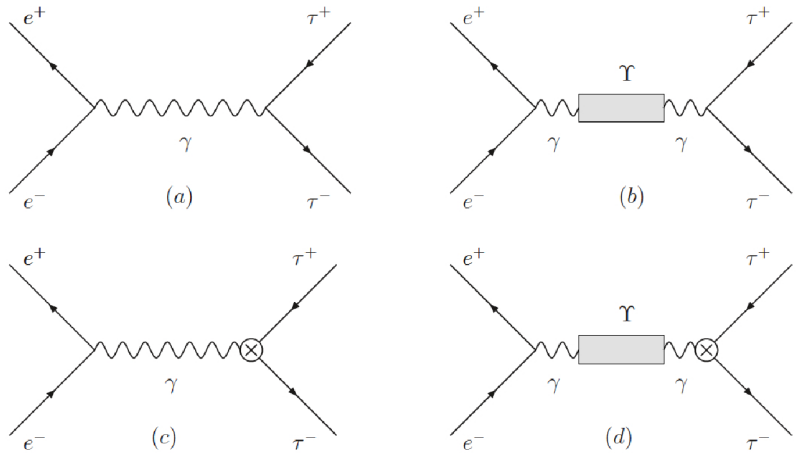

Figure 3: Diagrams. (a) direct γ exchange. (b) Υ production. (c) EDM in γ exchange. (d) EDM at the Υ-peak.

Lagrangian, the cross section of the $e^+e^- \to \tau^+\tau^-$ process is proportional to the squared spin density matrix:

$$\mathcal{M}^2_{prod} = \mathcal{M}^2_{SM} + Re(d_\tau)\mathcal{M}^2_{Re} + Im(d_\tau)\mathcal{M}^2_{Im} + |d_\tau|^2\mathcal{M}^2_{d^2}.$$

For the EDM measurement we adopt the same method used in previous existing measurements by the ARGUS and Belle experiments, the so-called optimal observable method, which maximizes the sensitivity to d_τ. The optimal observables are defined as:

$$\mathcal{O}_{Re} = \frac{\mathcal{M}^2_{Re}}{\mathcal{M}^2_{SM}}, \quad \mathcal{O}_{Im} = \frac{\mathcal{M}^2_{Im}}{\mathcal{M}^2_{SM}}. \tag{3}$$

The matrix elements $\mathcal{M}^2_i = \mathcal{M}^2_i(\vec{k}, \vec{S}_\pm)$ depend on the τ^+ momentum $\vec{k}$ and on the τ^+ and τ^- spin vectors $\vec{S}_\pm$ in the τ-pair rest frame. The complete reconstruction of these quantities is prevented by the presence of undetectable neutrinos in τ decays. The final state in which both τ's decay hadronically in $\tau^\pm \to \pi^\pm\nu$ has been analysed. The τ momentum measurement algorithm and the spin reconstruction formula have been studied and verified. The mean values of the optimal observables $\langle\mathcal{O}_{Re}\rangle$ and $\langle\mathcal{O}_{Im}\rangle$ are linear functions of d_τ:

$$\langle\mathcal{O}_{Re}\rangle = a_{Re} \cdot Re(d_\tau) + b_{Re}, \quad \langle\mathcal{O}_{Im}\rangle = a_{Im} \cdot Im(d_\tau) + b_{Im}. \tag{4}$$

In order to extract the value of d_τ from the observable means measured on the data, we have to know the coefficients a_j and the offsets b_j. The parameters a_j and b_j are extracted from

the correlations between $\langle \mathcal{O}_{Re} \rangle$ ($\langle \mathcal{O}_{Im} \rangle$) and $Re(d_\tau)$ ($Im(d_\tau)$) extracted by a full Monte Carlo (MC) simulation including the detector simulation with acceptance effects and event selection efficiency. The slopes a_j represent the real and imaginary EDM sensitivity, the offsets b_j represent the difference from zero of the observable mean when $d_\tau = 0$.

This EDM measurement method and the EDM sensitivity evaluation have been tested on a preliminary signal MC sample with no detector effects. Distributions of the real and imaginary optimal observables for $\tau^+\tau^- \to \pi^+\pi^-\nu_\tau\bar{\nu}_\tau$ events, from a MC sample with about the same statistics expected for Babar data, are shown in Fig.4. In Fig.5 the correlations between the

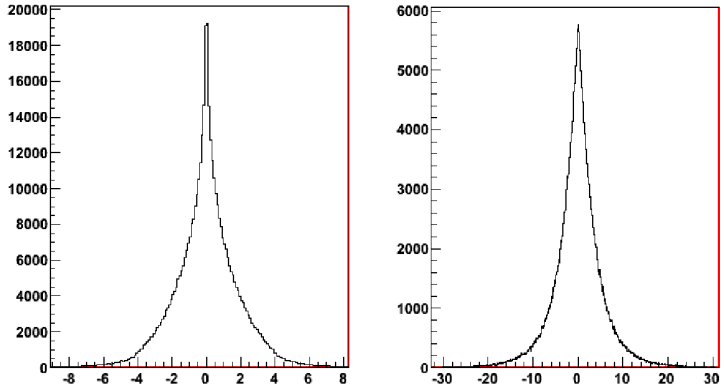

Figure 4: Optimal observables distribution for $\tau^+\tau^- \to \pi^+\pi^-\nu_\tau\bar{\nu}_\tau$ events. Left: O_{Re}; right: O_{Im}.

observable means $\langle O_{Re} \rangle$ and $\langle O_{Im} \rangle$ and d_τ of this MC sample are shown.

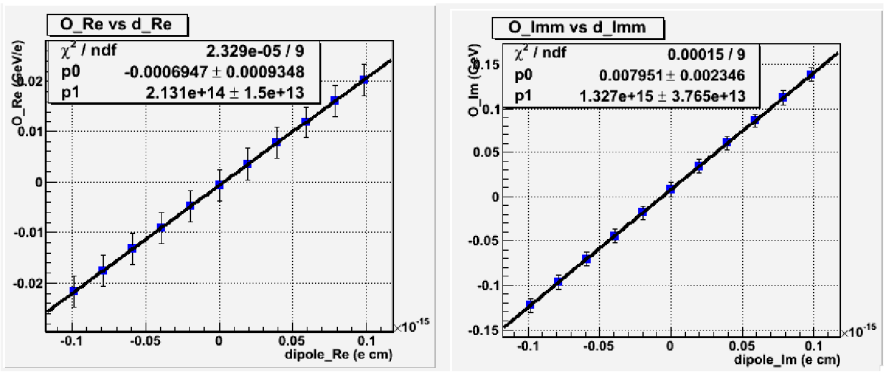

Figure 5: Correlation between the observable means $\langle O_{Re} \rangle$ (left) and $\langle O_{Im} \rangle$ (right) and d_τ for the analysed MC sample. Fit results are shown, p0 is the offset b_j and p1 is the slope, corresponding to the EDM sensitivity a_j.

The statistical sensitivity (one σ) to the $Re(d_\tau)$ expected with the full babar data sample extrapolated from the correlation plot (Fig.5, left) is $0.14 \cdot 10^{-16} ecm$, one order of magnitude higher than the one reached by Belle. The systematic uncertainties are now under evaluation with the ongoing analysis on the full realistic MC sample with detector acceptance and background effects included. We are confident to improve the present Belle experimental measurements.

6 List of Conference Talks in Year 2012

1. "*CP* Violation in Mixing at *BABAR*", R. de Sangro (*BABAR* Collaboration)
   International Conference on High Energy Physics, 4-11 July 2012, Melbourne, Australia.

References

1. **"Search for di-muon decays of a low-mass Higgs boson in radiative decays of the $\Upsilon(1S)$"**, J. P. Lees *et al.* , Phys. Rev. D 87, **031102**, (2013) (R)

2. **"Measurement of $D^0 - \bar{D}^0$ Mixing and CP Violation in Two-Body D^0 Decays"**, J. P. Lees *et al.* , Phys. Rev. D **87**, 012004 (2013)

3. **"Study of high-multiplicity 3-prong and 5-prong tau decays at BABAR"**, J. P. Lees *et al.* , Phys. Rev. D **86**, 092010 (2012).

4. **"Study of the baryonic B decay $B^- \to \Sigma_c^{++}\bar{p}\pi^-\pi^-$"**, J. P. Lees *et al.* , Phys. Rev. D **86**, 091102 (2012).

5. **"Measurement of the Time-Dependent CP Asymmetry of Partially Reconstructed $B^0 \to D^{*+}D^{*-}$ Decays"**, J. P. Lees *et al.* , Phys. Rev. D **86**, 112006 (2012).

6. **"Branching fraction and form-factor shape measurements of exclusive charmless semileptonic B decays, and determination of $|V_{ub}|$"**, J. P. Lees *et al.* , Phys. Rev. D **86**, 092004 (2012).

7. **"The branching fraction of $\tau^- \to \pi^- K_S^0 K_S^0(\pi^0)\nu_\tau$ decays"**, J. P. Lees *et al.* , Phys. Rev. D **86**, 092013 (2012).

8. **"A search for the decay modes $B^{+-} \to h^{+-}\tau^{+-}l$"**, J. P. Lees *et al.* , Phys. Rev. D **86**, 012004 (2012).

9. **"Observation of Time Reversal Violation in the B^0 Meson System"**, J. P. Lees *et al.* , Phys. Rev. Lett. **109**, 211801 (2012).

10. **"Measurement of B($B \to X_s\gamma$), the $B \to X_s\gamma$ photon energy spectrum, and the direct CP asymmetry in $B \to X_{s+d}\gamma$ decays"**, J. P. Lees *et al.* , Phys. Rev. D **86**, 112008 (2012).

11. **"Precision Measurement of the $B \to X_s\gamma$ Photon Energy Spectrum, Branching Fraction, and Direct CP Asymmetry $A_{CP}(B \to X_{s+d}\gamma)$"**, J. P. Lees *et al.* , Phys. Rev. Lett. **109**, 191801 (2012).

12. **"Study of $X(3915) \to J/\psi\omega$ in two-photon collisions"**, J. P. Lees *et al.* , Phys. Rev. D **86**, 072002 (2012).

13. **"Exclusive Measurements of $b \to s\gamma$ Transition Rate and Photon Energy Spectrum"**, J. P. Lees *et al.* , Phys. Rev. D **86**, 052012 (2012).

14. **"Search for the decay modes $D^0 \to e^+e^-$, $D^0 \to \mu^+\mu^-$, and $D^0 \to e\mu$"**, J. P. Lees *et al.* , Phys. Rev. D **86**, 032001 (2012).

15. **"Improved Limits on B^0 Decays to Invisible Final States and to $\nu\bar{\nu}\gamma$"**, J. P. Lees *et al.* , Phys. Rev. D **86**, 051105 (2012).

16. **"Search for resonances decaying to $\eta_c\pi^+\pi^-$ in two-photon interactions"**, J. P. Lees *et al.* , Phys. Rev. D **86**, 092005 (2012).

17. **"Evidence for an excess of $\bar{B} \to D^{(*)}\tau^-\bar{\nu}_\tau$ decays"**, J. P. Lees *et al.* , Phys. Rev. Lett. **109**, 101802 (2012).

18. **"Precise Measurement of the $e^+e^- \to \pi^+\pi^-(\gamma)$ Cross Section with the Initial-State Radiation Method at BABAR"**, J. P. Lees *et al.* , Phys. Rev. D **86**, 032013 (2012).

19. **"Measurement of Branching Fractions and Rate Asymmetries in the Rare Decays $B \to K^{(*)}l^+l^-$"**, J. P. Lees *et al.* , Phys. Rev. D **86**, 032012 (2012).

20. **"Study of the reaction $e^+e^- \to J/\psi\pi^+\pi^-$ via initial-state radiation at BaBar"**, J. P. Lees *et al.* , Phys. Rev. D **86**, 051102 (2012).

21. **"Search for lepton-number violating processes in $B^+ \to h^-l^+l^+$ decays"**, J. P. Lees *et al.* , Phys. Rev. D **85**, 071103 (2012).

22. **"Search for Low-Mass Dark-Sector Higgs Bosons"**, J. P. Lees *et al.* , Phys. Rev. Lett. **108**, 211801 (2012).

23. **"Study of CP violation in Dalitz-plot analyses of $B^0 \to K^+K^-K^0_S$, $B^+ \to K^+K^-K^+$, and $B^+ \to K^0_SK^0_SK^+$"**, J. P. Lees *et al.* , Phys. Rev. D **85**, 112010 (2012).

24. **"Initial-State Radiation Measurement of the $e^+e^- \to \pi^+\pi^-\pi^+\pi^-$ Cross Section"**, J. P. Lees *et al.* , Phys. Rev. D **85**, 112009 (2012).

25. **"B^0 meson decays to ρ^0K^{*0}, f_0K^{*0}, and ρ^-K^{*+}, including higher K^* resonances"**, J. P. Lees *et al.* , Phys. Rev. D **85**, 072005 (2012).

26. **"Study of $\bar{B} \to X_u\ell\bar{\nu}$ decays in $B\bar{B}$ events tagged by a fully reconstructed B-meson decay and determination of $\|V_{ub}\|$"**, J. P. Lees *et al.* , Phys. Rev. D **86**, 032004 (2012).

27. **"Search for the $Z_1(4050)^+$ and $Z_2(4250)^+$ states in $\bar{B}^0 \to \chi_{c1}K^-\pi^+$ and $B^+ \to \chi_{c1}K^0_S\pi^+$"**, J. P. Lees *et al.* , Phys. Rev. D **85**, 052003 (2012).

28. **"Observation and study of the baryonic B-meson decays B to D(*) p pbar (pi) (pi)"**, P. del Amo Sanchez *et al.* , Phys. Rev. D **85**, 092017 (2012).

29. **"Amplitude analysis and measurement of the time-dependent CP asymmetry of $B^0 \to K^0_SK^0_SK^0_S$ decays"**, J. P. Lees *et al.* , Phys. Rev. D **85**, 054023 (2012).

30. **"Search for the Decay $D^0 \to \gamma\gamma$ and Measurement of the Branching Fraction for $D^0 \to \pi^0\pi^0$"**, J. P. Lees *et al.* , Phys. Rev. D **85**, 091107 (2012).

31. **"Search for $\bar{B} \to \Lambda_c + Xl^-\nu_l$ Decays in Events With a Fully Reconstructed B Meson"**, J. P. Lees *et al.* , Phys. Rev. D **85**, 011102 (2012).

32. **"A Measurement of the Semileptonic Branching Fraction of the B_s Meson"**, J. P. Lees *et al.* , Phys. Rev. D **85**, 011101 (2012).

33. **"Search for CP Violation in the Decay $\tau^- \to \pi^-K^0_S(\geq 0\pi^0)\nu_\tau$"**, J. P. Lees *et al.* , Phys. Rev. D **85**, 031102 (2012), [Erratum-ibid. D **85**, 099904 (2012)]

34. **"Cross Sections for the Reactions $e^+e^- \to K^+K^-\pi^+\pi^-$, $K^+K^-\pi^0\pi^0$, and $K^+K^-K^+K^-$ Measured Using Initial-State Radiation Events"**, J. P. Lees *et al.* , Phys. Rev. D **86**, 012008 (2012).

BESIII

M. Anelli (Tecn.), R. Baldini Ferroli (ass.), M. Bertani (Resp.), A. Calcaterra,
R. Rosellini (Tecn.), Y. Wang (borsista), A. Zallo (ass.), A. Zossi (Tecn.)

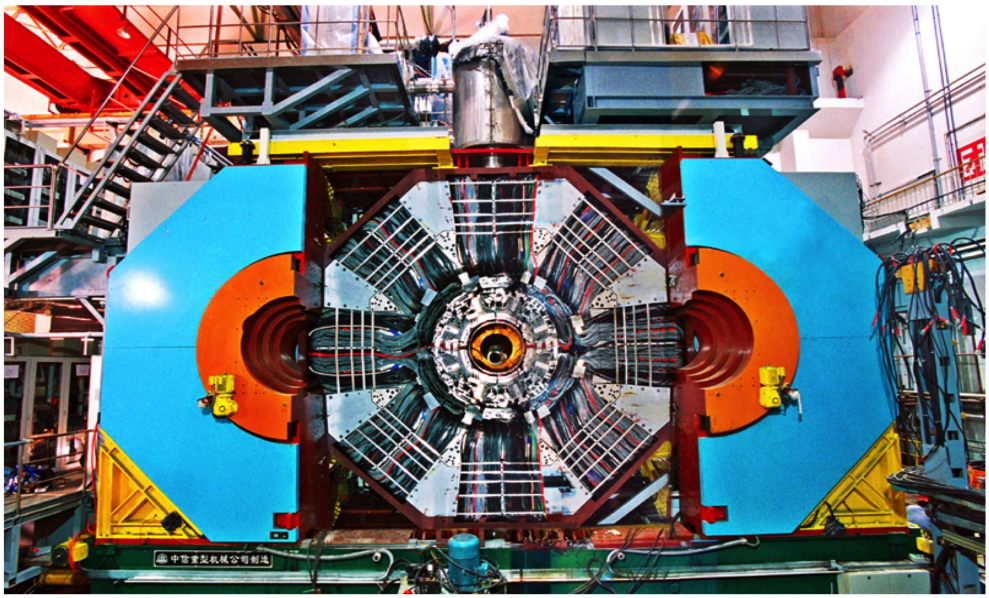

Figure 1: Overview of BESIII detector

1 The BESIII experiment

The BESIII experiment is taking data since 2009 at the Beijing Electron Positron Collider BEPC-II, at the Beijing Institute of High Energy Physics, IHEP. The BESIII detector, shown in fig. 1, is designed to study the τ-charm physics. The first physics event was observed on July 19, 2008. So far BESIII collected the world largest samples of J/ψ, $\psi(3686)$, $\psi(3770)$ and $\psi(4040)$. The actual maximum instantaneous value of the luminosity reached is 0.6×10^{33} cm^{-2} s^{-1} and the goal is to reach the goal value of 10^{33} cm^{-2} s^{-1} by 2013.
The LNF group joined the BESIII collaboration at the end of 2009 and has the full responsability of the detector for zero-degree photon tagging, ZDD, which was installed at BEPCII on 2011. In 2012 the group started to work on the proposal to upgrade the Inner BESIII tracking chamber with a Cylindrical GEM detector. They are involved in the physics analyses of processes mainly involving nucleons or light hadrons.

2 The zero degree detector

2.1 The initial state radiation technique

At τ-charm and b factories e^+e^- annihilation processes to hadrons can be investigated by means of the so-called initial state radiation technique (ISR). Such a technique consists in measuring

the reaction $e^+e^- \to H\gamma$, where H is a hadronic final state and the photon is emitted by one of the initial electrons. The differential cross section for this process is proportional to the direct $e^+e^- \to H$ cross section. The proportionality factor, the *radiator* function, gives the probability for the initial photon emission and can be computed to an accuracy better than 1%.
The angular distribution of the ISR photon in the center of mass (CoM) frame is peaked at small angles. Indeed the fraction of photons in the main detector, which has a typical geometrical acceptance $20^o \leq \theta \leq 160^o$, is lower than 20%. The possibility of measuring the small-angle photons, even in a few milliradians cone around the beam line, would increase the ISR acceptance by almost a factor of two.

2.2 The ZDD

The proposed ZDD is made of two simmetric detectors (ZDD_E and ZDD_W) located in two areas close to the beam line, about 3 m away in the East and West direction from the BESIII detector. They will be used to tag the ISR photons and measure their energy, and also to replace the present BESIII luminometer. Each detector is made of two modules $4 \times 6 \times 14$ cm^3, one "upper" and one "lower". The modules are composed by the same material used for the KLOE electromagnetic calorimeter: a mixture of scintillating fibers (60% of volume) embedded in a Pb matrix (40%), with the fibers oriented vertically direction, as shown in Fig. 2.

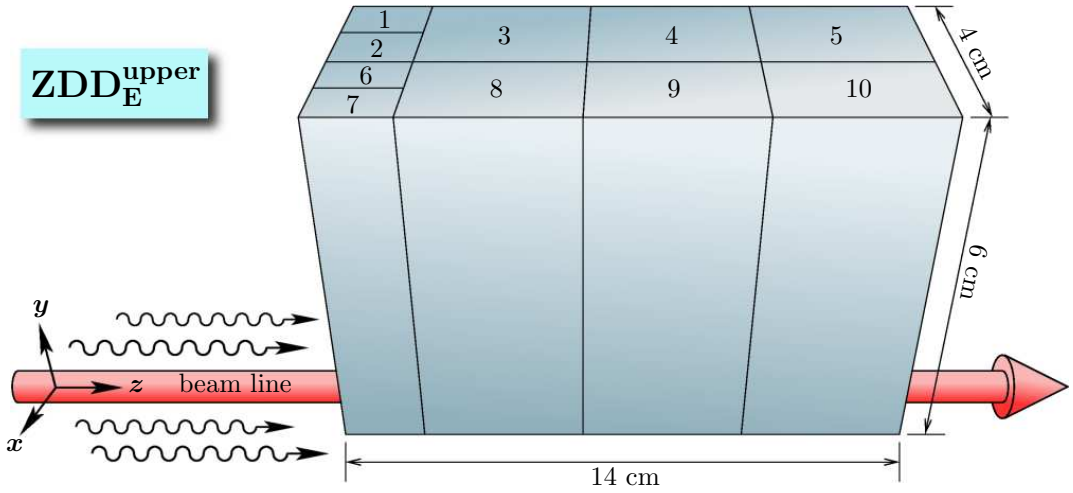

Figure 2: Upper module of the ZDD detector. The segmentation on the upper face indicates the ten reading sectors. The red arrow shows the direction of ISR (and Bremsstrahlung) photons. The lower module (not drawn) is located below the red arrow.

To avoid the severe background due to Bremsstrahlung photons produced in the process $e^+e^- \to e^+e^-\gamma$, which populate the very small polar angle region, the upper and lower modules of each ZDD station are separated by an empty space 10-mm wide along the vertical direction, so as to move each module approximately 5 mm away from the equatorial plane of the machine, on opposite sides. In this way, and considering that the angular distribution of Bremsstrahlungby photons is much narrower than the one for ISR photons, a big reduction of background is obtained, at the price of a small (additional) inefficiency for the ISR signal.

The scintillation light is channeled by bundles of clear optical fibers 2 m long to photomultipliers Hamamatsu H10828, that have a very fast response, and are selected to have uniform gains of $\sim 10^6$ at 1500 V. The PM signals are fed into preamplifiers ($\times 2$) located close to the experimental

area and sent, via RG58 cables 20 m long, to shaper, splitter and discriminator circuitry located in the BESIII DAQ crates.
The preamplifiers, as well as the readout electronics, are a project and realization of the "SELF" group of the LNF.

2.3 The ZDD as a luminometer

As previously said, the ZDD may be used in a parasitic way as a luminometer, giving a fast measurement of beam-to-beam relative BESIII luminosity via instantaneous rates of appropriate sums of channels. The signal used currently by BEPC-II is the analogic sum over the first 8 segments in the first layer impacted, 4 of which are shown in Fig. 2 with numbers 1–2–6–7. Fig. 3 shows a sample of ZDD data under this respect.

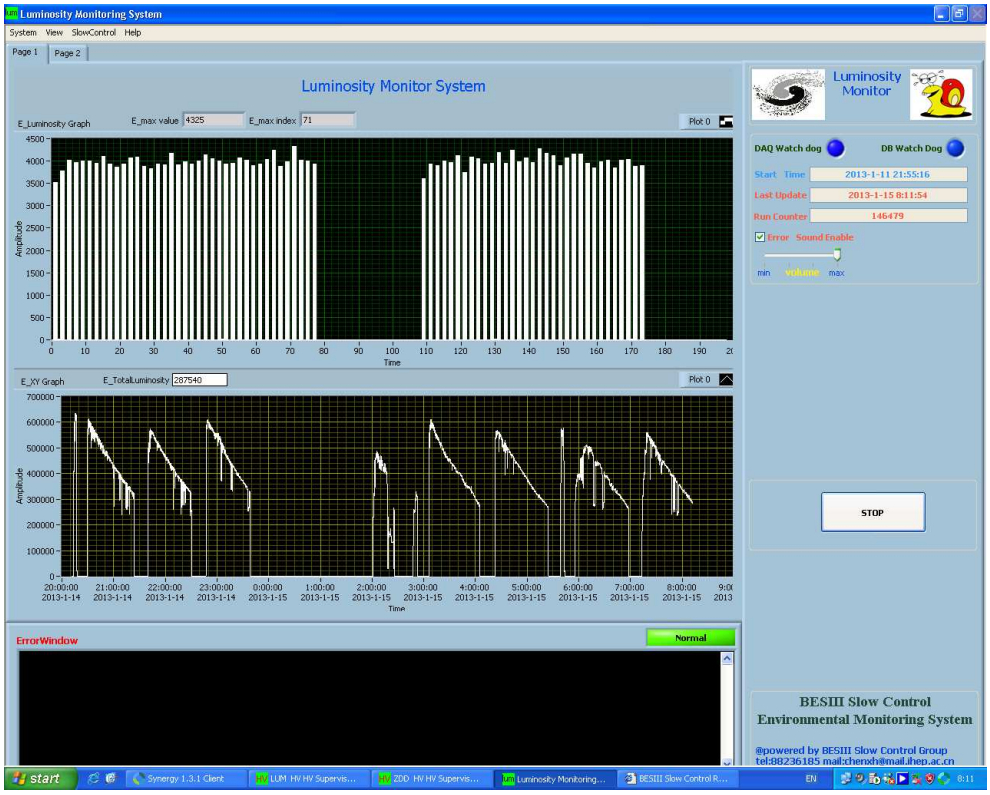

Figure 3: The ZDD as a luminometer. The top plot indicates the counting rates for the ZDD signal (see text) in 175 successive RF buckets (some buckets are empty).

2.4 ZDD upgrade

The photon impact point on the ZDD is largely unknown, and this affects adversely the energy resolution. One way to alleviate this is the 4-fold segmentation of the first layer, that could be used to obtain the impact point by some average of the energy partition between the 4 front channels.

Another method, for that fraction of photons that convert in the beam pipe, and hit the ZDD as a very close electron/positron pair, would be to use a system of very small scintillators.

Such a system, complete with its readout, has been almost completely readied in 2012, and will be installed as a ZDD upgrade in 2013.

Fig. 4 shows the finger array, currently under test at LNF. The array is read out by a Hamamatsu H7546A-200 multianode PM, and the frontend electronics is a project of INFN-SELF.

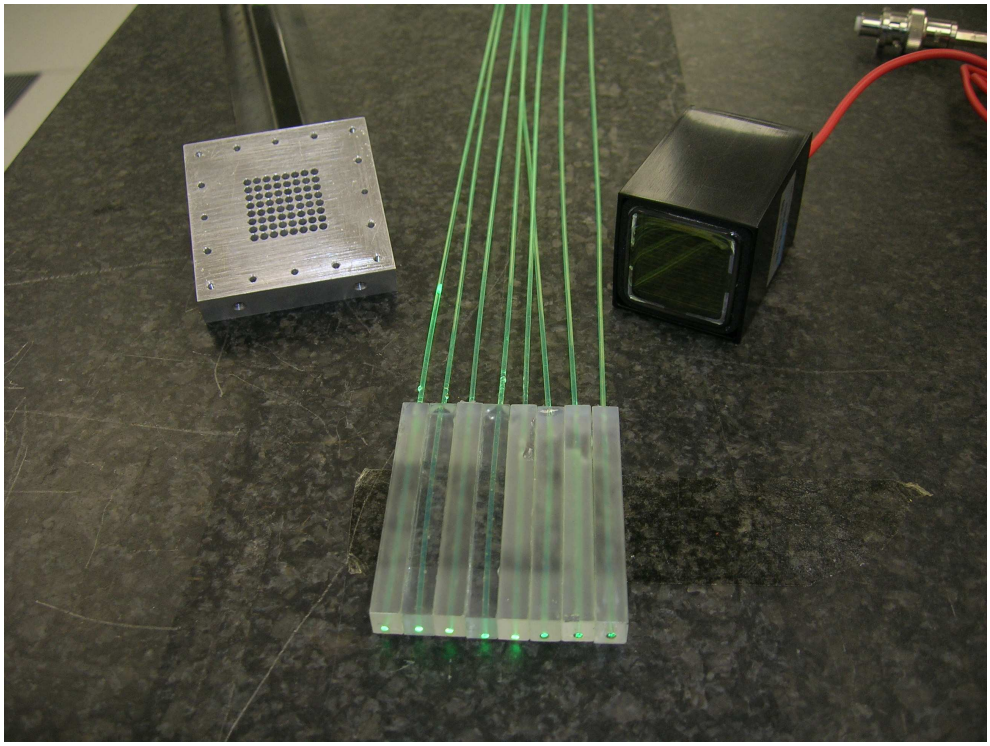

Figure 4: The finger array for measuring the impact point on the ZDD of (converted) ISR photons. Each indipendent scintillator, coupled to its own fiber, has dimensions 5x5x50 mm^3.

3 Proposal for the study of a BESIII inner tracker with Cylindrical GEMs

During the 2012 BESIII run it appeared that the increased backgrounds consequent to an increase in BEPC-II luminosity were starting to induce aging problems in the inner Drift Chamber, that is a physically separate section of the BESIII cylindrical Main Drift Chamber(MDC) carrying 8 layers of stereo wires very close to the beam, at radii from about 8 cm to about 18 cm. Since the BEPC-II is expected to further increase luminosity over the next 5 years of running, it was decided to investigate solutions alternative to the construction of a new inner Drift Chamber: the GEM (Gas Electron Multiplier) technique, already used at LNF for the KLOE2 Vertex Detector, looked very promising from the points of view of rate capability and radiation hardness.

In July 2012 INFN has encouraged and allowed the BESIII-Italy collaboration to ask the Ministry for External Affairs (MAE) cofinancing for a 3-year project destined to produce a finished layer of cylindrical detector, employing for the first time the technique of analog readout of cylindrical GEMs. This detector must have a radius and length adequate for forming in the future part of a multilayer device, should the BESIII Collaboration approve the use of GEMs in the detector.

In this connection, a workshop dedicated to cylindrical GEMs detectors was organized and held in LNF in the month of October, seeing participation by BESIII and KLOE2 physicists, and interested personnel from Russia and other countries.

In January 2013 the MAE has approved the project for participation in the Executive Programme and we have submitted an application for cofinancing the first year: an answer from MAE is expected by the end of March 2013.

4 Physics analysis

4.1 Study of $J/\psi \to p\bar{p}$ and $J/\psi \to n\bar{n}$

The decay of the J/ψ meson to a nucleon-antinucleon pair represents a good testbed for studying perturbative QCD. The $J/\psi \to N\overline{N}$ amplitude has a strong (QCD) and an electromagnetic (EM) contribution. The strong amplitude accounts for the lowest order QCD diagram where the decay is mediated by three gluons that produce the $N\overline{N}$ final state via single gluon-quark-antiquark vertices. The EM amplitude, instead, describes the $N\overline{N}$ production though one-photon exchange. Since the J/ψ meson has isospin zero, the strong amplitudes for decays in $p\overline{p}$ and $n\overline{n}$ should be the same. The EM amplitudes for protons and neutrons scale with the magnetic moments that are almost opposite ($\mu_p = 2.973$ and $\mu_n = -1.91$ in units of Bohr magneton). If all amplitudes are real (in phase), as it is expected at that energy, the interference terms between strong and EM part in case of $p\overline{p}$ and $n\overline{n}$ production have opposite sign so that we expect $\Gamma(J/\psi \to n\overline{n}) : \Gamma(J/\psi \to p\overline{p}) \simeq 1 : 2$. The physics analysis for the branching fractions of $J/\psi \to p\bar{p}$ and $J/\psi \to n\bar{n}$, based on a sample of 225 million J/ψ, has been performed at LNF during 2011 and 2012 and the results [12] are:

$$\Gamma(J/\psi \to n\overline{n}) = (2.07 \pm 0.01 \pm 0.17) \times 10^{-3}$$

$$\Gamma(J/\psi \to p\overline{p}) = (2.112 \pm 0.004 \pm 0.031) \times 10^{-3}$$

These results, that represent significant improvements over previous measurements, strongly support almost orthogonal EM and strong amplitudes. This means that, contrary to the expectation, there should be a relative phase of about 90 degrees between these amplitudes: if one is real the other must be purely imaginary. The origin of this unexpected phase is still under investigation.

4.2 Measurement of the phase between J/ψ strong and electromagnetic decay amplitudes by means of a resonance scan

To clarify the experimental situation in a model independent way, in 2011 the Italian group submitted to the BESIII Collaboration a proposal [1] which has been accepted, to measure the phase difference between EM and strong J/ψ decay amplitudes. The analysis consists in looking for an interference pattern, in all possible channels, between the resonant amplitude and the non resonant one, by means of an energy scan of the J/ψ.

More in detail, this study requires setting a continuum reference at $\sim$100 MeV below the J/ψ and then measuring the decay rate at different energy points lying between this reference point and the J/ψ mass. The choice of these energy points with the necessary integrated luminosity has been done to maximize the capability to discriminate between the extreme cases, *i.e.* relative phase equal to zero, maximum interference, and 90 degrees, no interference.

Data taking time was dedicated to this measurement in May 2012 after the J/ψ lineshape scan and data analysis has started in LNF. The work is in progress and will go on during 2013, for the moment we can report some preliminary results. An interference pattern in the $\mu^+\mu^-$ channel was identified and measured soon after the discovery of J/ψ at SLAC, the relative phase between the resonant and non-resonant amplitudes being in good agreement with what expected. In

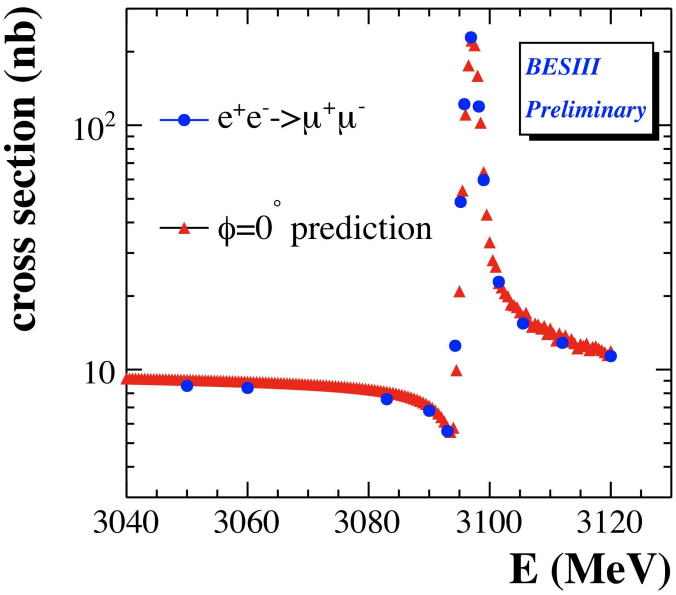

Figure 5: BESIII preliminary result on the lineshape scan of $e^+e^- \to \mu^+\mu^-$ confirming a full interference pattern between the resonant and non-resonant J/ψ amplitudes.

$e^+e^- \to 2\pi^+2\pi^-$ no strong decay is allowed because of G-parity conservation and full inteference between the e.m. decay and the continuum is expected. The sign of the interference is not established a priori and should be an interesting byproduct. In BESIII we started to analyse the $\mu^+\mu^-$ and $2\pi^+2\pi^-$ channels where interference is expected, the preliminary results are shown in figs. 5 and 6, and confirm full interference between J/ψ decay and continuum. The $\mu^+\mu^-$ result improves the significance of previous existing results, while the intereference in $2\pi^+2\pi^-$ is seen for the first time.
Work is in progress to improve to study the systematic errors and to fit the lineshapes to evaluate the phase angles. In the meantime the analysis of the $e^+e^- \to 2\pi^+2\pi^-\pi^0$ channel with strong interaction has started, results are expected for next year.

5 List of talks by LNF Authors in 2012

1. A. Zallo, "The Zero Degree Detector at BESIII", Frontier Detectors for Frontier Physics Workshop,La Biodola, Isola d'Elba, Italy, 20-25 May 2012.

2. A. Calcaterra, "A CGEM Prototype for a BESIII Inner Drift Chamber Upgrade", IHEP seminar, Beijing, 17 September 2012.

References

1. Y. Wang *et al.* "A proposal to measure the phase between J/ψ strong and electromagnetic decay amplitudes by means of an energy scan, BESIII Internal note (2011)

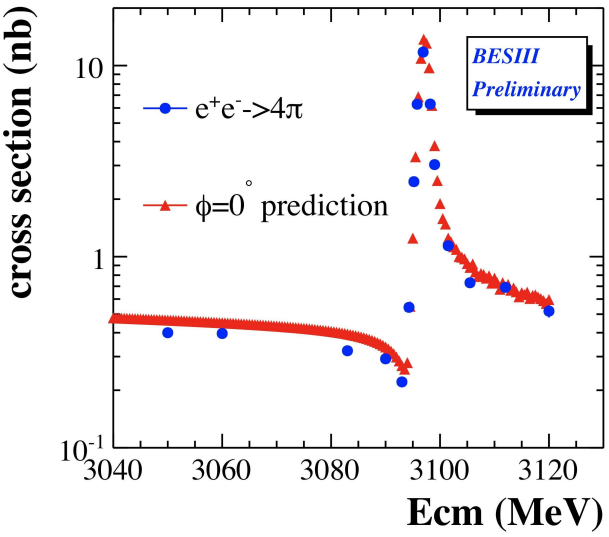

Figure 6: BESIII preliminary result on the lineshape scan of $e^+e^- \to 2\pi^+2\pi^-$ showing for the first time a full interference pattern between the resonant and non-resonant J/ψ amplitudes.

6 Publications in 2012

2. BESIII Collaboration (M. Ablikim *et al.*), Chin. Phys. C **36**, 915 (2012)
3. BESIII Collaboration (M. Ablikim *et al.*), Phys. Lett. **710**, 594 (2012)
4. BESIII Collaboration (M. Ablikim *et al.*), Phys. Rev. Lett. **108**, 112003 (2012)
5. BESIII Collaboration (M. Ablikim *et al.*), Phys. Rev. Lett. **108**, 182001 (2012)
6. BESIII Collaboration (M. Ablikim *et al.*), Phys. Rev. Lett. **108**, 222002 (2012)
7. BESIII Collaboration (M. Ablikim *et al.*), Phys. Rev. D **85**, 092012 (2012)
8. BESIII Collaboration (M. Ablikim *et al.*), Phys. Rev. D **85**, 112008 (2012)
9. BESIII Collaboration (M. Ablikim *et al.*), Phys. Rev. Lett. **109**, 042003 (2012)
10. BESIII Collaboration (M. Ablikim *et al.*), Phys. Rev. Lett. **109**, 172002 (2012)
11. BESIII Collaboration (M. Ablikim *et al.*), Phys. Rev. D **86**, 032008 (2012)
12. BESIII Collaboration (M. Ablikim *et al.*), Phys. Rev. D **86**, 032014 (2012)
13. BESIII Collaboration (M. Ablikim *et al.*), Phys. Rev. D **86**, 052004 (2012)
14. BESIII Collaboration (M. Ablikim *et al.*), Phys. Rev. D **86**, 052011 (2012)
15. BESIII Collaboration (M. Ablikim *et al.*), Phys. Rev. D **86**, 071101 (2012)

16. BESIII Collaboration (M. Ablikim *et al.*), Phys. Rev. D **86**, 072011 (2012)
17. BESIII Collaboration (M. Ablikim *et al.*), Phys. Rev. D **86**, 092008 (2012)
18. BESIII Collaboration (M. Ablikim *et al.*), Phys. Rev. D **86**, 092009 (2012)

CDF2

M. Cordelli (Resp.)

Not received

CMS

L. Benussi, S. Bianco (Resp.), M.A. Caponero (Ass.)
S. Colafranceschi (Dott.), F.L. Fabbri (Ass.), M. Ferrini (Ass.)
M. Parvis (Ass.), L. Passamonti (Tecn.), D. Piccolo
D. Pierluigi (Tecn.), G. Raffone, A. Russo (Tecn.), G. Saviano (Ass.), C. Vendittozzi (Dott.)

In collaboration with:
B.Dulach (SPECAS), D.Orecchini (SPECAS),

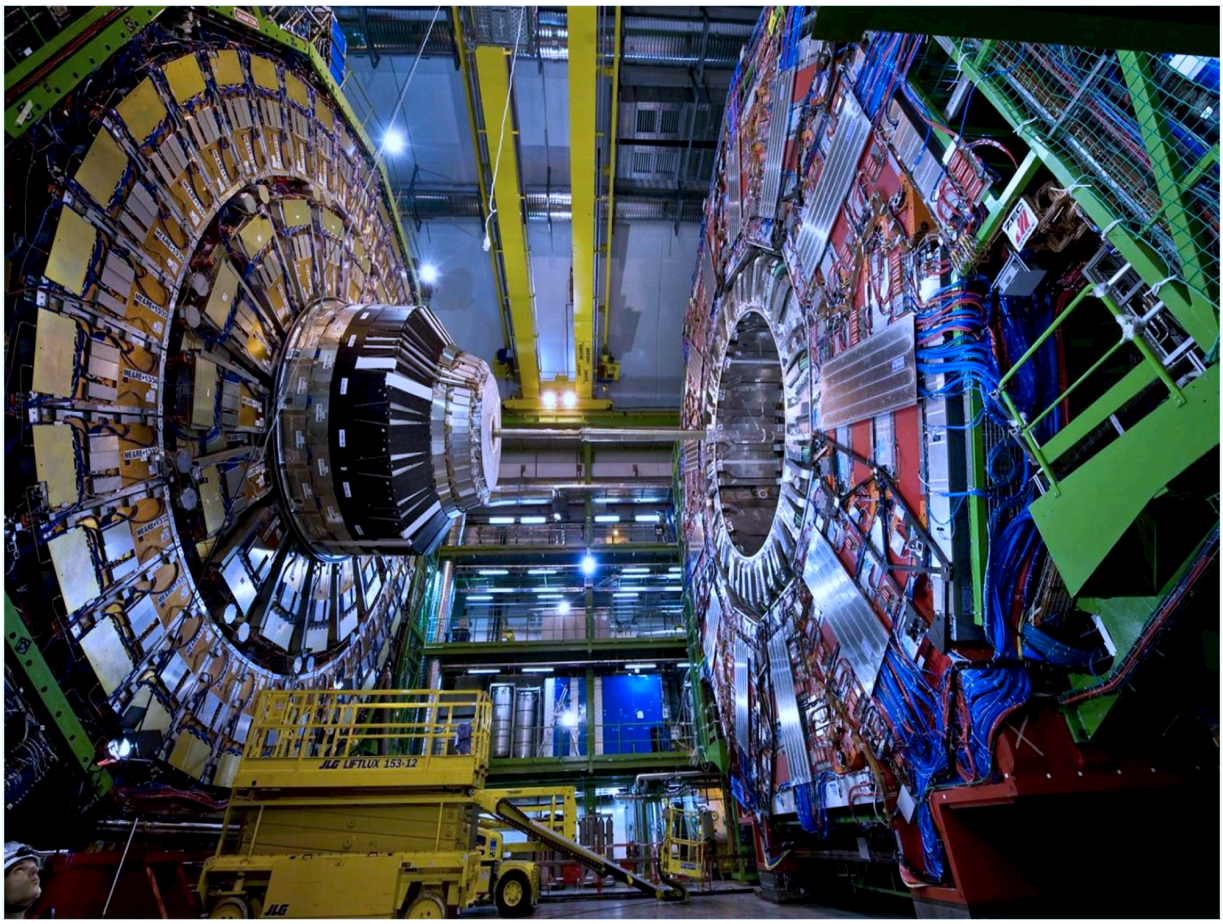

The Compact Muon Solenoid (CMS) experiment [1)] will search for the missing block of Nature - the Higgs boson - and for new exotic elementary particles that are predicted by theory and by cosmological observations. A key element of the CMS detector is a highly performing and redundant muon system. Drift tubes and Resistive Plate Chambers (RPC) in the Barrel and Cathod Strip Chambers and RPCs in the endcap are used for both triggering and tracking of muon particles. The activity of the CMS Frascati groups is centered on various responsibilities in the construction, operations and monitoring of the RPC detector, as well as in the quality control of data and physical data analysis.

1 Status of the CMS experiment

The year 2012 has been historic for CMS [2] Physics. The pinnacle of our physics programme was an observation of a new particle [3], a strong candidate for a Higgs boson, which has captured worldwide interest and made a profound impact on the field of particle physics. At the time of the discovery announcement on 4 July, 2012, prominent signals were observed in the high-resolution H $\rightarrow \gamma\gamma$ and H$\rightarrow$ ZZ $\rightarrow$ (4l) modes. Corroborating excess was observed in the H$\rightarrow W^+W^-$ mode as well. The fermionic channel analyses (H$\rightarrow$ bb, H$\rightarrow \tau\tau$), however, yielded less than the Standard Model (SM) expectation. Collectively, the five channels established the signal with a significance of five standard deviations. With the exception of the diphoton channel, these analyses have all been updated in the last months and several new channels have been added. With improved analyses and more than twice the integrated luminosity at 8 TeV, the fermionic channels are now more consistent with the SM expectation as can be seen in the figure 1. The larger dataset has also allowed for more precise studies of the properties of the new boson. The mass has been measured to be 125.8 $\pm$ 0.5 GeV and the data are now in favour of the 0 pseudo-scalar hypothesis, with a CLs value of 2.4%.

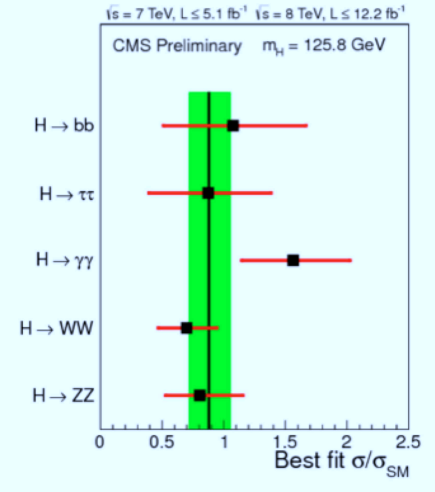

Figure 1: All five channels are consistent with the Standard Model expectation.

With the discovery of a strong candidate for a fundamental scalar, the question of what is stabilising its mass at 125 GeV has become a principle goal of our field. Though constrained by previous null results from the LHC, Supersymmetry remains a strong possibility for such a natural solution to this problem. Third-generation squarks play a special role in natural SUSY, so searches for stops and sbottoms have received increased attention in the SUSY Analysis. For stops/sbottoms produced via gluino cascades, searches have excluded gluino masses of 1.1 TeV for almost any stop/sbottom mass. For direct production of stops/sbottoms, 95% confidence level (CL)

limits reach 600 GeV. Several new analysis studying the EW production of chargino/neutralinos have now excluded masses up to 650 GeV . With these increasingly stringent limits on R-parity-conserving SUSY models, R-parity-violating (RPV) scenarios must also be considered. At HCP conference, CMS presented 95% CL limits on the mass of RPV stops of 850 1000 GeV.

Meanwhile CMS continues its broad search programme for physics beyond the Standard Model.

In addition to these searches, CMS has performed a number of important SM analyses. The TOP physics has entered a new phase of precision measurements wherein it has been measured the top-pair and single-top (t-channel) production cross-sections at both 7 and 8 TeV, and the top-quark mass has been measured with 1 GeV precision to be $173.4 \pm 0.4 \pm 0.9$ GeV, reaching the highest precision ever achieved by a single experiment. Other studies cover the physics programme of testing perturbative QCD and precision tests of electroweak interactions. In the B Physics field it has been demonstrated that CMS is competitive with dedicated experiments in the study of B-physics and quarkonia. In heavy-ion physics, CMS made a splash at the QM2012 conference where eight new analyses on 2.76-TeV PbPb collision data were presented. More recently, an observation of a ridge in proton-lead collisions based on a single pilot pPb run earlier this year (published in October) has captured the attention of the heavy-ion community.

There has also been a lot recent activity on the future physics of CMS. Physics studies have been carried out in the Higgs and Susy field to support the upgraded CMS detector of the pixel and Hadronic Calorimeter system. Similar performance studies have also been carried on to study the impact of the upgrade of the Level 1 trigger and of the Muon system. To conclude, the CMS Physics output has never been as rich as in the past six months. Nearly 85 new analyses on 7/8-TeV pp collision data, were presented at the ICHEP 2012 conference in July. In december 2012, CMS presented 25 new results on 8-TeV data at the HCP symposium in Kyoto. These preliminary results are being finalised for publication or have already been published, including the paper documenting the new boson discovery. CMS has also attained the milestone of 200 papers published with collision data from the LHC.

2 Status of the RPC Muon system

The RPC system operated in 2012 very smoothely, with an average chamber efficiency of about 95% and an average cluster size around 1.8. The average number of active channels is 97.7%. Eight chambers are disconnected and forty are working in single-gap mode due to high-voltage problems. The total luminosity lost due to RPCs in 2012 is only 88.46 pb^{-1} most of it due to dedicate calibration Runs required by the RPC system. One of the main goals of 2012 was to improve the stability of the endcap trigger that is strongly correlated to the performances of the detector, due to the 3-out-3 trigger logic. At beginning of 2011 the instability of the detector efficiency was about 10%. Detailed studies found that this was mainly due to the strong correlation between the performance of the detector and the atmospheric pressure (P). Figure 2 (red points) shows the linear correlation between the average cluster size of the endcap chamber versus P. This effect is expected for gaseous detectors and can be reduced by correcting the applied high-voltage working point (HVapp) according to the following equation: HVapp = HVeff (1 - α + α*P/P_0), where α is a parameter to estimate from the data ($\alpha \leq 1.0$) and HVeff is the effective HV working point (WP). By convention P_0 is chosen to 965 mbar.

Many improvements have been introduced since 2011 to stabilise the detector performance and they are: a slow (once per fill) WP automatic correction, with $\alpha = 1$, (July 2011); a fast WP

automatic correction (anytime it changes of 3 V) (July 2012); and a detailed analysis to quote the correct value of α estimated equal to 0.8 with the first data of the 2012. Thanks to the first two steps the chamber efficiency instability went down from 10% to 4÷5% and, finally, with α equal to 0.8, the amplitude of the oscillations due to atmospheric pressure variations has been reduced by a factor of 10 for the cluster size and by a factor of 4 for the efficiency (1÷2%). Still in figure 2 (blue points) the clear imprvement in the stability is visible.

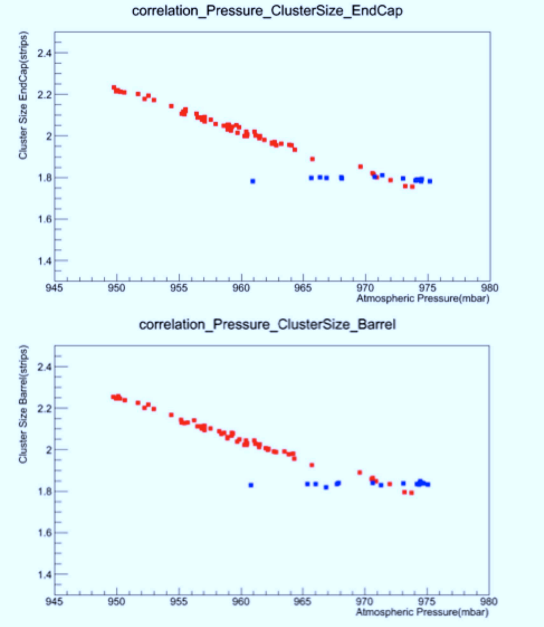

Figure 2: RPC Cluster size vs atmospheric pressure, before (red points) and after (blue points) authomatic HV correction.

A detailed study has also shown that the contribution of RPC hits to the standard Muon Reco is in a range of 1% to 7% [4]. The contribution reaches a value of 5÷7 % in some specific η regions: overlap between wheel 0 and 1 and overlap barrel-endcap. A new muon object, based on the matching between a Tracker track and RPC hits, has been released in the official code of CMS

One of the important activities started in 2012 has been the production of the first new RPC chambers that will be used to cover the outermost station of the endcap during the Long Shutdown of 2013-14. RPC gaps produced in Korea arrived at CERN for quality control, tests and assembling in the final chambers. Few imperfections on the graphite surface of the gaps have been detected and some improvements in the gap production have been already introduced. A first chamber has been produced at the laboratory of CERN and has been tested with cosmic rays in December. The RPC activities during 2012 were a big success thanks to a good organization

of the Run Coordination and to the expert and enthusiastic work of the pool of people covering the main tasks in the operation, maintenance and analysis of detector performance. Starting from 2013 a new regime of operations will be entered to meet the new requirements of the shutdown activities.

3 Activity of the CMS Frascati group in 2012

The Frascati group has joined CMS in the RPC muon detectors at the end of year 2005 and it is now very well inserted in the main activities. During the last years many important responsabilities were covered by members of the Frascati group. In 2010 and 2011 the RPC DPG (Detector Performance Group) coordinator was a Frascati charge. In 2011 and 2012 the RPC Run coordination was covered by Frascati. And at the end of 2012 a member of the group was elected as Italian National responsible for RPCs. The success of the RPC activities during 2012 was so also due to the important role covered by Frascati group in the CMS RPC collaboration. Also, during 2012, many of the activities of the group were devoted to the maintanance of the GGM (Gas Gain Monitor) system in charge to monitor the quality of the gas in the closed loop of the RPC system with a system of RPCs in the gas house. This system was projected and build by the group. In February 2012 the important International conference "XI Workshop on Resistive Plate Chambers and Related Detectors" has been held in Frascati, organized by our group together with other people. Many of the talks given in the conference were done by RPC CMS collabroation people and the conference was a great success.

The Frascati group was also involved in 2012 in the analysis of the single top production with specific studies of trigger and selection for the s-channel cross section.

Finally the 2012 was an important year to plan the future upgrades in view of the improved LHC luminosity during the shutdowns of 2018 and 2022. A Muon Strategy Group was formed with people from the different muon subdetectors and with the charge to analyze the performance detector perspective toward 2020 versus the foreseen trigger scheme and the background conditions.Frascati was representing the RPC community in this group.

3.1 Physics analysis: single top production

In LHC the top quark can be produced both in pairs or as a single top via Electroweak mechanism. The single top production is possible through three different diagrams: t-channel, tW channel and s-channel, each of them sensible to different possible effects of new physics. The precise measurement of the cross section of the single top production is so an important standard model check and a window for new physics. The Frascati group joined in 2012 the group of Analysis of the single top and was involved in two main activities: study of the hadronic cross-trigger efficiency and study of selection for the s-channel cross section measurement. While for the t-channel [5)] and tW channel CMS has produced papers with measurement, still no official measurement of the s-channel cross section is available. The signal coming from the s-channel single top production is very difficult to discriminate against background events (mainly single top t-channel and $t\bar{t}$). An apporoach based on multi-variate analysis is necessary and is under study to identify the signal events.

3.2 Gas Gain Monitoring System

The Gas Gain Monitoring (GGM) system of RPC detectors in CMS monitors the changes in working point due to gas variations, by means of monitoring of anodic charge in small RPC gaps

in a cosmic ray telescope. The system is composed of three subsystem of RPC single gaps, readout by 45cm x 45cm pads in a cosmic ray telescope located in the SGX5 gas building. Each subsystem is flushed with a different gas. The Reference subsystem is flushed with fresh open loop gas mixture. The MonitorOut subsystem is flushed with Closed Loop gas downstream of CMS RPCs. The MonitorIn subsystem is flushed with Closed Loop gas upstream of CMS RPCs. Each subsystem is composed of three gaps, whose high voltage is set to the standard working point voltage at the efficiency knee, and to 200 V above and below the knee respectively. Each cosmic ray track therefore provides completely correlated pulses in the three subsystems, allowing one to study the differential response of gaps and by disentangling any effect due to changes in the gas mixture. In case a working point change is detected, an alarm condition is released and the gas quality monitoring system will verify what the change of work point is due to.

4 Muon Strategy Group

The Frascati group was involved in the Muon Strategy Group with the goal to identify possible weak points in the present RPC system in view of the increased LHC luminosity. Data collected during 2011 and 2012 have been analyzed in order to quantify the correlation between background rate and LHC luminosity. The background affecting RPC response is mainly due to photons and neutrons and this rate has been shown to be with good approximation linear as a function of Luminosity (figure 3). The expected performance of the RPC system up to the higher LHC Luminosity expected above 2020 seems to be under control in all the system with some concerns in the region at very high η where the rate (and by conseuqence the integrated charge) will reach values close to the limit for a correct RPC operation. Future data will be useful to give more clear results. One important point covered by the Muon Strategy group has been the High η coverage of the muon system. At moment the Muon system is covered by three independent detectors giving high redundancy to the system (Drift tube and RPC in the barrel, and Cathode Strip Chambers and RPC in the endcap up to $\eta = 1.6$). In the region $1.6 \leq \eta \leq 2.4$ no RPC (with present technology) can work and only the Cathode Strip Chambers are present. This is the region with higher background and an additional detector has been shown to be able to improve the performance of the muon system in view of the higher background expected. The Gas Electron Multiplier (GEM) detector has been identified as a possible solution to cover this region in the next long shutdown (2018-19) and is at moment under review from the CMS management.

5 Activity planned for 2012

The 2012 is the first of two years of long shutdown of LHC in which the group will be involved in the installation and commissioning of the outermost RPC layer in the endcap system [6]. During this period 144 new RPC chambers will be installed on the detector with services, readout electronics and gas system. The Frascati group will be involved in the commissioning and installation of the Link Board system responsible for the readout and zero suppression of the RPC signals to be sent to the CMS trigger and DAQ system. This period will also be used to reparation of the present system and Frascati will give his contribution on the HV system and on the fix of gas leaks found in some region of the detector. Main reparation and maintainance of the GGM system will also be part of the Frascati activities.

At the same time a GEM collaboration has been setup in CMS in order to propose and realize a system based on GEM detectors for the coverge of the high η region of the CMS muon system [7].

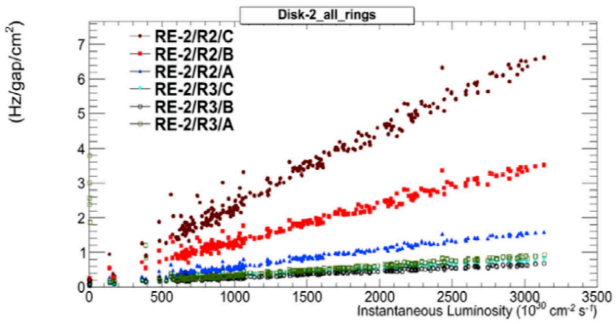

Figure 3: RPC background vs LHC luminosity for different regions of the endcap RPC system.

An approval of CMS is expected during the first half of 2012 and tdr should be prepared by the end of the year. Frascati is involved in this effort with a plan of R&D activities to be carried on in Frascati and with contributions to analysis of simulation data for the best layout definition. From the R&D point of view the Frascati group will study the tensioning of the GEM foils inside the CMS chambers. New techniques for the stretcing have been developed and used by the LHCb GEM collaboration but should be verified on the larger CMS chambers (120 cm x 60 cm). The quality control of this stretching in view of a massive chamber production and the long term monitoring are part of our R&D program. A crucial parameter for successfully operations of GEM at CMS is the time resolution that should be of the order of 4-5 ns in order to identify efficiently the LHC bunch crossing and to have a good discrimination power against photons and neutron backgrounds. These requirements will drive the Frascati group R&D that will be devoted to the studies of gas mixture and GEM geometry to improve the time resolution.

The Analysis of single top s-channel will be enforced during 2012. The Frascati group is well integrated and works in sinergy with the Napoli INFN group with the plan to finalize a paper with the measurement of the single top s-channel cross section by the end of the year. Also the studies of the hadronic cross trigger that will be important for the analysis of the single top will be finalized in the first half of 2012.

6 Conference Talks by LNF Authors

1. C. Vendittozzi et Al., "A model for the chemistery of defects in bakelite plates exposed to high-radiation environment" poster at RPC2102 conference, Frascati, Italy, February 2012.

2. S. Colafranceschi et Al., "Operational experience of the GGM at the CMS Experiment" poster at RPC2102 conference, Frascati, Italy, February 2012.

7 Papers

1. For the listing of CMS papers in 2012 see /www.slac.stanford.edu/spires/

2. L. Benussi, S. Bianco, S. Colafranceschi, L. Passamonti, D. Piccolo, D. Pierluigi, A. Russo and G. Saviano *et al.*, "Study of gas mixtures and high voltage in a single gap RPC monitoring system," PoS RPC **2012** (2012) 057.

3. S. Grassini, M. Ishtaiwi, M. Parvis, L. Benussi, S. Bianco, S. Colafranceschi and D. Piccolo, "SiOx coated plastic fiber optic sensor for gas monitoring in RPC," PoS RPC **2012** (2012) 072.

4. M. A. Caponero, A. Polimadei, L. Benussi, S. Bianco, S. Colafranceschi, L. Passamonti, D. Piccolo and D. Pierluigi *et al.*, "Use of fiber optic technology for relative humidity monitoring in RPC detectors," PoS RPC **2012** (2012) 073.

5. D. Abbaneo, M. Abbrescia, C. Armagnaud, P. Aspell, Y. Assran, Y. Ban, S. Bally and L. Benussi *et al.*, "Beam Test Results for New Full-scale GEM Prototypes for a Future Upgrade of the CMS High-eta Muon System," arXiv:1211.3939 [physics.ins-det].

6. D. Abbaneo, M. Abbrescia, P. Aspell, S. Bianco, K. Hoepfner, M. Hohlmann, M. Maggi and G. De Lentdecker *et al.*, "A GEM Detector System for an Upgrade of the High-eta Muon Endcap Stations GE1/1 + ME1/1 in CMS," arXiv:1211.1494 [physics.ins-det].

7. S. Bianco [CMS and ATLAS Collaborations], "Searches for supersymmetry and beyond the standard model physics in ATLAS and CMS," Frascati Phys. Ser. **54** (2012) 240.

8. S. Colafranceschi, R. Aurilio, L. Benussi, S. Bianco, L. Passamonti, D. Piccolo, D. Pierluigi and A. Russo *et al.*, "A study of gas contaminants and interaction with materials in RPC closed loop systems," PoS RPC **2012** (2012) 056 [arXiv:1210.1819 [physics.ins-det]].

9. S. Colafranceschi, L. Benussi, S. Bianco, L. Passamonti, D. Piccolo, D. Pierluigi, A. Russo and G. Saviano *et al.*, "Performance of the Gas Gain Monitoring system of the CMS RPC muon detector and effective working point fine tuning," JINST **7** (2012) P12004 [PoS RPC **2012** (2012) 046] [arXiv:1209.3893 [hep-ex]].

10. M. S. Kim, H. Seo, J. Goh, Y. Choi, K. Beernaert, A. Cimmino, S. Costantini and G. Garcia *et al.*, "CMS reconstruction improvement for the muon tracking by the RPC chambers," PoS RPC **2012** (2012) 045 [arXiv:1209.2646 [physics.ins-det]].

11. S. Costantini, K. Beernaert, A. Cimmino, G. Garcia, J. Lellouch, A. Marinov, A. Ocampo and N. Strobbe *et al.*, " Uniformity and Stability of the CMS RPC Detector at the LHC," PoS RPC **2012** (2012) 005 [arXiv:1209.1989 [physics.ins-det]].

12. M. Tytgat, A. Marinov, P. Verwilligen, N. Zaganidis, A. Aleksandrov, V. Genchev, P. Iaydjiev and M. Rodozov *et al.*, "The Upgrade of the CMS RPC System during the First LHC Long Shutdown," PoS RPC **2012** (2012) 063 [JINST **8** (2013) T02002] [arXiv:1209.1979 [physics.ins-det]].

13. P. Paolucci, R. Hadjiiska, L. Litov, B. Pavlov, P. Petkov, A. Dimitrov, K. Beernaert and A. Cimmino *et al.*, "CMS Resistive Plate Chamber overview, from the present system to the upgrade phase I," PoS RPC **2012** (2012) 004 [arXiv:1209.1941 [physics.ins-det]].

14. D. Abbaneo, M. Abbrescia, M. Alfonsi, C. Armaingaud, P. Aspell, M. G. Bagliesi, Y. Ban and S. Bally *et al.*, "An overview of the design, construction and performance of large area triple-GEM prototypes for future upgrades of the CMS forward muon system," JINST **7** (2012) C05008.

15. L. Benussi, S. Bianco, S. Colafranceschi, F. L. Fabbri, M. Giardoni, L. Passamonti, D. Piccolo and D. Pierluigi *et al.*, "A New approach in modeling the response of RPC detectors," Nucl. Instrum. Meth. A **661** (2012) S182 [arXiv:1012.5508 [physics.ins-det]].

16. Benussi:2010yx L. Benussi, S. Bianco, S. Colafranceschi, F. L. Fabbri, F. Felli, M. Ferrini, M. Giardoni and T. Greci *et al.*, "Study of gas purifiers for the CMS RPC detector," Nucl. Instrum. Meth. A **661** (2012) S241 [arXiv:1012.5511 [physics.ins-det]].

8 Volumes

L. Benussi, S. Bianco, D. Piccolo et Al. (Eds.), "XI Workshop on Resistive Plate Chambers and Related Detectors International Conference, RPC12 2012, Frascati, Italy, February 5-10, 2012" *PoS RPC2012 (2012) nonconsec. pag.*

References

1. CMS Collaboration home page is /cms.cern.ch/.

2. R. Adolphi *et al.*, "The CMS experiment at the CERN LHC," JINST **3** (2008) S08004

3. S. Chatrchyan et al., "Observation of a new boson at a mass of 125 GeV with the CMS experiment at the LHC", Phys. Lett. B 716 (2012) 30

4. M. S. Kim, *et al.*, "CMS reconstruction improvement for the muon tracking by the RPC chambers," PoS RPC **2012** (2012) 045 [arXiv:1209.2646 [physics.ins-det]].

5. S. Chatrchyan et al., "Measurement of the single-top-quark t-channel cross section in pp collisions at $sqrts = 7$ TeV " Phys. Lett. B 716 (2012) 30

6. M. Tytgat, *et al.*, "The Upgrade of the CMS RPC System during the First LHC Long Shutdown," PoS RPC **2012** (2012) 063 [JINST **8** (2013) T02002] [arXiv:1209.1979 [physics.ins-det]].

7. D. Abbaneo, *et al.*, "A GEM Detector System for an Upgrade of the High-eta Muon Endcap Stations GE1/1 + ME1/1 in CMS," arXiv:1211.1494

KLOE/KLOE-2

The KLOE/KLOE-2 Collaboration at the LNF

D. Babusci, G. Bencivenni, C. Bloise (Resp.), F. Bossi, G. Capon (Ass.), P. Ciambrone, E. Czerwinski (Bors. PD), E. Dane' (Art. 23), E. De Lucia, P. de Simone, D. Domenici (Art. 23), J. Dong (Bors. EU), G. Felici, G. Fortugno (Tecn.), S. Giovannella, F. Happacher, E. Iarocci (Ass.)*, M. Iannarelli (Tecn.), J. Lee-Franzini (Ass), B. Leverington (Bors. PD), M. Martini (Ass)**, S. Miscetti, V. Patera (Ass.)*, G. Pileggi (Tecn.), B. Ponzio (Tecn.), R. Rosellini (Tecn.), F. Roukoutakis (Bors. EU), P. Santangelo, A. Saputi (Tecn.), I. Sarra (Dott.), F. Sborzacchi (Tecn.), B. Sciascia, A. Sciubba (Ass)*, E. Turri (Tecn.), G. Venanzoni.

In Collaboration with "LNF-SEA"
A. Balla, G. Corradi, U. Denni, A. Frani, M. Gatta, C. Paglia, G. Papalino
and "LNF SPAS"
S. Cerioni

*Also Dipartimento di Scienze di Base ed Applicate per l'Ingegneria, "Sapienza" University, Rome, Italy
**Also Dipartimento di Scienze e Tecnologie applicate,"Guglielmo Marconi" University, Rome, Italy

1 Introduction

The operation of the KLOE detector at DAΦNE continued during the year, except for the summer shutdown in July-August, in order to follow the machine studies providing the measurements of the luminosity, background levels, beam energy and beam position at the interaction region (IP). In August, the Amadeus Collaboration inserted a thin carbon target inside KLOE to collect data on kaon-nucleus interactions. Data taking for nuclear physics went on, mostly during nights and weekends, from November, with 100 pb^{-1} of integrated luminosity that should increase by a factor of three the data sample of K-N interactions previously selected from the 2.5 fb^{-1} of KLOE data. From the machine running, several results have been reached by the accelerator experts: i) with 102 bunches (1.1 A of electrons and 0.8 A positrons) and crab-waist sextupoles at half strength, DAΦNE operated at $1.4{\cdot}10^{32}$ cm^{-2} s^{-1}, with 4 pb^{-1} delivered in 12 hours; ii) in these conditions the luminosity is almost linear with current; iii) there is significantly scope for further luminosity improvements increasing current, an issue linked to the consolidation program planned for the 6-month shutdown started in December; iv) the expected performance increasing current is 2.0-2.5 fb^{-1} delivered in 250 running days assuming 50% global efficiency. Such results confirmed the program for DAΦNE consolidation, and running starting from June 2013. During the winter shutdown KLOE-2 will proceed with the installation of the upgrades, inner tracker and calorimeters, whose construction and test have been mostly finalized during the year, as presented in Sec.2-3. Detector installation and integration on the beam pipe is a crucial task both, for the importance of IP alignment and cooling for the DAΦNE performance, and for the impact on the operation of the detectors. Most of the procedures have been studied and tested on a mockup; cabling and cooling systems are being finalized.

Several analyses have been completed, i) on the hadronic cross section, Sec.4, ii) on the η production from γ–γ fusion [1)], iii) on the $\eta \to \pi\pi\gamma$ decays [2)], iv) on the U-boson searches, Sec.5, and other physics studies have been started as doctoral theses in Italy, Poland, and Sweden, reported in Sec.7.

2 The KLOE-2 inner tracker

Tracking detectors based on the Gas Electron Multiplier (GEM) technology have been used so far to equip forward regions of experiments at hadron machines (LHCb, COMPASS, TOTEM) fully exploiting their excellent rate capability (to 1 MHz/mm^2). At DAΦNE, where radiation flux is well below such a scale, the unique lightness of the GEM detector suggested the R&D for a cylindrical GEM, whose material budget could be kept lower than 2% of X_0. This feature is of utmost importance in KLOE-2, to limit the multiple scattering of low-momentum particles, photon conversions and K_S regeneration.

KLOE-2 is the first experiment using the GEM technology with a cylindrical geometry, developed at the LNF within the CERN RD51 Collaboration, aiming for technological advances of Micropattern Gas Detectors. The construction of the Inner Tracker (IT) has started in mid 2011; since then three layers have been completed and construction of the fourth (last) layer started in November 2012. Each layer is a triple-GEM detector composed by five concentric cylindrical electrodes: the cathode, to set the drift field, the 3 GEM foils for electron multiplication, and the anode that is also the readout circuit (Fig. 1,left). The IT is composed by four concentric CGEM

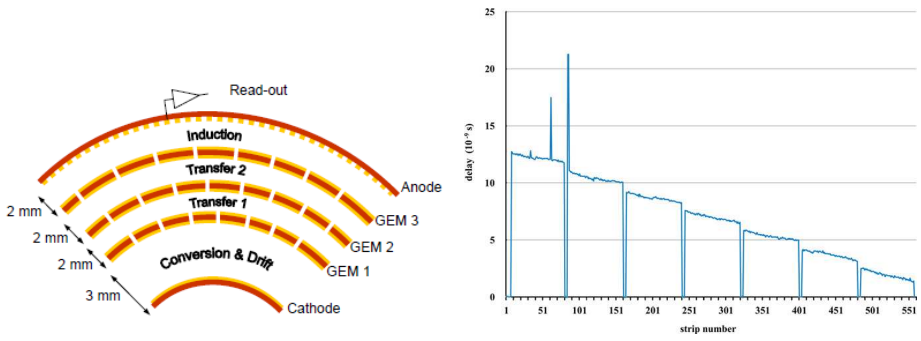

Figure 1: Cross-section of the triple-GEM cylindrical detector (left); Delay time measured for the V-view strips of half an anode foil of the second CGEM layer (right).

layers at radii from 13 cm, to preserve the K_S-K_L quantum interference region, to 20.5 cm, imposed by the KLOE DC inner wall, at 25 cm. The total active length for all layers is 70 cm. The anode readout of each CGEM is patterned with longitudinal X strips, 650 μm pitch, interleaved, on the same substrate and at the same level, with pads connected through internal vias to form V strips at an angle within 25°÷27° and with 650 μm pitch, for a total of about 30,000 FEE channels. The insertion of the IT is expected to improve by a factor of three the vertex resolution close to the interacton region, IP [3].

A dedicated readout system has been developed within the KLOE-2 collaboration. The Front-End Electronics is based on the new GASTONE ASIC [4], a 64 channels chip composed by four different stages: a charge preamplifier with 20 mV/fC sensitivity, a shaper, a leading-edge discriminator with a programmable threshold and a monostable stretcher of the digital signal, to synchronize with the KLOE Level1 trigger. GASTONE boards are one of the three elements of the IT data acquisition system together with the general interface boards (GIB) and the readout driver (ROD). The GIB board is based on a Xilinx Virtex 4FX Field Programmable Gate Array (FPGA) with an embedded IBM Power PC (PPC405) running at 300MHz. It has been designed to set up the front-end chip parameters, deliver the power supply and download data from a maximum of eight GASTONE. Data are then delivered from the 2 Gb/s optical port of the GIB board to the

ROD, which performs a first-level event-building, transfers data from GIBs to a VME CPU-board sending data to the online farm.

The IT project has been finalized after 3 years of intense R&D, from 2008 to 2010, with several prototypes built and tested with X-rays, cosmic-ray muons and pion beams at CERN. The three main stages have been: i) the construction and complete characterization of a full-scale CGEM prototype [5]; ii) the study of the readout system with a planar XV GEM chamber operated also in magnetic field, from 0.4-1.5 T, at the RD51 CERN-SPS facility [6]; iii) the construction and characterization of a large-area planar GEM realized with the new single-mask photolitografic technique [7]. The CGEM operation in magnetic field (B orthogonal to E) has been studied with 150 GeV/c pion beams, using two different gas mixtures at a gain of $\sim 10^4$: Ar/CO_2 (70/30) and $Ar/i\text{-}C_4H_{10}$(90/10). Spatial resolution in the bending plane increases with the magnetic field due to the Lorentz force spreading the charge over the readout plane.The resolution in the bending plane measured at 0.52 T (the value of the KLOE magnetic field) is $\sigma_{r\phi} \sim 200$ μm. Spatial resolution in the transverse direction to the bending plane is $\sigma_z \sim 350$ μm, insensitive to the magnetic field. Due to IT dimension, R&D was needed for a new GEM manufacturing procedure. The TE-MPE-EM CERN group produced GEM foils of unprecedented size (up to 50x100 cm^2) using single-mask electro-chemical etching of the micro-holes. Exploiting the intrinsic lightness of GEM foils (50 μm thick polyimide doubly clad with 2 μm copper films) and their extreme flexibility, we managed to manufacture a cylindrical GEM foil with only 2 mm wide overlap gluing region. The (Ar/iC_4H_{10}) gas mixture has been chosen after testing several alternatives (either Argon or Helium based mixtures), taking into account the most important operating parameters. In the cylindrical triple-GEM detector all the electrodes are made of polyimide foils. The uniformity of GEM holes, directly affecting the gain, has been measured over a surface as large as 70x30 cm^2. The anode quality check has been perfomed with 100 ps precision: the strip can be regarded as a transmission line and its length and possible damages can be evaluated by measuring the delay of the reflected input signal [8]. Fig. 1 (right) shows the distribution of the delay time measured for the V-view strips of half an anode foil of the second CGEM layer: the peaks represent shorts in the readout strips. After quality controls, the construction of the detector starts with the splicing of three separate foils to obtain a single electrode with dimensions of about 100x70 cm^2. The splicing is performed by distributing an epoxy glue (Araldite 2011) along the overlap between foils (2 mm wide) and then pressing the foils with a vacuum bag on a machined assembly table, for the 24 hours epoxy curing cycle. This large electrode foil is wrapped around an aluminum cylindrical mold, glued on a 2 mm wide overlap and finally enveloped in a vacuum bag. Two fiberglass rings are glued at the ends of the barrel, acting as spacers between electrodes, and as mechanical support. The surface of the mold is covered by a PTFE film, providing a low-friction surface, allowing the GEM to be extracted without damages. The cathode and the anode cylindrical electrodes are manufactured with a similar process, the only difference with respect to the GEM electrodes is that they are both reinforced with a 3 mm thick honeycomb structure coupled with thin external skins: 50 μm kapton foil for the cathode and 90 μm carbon foil for the anode. The assembly of the final detector is performed by inserting one into the other the cylindrical electrodes, starting by the anode and ending with the cathode. To this extent a dedicated machine has been built. The machine allows the insertion of the electrodes with a ~ 100 μm axial alignment over a length of about 1.5 m. The detector is then sealed at both ends to ensure gas tightness.
The three innermost CGEM layers of the Inner Tracker have been built, all of them tested in current mode with 5.9 keV X-rays, and equipped with GASTONE FEE.

While constructing the second CGEM layer, during DAΦNE commissioning, the beam pipe at the interaction region reached temperatures much higher than expected ($> 50°$C). For this reason on the second layer we made tests of operation at increasing temperatures showing some instability for T $> 35°$-$40°$C, due to the mechanical relaxation of the GEM electrodes. Although DAΦNE

operation at normal temperature was resumed since then, a cooling system for the interaction region was designed and tested to keep the temperature below 30°C. Moreover, to cope with possible accidents causing the mechanical relaxation of GEM foils, the third and the fourth CGEM layers have been built introducing between GEM electrodes a 300 μm support grid made of PEEK, a clean organic thermoplastic polymer(Fig. 2).

Figure 2: The PEEK grid is fixed on the kapton outside the GEM foil active area with epoxy glue.

To validate CGEM construction we have used cosmic-ray muons and a ^{90}Sr source that has been used to check each HV sector. Muon tracks at the cosmic ray stand have beem used for the measurement of cluster efficiency and spatial resolution. A test stand has been setup at the LNF with the final high voltage supply system, GASTONE, GIB and ROD boards. While testing the second CGEM layer, a correlated noise of the order of 10% was observed, analougously to what noticed for the first time on LHCb-GEMs. It has been explained as cross-talk due to the capacitive coupling between GEM3$_{bottom}$ and the readout plane. In events with large charge deposit, the current on the common GEM3$_{bottom}$ can induce signals on all the strips facing the GEM3 HV sector, originating "splash" events with high hit multiplicity. These events can be strongly suppressed by the insertion of a blocking capacitor (BC): with suitable tuning of the resistor R and capacitor C, the current induced on GEM3$_{bottom}$ flows through the BC rather than through the detector. Afterwards BCs have been mounted on all CGEM layers, the same solution adopted for the LHCb-GEMs.

In conclusion, after three years of R&D which has demonstrated the feasibility of cylindrical triple-GEM detector (CGEM) with an XV readout providing $\sigma_{r\phi} \sim 200$ μm and $\sigma_z \sim 350$ μm, completion of the KLOE-2 Inner Tracker is expected in January 2013. In fact, the three innermost CGEM layers have been built and the construction of the fourth has started. The IT insertion inside the KLOE apparatus and the integration with the DAΦNE beam pipe is planned during spring 2013.

3 Calorimeters for the KLOE upgrade

The QCALT calorimeter has been realized mostly to increase the KLOE acceptance for photons from neutral and radiative kaon decays in the drift chamber (DC). In fact, those photons crossing the DAΦNE beam pipe region can be lost due to the interactions with the focusing magnets or the beam pipe support. The calorimeters, on both sides of the IP, cover a total of 2 out of 3.6 m of the DC internal length (Fig.3, left). Fig.3, right, shows the half QCALT calorimeters whose construction has been completed in December 2012. They are constituted by 12 trapezoidal units,

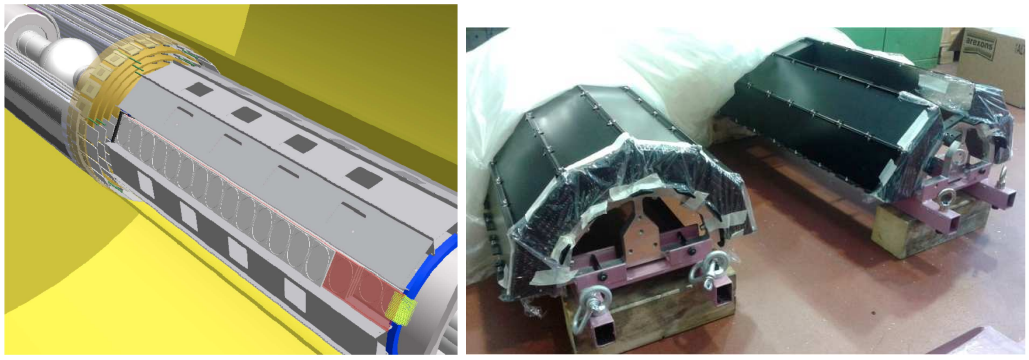

Figure 3: Inner tracker and QCALT calorimeter on the DAΦNE beam pipe (left) and half QCALT calorimeters (right).

5 layers each, with scintillator tiles interleaved with tungsten planes, for a total depth of 5.5 X_0. Each of the 18 tiles assembled in one layer has been machined to place one optical WLS fiber for light transport to a silicon photomultiplier (SiPM) of 1.2 mm diameter, at one end of the calorimeter, for a total of 2000 channels. SiPMs are custom device prepared in collaboration with the Advansid company, soldered on alumina PCBs, one PCB for each calorimeter module (80 channels). The alumina has been chosen to ensure a planarity better than 0.1 mm, and good heat dissipation. Such precision planarity is needed for optical coupling between PCB and fiber holder, mounted at the end of each module. As shown in Fig.3, right, one of the modules is kept free for the insertion of the LET (Low Energy Tagger) calorimeter, which is used as $\gamma\gamma$ tagger [9].

The electronic service of the LNF has developed custom electronics to manage the signals from many channels (Fig.4). The on–detector board contains pre-amplifiers and voltage regulator; a multifunction NIM board supplies the V_{bias} to the photodetectors with a precision of 2 mV and a stability at the level of 0.03 permill.

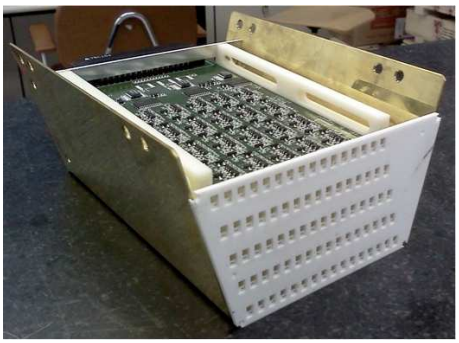

Figure 4: Cards with voltage regulators and readout circuits for the SiPMs that are mounted on the alumina (white) layer.

During construction, any single layer has been tested using a ^{90}Sr source to check all of the optical couplings between fibers and scintillator tiles. The result on the uniformity in light response was at the 10% level, fully compatible with the attenuation length of the fibers (WLS

multicladding, 1 mm diameter fibers produced by Bicron).

Tooling for QCALT installation on the beam pipe has been designed and is being realized. It consists of a mechanical system prepared to place half QCALT below beam pipe moving the other half on top of it. When the two halves are in contact, a screw system, both on modules and on steel rings, closes the calorimeter. The tooling also include a rotation system, allowing each calorimeter to reach the final angular position imposed by the LET detector.

Test of final QCALT electronics is in progress, including i) the check of the HV regulators to control their functionality, precision and stability in voltage setting; ii) a pulse test, in collaboration with the LNF Electronic Service, to check the discriminator thresholds; iii) the test of final FEE chain, with PCBs and DAQ system separately operated using both laser distributor and calorimeter modules.

The calorimeter at low polar angle, CCALT, is made by 96 LYSO crystals readout by silicon photomultipliers (SiPM). Calorimeter characterization has been obtained with the beam test at the LNF facility using 100 MeV electrons. The results on time resolution, $\sigma(t) \simeq$ 250 ps, is adequate to deal with the background rates observed in the DAΦNE interaction region, and the spatial resolution of 2-3 mm (at $\sim$15 cm from the IP) will improve event reconstruction by additional constraints on the kinematical fits. The CCALT position on the beam pipe and the calorimeter

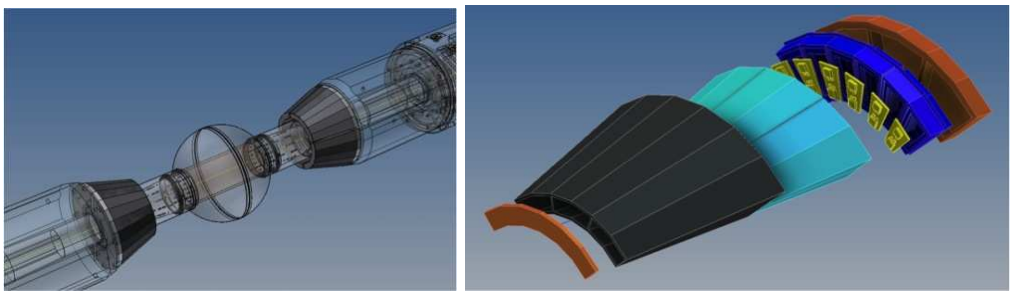

Figure 5: CCALT position on the DAΦNE beam pipe (left), and the components, PVC ring, mechanical structure, LYSO crystals, PCBs, PVC closing cap, and PVC support (right)

modularity are shown in Fig.5. In year 2012 both, the detector, and the FEE elements have been realized, including,

- LYSO crystals, produced by SICCAS in China,
- SiPMs, produced by Advansid in Italy,
- PCBs,
- mechanical structure,
- PVC holders for the readout cards containing both, SiPMs, and calibration LEDs.

The readout cards are being mounted. Crystal quality has been checked with a ^{22}Na source and each LYSO element wrapped in reflective Tyvek layers for optical decoupling from the others. A final test with the assembled crystals is scheduled before the calorimeter installation on the beam pipe, by mid March 2013.

4 Results on hadron physics

The analysis of the ISR $\mu\mu\gamma$ sample for the measurement of the hadron vacuum polarization contribution to muon anomaly, has been finalized and the paper submitted to PLB at end of 2012. Most of the analysis procedure is reported on the 2011 Activity Report (this series).

We summarize recent, final results, mostly on systematics and background subtraction relating to the $\mu\mu\gamma$ spectrum. Event selection includes:

- reconstruction of at least two tracks of opposite sign, with origin at the IP and polar angle satisfying $50^\circ < \theta < 130^\circ$. The momenta satisfy $p_\perp > 160$ MeV or $|p_z| > 90$ MeV, to ensure good reconstruction and efficiency;
- polar angle $\theta_{\mu\mu}$ of the the dimuon system ($\mathbf{p}_{\mu\mu} = \mathbf{p}_+ + \mathbf{p}_-$) satisfying $|\cos\theta_{\mu\mu}| < \cos(15^\circ)$;
- computed mass for the two observed particles, as obtained from kinematical constraints assuming ISR $xx\gamma$ events, in the range $80 < m_x < 115$ MeV;
- PID estimator, $L_\pm$, which uses time of flight information and energy deposit of each charged particle in the calorimeter, compatible with muon hypothesis at least for one track.

Residual $e^+e^-\gamma$, $\pi^+\pi^-\gamma$ and $\pi^+\pi^-\pi^0$ backgrounds are evaluated by fitting the observed m_x spectrum with a superposition of Monte Carlo simulation (MC) distributions describing signal and $\pi^+\pi^-\gamma$, $\pi^+\pi^-\pi^0$ backgrounds, and a distribution obtained from data for the $e^+e^-\gamma$ background. In the ρ mass region, the fractional $\pi^+\pi^-\gamma$ yield in the $\mu\mu\gamma$ acceptance region is about 15% of the sample. To improve the MC description of the low energy m_x tail of $\pi^+\pi^-\gamma$ events in the muon peak, we apply a data/MC resolution correction, function of s_μ. This correction is evaluated from a high–purity sample of $\phi \to \pi^+\pi^-\pi^0$ events, with the results shown in Fig.6.

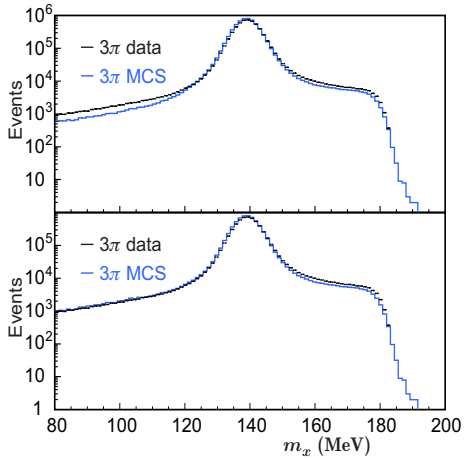

Figure 6: Data and MC m_x distributions for the $\pi^+\pi^-\pi^0$ control sample, before (upper) and after (lower) resolution correction.

Contributions from $e^+e^- \to e^+e^-\mu^+\mu^-$ and $e^+e^- \to e^+e^-\pi^+\pi^-$ processes are evaluated using the `Nextcalibur` [10] and `Ekhara` [11] MC generators. After analysis cuts, the $e^+e^- \to e^+e^-\pi^+\pi^-$ process is found to be negligible, while the $e^+e^- \to e^+e^-\mu^+\mu^-$ background contribution is between 0.6% and 0.1%, in the low $M^2_{\mu\mu}$ region and is subtracted from the data spectrum. Systematic errors in the background subtraction include: (*i*) errors on the parameters from the fit

procedure: these decrease monotonically from 0.7% to 0.1% with respect to s_μ; (*ii*) the uncertainty on the data/MC resolution corrections: about 1% in the ρ mass region, smaller at higher s_μ, negligible at lower s_μ values; (*iii*) the uncertainty on the $e^+e^- \to e^+e^-\mu^+\mu^-$ process: about 0.4% at low s_μ values, rapidly falling to 0.1% for $s_\mu > 0.5\,\mathrm{GeV}^2$. The correctness of the background estimate has been checked by two independent methods.

- We perform a kinematic fit of the two track events assuming it is a $\mu\mu\gamma$ state. The χ^2 value obtained is used as discriminant variable, instead of m_x, in the fitting procedure described above;
- we improve the π-μ separation by use of m_x, applying a quality cut on the helix fit for both tracks. This cut reduces the dipion background in the dimuon signal region by more than a factor of two.

The background fractions obtained for both cases are in good agreement with the standard procedure.

The differential $\mu^+\mu^-\gamma$ cross section is obtained from the observed event count $N_{\rm obs}$ and background estimate $N_{\rm bkg}$, as

$$\frac{\mathrm{d}\,\sigma_{\mu\mu\gamma}}{\mathrm{d}\,s_\mu} = \frac{N_{\rm obs} - N_{\rm bkg}}{\Delta s_\mu}\,\frac{1}{\epsilon(s_\mu)\,\mathcal{L}}. \tag{1}$$

where $\mathcal{L}$ is the integrated luminosity from Ref. [12] and $\epsilon(s_\mu)$ the selection efficiency. Figure 7 top, shows the measured $\mu^+\mu^-\gamma$ cross section compared with the QED calculations to NLO, using

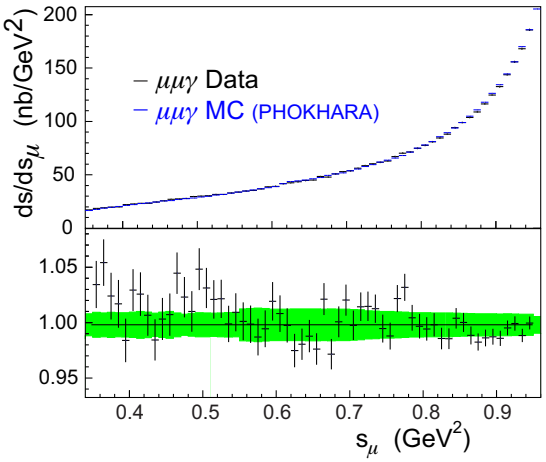

Figure 7: Top. Comparison of data and MC results for $\mathrm{d}\,\sigma_{\mu\mu\gamma}/\mathrm{d}\,s_\mu$. Bottom. Ratio of the two spectra. The green band shows the systematic error.

the MC code `Phokhara` [13]. Figure 7 bottom, shows the ratio between the two differential cross sections. The green band indicates the systematic uncertainty, experimental and theoretical, of the measured cross section. The average ratio, using only statistical errors, is 0.9981 ± 0.0015, showing a good agreement within the quoted systematic uncertainties.

From the bin-by-bin ratio between our published [14] $\pi^+\pi^-\gamma$, and the $\mu^+\mu^-\gamma$ differential cross sections described above, we obtain the bare cross section $\sigma^0_{\pi\pi(\gamma)}$ (inclusive of FSR, with VP effects removed) which is used in the dispersion integral for computing $\Delta^{\pi\pi}a_\mu$. Figure 8 shows the

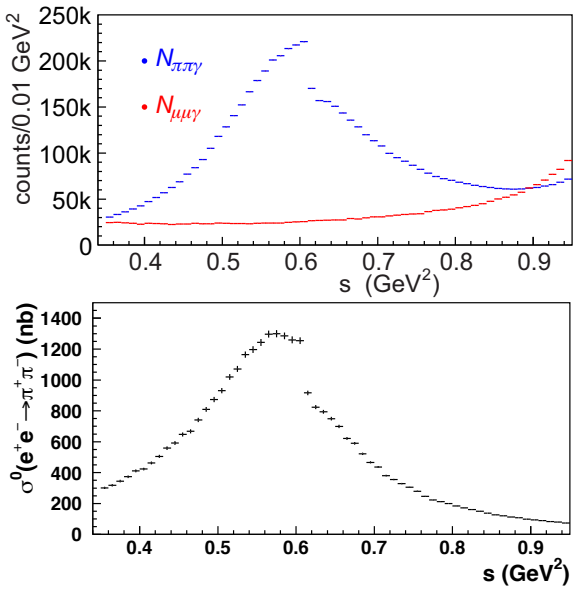

Figure 8: Square invariant mass distributions of $\pi^+\pi^-\gamma$ (blue) and $\mu^+\mu^-\gamma$ (red) events after background subtraction and data/MC corrections (top); the bare cross section from the $\pi^+\pi^-\gamma/\mu^+\mu^-\gamma$ ratio (bottom).

$\pi^+\pi^-\gamma$ and $\mu^+\mu^-\gamma$ event spectra after background subtraction and data/MC corrections (top) and the bare cross section $\sigma^0_{\pi\pi(\gamma)}$ (bottom). Systematic uncertainties on $\sigma^0_{\pi\pi(\gamma)}$ are smaller than the individual uncertainty on $\pi\pi\gamma$ and $\mu\mu\gamma$ due to correlation between the two measurements [15].

The dispersion integral for $\Delta^{\pi\pi}a_\mu$ is computed as the sum of the values for $\sigma^0_{\pi\pi(\gamma)}$ times the kernel $K(s)$, times $\Delta s = 0.01$ GeV^2 :

$$\Delta^{\pi\pi}a_\mu = \frac{1}{4\pi^3}\int_{s_{min}}^{s_{max}} \mathrm{d}\, s\, \sigma^0_{\pi\pi(\gamma)}(s)\, K(s)\ , \tag{2}$$

where the kernel is given in in Ref. [16].

Equation 2 gives $\Delta^{\pi\pi}a_\mu = (385.1 \pm 1.1_{\rm stat} \pm 2.6_{\rm exp} \pm 0.8_{\rm th}) \times 10^{-10}$ in the interval $0.35 < M^2_{\pi\pi} < 0.95\,\mathrm{GeV}^2$.

This result, with comparable total experimental uncertainty and a theoretical error reduced by about 70% with respect to our previous measurements [14], confirms the current discrepancy between the standard model prediction and the experimental value of a_μ.

5 Searches for U–boson

Some models of physics beyond the SM predict the existence of light neutral vector particles (called U–bosons) mediator of new gauge interactions under which ordinary matter is uncharged [17, 18]. Motivated by astrophysical arguments, their mass, M_U, is expected to be of order 1 GeV or lighter [19, 20]. Coupling of SM particles with the U is possible via kinetic mixing between the U and the ordinary photon [21], regulated by a dimensionless parameter ϵ, expected to be of order $\epsilon \sim 10^{-3}$ or lower.

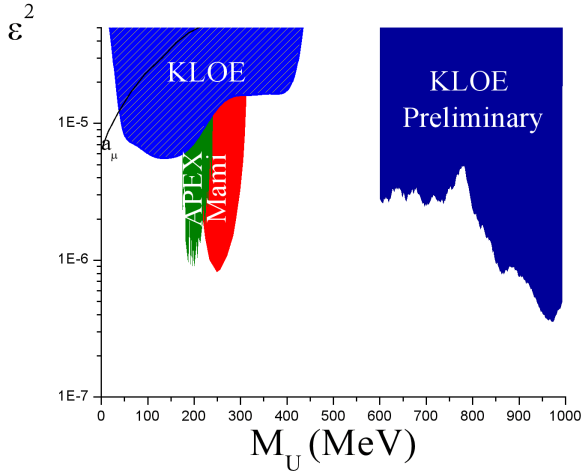

Figure 9: KLOE-2 limit in the plane M_U–ϵ^2. Results are shown for the $\phi \to \eta e^+e^-$ analysis and for the $e^+e^- \to \mu^+\mu^-\gamma$ one. The results from the APEX and MAMI-A1 experiments are also shown

These new particles can be observed as sharp resonances at M_U in the invariant mass distribution of charged lepton or pion pairs in reactions of the type $e^+e^- \to l^+l^-\gamma$ or $V \to Pl^+l^-$, where V (P) stands for any vector (pseudoscalar) meson, and $l^\pm$ can be muons, electrons or charged pions.

KLOE has searched for U boson production in both modes, using $\phi \to \eta e^+e^-$ events (a), and $e^+e^- \to \mu^+\mu^-\gamma$ events (b).

As for reactions (a), a first paper has been published [22] in which the presence of the η meson was tagged using its $\pi^+\pi^-\pi^0$ decays; a second paper has been subsequently issued [23] in which also the $3\pi^0$ decay channel of the η was used. In both cases a sample corresponding to 1.7 fb^{-1} of data at the ϕ peak was used; no evidence of the U boson is found, and the exclusion plot, in the interval $30 < M_U < 400$ MeV, has been obtained (Fig. 9).

Reaction (b) was studied on the sample used for the measurement of the ratio, $R = \sigma(e^+e^- \to \pi^+\pi^-)/\sigma(e^+e^- \to \mu^+\mu^-)$, presented in the previous section, exploiting the precision MC simulation of the QED process $e^+e^- \to \mu\mu\gamma$ reported in Fig. 7. The exclusion plot is obtained using the CL_S technique. The preliminary result shown in Fig. 9 covers the mass region $600 < M_U < 1000$ MeV and is currently being extended to 500 MeV.

If the hidden symmetry is broken by the Higgs mechanism, there is the possibility of the existence also of a non SM higgs-type particle, the h'. This can be produced together with the U–boson in reactions of the type $e^+e^- \to Uh'$ (the so called $higgs' - stralhung$ process). Then, if the h' is ligther than the U its lifetime becomes long, giving rise to event of the type $e^+e^- \to l^+l^- + missing\ energy/momentum$. These have been searched by KLOE, in the hypothesis $l = \mu$ in both, on-peak, and off-peak data. Again, no evidence of signal is found.

Results of the last two analyses are still preliminary. They are expected to be finalized in year 2013.

6 Doctoral theses completed in year 2012

1. Ivano Sarra, Tor Vergata University, Rome, Italy *Search for a dark force mediator in the $\phi \to \eta e^+ e^-$ decay at KLOE*; Supervisors: Prof. P. Picozza, Dr. S. Giovannella and Dr. S. Miscetti

2. Michal Silarski, Jagiellonian University of Krakow, Poland *Search for CP symmetry violation in the decay of K_S mesons using the KLOE detector*; Supervisor: Prof. P. Moskal

3. Cecilia Taccini, Roma-3 University, Rome, Italy *Measurement of η meson production in $\gamma\gamma$ interactions and $\Gamma(\eta \to \gamma\gamma)$ with the KLOE detector*; Supervisors: Prof. F. Ceradini and Dr. F. Nguyen

7 Ongoing Doctoral theses

1. Izabela Balwierz-Pytko, Jagiellonian University of Krakow, Poland *Study of K_S regeneration in the berillium beam pipe and in the carbon fiber wall of the drift chamber of the KLOE detector for the measurement of the cross sections at kaon momenta close to 100 MeV*; Supervisor: Prof. P. Moskal

2. Li Caldeira Balkestahl, Uppsala University, Sweden *Study of the $\eta \to \pi^+\pi^-\pi^0$ Dalitz plot with the KLOE detector for improving sensitivity on the light-quark mass ratio*; Supervisor: Dr. A. Kupsc

3. Francesca Curcianello, Messina University, Italy *Study of the $e^+e^- \to \mu\mu\gamma$ process with the KLOE detector to search for Dark photons*; Supervisors: Prof. G. Giardina, Dr. G. Mandaglio and Dr. G. Venanzoni

4. Veronica De Leo, Messina University, Italy *Study of the $e^+e^- \to \mu\mu\gamma$ process with the KLOE detector for probing vacuum polarization effects*; Supervisors: Prof. G. Giardina, Dr. G. Mandaglio and Dr. G. Venanzoni

5. Lena Heijkenskjld, Uppsala University, Sweden *Study of the $\omega \to \pi^+\pi^-\pi^0$ Dalitz plot with the KLOE detector for testing ChPT predictions*; Supervisor: Dr. A. Kupsc

6. Matteo Mascolo, Tor Vergata University, Rome, Italy *Study of the $e^+e^- \to \pi^0 e^+ e^-$ process with the KLOE detector for the measurement of the transition form factor*; Supervisors: Prof. R. Messi, Dr. D. Moricciani and Dr. D. Babusci

7. Ivan Prado Longhi, Roma-3 University, Rome, Italy *Study of the $\pi^0\pi^0$ production in $\gamma\gamma$ interactions with the KLOE detector for the measurement of the two-pion invariant mass distribution and the comparison with ChPT predictions*; Supervisors: Prof. F. Ceradini and Dr. A. Passeri

8. Jaroslaw Zdebik, Jagiellonian University of Krakow, Poland *Study of the $\phi \to \eta e^+ e^-$ Dalitz decays using KLOE data*; Supervisors: Prof. P. Moskal and Dr. S. Giovannella

8 Papers

1. D. Babusci, H. Czyz, F. Gonnella *et al. On the possibility to measure the $\pi^0 \to \gamma\gamma$ decay width and the $\gamma * \gamma \to \pi^0$ transition form factor with the KLOE-2 experiment* Eur. Phys. J. **C72** (2012) 1917

2. F. Archilli *et al.* (KLOE-2), *Search for a vector gauge boson in phi meson decays with the KLOE detector*, Phys. Lett. **B706** (2012) 251

3. D. Babusci *et al.* (KLOE), *Measurement of* $\Gamma(\eta \to \pi^+\pi^-\gamma)/\Gamma(\eta \to \pi^+\pi^-\pi^0)$ *with the KLOE Detector*, Phys. Lett. **B718** (2013) 910

4. D. Babusci *et al.* (KLOE-2), *Measurement of* η *meson production in* $\gamma\gamma$ *interactions and* $\Gamma(\eta \to \gamma\gamma)$ *with the KLOE detector*, J. of High Energy Phys. **1301** (2013) 119

5. G. Bencivenni, E. Czerwinski, E. De Lucia *et al.*, *A Time Domain Reflectometer with 100 ps precision implemented in a cost-effective FPGA for the test of the KLOE-2 Inner Tracker readout anodes*, Nucl. Inst. & Meth. **A698** (2013) 185

9 Talks and Conference Proceedings

1. S. Giovannella *et al.*, (KLOE-2) *KLOE searches on Dark Matter*, Talk at the Les Recontres de Physique de la Vallee d'Aoste, February 26-March 3 (2012), La Thuile, Italy

2. I. Sarra *et al.*, *Ricerca di Dark forces a KLOE*, Talk at the Incontri di Fisica della Alte Energie, IFAE 2012, April 11-13 (2012), Ferrara, Italy

3. A. Saputi *et al.*, *QCALT: a tile calorimeter for KLOE-2*, Talk at the 12th Pisa Meeting on Advanced Detectors, May 20-26 (2012), La Biodola, Italy

4. S. Giovannella *et al.*, *CCALT: a crystal calorimeter for the KLOE-2 experiment*, Talk at the 12th Pisa Meeting on Advanced Detectors, May 20-26 (2012), La Biodola, Italy

5. D. Domenici *et al.*, *Production and test of first layers of the KLOE-2 inner tracker*, Talk at the 12th Pisa Meeting on Advanced Detectors, May 20-26 (2012), La Biodola, Italy

6. E. Czerwinski *et al.*, (KLOE-2) *KLOE results on flavour physics*, Talk at the Fourth Capri Workshop on Theory, Phenomenology and Experiments on flavour physics, June 11-13 (2012), Capri, Italy

7. F. Bossi *et al.*, (KLOE-2) *Recent results from KLOE-2* , Talk at the 7th International Workshop on Chiral Dynamics, CD12, August 6-10 (2012), Newport News, Virginia, USA

8. I. Sarra *et al.*, (KLOE-2) *U-boson search at KLOE-2* , Talk at the International Workshop on Dark forces at Accelerators, DARK2012, October 16-19 (2012), Frascati, Italy

9. E. De Lucia *et al.*, *Production and test of first layers of the KLOE-2 inner tracker*, Talk at the 2012 Nucl. Sc. Symp. and Medical Imaging Conf., NSS/MIC 2012, Oct 19-November 3 (2012), Anaheim, California, USA

10. S. Miscetti, *Hadronic Physics at KLOE/KLOE-2* , Seminar at the Thomas Jefferson Lab, December 19th 2012, Newport News, Virginia, USA

11. M. Cordelli *et al.*, *Test and Simulation of a LYSO+APD matrix with a tagged Photon Beam from 40-MeV to 300-MeV*, J. Phys. Conf. Ser. **404** (2012) 012027; Proceedings of the 15th International Conference on Calorimetry in High Energy Physics (CALOR 2012)

12. C. F. Redmer *et al.*, (KLOE-2) *Measurement of* $\eta' \to \eta\pi\pi$ *with KLOE and KLOE-2*, EPJ Web Conf. **37** (2012) 09030; Proceedings of the 12th International Workshop on Meson Production, Properties and Interaction (MESON 2012)

13. Li Caldeira Balkestahl *et al.*, (KLOE-2) *Study of the $\eta \to \pi^+\pi^-\pi^0$ Dalitz plot with the KLOE detector*, EPJ Web Conf. **37** (2012) 09002; Proceedings of the 12th International Workshop on Meson Production, Properties and Interaction (MESON 2012)

14. M. Silarski *et al.*, (KLOE-2) *Search for the $K_s \to 3\pi^0$ decay with the KLOE detector*, EPJ Web Conf. **37** (2012) 05004 ; Proceedings of the 12th International Workshop on Meson Production, Properties and Interaction (MESON 2012)

15. F. Nguyen *et al.*, (KLOE-2) *Results and prospects on light meson spectroscopy with KLOE/KLOE-2*, Nucl. Phys. Proc. Suppl. **225-227** (2012) 121; Proceedings of the 8th International Workshop on e^+ e^- Collisions from Phi to Psi (PHIPSI 11)

16. P. Lukin *et al.*, (KLOE-2) *KLOE measurement of e^+ $e^- \to \pi\pi(\gamma)$ with initial state radiation and the $\pi\pi$ contribution to the muon anomaly*, Nucl. Phys. Proc. Suppl. **225-227** (2012) 265; Proceedings of the 8th International Workshop on e+ e- Collisions from Phi to Psi (PHIPSI 11)

17. A. De Santis *et al.*, (KLOE-2) *Recent results on CP and CPT tests at KLOE*, PoS **HQL2012** (2012) 018; Proceedings of 11th International Conference on Heavy Quarks and Leptons (HQL 2012)

18. F. Nguyen *et al.*, (KLOE-2) *Hadron physics at KLOE/KLOE-2*, AIP Conf.Proc. **1441** (2012) 347; Proceedings of the 19th International Conference on Particles and Nuclei (PANIC 11)

References

1. D. Babusci et al. (KLOE-2 Collaboration), JHEP **1301**, 119 (2013), 1211.1845
2. D. Babusci et al. (KLOE Collaboration), Phys.Lett. **B718**, 910 (2013), 1209.4611
3. F. Archilli et al. (KLOE-2 Collaboration) (2010), 1002.2572
4. A. Balla, G. Bencivenni et al., Nucl.Instrum.Meth. **A604**, 23 (2009)
5. G. Bencivenni, S. Cerioni et al., NSS CR 2008. IEEE **6**, 4666 (2007)
6. A. Balla, G. Bencivenni et al., Nucl.Instrum.Meth. **A628**, 194 (2011), 1003.3770
7. M. Alfonsi, G. Bencivenni et al., Nucl.Instrum.Meth. **A617**, 151 (2010)
8. G. Bencivenni, E. Czerwinski et al., Nucl.Instrum.Meth. **698**, 185 (2013)
9. D. Babusci, C. Bini, P. Ciambrone et al., Nucl.Instrum.Meth. **A617**, 81 (2010), 0906.0875
10. F.A. Berends et al., Comput.Phys.Commun. **136**, 148 (2001), hep-ph/0011031
11. H. Czyz, E. Nowak-Kubat, Phys.Lett. **B634**, 493 (2006), hep-ph/0601169
12. F. Ambrosino et al. (KLOE), Eur. Phys. J. **C47**, 589 (2006), hep-ex/0604048
13. H. Czyz, A. Grzelinska, J.H. Kuhn, G. Rodrigo, Eur.Phys.J. **C39**, 411 (2005), hep-ph/0404078
14. F. Ambrosino et al. (KLOE Collaboration), Phys.Lett. **B670**, 285 (2009), 0809.3950
15. P. Lukin et al., http://www.lnf.infn.it/kloe2/tools/getfile.php?doc_fname=K2PD-6.pdf&doc_ftype=docs
16. B. Lautrup, A. Peterman, E. De Rafael, Nuovo Cim. **A1**, 238 (1971)

17. P. Fayet, Phys. Lett. **B95**, 285 (1980)

18. B. Batell, M. Pospelov, A. Ritz, Phys. Rev. **D80**, 095024 (2009), 0906.5614

19. N. Arkani-Hamed, N. Weiner, JHEP **12**, 104 (2008), 0810.0714

20. M. Pospelov, A. Ritz, M.B. Voloshin, Phys. Lett. **B662**, 53 (2008), 0711.4866

21. B. Holdom, Phys. Lett. **B166**, 196 (1986)

22. F. Archilli et al., Phys.Lett. **B706**, 251 (2012), 1110.0411

23. D. Babusci et al. (KLOE-2 Collaboration), Phys.Lett. **B720**, 111 (2013), 1210.3927

LHCb

M. Anelli (Tecn.), F.Archilli (Ass. Ric.), G. Bencivenni, P. Campana,
P. Ciambrone, P. De Simone, G. Felici, G. Lanfranchi, F. Murtas,
M. Palutan, R. Rosellini (Tecn.), M. Santoni (Tecn.), A. Saputi (Tecn.),
A. Sarti (Ass.), B.Sciascia, A. Sciubba (Resp. Ass.), F. Soomro (Bors. PD)

In collaboration with "LNF-SEA"
A. Balla, M. Carletti, G. Corradi, M. Gatta

1 Introduction

The LHCb experiment 2012 data taking campaign was very succesful, with 2.2 fb^{-1} of pp collisions integrated at $\sqrt{s} = 8$ TeV. This was possible thanks to the performance of the LHC, to the luminosity leveling technique, consisting of taking data at constant instantaneous luminosity of 4×10^{32} cm^{-2} s^{-1} , and to the excellent run of the detector, which was capable to work at full efficiency far beyond its design parameters. The acquired data add up to the 1 fb^{-1} integrated in 2011 at $\sqrt{s} = 7$ TeV, leading to an unprecedented sample of b and c decays which will allow to considerably increase our sensitivity in the search of physics beyond the Standard Model (SM) in the flavor sector. Already in 2012 LHCb published several "world record" measurements in the core physics channels: the CP violation phase ϕ_s in the B_s^0 decays, the rare decays $B_s^0 \to \mu^+\mu^-$ and $B^0 \to K^*\mu^+\mu^-$, and in charm physics.

Among these, most relevant is the evidence for a $B_s^0 \to \mu^+\mu^-$ signal with $3.5\,\sigma$ significance, as discussed in sec. 2, which is the result of the joint analysis of 2011 data and $1.1\,\text{fb}^{-1}$ of the 2012 data. This eagerly awaited result, presented at HCP conference in november 2012 and recently published in Physical Review Letters [8], collecting more than sixty citations in less than two months, represents a milestone in the flavor physics landscape. The LNF team contributed substantially to this achievement, partecipating in all of the aspects of the analysis, and coordinating the effort of the international analysis working group (with G. Lanfranchi and M. Palutan serving as convenors).

In parallel, considerable efforts have been spent by the team on the muon system, covering both aspects of detector operation/maintenance and performance assessment/monitoring. On the first item, we contributed as muon piquet shifters to the daily operation of the detector during the whole data taking period, and thanks to our technical staff we could contribute also to the spare chamber reparation, to the

readout board maintenance and we took care of keeping updated the online control software. All these aspects were fundamental to achieve a reliable and efficient operation of the muon trigger, and to ensure a high data quality. On the second item, we developed and ran intensively the software needed to monitor the chamber efficiency. Moreover, we also performed a full scan of the offline muon identification performances on the whole 2011 and 2012 data sets. This study provides, as a function of the time and data taking conditions, the algorithm efficiency on true muons, as measured on J/ψ decays, and the misidentification probability of proton, kaon and pions, as measured on Λ and D decays. These calibrations have been widely used in many LHCb analyses involving muons in the final state.

Even though the physics harvest is now in full flow, the collaboration is already planning for an upgrade of the experiment, intended to collect ~ 50 fb^{-1} starting in 2019, after the long shutdown 2 of LHC. This very large sample should allow to determine several SM variables in the flavor sector to a precision comparable with the ultimate theoretical uncertainty. The LNF team will guarantee the full operation of the muon system readout in the upgrade conditions, the production of the needed spare muon chambers, and the production of new chambers based on GEM technology, on which the group has a leadership position. Detailed studies on the detector hardware performances in special high luminosity runs have been performed at LNF, which are driving the choices for the muon detector upgrade.

As demonstrated above, the LHCb LNF group has a leadeship role in many aspects, and this has been fully recognized by appointing Pierluigi Campana as spokeperson of the LHCb collaboration, with a three years mandate starting June 2011.

2 First evidence of the decay $B_s^0 \to \mu^+\mu^-$

The rare decays $B_s^0 \to \mu^+\mu^-$ and $B^0 \to \mu^+\mu^-$ are highly suppressed in the SM. Precise predictions of their branching fractions, $\mathcal{B}(B_s^0 \to \mu^+\mu^-) = (3.23 \pm 0.27) \times 10^{-9}$ and $\mathcal{B}(B^0 \to \mu^+\mu^-) = (1.07 \pm 0.10) \times 10^{-10}$, make these modes powerful probes in the search for deviations from the SM, especially in models with a non-standard Higgs sector.

Previous searches already constrain possible deviations from the SM predictions. The lowest published limits are $\mathcal{B}(B_s^0 \to \mu^+\mu^-) < 4.5 \times 10^{-9}$ and $\mathcal{B}(B^0 \to \mu^+\mu^-) < 1.0 \times 10^{-9}$ at 95 % confidence level (CL) from the LHCb collaboration using 1.0 fb^{-1} of data collected in pp collisions in 2011 at $\sqrt{s} = 7$ TeV [6]. Here we discuss the update of this search with 1.1 fb^{-1} of data recorded in 2012 at $\sqrt{s} = 8$ TeV.

The analysis of 2012 data was similar to what we did in the past (and described in Ref. [6]), but we greatly improved our estimate of the exclusive backgrounds. To avoid potential bias, the events in the signal region were not examined until all the analysis choices were finalized. The updated estimate of the exclusive backgrounds is also applied to the 2011 data [6] and the results re-evaluated.

The $B^0_{(s)} \to \mu^+\mu^-$ candidates are selected by requiring two high quality muon candidates [4) 5)] displaced with respect to any pp interaction vertex (primary vertex, PV), and forming a secondary vertex separated from the PV in the downstream direction by a flight distance selection. The surviving background comprises mainly random combinations of muons from semileptonic decays of two different b hadrons ($b\bar{b} \to \mu^+\mu^- X$, where X is any other set of particles).

Two channels, $B^+ \to J/\psi K^+$ and $B^0 \to K^+\pi^-$, serve as normalization modes. The first mode has trigger and muon identification efficiencies similar to those of the signal, but a different number of tracks in the final state. The second mode has a similar topology, but is triggered differently. The selection of these channels is as close as possible to that of the signal to reduce the impact of potential systematic uncertainties.

A multivariate analysis, based on a boosted decision tree (BDT), is used to fully exploit the kinematic and topological information of the event to discriminate the signal from the background. The BDT output is then used, together with the dimuon invariant mass, to classify the selected candidates. The BDT discriminant is trained using simulated samples consisting of $B^0_s \to \mu^+\mu^-$ for signal and $b\bar{b} \to \mu^+\mu^- X$ for background. The BDT response is defined such that it is approximately uniformly distributed between zero and one for signal events and peaks at zero for the background. The BDT response is independent of the invariant mass for signal inside the search window. The probability for a $B^0_{(s)} \to \mu^+\mu^-$ event to have a given BDT value is obtained from data using $B^0 \to K^+\pi^-$, $\pi^+\pi^-$ and $B^0_s \to \pi^+K^-$, K^+K^- exclusive decays selected as the signal events.

The invariant mass lineshape of the signal events is described by a Crystal Ball function. The peak values for the B^0_s and B^0 mesons, $m_{B^0_s}$ and m_{B^0}, are obtained from the $B^0_s \to K^+K^-$ and $B^0 \to K^+\pi^-$, $B^0 \to \pi^+\pi^-$ samples. The resolutions are determined with a power-law interpolation between the measured resolutions of charmonium and bottomonium resonances decaying into two muons. The results are $\sigma_{B^0_s} = 25.0 \pm 0.4\,\mathrm{MeV}/c^2$ and $\sigma_{B^0} = 24.6 \pm 0.4\,\mathrm{MeV}/c^2$, respectively.

The $B^0_s \to \mu^+\mu^-$ and $B^0 \to \mu^+\mu^-$ yields are translated into branching fractions using

$$\begin{aligned} \mathcal{B}(B^0_{(s)} \to \mu^+\mu^-) &= \frac{\mathcal{B}_{\rm norm}\,\epsilon_{\rm norm}\,f_{\rm norm}}{N_{\rm norm}\,\epsilon_{\rm sig}\,f_{d(s)}} \times N_{B^0_{(s)}\to\mu^+\mu^-} \\ &= \alpha^{\rm norm}_{B^0_{(s)}\to\mu^+\mu^-} \times N_{B^0_{(s)}\to\mu^+\mu^-}, \end{aligned} \tag{1}$$

where $\mathcal{B}_{\rm norm}$ represents the branching fraction, $N_{\rm norm}$ the number of signal events in the normalization channel obtained from a fit to the invariant mass distribution, $\alpha^{\rm norm}_{B^0_{(s)}\to\mu^+\mu^-}$ the normalization factors, and $N_{B^0_{(s)}\to\mu^+\mu^-}$ is the number of observed signal events.

The factors $f_{d(s)}$ and $f_{\rm norm}$ indicate the probabilities that a b quark fragments into a $B^0_{(s)}$ meson and into the hadron involved in the given normalization mode,

respectively. We assume $f_d = f_u$ and use $f_s/f_d = 0.256 \pm 0.020$ measured in pp collision data at $\sqrt{s} = 7$ TeV

The efficiency $\epsilon_{\rm sig(norm)}$ for the signal (normalization channel) is the product of the reconstruction efficiency of the final state particles including the geometric detector acceptance, the selection efficiency and the trigger efficiency. The normalization factors $\alpha^{\rm norm}_{B^0_{(s)}\to\mu^+\mu^-}$ for $B^+ \to J/\psi K^+$ and $B^0 \to K^+\pi^-$ are in agreement within the uncertainties, and their weighted average, taking correlations into account, gives $\alpha_{B^0_s\to\mu^+\mu^-} = (2.52 \pm 0.23) \times 10^{-10}$ and $\alpha_{B^0\to\mu^+\mu^-} = (6.45 \pm 0.30) \times 10^{-11}$.

In the 2012 data sample, 24 044 muon pairs with invariant mass between 4900 and 6000 MeV/c^2 pass the trigger and selection requirements. Given the measured normalization factors and assuming the SM branching fractions, the 2012 data sample is expected to contain about 14.1 $B^0_s \to \mu^+\mu^-$ and 1.7 $B^0 \to \mu^+\mu^-$ decays. The signal regions are defined by $m_{B^0_{(s)}} \pm 60$ MeV/c^2.

The expected number of combinatorial background events is determined by interpolating from the invariant mass sideband regions defined as $[4900\,{\rm MeV}/c^2, m_{B^0} - 60\,{\rm MeV}/c^2]$ and $[m_{B^0_s} + 60\,{\rm MeV}/c^2, 6000\,{\rm MeV}/c^2]$. The low-mass sideband and the B^0 and B^0_s signal regions are potentially polluted by exclusive backgrounds with or without misidentification of the muon candidates.

The first category includes $B^0 \to \pi^-\mu^+\nu_\mu$, $B^0_{(s)} \to h^+h'^-$, $B^0_s \to K^-\mu^+\nu_\mu$ and $\Lambda^0_b \to p\mu^-\overline{\nu}_\mu$ decays. The second category includes $B^+_c \to J/\psi(\mu^+\mu^-)\mu^+\nu_\mu$, $B^0_s \to \mu^+\mu^-\gamma$ and $B^{0(+)} \to \pi^{0(+)}\mu^+\mu^-$ decays. Apart from $B^0_{(s)} \to h^+h'^-$, all background modes are normalized relative to the $B^+ \to J/\psi K^+$ decay. The $B^0 \to \pi^-\mu^+\nu_\mu$, $B^0_{(s)} \to h^+h'^-$ and $B^{0(+)} \to \pi^{0(+)}\mu^+\mu^-$ decays are the dominant exclusive modes in the range BDT > 0.8, which accounts for 70 % of the sensitivity. Of these, $B^0_{(s)} \to h^+h'^-$ double misidentified events are the only contributing significantly in the signal region.

The compatibility of the observed distribution of events with that expected for a given branching fraction hypothesis is computed using the binned $\rm CL_S$ method. The method provides $\rm CL_{s+b}$, a measure of the compatibility of the observed distribution with the signal plus background hypothesis, $\rm CL_b$, a measure of the compatibility with the background-only hypothesis, and $\rm CL_s = CL_{s+b}/CL_b$. As inputs to the $\rm CL_S$ computation, we count the number of observed candidates, and compute the expected number of signal and background events in each bin of the two-dimensional space formed by the dimuon mass and the BDT output.

The expected and observed $\rm CL_S$ values for $B^0 \to \mu^+\mu^-$ as a function of the branching fraction are shown in Fig. 1. The observed $\rm CL_b$ value at $\rm CL_{s+b} = 0.5$ is 89 %, corresponding to a p-value for background-only observation of 11%. From our data we constrain the $B^0 \to \mu^+\mu^-$ branching fraction to be less than 9.4×10^{-10}, at 95% CL [8], which is the world-best limit from a single experiment.

The probability that background processes can produce the observed number of $B^0_s \to \mu^+\mu^-$ candidates or more is 5×10^{-4} and corresponds to a statistical significance of $3.5\,\sigma$. The value of the $B^0_s \to \mu^+\mu^-$ branching fraction is obtained

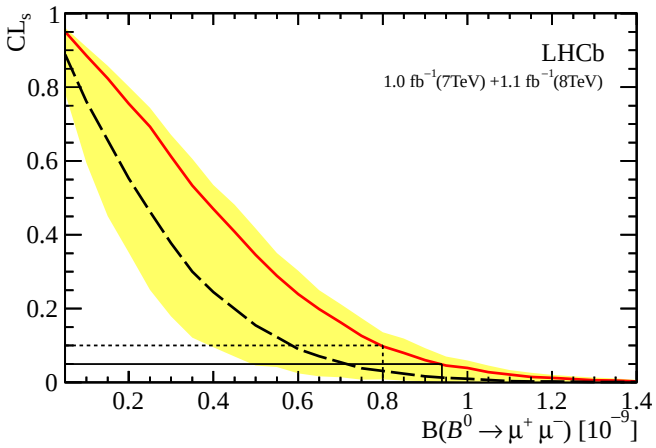

Figure 1: CL_S as a function of the assumed $B^0 \to \mu^+\mu^-$ branching fraction for the combined 2011+2012 dataset. The dashed gray curve is the median of the expected CL_S distribution if background and SM signal were observed. The shaded yellow area covers, for each branching fraction value, 34 % of the expected CL_S distribution on each side of its median. The solid red curve is the observed CL_S.

from an unbinned likelihood fit to the mass spectrum, performed simultaneoulsy in different BDT bins. We obtain [8]

$$\mathcal{B}(B_s^0 \to \mu^+\mu^-) = (3.2\,^{+1.4}_{-1.2}(\text{stat})\,^{+0.5}_{-0.3}(\text{syst})) \times 10^{-9},$$

which is in agreement with the SM expectation. This is the first evidence for the decay $B_s^0 \to \mu^+\mu^-$. The invariant mass distribution of the $B^0_{(s)} \to \mu^+\mu^-$ candidates with BDT > 0.7 is shown in Fig. 2.

After decades of experimental efforts, the present result represents a major achievement of the LHC. However the current precision on the decay rate is not sufficient to exclude contributions from new physics processes. In particular, even if strong enhancements from scalar Higgs have been already ruled out, we start to experimentally probe only now possible new physics contributions from the semileptonic operators.

Present effort by the LNF group is in the finalization of the analysis on the full 2012 dataset, adding more than 1 fb^{-1} to what used to publish the above result. All data have been reprocessed for this purpose, with a better tracking alignement and optimized calibration parameters. For what concern the analysis we're aiming at improving the signal sensitivity by means of a better performing multivariate discriminant, based on a novel algorithm and new training procedure.

3 The LHCb upgrade

The LHCb experiment, by the end of 2017, will collect ~ 5 fb^{-1} at the energy of $\sqrt{s} = 14$ TeV. However, pinning down the theoretical error on several variables on

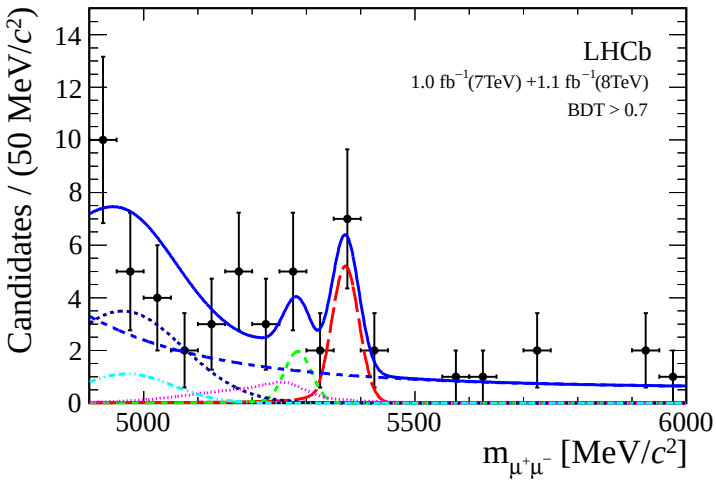

Figure 2: Invariant mass distribution of the selected $B^0_s \to \mu^+\mu^-$ candidates (black dots) with BDT > 0.7 in the combined 2011+2012 dataset. The result of the fit is overlaid (blue solid line) and the different components detailed: $B^0_s \to \mu^+\mu^-$ (red long dashed), $B^0 \to \mu^+\mu^-$ (green medium dashed), $B^0_{(s)} \to h^+h'^-$ (pink dotted), $B^0 \to \pi^-\mu^+\nu_\mu$ (black short dashed) and $B^{0(+)} \to \pi^{0(+)}\mu^+\mu^-$ (light blue dot dashed), and the combinatorial background (blue medium dashed).

which SM is able to provide theoretically precise predictions, such as γ, the angular variables of the $B^0 \to K^*\mu^+\mu^-$ decay, ϕ_s or the $B^0 \to \mu^+\mu^-/B^0_s \to \mu^+\mu^-$ ratio, will require more statistics. The main limitation of current LHCb experiment is due to the built-in maximum bandwidth of 1 MHz. Even increasing the luminosity, the efficiency for channels with hadrons will decrease, caused by the need of increasing the E_T threshold, to stay within the bandwidth limit. Consequently, the LHCb upgrade plans to remove this limitation, allowing for a fully software 40 MHz readout trigger. To achieve this challenging goal, and to perform optimally up to a luminosity of $\sim 2 \times 10^{33}$ cm^2 s^1 and at an average pile-up of ~ 4, intense planning is underway for a detector upgrade, which foresees a new vertex detector, a new tracking system and 40 MHz readout on all subsystems. The plan is to have the experiment ready to restart data taking just after the long shutdown 2 (LS2) in 2019 and to collect 50 fb^{-1} afterwards.

In preparation of the upgrade, an intense phase of RD has started, with the aim of preparing a TDR for the end of 2013. At LNF, several activities have been scheduled for this year, focussing on the muon detector.

First, in order to test the muon system performances in the upgrade conditions, special high-luminosity runs have been performed at the end of the 2012 data taking period. Here at LNF a careful analysis of these data is being performed, with the tools developed for muon chamber efficiency monitoring. The preliminary results of

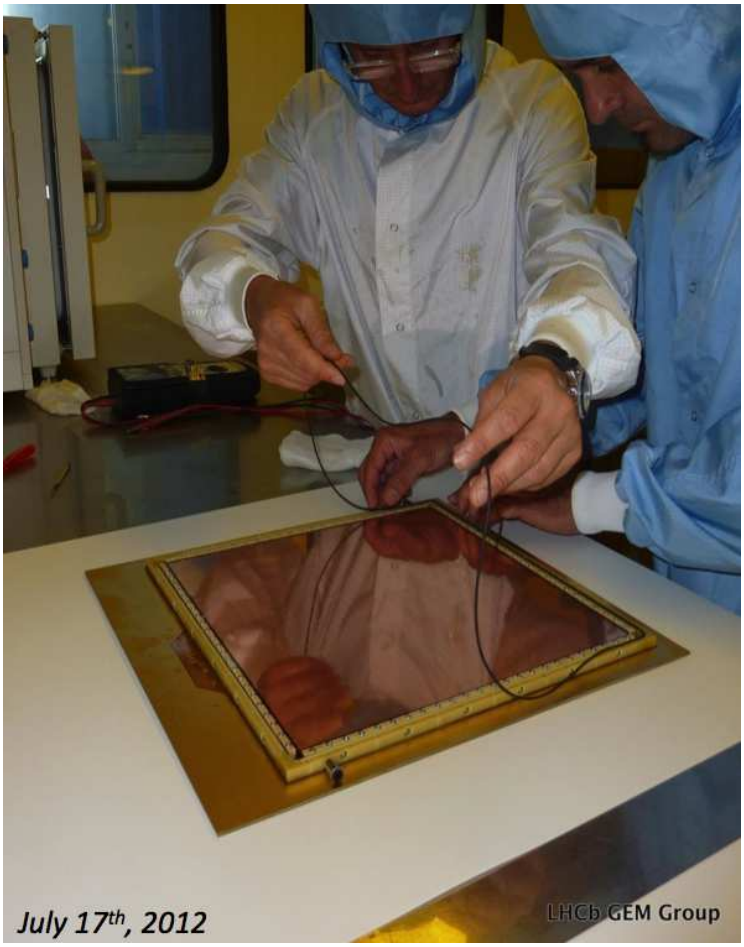

Figure 3: Assembly of a GEM detector.

this survey show a good performance of the muon detector, and suggest that the reduction of efficiency, estrapolated to the upgrade scenario, will not have dramatic effects on muon trigger performances. However, due to ageing effects, the MWPC installed in the inner regions are not adequate to stand the whole upgrade phase. For this reason, we definitely need to build new detectors: the baseline choice is triple-GEM detectors with PAD readout. Prototypes of these detectors will be built at LNF in 2013, using a novel assembly tecnique, developed in cooperation between LNF and CERN (see Fig. 3).

Besides that, additional efforts will be spent in the preparation of the new readout boards, which will be able to increase the data bandwidth towards the data acquisition system up to a design rate of 40 MHz. A dedicated RD has been scheduled this year at LNF, which aims at putting in operation one of such acquisition chains.

4 List of Conference Talks by LNF Authors in Year 2011

1. F. Archilli, "Rare heavy flavour decays at LHCb", International Conference on Heavy Quarks and Leptons 2012, Prague, Jun 2012.

2. F. Archilli, "Search for rare purely leptonic decays at LHCb" , CKM 2012, Cincinnati, Ohio, Sep 2012.

3. G. Bencivenni, A. Cardini, P. De Simone, "Operational Experience of the Triple-GEM Detectors of the LHCb Muon System: Summary of 2 years of data taking", 2012 IEEE Nuclear Science Symposium and Medical Imaging Conference, Anaheim, California, USA, Oct 2012.

4. P. Campana , "Heavy flavour physics at the LHC", Symposium "Symmetries and Phases in the Universe" 2012, Kloster Irsee, Germany, Feb 2012.

5. P. Campana , "Recent results from LHCb and future prospects" , Fifth Annual Meeting of the US LHC Users Organization, Fermilab, Batavia, Illinois, Oct 2012.

6. P. Campana , "Recent results from LHCb and future prospects", 10th International Conference on Beauty Charm Hyperons in Hadronic interactions, Wichita, Kansas, USA, Jul 2012.

7. P. Campana , "The LHCb Upgrade", XL International Meeting on Fundamental Physics, Benasque, Spain, May 2012.

8. P. Campana , "Recent results from LHCb and future prospects", Fermilab - Joint Experimental-Theoretical Seminar, Batavia, Illinois, USA, Feb 2012.

9. P. De Simone, "Heavy flavour production and spectroscopy at LHCb", 10th International Conference on Beauty Charm Hyperons in Hadronic interactions, Wichita, Kansas, USA, Jul 2012.

10. G. Lanfranchi, " CP violation and Rare Decays", 24th Rencontres de Blois on Particle Physics and Cosmology, Blois, Loire Valley, France, May 2012.

11. G. Lanfranchi, "Rare decays at LHCb", 3rd Meeting on Implications of LHC Results for TeV-scale Physics, CERN, Geneva, Switzerland, Jul 2012.

12. G. Lanfranchi, convener of the WG III *Rare Decays* at the CKM Conference, Cincinnati, Ohio, Sep 2012.

13. M. Palutan, "New results in the search for $B^0_{(s)} \to \mu^+\mu^-$ from LHCb", LHC seminar, CERN, Geneva, Switzerland, Nov 2012.

14. A. Sarti, "Rare decays at LHCb", APS April Meeting 2012: 100 Years of Cosmic Ray Physics, Atlanta, Georgia, United States, Mar 2012.

15. B. Sciascia, "Rare B decays as probe for new physics", 1st International Conference on New Frontiers in Physics, Kolymbari, Crete, Greece, Jun 2012.

16. B. Sciascia, convener of the WG I *Precise determination of* V_{ud} *and* V_{us} at the CKM Conference, Cincinnati, Ohio, Sep 2012.

17. F. Soomro, "Rare decays at LHCb", Cracow Epiphany Conference on Present and Future of B-physics, Krakow, Poland, Jan 2012.

18. F. Soomro, "Recent LHCb Results", Miami 2012, Fort Lauderdale, Florida, USA, Dec 2012.

5 Publications and internal notes

References

1. C. Adrover *et al.*, "Search for the rare decays $B_s^0 \to \mu^+\mu^-$ $B^0 \to \mu^+\mu^-$ with 1.02 fb−1", CERN-LHCb-ANA-2011-102.

2. F. Archilli, G. Lanfranchi and F. Soomro, "Searches for the lepton flavour violating decays $B_s \to e\mu$ and $B_d \to e\mu$ at LHCb", CERN-LHCb-ANA-2012-079

3. C. Adrover *et al.*, "Search for the rare decays $B_s^0 \to \mu^+\mu^-$ $B^0 \to \mu^+\mu^-$ with 1 fb−1 of 2012 data", CERN-LHCb-ANA-2012-081.

4. X. Cid Vidal *et al.*, "Performance of the Muon Identification in LHCb with 2011 data", CERN-LHCb-INT-2012-016.

5. X. Cid Vidal *et al.*, "Muon Identification efficiency and non-muon misidentification rates: 1 fb^{-1} results", CERN-LHCb-INT-2012-004.

6. R. Aaij *et al.*, The LHCb Collaboration, "Strong constraints on the rare decays $B_s^0 \to \mu^+\mu^-$ and $B^0 \to \mu^+\mu^-$", Phys. Rev. Lett. 108 (2012) 231801.

7. The ATLAS, CMS and LHCb Collaborations, "Search for the rare decays $B_{(s)}^0 \to \mu^+\mu^-$ at the LHC with the ATLAS, CMS and LHCb experiments", LHCb-CONF-2012-017.

8. R. Aaij *et al.*, The LHCb Collaboration, "First evidence for the decay $B_s^0 \to \mu^+\mu^-$", Phys. Rev. Lett. 110 (2013) 021801.

9. R. Aaij *et al.*, The LHCb Collaboration, "Implications of LHCb measurements and future prospects", CERN-PH-EP-2012-334, submitted to Eur. Phys. J. C.

NA62

A. Antonelli (Resp.), M. Moulson,
F. Gonnella (Ass. Ric.), M. Raggi (Art. 23), T. Spadaro,

In collaboration with
E. Capitolo, R. Lenci, B. Ponzio, V. Russo,
M. Santoni, S.Valeri, T. Vassilieva;
the Servizio di Progettazione Apparati Sperimentali (SPAS):
C. Capoccia, A. Cecchetti;
the Servizio di Sviluppo e Costruzione Rivelatori (SSCR):
G. Bisogni, A. Franceschi
the Divisione Acceleratori, Servizio di Vuoto:
R. Di Raddo, V. Lollo
and the Servizio di Elettronica:
G. Corradi, C. Paglia, D. Tagnani

1 The NA62 Experiment

The branching ratio (BR) for the decay $K^+ \to \pi^+\nu\bar{\nu}$ can be related to the value of the CKM matrix element V_{td} with minimal theoretical uncertainty, providing a sensitive probe of the flavor sector of the Standard Model. The measured value of the BR is $1.73^{+1.15}_{-1.05} \times 10^{-10}$ on the basis of seven detected events [1]. The goal of the NA62 experiment at the CERN SPS is to detect $\sim$100 $K^+ \to \pi^+\nu\bar{\nu}$ decays with a S/B ratio of 10:1 [2]. The experimental layout is illustrated in Fig. 1.

The experiment will make use of a 75 GeV unseparated positive secondary beam. The total beam rate is 800 MHz, providing $\sim$50 MHz of K^+'s. The decay volume begins 102 m downstream of the production target. 5 MHz of kaon decays are observed in the 65-m long fiducial vacuum decay region. Ring-shaped large-angle photon vetoes are placed at 12 stations along the decay region and provide full coverage for decay photons with 8.5 mrad $< \theta <$ 50 mrad. The last 35 m of the decay region hosts a dipole spectrometer with four straw-tracker stations operated in vacuum. The NA48 liquid krypton calorimeter [3] is used to veto high-energy photons at small angle. Additional detectors further downstream extend the coverage of the photon veto system (e.g. for particles traveling in the beam pipe).

The experiment must be able to reject background from, e.g., $K^+ \to \pi^+\pi^0$ decays at the level of 10^{12}. Kinematic cuts on the K^+ and π^+ tracks provide a factor of 10^4 and ensure 40 GeV of electromagnetic energy in the photon vetoes; this energy must then be detected with an inefficiency of $\leq 10^{-8}$. For the large-angle photon vetoes, the maximum tolerable detection inefficiency for

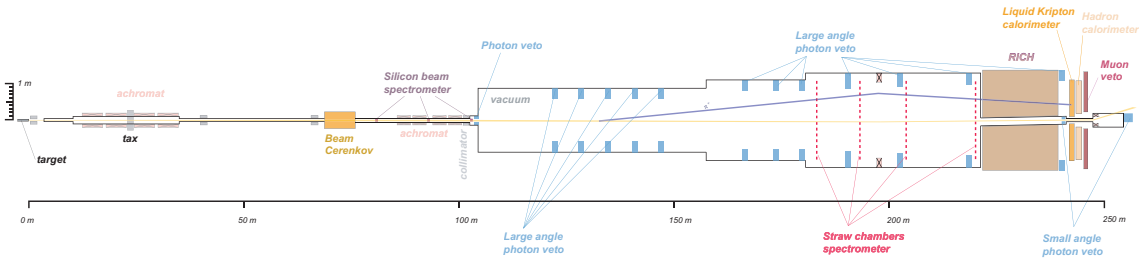

Figure 1: *The NA62 experimental layout.*

photons with energies as low as 200 MeV is 10^{-4}. In addition, the large-angle vetoes (LAVs) must have good energy and time resolution and must be compatible with operation in vacuum.

The principal involvement of the LNF NA62 group is in the design and construction of the LAV system.

In 2012, the main responsibilities of the LNF NA62 group were the following:

- Continued processing of lead-glass blocks for use in LAV stations A9, A10, and A11 (structural reinforcement, cleaning, characterization, and testing).
- Assembly and transport to CERN of A8 and A11.
- Production of final drawings for station A12, which is operated in air and thus of a different design from the other stations.
- Installation of the first 8 stations into the NA62 beamline.
- Vacuum-testing and measurement of outgassing for the stations installed.
- Mass production and testing of the LAV front-end electronics boards.
- Commissioning of the electronics for the first 3 stations.
- Development of level-zero trigger firmware for the LAV system.
- Coordination of the NA62 Photon Veto working group.

2 Large-Angle Photon Vetoes

The LAV design is based on the reuse of the lead-glass blocks from the central part of the OPAL electromagnetic calorimeter barrel [4]. The blocks are made of SF57 lead glass and have an asymmetric, truncated square-pyramid shape. The front and rear faces of the blocks measure about 10×10 cm^2 and 11×11 cm^2, respectively; the blocks are 37 cm long. The modules are read out at the back side by Hamamatsu R2238 76-mm PMTs, coupled via 4-cm cylindrical light guides of SF57. The LAV system consists of 12 stations. The diameter of the stations increases with distance from the target, as does the number of blocks in each, from 160 to 256, for a total of about 2500 blocks. Each station consists of four or five rings of blocks, with the blocks staggered in azimuth in successive rings. The total depth of a five-layer station is 27 radiation lengths. This structure guarantees high efficiency, hermeticity, and uniformity of response. The final design for the first five stations is illustrated in Fig. 2, left.

2.1 LAV construction and installation at CERN

The first LAV station, ANTI-A1, was constructed in 2009 and served as a prototype; three more of the upstream LAV stations, ANTI-A2, A3, and A4, were built at LNF during 2010. In 2011, with the construction of A5, the series of stations of small diameter was completed. Stations A6 and A7, of intermediate diameter, were also constructed in 2011 [5]. Following the delivery of A7 to CERN in early 2012, stations A8 and A11 were constructed and delivered. A11 was the first station of large diameter to be completed and required the development of new technical solutions for aspects of the cabling and assembly. As of the end of 2012, 9 of the 12 stations have been completed and delivered to CERN. So far during the construction of the LAV detectors, more than 1760 lead-glass blocks from the OPAL electromagnetic calorimeter have been processed (structural reinforced, cleaned, characterized, and tested), corresponding to $\sim 70\%$ of the total to be used in NA62.

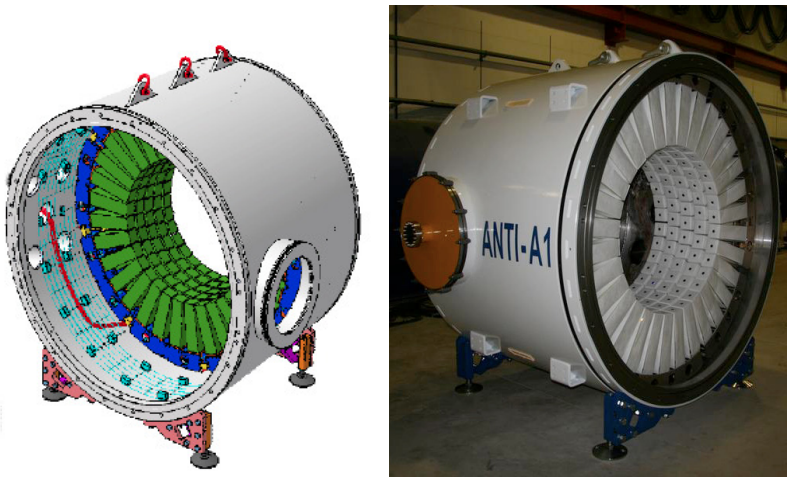

Figure 2: *Left: Design study for the upstream LAV stations. Right: Photograph of the prototype ANTI-A1.*

Much progress has also been made on the mechanical design for stations A9 and A10. Since these two stations will be operated in the vicinity of the NA62 spectrometer magnet, the vacuum vessels in which they are housed must be constructed from high-quality, non-magnetic stainless steel. In 2012, significant effort was dedicated to identifying and procuring an appropriate grade of non-magnetic stainless steel, and to developing techniques for its machining and welding. The contract for the fabrication of the vessels for A9 and A10 was awarded to Fantini SpA in mid-2012, with whom this work was carried out in collaboration. Construction of the A9 vessel was begun in September and for the A10 vessel shortly thereafter. These vessels are expected to be delivered to Frascati during the first half of 2013.

By the end of 2012, the basic design of the A12 station was completed. In particular, the arrangement of the blocks, the mechanical structure, and the basic cabling scheme were all finalized. The design of the A12 station, illustrated in Fig.3, is different from that of the other 11 stations in many important aspects: it is operated in air rather than in vacuum, it is modular rather than monolithic because of its large size, and its installation into the closed space at the downstream end of the beamline will require a delicate insertion procedure.

Also in 2012, stations A1 to A8 were installed in the beamline and vacuum tested. A11 was not installed only because the beam line is not yet ready at the installation point. The installation required a total of 26 person-weeks of continuous presence at CERN. In August, stations A1 to A3 were cabled, equipped with front-end electronics and digital readout cards, and read out with the NA62 data acquisition system in preparation for the first NA62 technical run, which took place in November 2012 (see Fig. 6).

3 LAV readout

The LAV system will mainly detect photons from kaon decays, as well as muons and pions in the beam halo. For each incoming particle, the veto detectors are expected to provide a time measurement with $\sim$1 ns resolution and an energy measurement of moderate precision (of order 10%). The system must be able to operate with thresholds of a few millivolts, well below the signal amplitude for minimum-ionizing particles (MIP) traversing the blocks, in maintain the detection efficiency as high as possible for muons and low energy photons.

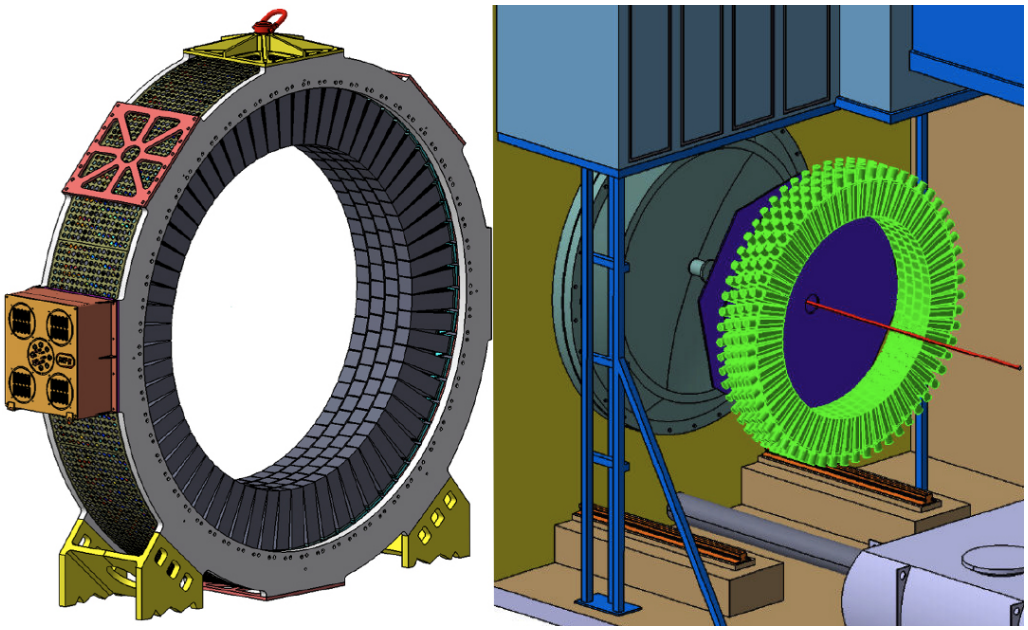

Figure 3: *The LAV ANTI-A12 station (left) and its insertion point in the NA62 experimental hall (right).*

Because of the intrinsic time resolution of the lead-glass blocks (<1ns) and the rise time of the Hamamatsu R2238 PMTs (∼5 ns), the requirements on the precision of the time measurement are not stringent. On the other hand, the amount of energy deposited in the LAV stations from photons from π^0 decays spans a very wide range, from 10 MeV up to 30 GeV. Using the measured average photoelectron yield of 0.3 p.e./MeV and a nominal gain of $1 \cdot 10^6$ for the R2238 PMT, one expects a signal charge of ∼4.5 pC for a MIP, corresponding to a signal amplitude of ∼20 mV on a 50Ω load. At the upper end of the photon energy range, signals from 20 GeV showers can reach an amplitude of 10V. The readout chain for the LAV stations consists of two different types of boards

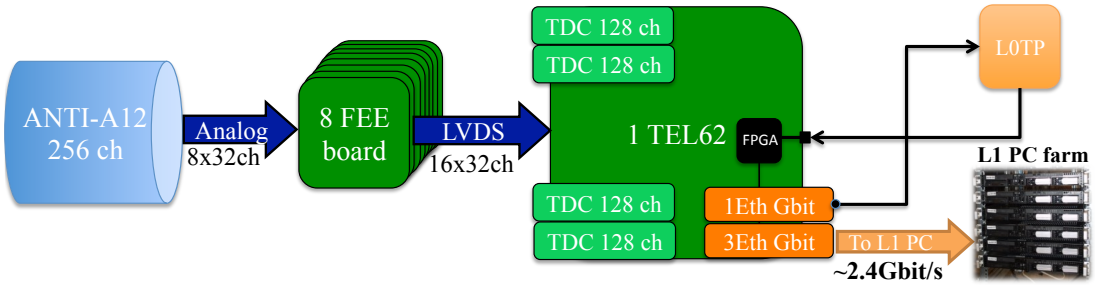

Figure 4: *The LAV readout scheme. The ANTI-A12 station has been used as example.*

(see Fig. 4): a dedicated front-end board developed for the LAV detector, and a common digital readout board called TEL62, used by most of the NA62 detectors. The LAV front-end board splits the analog signal from the PMT into two copies and converts each into a logical LVDS signal, using two comparators with independently adjustable thresholds. The duration of the LVDS pulses is

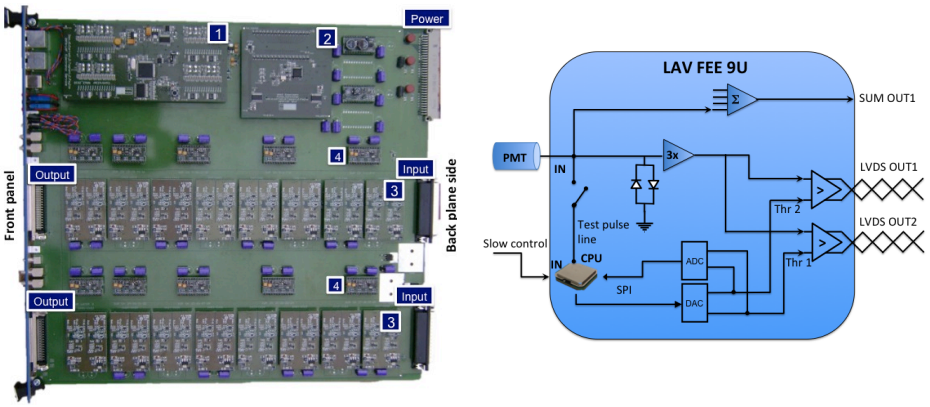

Figure 5: *The LAV front end board (left) and its block diagram (right).*

equal to the time during which the analog signal is above the programmed threshold. The LVDS logic signals are sent to the TEL62 readout board, in which a custom-designed TDC mezzanine converts each signal into digital leading and trailing times. The FPGAs on board the TEL62 are used to correct raw hit times for slewing and to produce a level-zero (L0) trigger primitive (see Fig. 5), which is sent to the L0 trigger processor using a dedicated gigabit Ethernet interface. Upon receiving a L0 trigger request, the TEL62 sends its buffered data to the level-one (L1) PCs over three additional gigabit Ethernet interfaces. The whole LAV system has ~ 2500 analog input channels and ~ 5000 digital output channels in total. The system is designed to sustain hit rates of up to 100KHz per channel and to be able to transmit a data volume to the L1 PC farm of up to 2.4 Gbit/s for each station.

3.1 LAV front-end electronic board

Since 2010, the LNF group has been responsible for the design and construction of the front-end electronics for the large-angle veto system. The basic idea is to exploit the time-over-threshold technique to measure the signal charge over a broad interval. A custom 9U board designed by the LNF Servizio di Elettronica converts the analog signals from the PMTs into logical LVDS signals of equivalent width, as described above. The LAV front end board is implemented on a 9U VME standard layout with the J1 power connector only at the top of the backplane side. No VME bus line is connected to the board; only custom ± 7.5 V power lines are used. At the bottom, the 32 analogue inputs are connected to the board using two DB37 connectors (see fig 5). The signal from each analog input channel is discriminated at two different, programmable levels to produce two logical outputs. The resulting 64 LVDS outputs are available on two SCSI2 connectors placed on the front panel of the board for connection to the TDCs. Analog sums of groups of 4 and 16 channels are provided on $8 + 2$ LEMO00 connectors for monitoring of the analog signals. Communications with the board (e.g., for threshold programming) are managed by the CAN-Open protocol via two RJ-45 connectors. To simplify maintenance and reduce costs, the board has a modular structure. The 9U motherboard manages input, output, and power distribution while all other functions are implemented on mezzanines of four different types. A detailed description of each mezzanine can be found in [6]. Five prototype 9U boards complete with their mezzanines were assembled and tested in 2011.

The year 2012 was dedicated to the mass production and testing of LAV front-end boards. One-hundred fully equipped boards have been produced, for a total of 1600 time-over-threshold

mezzanines. Thirty boards were tested and characterized in advance of the NA62 technical run in November 2012 (see Fig. 6). The characterization and testing was performed at LNF using the automatic system described below. Twenty-six of these were delivered to CERN and installed for the technical run.

4 Testing LAV front-end boards

In order to test and characterize the 100 LAV front-end boards, an automated test stand was set up at LNF at the beginning of 2012.

4.1 Test setup

A pulse generator (Agilent 81110A) is used to generate test signals with a fixed rise time of 5 ns, a fall time of 16 ns, and variable amplitude. The signal is passively split into 32 copies and fed into the input DB37 connectors of a front-end board. The 64 LVDS outputs are connected to a VME commercial board (CAEN V1190B), which makes use of the same TDC ASIC as the actual TEL62 readout (HPTDC). The digital data from the TDCs are collected through a VME controller (CAEN V1718) and stored on a PC. The PC additionally sets the threshold values on the front-end boards via USB, and varies the amplitude of the signals from the pulse generator via GPIB. The procedure is fully automated; a complete test of a front-end board takes about 15 minutes.

4.2 Test results

Minimum threshold and time resolution measurements are performed for each board.To determine the minimum threshold, the amplitude of the input signal is varied over the range from 5 mV up to 20 mV. The threshold is set to the nominal value of 2 mV. This is the lowest value at which the noise rate is less than 100 Hz on each channel. The efficiency for each channel is measured as the number of pulses detected divided by the number delivered. An example of the result of this measurement is shown in Fig. 6, left. The minimum threshold is defined as the smallest value of the signal amplitude for which the efficiency is greater than 95%, as illustrated in the figure by the dashed red lines.

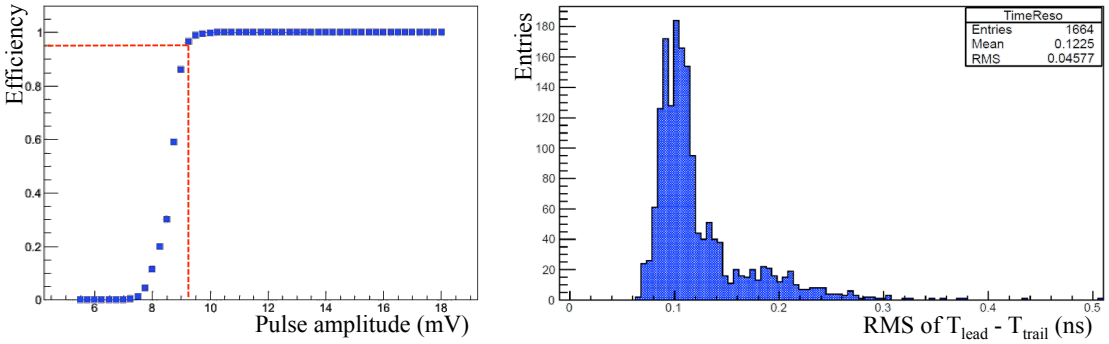

Figure 6: *Left: threshold profile. Right: distribution of the RMS of repeated time measurements of a probe signal, performed with every channel. The probe signal has an amplitude of 100 mV and a fixed width of 30 ns to within 40 ps RMS.*

The time resolution is obtained by performing repeated measurements of the time difference between the leading and the trailing edges of a test input signal. The test signal is supplied by a pulse generator with a width of 30 ns and an RMS variation of less than 40 ps. The time resolution is then evaluated as the RMS of the distribution of the leading-trailing time difference. The distribution of the resulting values of the time resolution, for all channels on 26 boards, is shown in Fig. 6, right. Most channels have a time resolution on the order of 100 ps. The tail towards higher values is due to noisy channels that are still under study. If needed, the performance of these channels can be improved by replacing the noisy ToT mezzanines, thanks to the modular design of the front-end board.

5 LAV trigger-generating firmware

For all of the NA62 detectors, the digital readout is based in the TEL62 board [7], which collects the data from TDC mezzanines and transfers them to the L1 PC farm via a gigabit Ethernet link upon receipt of a L0 trigger. Some of the detector subsystems, including the LAVs, must also generate the L0 trigger primitives. An L0 primitive is the value of the time at which some specific physics event occurred. To recognize this event and generate the primitive requires the development of detector-specific firmware for the FPGAs on board the TEL62s. In the case of the LAVs, the event which causes an L0 primitive to be generated is simply the receipt of a signal crossing both the low and high thresholds on the same block.

In 2012, the firmware to generate the L0 primitive for the LAVs was developed at LNF. The data stream for L0 primitive generation is independent of and parallel to that for the acquisition of LAV data. As a first step, events are distributed among different FIFOs, one for each low and high threshold channel. While the FIFOs are filled, a finite state machine searches for an event, i.e., a block with both thresholds crossed. Once the two hits are associated, the event time is determined, with slewing (time-walk) corrected according to the following formula:

$$t = t_{low} - \frac{(t_{high} - t_{low}) \cdot t_{low}}{V_{high} - V_{low}}$$

where V_{high} and V_{low} are the high and low threshold voltages and t_{high} and t_{low} are the respective crossing times. Events occurring within a specific time window (programmable up to ~ 25 ns) are then grouped together to form a cluster whose time is calculated as the average of single times. Finally, the time values of the clusters are sorted and delivered to the last firmware block to build the trigger primitives and send them to the experiment's L0 trigger processor.

6 NA62 Technical Run

The first NA62 technical run was carried out in November 2012. The goal of this run was to test the full readout chain and data acquisition system. The detectors involved in the test were the charged and neutral hodoscopes from NA48 (CHOD and NHOD), the charged-particle veto (CHANTI), LAV stations A1 to A3, muon vetoes (MUV) 1 to 3, the small-angle photon veto (SAC), and the beam Cerenkov counter (CEDAR). The LAV front-end boards were used to read out most of the detectors involved in the test. The 26 LAV front-end boards available were installed in the readout chains of the CHOD (4 boards), NHOD (1), LAV (15), MUV (4), SAC (1), and CHANTI (1). The summed analog outputs from the front-end boards used to read out the CHOD and NHOD were used to produced a one-track L0 trigger signal for all detectors for the entire run.

During the technical run, three complete LAV stations were powered up with the definitive HV systems and data were acquired with the final acquisition chain with muon and kaon beams. The entire readout chain was tested, with data recorded in the L1 PC farm. The data taken

during the technical run were used to verify that all channels and the associated electronics for LAV stations 1 to 3 were fully operational.

7 Conference talks by NA62 LNF members

- A. Antonelli: Vulcano Workshop 2012 - Frontier Objects in Astrophysics and Particle Physics.
  Vulcano (ME), Italy, 28 May - 2 June 2012.
  Talk: "NA62 Experiment".
- M. Moulson: XVth International Conference on Calorimetry in High Energy Physics.
  Santa Fe NM, USA, 4 - 8 June 2012.
  Talk: "The NA62 large-angle photon veto system".
- T. Spadaro: VII International Workshop on Chiral Dynamics (CHIRAL2012).
  JLAB, Newport News, VA, USA, August 6 - 10, 2012.
  Talk: "ChPT studies at NA62".
- A. Antonelli: 20th Int. Conf. on SUSY and Unification of Fundamental Interactions.
  Peking University, Beijing, China, 13 - 18 August 13 2012.
  Talk: "Search for New Physics at NA62".
- F. Gonnella: Topical Workshop on Electronics for Particle Physics.
  Oxford (Oxfordshire), United Kingdom, 17 - 21 September 2012.
  Poster: "Performance of the NA62 LAV front-end electronics".
- M. Moulson: Particle Physics Seminar, Columbia University.
  New York NY, USA, 3 October 2012.
  Talk: "The NA62 experiment: Rare kaon decays at the CERN SPS".
- M. Raggi: Quark Confinement and the Hadron Spectrum X.
  Munich, Germany, 8 - 12 October 2012.
  Talk: "ChiPT tests at NA62".

References

1. E949 Collaboration, A. Artamonov *et al.*, Phys. Rev. Lett. **101**, 191802 (2008).
2. F. Hahn *et al*, NA62 Technical Design Document, NA62-10-07 (2010).
3. NA48 Collaboration, V. Fanti *et al.*, Nucl. Instrum. Meth. A **574**, 433 (2007).
4. OPAL Collaboration, K. Ahmet *et al.*, Nucl. Instrum. Meth. A **305**, 275 (1991).
5. F. Ambrosino *et al.*, arXiv:1111.4075 [physics.ins-det].
6. A. Antonelli *et al.*, JINST **8**, C01020 (2013)
7. B. Angelucci *et al.*, JINST **7** (2012) C02046.

The Super$B$ Project

M. Beretta, R. de Sangro, G. Felici, G. Finocchiaro (Resp.),
C. Gatti, S. Lauciani, A. Martini, P. Patteri, I. Peruzzi (Ass.), M. Piccolo, M. Rama, E. Vilucchi

In collaboration with:
E. Capitolo (SPECAS), M. Gatta (SELF)

1 Introduction

Motivated by the enormous impact shown by the B Factories on Flavour Physics and in several other areas, an Italian led, INFN hosted, collaboration of scientists have worked together to design and propose a high luminosity asymmetric B-Factory project. This project, called Super$B$, exploits a novel collision scheme based on very small beam dimensions and betatron function at the interaction point, on large crossing and Piwinsky angle and on the "crab waist" scheme [1]. This approach allows to reach a luminosity of $10^{36}\,\mathrm{cm}^{-2}\mathrm{s}^{-1}$ and at the same time overcome the difficulties of early super e^+e^- collider designs, most notably very high beam currents and very short bunch lengths. The wall-plug power and the beam-related background rates in the detector are therefore kept within affordable levels.

In the course of the years Super$B$ has evolved into a full-fledged project, with a Conceptual Design Report published in 2007 [2], progress reports on the Physics potential [3], on the detector [4] and on the accelerator design [5] in 2009 [3] and a formal collaboration structure set up in 2010 with hundreds of members from several countries. All aspects of the project, physics potential, accelerator design, detector design, successfully passed several international reviews setup by INFN. In 2010 Super$B$ was inserted in the Italian Research Ministry National Research Plan as Flagship Project, and a good fraction of the required funds were allocated, although not the full amount. The decision to build Super$B$ on the land of the University of Rome Tor Vergata led, in 2011, to the formation of the Cabibbo Laboratory consortium between INFN and TorVergata, with the explicit mission of constructing and managing a new research infrastructure for flavour physics. A ministerial cost and schedule review of the accelerator project was held in fall 2012. A combination of a more realistic cost estimates and the unavailability of funds due of the global economic crisis led to a formal cancelation of the project on Nov 27, 2012.

Despite the project cancelation, it was decided to document the huge work done by the Super$B$ collaboration and by the LNF group in particular to optimize the design of a detector capable of matching the challenges posed by the extreme project luminosity of the accelerator project in a Technical Design Report. This document (almost 500 pages long) is undergoing final review at the time of writing the present report.

2 Activities in the LNF Group

The LNF group has been involved in the design of the Super$B$ Drift Chamber with major responsibilities. In particular, a member of the group is co-convening the general Super$B$ DCH group, which includes other Italian (Lecce University and INFN, RM3 University and INFN), as well as several Canadian Institutions. Another member of the LNF grup is convening the *Physics Tools* and the *Detector Geometry Working Groups* (see secs. 4).

3 The Super$B$ Drift Chamber

The Super$B$ Drift Chamber (DCH) is the main tracking detector of the Super$B$ experiment. Immersed in a 1.5 T solenoidal magnetic field, the DCH provides several position measurements along the track for a precise reconstruction of the particle momentum. It also measures the ionization energy loss used for particle identification. In fact, the DCH is the primary device in Super$B$ to measure velocities of particles having momenta below approximately 700 MeV/c and, at least in the initial phase of the experiment when no forward PID device is foreseen, it is the the only particle identification device for tracks with $\vartheta \leq 25°$.

Finally the drift chamber, together with the electromagnetic calorimeter, will provide the trigger of the experiment.

The baseline of the Super$B$ tracking detector is the *BABAR* drift chamber, which was already optimized to perform measurements of B-physics events, and has been working quite well for the entire *BABAR* lifetime. In particular, the Super$B$ Drift Chamber will operate with a Helium-based gas mixture to minimize the multiple scattering contribution to the momentum resolution. The main differences, with respect to *BABAR*, relevant to the Super$B$ tracking system are:

- reduced center-of-mass boost ($\beta\gamma = 0.24$ compared to 0.56 in *BABAR*);
- higher occupancy due to electron-pair backgrounds from two-photon processes and radiative Bhabha events scattered in the tracking devices by bending/focussing elements of the machine optics; minimization of this occupancy requires thick Tungsten shields which could somewhat limit the Drift Chamber inner radius;
- possible presence in the backward region of an electromagnetic calorimeter.

The items mentioned above require a device possibly lighter in terms of radiation lengths with respect to *BABAR*, faster and with lighter endplates too. Super$B$'s lower boost also points toward a detector introducing minimal multiple scattering.

4 Development of Simulation Tools for Detector Design and Physics Studies

The design of the Super$B$ detector and the study of the physics reach of the experiment require specific simulation tools. Depending on the nature of the study, a detailed simulation (Geant4) or a fast simulation are needed. The use of the latter has been mandatory at the to perform those studies that require the generation and complete reconstruction of the physics event. A member of our group has coordinated the *Physics Tools* group, whose main goal was the development and maintainance of the simulation and analysis tools needed to perform the physics and detector studies. The core of the Super$B$ physics tools is the fast Monte Carlo (*FastSim*), which includes a simplified and flexible detector element description, a full modeling of particles interaction with the detector, the parameterization of the detector response and the event reconstruction. It also allows to plug in the machine background simulated with Geant4. FastSim has been used to perform all physics studies and a large fraction of the detector optimization studies of Super$B$.

5 Optimization of the Drift Chamber Geometry

We have made extensive simulation studies to evaluate the impact on track reconstruction and ionization energy loss measurement of a number of design choices concerning both the external structure and the internal layout. These performance studies have been carried out using the Super$B$ fast simulation tool FastSim using signal samples with both high (*e.g.* $B \to \pi^+\pi^-$), and medium-low (*e.g.* $B^0 \to D^{*-}K^+$) momentum tracks (see previous section), and concerned: radius

and thickness of the inner wall; drift chamber length and position and shape of the endcaps, both on the forward and on the backward directions; gas and wire material; layout of the stereo angles (stereo-only layers vs. axial+stereo) and the possible improvements due to cluster counting.

A side view of the drift chamber as resulting from the studies just sketched above and satisfying all the constraints from the other Super$B$ sub-detectors is shown in Fig. 1.

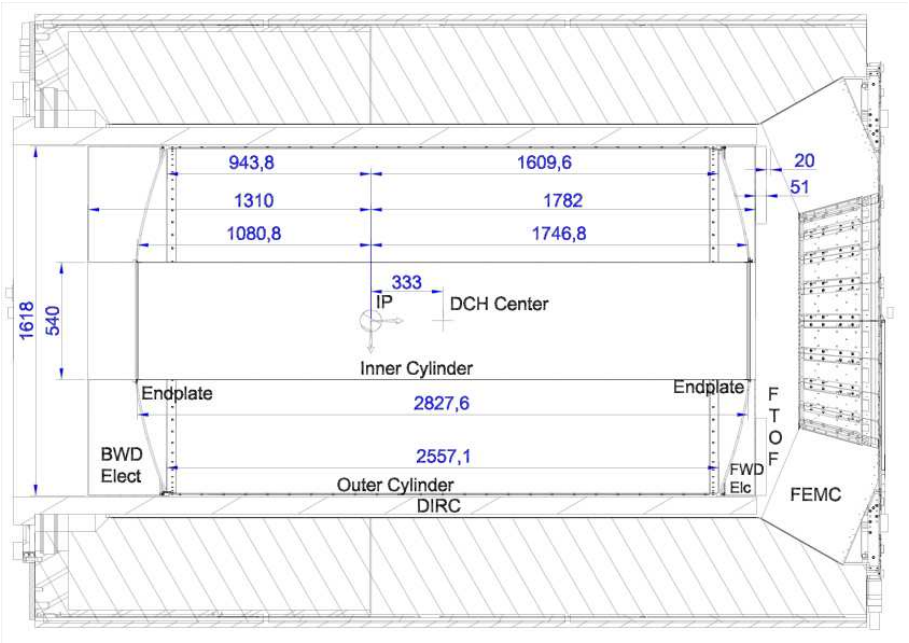

Figure 1: *Longitudinal section of the DCH with principal dimensions.*

6 R&D for the Super$B$ Drift Chamber

Various R&D programs have been carried out towards the definition of an optimal drift chamber for Super$B$. A possibility being considered to improve the performances of the gas tracker is the use of the *cluster counting* method, which in principle holds the promise of a better resolution both in the spatial and in the energy loss measurements. The ability to count the individual ionization clusters and measure their drift times strongly depends on the average time separation between them, which is, in general, relatively large in He-based gas mixtures thanks to their low primary yield and slow drift velocity. Other requirements for efficient cluster conting include good signal-to noise ratio but no or limited gas-gain saturation, high preamplifier bandwidth, and digitization of the signal with a sampling speed of the order of 1Gs/sec. Finally, it is necessary to extract online the relevant signal features (*i.e.* the cluster times), because the DAQ system of the experiment would hardly be able to manage the enormous amount of data from the digitized waveforms of the about 10 000 drift chamber channels.

During 2012 the LNF group continued the R&D program to study the feasibility of counting and measuring the drift times of the single ionization clusters. The full-length drift chamber prototype designed and built at LNF to study cluster counting in a realistic environment, including signal distortion and attenuation along 2.5 meter long wires was exposed to cosmic rays and beam test particles. The spatial resolution measured from tracks fitted through the eight layers of the detector operated in a 90%He-10%iC_4H_{10} gas mixture is shown in Figg. 2 and 3 as a function of

the drift distance. This spatial resolution matches the requirements on the needed momentum

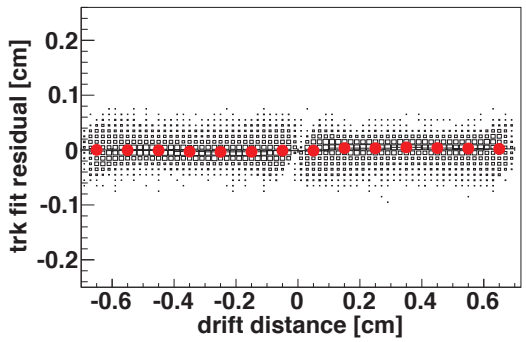

Figure 2: *Track fit residuals as a function of the drift distance from trcks fitted in the rectangular cells of the long prototype, operated in a 90%He-10%iC_4H_{10} gas mixture.*

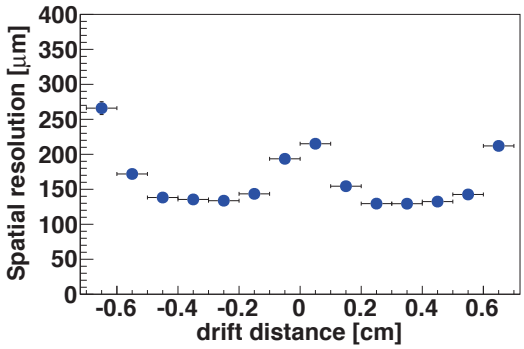

Figure 3: *Spatial resolution as a function of the drift distance from trcks fitted in the rectangular cells of the long prototype, operated in a 90%He-10%iC_4H_{10} gas mixture.*

resolution obtained with our simulation physics studies.

In Fig. 4 we show the dE/dx resolution from a truncated mean technique as a function of the number of associated hits along the tracks. Scaling this figure to the number of samples in the real Super$B$ drift chamber (40 layers) would extrapolate to a relative dE/dx resolution of 6.7%, somewhat better than in the *BABAR* drift chamber. Studies comparing the particle identification

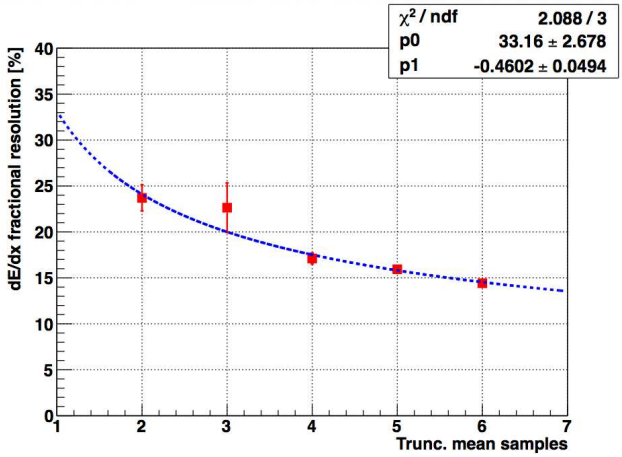

Figure 4: dE/dx *resolution as a function of the number of associated hits.*

capabilities of the detector with the standard dE/dx and the *cluster counting* are currently in progress.

7 Mechanical Design

The drift chamber mechanical structure must sustain the wire load with small deformations, while at the same time be as light as possible to minimize the degradation of the performances of the surrounding detectors. The structure is also required to ensure tightness for the gas filling the drift

volume. We opted for a structure entirely in Carbon Fiber (CF) composite, with an approximately cylindrical geometry. Given the studies mentioned in Sec. 5 the active length of the chamber has been maximized. In particular the length in the backward direction is increased with respect to *BABAR* despite the 160 mm reserved in Super*B* for the possible backward EMC to be installed at a later stage; this is possible thanks to the new design of the drift chamber front-end electronics, which require substantially less space than *BABAR*.

Detailed studies of static deformations and buckling instabilities have been performed with the aid of Finite Element Analysis programs. These studies allowed to tune the mechanical design to minimize the deformation under the wire load and the material thickness at the same time, finally leading to the drawing shown in Fig.1. Examples of the calculated buckling shapes for the endplates, inner and outer cylinder are shown in Fig. 5.

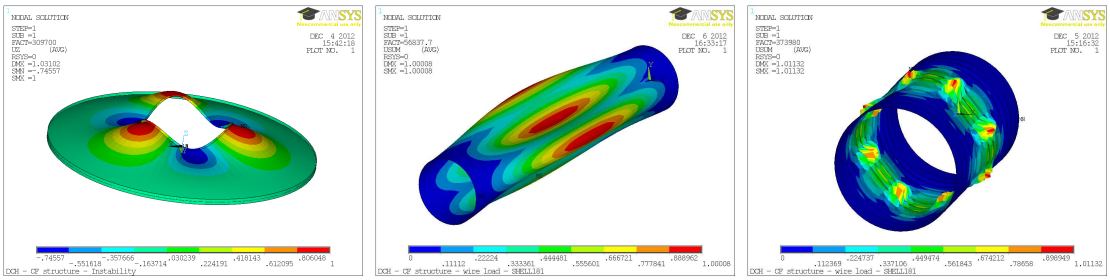

Figure 5: *Calculated first buckling shape of the endplates (left), inner cylinder (middle), outer cylinder (right).*

Details of how the the inner and outer flanges are connected to the endplates (all elements are in Carbon Fiber composite) are shoen in Fig.6.

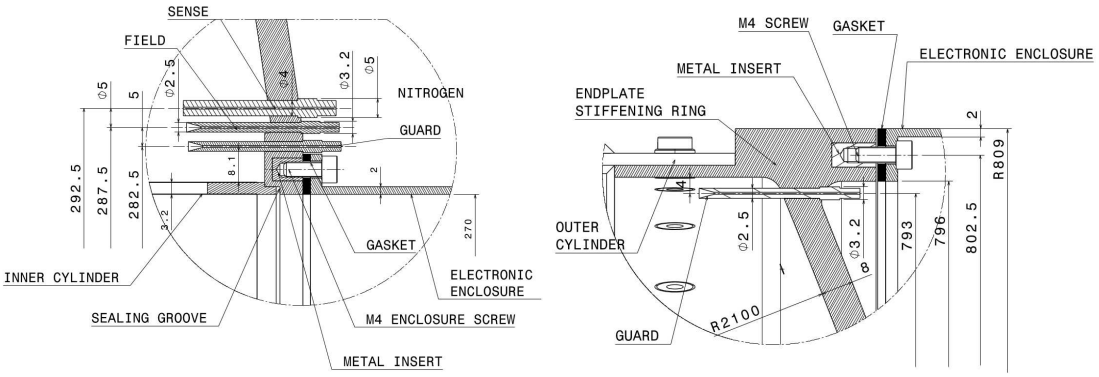

Figure 6: *Left: coupling of the DCH inner cylinder to the endplate; right: Detail of the outer flange of the DCH endplates.*

8 List of Presentations and Conference Talks in Year 2012

1. M. Rama, *Status of the SuperB project*, BEACH 2012, Wichita (KS), USA.
2. G. Finocchiaro, *SuperB Status and Prospects*, Belle2 Open Meeting, Bad Aibling, July 2012.

3. G. Finocchiaro, *Prospects at Future B Factories*, CKM 2012, Cincinnati (OH), USA.

References

1. *P. Raimondi*: Talk given at the 2^{nd} Super B-Factory Workshop, `http://www.lnf.infn.it/conference/superb06/talks/raimondi1.ppt`; *P. Raimondi, D. Shatilov, M. Zobov*: arXiv:physics/0702033v1 [physics.acc-ph].
2. *SuperB Conceptual Design Report*, `http://www.pi.infn.it/SuperB/CDR` arXiv:0709.0451v2 [hep-ex]
3. *B. O'Leary et al.: SuperB Progress Report - Physics*; arXiv:1008.1541v1 [hep-ex].
4. *E. Grauges et al.: SuperB Progress Report - Detector*; arXiv:1007.4241v1 [hep-ex].
5. *M. E. Biagini et al.: SuperB Progress Report - Accelerator*; arXiv:1009.6178 [physics.acc-ph].
6. *G. Finocchiaro: Prospects at Future B Factories*; arXiv:1212.6758 [hep-ex].

The MU2E project

M. Cordelli, S. Giovannella, F. Happacher, A. Luca (Laur.), S. Miscetti (Resp.),
A. Saputi (Tecn.), I. Sarra (Dott.), V. Stomaci (Laur.)

1 The Mu2e experiment

The Mu2e experiment, proposed at Fermilab, aims to search for the neutrinoless, coherent conversion of a negative muon into an electron in the Coulomb field of a nucleus [1]. The measurement will be expressed by the ratio of the muon-to-electron conversion rate relative to the ordinary muon capture rate on an aluminium nucleus:

$$R_{\mu e} = \frac{\Gamma(\mu^- + Al \rightarrow e^- + Al)}{\Gamma(\mu^- + Al \rightarrow \nu_\mu + Mg)} \,. \tag{1}$$

The process of muon to electron conversion is an example of Charged Lepton Flavor Violation (CLFV). While it is strongly suppressed in the Standard Model (SM), (BR($\mu \rightarrow e$) $\approx 10^{-54}$), many scenarios of physics beyond the SM, predict enhanced BRs close to the reaches of current or near future experiments. Therefore, any signal is a compelling evidence of New Physics. If no events are seen in the signal window, the experiment is designed to set an upper limit of $R_{\mu e} \leq 6 \times 10^{-17}$ at 90% C.L. in three years of running. This value represents an improvement of four orders of magnitude over the current best experimental limit $R_{\mu e}(Au) < 7 \times 10^{-13}$, from the SINDRUM II experiment [2]. The conversion of a muon to an electron in the field of a nucleus occurs coherently, resulting in a monoenergetic electron with an energy equal to the muon rest mass, apart from corrections for the nuclear recoil and the K-shell binding energy of the muon (E_e = 104.97 MeV). This distinctive signature has several experimental advantages, including the near-absence of background from accidentals and the suppression of background electrons near the conversion energy from muon decays. At the proposed Mu2e sensitivity, the most important background sources are: (1) intrinsic processes that include muon *Decay-In-Orbit* (or DIO) and radiative muon capture (RMC), (2) *delayed* processes due to particles that spiral slowly down the muon beamline, such as antiprotons, (3) prompt processes where a beam particle can arrive at the muon stopping target nearly coincident in time with the the detected electron, (4) electrons that are initiated by cosmic rays, (5) events that result from reconstruction errors in the detector.

Among the potential backgrounds, the muon *Decay-In-Orbit* is of particular concern, contributing about half the total background in the signal energy region. The process is $[\mu^- \; Al]^{1s}_{bound} \rightarrow e^- \; Al \; \nu_\mu \; \overline{\nu}_e$, with a bound muon which decays in orbit in aluminium and produces an electron that can mimic the signal: the outgoing electron recoils off the nucleus and will have exactly the conversion energy, in the limit that the neutrinos have zero energy. The bulk energy is below $m_\mu/2 \approx 52.8$ MeV, which corresponds to the Michel endpoint for free muon decay, and the nuclear recoil gives rise to a small tail that extends out to the conversion energy (Fig. 1). Since the DIO rate falls as $\approx (E_{conversion} - E)^5$ as the electron energy approaches the endpoint, this background can be overcome through adequate electron energy resolution.

The overall design of Mu2e is driven by the need to suppress potential backgrounds and to produce a high intensity, low energy muon beam that should provide around 10^{18} stopped muons on target. The desired Mu2e muon beam will be produced using the Fermilab accelerator complex, which will deliver 8 GeV protons into the *Mu2e beamline*. A pulsed structure of beam and a veto gate allow prompt beam background to die down during 750 ns, after which the detector is activated to look for μ-atom decays. The Mu2e beamline consists in an evacuated inner bore (to 10^{-4} Torr) of

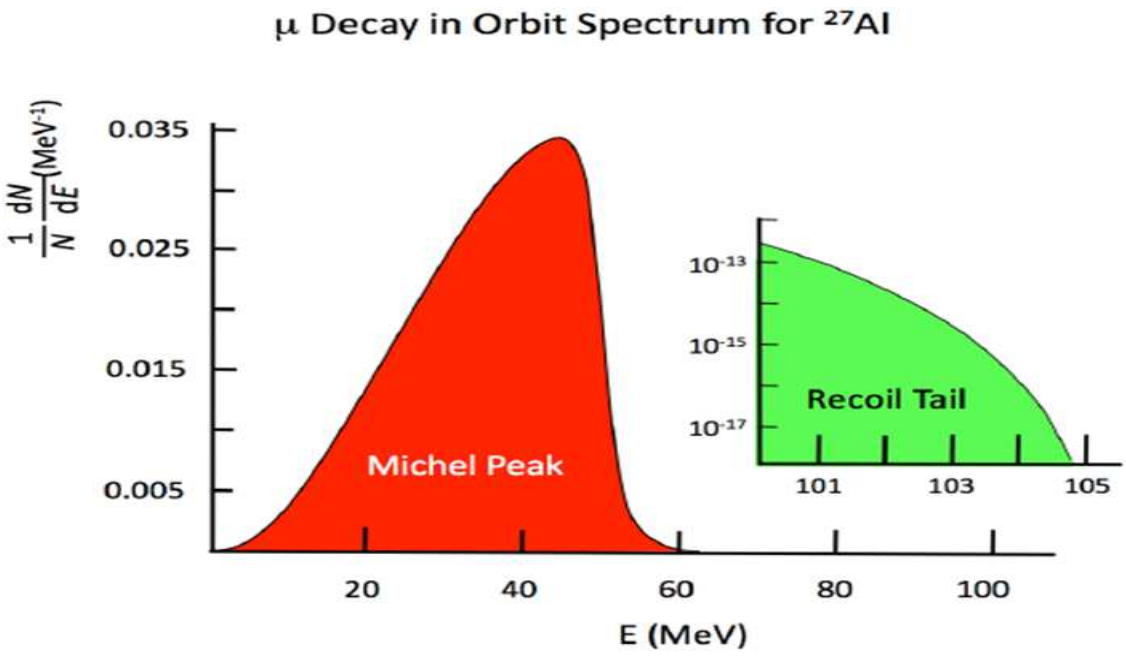

Figure 1: *The electron energy spectrum for muon decay in orbit in aluminum. The recoiling nucleus results in a small tail (blown up on the right) that extends out to the conversion energy.*

a series of superconducting solenoids which form a graded magnetic field: the Production Solenoid (PS), the Transport Solenoid (TS) and the Detector Solenoid (DS). The PS contains the production target that intercepts the proton beam. Pions produced by target interactions and the muons into which they decay are captured. The muon stopping target composed of a set of thin aluminium foils and has a graded magnetic field. The graded field increases the acceptance for conversion electrons and plays a key role in rejecting certain backgrounds. The downstream section of the DS has a nearly uniform field ($< 1\%$ non-uniformity) in the region occupied by the Tracker and the Calorimeter that accurately analyze electrons emerging from the stopping foils. The detector system must be cylindrical with a central hole where the remnant muon beam and most of the DIO electrons pass through (executing helices with small radii). Fig. 2 shows the muon beamline and the detector system. A description of the solenoidal systems and of the main backgrounds expected in the experiment can be found in Ref. [3].

The LNF group, together with INFN groups of Pisa and Udine is in charge of the construction of the calorimeter, EMC, with an assigned role of L2 management. An INFN group from Lecce is proposing an alternative system for the tracking based on a cilindrical drift chamber.

In this report, we show the design of the calorimeter, the results obtained at 100 MeV with a small size prototype and the excellent data-MC comparison for these data. We also show the simulation of the calorimeter in the Mu2e software framework and the plans for R&D and calibration.

During 2012, our group partecipated to many technical reviews at Fermilab and was in charge for the preparation of the CDR chapter on calorimetry, the cost estimate (BOE, WBS) and the schedule preparation. On June 2012, the CD-1 review meeting was succesfully held. The experiment got CD-1 approval on July 11.

2 The Mu2e electromagnetic calorimeter

The calorimeter has to match a given set of requirements driven by the need of confirming that the candidates reconstructed by the extremely precise tracker system are indeed conversion electrons.

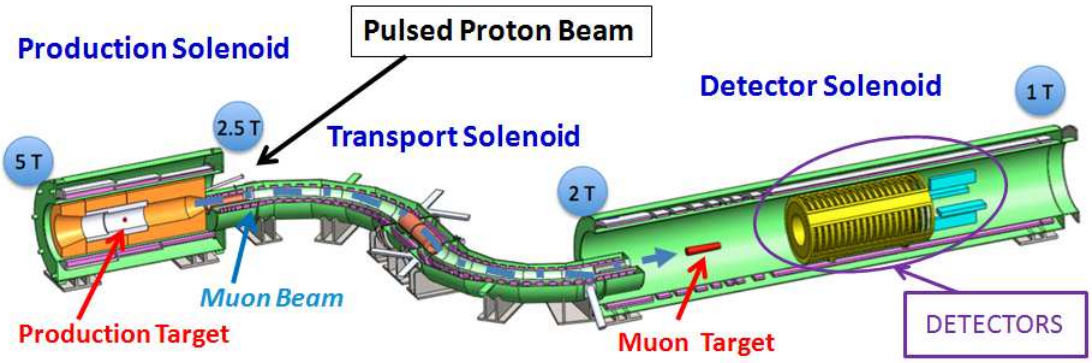

Figure 2: *An overview of the Mu2e detector.*

We therefore look for a calorimeter with a large acceptance for signal events, an excellent energy resolution $\mathcal{O}(2\%)$ and a reasonable position (time) resolution of few mm (< 1 ns) to compare the impact point (the arrival time) of the tracks on the calorimeter surface. Moreover, the calorimeter should also provide a trigger (or a reduction filter) for the experiment and be able to perform a powerful μ^-/e^- particle identification. Finally, it should be able to keep functionality in an environment where the n, p and γ background coming from muon capture processes and beam flash events deliver a dose of ~ 200 Gy/year in the hottest area. It will also need to work immersed in 1 T axial magnetic field and in a 10^{-4} torr vacuum enclosure inside the Detector Solenoid.

In order to achieve the required energy resolution at 100 MeV, a total absorption homogeneous calorimeter is needed. Among the potential materials for such a calorimeter we focused on two types of scintillating crystals: an improved version of the classical lead tungstate $PbWO_4$ which has been developed for the PANDA calorimeter [4)] and the Cerium-doped Lutetium Yttrium Oxyorthosilicate, LYSO. They both have certain desirable characteristics: they have fast scintillation decay times, similar Molière radii, reasonable mechanical properties and are not hygroscopic. There are differences, however: LYSO has a slightly lower density and a slightly longer radiation length, but has a light yield a factor of ~ 200 better than the $PbWO_4$ at room temperature. It is more radiation hard, and its scintillation light output has a much reduced dependence on temperature with respect to $PbWO_4$ crystals. The light emission spectrum of LYSO peaks at 402 nm, slightly lower that of $PbWO_4$, but both are compatible with APD readout. LYSO has been selected as the primary choice since the energy resolution terms will be dominated by leakage and intrinsic uniformity of the crystal. The noise and photostatistic term can be easily reduced to be negligible.

The proposed calorimeter consists of 1952 LYSO crystals located downstream of the tracker and arranged in four homogeneous parallelepiped vanes as shown in Fig. 3. The inner radius (36 to 39 cm) allows DIO electrons with $p_T > 55$ MeV to pass through the central hole, without registering a hit. Each vane is an array of 11×44 crystals, $(3\times3\times11)$ cm^3 each, and will be equipped with two Avalanche Photodiodes (APDs) which work well in a magnetic field. The usage of two APDs per crystal increases the light yield, provides redundancy and allows for the correct energy to be determined if a charged particle passes through one of the APDs. APD signals are amplified and

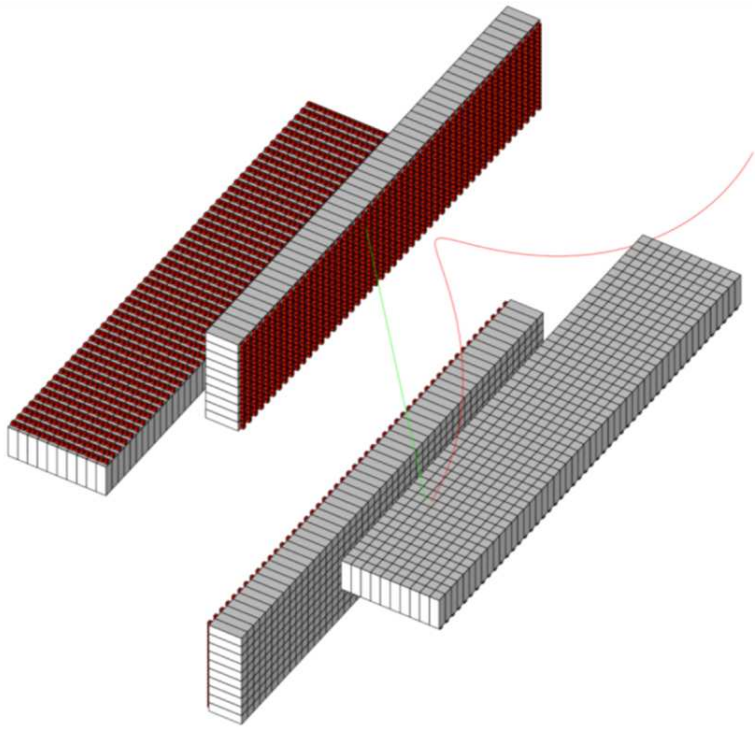

Figure 3: *The electromagnetic calorimeter is composed of four vanes. An electron, exhibiting a spiral path, hits the active face. The opposite face houses an APD based readout package.*

shaped and then readout through 200 MSPS waveform digitizers optically connected to the DAQ system. An alternative geometry that improves acceptance by using a disk-based geometry is also currently under evaluation.

An absolute calibration will be performed using a *source calibration system*. This system, successfully used in the BaBar experiment [5)], is based on an activated compound which produces the decay chain $^{19}F + n \rightarrow^{16} N + \alpha$, $^{16}N \rightarrow^{16} O^* + e^- + \nu_e$, $^{16}O^* \rightarrow^{16} O + \gamma$. The resulting energy spectrum (see Fig. 4) has a peak corresponding to the 6.13 MeV photon line from ^{16}O* and two escape peaks at 5.62 MeV, 5.11 MeV. Thus, such an approach can also provide a measurement of linearity. We plan to monitor, in a more continuous way than with the source, the variations of the crystal optical transmittance and of the APD gains by means of a laser system: blue and red light will be transported with optical fibers to the back of each LYSO crystal.

We have tested the EMC capabilities with a full simulation of signal and DIO background events in the Mu2e Framework software. One important achievement is obtained with a simple trigger algorithm that could be implemented in hardware to drastically reduce the bandwidth of DAQ system. This method just applies different threshold values to the reconstructed energy clusters and gives an efficiency of $\sim 91\%$ on signal events with a DIO reduction rate of a factor of 120 (i.e. 1.5 kHz maximum rate) with respect to tracker, at 64 MeV. This study is performed as a function of achievable calorimeter energy resolution (1, 1.5, 5 and 10 MeV), as shown in Fig. 5. We have developed a clustering method based on contiguity of fired cells. We have also developed a technique to reconstruct the impact point position along z. We get a resolution of about 1 mm for the Gaussian core (80% of the events) and 6 mm for the tails (20%). We have also studied the Pion Identification Capability of the calorimeter with respect to muons and electrons.

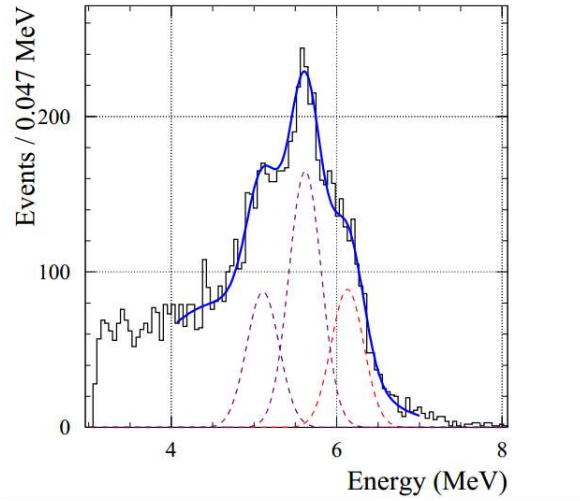

Figure 4: *Energy spectrum in a BaBar CsI(Tl) crystal irradiated with 6.13 MeV photons from an* $^{16}O^*$ *source.*

2.1 Test results with photon beams

We have tested a calorimeter prototype with a clean tagged photon beam at MAMI (Mainz Microtron) facility in Germany. The matrix prototype was built in February 2011, with transverse dimensions corresponding to ~ 2.8 R_M and longitudinal dimensions of 13-15 cm ($\sim 11 \div 12$ X_0). The prototype consists of an inner matrix of 9 LYSO crystals by SICCAS ($2 \times 2 \times 15$ cm^3) readout by APDs S8664 (10×10 mm^2 produced by Hamamatsu) and an outer matrix for leakage recovery, composed by 8 $PbWO_4$ crystal sectors (being constrained by budget), readout by standard Hamamatsu Bialcali photo multipliers of 1 inch of diameter. The realization of such a prototype has been a joint work with KLOE-2 Collaboration.

In the facility hall A2 the electron beam is converted to an intense beam of real photons through bremsstrahlung in a thin metal foil radiator. The scattered electrons in this process are momentum analyzed by plastic scintillator spectrometer which provides a determination of the energy of the associated bremsstrahlung photon with a resolution of few per mil. The tagged photon beam is excellent, having Δp(FWHM) = 1 MeV and a cross section on the calorimeter front face of about 8 mm diameter. The calorimeter prototype was installed over a movable table allowed to adjust the position of the matrix with respect to the photon beam.

We have triggered by using a coincidence between the OR signal from the inner matrix and the signal from the beam tagging system. We acquired data with a CAMAC system, reading out LeCroy ADC and TDC boards with a sensitivity of 250 fC/count and 100 ps/count, respectively. The data acquisition was writing on disk at $\sim$ 10 Hz. The temperature of the experimental hall ($\sim$ 24 °C) was continuously monitored with thermo-sensors attached to the electronics and preamplifiers and was stable at the level of ± 0.5°C.

The FEE has been developed by a collaboration of Laboratori Nazionali of Frascati and Roma 2 University. This consists in an amplifier first stage, composed by a MAR8A + discrete amplifier by Microcircuits with a gain of $\sim$ 20, and second stage buffer, made of a LMH6559 high-speed buffer by National Semiconductor. In order to minimize the gain variation we have also developed a new High Voltage board. This shows a stability of 20-30 mV, corresponding to δG/G $\sim$ 1%. Moreover it can be remotely adjusted and monitored with a sensibility of 30 mV.

We have taken data in March 2011 with the photon beam (100-500 MeV) impinging at the center of the inner crystal matrix. The same photon energy (100 MeV) was used for the position dependence scan. Pedestal and test pulse runs were performed once every few hours during the

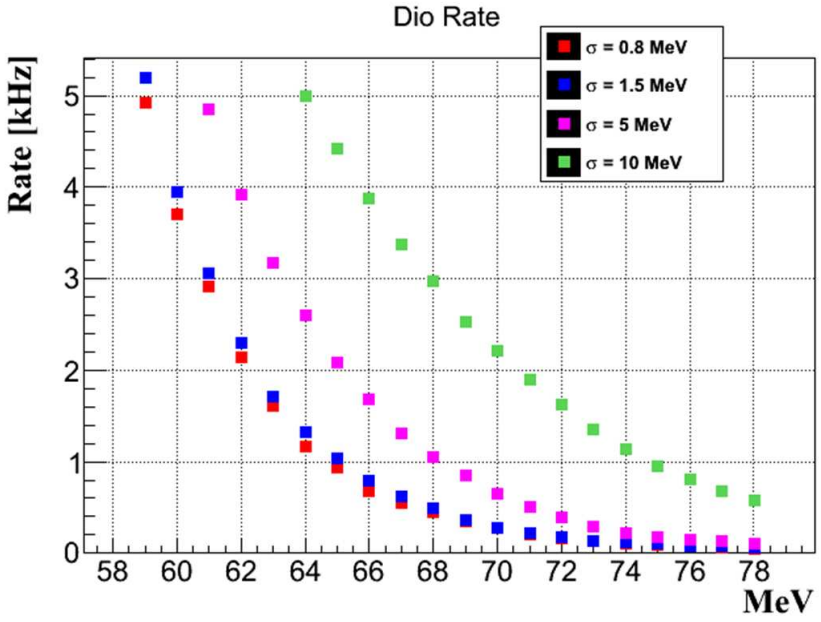

Figure 5: *DIO rate on fiducial calorimeter faces as a function of energy thresholds, for different energy resolution values.*

beam time to check the system stability. Cosmic Rays (CR) were used for the calibration. We took CR calibration data during the off-beam periods by means of an external trigger provided by a coincidence of a pair of scintillator counters. We have calibrated the calorimeter response of each channel with minimum ionizing particles (MIPs), crossing the calorimeter orthogonally to the crystal axis. The energy scale has been set looking at the linearity in response with the photon beam, and is set to 18.8 MeV per MIP consistently with average LYSO number. We get $\sigma_{\rm ped}$ of 3 (2) counts and a MIP peak around 120 (250) counts for the inner (external) crystals. The statistical precision on the peak determination is $\sim 2\%$.

The total response of the detector is defined as $Q_{TOT} = \sum_i (Q_i - P_i) \cdot 1/M_i$, where Q_i and P_i are the collected charge and the pedestal of the i-th channel and M_i is the minimum ionization peak. To understand the different terms contributing to the energy resolution, we have carried out a full simulation of the prototype based on Geant-4. Fig. 6 left shows a comparison between experimental data (black circles) and MC results (red distributions), for the energy deposit in the whole matrix, normalized to the beam energy at 100 MeV. We added a 4% Gaussian smearing for each channel in MC to reproduce data, obtaining a good data-MC agreement.

We have selected different beam energy values and fitted the corresponding energy distributions with a logarithmic Gaussian function [6], in order to quote the energy response and resolution. In Fig. 6 right, we show the energy dependence of the energy resolution which has been fitted with the following equation:

$$\sigma_E/E = a/\sqrt[4]{E[GeV]} \oplus b/E[GeV] \oplus c\,. \qquad (2)$$

For experimental data, we found the stochastic term, a, to be $2.1 \pm 0.1\%$ and the constant term, c, to be $3.6 \pm 0.3\%$. The noise term b is practically negligible. The observed energy resolution (black points) well agrees with the expected one from MC with the 4% additional smearing (red points). Pink points refer to MC results without the degradation, which is believed to be due to the large variation in longitudinal uniformity. Longitudinal uniformity is an important specification for meeting the overall energy resolution goals. The calorimeter group has devised a method (involving

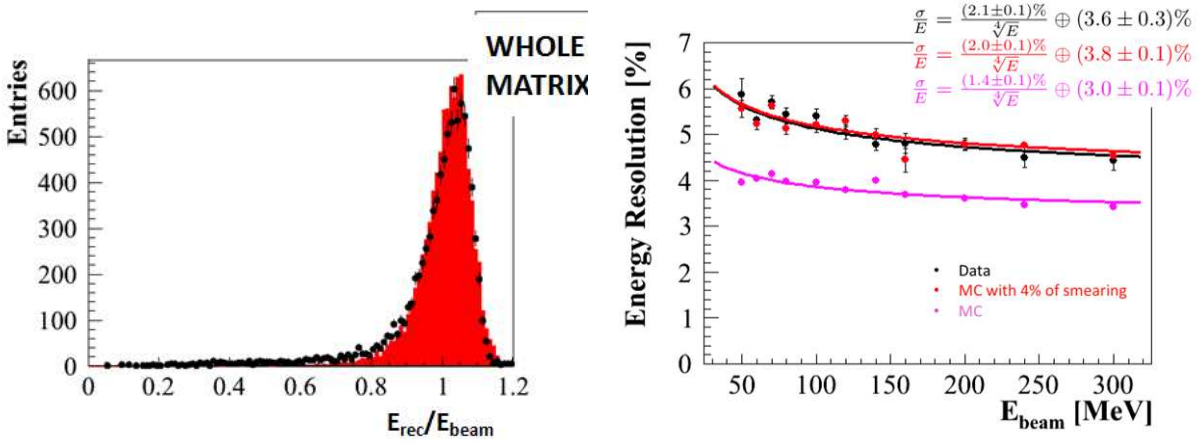

Figure 6: *Left: data (black) MC (red) comparison of energy deposit sum in the whole matrix, normalized to the beam energy, at 100 MeV. Right: data-MC comparison of the energy resolution as a function of beam momentum. Black points are data, red (pink) points are MC expectations with (without) the 4% correction.*

roughening one surface) to improve longitudinal uniformity by means of diffuse reflection. The crystals will be treated in this manner and re-exposed to a test beam prior to CD-2 to validate the anticipated energy resolution.

3 R&D and plans

One of the most crucial job for next year is to carry out simulation in the experiment and partecipating to the code development for a final version of the hit and cluster reconstruction. Moreover, we are carrying out R&D on many points:

1. measurement of the longitudinal response uniformity of the crystals;
2. measurement and choice of the photosensors ;
3. realization of the FEE and design of the digitizer algorithm;
4. calibration system based on the laser;
5. mechanical support.

We expect that during 2013 we will conclude the R&D for the crystals and photosensors and prepare a solid QC (Quality Control) specification for the crystal large size production. Engineering design of the QC station will be prepared. Prototypes of FEE amplification and HV regulation boards will be done. The goal is to get R&D completed for spring 2014, in order to succesfully complete the CD-2 review.

The other basic milestone we are facing, it is that of completing another set of test beams with a larger size matrix and better FEE and system stability. We aim to reach experimental proof of getting an energy resolution of 2-2.5% at 100 MeV.

Acknowledgments

The authors are grateful to many people for the successful realization of the matrix. In particular, we thank all the LNF mechanical shop for the realization of the support and APD boxes, expecially G. Bisogni, U. Martini and A. De Paolis. We thank B. Ponzio for the realization of the HV board and G. Pileggi for the help on the mechanical support of the matrix. We also thank the MAMI staff for providing the beam time. The realization of the preamplifiers was done in collaboration with E. Reali from Roma-2 University.

4 List of Conference Talks by LNF Authors in Year 2012

1. A. Lucà, "**The calorimeter project for the Mu2e experiment**", 12th Pisa Meeting on Advanced Detectors, 20-26 May 2012, La Biodola, Isola d'Elba, Italy
2. I. Sarra,"**Test and Simulation of a LYSO+APD matrix with a tagged photon beam from 40 to 300 MeV**", XVth International Conference on Calorimetry in High Energy Physics (CALOR2012), 48 June 2012, Santa Fe, USA

5 List of Papers/Proceedings

1. The Mu2e project and Collaboration, "**Mu2e Conceptual Design Report**", http://arxiv.org/abs/1211.7019
2. J. Budagov *et al.*, "**The calorimeter project for the Mu2e experiment**", http://dx.doi.org/10.1016/j.nima.2012.11.177
3. M. Cordelli *et al.*, "**Test and Simulation of a LYSO+APD matrix with a tagged photon beam from 40 to 300 MeV**", J. Phys. Conf. Ser. **404** 012027 (2012)

References

1. The Mu2e Collaboration, R. M. Carey *et al.*, http://mu2e-docdb.fnal.gov, document 388-v1.
2. W. Bertl *et al.*, Eur. Phys. J. C **47**, 337 (2006).
3. The Mu2e Collaboration, R. J. Abrams *et al.*, http://arxiv.org/abs/1211.7019.
4. M. Kavatsyuk *et al.*, Nucl. Instr. Meth. A **648**, 77-91 (2011).
5. B. Aubert *et al.*, Nucl. Instr. Meth. A **479**, 1 (2002).
6. H. Ikeda *et al.*, Nucl. Instr. Meth. A **441** 401-426 (2000).
7. M. Cordelli *et al.*, Nucl. Instr. Meth. A **671** 109-112 (2010).

UA9: Crystal Collimation Experiment at CERN

S.B. Dabagov (Resp. Loc.), A. Babaev (Osp.), O. Bogdanov (Postdoc), G. Claps (Bors.), A. Dik (Bors.), E. Frolov (Bors.), D. Hampai (art. 23), F. Murtas

Participant Institutions:

Italy: INFN Laboratori Nazionali di Frascati

Russia: RAS P.N. Lebedev Physical Institute, Moscow
National Research Nuclear University "MEPhI", Moscow
Tomsk Laboratory of Computational Physics, Tomsk
Tomsk Polytechnic University, Tomsk

The main UA9 scope is to study experimentally and theoretically fundamental properties of interactions for relativistic channeled particles (protons and ions) in crystals that aim in the crystal-assisted collimation of the CERN SPS ring beams. After a set of successful experiments on the beam collimation by various schemes of crystal bent systems the project is suggested to be continued in order to investigate the crystal technique feasibility for the LHC beams collimation (a "LUA9" project).

For 2012 the LNF team activity was dedicated to the experiments on the GEM & Medipix detectors optimization and to theoretical studies on simulation of inelastic scattering of relativistic protons and heavy ions in aligned bent crystals. Additional activity was performed to continue our research on relativistic electron/positron beams channeling in various straight crystals, from thin to thick ones. The particle loss in the volume of a bent crystal when relativistic ions pass through the bent crystal under channeling and quasichanneling conditions is simulated. Multiple passage of projectiles through an idealized crystal collimator is considered. The crystal orientation dependence for a particle loss function is obtained.

1 Introduction

As in previous years the project aims in preparation, installation and managing GEM & Medipix detectors to be used at CERN as well as in computer simulations of relativistic proton & ion beams deflection by bent crystal potentials taking into account all the processes of beam scattering in a crystal. Within the project we have established a new testing facility at X-Lab Frascati to characterize the crystals. This facility deals with various X-ray techniques like diffraction and stress analysis, including also a possibility for elemental mapping. Within theoretical part of the collaboration research we have developed several codes dedicated to computer simulations of relativistic beams (electrons, positrons, protons, ions) passage through aligned to the beam straight and bent crystals.

During 2012 we have developed new "Mathematica" codes to study relativistic electrons diffusion/scattering in aligned straight crystals based on both Fokker-Planck equations and multiple scattering simulations. By means of these codes we have analyzed in details the features of axial and planar electron channeling in the crystals of various thicknesses. A special code for simulating relativistic proton/ion beam crystal collimation has been upgraded that allows the peculiarities of inelastic scattering at proton/ion channeling in bent crystals to be taken into account.

One of the important aims of present projects based on the bent crystal technology is to collimate the beam of relativistic protons or ions. However, when the crystal is used to deflect the

beam, one has to consider the problem of beam particles interactions in a crystal characterized by energy loss. The important origins of the loss are inelastic nuclear interactions (i.e. close collisions of beam nuclei with crystal nuclei) and electromagnetic dissociation (i.e. the nucleus decay at crystal electric field influence). Using earlier developed computing code successfully applied for protons, we have analyzed the probability of a particle loss in dependence on crystal orientation for the case of relativistic Pb ions moving into bent crystals.

2 Activity in 2012

2.1 Theory and simulations

Let us follow some basic principles of a simple method for the idealized experiment. Namely, let a non-divergent beam of the intensity I enter the experimental setup. Main unit of this setup is a bent crystal, which scatters αI ($\alpha \leq 1$) particles at different directions. Projectiles penetrate into the crystal at small incident glancing angle θ_0 to bent planes, so they can move through the crystal under channeling or quasichanneling conditions. Another element of the setup is the absorber, which stops the particles deflected at the angles exceeding the cutting angle θ_b. Non-caught particles pass to the 'focusing system' restoring the beam profile. Obviously, simulation of real collimator systems should include the change in a beam profile. Nevertheless, dedicated equipment of the focusing system is omitted here to avoid the technical details and, moreover, to clarify the nature of the particle loss with respect to the crystal orientation defined by the angle θ_0. Behind the focusing system non-divergent beam is again delivered to the setup entrance. So, the model permits describing particle's multiple passage through the crystal. Obviously, if the number Z of lost particles due to the interactions into the crystal volume is much less than that of the initial beam, $Z << I$, the angular distributions of scattered particles remain the same at every turn of a beam.

To estimate the intensity of particle loss at single particles passage through the setup, the average probability of interactions P (API) between a beam particle and nuclei of a crystal can be introduced. In amorphous solid API can be defined by the expression $P = \sigma N z$, while $P << 1$. Here z is the particle path length in a solid, σ is the particle loss cross-section due to the particle interaction with one atom, N is the nuclear density. In aligned crystal, for both channeling and quasichanneling conditions, the nuclear density N strongly depends on the distance from crystallographic planes due to the nuclei thermal oscillations near the equilibrium position located on a plane. Then, for aligned crystal API can be rewritten as follows $P = \sigma \langle N \rangle_{tr} z$, where $\langle N \rangle_{tr}$is the averaged nuclear density over the projectile path. In simulations we used the Gaussian distribution for the displacement of nuclei from the plane.

The beam divergence in recent experiments on beam collimation is very small (for example, experimental horizontal beam emittance was 0.011 μm_rad). So, for estimation let now consider a non-divergent beam hitting a bent crystal at the incident angle θ_0. The particle trajectory in the crystal is defined by its initial position in a channel. It is important to underline that the width of a channel is about a few Angstroms, whereas the characteristic transverse beam size is about a few tens of μm. Hence, to perform simulations for a beam, the projectile has to be characterized by random initial distance that results in equal probability for a particle to move over any possible trajectory (of course, taking into account a weight factor due to space distribution of particles in a beam). If the beam contains a large number of particles, in simulations we deal with the variety of defined trajectories in a crystal. Therefore, one can evaluate a lot of trajectories with equidistant initial points. Then calculating the averaged nuclear density $\langle N \rangle_{tr}$ over each trajectory, we have to define the averaged nuclear density $N(\theta_0)$ at the crystal orientation angle θ_0. This approach allows getting the API value in a crystal volume without each trajectory examination $P = \sigma N(\theta_0) z$ for one arbitrary projectile, where z is the crystal thickness. As above said, the expression is valid

while $P << 1$.

To obtain the density $N(\theta_0)$ the evaluation of 100-1000 trajectories is enough, whereas the beam can contain about 10^8-10^{10} particles. That makes suggested approach effectively applied without the necessity to consider the trajectories for all beam particles.

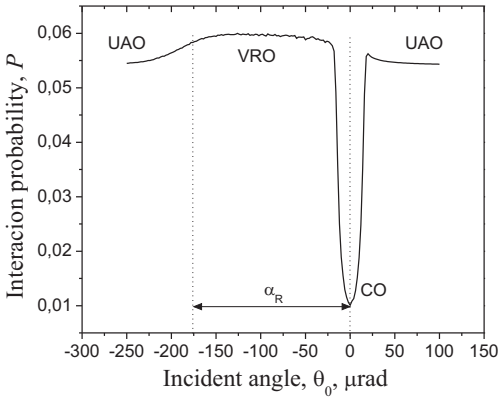

Figure 1: The API dependence P versus the incident angle θ_0.

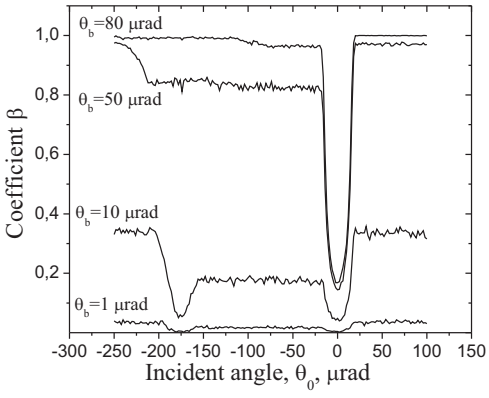

Figure 2: The coefficient β as a function of the incident angle θ_0 at different cutting angles θ_b. Each cutting angle corresponds to different relative position of the absorber in respect with the crystal.

The results of simulations revealed are presented in Fig. 1. The beam of Pb ions with the momentum 9840 GeV/c passed a Si crystal bent along (110) planes over the angle $\phi_R = 167$ μrad was considered. The crystal thickness $z = 2$ mm and the interaction cross-section $\sigma = 5.414 \cdot 10^{-24}\text{cm}^2$ were chosen to be in agreement with other results. One can see in the figure three areas corresponding to different crystal orientations with respect to the beam direction: CO corresponds to the "channeling orientation", VRO – the "volume reflection orientation", UAO – the "unaligned orientation" (no coherent interactions). These areas reflect distinct characteristics of the projectiles motion. In the CO regime most of the particles cross the crystal being channeled. These particles remain in a central area of the planar channels characterized by the minimal nuclear density. Hence, one can see a sharp deep at CO. At both UAO and VRO most of the projectiles are quasichanneled. They cross bent planes where the local density of crystal nuclei is maximal; API for both orientations becomes many times larger than at the CO orientation. At VRO the volume reflection effect takes place for quasichanneled projectiles: particle moving initially to the center of crystal curvature changes its direction. Near the "reflection point", where the direction has been changed, the projectile moves along bent plane with extremely high nuclear density. Finally, at the VRO conditions API is revealed to be higher than at UAO.

When the bent crystal is used as a collimator in real experiments with ion beams, the beam particles can pass through experimental setup many times. To investigate the multiple passage of particles through the bent crystal, a theoretical model earlier proposed introduces the coefficient β , which characterizes the fraction of particles crossing the crystal and successfully passing to the ring focusing system. This coefficient can be evaluated from the angular distribution of projectiles behind the crystal. The dependencies $\beta(\theta_0)$ at different cutting angles θ_b for the considered parameters are presented in Fig. 2. All curves in the figure demonstrate a deep for the CO area. Indeed, channeled projectiles are deflected by a bent crystal at large angles θ close to the crystal bent angle α_R. Hence, all channeled particles hit the absorber and, thus, leave the beam ($|\theta| > \theta_b$).

At small cutting angle $\theta_b = 1$ μrad some projectiles scattered by a crystal passes to the focusing system revealing a slight variation at the orientation angle θ_0; therefore, the corresponding coefficient β changes slightly. On the contrary, at largest cutting angle $\theta_b = 80$ μrad almost all projectiles pass to the focusing system except those for CO. Therefore, one can see $\beta \approx 1$ except the sharp decrease at CO. For intermediate angles the coefficient β

demonstrate quite different behavior in the transition area from VRO to UAO. Namely, for the case $\theta_b = 10$ μrad one can see the β parameter suppression for large incident angles ($\sim$175 μrad) whereas for the case $\theta_b = 50$ μrad it disappears. This feature is related to the scattered beam splitting at corresponding orientation angles. One part of the projectiles moves under the volume reflection condition while other projectiles are deflected mainly due to multiple scattering. Therefore, the first particles are deflected jointly at large angles whereas the deflection angles of second particles are distributed close to the initial beam direction. Hence the beam is split. The observer watching the projectiles at the entrance of focusing system scans both produced beams at $\theta_b = 50$ μrad, i.e. he observes the smooth transition from VRO to UAO (the splitting is absent at both areas). But at condition $\theta_b = 10$ μrad the observer registers only one beam (the second is cut off by absorber). As a result, the number of particles passing to the focusing system decreases with respect to VRO as well as to UAO.

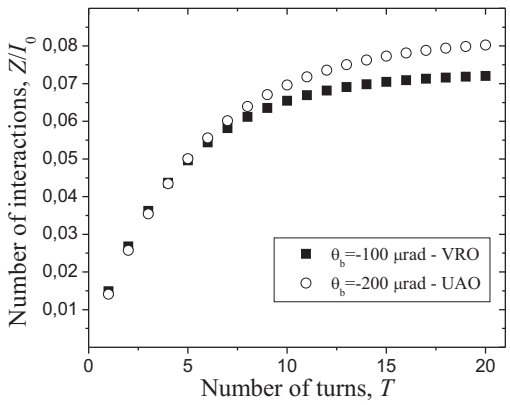

Figure 3: The number of loss Z divided to the initial number of nuclei I_0 as a function of the turns number T at $\alpha = 0.25$, $\theta_b = 10$ μrad.

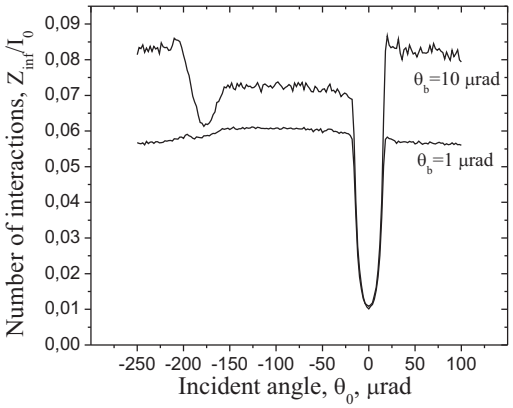

Figure 4: The number of loss for the saturation state $Z_{\rm inf}$ with respect to the initial number of nuclei I_0 in dependence on the incident angle θ_0 at different cutting angles θ_b.

Successfully, total number Z of the projectile loss in a crystal volume over T turns under the condition $\beta < 1$ (i.e. when the absorber catches particles) is defined by the expression $Z = \frac{1-(1-\alpha+\alpha\beta)^T}{1-\beta} PI_0$, Z tends to saturate with the increase of the number of turns approaching the following limit $Z_{\rm inf} = \frac{P}{1-\beta} I_0$, where I_0 is the initial number of particles in a beam. Fig. 3 presents the evolution of this saturation effect. As seen, the number of interactions is initially larger at VRO with respect to the UAO case that is in agreement with the results of Fig. 1. However, the situation becomes inverted starting from the 5-th turn. Indeed, at UAO the ions are deflected at small angles close to initial beam direction whereas at VRO the ions can be deflected at large angle from this direction. Therefore, at UAO selected ion has a chance to make more turns before being deflected by the angle $|\theta| > \theta_b$(when it will be caught by the absorber, i.e. this ion leaves the beam definitively) in comparison with the number of turns at VRO. Due to the fact that probability of interaction grows with the increase of the number of turns, multiple passage at VRO

is characterized by reduced interaction probability with respect to UAO. This conclusion is also proved by Fig.4, where the dependences of projectile loss in saturation regime are shown for two different cutting angles θ_b. At small cutting angle $\theta_b = 1$ μrad particle passes through the crystal one time only being deflected into the absorber. As seen, the curve at $\theta_b = 1$ μrad is almost the same as the API dependence of Fig. 2. Hence, the projectile loss under the VRO conditions is more than that for the UAO conditions. On the contrary, at moderate cutting angle $\theta_b = 10$ μrad the reflected particle is deflected to the absorber, whereas non-reflected quasichanneled particle can pass several times through the crystal. Finally, the loss at UAO becomes more than at VRO.

As regards the curves in Fig. 4, the deep in the CO area is due to the deflection of channeled ions at large angles (Fig. 2) combined with the API decrease (Fig. 1). The left deep at $\theta_b = 10$ μrad is related to the splitting of angular distribution in this area as described above.

It is remarkable that the cross-section for ions considered in this work is 10 times larger than that for protons. It brings us to the conclusion that at large cutting angles the ratio $Z_{\rm inf}/I_0$ should approach 1 at both UAO and VRO, and the deep remains only at CO.
Obviously, when bent crystal is used to deflect the beam, the orientation optimized for beam channeling is preferable to reduce the number of particle loss in the crystal volume. However, in this case a precise crystal orientation is required because of the fact that small deviations from the optimal value $\theta_0 = 0$ lead to essential increase in the loss intensity. The total loss can exceed 5%.

3 Conclusions

We have applied earlier developed theory that describes inelastic nuclear interactions at proton multiple passage through bent crystals, to the crystal collimation studies for ions. Originally, the approach is valid for small particle loss with respect to total intensity hitting the crystal entrance for each system passage ($P << 1$). In this case the loss of projectiles does not essentially influence the angular distribution of scattered ions. As seen in Fig. 1, for relativistic ions considered here we are practically in the limit of proposed theory applicability.

Nevertheless, we have to underline that for heavy ions beam the particle loss cross-section may exceed the one for Pb nuclei. In this case the influence of projectile loss on angular distributions should be included in the model. For example, reflected ions undergo a strong loss. Hence, in angular distributions the intensity of reflected ions may be noticeably changed in comparison with the case when the ion loss is not taken into account. On the contrary, channeled ions almost do not interact with the nuclei of a crystal that results in the negligible change in angular distribution even at very large cross-sections. Therefore, the method to study the angular distributions of scattered ions versus the particle loss should be developed in future.

CUORE

M. A. Franceschi (Resp.)

Not received

ICARUS

H.Bilokon (Resp.), G. Mannocchi (Ass.), P.Picchi (ass.)

We are working on the optimisation of noble liquid cryogenic detectors using photo-dopants, namely argon detector with double phase (liquid and gas) doped with TMG (Tetramethyl-Germanium). The TMG has a very large cross section for photo-absorption (62 Mb) and a high quantum efficiency to convert ultraviolet photons of argon scintillation (128 nm) in photo-electrons. Double phase detectors are able to combine a large mass with a low energy threshold; they are suitable for measuring rare events in the keV energy region (e.g.: neutrino coherent interactions and Dark Matter search). Photo-electrons are separated by several mm, depending on the concentration of TMG, and can therefore be considered isolated electrons. An electric field drives electrons toward the surface of the liquid and pulls them into the gaseous phase, where they meet one or more GEM (Gas Electron Multiplier) in cascade that, working in streamer mode, have the sensitivity to detect single electrons.
We continue the participation in the development of a new detector (LEM: Large Electron Multiplier), which exploits the avalanche multiplication in ultra pure noble gases in the absence of quencher with large gains and good spatial and energy resolution. This line of research began as an activity of Gruppo-V (LEM Project) and was most recently inserted in the RD51 international collaboration. This technique can be applied in many areas of fundamental physics: ionization signal detection at very low energy (e.g. for dark matter searches), the single photon UV detection on large areas (e.g. fast trigger for large TPC), ionization signals detection on large areas (pixels) for medical images. The LEM is a coarse-grained Gas Electron Multiplier obtained with approximately millimeter diameter holes in a G10 (copper cladded PCB) with thickness of about 2 mm. Gains of 10^3 - 10^4 in pure noble gases such as Ar and Xe has been obtained. The system was tested successfully also in conjunction with CsI photo-cathodes. These exceptional gains obtained without quencher are possible because the walls of the G-10 holes act as mechanical quencher absorbing UV photons produced by the electron avalanche in a confined space.
From October 2010 the ICARUS T600 detector is working in the Gran Sasso Laboratories, recording CNGS neutrino interactions events with efficiency greater than 95%. The characteristics of LAr-TPC as tracking and calorimetric detector as well as an excellent discrimination of electrons from π^0, allow good rejection of neutral current, without significant loss of efficiency for electron neutrino identification. In the current phase of data taking, we are participating to the support activities of the experiment such as the visual scanning of the collected events and their classification. This work will continue also during 2013. As a next step the detector ICARUS T600 will be moved from LNGS to CERN during the LHC and LSND long shut down in 2013-1214. The T600 should be located in a position where it can be used as a "FAR detector" in a short baseline “dual detector” experiment for the search of sterile neutrinos (LSND anomaly).

1) Experimental search for the LSND anomaly with the ICARUS LAr TPC detector in the CNGS beam
By M Antonello, B Baibussinov, P Benetti, E Calligarich, N Canci, S Centro, A Cesana, K Cieslik et al..
arXiv:1209.0122 [hep-ex].

2) Precision measurement of the neutrino velocity with the ICARUS detector in the CNGS beam
By M. Antonello, B. Baibussinov, P. Benetti, E. Calligarich, N. Canci, S. Centro, A. Cesana, K. Cieslik et al..
arXiv:1208.2629 [hep-ex].

3) Search for anomalies in the neutrino sector with muon spectrometers and large LArTPC imaging detectors at CERN
By A. Antonello, D. Bagliani, B. Baibussinov, H. Bilokon, F. Boffelli, M. Bonesini, E. Calligarich, N. Canci et al..
arXiv:1208.0862 [physics.ins-det].

4) Development and preliminary tests of resistive microdot and microstrip detectors
By V. Peskov, P. Fonte, E. Nappi, P. Martinengo, R. Oliveira, F. Pietropaolo, P. Picchi.
arXiv:1203.3658 [physics.ins-det].

5) Measurement of the neutrino velocity with the ICARUS detector at the CNGS beam
By ICARUS Collaboration (M. Antonello et al.).
arXiv:1203.3433 [hep-ex].
Phys.Lett. B713 (2012) 17-22.

6) Search for 'anomalies' from neutrino and anti-neutrino oscillations at Delta_m^2 $\sim$ 1eV^2 with muon spectrometers and large LAr-TPC imaging detectors
By M. Antonello, D. Bagliani, B. Baibussinov, H. Bilokon, F. Boffelli, M. Bonesini, E. Calligarich, N. Canci et al..
arXiv:1203.3432 [physics.ins-det].

7) Development of novel designs of spark-protected micropattern gaseous detectors with resistive electrodes
By V. Peskov, P. Martinengo, E. Nappi, R. Oliveira, P. Pietropaolo, P. Picchi.
JINST 7 (2012) C01005.

8) A Search for the analogue to Cherenkov radiation by high energy neutrinos at superluminal speeds in ICARUS
By ICARUS Collaboration (M. Antonello et al.).
arXiv:1110.3763 [hep-ex].
Phys.Lett. B711 (2012) 270-275.

9) Advances in the Development of Micropattern Gaseous Detectors with Resistive Electrodes
By P. Fonte, P. Martinengo, E. Nappi, R. Oliveira, V. Peskov, F. Pietropaolo, P. Picchi.
arXiv:1005.1477 [physics.ins-det].
Nucl.Instrum.Meth. A661 (2012) S153-S155.

JEM-EUSO-RD

A. Franceschi, A. Marini, G. Modestino, T. Napolitano, M. Ricci (Resp.), F. Ronga (Ass.)

Participant Italian Institutions:

INFN LNF, INFN and Universities of Bari, Catania, Napoli, Roma Tor Vergata, Torino; ASI (Italian Space agency)

Participant International Countries:

JAPAN, USA, FRANCE, GERMANY, MEXICO, RUSSIA, SOUTH KOREA SWITZERLAND, SPAIN, POLAND, SLOVAKIA, BULGARIA

1 Introduction

The origin and nature of Ultra-High Energy Cosmic Rays (UHECRs) remain unsolved in contemporary astroparticle physics. A cutoff in the cosmic ray energy spectrum clearly appears at $\sim 10^{20}$ eV in the data of HiReS [1)], Telescope Array [2)] and Auger [3)] on ground experiments. It is well known that the detection of events with energy $\geq 10^{20}$ eV is challenged by the GZK effect [4, 5)], which limits the highest detectable energy at $\sim 10^{20}$ eV due to photopion production in the interaction of UHECR on the microwave fossil radiation of the Big Bang, as suggested also by the HiReS and Telescope Array data, or by nuclei photodisintegration as indicated by the Auger results. However, the possibility that the cutoff at $\sim 10^{20}$ eV can be intrinsic to the acceleration power of the astrophysics cosmic ray sources remains alive. Moreover, indications of sources or excesses in the arrival direction distribution of UHECRs have been claimed by the Auger experiment, though not fully confirmed. To give an answer to these questions is rather challenging because of the extremely low flux of a few per km^2 per century at extreme energies such as $E > 5 \times 10^{19}$ eV.

The JEM-EUSO experiment, Extreme Universe Space Observatory at the Japanese Experiment Module of the International Space Station, is the first space mission devoted to the scientific research of cosmic rays at the highest energies. Its super-wide-field telescope looks down from the International Space Station onto the night sky to detect UV photons emitted from air showers generated by UHECRs in the atmosphere.

13 Countries, 77 Institutes and about 280 researchers are collaborating in JEM-EUSO, with the support of the most important International and National Space Agencies and research funding institutions. JEM-EUSO is currently in the evaluation phase (Phase A) by the Japanese Space Agency (JAXA).

2 The JEM-EUSO Mission

JEM-EUSO on the International Space Station is a new type of observatory, based on a UV telescope, which uses the whole Earth as detector. It will observe, from an altitude of ~ 400 km, the fluorescence tracks produced at $(330 \div 400)$ nm by Extensive Air Showers (EAS) originated by UHE primaries which traverse the Earth's atmosphere at ultra-relativistic speed. JEM-EUSO will be launched by an H2B rocket and will be conveyed to the ISS by the H-II Transfer Vehicle (HTV). It will be then attached to one of the ports for non-standard payloads of the Exposure Facility (EF) of the Japanese Experiment Module (JEM). Data will be transmitted via TDRS (Tracking

and Data Relay Satellite) to the Mission Operation Center hosted by JAXA in the Tsukuba Space Centre (Fig.1).

The launch is foreseen for 2017 and the mission will last at least 5 years. JEM-EUSO will be operated for three years in Nadir configuration to maximize statistics at the lowest energies in order to cross calibrate with the current generation of ground-based detectors. The instrument will be then tilted (about 30°) with respect to Nadir in order to exploit a larger amount of atmosphere and to maximize the statistics of events at the highest energies. JEM-EUSO will significantly increase the exposure to UHECRs compared to the largest ground-based air shower arrays presently in operation.

Two pathfinder test experiments are currently prepared; one to observe the fluorescence background from the edge of the Atmosphere (EUSO-Balloon) and the other at ground for an inter-calibration with the fluorescence detector (EUSO-TA) of the Telescope Array experiment. The main parameters of the mission at ISS are described in Table 1.

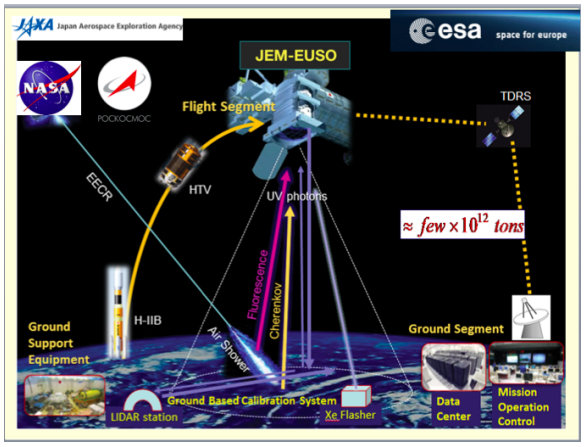

Figure 1: The JEM-EUSO Mission concept

Table 1: JEM-EUSO Main Parameters

Expected launch date	JFY 2017
Mission Lifetime	3+2 year
Launch Rocket	H2B
Transport Vehicle	HTV
Accommodation on JEM	EF n.2 (or 9)
Instrument Mass	1938 kg
Height of the Orbit	400 km
Inclination of the Orbit	51.6

3 The Science Case

JEM-EUSO will address basic problems of fundamental physics and high-energy astrophysics studying the nature and origin of the Ultra High Energy Cosmic Rays ($E > 3 \times 10^{19}$ eV).

JEM-EUSO will pioneer the investigation from Space of UHECR-induced Extensive Air Showers making precise measurements with unprecedented statistical accuracy of the primary energy, arrival direction and composition of UHECRs, using a target volume far greater than it is possible from the ground. Such data will shed light on the origin of the UHECRs, on the sources that are producing them, on the propagation environment from the source to the Earth and, possibly, on the particle physics mechanisms at energies well beyond the ones achievable in man-made accelerators. Moreover, exploratory objectives such as constraining the galactic and extragalactic magnetic fields, the detection of extreme energy neutrinos and gamma rays, the verification of special relativity at extremely large Lorentz factors, the examination of possible quantum gravity effects at extreme energies, and the systematic surveillance of atmospheric phenomena, complete the scenario of the JEM-EUSO science goals.
Below, the scientific objectives of the JEM-EUSO mission are summarized.

Astrophysics and Cosmology

Main Science Objectives:
- Identification of UHE sources
- Measurement of the energy spectra of individual sources
- Measurement of the trans-GZK spectrum

Exploratory objectives:
- Discovery of UHE neutrinos
- Discovery of UHE Gamma-rays
- Study of the galactic and local extragalactic magnetic field

Atmospheric Science
- Nightglow
- Transient Luminous Events (TLE)
- Meteors and Meteoroids

A new window on the unknown
- Particle Physics: String Theory
- Relativity and quantum gravity effect

4 Observational Principle

In the JEM-EUSO mission, the UHECR observation is based on the measurement of the fluorescence and Cherenkov photons produced in the extensive air shower (EAS) phenomenon. An UHECR, interacting with atmospheric nuclei, produces secondary particles that in turn collide with the air atoms giving rise to a propagating cascade of particles. The number of the secondary particles in an EAS is related to the energy of the primary UHECR. The most dominant particles in EAS are electrons moving through the atmosphere, which excite metastable energy levels in atmospheric atoms and molecules, in particular nitrogen, that return to ground state emitting characteristic fluorescence light in the ultraviolet (UV) band with wavelengths between 330 and 400 nm. The emitted light is isotropic and its intensity is proportional to the energy deposited

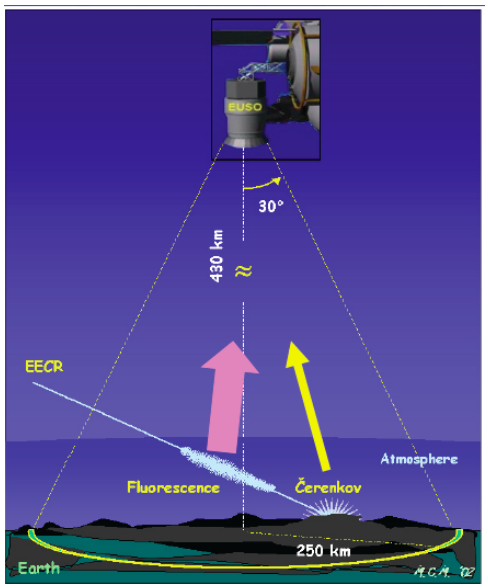

Figure 2: Artistic view of the JEM-EUSO Observational Principle

in the atmosphere. An UHECR-induced EAS then forms a significant streak of fluorescence light along its passage in the atmosphere, depending on the energy and zenith angle of the primary UHECR. Numerous secondary particles have velocities higher than that of the light and therefore they emit Cherenkov photons. These Cherenkov photons are highly beamed within a cone of $< 1.3°$ radius along the trajectory and may be scattered by the molecular and aerosol content in the atmosphere. Part of these photons will be isotropically diffused when reaching land, sea or clouds. Looking downward the dark Earth atmosphere, the JEM-EUSO telescope will detect such fluorescence light as sketched in Figure 2. EAS appears as a small disc-shaped luminous object which, when viewed continuously, moves on a straight path at the speed of light. The recorded amount of light is nearly proportional to the shower size at the various depths in the atmosphere. By imaging the motion of the streak every few microseconds, it is possible to determine the arrival direction of the primary UHECR. The integral of light recorded is an important information to determine the energy of the primary UHECR. The cascade shape (especially the position of the shower maximum in the traversed slant depth) gives an indication about the nature of the primary.

5 The Instrument

The JEM-EUSO instrument (Fig.3) basically consists of an UHECR telescope assisted by an atmosphere monitoring device and controlled by a calibration system.

The JEM-EUSO telescope is a fast, high-pixelized, large-aperture and large field-of-view digital camera, working in the near-UV wavelength range ($330 \div 400$ nm) with single photon counting capability. The main components of the telescope are the collecting optics, the focal surface detector, the electronics and the structure. The optics system is composed of two Fresnel lenses and one diffractive precision Fresnel lens. The focal surface detector is composed by a grid of $\sim$ 5000 multi-anode photomultipliers (MAPMT), 64 pixels in each, that convert the energy of the incoming photons into electric pulses. They are arranged in 137 PDM (Photo Detector Module), with 2304 pixels in each. The electronics counts-up the number of the electric pulses in

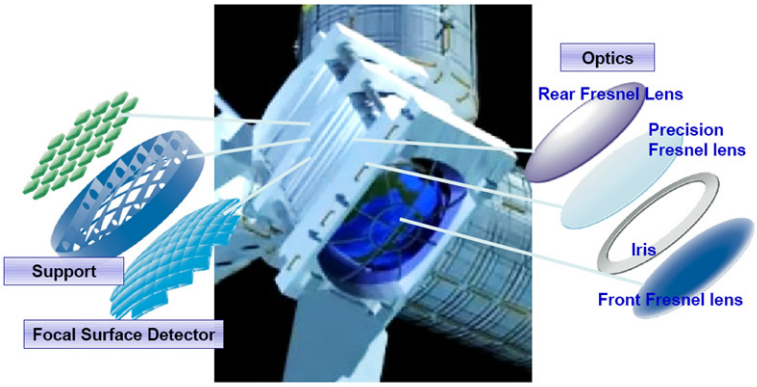

Figure 3: The JEM-EUSO Instrument

time periods of 2.5 μs. The JEM-EUSO atmosphere monitoring will use an infrared (IR) camera and a Lidar (Light Detection and Ranging) with ultraviolet laser to observe the conditions of the atmosphere in the field of view of the telescope.

JEM-EUSO will be calibrated through instrumentations both onboard and on ground. The onboard calibration system is composed of a set of three LEDs with different wavelengths (from 300 to 500 nm) that will be installed in the telescope cylinder as diffusive light sources. On ground, the monitoring and calibration will be performed by a Global Light System (GLS) of lasers and xenon light sources located in 12 sites around the world, supplemented with an aircraft system.

6 The Pathfinders: EUSO-TA and EUSO-Balloon

The JEM-EUSO collaboration is currently involved in the development of two pathfinders for the JEM-EUSO mission: a ground-based telescope (EUSO-TA) and a space-based one (EUSO-Balloon). EUSO-TA is a ground-based telescope formed by one Photo Detector Module and two fresnel lenses, protoypes of those foreseen in JEM-EUSO. It will be located at Telescope Array site (Utah) in early 2013. The principle of such instrument is to monitor the UV light ($290 \div 430$ nm) in the atmosphere in its field of view (FoV) of 4 degrees, continuously, during the night, at a rate of 4×10^5 frames/s. The telescope is sensitive also to air showers with energies $E > 10^{18}$ eV falling in the FoV.

EUSO-Balloon is developed as a demonstrator for the technologies and methods featured in the space instrument. EUSO-Balloon is an imaging UV telescope as JEM-EUSO. The balloon-borne instrument points towards the Nadir from a float altitude of about 40 km. With its Fresnel Optics and Photo-Detector Module similar to TA-EUSO, the instrument monitors a $12^\circ \times 12^\circ$ wide field of view at the same rate as TA-EUSO. The instrument is presently built by various institutes of the entire JEM-EUSO collaboration. Balloon flights will be managed and performed by the balloon division of the French Space Agency CNES; a first flight is scheduled in 2014.

7 The participation and contribution of the italian groups

JEM-EUSO in Italy is presently funded by the Istituto Nazionale di Fisica Nucleare (INFN) within the National Scientific Committee for Astroparticle and Neutrino Physics; funds have been provided

for several years also by the Italian Space Agency (ASI). The full commitment of ASI is depending on the final approval of the mission. The tasks and responsibilities, briefly summarized, are the following:

Focal Surface Subsystem:

- PDM Structure
- Focal Surface Structure
- Focal Surface integration

Data Handling Subsystem:

- Mission Data Processor
- Telemetry Command Unit
- Data Acquisition Interface Board
- Clock Board

Atmospheric Monitoring Subsystem

Simulation Tools

The Italian Collaboration is presently fully involved also in the realization of the two pathfinders, EUSO-Balloon and EUSO-TA. CPU, Telemetry, Clock and transmission system have been integrated and tested. For EUSO-TA, moreover, the mechanical supporting structure of the instrument, with a dedicated inclination system, has been constructed.

8 Activity of the LNF group during year 2012 and for 2013

The LNF JEM-EUSO group is responsible (in collaboration with the SPCM LNF Service) of the design of the Focal Surface (FS) mechanical structure and of the 137 PDMs which cover the entire FS and where the 4932 multi anode Photomultipliers Hamamatsu M64 are accommodated (Fig.4).

So far, the engineering studies have been carried out, including 3D CAD design of the structure, finite element model calculations, vibration mode studies related to the launch vehicle parameters. In 2012, first assembled prototypes of PDMs for testing and for both EUSO-TA and EUSO-Balloon have been produced. Members of the group are involved in the JEM-EUSO Editor's Team, which takes care of the editing of successive updated versions of the Technical Reports, and in the JEM-EUSO Speaker's Bureau which manages and organizes the activities related to publications and conferences. The group participates and contributes also to the definition and assessment of the scientific objectives of the mission. In 2013, the activity will be mainly dedicated to the continuation of the engineering project of the FS structure, to the production of more PDMs, in an updated configuration as far as the front end, the DAQ and the power supply electronic boards design is consolidated, in view of reaching the successive Technical Readiness Levels required by a Space mission. The activities related to publications, presentation at Conferences and contact and meetings with national aerospace Companies constitute a relevant part of the tasks foreseen in 2013.

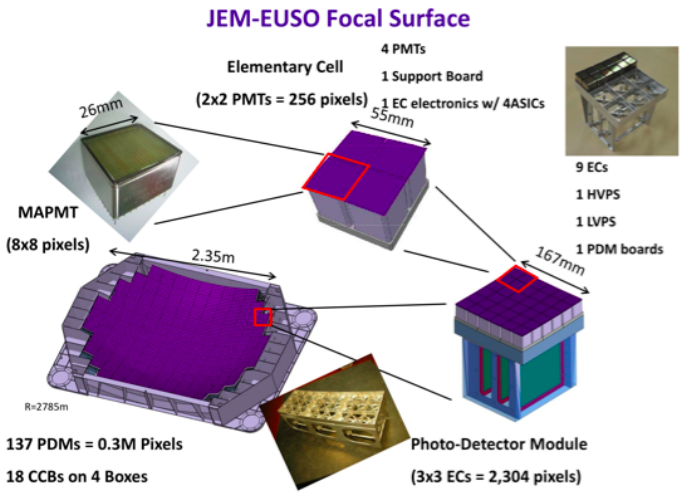

Figure 4: The JEM-EUSO Focal Surface Structure components

9 Recent publications

1. The JEM-EUSO Collaboration: J.H. Adams *et al.*, "An Evaluation of the Exposure in Nadir Observation of the JEM-EUSO Mission", Astrop. Phys. **44**, 76 (2013).
2. J.H. Adams *et al.*, "Summary Report of JEM-EUSO Workshop at KICP in Chicago ", arXiv:1203.3451v2 [astro-ph.IM] (2012).
3. M.Ricci for the JEM-EUSO Collaboration, "The JEM-EUSO Mission", 12th International Conference on Topics in Astroparticle and Underground Physics (TAUP 2011, Munich) Journal of Physics: Conference Series **375**, 052009 (2012).
4. The JEM-EUSO Collaboration: J.H. Adams *et al.*, "The JEM-EUSO Mission: Status and Prospects in 2011"; Proc.32nd International Cosmic Ray Conference, Beijing, August, 2011, arXiv:1204.5065v1 [astro-ph.IM].
5. T. Ebisuzaki, for the JEM-EUSO Collaboration, "The JEM-EUSO Mission", AIP Conf.Proc. **1367**, 120 (2011) XVI International Symposium on Very High Energy Cosmic Ray Interactions, ISVHECRI 2010, Batavia, IL, USA; arXiv:1101.1909v1 [astro-ph.HE].

References

1. P. Sokolsky and G.B. Thomson, J.Phys. **G34**, R401 (2007).
2. T. Abu-Zayyad *et al.*, Astroph. J. **757**, 26 (2012).
3. The Pierre Auger Collaboration: P. Abreu,*et al.*, Contributions to the 32nd International Cosmic Ray Conference, Beijing, China, August 2011 - arXiv:1107.4809v1 [astro-ph.HE].
4. K. Greisen, Phys.Rev.Lett., **16**, 748 (1966)
5. G.T. Zatsepin and V.A. Kuz'min, JETP Lett., **4**, 78 (1966)

NEMO

O. Ciaffoni (Tecn.), M. Cordelli, A. Martini (Resp.), L. Trasatti (Ass.),
R. Habel (Ass.)

The NEMO collaboration (km3 from January 2013), in the framework of the KM3Net initiative, aims at building a km^3 scale Cerenkov neutrino detector in the Mediterranean Sea. During the year 2012 the collaboration has completed the construction of NEMO Phase II, an 8 floor tower to be deployed at the final site, 100 km SE of Capo Passero, in the spring of 2013, taking advantage of the electrooptical cable already deployed from the site to the counting room in Portopalo.
In 2012 the LNF group installed four PORFIDO probes in the NEMO Phase II apparatus with the assistance of the LNS group responsible for the assembly of the Optical Modules.
In the mean time the KM3Net collaboration is developing the design of the PPM, (PreProduction Module), to be deployed in 2014, containing the DOM (Digital Optical Module), a 17" glass sphere containing 31 small PMTs. The LNF group, as a consequence, has developed PORFIDOM, a version of PORFIDO that can be fitted in the new DOM.
In 2012 the LNF group has continued the development of the PORFIDO probes adding a 24 bit ADC with a PT100 temperature probe, that is read by the WISP and provides a temperature measurement with the accuracy of 0.001°C. Alternately we are developing a salinity monitor that can be connected to the same ADC with a resolution of about 1 ppm.
These new developments will be installed on the Phase 3 towers.

Publications

KM3NeT Collaboration (S. Adrian-Martinez et al.),
Detection Potential of the KM3NeT Detector for High-Energy Neutrinos from the Fermi Bubbles, arXiv:1208.1226 [astro-ph.HE], in press.

NESSiE

A. Longhin, A. Paoloni (Resp.)

in collaboration with
LNF-SPAS (Div. Ric.): A. Cecchetti, D. Orecchini

1 Introduction

Several experimental results provide indications for the existence of additional neutrinos beyond the three known states which couple via the electro-weak force (sterile neutrinos): a deficit of $\bar{\nu}_e$ from nuclear reactors measured at distances of $\mathcal{O}$(10-100 m) from the core [2)], a deficit of ν_e from MCi ^{51}Cr and ^{37}Ar calibration sources at $\mathcal{O}$(m) distances (SAGE, GALLEX [3)]), an excess of ν_e and $\bar{\nu}_e$ in artificial ν_μ and $\bar{\nu}_\mu$ at distances of $\mathcal{O}$(km) (LSND [4)], MiniBooNE [5)]). Furthermore, current cosmological fits based on CMB data show a moderate preference for extra neutrino states [6)]. All these inputs triggered the community towards an experimental effort with the goal of, either disproving with large significance the existing indications, or leading to a ground-breaking discovery.

The ICARUS-NESSiE experiment (SPSC–P–347 [1)]) is a joint proposal for the search for sterile neutrinos with a short-baseline neutrino beam based at CERN. The experiment concepts consists in exposing two almost identical detectors at two distances (640 and 1600 m) from a $\nu_\mu/\bar{\nu}_\mu$ neutrino source with a peak energy of about 2 GeV. The existence of extra neutrinos with a squared mass difference with respect to the three known states of $\mathcal{O}(\mathrm{eV}^2)$ is expected to manifest itself both with an energy-dependent disappearance of the ν_μ and/or appearance of ν_e above the instrinsic beam contamination. Each setup is composed of a liquid-Argon Time Projection Chamber (LAr-TPC) which is optimal for the reconstruction of the electronic component followed by a magnetic spectrometer for a complete reconstruction of muonic final states (Fig.1). A substantial part of the far-site LAr-TPC will consist of the ICARUS detector which will be transported from the LNGS underground laboratories. The muon spectrometers at the far and near sites will be build by the NESSiE (Neutrino Experiment with SpectrometerS in Europe) Collaboration which is currently composed by groups from Bari, Bologna, Lecce, LNF, Roma-1 and Padova. The final decision on the construction of the beamline in the North-Area (CENF, CErn Neutrino Facility) which would give the green-light for the startup of the program is expected by CERN before Summer 2013.

In order to measure with high precision the charge and the momentum of muons produced by neutrino interactions in the LAr target and those interacting in the spectrometer itself, two complementary spectrometers will be installed (Fig.1): an air-core magnet (ACM), followed by an iron-core magnet (ICM). The ICM is dedicated to the precise reconstruction of high-energy muons (up to 30 GeV) and to reach few % precision, through range measurement, on the momentum of muons with energy lower than 3 GeV while the ACM covers the low momentum region where it ensures high momentum resolution and charge discrimination (allowing to separetely study the ν

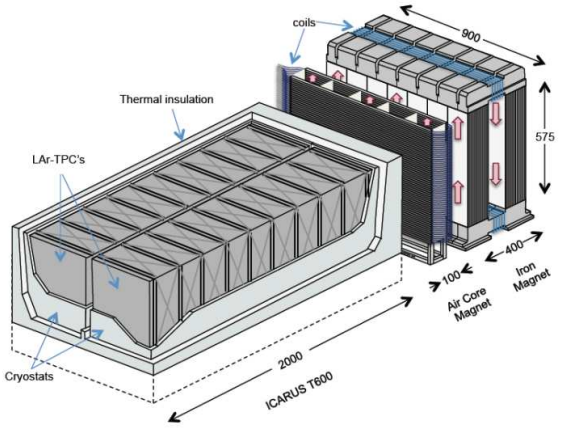

Figure 1: Sketch of the ICARUS-NESSiE experiment far location at 1600 m from the proton target.

and $\bar{\nu}$ components).

2 Activities of the LNF group

2.1 Iron-core magnets

The NESSiE collaboration can profit of the experience acquired with the OPERA experiment for the design and realization of the ICM. The two OPERA spectrometers are made of two arms, each composed by 12, 5 cm thick, iron slab layers alternated to 11 layers instrumented with Resistive Plate Chambers; two iron yokes, on top and on bottom, close the magnetic flux, providing a constant magnetic field of 1.5 T with opposite directions inside the two arms. The deflection of muons crossing the spectrometers is measured by means of drift tubes stations (two before, two in the middle and two after each magnet), reaching precisions of about 20% on momenta lower than 30 GeV and a charge confusion of 0.3% in the same energy range.

About 40 iron slabs of 5 cm thickness are needed to stop muons up to 3 GeV energy, but given the height of the ICARUS experiment, almost all of the iron needed for the far and the near site can be recovered from OPERA, cutting the present slabs and installing two iron core magnets, each with 24 magnetized slab layers, in order to recover also the yokes. The about 1000 resistive plate chambers installed in the OPERA spectrometers, for the same reasons, are sufficient to instrument both the near and far site spectrometers. The RPC gas system, two power supplies and the refrigerating system for the magnet coils of the OPERA spectrometers can also be recovered.

The LNF OPERA group, in sinergy with the SPAS service, is actively involved in the proposal since the beginning of the project and is playing a crucial role thanks to the recognised expertise gained during the design and construction of the OPERA ICM spectrometers. The schedule of the project in its present form is naturally connected with the dismantling of the OPERA detector, activity in which the group is naturally committed (definition of the schedule, costing, optimization).

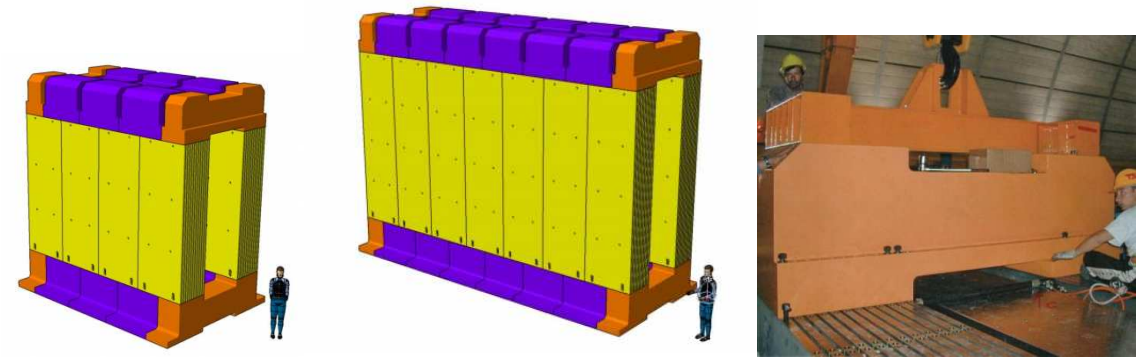

Figure 2: Mechanical model of the near ICM (left), far ICM (center) from the SPAS and a phase of the installation of the OPERA top yokes for the OPERA spectrometers in 2004 (right).

2.2 Simulation and optimization of the neutrino flux

Furthermore the Frascati group, in cooperation with CERN, is active in the optimization of the horn optics to maximize the neutrino flux produced by the 100-GeV SPS protons. The goal is to produce a high-intensity ν_μ flux with a low ν_e contamination and with a spectrum well matched to the region of interest in terms of the sterile oscillation phenomenology (and suppressed high-energy tails). In particular a systematic search based on a fine sampling of the space of possible configurations of a horn-reflector system has been conducted with a GEANT4-based simulation. Promising results in terms of enhancement of flux with a reduced horn current have been obtained recently. An example of a candidate configuration is shown in Fig. 3.

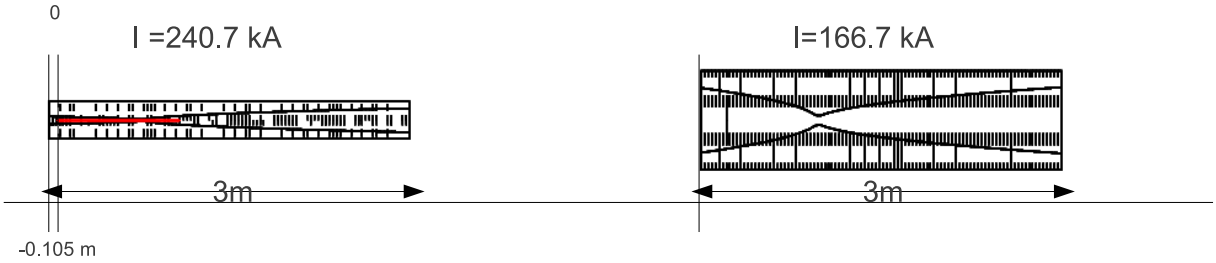

Figure 3: Sketch of an optimized bi-parabolic horn-reflector system for the neutrino flux for the ICARUS-NESSiE experiment.

3 Public presentations by group members

We have presented the status and perspectives of the ICARUS-NESSiE experiment at the following workshops/conferences:

- A. Longhin: "Search for sterile neutrinos at a new SBL neutrino beam at CERN: the ICARUS-NESSiE experiment", at the "GDR neutrino" meeting [7] in Caen (FR), 31 October 2012.

- N. Mauri:"Search for sterile neutrinos at a new SBL CERN beam" at the "24^{th} Rencontres de Blois (Particle Physics and Cosmology)" [8] (FR), in May 27-June 1, 2012.

3.1 More studies on future scenarios: leptonic CP violation

Following the confirmation of a large θ_{13} angle by the Daya-Bay and RENO experiments in March 2012 we have also engaged in a phenomenological study involving the possibility to measure the δ_{CP} phase with a future long-baseline neutrino beam based in Europe with a particular focus on possible opportunities for the CERN-to-Gran Sasso baseline. The results have been presented at the:

- "nuTURN" workshop, LNGS (IT), 20/09/2012, "Study of possible opportunities for leptonic CP violation and neutrino mass hierarchy at LNGS" (A. Longhin).
- SIF Congress, Napoli (IT), 20/09/2012, "Opportunitá per la violazione di CP leptonica e la gerarchia di massa ai laboratori del Gran Sasso nell'era di θ_{13} $\mathcal{O}(10^{-1}$" (A. Longhin).

A corresponding paper (whose content is also available on the arXiv [9]) is in the process of publication in the EPJ-C journal.

References

1. P. Bernardini *et al.* (NESSiE Coll.) SPSC–P–343, arXiv:1111.2242v1 (2011). M. Antonello *et al.* (ICARUS-NESSiE Coll.), SPSC–P–347 (2012), arXiv:1203.3432 (2012), arXiv:1208.0862v2 (2012).
2. G. Mention, *et al.*, Phys. Rev. D**83** 073006 (2011).
3. J.N. Abdurashitov *et. al* (SAGE Coll.) Phys. Rev. C**73**, 045805 (2006). M.A. Acero, C. Giunti, M. Laveder, arXiv:0711.4222 (2007). C. Giunti, M. Laveder, arXiv:1006.3244 (2010).
4. A. Aguilar *et al.* (LSND Collaboration), Phys. Rev. D 64, 112007 (2001).
5. A. A. Aguilar-Arevalo (MiniBooNE Coll.), Phys. Rev. Lett. 102, 101802 (2009). A. A. Aguilar-Arevalo *et al.* (MiniBooNE Coll.), arXiv:1007.1150. F. Mills, ICHEP 2010, Paris, France. R. Van de Water, Neutrino 2010, Athens, Greece. E.D. Zimmerman, PANIC 2011, Cambridge, U.S.A.. A. A. Aguilar-Arevalo (MiniBooNE Coll.), arXiv:1207.4809.
6. E. Komatsu *et al.*, Astrophys. Jour. Suppl. 192:18, (2011). J. Dunkley *et al.*, Astrophys. Jour. 749 90 (2012). J. Hamann *et al.*, Phys. Rev. Lett. 105:181301, (2010). Y. I. Izotov, T. X. Thuan, Astrophys. Jour. Lett. 710 (2010).
7. GDR neutrino, Caen (FR), 31 Oct. 2012, `https://indico.cern.ch/getFile.py/access?contribId=4&sessionId=6&resId=0&materialId=slides&confId=207406`.
8. 24^{th} Rencontres de Blois 2012, `http://blois.in2p3.fr/2012/transparencies/tuesday_afternoon/neutrinos/Mauri.pdf`.
9. S. Dusini, A. Longhin, M. Mezzetto, L. Patrizii, M. Sioli, G. Sirri, F. Terranova. hep-ph//1209.5010v1

OPERA

V. Chiarella, F. Grianti (Ass.), A. Gambarara (Tecn., Ass.),
N. Intaglietta (Tecn., art.15), A. Mengucci (Tecn.), N. Mauri (Ass. Ric.),
A. Paoloni (Resp.), M. Spinetti, F. Terranova, T. Tonto (Tecn.),
M. Ventura (Tecn.), L. Votano

in collaboration with

LNF-SEA (Div. Ric.): U. Denni, G. Papalino
LNF-SPAS (Div. Ric.): A. Cecchetti, D. Orecchini

1 The experiment

OPERA [1)] has been designed to provide a very straightforward evidence for $\nu_\mu \to \nu_\tau$ oscillations in the parameter region indicated by Super-Kamiokande as the explanation of the zenith dependence of the atmospheric neutrino deficit. It is a long baseline experiment located at the Gran Sasso Laboratory (LNGS) and exploiting the CNGS neutrino beam from the CERN SPS. The detector [2)] is based on a massive lead/nuclear emulsion target. The target is made up of emulsion sheets interleaved with 1 mm lead plates and packed into removable "bricks" (56 plates per brick). Each brick is equipped with a detachable emulsion doublet ("Changeable Sheet", CS), which is scanned before the full development of the brick emulsions. The bricks are located in a vertical support structure making up a "wall". These bricks were produced in situ by a "brick assembly machine" (BAM) located near the OPERA experimental Hall; they are inserted into the wall support structure by a dedicated robot (BMS). Nuclear emulsions are used as high resolution tracking devices for the direct observation of the decay of the τ leptons produced in ν_τ charged current interactions. Electronic detectors positioned after each wall locate the events in the emulsions. They are made up of extruded plastic scintillator strips read out by wavelength-shifting fibers coupled with photodetectors at both ends. Magnetized iron spectrometers measure charge and momentum of muons. Each spectrometer consists of a dipole magnet made of two iron walls interleaved with pairs of precision trackers. The particle trajectories are measured by these trackers, consisting of vertical drift tube planes. Resistive Plate Chambers (RPC) with inclined strips, called XPC, are combined with the precision trackers to provide unambiguous track reconstruction in space. Moreover, planes of RPC are inserted between the magnet iron plates. They allow for a coarse tracking inside the magnet to identify muons and ease track matching between the precision trackers. They also provide a measurement of the tail of the hadronic energy leaking from the target and of the range of muons which stop in the iron. A block of 31 walls+scintillator planes, followed by one magnetic spectrometer constitutes a "super-module". OPERA is made up of two super-modules (SM) located in the Hall C of LNGS (see Fig. 1). Since 2008 all bricks have been inserted, for a total of 150036 bricks, corresponding to a target mass of 1.25 kton, now decreased to 1.15 kton after the extraction of the bricks analyzed so far.
OPERA is able to observe the ν_τ signal with an impressively low background level. The direct and

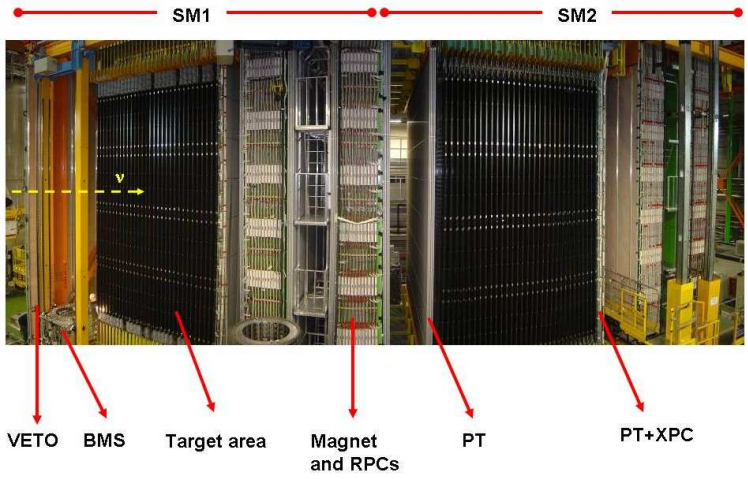

Figure 1: *A fish-eye view of the OPERA experiment. The upper red horizontal lines indicate the position of the two identical super-modules (SM1 and SM2). The "target area" is made up of planes of walls filled with lead-emulsion bricks interleaved with planes of plastic scintillators (TT): the black covers visible in the photograph are the end-caps of the TT. Arrows show also the position of the VETO planes, the drift tubes (PT) followed by the XPC, the magnets and the RPC installed among the magnet slabs. The Brick Manipulator System (BMS) is also visible. The direction of incoming neutrinos from CERN is indicated by the yellow arrow.*

unambiguous observation of $\nu_\mu \to \nu_\tau$ appearance will constitute a milestone in the study of neutrino oscillations. Moreover, OPERA has some sensitivity to the sub-dominant $\nu_\mu \to \nu_e$ oscillations [3]. The potential of the experiment for the research of oscillations into sterile neutrinos and non standard interactions has also been investigated [4, 5].

Opera is an international collaboration (Belgium, Croatia, France, Germany, Israel, Italy, Japan, Russia, Switzerland, Tunis and Turkey) and the INFN groups involved are Bari, Bologna, LNF, LNGS (Gran Sasso), Naples, Padova, Rome and Salerno. The Technical Coordinator (A. Paoloni) is a LNF researcher.

2 Overview of the OPERA activities in 2012

The CNGS complex ended its operation after the 2012 run, with 4.84×10^{19} protons delivered on target, corresponding to 3493 events inside the OPERA bricks, with an overall duty-cycle for the accelerator complex of 81%. The corresponding live-time of the detectors on the beam has been greater than 99%.

Considering all the years of data taking with the bricks inside the target, i.e. from to 2008 to 2012, the CNGS accumulated in total 18.22×10^{19} proton-on-target, about 80% of the statistics considered in the OPERA proposal, corresponding to 17330 events inside the OPERA bricks. To speed up the research of tau candidates in the exposed bricks, the collaboration has decided to postpone the analysis of those events in which the neutrino vertex is not localized in the first

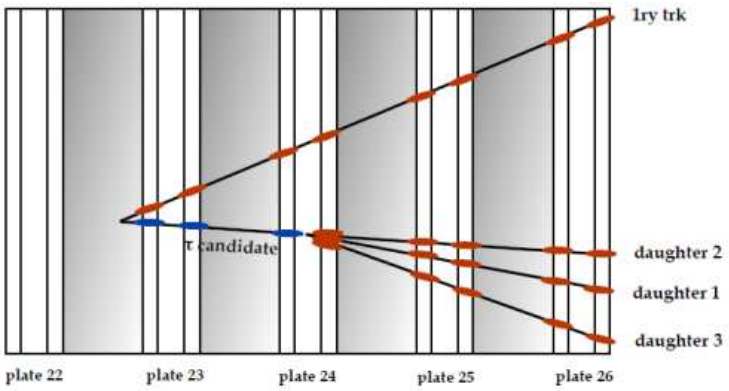

Figure 2: *The second OPERA tau candidate event.*

scanned brick and to give priority to events without muons or with muons of momentum lower than 15 GeV. Up to the end of 2012, about 9000 bricks have been scanned and 5500 events located.

During 2012, the collaboration reported the observation of the second observed tau candidate, interpreted as a 3 prong hadronic decay, whose picture is shown in Fig.2, The expected number of ν_{mu} into ν_τ oscillations is 2.1 with 0.18 background events.

The analysis of the oscillation into electron neutrinos was also completed for the 2008+2009 data sample (corresponding to 5.25×10^{19} pot). We observed 19 events, compatible with the non-oscillation expectation of 19.8 ± 2.8 events.

The experiment revised the measurement of the neutrino velocity using the electronics detectors data acquired on CNGS beam from 2009 to 2011 [6)] and performed a new measurement with the data acquired during 2012 run. Both measurements show that neutrinos are traveling at the speed velocity within experimental errors.

The analysis of the events in the bricks will continue in the next years.

3 Activities of the LNF group

The Frascati group has been responsible for the design and the construction of the dipole magnets and the general support structure of the sub-detectors. It shares responsibility with INFN Padova and LNGS for the construction and running of the bakelite RPC planes. Frascati and Naples also designed and prototyped the wall support structures housing the lead/emulsion bricks and LNF was responsible for their production and installation. The Frascati group has been also involved, with the University of Hamburg, in the trigger of the drift tubes, performed by the Resistive Plate Chambers.

On the emulsion side, LNF was highly involved in the construction and operation of the Brick Assembly Machine (BAM) and, since 2008, contributes to the emulsion scanning with one dedicated microscope located in Frascati. Finally, since 2007 LNF follows the brick handling of OPERA, with the management of the X-ray marking facilities and the automation of the temperature control of the development tanks.

The group is contributing also to data analysis, with particular interest in electronic detectors (cosmic ray studies, RPC data quality checks, neutrino velocity measurement) and in the statistical significance assessment of the observed ν_μ into ν_τ oscillations.

3.1 Resistive Plate Chambers

After major contributions in the construction of the RPC system, the LNF group has been highly involved in its running during the CNGS data taking. One of the duties of the group is the monitoring of the performances as a function of time. In OPERA, Resistive Plate Chamber with bakelite electrodes are arranged into layers, 22 in each spectrometer, inserted into 2 cm gaps inside the magnetized iron. Two additional layers, called XPCs because of the inclined read-out strips, are placed in each Super-Module between the Target Tracker and the spectrometer. The XPC layers and 7 out of 22 RPC layers in each spectrometer are instrumented with dedicated Timing Boards (TBs) for triggering the drift tubes. A complete description of the OPERA RPC system can be found on [2, 9, 10].

The detectors are operated in streamer mode at 5.7 kV with the gas mixture $Ar/C_2H_2F_4/i-C_4H_{10}/SF_6 = 75.4/20.0/4.0/0.6$ [11]. An automatic correction is applied for the pressure, according to [12]; the temperature is quite stable, between 15 and 18^{o}C, depending on the detectors position. Signals from the vertical strips, measuring the bending coordinate, are discriminated at 40 mV, while the threshold for the horizontal strips is 26 mV, in order to correct for the different impedance matching with the read-out twisted flat cables.

The full RPC system ran smoothly during the 2012 run, with almost no dead-time and with performances similar to those observed in previous years [7], matching the required specifications, with efficiency greater than 90% and time resolutions better than 5 ns.

The main aging effect observed on OPERA RPCs is the progressive increase of electrode resistivity due to the drying of the bakelite. Since the gas mixing is in common between the bakelite RPCs (instrumenting the spectrometers) and the glass ones (instrumenting the VETO system), both detectors are indeed flushed with a dry mixture. The chambers in the spectrometers are disposed in rows of three chambers, with the gas flowing from column 1 to column 3. In figure 3 it is shown the average efficiency measured on cosmic rays as a function of the RPC position along the gas flow. During the years of operation, detector efficiencies have slightly decreased, especially at the entrance of the gas, as expected.

3.2 Cosmic rays analysis with OPERA detector

Beside its main goal of neutrino oscillation appearance, the OPERA experiment is perfectly suited as a cosmic ray detector due to its interesting physics capabilities. OPERA is located in the underground Gran Sasso Laboratory, at an average depth of 3800 meters of water equivalent (m.w.e.). The rock overburden naturally selects very energetic muons. The detector observes underground muons with a minimum surface energy of 1 TeV and the mean value of their energy spectrum is about 2 TeV. The analysis of the atmospheric muon charge ratio $R_\mu = N_{\mu^+}/N_{\mu^-}$ in the highest energy region with the whole OPERA statistics over five years is in progress.

Another important item is the search for coincident events between the LVD and OPERA detectors, respectively located in Hall A and C at LNGS. The idea is to look for shower events

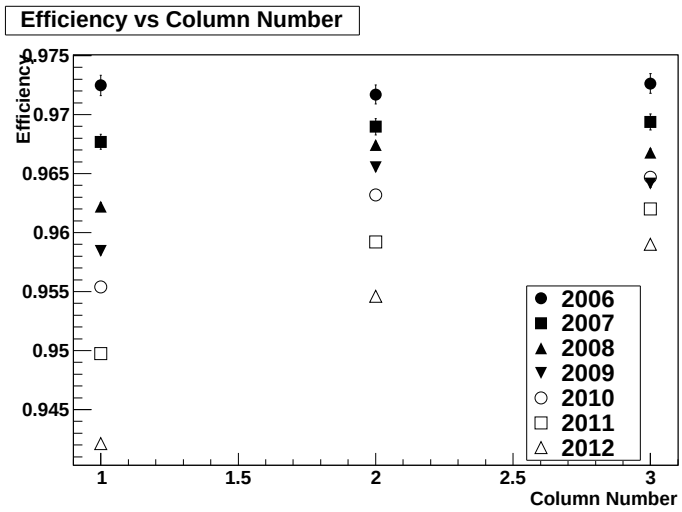

Figure 3: *Average RPC efficiency along the gas flow for the different data taking years.*

intercepted by both detectors as a tool for study high p_t events in cosmic rays. Given the large distance between the two detectors ($d \sim 170$ m) coincident muon bundles would allow to address the boundary region where pQCD gives way to soft physics, a region of particular interest for the modeling of high energy Monte Carlo codes. Possibly CNGS-correlated coincident events would also allow the study of large angle di-muon events from charmed particles produced by charge-current neutrino interaction in the rock upstream the detectors. The analysis was jointly carried out by the two Collaborations after a formal agreement.

A preliminary analysis showed no interesting events related to muon bundles. We observed several events with a large ($\sim$ 600 ns) time difference between the two detectors. After visual scanning these events were identified as single muon events, hitting OPERA first and then LVD, coming from the so called Teramo Valley, a peculiar region in the Gran Sasso orography with large zenith angles ($>$ 80 deg) and modest rock thickness ($\sim$ 2200 m).

After the first release of the neutrino velocity measurement, showing an anomalous anticipation of the neutrino time-of-flight, by continuing the campaign of cross checks, the fiber delay measurement was repeated in December 2011. The result was different from the one obtained in 2007 and quoted in the analysis. The Bologna and LNF groups used the high energy muon beam ($\sim$ 270 GeV) from the Teramo Valley as a probe to cross-calibrate the two detector timing systems.

We extended the OPERA-LVD coincidence analysis to a larger period (2007-2012 Runs' data). We found a discontinuity in the muon time-of-flight around summer 2008 of the same size of the fiber delay anomalous result. The analysis also confirmed the existence of a drift in the OPERA internal clock [13].

This led to a model able to explain all the effects, historicizing when the two issues arose. The coincidence analysis solved the neutrino velocity anomaly and contributed to reassess the measurement eventually presented in Ref. [6].

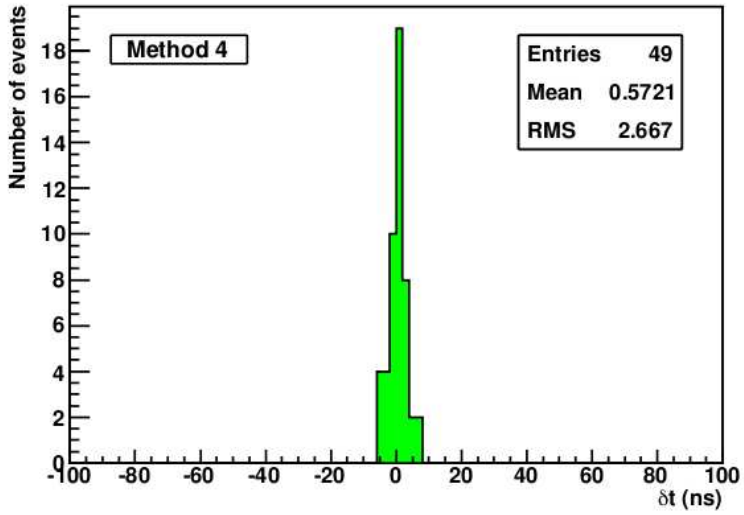

Figure 4: *CNGS neutrinos timeofflight distribution: δt=L/c-TOF, where L=baseline CERN-LNGS and TOF=measured time-of-flight.*

3.3 Neutrino velocity measurement

After the measurement of the CNGS neutrinos velocity with the data acquired from 2009 to 2011, the OPERA experiment performed several improvements on the setup for the 2012 bunched beam run [14].

One of these improvements is the duplication of the DAQ for the resistive plate chambers with a new VME based system, in order to perform cross-checks on eventual data anomalies. The key element of the new system is a custom VME board receiving through an optical fiber the synchronization signal of the Gran Sasso atomic clock (PPmS), reading its UTC time (coded with ms precision) and distributing it to the readout electronics in standard NIM logic. The module, originally designed for the NAUTILUS experiment by the LNF electronic workshop, has been adapted for the operation in the underground Gran Sasso laboratory, with the addition of large bandwidth amplifier to compensate for the light attenuation over the 8 km optical fiber connecting the module to the atomic clock located in the external laboratory.

The repeated PPmS and the OR signals of the 14 RPC layers instrumented with the Timing Boards are acquired by a VME TDC with 800 μs range and 1 ns precision; their time difference is the sub-ms component of the corresponding UTC times. The custom VME PPmS receiver module provides also a reference 5 kHz frequency for calibrating and verifying the stability of the internal TDC frequency.

The measured time of flight is consistent with the neutrinos traveling at the speed of light, while the rms of the distribution, shown in figure 4, is 2.7 ns, the best among all the experiments at GranSasso. The systematic error on the measurement is around 3 ns, dominated by the knowledge of the RPC detector intrinsic response delay.

This delay has been measured on purpose in the external LNGS laboratories triggering cosmic rays with a time-calibrated detector (a scintillator read-out by a photomultiplier), acquiring the analog signals by means of a 5 GSample/sec digitizer. We have found that the intrinsic delay in the response of OPERA RPCs (gas gap=2mm, operated in streamer mode) is 24 ± 2 ns.

3.4 Analysis of the OPERA emulsion detectors at the LNF scanning station

The OPERA brick is based on the Emulsion Cloud Chamber (ECC) detector concept, fulfilling the requirements of high granularity and micrometric resolution necessary to distinguish the τ decay vertex from the primary ν_τ interaction. Each ECC can act as a standalone detector that can be selectively removed from the target, developed and analyzed after the interaction took place.

A detailed description of the automatic microscopes developed for the analysis of OPERA ECCs can be found in Ref. [15]. The ECC (or "brick") dimensions and length are optimized to contain the primary as well the decay vertex and to provide particle identification and kinematical reconstruction. The use of passive material, combined with high accuracy tracking devices, allows for momentum measurement of charged particles via multiple Coulomb scattering (MCS) and for electromagnetic shower identification [16].

The bricks selected by the electronic detectors as containing a neutrino interaction vertex are extracted from the OPERA target and equally shared between Japan and Europe for the scanning. The CS doublet acts as a confirmation of the trigger provided by the Target Tracker: the brick is developed only if the prediction is confirmed, otherwise the CS is replaced and the brick is put back in the target. For events assigned to the European community the CS doublets are analyzed at the LNGS scanning station and the scanning load is shared among a group of specialised shifters. Since 2008 the LNF group contributes to the CS doublets scanning performing shifts at the LNGS station, in addition to the work load at the home scanning laboratory. The LNF scanning station [18] is part of the network of italian scanning groups including Bari, Bologna, LNGS, Napoli, Padova and Roma1 to which the emulsions developed at LNGS are sent for the final analysis.

The LNF emulsion scanning station (Building 29) is hosted in a climatised environment to ensure good conditions for emulsion storage. The station is equipped with a motorized optical microscope instrumented with a system for the emulsion plates loading on the microscope stage (Plate Changer). The whole chain for brick scanning at LNF is fully operational since 2008. It consists of three phases: the brick scanning, the event reconstruction and the data publication on the central database.

After concentrating on the specific task of studying the event kinematics in the emulsions (see the report for 2011), since February 2012, the LNF scanning station has resumed the vertex location activities on a signal enriched sample of NC-like interactions registered by the detector in 2011 and 2012 with the aim of exploring as much as possible the occurrence of new τ candidates. In 2012 a total number of about 40 bricks has been treated. The event display of a remarkable event with a high-energy electromagnetic shower identified with our microscopes during this campaign is shown in Fig. 5. The scanning and analysis flow is smoothly running on-time with the brick assignment. The LNF scanning laboratory shows good performances with a 75% location efficiency, in agreement with the expectations.

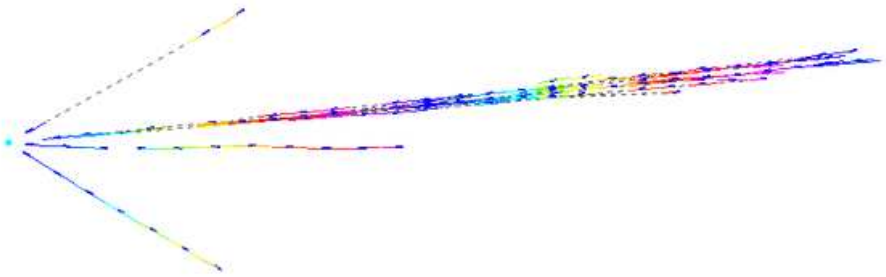

Figure 5: *A neutrino interaction in an OPERA brick found at the LNF scanning station. An animated 3D view is available at* [18].

Besides the scanning activity we are also deeply involved in the development of the simulation and the global analysis of the emulsion data in view of upcoming publications.

4 List of Conference Talks by LNF Authors in Year 2012

1. A. Longhin "Results from OPERA", Moriond EWK, La Thuile, Italy, 04 March 2012.
2. A. Paoloni, "Performance and aging of OPERA bakelite RPCs", XI Workshop on Resistive Plate Chambers and Related Detectors, LNF, Italy, 6-10 February 2012.
3. N. Mauri, "Highlights from the OPERA experiment" ICFP 2012, International Conference on New Frontiers in Physics Kolymbari, Crete, Greece, 10-16 June 2012.

5 Publications

1. N. Agafonova *et al.* [LVD and OPERA Collaborations], "Determination of a time-shift in the OPERA set-up using high energy horizontal muons in the LVD and OPERA detectors" Eur. Phys. J. **127**, 71 (2012).
2. A. Paoloni *et al.*, "Long term performances of OPERA bakelite RPC system.", Nucl. Instrum. Meth., **A661**, S60 (2012).
3. N. Agafonova *et al.* [OPERA Collaboration], "Search for $\nu_\mu \Rightarrow \nu_\tau$ oscillation with the OPERA experiment in the CNGS beam", New J.Phys. **14**, 033017 (2012).
4. N. Agafonova *et al.* [OPERA Collaboration], "Momentum measurement by the Multiple Coulomb Scattering method in the OPERA lead emulsion target.", New J.Phys. **14**, 013026 (2012).

5. T. Adam *et al.* [OPERA Collaboration], "Measurement of the neutrino velocity with the OPERA detector in the CNGS beam", JHEP **10**, 093 (2012).
6. A. Paoloni *et al.*, "Performance and aging of OPERA bakelite RPCs", PoS (RPC2012), 010 (2012).

References

1. M. Guler *et al.*, OPERA proposal, CERN/SPSC 2000-028, SPSC/P318, LNGS P25/2000.
2. R. Acquafredda *et al.*, JINST **4**, P04018 (2009).
3. M. Komatsu, P. Migliozzi, F. Terranova, J. Phys. **G29**, 443 (2003); P. Migliozzi, F. Terranova, Phys. Lett. **B563**, 73 (2003).
4. A. Donini, M. Maltoni, D. Meloni, P. Migliozzi and F. Terranova, JHEP **0712**, 013 (2007).
5. M. Blennow, D. Meloni, T. Ohlsson, F. Terranova and M. Westerberg, Eur. Phys. J. **C56**, 529 (2008).
6. T. Adam *et al.* [OPERA Collaboration], JHEP **10**, 093 (2012).
7. See "LNF 2009 Annual Report", D. Babusci ed., LNF-10/15 (IR), p.97, "LNF 2008 Annual Report", D. Babusci ed., LNF-09/04 (IR), p.99, "LNF 2007 Annual Report", M. Antonelli ed., LNF-08/20 (IR), p.103; "LNF 2006 Annual Report", M. Antonelli ed., LNF-07/10 (IR), p.87; "LNF 2005 Annual report", E. Nardi ed., LNF-06/10 (IR), p.78; "LNF 2004 Annual Report", E. Nardi ed., LNF-05/5 (IR), p.70; "LNF 2003 Annual Report", S. Dell'Agnello ed., LNF-04/08 (IR), p.64.
8. A. Cazes *et al.*, JINST **2**, T03001 (2007).
9. S. Dusini *et al.*, Nucl. Instrum. Meth., **A602**, 631 (2009).
10. A. Paoloni *et al.*, Nucl. Instrum. Meth., **A602**, 635 (2009).
11. A. Mengucci, A. Paoloni, M. Spinetti, L. Votano, Nucl. Instrum. Meth., **A583**, 264 (2007); A. Paoloni *et al.*, LNF Technical Note **LNF-08/14(NT)** (2008).
12. M. Abbrescia *et al.*, Nucl. Instrum. Meth., **A359**, 603 (1995).
13. N. Agafonova *et al.*, Eur. Phys. J. **127**, 71 (2012).
14. A. Balla *et al.*, OPERA internal note **156** (2012)
15. N. Armenise *et al.*, Nucl. Instrum. Meth. **A551**, 261 (2005).
16. L. Arrabito *et al.*, JINST **2**, P05004 (2007).
17. A. Anokhina *et* al. [OPERA Coll.], JINST **3**, P07005 (2008).
18. LNF scanning station.
    `http://www.lnf.infn.it/esperimenti/opera/scanning.html`,
    `http://www.lnf.infn.it/esperimenti/opera/scanning/figs/animation_54105.gif`

ROG

G. Giordano (Resp.), M. Iannarelli (Tecn.), R. Lenci (Tecn.),
A. Marini (Ass.), G.P. Murtas (Ass.), G. Pizzella (Ass.),
F. Ronga (Ass.), E. Turri (Tecn.)

ROG Collaboration includes groups at :
University of Rome La Sapienza and INFN Roma 1,
University of Rome Tor Vergata and INFN Roma 2

1 Introduction

The ROG group is currently operating the cryogenic gravitational wave (GW) bar detector NAUTILUS, hosted in Frascati National Laboratory. The other detector that was operated by the ROG group, EXPLORER at CERN, ceased its operation on June 2010, by decision of INFN. The main goal of this search is the direct detection of the GW's that could be emitted by astrophysical sources (such as Supernovae or Coalescent Binaries). Such detection would be of enormous interest for general relativity and astrophysics.

The NAUTILUS detector consists of an aluminum cylindrical bar having a mass of $\simeq 2.3$ tons, with a capacitive resonant transducer mounted on one of the bar faces. It is contained in a vacuum cryostat, cooled at cryogenic temperatures (at present $\simeq 3$ K, but a temperature as low as 0.1 K can be reached) to reduce thermal noise, and isolated from seismic and acoustic disturbances.

The capacitive transducer is coupled to a very low noise superconducting amplifier (d.c. SQUID) whose output is acquired by a VME ADC board, sampled at 5 kHz.

A GW signal would excite the mechanical resonant modes of the bar-transducer system. When searching for impulsive signals, the data are filtered with an adaptive filter matched to a delta-like signal. This search for bursts is suitable for any transient GW which shows a nearly flat Fourier spectrum at the two resonance frequencies of the detector.

Both EXPLORER and NAUTILUS have been kept in continuous observational mode since 2003, with a duty cycle between 80 and 90%, mainly limited by the necessary periodic cryogenic operations.

The LNF group has major responsibilities in the maintenance and running of NAUTILUS (including the production of liquid Helium), in the maintenance, upgrading and running of the cosmic ray detectors, in the data acquisition and in many items of data analysis.

2 NAUTILUS and EXPLORER

The ultra-cryogenic detector NAUTILUS is operating at the INFN Frascati National Laboratory since December 1995. It is equipped with a cosmic ray detector based on a streamer tube assembly.

The present data taking started in 2003, with a new bar tuned at 935 Hz, where a pulsar, remnant of the SN1987A, is supposed to emit GW's, with a more sensitive readout chain (the same as for EXPLORER), and a new suspension cable, to provide a more stable position setting. At present, the temperature of the bar is 3.5 K and the resulting strain noise (the minimum detectable spectral density) is $\tilde{h} \simeq 1 \cdot 10^{-21} \, / \sqrt{Hz}$ around 935 Hz, and $\tilde{h} \leq 10^{-20} \, / \sqrt{Hz}$ over about 50 Hz. At the beginning of 2009, we discovered that some wide-band noise was due to a malfunctioning of the UPS system. After changing the UPS and some adjustments in the SQUID electronic chain, the noise temperature decreased down to less than 1 mK, corresponding to an adimensional amplitude of GW bursts $h \simeq 2.4 \cdot 10^{-19}$.

The EXPLORER antenna was located at CERN and was very similar to NAUTILUS. Also its duty cycle was very high (of the order of 90%), its noise temperature was about 2 mK, with a strain sensitivity $\tilde{h} \simeq 2 \div 3 \cdot 10^{-21} / \sqrt{Hz}$ around the two resonances at 904 Hz and 927 Hz, and $\tilde{h} \leq 10^{-20} / \sqrt{Hz}$ over about 30 Hz. EXPLORER was equipped with a cosmic ray detector, based on a set of long plastic scintillators.

The read-out systems installed in 2001 on EXPLORER and in 2003 on NAUTILUS, obtained a larger bandwidth and consequently improved the time resolution (a few ms), as it is also been checked with the events due to cosmic ray showers.

In the last years a continuos effort has been paid in improving the data analysis system already present and in testing independent algorithms and new methods. As a result of these, still going, efforts we were able to improve the accuracy in the reconstruction of both the amplitude and time characteristic of the signals. At the same time, we performed detailed studies of the detectors response to other class of signals than the simple delta-like burst previously considered. All this was done also with a particular eye on the perspective of performing joint analyses with the interferometric type of GW detectors, which do have a much better sensitivity than the resonant bar detectors, but up to now have suffered from very long interruptions in their operation. At present, both the US interferometers (LIGO) and the french-italian one (VIRGO) are down for a major upgrade that will remain inoperative for at least 4 years, leaving the INFN bar detectors (AURIGA and NAUTILUS) the only continually operational GW detectors.

2.1 Analysis of EXPLORER-NAUTILUS data

We continued to study all possible wide-band noises that can result in a candidate event and also, through simulations and software injections of signals, to find the event characteristics (e.g. length vs. amplitude) that an event due to a real excitation must have. All this was used to reduce the number of candidate events by putting vetos on periods or single events with understood instrumental noise excess, in addition to the usual vetos on events triggered by cosmic rays showers.

In 2010, up to the EXPLORER shutdown in June 10^{th}, we had a total of $\simeq 113$ days of good data periods in the overlap between EXPLORER and NAUTILUS.

We have finished the analysis of the last period of NAUTILUS- EXPLORER overlapping operations, from April 2007 to June 2010. The analysis of this period of data, about 3 years long, was performed improving the methods used in the past, including a detailed study of the efficiencies of both detectors through the use of software injections. The search for coincidences of possible delta-like excitations, at the level of 0.1 accidentals expected in the whole period, produced a null result. We produced upper limits on the rate of GW short signals impinging on the Earth, also in this case with more refined techniques, including optimization procedures at each amplitude. The computed upper limits, at least in the high-amplitude range, are the lowest ever produced, and in all ranges improved the results previously published by resonant detectors. A paper with this analysis have been submitted for publication [1)].

2.2 Other types of analyses

- Cosmic Rays - The study of the response of our detectors to cosmic ray showers continues to demonstrate experimentally the actual capability to detect very small mechanical excitations of the bars. While the study of the timing characteristics of the larger events produced by the rare very high density showers allows us a real measure of the accuracy in the time reconstruction, the study of the much more numerous cases of low density showers, performed with a cumulative-type analysis, constitutes an independent cross-check of the amplitude response calibration.

- Exotic particles - We continued the studies for exotic particles impinging on Nautilus or Explorer. Such particles could be with a quark "s" (nuclearites) and particles with only gravitational

interactions.
- Astrowatch - Since the large interferometric GW detectors (LIGO, Virgo) have suspended operations for major upgrades, in the next 3-4 years the only continually operating GW detectors will be NAUTILUS and AURIGA, at Legnaro National Laboratory. The two groups have reached an agreement to be in a coordinated "astrowatch operation". The intent is to be ready for a common data analysis in case an important astrophysical event (that is an event thought to be a source of GW radiation) would happen. This would lead to at least the establishment of an upper limit on the amount of GW delivered by the event, or, in the most optimistic case, if the data would show a clear behavior above any reasonable possibility of a noise fluctuation and in agreement with the expectations for that event, to a claim for detection.

In 2012, the interferometric detector GEO (Hannover, Germany) has joined this agreement for astrowatch operation. GEO operations is not continuos, being on mainly on weekends and nights, since its main operation is devoted to upgrade and operational studies.

3 List of Conference Talks by LNF Authors in Year 2010

1. F. Ronga, Vulcano workshop 2012 - Frontier objects in astrophysics and particle physics. Vulcano (Italy)

4 Publications

References

1. P. Astone *et al.*, "Analysis of 3 years of data from the gravitational wave detectors EXPLORER and NAUTILUS", arXiv:1212.5202 [gr-qc].

2. M. Bassan *et al.*, "Measurement of the thermal expansion coefficient of the Al 5056 alloy in the $0.3 < T < 2$ K temperature range", arXiv:1212.0368 [cond-mat.mtrl-sci].

3. M. Bassan *et al.*, "Vibrational excitation induced by electron beam and cosmic rays in superconductive aluminum bars", J. Phys. Conf. Ser. **375** (2012) 062006 (arXiv:1105.4724 [gr-qc]).

4. F. Ronga, "Analysis of the MACRO experiment data to compare particles arrival times under Gran Sasso", arXiv:1208.0791 [hep-ex].

WIZARD/PAMELA

G.Basini, M.Martucci (Dott.), G. Pizzella (ass.), M.Ricci (Resp.)

Participant Institutions:

ITALY: INFN Bari, LNF, Firenze, Napoli, Roma 2-Tor Vergata, Trieste;
CNR Ist. Fisica Applicata "Nello Carrara" Firenze;
ASI (Italian Space agency);
Electronic Engineering Department, University of Roma 2 "Tor Vergata";
RUSSIA: MePhi Moscow;
FIAN Lebedev Moscow;
IOFFE St Petersburg;
TsSKB-Progress Samara;
SWEDEN: KTH Stockholm;
GERMANY: Siegen University;

1 The satellite mission PAMELA

PAMELA, a part of the WIZARD international experimental program on balloon, satellite and Space Station activities, is a cosmic ray space experiment installed and running on board a Russian satellite (Resurs-DK1) which has been successfully launched on June 15th, 2006 from the cosmodrome of Baikonur, Kazakhstan, by a Soyuz TM2 rocket.

The satellite is flying in a low altitude, elliptic orbit (350-610 km) with an inclination of 70.0 degrees. The PAMELA telescope consists of a magnetic spectrometer composed of a permanent magnet coupled to a silicon tracker, an electromagnetic silicon-tungsten calorimeter, a time-of-flight system, an anticoincidence system, a shower tail catcher scintillator and a neutron detector [1, 2].

The total height of PAMELA is ~ 130 cm, the mass is 470 kg and the power consumption is 355 W.

The observational objectives of the PAMELA experiment are to measure the spectra of antiprotons, positrons and nuclei in the cosmic rays over an extended range of energies, to search for antimatter and for indirect signatures of dark matter and to study cosmic ray fluxes over a significant portion of the Solar cycle.

The main scientific goals can be schematically listed as follows:

a) measurement of the antiproton spectrum in the energy range 80 MeV-190 GeV;
b) measurement of the positron spectrum in the energy range 50 MeV-300 GeV;
c) measurement of the electron spectrum up to 500 GeV;
d) measurement of the proton spectrum up to 700 GeV;
e) measurement of the electron+positron spectrum up to ~ 1 TeV;
f) measurement of light nuclei spectra (He/Be/C) up to 200 GeV/n;
g) search for antinuclei with a sensitivity of 3×10^{-8} in the $\overline{He}/He$ ratio.

Additional objectives achievable all over the duration of the mission are:
- Long-term monitoring of the solar modulation of cosmic rays;
- Measurements of Energetic Particles from the Sun;

- High-energy Particles in the Earth magnetosphere and Jovian electrons.

2 PAMELA Main results

After almost seven years of operation, both the satellite and the PAMELA instrument have shown to be properly functioning and the performance of the detectors to be fairly good. Every day, an average of 14 GBytes of data are transmitted to the main Receiving Station NTsOMZ located in Moscow where quick-look and first control of the performances of the instrument are performed. Then, all data are transferred through high-speed networks to CNAF, Bologna and to the participating institutions of the PAMELA International Collaboration for the full analysis of data. PAMELA, at present, has collected some 33 TBytes of data corresponding to about 3.5 billion events.

Due to the overall good performance of both the satellite and the instruments on board, and according to the latest agreements between the Russian Space Agency Roscosmos and INFN for the extension of the mission of one more year, PAMELA will continue running and taking data in 2013 (the mission was initially planned for three years).

2.1 Antiprotons

The antiproton energy spectrum and the antiproton-to-proton flux ratio measured by PAMELA [3] in the energy interval between 60 MeV and 180 GeV are shown respectively in Fig.1 and Fig.2, along with other recent experimental data and theoretical calculations done assuming pure secondary production of antiprotons during the propagation of cosmic rays in the galaxy. The curves were calculated for solar minimum, which is appropriate for the PAMELA data taking period, using the force field approximation [4]. The PAMELA results are in agreement with the previous measurements. They reproduce the expected peak around 2 GeV in the antiproton flux (due to the kinematic constraints on the antiproton production) and are in overall agreement with a pure secondary production. The experimental uncertainties are smaller than the spread in the different theoretical curves and, therefore, the data provide important constraints on parameters relevant for secondary production calculations. However, a possible contribution from non thermally produced dark matter annihilation is suggested by some authors [5].

2.2 Positrons

The positron to all electron (i.e. electron + positron) ratio measured by the PAMELA experiment [6] is given in Fig.3, compared with other recent experimental results.

The calculation, shown in the same figure, for pure secondary production of positrons during the propagation of cosmic rays in the Galaxy without re-acceleration processes provides evidence that the positron fraction is expected to fall as a smooth function of increasing energy if secondary production dominates. The data, covering the energy range 1.5 - 100 GeV, show two clear features. At low energies, below 5 GeV, the PAMELA results are systematically lower than data collected during the 1990s; this can be convincingly explained by effects of charge-dependent solar modulation. At high energies, above 10 GeV, data show a positron fraction significantly increasing with energy. The background propagation model considered in Fig.3 is clearly not able to fully account for the experimental data. In particular, the rising at $E > 10$ GeV seems a very difficult feature to be reproduced by a pure secondary component without using an unrealistic soft electron spectrum [7], suggesting the existence of other primary sources [8].

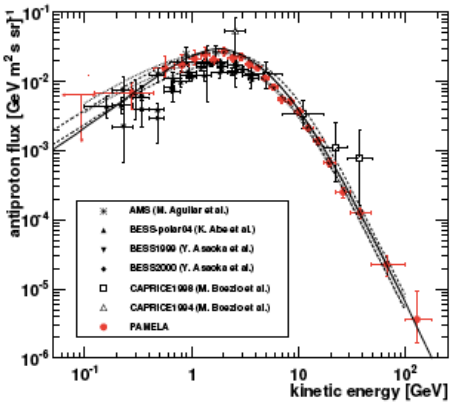

Figure 1: The PAMELA antiproton energy spectrum compared with recent measurements (see references in [3]).

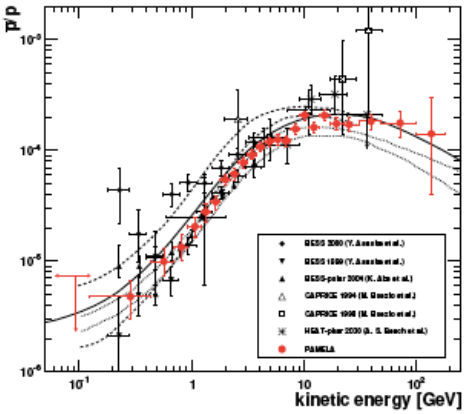

Figure 2: The PAMELA antiproton-to-proton flux ratio compared with recent measurements (see references in [3]).

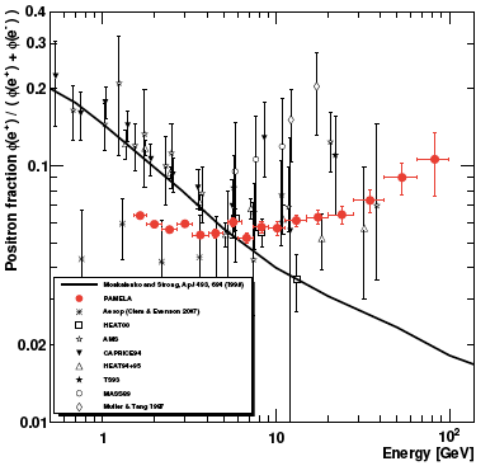

Figure 3: The PAMELA positron fraction compared with other recent experiments (see references in [6]).

The most problematic theoretical challenge posed by the PAMELA results is the asymmetry between leptonic (positron fraction) and hadronic (antiproton-proton ratio) data, difficult to explain in the framework in which the neutralino is the dominant dark matter component. A suitable explanation requires a very high mass (M >10 TeV) neutralino [9], which is unlikely in the context of allowable energy supersymmetry breaking models. Better descriptions are obtained in terms of leptonic annihilation channels for a wide range of the WIMP masses [9]. Furthermore, all explanations in terms of dark matter annihilation require a boost factor for the annihilation standard rate ranging between 10^2 to 10^3. Among the models proposed to explain the PAMELA data, it is worth to cite also the Kaluza-Klein (KK) dark matter [10], in the Universal Extra Dimension framework. Besides particle physics interpretations, a variety of astrophysical models have been put forward to explain the positron excess. One plausible explanation relates to a contribution from nearby and young pulsars, objects well known as particle accelerators. Only a few months before the publication of PAMELA positron data, the ATIC collaboration reported an excess in the galactic all electron (sum of electrons plus positrons) energy spectrum at energies of $\sim 500 - 800$ GeV [11], which led to the speculation over the existence of a nearby source of energetic electrons, either of astrophysical or exotic nature. Later in 2009, the Fermi collaboration released results about the all electron spectrum up to 1 TeV [12]. Fermi high precision data show that this spectrum falls with energy as $E^{-3.0}$ - harder than the conventional diffusive model - but does not exhibit the same prominent spectral features of ATIC. The significant flattening of the Fermi data may suggest the presence of one or more local sources of high energy CR electrons, but also dark matter scenarios cannot be excluded. Many different articles appeared, which took into account in the same theoretical frame the data from PAMELA, ATIC and Fermi.

2.3 Proton and Helium spectra

PAMELA has measured the absolute cosmic ray proton and helium spectra [13] in the rigidity interval between 1 GV and 1.2 TV (Fig.4). The results are consistent with those of other experiments within the statistical and systematic uncertainties. The differences at low energies (< 30 GeV) are caused by solar modulation effects. PAMELA results overlap with ATIC-2 data [14] between $\sim$ 200 and $\sim$ 1200 GV, but differ both in shape and absolute normalization at lower energies. The extrapolation to higher energy of the PAMELA fluxes suggest a broad agreement with those published by CREAM [15] and JACEE [16] but are higher than the RUNJOB [17] helium data. To gain a better understanding of the spectra, the results have been re-analyzed in terms of rigidity instead of kinetic energy per nucleon (Fig.5). Two important conclusions can be drawn from the PAMELA data.

Firstly, the proton and helium spectra have different spectral shapes. If a single power law is fit to the data between 30 GV and 1.2 TV, the resulting spectral indices show a significant difference. Secondly, the PAMELA data show clear deviations from a single power law model. The spectrum of protons gradually softens in the rigidity range 30 - 230 GV. At 230 - 240 GV the proton and Helium data exhibit an abrupt spectral hardening. This hardening could be interpreted as an indication of different populations of cosmic ray sources. Analysis of further data is in progress and more details of these results and of the analysis procedure can be found in [13].

2.4 Geomagnetically trapped cosmic-ray antiprotons around Earth

The most recent major result obtained by PAMELA is the observation - for the first time - of antiprotons trapped in Earth's inner radiation belt [18]. The antiparticle population originates from CR interactions in the upper atmosphere and subsequent trapping in the magnetosphere.

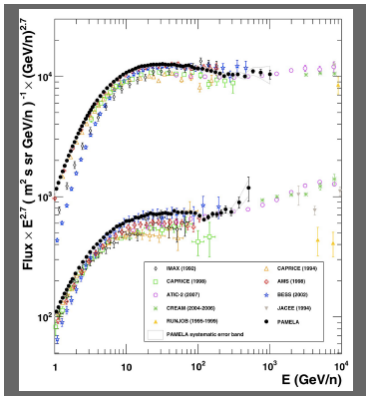

Figure 4: Proton (top points) and Helium (bottom points) absolute fluxes measured by PAMELA above 1 GeV/n compared with previous experiments (see details and references in [13]).

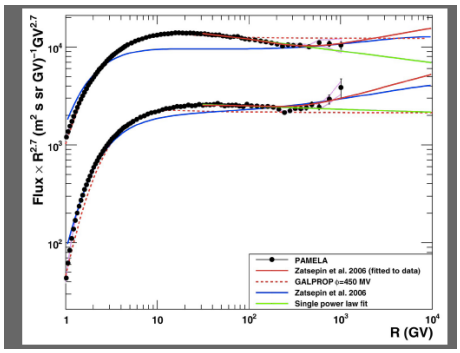

Figure 5: Proton (top points) and Helium (bottom points) data measured by PAMELA in the rigidity range 1 GV - 1.2 TV. The shaded area represents the estimated systematic uncertainty (see details and references in [13]).

PAMELA data confirm the existence of a significant antiproton flux in the South Atlantic Anomaly (SAA) region below ~ 1 GeV in kinetic energy, as shown in Fig.6.

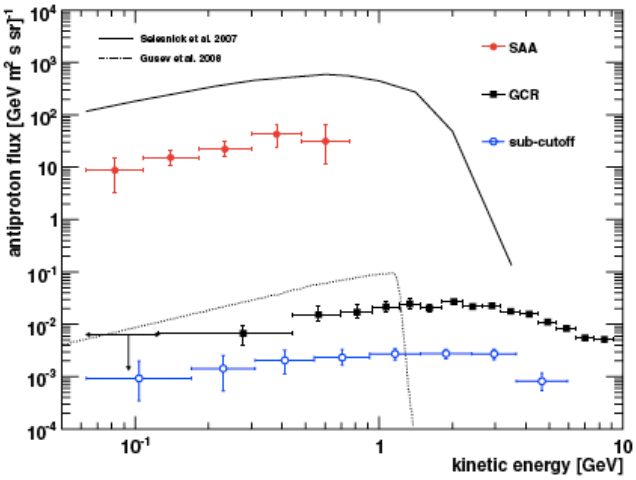

Figure 6: Geomagnetically trapped antiproton spectrum measured by PAMELA in the SAA region (red full circles). The error bars indicate statistical uncertainties. Trapped antiproton predictions by [19] for the PAMELA satellite orbit (solid line), and by [20] at L-shell = 1.2 (dotted line), are also reported. For comparison, the mean atmospheric under-cutoff antiproton spectrum outside the SAA region (blue open circles) and the galactic CR antiproton spectrum (black squares) measured by PAMELA ([3]) are also shown.

The flux exceeds the galactic CR antiproton flux by three orders of magnitude at the current solar minimum, thereby constituting the most abundant antiproton source near the Earth.

A measurement of the sub-cutoff antiproton spectrum outside the SAA region is also reported. PAMELA results allow CR transport models to be tested in the terrestrial atmosphere and significantly constrain predictions from trapped antiproton models, reducing uncertainties concerning the antiproton production spectrum in Earth's magnetosphere.

2.5 Solar events observation by PAMELA

The wide interval of measured energies makes PAMELA a unique instrument for solar energetic particle (SEP) observations filling the energy gap between the highest energy particles measured in space and the ground-based domain. Furthermore, these data can be used to study the effect of solar modulation in great detail. Since the start of Solar Cycle 24, PAMELA has observed and collected data during several solar events. A new collaboration for joint analysis of PAMELA data in comparison with other dedicated space missions has been established with the New Mexico State University, the University of New Hampshire and the NASA Goddard Space Flight Center. Data analysis is in progress and the extension of the PAMELA mission for one more year in 2013 will contribute to increase the statistics over a relevant part of an entire solar cycle.

3 Activity of the LNF group during year 2012 and for 2013

The LNF PAMELA group has been fully involved in all the previous balloon and present satellite programs in the design, prototyping, test and instrumental R&D for space. During the year 2012 the LNF group has continued the activity in the analysis, running and quick-look control of the mission. In particular, it is fully involved in the analysis of solar events (Solar Flares, SEP, Forbush decrease) which is also the argument of a doctoral thesis. The same activity will continue in 2013, including presentations at the International Cosmic Ray Conference (ICRC 2013), Rio de Janeiro. Final publications are expected from the analysis of the latest data.

References

1. M. Casolino *et al.*, Adv. Space Res. **42**, 455 (2008)
2. P. Papini *et al.*, Nucl. Instr. and Meth. Phys. Res. **A588**, 259 (2008)
3. O. Adriani *et al.* (PAMELA Collaboration) *Phys. Rev. Lett.* **105**, 121101 (2010).
4. L.J. Gleeson and W.I. Axford *Astrophys. J.* **154**, 1011 (1968).
5. G. Kane *et al.Phys. Lett. B* **681**, 151 (2009).
6. O. Adriani *et al.*(PAMELA Collaboration) *Nature* **458**, 607 (2009).
7. T. Delahaye *et al. Astron. Astrophys.* **501**, 821 (2009).
8. P.D. Serpico *Phys. Rev. D* **79**, 021302 (2009).
9. M. Cirelli *et al. Nucl. Phys. B* **813**, 1 (2009).
10. D. Hooper and K.M. Zurek *Phys. Rev. D* **79**, 103529 (2009).
11. J.Chang *et al.* (ATIC Collaboration) *Nature* **456**, 362 (2008).
12. A.A. Abdo *et al.* (Fermi LAT Collaboration) *Phys. Rev. Lett* **102**, 181101 (2009).

13. O. Adriani *et al.* (PAMELA Collaboration) *Science* **332**, 69 (2011).

14. J.P. Wefel *et al.* (ATIC Collaboration) *Proc. 30th ICRC, Merida* **2**, 31(2007).

15. H. S. Ahn *et al.*(CREAM Collaboration) *Astroph. J. Lett.* **714**, L89 (2010).

16. K. Asakimori *et al.* (JACEE Collaboration) *Astroph. J.* **502**, 278 (1998).

17. M. Areyama (RUNJOB Collaboration) *J. Phys. Conf. Ser.* **31**, 159 (2006).

18. O. Adriani *et al.* (PAMELA Collaboration) *Astroph. J. Lett.* **737**, L29 (2011).

19. R.S. Selesnick *et al.Geophys.Res. Lett.* **34**, 20 (2007).

20. A. Gusev *et al.Adv. Space Res.* **42**, 1550 (2008).

ALICE

N. Bianchi, G.P. Capitani (Ass.), A. Casanova Diaz (Ass.), L. Cunqueiro (Ass.),
P. Di Nezza (Resp. Loc.), A. Fantoni, P. Gianotti, S.Liuti (Ass.), A. Moregula (Ass.), V. Muccifora,
A. Orlandi (Tecn.), A.R. Reolon, F. Ronchetti (Ass.), A. Viticchié (Tecn.)

1 Introduction

ALICE is an experiment at CERN which involves about 1100 physicists from more than 100 Institutions from several Countries. Italy participates with 12 groups and about 200 physicists. The Frascati group is deeply involved in the electromagnetic calorimeter project (EMCal), both on the hardware and software side taking, in addition, the responsibility of System Run Coordinator for the full year. On the data analysis side the group is focused on the physics of the jets. This choice comes from the fact that the EMCal enables ALICE, like no other experiment before, to explore the physics of jet quenching, i.e. the interaction of energetic partons with the QCD hot and dense medium, over the large kinematic range provided by the LHC. The EMCal provides both fast triggers (level 0 and 1) for photons, electrons, and jets and a High Level Trigger (HLT) as well. The EMCal also measures the neutral energy component of jets, enabling full jet reconstruction in all collision systems, from proton-proton to Pb-Pb, passing through the p-Pb collisions scheduled for the 2013. The combination of the EMCal, the excellent ALICE charged tracking capabilities, and the modest ALICE magnetic field strength, is a preferred configuration for jet reconstruction in the high background environment of heavy-ion collisions, allowing detailed optimization of background rejection while preserving the crucial jet quenching signals at low transverse momenta. The first paper on jets had the Frascati group as co-first author while, at the moment, a new analysis investigating the hadron-jet correlation, close to be published, sees the Frascati group as the main author. ALICE data open the frontiers to rare events, to very high transverse momentum jets and give new tools for investigating the QCD and the Quark Gluon Plasma physics. An EMCal extension, called DCal, has been completed and is ready to be installed during the LHC long shutdown 2013-2014.

2 EMCal

The calorimeter was fully working for the whole data taking of the ALICE spectrometer. Together with the Inner Tracking System, it was the most efficient detector, participating at the 94% of the data taking time. The status of the system is shown in Fig.1 where the percentage of the dead calorimetric cells is plotted for the 15 periods of the 2012 full data taking; the number of inefficiencies is always $\leq$2%. In Fig.2 is shown the average number of clusters per event for a sample of runs and for each of the 10 Super-Modules. Also in this case the stability of the system is clear.

2.1 High Level Trigger optimization of the new clustering algorithms using p-p collisions

The EMCal HLT Clusterizer component merges individual signals (digits) of adjacent cells into structures called clusters. Since the typical cluster size in the EMCal can vary according to the detector occupancy due to shower overlap effects, which are much different for pp and heavy-ion collisions, clustering algorithms with and without a cutoff on the shower size have been developed (both in offline and in the HLT) to optimize the cluster reconstruction for the different cases. Events originating from pp collisions, tends to generate smaller, spherical and well-separated clusters in the EMCal, at least up to 10 GeV/c. At higher transverse momenta, the overlapping of the showers

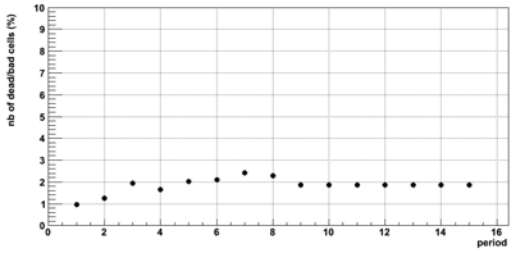

Figure 1: Percentage of the dead calorimetric cells for the 16 periods of the 2012 full data taking.

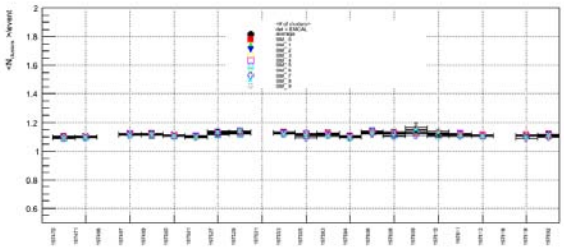

Figure 2: Average number of clusters per event for each of the 10 Super-Modules plotted for a sample of runs.

requires a shape analysis to extract the single shower energy. Above 30 GeV/c the reconstruction can be performed only with more sophisticated algorithms such as isolation cuts to identify direct photons.

The identification of an isolated single electromagnetic cluster in the EMCal can be performed using different strategies: summing up all the neighboring cells around a seed-cell over threshold until no more cells are found or adding up cells around the seed until the number of clustered cells reaches the predefined cutoff value. The first approach is more suitable for an accurate reconstruction. A further improvement to this clustering algorithm would be the ability to unfold overlapping clusters as generated from the photonic decay of high-energy neutral mesons, however this procedure usually requires computing intensive fitting algorithms. Such performance penalty must be avoided in the online reconstruction so the cutoff technique is preferred. In the EMCal HLT reconstruction a cutoff of 9 cells is used (according to the geometrical granularity of the single cell size), so the clusterization is performed into a square of 3x3 cells. In pp collisions the response of the two methods is very similar since the majority of clusters are well separated, while in Pb-Pb collisions, especially in central events, the high particle multiplicity requires the use of the cutoff (or unfolding in offline) to disentangle the cluster signals from the underlying event to avoid the generation of artificially large clusters.

The reconstruction quality of the EMCal online clusterizer algorithms implemented in the HLT chain were checked against offline as shown in Figs.3 and 4, where it can be seen that the performance is in a reasonable agreement in all cases. Since the EMCal HLT reconstruction is mainly targeted for triggering, a small penalty in the accuracy of the energy reconstruction of the clusters is accepted as a trade off in favor of faster performance, and for this reason the cutoff clustering method was used, especially for Pb-Pb collisions.

2.2 High Level Trigger development for correlation measurements in heavy ion collisions

The online HLT chain is capable of producing trigger decisions based on full event reconstruction. In terms of EMCal event rejection, the following relevant trigger observables have been implemented:

- neutral cluster trigger;
- electron and jet trigger.

The single shower triggering mode is primarily targeted to trigger on photons and neutral mesons. In all collision systems, the high level trigger post-filtering can improve the hardware L0 and L1 trigger response by using the current bad channels map information and calibration factors.

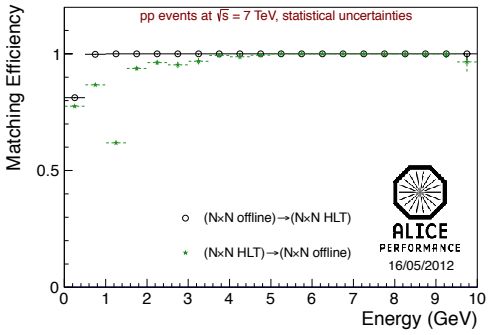

Figure 3: Reconstruction efficiency for the $N \times N$ algorithm (cutoff) in offline and HLT. The notation $(A) \rightarrow (B)$ indicates the fraction of clusters found using method A that are also found using method B.

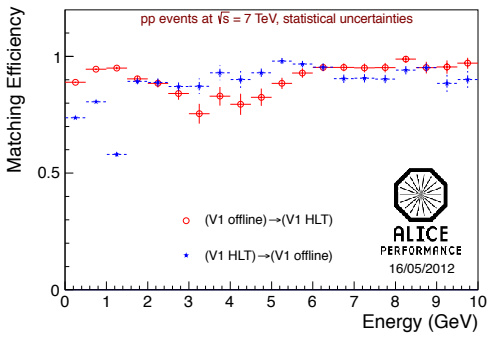

Figure 4: Reconstruction efficiency for the $V1$ algorithms (no cutoff) in offline and HLT. The notation $(A) \rightarrow (B)$ indicates the fraction of clusters found using method A that are also found using method B.

For the electron trigger, the cluster information reconstructed online by the EMCal HLT analysis chain is combined with the central barrel tracking information to produce complex event selection as a single electron trigger (matching of one extrapolated track with an EMCal cluster).

Performance and accuracy studies of the track matching component developed for this purpose have been done using simulated and real data taken during the 2011 LHC running period 1).

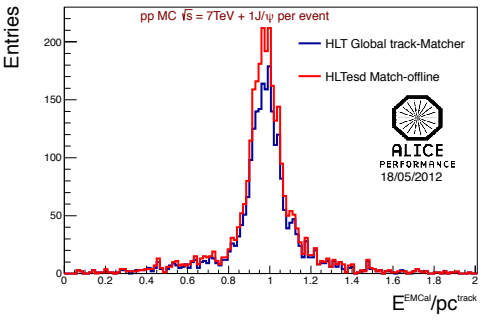

Figure 5: E/pc distributions obtained with the track extrapolation - cluster matching via the online algorithms compared to the ESD-based tracking (red).

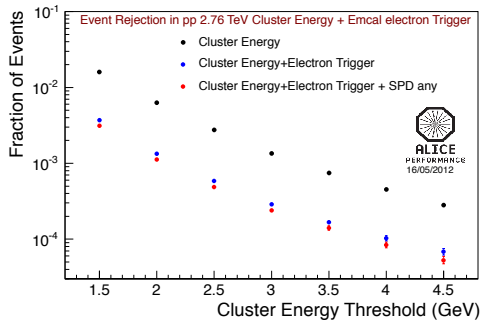

Figure 6: Improvement in the event selection for $E_{e^-} > 1$ GeV from simulation with minimum bias pp at $\sqrt{s} = 2.76$ TeV.

In addition to the extrapolation of the track from the central barrel to the EMCal interaction plane and the matching with a compatible nearby cluster, the electron trigger component must finally perform particle identification to issue a trigger decision. The selection of electron candidates is done using the E/pc information where the energy is measured from the EMCal cluster, and the momentum from the central barrel track as shown in Fig.5. To determine the possible improvement of the event selection for electrons with energies above 1 GeV, simulations of the HLT chain using pp minimum bias data at 2.76 GeV and the EMCal geometry have been used. These studies have shown that at least a factor 5 to 10 in event selection can be gained compared to the single shower

trigger, as shown in Fig.6, where the red points are obtained with the requirement of one hit in one of the inner tracker silicon pixel (SPD) layers to reject a higher fraction of photon conversions.

The EMCal online jet trigger component was developed to provide an unbiased jet sample by refining the hardware L1 trigger decisions. In fact, the HLT post-processing can produce a sharper turn on curve using the track matching capabilities of the online reconstruction chain. In addition, a more accurate definition of the jet area than the one provided by the hardware L1 jet patch, is obtained choosing a jet cone based on the jet direction calculated online. The combination of the hadronic and electromagnetic energy provides a measurement of the total energy of the jet by matching the tracks identified as part of the jet with the corresponding EMCal neutral energy.

The use of the HLT jet trigger also allows a better characterization of the trigger response as a function of the centrality dependent threshold by re-processing the information from the V0 detector directly in HLT. Performance considerations, due to the high particle multiplicity in Pb-Pb collisions, impose that the track extrapolation is done only geometrically without taking into account multiple scattering effects introduced by the material budget in front of the EMCal. The pure geometrical extrapolation accounts for a speedup factor of 20 in the execution of the track matcher component with respect to the full-fledged track extrapolation used for pp collisions. The identification of the jet tracks is performed using the anti-k_T jet finder provided by the FastJet package which was embedded in the HLT framework.

3 DCal

The first upgrade approved by the ALICE collaboration was an extension of EMCal, denominated DCal (Di-jet Calorimeter) [2]. The DCal expands the physics capabilities of the EMCal by enabling back-to-back correlation measurements that are essential to obtain a complete picture of the physics addressed by the EMCal. Together, DCal and EMCal form a two-arm electromagnetic calorimeter. The EMCal subtends 110° and the DCal subtends 67° in the azimuthal angle ϕ, with both detectors covering $|\eta|$ <0.7, thereby providing good acceptance for di-jets with radii R<0.4 up to transverse momenta $p_T \sim 150$ GeV/c. Simulation studies of the DCal have been carried out and have verified that the technology, originally developed for and implemented in the EMCal, meets all the needs of the DCal project. As a consequence, from a technical perspective, DCal is an extension of EMCal having super-modules built exactly as they are in the EMCal, out of strip-modules, but with reduced length in η: in fact, each DCal super-module contains 16 strip-modules instead of 24 present in the previous calorimeter. Also in this case, there are 2 extensions made of reduced super-modules 1/3 (each of them done by 16 strips with 4 modules), matching the angular coverage back-to-back for the EMCal extension.

DCal will be situated immediately adjacent to PHOS on both the ALICE "A" and "C" sides, causing unavoidably a small gap in η ($\delta\eta \sim 0.02$) between the sensitive volumes of the two detectors, due to the super-module structure. DCal+PHOS can be considered as one integrated detector system for the study of jets, consequently all simulations done include PHOS as well as DCal super-modules.

In Fig. 7 is shown a schematic view of the 6 DCal super-modules together with the 2 reduced width (1/3) DCal super-modules and with the PHOS super-modules in between.

The DCal Collaboration is the EMCal one plus the Tsukuba (Japan) and Wuhan (China) groups. The Frascati group has the responsibility of coordinating the construction and assembly in the European-Asiatic zone. Moreover the Frascati group provided all WLS fibers for 1.5 DCal super-module and for the 2 reduced length super-modules including cutting, ice-polishing and aluminizing procedure. A total of about 62000 fibers, grouped in 1700 bundles, with 36 fibers each have been produced at LNF, part of those in collaboration with the Wuhan group. As for EMCal, each fiber bundle is built of two sub-bundles to match the different path lengths between

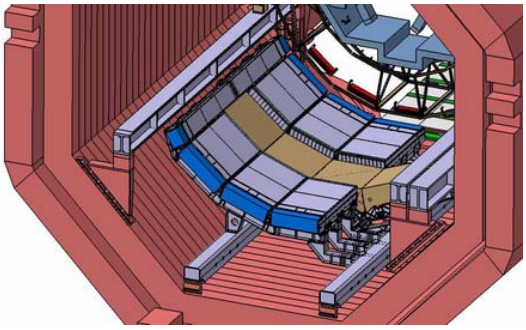

Figure 7: 6 DCal (in blue) super-modules plus the 2 with reduced length (1/3) with the PHOS super-modules (in violet) in between.

Figure 8: Left: picture of 1 full DCal super-module. Right: photo of the 2 reduced DCal super-modules.

central and peripheral fibers in the four towers of the single module. The module assembly started in 2011 and has been completed in 2012. All fibers have been inserted in the modules and the corresponding strip-modules have been assembled and calibrated in Grenoble (France). In Fig. 8 is shown a picture of one full DCal super-module after calibration (left panel) and a picture of the two reduced width DCal super-modules (right panel).

All DCal super-modules will be installed in ALICE during the LHC long shutdown (LS1) in 2013-2014. Concerning the mechanical DCal installation, the common PHOS-DCal support structure has been shipped to CERN and load-tested successfully as shown in Fig.9.

A preparatory work of the calorimeters has also been coordinated in order to have interventions during the LHC LS1. In particular, it was planned to switch from the RCU GTL-bus based readout to the new parallel (SRU) point-to-point readout (same as DCal) which will enable the EMCal/DCal to sustain the 50 kHz Pb-Pb interaction rate foreseen for running the central barrel detectors after 2018.

The preparation of the insertion tooling (different from the one used for the EMCal since the super-module size is different) is underway and the detector installation is foreseen for September 2013.

Figure 9: Common DCal-PHOS support structure under load test at the CERN P2.

4 Physics results

Frascati group contributed to the development of the field of jets in heavy ion collisions with two publications [3] [4] and a preliminary experimental analysis [5].

While studies at hadron level have been crucial in order to establish the existence and to gain understanding on the jet quenching phenomenon, the study of jets was proposed long ago as a complementary possibility. Specifically, single hadron spectra are supposed to be mostly sensitive to the medium-induced energy loss of the leading parton coming from a hard scattering, while jet-related observables should offer information about the medium modifications on the QCD branching process. The latter are expected to be affected by potential biases in a different manner than the former and, thus, they offer a possibility to additionally constrain the mechanism of energy loss and characterize the medium produced in the collisions. In the last two years several jet-related analysis have been performed at the LHC, that have triggered great interest and a large experimental, phenomenological and theoretical activity. Summarizing, the results show: (i) a larger imbalance of the transverse energy of leading and subleading jets in Pb-Pb collisions than in pp and increasing with centrality, which indicates the existence of medium-induced energy loss; (ii) a similar azimuthal distribution between leading and subleading jets in central Pb-Pb collisions to that in pp, apparently pointing to the absence of sizable medium-induced broadening in transverse momentum; (iii) an excess of soft particles at large angles with respect to the subleading jet in Pb-Pb collisions and increasing with increasing dijet momentum imbalance, compared to Monte Carlo expectations which reproduce pp data; (iv) a lack of sizable modifications of the hard jet fragmentation (i.e. the fragmentation into particles with energies close to the jet energy) between pp and Pb-Pb collisions. These observations look, at first sight, challenging for the standard explanation of jet quenching in terms of medium-induced gluon radiation in which energy loss and broadening are linked and the induced radiation is semi-hard.

In ALICE, we published the first studies [4] on event background fluctuations and their impact on the jet spectrum. Jet reconstruction in the complex environment of a heavy-ion collision requires a quantitative understanding of background-induced fluctuations of the measured jet signal and the effects of the underlying heavy-ion event on the jet finding process itself. Here, region-to-region background fluctuations are the main source of jet energy or momentum uncertainty and can have a large impact on jet structure observables, such as the fraction of energy inside the jet core or the shape of the jet, and will distort the measured jet energy balance even in the absence of medium effects. The conclusion of this first detailed study of event background fluctuations for jet reconstruction is that the standard deviation of the fluctuations in the 10% most central events is $\sigma = (10.98 \pm 0.01)$ GeV/c within a rigid cone of $R = 0.4$ and for a low p_T cut-off of 0.15 GeV/c. It has been shown that the non-statistical sources of fluctuations are

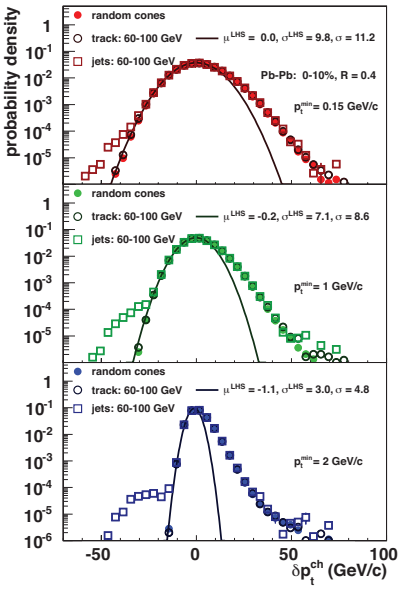

Figure 10: Fluctuations distributions for different minimum particle momentum cutoff and different objects embedded.

driven in part by the anisotropy of the particles emitted from the collision (elliptic and triangular flow). It was also concluded that the anti-k_T algorithm has a modest dependence on the method used to characterize the fluctuations, in particular, on the jet fragmentation pattern. The use of reconstructed charged particles down to $p_T^{min} = 0.15\,\mathrm{GeV}/c$ allows a comparison of the impact of background fluctuations with a minimal bias on hard fragmentation in jet finding to the case with increased bias ($p_T^{min} \geq 1\,\mathrm{GeV}/c$). The observed reduction, Fig.10, of the standard deviation to $\sigma = (4.82 \pm 0.01)\,\mathrm{GeV}/c$ for the $p_T^{min} = 2\,\mathrm{GeV}/c$ case, is driven by the smaller number of particles and the reduced influence of soft region-to-region fluctuations. The asymmetric shape of the δpt distribution with a tail towards positive fluctuations has a large impact on the jet measurement, compared to purely Gaussian case, though the role of signal jets contributing to the tail has to be considered. Using different assumptions on the shape of the true jet spectrum it is found that for $p_T^{min} = 0.15\,\mathrm{GeV}/c$ fluctuations can have a large influence on the charged jet yield for transverse momenta up to $100 \pm 15\,\mathrm{GeV}/c$. The conclusions of this paper are key ingredients to upcoming ALICE papers measuring the jet spectrum.

In [3] we address the question of the effects of jet reconstruction and background subtraction in high-energy heavy-ion collisions on different jet observables. Our aim is to gain insight on how these issues affect the understanding and detailed characterization of the produced medium through present jet observables (using the experimental data on the dijet asymmetry and azimuthal correlation and on the missing transverse momentum as references). For this purpose, we use a highly flexible toy model for the background - where particles are simulated according to a thermal spectrum matched to a power law at larger transverse momentum - that allows fluctuations both among different events and, more importantly, event-by-event. By changing the slope of the exponential function, T, we can set different values for the background fluctuations, σ_{jet}, and for the average level of energy deposition, ρ. The results of the toy model have also been checked and found in agreement with those using a detailed Monte Carlo simulator for the background, the PSM model. Jets are generated through pp events in PYTHIA for vacuum jets. In order to address possible interplays between a different structure of in-medium quenched jets, we also generated samples of jets with different degrees of quenching through pp collisions in Q-PYTHIA. We have studied two background subtraction techniques: the FastJet area-based method, where the estimation of the background parameters is made at jet level; and a pedestal method, where the background estimation is made at a calorimetric level and uses a pedestal subtraction.

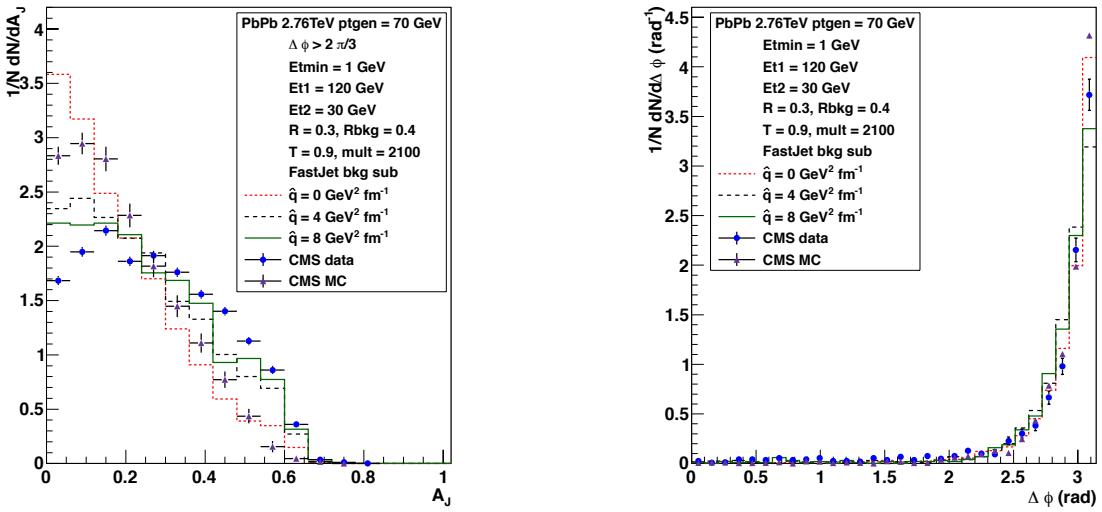

Figure 11: Dijet observables for a simulation using Q-PYTHIA with different $\hat{q}$ embedded in a background with $T = 0.9$ GeV ($\sigma_{jet} \simeq 11$ GeV). The red dotted lines corresponds to $\hat{q} = 0$, the black dashed ones to $\hat{q} = 4$ GeV^2 fm^{-1} and the green solid ones to $\hat{q} = 8$ GeV^2 fm^{-1}. The blue dots are the CMS data with the corresponding error bars, and the purple triangles the CMS Monte Carlo. The background subtraction method is the area-based FastJet one.

From this study, when using the toy model to simulate the background, or a more realistic Monte Carlo simulator, we conclude that for the FastJet background subtraction, an average ρ and σ_{jet} are sufficient to characterize a background, since no apparent dependency was found. As for the pedestal method, we find a higher sensitivity to the background intrinsic structure which requires a tuning of the parameters in the method, specifically the value $E_{T,jets}$ that separates those jets whose constituents are included in the background estimation from those whose constituents are not included, and the value κ that sets the level of background subtraction above the average and leads to larger empty cells for reconstruction. We investigated the dijet asymmetry (A_J) and the average missing transverse momentum observables by comparing Q-PYTHIA embedded in a background with the CMS results. We checked first a Q-PYTHIA simulation without medium effects ($\hat{q} = 0$) which results in qualitative agreement with the CMS simulation (PYTHIA events embedded in a HYDJET background). Then, switching quenching on, we found that Q-PYTHIA has the same trend than CMS data for A_J, meaning an excess of events with large energy imbalance, as shown in Fig.11. Concerning the missing p_T, a softer composition in the subleading jet direction that persists even at large angles from the dijet direction is found. Considering that both this fact and the interpretation of the dijet asymmetry and azimuthal correlations as energy loss without broadening defy the 'standard' understanding of radiative medium-induced energy loss (in which energy loss and broadening are linked and radiation is semi-hard and takes place at large angles), we find this qualitative agreement between Q-PYTHIA and data noteworthy.

From our study, it seems unavoidable to conclude that the naive expectation that background subtraction methods are enough for phenomenological jet studies to extract medium characteristics without considering the background, becomes strongly weakened. Indeed, it seems that realistic - even real - background events and the use and detailed understanding of the background subtraction method used in each experiment are required in order to achieve the medium characterization through jet observables.

In [5] we presented the analysis of the semi-inclusive distribution of reconstructed charged particle jets recoiling from a high p_T hadron trigger in central Pb-Pb collisions at $\sqrt{s} = 2.76$ TeV. Since a high p_T hadron trigger isolates a single high Q^2 interaction within the complex fireball of a central Pb-Pb collisions, we expect to have a similar true coincidence rate per trigger in central Pb-Pb collisions as in pp, modulo quenching, initial-k_T, and other nuclear effects such as shadowing. However, the very large multiplicity in such collisions, which originates almost entirely from interactions that are incoherent with hard interaction generating the hadron trigger, will generate a population of uncorrelated (mainly combinatoric) jets in the recoil acceptance at the rate of a few per trigger, forming a very large background relative to the expected true coincidence rate of a few percent.

Model studies show that an attempt to measure the hard jet distribution by unfolding background fluctuations without prior removal of the combinatorial jet component is not a mathematically well-posed problem, leading to unstable and wildly wrong results. In order to suppress the non-coincident jet contribution without introducing infra-red unsafe or collinear-unsafe cuts, we utilize the differential coincidence observableΔ_{Recoil}. The technique is based on the realization that the distribution of combinatorial background jets is, by definition, *uncorrelated* with p_T^{trig}. This raises the possibility of a purely data-driven elimination of the combinatorial jet population, by considering the measurement of the *difference* of the recoil jet distributions for two *exclusive* hadron trigger classes, "signal" and "reference":

$$\text{Signal} : p_{T,low}^{Sig} < p_T^{trig} < p_{T,high}^{Sig} \tag{1}$$

$$\text{Reference} : p_{T,low}^{Ref} < p_T^{Ref} < p_{T,high}^{Ref}, \tag{2}$$

where $p_{T,low}^{Sig} > p_{T,high}^{Ref}$. Then the differential observable Δ_{Recoil} is defined as:

$$\Delta_{Recoil} = \frac{1}{N_{trig}^{Sig}} \frac{dN}{dp_T^{jet}} \mid_{Sig} - c \cdot \frac{1}{N_{trig}^{Ref}} \frac{dN}{dp_T^{jet}} \mid_{Ref} . \tag{3}$$

The scaling factor c of the Reference distribution is applied to account for the observed strict conservation (at the per mille level) of jet density in the experimental acceptance, which results in increasing displacement of combinatorial jets by true, hard coincidence jets as p_T^{trig} increases. The scaling factor c is measured in the region of negative and low jet p_T where the combinatorial contribution dominates, and differs from unity by less than 4%.

Δ_{Recoil} represents the *evolution* of the coincident recoil jet distribution, i.e. from the same hard interaction, as the trigger p_T evolves from the lower p_T trigger interval ("reference") to the higher p_T trigger interval ("signal"). This observable, while uncommon, is nevertheless perturbatively well-defined.

The Pb-Pb measurements are compared to a pp PYTHIA reference distribution generated at the same energy. Modification of the jet structure due to quenching is explored by varying the cone radius R (0.2, 0.4) and the lower p_T cutoff of the charged particle constituents (0.15, 2.0 GeV/c). To explore the energy redistribution within the recoil jets, we consider the ratio for the measured Δ_{recoil} distribution over the same observable calculated with PYTHIA,$\Delta_{\text{IAA}}^{\text{PYTHIA}}$. This ratio is presented in Fig.12 for $R = 0.4$ and $p_{\text{T}}^{\text{const}} > 0.15$ GeV, for $R = 0.2$ and $p_{\text{T}}^{\text{const}} > 0.15$ GeV and for $R = 0.4$ and $p_{\text{T}}^{\text{const}} > 2$ GeV. Comparison of these distributions does not indicate a large energy redistribution, relative to PYTHIA, transverse to the jet axis, or towards lower p_T constituents, though more precise statements will be possible with reduced systematic uncertanties and higher statistics data.

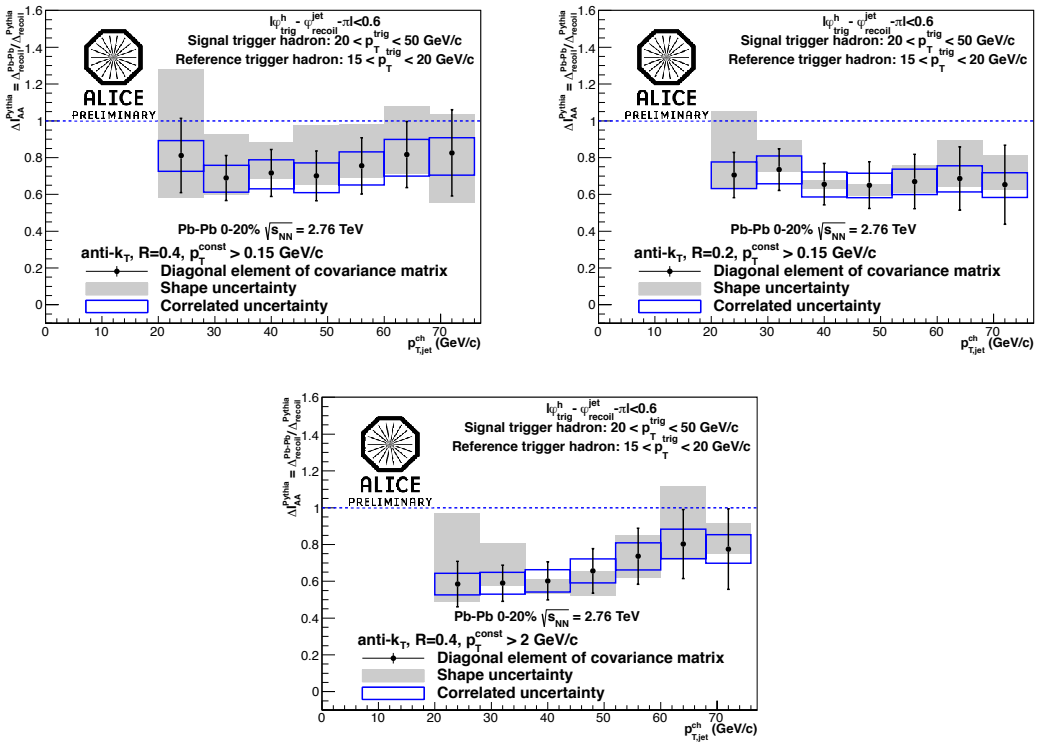

Figure 12:$\Delta\ {}^{PYTHIA}_{IAA}$ distributions for different radius.

5 Activity in the Seventh Framework Programme in HadronPhysics3

Part of the activities of the LNF group described in the present activity report, have been performed in HadronPhysics3 in the Seventh Framework European Programme. In particular a Joint Research Activity has been developed in collaboration with the Centre National de la Recherche Scientifique CNRS/IN2P3 and the Universidad de Santiago de Compostela, with the aim to expand the physics capabilities of the ALICE Electromagnetic Calorimeter (EMCal) by enabling back-to-back correlation measurements.

The collaboration among these institutes concentrated the efforts on the first LHC runs showing that the EMCal has superb capabilities for inclusive jet measurements. However, as discussed in the previous sections, a critical consideration in the detector design for the measurement of the correlations is the capability to deliver acceptance adequate for dijet measurements with p_t up to 150 GeV/c, and an energy resolution and an electromagnetic shower shape determination sufficient for γ/π_0 discrimination, up to at least $p_t \simeq 30$ GeV/c, in central Pb-Pb collisions. The simulation studies carried out verified that the technology originally developed for the EMCal meet these requirements. As a consequence, the technical solutions developed in the framework of the electomagnetic calorimeter constuction, as well as the developed tools for the calorimeter assembling and tests and the dedicated infrastructure, have be used for the DCal construction.

An essential capability for the measurement of hadron-, jet- and γ- jet correlations is a fast and efficient Level 1 (L1) trigger, (obtained by means of a "jet patch"on total energy summed over

finite phase space area), provided by the combination of electromagnetic calorimeters EMCal and DCal. The L1 trigger architecture developed for EMCal will be used for DCal and applied in the correlation measurements. However, at the L1 the jet trigger operates only on the Electromagnetic Calorimeter response and a full energy measurement is possible only at High Level Trigger (HLT), where the charged particle momenta become available as input to the trigger algorithms. More specifically: i) in pp collisions HLT can re-evaluate the L0/L1 hardware trigger decision and can be used for both monitoring of the triggers and post-filtering of the triggered events. ii) in Pb-Pb collisions the primary role of the HLT is to provide further rejection power. In particular, HLT is designed to increase the statistics of recorded physics events of interest by a factor of 10 for Pb-Pb collisions. Thus, to fully exploit the broad range of correlation measurements that will be performed by the overall EMCal + DCal calorimeters, the trigger optimization using the HLT response for the full event reconstruction is mandatory. The activity performed in 2012 concerning the HLT development has been focused on the optimization of clustering algorithms using p-p collisions and on the development for correlation measurements in heavy collisions. A significant amount of effort in this framework has been placed in the development of the jet reconstruction and background subtraction. This activity mainly included the introduction of new jet algorithms, the comparison between different algorithms, the study of new techniques for the subtraction of the underlying event. In 2012 we perform an extensive study of jets with focus on dijet asymmetry and missing transverse momentum. We addressed the question to which extent the most commonly used subtraction techniques are able to eliminate the effects of the background on the most commonly discussed observables at present: single inclusive jet distributions, dijet asymmetry and azimuthal distributions. The analysis of the influence of background subtraction and quenching on jet observables in heavy ion collisions have been completed.

References

1. F. Ronchetti, F. Blanco, M. Figueredo, A.G. Knospe and L. Xaplanteris, *The ALICE electromagnetic calorimeter high level triggers* Journal of Physics: Conference Series 396 (2012) 012045;

2. J. Allen *et al.*, *ALICE DCal: An addendum to the EMCAL Technical Design Report*, CERN LHCC-2010-011, 20 June 2010;

3. N. Armesto, L. Apolinario, L. Cunqueiro *An analysis of the influence of background subtraction and quenching on jet observables in heavy ion collisions*, JHEP **1302** (2013) 022;

4. ALICE Collaboration, *Measurement of Event Background Fluctuations for Charged Particle Jet Reconstruction in Pb-Pb collisions at* $\sqrt{s_{NN}} = 2.76$ *TeV*, JHEP **1203** (2012) 053;

5. L.Cunqueiro, *Jet structure at* 2.76 *TeV collisions at ALICE*, arXiv: 1210.7610, QM 2012, to be published in Nuclear Physics, Section A.

Publications

The ALICE Collaboration has published 26 papers in 2012. The publications are accessible at the link: http://aliceinfo.cern.ch/ArtSubmission/publications

1. N. Armesto, L. Apolinario, L. Cunqueiro, *An analysis of the influence of background subtraction and quenching on jet observables in heavy ion collisions*, JHEP **1302** (2013) 022.

Conference Talks

1. N. Bianchi, *Hadron multiplicities in SIDIS off nucleons and nuclei*, HEP in the LHC Era, Valparaiso, Chile, January 2012;
2. L. Cunqueiro *Jet Physics with ALICE*, 7^{th} International Workshop on High-pT physics, March 2012, Hanau-Frankfurt;
3. F. Ronchetti, *The ALICE electromagnetic calorimeter high level triggers*, Computing in High Energy and Nuclear Physics (CHEP), May 2012, New York;
4. A. Fantoni, *An overview of the ALICE experiment at LHC*, LatinoAmerican Workshop on High Energy Physics: Particles and Strings, July 2012 - Havana, Cuba (invited talk);
5. L. Cunqueiro, *ALICE latest results*, Fundamental Physics Coference, July 2012, Benasque, Spain (invided talk);
6. P. Di Nezza, *Probing the medium with hard probes in ALICE*, Heavy Ion Collisions in the LHC Era, July 2012, Qui Nhon, Vietnam (invited talk)
7. L. Cunqueiro, *Jet structure in 2.76 TeV Pb-Pb Collisions at ALICE*, Quark Matter, August 2012, Washington.

Conferences Organization

1. High Level Trigger Meeting, LNF 9-11 February, 2012;
2. Alice Physics Week, LNF 16-20 April, 2012.

Proceeding and Notes

1. F. Ronchetti et al., *The ALICE electromagnetic calorimeter high level triggers* Journal of Physics: Conference Series 396 (2012) 012045;
2. L. Apolinario, N. Armesto and L. Cunqueiro, *Background subtraction and jet quenching on jet reconstruction*, arXiv:1207.6587, Hard Probes 2012;
3. L.Cunqueiro, *Jet structure at* 2.76 *TeV collisions at ALICE*, arXiv: 1210.7610, QM 2012, to be published in Nuclear Physics, Section A;
4. P. Di Nezza, *Probing the medium with hard probes in ALICE*, to be published on IOP Conference Series;
5. B.Abelev et al., *Upgrade of the ALICE Experiment*, CERN-LHCC-2012-012.

JLAB12

M. Aghasyan (Art. 23), A. Courtoy (Ass.), S. Anefalos Pereira (Ass.), E. De Sanctis (Ass.), D. Hasch, M. Hoek (Ass.), V. Lucherini, M. Mirazita (Resp.), R. Montgomery (Ass.), J. de Oliveira Echeimberg (Bors. PD), D. Orecchini (Tecn.), A. Orlandi (Tecn.), J. Phillips (Ass.), S. Pisano (Ass.), E. Polli (Ass.), P. Rossi, L. Trevisan (Bors.), M. Turisini (Ass.), A. Viticchié (Tecn.)

1 Introduction

The Frascati JLAB12 group participates into the physics program carried on by the CLAS collaboration in the Hall B of the Jefferson Laboratory (JLab). The Continuous Electron Beam Accelerator Facility (CEBAF) ran with maximum energy of 6 GeV till may 2012, when it has been shut down to start the upgrade of the facility that will bring the maximum electron energy to 12 GeV. The new CLAS12 spectrometer is also under costruction.

The physics program of the group is focused on the precision study of the three-dimensional structure of the nucleon and its internal dynamics. This is achieved through the determination of new parton distribution functions, the so-called TMDs, which include information not only on the longitudinal but also on the transverse distributions of partons in a fast moving hadron. TMDs can be studied through the measurement of azimuthal asymmetries in Semi-Inclusive Deep Inelastic Scattering (SIDIS) processes, in which one (or more) hadron is detected in coincidence with the scattered electron.

In the period covered by this report, the group has continued to work to the analysis of already available experimental data with 6 GeV and in the $R\&D$ for the construction of a RICH detector for CLAS12.

2 Transverse Momentum Dependent parton distribution functions (TMDs)

The exploration of the internal structure of the hadrons has undergone enormous progress in the last decades. The Transverse Momentum Dependent (TMD) parton distribution and fragmentation functions [1, 2] are one of the framework to obtain information towards a genuine multi-dimensional picture of the nucleon structure. They are the three-dimensional generalization of the collinear Parton Distribution Functions (PDFs) introduced in the 60s to explain the Deep Inelastic Scattering (DIS) experiments. A major role in the TMD study is played by by Semi-Inclusive Deep-Inelastic Scattering (SIDIS) processes, where in addition to the scattered lepton, also a hadron is detected in the final state. This hadron is generated in the fragmentation of the scattered quark, the so-called Current Fragmentation Region (CFR).

There are eight leading-twist quark TMD distributions. Three of them survive after integration over the transverse momenta: the unpolarized and helicity distributions already introduced in the DIS experiments and the transversity distribution, which is related to transverse polarization of quarks. The other five distributions describe the correlations between the transverse momentum of quarks, their spin and/or the spin of the nucleon and provide a way to access the orbital angular momentum of the partons. Similar spin-orbit correlations arise in the hadronization process of the struck quark into the final hadron, described by TMD fragmentation functions. Besides the unpolarized one, the other relevant TMD fragmentation function is the Collins function [3],

representing a correlation between the transverse polarization of the fragmenting quark and the transverse momentum of the produced hadron.

The connection between TMDs and the physics observables was put on a firm theoretical basis with the appropriate factorization proof [4, 5]. The cross section for hadron production in SIDIS processes can be written [2] as a Fourier expansion in the azimuthal angle ϕ of the hadron

$$\sigma \propto \sigma_{UU} + \lambda\sigma_{LU}\sin(\phi) + S_{\parallel}\sigma_{UL}\sin(\phi) + \lambda S_{\parallel}\sigma_{LL} + ... \quad (1)$$

where λ and $S_{\parallel}$ are the electron helicity and longitudinal nucleon target spin and the labels indicate unpolarized (U) or longitudinally polarized (L) beam or target, the first index referring to the beam and the second to the target. The dots represent other contributions, including transverse polarization (T) terms. The different Fourier components of the cross section, each containing a well defined convolution of distribution and fragmentation functions, can be isolated by measuring beam and/or target spin asymmetries.

TMDs studies are one of the primary goal of experiments at JLab with the 12 GeV electron beam, but their investigation has already started with the 6 GeV beam using unpolarized and polarized targets.

3 Data analysis activity

The data analysis activity has been devoted to the following two main items:

3.1 *Studies of new methodes to extract the TMDs from the experimental data*

The TMDs enter in the observables through convolution integrals that makes their extraction a complicated task. A common way to deal with this problem is to use phenomenological parametrizations of the TMDs (for example, gaussian distributions for their transverse momentum dependence) and to fit them to the experimental data. A different approach is to introduce the so-called weighted asymmetries, defined as

$$A^w = \frac{\int w(\sigma^+ - \sigma^-)}{\int(\sigma^+ + \sigma^-)} \quad (2)$$

where the weight function w can be appropriately chosen to project out the relevant azimuthal modulation in eq. (1).

In a recent paper [6], Bessel-weighted asymmetries in the Fourier space, conjugated to the outgoing hadron transverse momentum, have been introduced. Besides some other theoretical advantages, the resulting compact expression of the asymmetries is a simple product of Fourier transformed TMDs, that can be now directly extracted from the experimental data.

The experimental study of Bessel-weighted asymmetries has been initiated using simulated data produced with a new Monte Carlo event generator for SIDIS reactions, based on the parton model [7] and on some of the latest parametrizations of the TMDs. It has been found that the correlations between the parton and hadron momenta can heavily distort the expected kinematical distributions, particularly in the transverse momentum. These correlations may also be important in the understanding of asymmetries (for example, the Cahn effect) that model calculations were in general not able to reproduce. The extraction of Bessel weighted TMDs from these simulated data is currently underway for a set of benchmark reaction channels, in order to understand uncertainties and limitations due to experimental effects. Preliminary results of this studies have been shown in International Conferences.

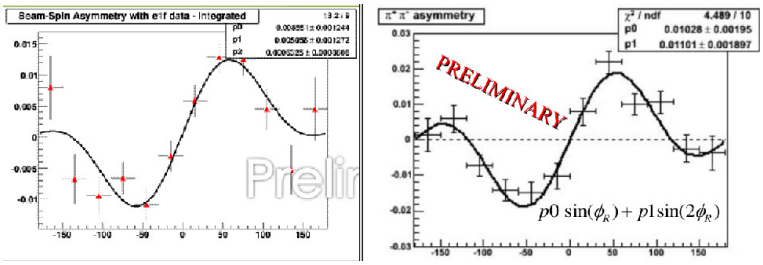

Figure 1: *Comparison between the preliminary CLAS results for Beam Single Spin Asymmetry in two pion SIDIS production extracted from the two data sets under analysis.*

3.2 *Two pion semi-inclusive electroproduction*

When two hadrons are semi-inclusively produced in the CFR, the cross section takes a simpler form than in the single pion case [8]. The Fourier components of eq. (1) are in fact given by a simple product of a TMD distribution function and a TMD DiHadron Fragmentation Function (DiFF). Thus, extraction of TMD information from this process is easier. In addition, the two hadron SIDIS processes, allow access to the sub-leading PDFs e, h_L and g_T that, together with the well known f_1 and g_1 and the transversity h_1, provide the complete description of the collinear (i.e. transverse momentum integrated) structure of the nucleon.

The study of two pion SIDIS electroproduction with CLAS data is underway with 6 GeV polarized electron beam and unpolarized as well as longitudinally polarized hydrogen target. Because of the polarized targets, the two data sets have different kinematic coverage and acceptance. The measured observables are single (beam or target) and double (beam and target) spin asymmetries, both of them having a $\sin(\phi_R)$ Fourier component (where ϕ_R is the azimuthal angle of the relative momentum of the detected hadron pair). Both asymmetries are small (few percent), but non-zero in the whole kinematical plane covered by the experiments. As an example, in Fig. 1, the comparison of the Beam Spin Asymmetry measured from the two data sets is shown. Good agreement between the two measurements has been found.

Preliminary results of these analyses have been presented in International Conferences. Currently, the acceptance effects and other systematic uncertainties are under evaluation.

4 The RICH detector for CLAS12

The CLAS12 large acceptance spectrometer in the Hall-B of JLab will have unique features (luminosity and resolution) to allow substantial progresses in the TMD studies. However, the approved physics program requires discrimination between kaons and other hadrons for momenta up to about 8 GeV/c that is not achievable in the present configuration of the detector. For this reason, the group proposed the construction of a RICH detector of large area to extend the measurements in the most interesting kinematical region.

The present solution [9] foresees a hybris proximity and mirror focusing configuration, that uses variable thickness aerogel radiator and multi-anode photomultipliers (MAPMTs) as photon detectors. A large elliptical mirror will be used to direct the Cerenkov light produced at large angles toward the MAPMTs, that will cover about 1 m^2. The project presents some critical points, that have been addressed in laboratory as well as in test beam measurements.

Laboratory tests performed in Frascati using a low intensity, high stability laser in the 400nm wave length region have shown that the Hamamatsu H8500 MAPMTs (8x8 pixels of 6mm pitch size)

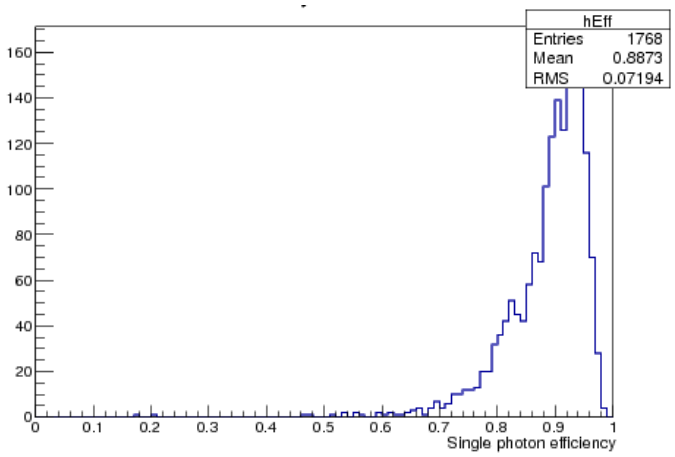

Figure 2: *Distribution of the pixel-by-pixel single photon detection efficiency measured for 28 H8500 MAPMTs in laser tests.*

provide high efficiency (about 80% or more) and uniformity of response as single photon detectors. The Fig. 2 shows the distribution of the pixel-by-pixel single photon efficiency measured in our tests of 28 H8500 MAPMTs. On average, an efficiency bigger than 80% has been measured, with a small tail of pixel with efficiency below 75%.

For the Data Aquisition, we have used an integrated electronics based on the MAROC3 chip, that provides analog information of up to 4096 channels in a very compact system. Test and setup of this electronics and of the Data Aquisition system have been performed in laboratory and also in a real experiment environment at the LNF Beam Test Facility in July 2012.

A large scale prototype has been designed and constructed at LNF in order to study the main feature of the final RICH detector. Test using a monochromatic hadron beam, composed by about 98% of pions and 2% of kaons, has been performed at the T9 beam line of the CERN in two runs in summer and winter 2012. The prototype was made by a large black box (about 2x2x2 m^3) containing an array of 28 H8500 MAPMTs, two supports for the aerogel radiator tiles and spherical and planar mirrors. The experimental setup was completed by two planar GEM chambers for particles tracking, two small plastic scintillators for triggering and a gas threshold Cerenkov detector for π/K separation. The data have been taken in two different configurations, as schematically shown in Fig. 3. In the direct light configuration, the Cerenkov photons produced by the beam particles were directly detected on the MAPMTs array. In the reflected light one, the Cerenkov photons were produced on a second radiator, then reflected by a system of a spherical plus planar mirrors toward the MAPMTs. In front of the planar mirrors, aerogel tiles were placed in order to mimic the geometry of the final detector and to study the light absorption. A picture of the prototype is shown in Fig. 4.

During the data taking, several elements of the prototype have been changed in order to fully test the features of the RICH. For the direct light measurements, we ran with:

- aerogel with different refractive index (n = 1.04, 1.05 and 1.06) and thickness (t = 2, 3 and 4 cm) to study the photon yield production;
- various optical filters placed in front of the radiator, in order to study the chromatic contribution to the single photon detection resolution;

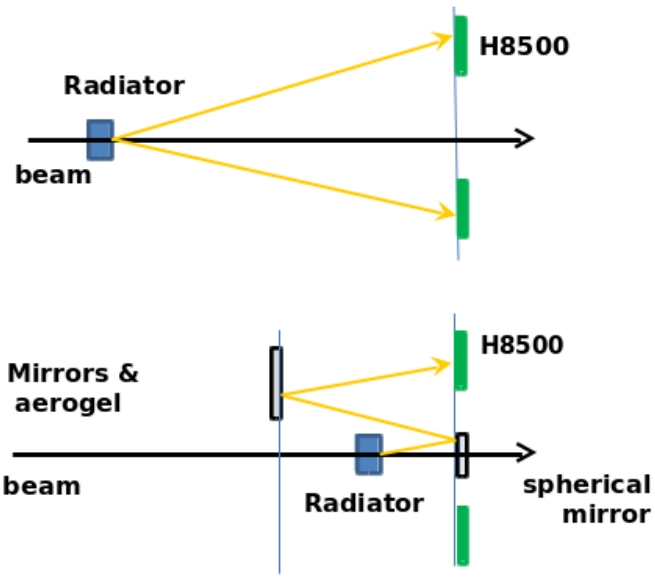

Figure 3: *Schematic of the two configurations of the RICH prototype for direct (upper plot) and reflected (lower plot) light measurements.*

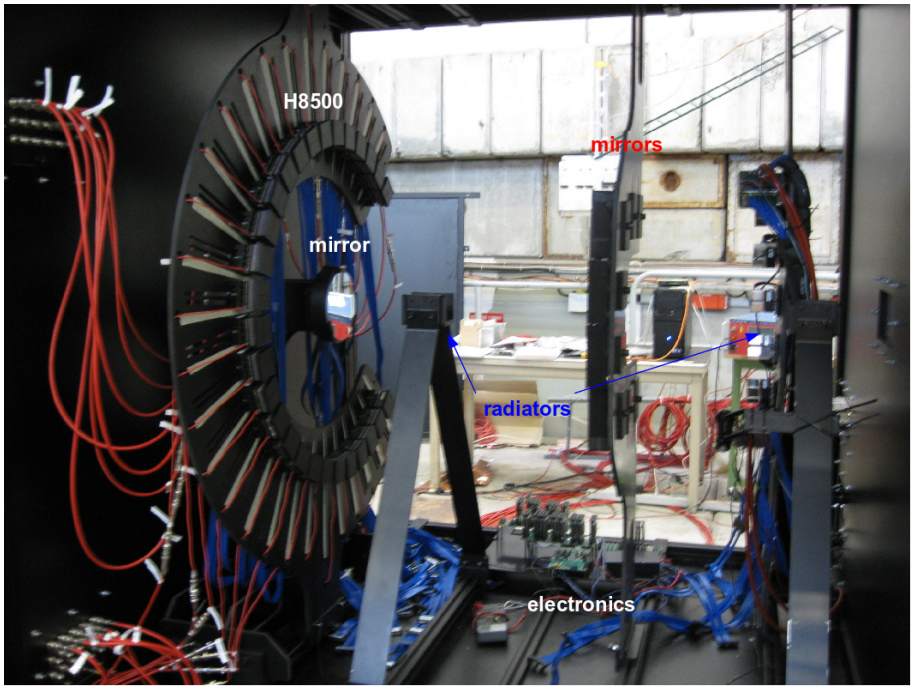

Figure 4: *Picture of the inner elements of the RICH prototype.*

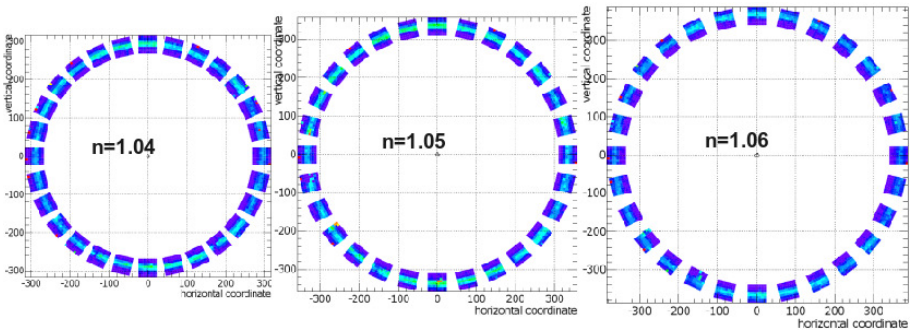

Figure 5: *Examples of Cerenkov rings measured in the direct light configuration for aerogel with n=1.04 (left), n=1.05 (center) and n=1.06 (right) refractive index.*

- MAPMTs moved away from the expected Cerenkov ring, to study background Rayleigh photon production;
- beam energy of 6, 7 and 8 GeV/c, to study momentum dependence in the π/K separation;

Main goal of these data is to fully exploit the kaon identification of the RICH, possibly estimating a detection efficiency using the gas Cerenkov detector as reference.

In the reflected light configuration, data were taken with a beam energy of 6 GeV/c (the maximum reachable in the real RICH detector for this configuration) and with:

- aerogel radiator with different refractive index (n = 1.04, 1.05 and 1.06) and thickness (from 2 to 8 cm);
- without the aerogel in front of the mirror and with aerogel of various thickness and quality;

Main goal here is to study the absorption of Cerenkov photons when passing multiple times through the aerogel.

An example of the measured Cerenkov rings in the direct light configuration is shown in the on-line monitoring plots reported in Fig. 5. The analysis of the data taken is currently underway. A document reporting the project of the final detector is also in preparation.

5 List of Conference Talks by JLAB12 members in 2011

1. D. Hasch, *Data analysis of hard exclusive and semi-inclusive DIS processes* - Lecture for the Doctoral Training Programme of the ECT* Trento on the 'THE 3-DIMENSIONAL NUCLEON STRUCTURE', 30. April - 15 June 2012, Trento (Italy).
2. S. Anefalos Pereira, *Probing the nucleon structure at Jefferson Lab* - QCD2012, July 2 - 7, 2012, Montpellier (France).
3. S. Pisano, *Analyzing nucleon spin structure through SIDIS at Jefferson Lab* - ENPC 2012, September 17 - 21, 2012, Bucharest (Romania).
4. M. Aghasyan, *Fully Differential Monte-Carlo Generator Dedicated to TMDs and Bessel-Weighted Asymmetries* - QCD-N12, October 22-26, 2012, Bilbao (Spain).
5. M. Mirazita, *From partons to hadrons: a challenge for the QCD* National workshop on Nuclear Physics- November 12-14, 2012, Catania (Italy)

6 Publications

1. Transverse Polarization of $\Sigma^+(1189)$ in Photoproduction on a Hydrogen Target CLAS Collaboration, C.S. Nepali *et al.*, submitted to Phys. Rev. C.

2. Measurement of the $\Sigma\pi$ Photoproduction Line Shapes Near the $\Lambda(1405)$ CLAS Collaboration, K. Moriya *et al.*, submitted to Phys. Rev. C.

3. Measurement of Transparency Ratios for Protons from Short-Range Correlated Pairs CLAS Collaboration, H. Hakobyan *et al.*, submitted to Phys. Rev. C.

4. Separated Structure Functions for Exclusive K^+ Λ and K^+ Σ^0 Electroproduction at 5.5 GeV with CLAS CLAS Collaboration, D.S. Carman *et al.*, submitted to Phys. Rev. C.

5. Near Threshold Neutral Pion Electroproduction at High Momentum Transfers and Generalized Form Factors CLAS Collaboration, P. Khetarpal *et al.*, submitted to Phys. Rev. C.

6. Shrunken particles pass freely through nuclear matter CLAS Collaboration, L. El Fassi *et al.*, Phys. Lett. **B 712** (2012) 326.

7. Probing Strangeness in Hard Processes: The science case of a RICH detector for CLAS12 H. Avakian *et al.*, arXiv:1202.1910

8. Deep exclusive π^+ electroproduction off the proton at CLAS CLAS Collaboration, K. Park *et al.*, Eur. Phys. J. **A 49** (2013) 16.

9. Measurement of Exclusive π^0 Electroproduction Structure Functions and their Relationship to Transversity GPDs CLAS Collaboration, I. Bedlinskiy *et al.*, Phys. Rev. Lett. **109**, 112001 (2012).

10. A study of the P11(1440) and D13(1520) resonances from CLAS data on $ep \to e'\pi^+\pi^- p'$ CLAS Collaboration, V. Mokeev *et al.*, Phys. Rev. **C 86**, 035203 (2012).

11. A comparison of forward and backward pp pair knockout in 3He(e,e'pp)n CLAS Collaboration, H. Baghdasaryan *et al.*, Phys. Rev. **C 85**, 064318 (2012)

12. Measurement of the generalized form factors near threshold via $\gamma p \to n\pi^+$ at high Q^2 CLAS Collaboration, K. Park *et al.*, Phys. Rrv. **C 85**, 035208 (2012)

13. Branching Ratio of the Electromagnetic Decay of the $\Sigma^+(1385)$ CLAS Collaboration, D. Keller *et al.*, Phys. Rev. **D 85**, 052004 (2012)

14. Comment on the narrow baryon peak reported by Amaryan et al. CLAS Collaboration, V.D. Burkert *et al.*, Phys. Rev. **C 86**, 069801 (2012)

15. Amplitude analysis of $\gamma n \to \pi^- p$ data above 1 GeV W. Chen *et al.*, Phys. Rev. **C 86**, 015206 (2012)

16. Measurement of the neutron F_2 structure function via spectator tagging CLAS Collaboration, N. Baillie *et al.*, Phys. Rev. Lett. **108**, 142001 (2012)

17. Upper limits for the photoproduction cross section for the $\Phi^{--}(1860)$ pentaquark state off the deuteron CLAS Collaboration, H. Egiyan *et al.*, Phys. Rev. **C 85**, 015205 (2012)

References

1. P.J. Mulders and R.D. Tangerman, Nucl. Phys. **B461**, 197 (1996).
2. A. Bacchetta et al., JHEP **02**, 093 (2007).
3. J.C. Collins, Nucl. Phys. **B396**, 161 (1993).
4. J.C. Collins and D.E. Soper, Nucl. Phys. **B193**, 381 (1981).
5. X. Ji, J. Ma and F. Yuan, Phys. Rev. **D71**, 034005 (2005).
6. D. Boer, L. Gamber, B. Musch and A. Prokudin, JHEP **1110** 021 (2011).
7. M. Anselmino et al., Phys. Rev. **D71** 074006 (2005).
8. A. Bacchetta and M. Radici, Phys. Rev. **D69**, 074026 (2004).
9. M. Contalbrigo et al., NIM **A639** (2011) 302.

KAONNIS

M. Bazzi (Art. 23), C. Berucci (Assoc.), M. Bragadireanu (Bors. UE), A. Clozza,
C. Curceanu (Resp. Naz.), A. D'Uffizi (Ass. Ric.),
C. Guaraldo, M. Iliescu (Art. 23), P. Levi Sandri, F. Lucibello (Tecn.),
S. Okada (Art. 23), D. Pietreanu (Ass.), K. Piscicchia (Bors.),
M. Poli Lener (Art. 23), A. Rizzo (Bors.), E. Sbardella (Bors.),
A. Scordo (Ass. Ric.), D. Sirghi (Art. 23), F. Sirghi (Bors. UE),
I. Tucakovic (Bors.), O.Vazquez Doce (Ass.)

1 The KAONNIS scientific program

KAONNIS represents an integrated program in the field of the low-energy kaon-nucleon/nuclei interaction studies. Under KAONNIS the following activities are performed:

- the study of kaonic atoms by the SIDDHARTA and SIDDHARTA-2 experiments
- the study of kaon-nuclei interaction at low energies in the framework of AMADEUS.

We present in what follows these scientific lines, together with the 2012 activities and the plans for 2013. The KAONNIS scientific program and its realization are partially financed within the FP7 HadronPhysics2 and HadronPhysics3 EU programs.

2 The SIDDHARTA and SIDDHARTA-2 experiments

The objective of the SIDDHARTA (Silicon Drift Detector for Hadronic Atom Research by Timing Application) experiment and of its successor, SIDDHARTA-2, is to perform high precision measurements of X-ray transitions in exotic (kaonic) atoms at DAΦNE.

The precise measurement of the shift and width of the $1s$ level with respect to the purely electromagnetic calculated values, in kaonic hydrogen and kaonic deuterium, generated by the presence of the strong interaction, through the measurement of the X-ray transitions to this level, will allow the first precise experimental extraction of the isospin dependent antikaon-nucleon scattering lengths, fundamental quantities in understanding low-energy QCD in strangeness sector.

The accurate determination of these scattering lengths will place strong constraints on the low-energy K^-N dynamics, which, in turn, constraints the SU(3) description of chiral symmetry breaking in systems containing the strange quark. The implications go from particle and nuclear physics to astrophysics.

SIDDHARTA performed the most precise measurement of kaonic hydrogen and the first exploratory one of kaonic deuterium. Moreover, the kaonic helium 4 and 3 transitions to the 2p level were measured, for the first time in gas in He4 and for the first time ever in He3. Presently, a major upgrade of SIDDHARTA, namely SIDDHARTA-2, is under way, with the aim to measure kaonic deuterium and other types of kaonic atoms in the coming years.

2.1 The SIDDHARTA setup

SIDDHARTA represented a new phase in the study of kaonic atoms at DAΦNE. The previous DEAR experiment's precision was limited by a signal/background ratio of about 1/70 for the kaonic hydrogen measurement. To significantly improve this ratio, a breakthrough was necessary.

An accurate study of the background sources present at DAΦNE was redone. The background includes two main sources:

- synchronous background: coming together with the kaons -related to K^- interactions in the setup materials and also to the ϕ-decay processes; it can be defined as hadronic background;
- asynchronous background: final products of electromagnetic showers in the machine pipe and in the setup materials originating from particles lost from primary circulating beams either due to the interaction of particles in the same bunch (Touschek effect) or due to the interaction with the residual gas.

Accurate studies performed by DEAR showed that the main background source in DAΦNE is of the second type, which shows the way to reduce it. A fast trigger correlated to a kaon entering into the target would cut the main part of the asynchronous background. X rays were detected by DEAR using CCDs (Charge-Coupled Devices), which are excellent X-ray detectors, with very good energy resolution (about 140 eV FWHM at 6 keV), but having the drawback of being non-triggerable devices (since the read-out time per device is at the level of 10 s). A new device, which preserves all good features of CCDs (energy resolution, stability and linearity), but additionally is triggerable - i.e. fast (at the level of 1μs), was implemented. The new detector was a large area Silicon Drift Detector (SDD), specially designed for spectroscopic application. The development of the new 1 cm^2 SDD device, together with its readout electronics and very stable power supplies, was partially performed under the Joint Research Activity JRA10 of the I3 project"Study of strongly interacting matter (HadronPhysics)" within FP6 of the EU.

The trigger in SIDDHARTA was given by a system of scintillators which recognized a kaon entering the target making use of the back-to-back production mechanism of the charged kaons at DAΦNE from ϕ decay: of the type:

$$\phi \rightarrow K^+K^-. \tag{1}$$

The SIDDHARTA setup contained 144 SDD chips, 1 cm^2 each, placed around a cylindrical target, containing high density cryogenic gaseous hydrogen (deuterium or helium). The target was made of kapton, 75μm thick, reinforced with aluminium grid.

The SIDDHARTA setup was installed on DAΦNE in late summer 2008, see Figure 1 - and the period till the end of 2008 was used to debug and optimize the setup performances (degrader optimization included). The kaonic atoms (hydrogen, deuterium, helium4 and 3) measurements were done in 2009 and data analysis followed by the data analyses.

2.2 SIDDHARTA activities in 2012

SIDDHARTA was in data taking until 9 November 2009. In 2012 the group activity was dedicated to the kaonic deuterium analysis and to the upgrade of the setup, SIDDHARTA-2, to perform in the future the kaonic deuterium and other precision kaonic atoms measurements.

2.2.1 Kaonic deuterium results

The X-ray spectrum from the kaonic deuterium experiment is shown in Fig. 2. The data analysis had the aim to extract the yield of the K-transitions. We obtained, after adding the error components quadratically:

- total Kd K-series yield: Y(K_{total})= 0.0077 ± 0.0051
- This corresponds to a Kd yield Y(K_α)= 0.0019 ± 0.0012

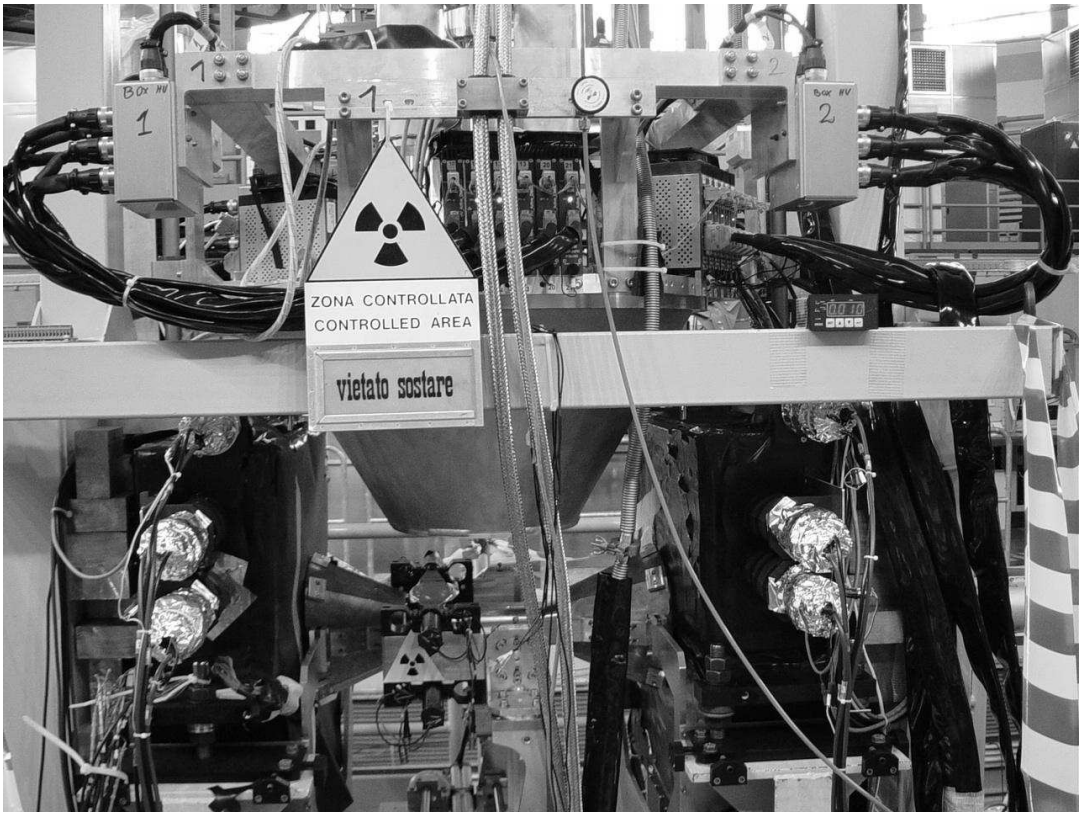

Figure 1: The SIDDHARTA setup installed at DAΦNE

Such values are compatible with what is expected, namely a yield of a factor about 10 smaller then the KH yield, estimated to be to 2% for K_α. For the yield values given above, the upper limits for the yields are (CL 90%):

- $\mathrm{Y}(K_{total}) < 0.00143$
- $\mathrm{Y}(K_\alpha) < 0.0039$

2.3 *SIDDHARTA-2*

In 2010 the proposal for the SIDDHARTA upgrade was put forward. The upgrade of SIDDHARTA to SIDDHARTA-2 is based on four main modifications:

- Trigger geometry and target density: By placing the upper kaon-trigger detector close in front of the target entrance window, the probability that a triggered kaon really enters the gas and is stopped there is much improved. Making the detector smaller than the entry area gives away some signal, but suppresses efficiently the kaonic lines from "wallstops" (kaons entering the gas volume, but passing from the inside of the target to the cylindrical walls). The number "signal per trigger" goes up, which also reduces the accidental background coming along with every trigger. We plan as well to double the gas density which enhances the gas stops and further reduces the wall-stops.
- K^+ discrimination to suppress kaon decay background: A "kaon stopper" scintillator is placed directly below the lower kaon trigger scintillator. When a K^- is stopped there, only one (large) signal from pileup of stopping and kaon-absorption secondaries is seen, whereas when

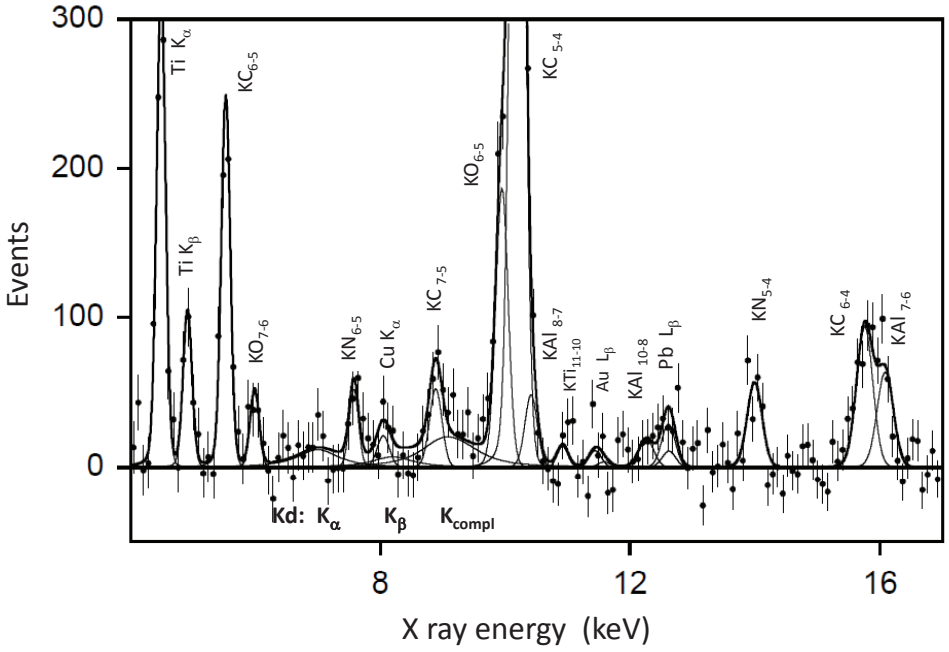

Figure 2: X-ray spectrum from the kaonic deuterium experiment. The continous background fit-component is already subtracted. Fit with fixed Kd transitions shift and width (-805,750 eV) and fixed yield ratio of the individual K-transitions. Integrated luminosity 100 pb^{-1}. The lines from the kaonic X-rays due to stops in the window foils and from X-ray fluorescence excited by background are labeled. Note the excess of events in the region of a possible signal.

a K^+ is stopped, the kaon-decay particles are seen after the signal from the stopping (mean K^+ lifetime 12.8 ns). Using a flash-ADC we will be able to efficiently distinguish the 2 cases. In addition, we will use scintillators surrounding the target to measure K^- absorption secondaries pions). The time window for gas stops is about 4 ns wide. By this condition we also suppress stops in the entry window.

- Active shielding: The scintillators surrounding the target will also be used in prompt anti-coincidence if the spatial correlation of SDD and scintillator hits indicates that it originated from a pion ("charged particle veto"). An anticoincidence covering the SDD time window of about 600 ns (with the exception of the 4 ns of the gas stopping time) will reduce the accidental background. Although the scintillators have only low efficiency for gammas, the abundance of secondaries from the electromagnetic showers allows a relevant reduction of accidental ("beam") background. The upper trigger scintillator has 2 functions, it is also used as an anticoincidence counter: after the kaon and eventual prompt kaon-absorption secondaries pass, it vetos beambackground.

- Operating SDDs at a lower temperature: tests indicate that an improvement of the timing resolution by a factor of 1.5 is feasible by more cooling. The signal enhancement by a factor 2 to 3 is due to moving the target cell closer to the IP, by changing its shape, by a better solid angle of the SDDs and by the higher gas density. In such conditions, with an integrated luminosity of 800 pb$^-$1 a precision of about 70 eV for the shift, and 160 eV for the width are attainable, resulting in a relative precision similar to that obtained for kaonic hydrogen.

In 2012 various tests on prototypes were performed, together with Monte Carlo simulations to optimize the setup.

More details can be found in the various presentations to the LNF International Scientific Committee on the LNF-INFN web-site.

2.4 Activities in 2013

The LNF group main activities in SIDDHARTA and SIDDHARTA-2 for 2013 are the following ones:

- analysis of widths of kaonic helium transitions to 2p level and publications;
- analysis of the yields for kaonic hydrogen and helium and publication of results;
- Monte Carlo simulations for the SIDDHARTA-2 setup and physics;
- construction of the SIDDHARTA-2 setup: target, veto counters, new trigger, new cryogenic systems;
- definition of the strategy for SIDDHARTA-2 measurements (including interaction region definition and construction).

The SIDDHARTA scientific program is important part of the Network LEANNIS (WP9) in the framework of the EU FP7 HadronPhysics3 program.

3 The AMADEUS proposal and 2012 activities

The low-energy (< 100 MeV/c) kaon-nuclei interaction studies represents the main aim of the AMADEUS experiment. In order to do these type of measurements, in a most complete way, by detecting all charged and neutral particles coming from the K^- interactions in various targets with an almost 4π acceptance, the AMADEUS collaboration plans to implement the existent KLOE detector in the internal region of the Drift Chamber with a dedicated setup (see Figure 3). The dedicated setup contains the target which can be either solid or a gaseous cryogenic one, a trigger (TPC-GEM) and a tracker system (scintillating fibers read by SiPM detectors).

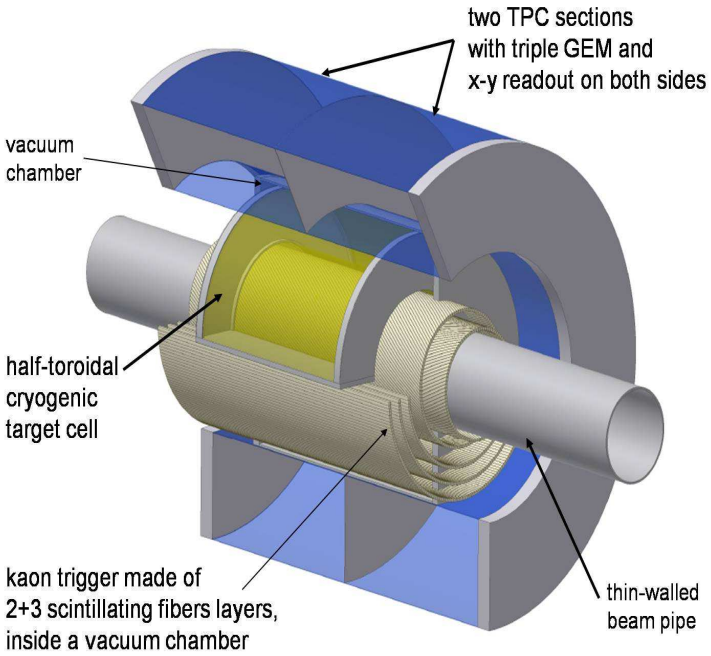

Figure 3: The AMADEUS dedicated setup implemented in the Drift Chamber of the KLOE detector. In this situation a cryogenic gaseous target is used.

The negatively charged kaons can stop inside the target or interact at low energies, giving birth of a series of processes we plan to study. Among these, a key-role is played by the generation of $\Lambda(1405)$ which can decay into $\Sigma^0\pi^0$, $\Sigma^+\pi^-$ or $\Sigma^-\pi^+$. We plan to study all these three channels in the same data taking. Another important item is represented by the debated case of the "kaonic nuclear clusters", especially the K^-pp, and K^- -ppn cases. We can study these channels by measuring, for example, their decays to Λp and to Λd. In the same time, many other kaon-nuclei processes will be investigated, either for the first time, or in order to obtain more accurate results

than those actually reported in literature. Cross sections, branching ratios, rare hyperon decay processes will be investigated, taking advantage of the unique kaon-beam quality delivered by DAΦNE and of the unique characteristics of the KLOE detector.

As targets to be employed, we plan to use gaseous ones, like d, ^{3}He or ^{4}He and solid ones as C, Be or Li. In the summer of 2012 a first dedicated target, half cylinder done in pure carbon was realized and installed inside the Drift Chamber of KLOE as a first setup towards the realization of AMADEUS (see Figure 4). The target thickness was optimized such as to have a maximum of stopped kaons (about 24% of the generated ones) without degrading too much the energy of resulting charged particles inside the target material. In the period of data taking a total integrated luminosity of about 80 pb^{-1} was achieved. The analysis of these data will provide new insights in the low-energy interactions of charged kaons in the nuclear matter. For the future, other targets are planned to be used compatible with the beam assignment.

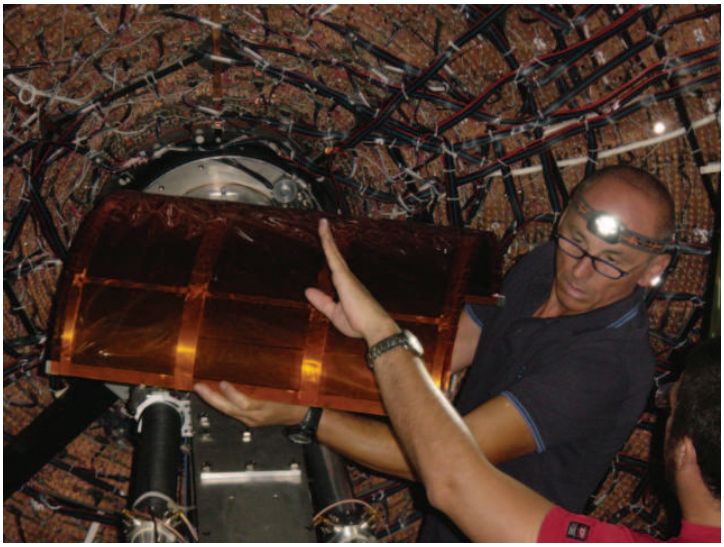

Figure 4: The AMADEUS carbon target (half cylinder) installed inside the Dift Chamber of KLOE detector.

Other activities done in 2012:

- R&D for the trigger system: a prototype based on scintillating fibers read by Silicon Photo-Multipliers (see Fig. 5) was tested at the PSI pion beam.
- R&D for the inner tracker - a small TPC-GEM prototype, Fig. 6, for traking performance.
- Monte Carlo simulations.

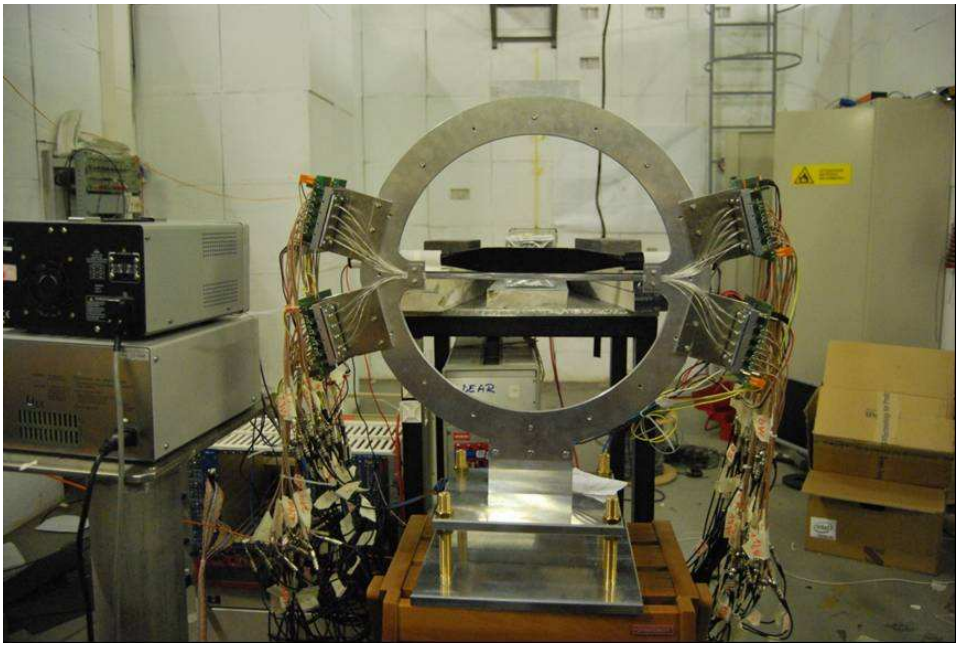

Figure 5: The AMADEUS trigger ptototype, based on scintillating fibers read at both ends by SiPM

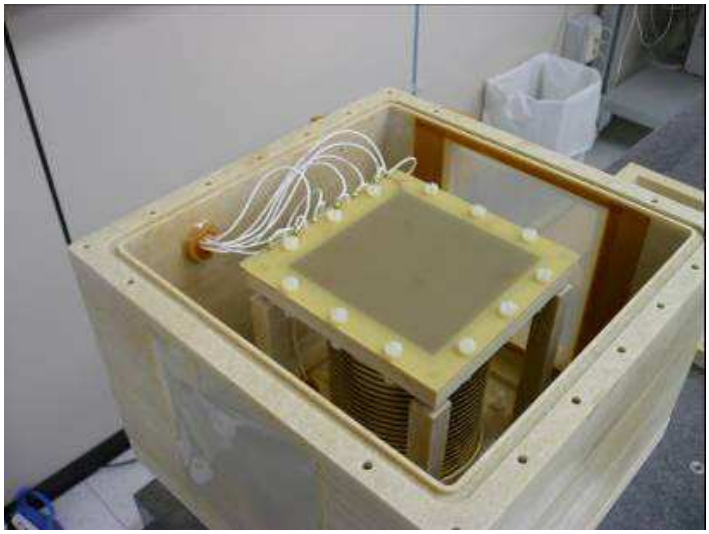

Figure 6: The TPC-GEM prototype

3.1 AMADEUS activities in 2013

The main activities of AMADEUS in 2013 will be:

- continuation of the R&D for the trigger system: tests of the prototype and readout electronics at BTF-LNF and PSI:
- continuation of the R&D for the inner tracker: tests of the prototype at BTF-LNF and PSI
- Monte Carlo simulations:
- finalization of the KLOE 2002-2005 data analyses for the search of processes due to K^-interaction in the Drift Chamber volume and publication
- analyses of data with carbon target
- definition of the experiment strategy

To be mentioned that the AMADEUS activities are supported in the framework of the EU FP7 HadronPhysics3, as WP24 (GEM), WP28 (SiPM) and WP9 (Network on kaon-nuclei interaction studies at low energies) programs.

Acknowledgements
The support from HadronPhysics3 FP7 project is acknowledged.

4 List of Conference Talks by LNF Authors in Year 2012

1. O. Vazquez Doce, Experimental studies of strong interaction in exotic atoms, Seminar at Excellence Cluster Universe, 8 February 2012, TUM, Munich.
2. O. Vazquez Doce, Lambda-p and Lambda-d correlations from K^- interactions in the KLOE Drift Chamber, New trends in the low-energy QCD in the strangeness sector: experimental and theoretical aspects, ECT*, 15-19 October 2012, Trento, Italy.
3. M. Iliescu, Kaon-nucleon strong interaction in kaonic atoms: the SIDDHARTA program, The 20th International IUPAP Conference on Few-Body Problems in Physics (FB20), 20-25 August 2012, Fukuoka International Congress Center in Fukuoka city, Japan.
4. D. Sirghi, Kaonic helium 4 and kaonic helium 3 exotic atoms, New trends in the low-energy QCD in the strangeness sector: experimental and theoretical aspects, ECT*, 15-19 October 2012, Trento, Italy.
5. K. Piscicchia, Themodynamics for a self-gravitating system with cutoff enery, Seminar at Univerista degli Studi di Roma La Sapienza, 9 March 2012, Roma, Italy.

6. K. Piscicchia, Kaon-nuclei interaction studies at low energies (the AMADEUS project), Incontri di Fisica delle Alte Energie, 11-13 April 2012, Univeristy of Ferrara, Ferrara, Italy.

7. K. Piscicchia, Kaon-nuclei interaction studies at low energies (the AMADEUS project), 12th International Workshop on Meson Production, Properties and Intercation, MESON2012, 31 May-5 June 2012, Krakow, Poland.

8. K. Piscicchia, Production of $\Lambda(1405)$ by stopped and in-flight absorption K^- in ^{4}Helium and ^{12}C, Mini-Workshop: The quest for Dense and Strange Hadronic Matter Role of the $\Lambda(1405)$ Hyperon, 31 July 2012, TUM, Munchen, Germany.

9. K. Piscicchia, Low energy kaon nuclei interaction studies through $\Sigma^0\pi^0$ channel with the KLOE detector, New trends in the low-energy QCD in the strangeness sector: experimental and theoretical aspects, ECT*, 15-19 October 2012, Trento, Italy.

10. H. Tatsuno, Kaonic ^{3}Helium and ^{4}Helium measurements in the SIDDHARTA experiment at the DAΦNE collider, New trends in the low-energy QCD in the strangeness sector: experimental and theoretical aspects, ECT*, 15-19 October 2012, Trento, Italy.

11. A. Scordo, Investigating low energy QCD with kaonic atoms: the SIDDHARTA experiment at DAΦNE, Poster presentation at the 50th International Winter meeting on Nuclear Physics, 22-27 January 2012, Bormio, Italy.

12. A. Scordo, Kaon nuclei interactions studies at low energy with a carbon target inside KLOE as a first step towards AMADEUS realization, New trends in the low-energy QCD in the strangeness sector: experimental and theoretical aspects, ECT*, 15-19 October 2012, Trento, Italy.

13. A. Rizzo, Kaonic atoms measurements at the DAΦNE collider: the SIDDHARTA experiment, Young Researcher Meeting in Rome -3rd edition, 20 Junary 2012, Universita degli Studi di Roma "Tor Vergata", Roma, Italy.

14. C. Curceanu, Unlocking the secrets of the kaon-nucleon/nuclei interactions at low energies: the SIDDHARTA and the AMADEUS experiments at the DAΦNE collider, HYP2012, 1-5 Octiber 2012, Barcelona, Spain.

15. C. Curceanu, From DEAR to SIDDHARTA - the strangeness adventure, New trends in the low-energy QCD in the strangeness sector: experimental and theoretical aspects, ECT*, 15-19 October 2012, Trento, Italy.

5 Publications

References

1. K. Piscicchia *et al* (AMADEUS collaboration), Kaon-nuclei interaction studies at low energies (the AMADEUS project) , EPJ Web Conf. 37 (2012) 07002.

2. M. Poli Lener *et al* (AMADEUS collaboration), Performances of a GEM-based Time Projection Chamber prototype for the AMADEUS experiment, arXiv:1302.3054 [physics.ins-det].

3. A. Scordo *et al*, Characterization of a scintillating fibers read by MPPC detectors trigger prototype for the AMADEUS experiment arXiv:1301.7268 [physics.ins-det].

4. H. Tatsuno *et al* (SIDDHARTA collaboration), Kaonic He-3 and He-4 measurements in the SIDDHARTA experiment at the DAΦNE collider, EPJ Web Conf. 37 (2012) 02002.

5. A. Scordo *et al* (SIDDHARTA collaboration), Investigating low energy QCD with kaonic atoms: The SIDDHARTA experiment at DAΦNE, PoS BORMIO2012 (2012) 009.

6. A. Rizzo *et al* (SIDDHARTA collaboration), Kaonic atoms measurements at the DAΦNE collider: The SIDDHARTA experiment, J.Phys.Conf.Ser. 383 (2012) 012004.

7. K. Agari *et al*, The K1.8BR spectrometer system at J-PARC,arXiv:1206.0077 [physics.ins-det].

8. M. Bazzi *et al* (SIDDHARTA collaboration), Measurements of the strong-interaction widths of the kaonic ^{3}Helium and ^{4}Helium 2p levels, Phys.Lett. B714 (2012) 40-43.

9. A. Rizzo *et al* (SIDDHARTA collaboration), Kaonic atoms measurements at the DAΦNE collider: The SIDDHARTA experiment, J.Phys.Conf.Ser. 348 (2012) 012003.

10. M. Bazzi *et al* (SIDDHARTA collaboration), Kaonic hydrogen X-ray measurement in SIDDHARTA, Nucl.Phys. A881 (2012) 88-97.

11. M. Bazzi *et al*, Experimental tests of the trigger prototype for the AMADEUS experiment based on Sci-Fi read by MPPC, Nucl.Instrum.Meth. A671 (2012) 125-128.

12. K. Piscicchia *et al* (AMADEUS collaboration), Kaon-nuclei interaction studies at low energies (the AMADEUS project), Il Nuovo Cimento, Vol. 36 (2013), 191.

13. M. Bazzi *et al* (SIDDHARTA collaboration), Study of kaonic deuterium X-rays by the SIDDHARTA experiment at DAΦNE, arxiv:1302.2797.

MAMBO

D. Babusci, P. Levi Sandri (Resp), D. Pietreanu (Ass.), A. Saputi (Tecn.)

1 Introduction

MAMBO groups together three complementary INFN activities in Germany: the experimental activity with the MAMI-C microtron in Mainz, the development of MRPC counters and the preliminary measurements towards a full proposal to measure the electric dipole moments (EDM) of proton and deuteron, and the new BGO-OD experiment at Bonn-ELSA. LNF are involved in the last two activities.

2 BGO-OD experiment

The BGO-OD esperiment is performed in collaboration between INFN sections of Roma2, LNF, Messina, Pavia, ISS-Roma1 and Torino, the University of Bonn, Physikalisches Institut, ELSA department, the University of Bonn, Helmholtz Institut für Strahlen- und Kernphysik, the University of Edinburgh, the National Science Center Kharkov Institute of Physics and Technology, the University of Moscow, Russia, the Petersburg Nuclear Physics Institute (PNPI), Gatchina and the University of Basel. More that 70 physicists participate to this experimental program foreseen to last until 2017 with possible extention.

The INFN contribution consist in the *Rugby Ball* calorimeter and associated detectors previously used at GRAAL, the target system, the cylindrical tracking chambers and the MRPC detector.

3 Activity in 2012

During the year 2012 the installation of the detector in the S-Beamline at ELSA was continued and the debugging of the experiment was started. The *Rugby Ball* calorimeter was completely installed with its new electronic based on S-ADC's that will allow to obtain time information with 3 ns resolution. Also the Barrel was installed and tested. Small maintenance issues were found ad fixed. Extra shielding to the residual magnetic field of the dipole is needed for the forward and upper part of the calorimeter. This issue is under studies through dedicated simulations. All the forward tracking detectors were installed and tested. No damages were detected as a consequence of the fire in June 2011, apart for some bars of the T.O.F. wall which need to be replaced. In Fig. 1 a schematic view of the complete apparatus is dispayed together with a photograph of the progress in the setup installation at the end of 2012.

4 Planned activity in 2013

The activity in 2013 will be mainly focused on the completion of the experimental apparatus. The full tagging system is expected to be ready in summer. The MRPC and the MPWC chambers under the INFN (Roma2 and Pavia) responsibility should be installed before the end of the year. The TOF wall (under the responsibility of Bonn PI) should also be completed this year. The first data taking is expected to start in november 2013.

$\overline{\text{P}}$ANDA

N. Bianchi, A. M. Bragadireanu (Ass.), B. Dulach (Ass.), P. Gianotti (Resp. Naz.),
M. Giardoni (Ass.), C. Guaraldo (Ass.), M. A. Iliescu (Ass.), V. Lucherini,
D. Orecchini (Tecn.), E. Pace, L. Passamonti (Tecn.), D. Piergluigi (Tecn.), F. Ronchetti,
A. Russo (Tecn.), D. L. Sirghi Diana (Ass.)

1 Introduction

$\overline{\text{P}}$ANDA is one of the biggest experiments of hadron and nuclear physics that will be carried out at the new Facility for Antiproton and Ion Research (FAIR) at Darmstadt, Germany. It is dedicated to the study of the annihilations of antiprotons on nucleons and nuclei up to a maximum center-of-mass energy in $\overline{\text{p}}$p of 5.5 GeV.

The $\overline{\text{P}}$ANDA collaboration consists of 420 physicists from 17 countries spread all over the world. The Italian groups involved are: Torino, University, Politecnico and INFN, Trieste, University and INFN, Genova INFN, Pavia, University and INFN, Ferrara, University and INFN, Legnaro INFN laboratory and Frascati INFN laboratory. The LNF group is involved in the design and construction of the central straw tube tracker of the $\overline{\text{P}}$ANDA detector.

2 $\overline{\text{P}}$ANDA experiment

A new facility for hadronic physics is under construction in Germany. It consists of a major upgrade of the presently running GSI accelerator complex of Darmstadt [1)]. An intense, high momentum

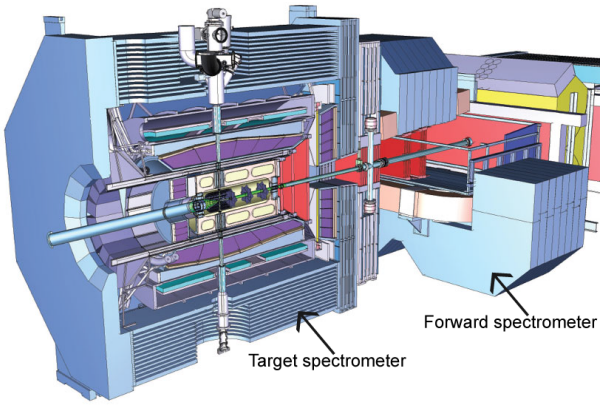

Figure 1: *A schematic view of the $\overline{\text{P}}$ANDA apparatus consisting of two distinct detectors: the target spectrometer (left) and the forward spectrometer (right).*

resolution antiproton beam, with momenta between 1.5 and 15 GeV/c, will be available at the High Energy Storage Ring (HESR), and the experimental activity will be carried out using a general purpose detector $\overline{\text{P}}$ANDA that will be build surrounding an internal target station installed in one of the two straight sections of the storage ring. Figure 1 shows a schematic drawing of the $\overline{\text{P}}$ANDA apparatus. It is designed as a large acceptance multi-purpose detector consisting of two distinct parts: a solenoidal spectrometer, surrounding the interaction target region, and a forward spectrometer to cover the solid angle between 5 and 22 degrees. It will allow the detection and the identification of either the neutral and the charge particles emitted following $\bar{p}$ annihilation.

3 The $\overline{\text{P}}$ANDA Central Tracker

For tracking charge particles in the target spectrometer, $\overline{\text{P}}$ANDA will use different detectors: a silicon Micro Vertex Detector (MVD) a Straw Tube Tracker (STT) and a set of forward GEM chambers [3]. Figure 2 shows the layout of the Target Spectrometer tracking system.

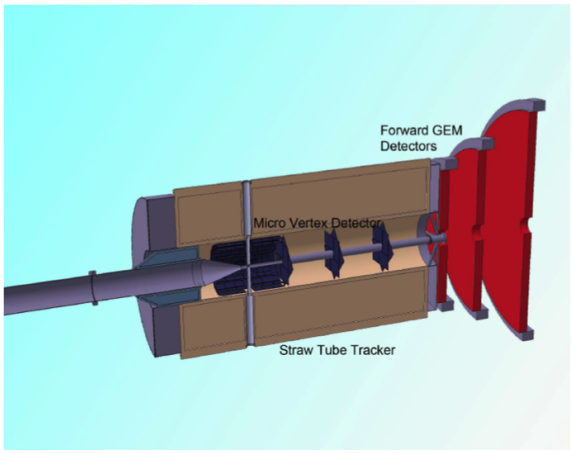

Figure 2: *The $\overline{P}$ANDA tracking system of the Target Spectrometer. It consists of three detectors: Micro Vertex Detector, Straw Tube Tracker, Forward GEM.*

The requirements for this system are:

- almost full solid angle coverage;
- momentum resolution $\delta p/p \sim 1.5\%$;
- low material budget $X/X_0 \sim$ few %;
- good spatial resolution $\sigma_{r,\phi} = 150$, μm, $\sigma_z =$ few mm.

The Technical Design Report (TDR) of the STT has been completed in April 2012 and it has been positively evaluated by the FAIR technical committee (ECE).

The LNF $\overline{\text{P}}$ANDA group is deeply involved in the STT realization and has the responsibility of the mechanics of the whole tracking system.

3.1 Layout of the straw tube detector

The $\overline{\text{P}}$ANDA STT will consist of two identical chambers separated by the beam-target cross-pipe that is cutting the x, y plane in two halves (see fig. 3). Each chamber is made of aluminized mylar straw tubes, diameter 10 mm, length 1500 mm, thickness 30 μm, arranged in planar double layers.

Inside a double layer the tubes are glued together and operated with an Ar+CO_2 (90+10) gas mixture with an over-pressure of 1 bar. This solution has been chosen to avoid strong support structures and to keep the detector design modular and simple. To measure also particle z coordinate, some layers will be mounted with a skew angle $\pm 3^o$ with respect to the beam axis.

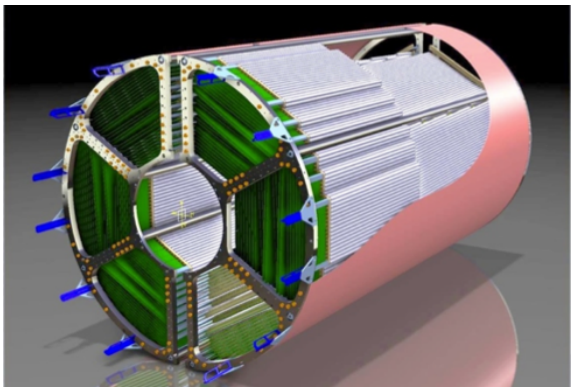

Figure 3: *CAD drawing of the $\overline{P}$ANDA Straw Tube Tracker*

4 Activity of the LNF $\overline{P}$ANDA group

The STT mechanical structure has to support also the beam-target cross-pipe and the MVD. This frame, has to be extremely light and has to allow the movements of the whole block of detectors during the installation procedure or the maintenance operations.

Figure 4 shows the prototype of the mechanical structure of the whole $\overline{P}$ANDA Central Tracking (CT). It has been designed by LNF SPAS and realised with the cooperation of the Torino INFN mechanical workshop.

Figure 4: *The prototype of the Central Tracker mechanics hold by the insertion support system.*

The activity of the LNF $\overline{P}$ANDA group during 2012 has been devoted to the following tasks:

- test of straw tubes prototypes in oder to determine the detector performances;
- development, together with the Torino INFN group, of the mechanical structure for the CT;
- TDR editing.

Concerning the first item, LNF $\overline{\text{P}}$ANDA group has collected data with radioactive sources, cosmic rays that have been included in the detector TDR.

Since the TDR of the STT has been approved, we can consider almost completed the R&D phase for this system. At present, the tracking group is defining the protocols for the straw tube construction and the module's assembly. Quality tests and quality assurance procedures are being defined in order to start soon the mass production that will be the main activity during 2013.

5 List of Conference Talks presented by LNF group members in Year 2012

1. P. Gianotti, "Future facilities for hadron spectroscopy", invited talk at the *International Workshop on new partial wave analysis tools for next generation hadron spectroscopy experiments (ATHOS 2012)*, Camogli, Italy, 20-22 Giugno 2012.

2. P.Gianotti, "The antiproton physics program of the PANDA experiment", invited talk at the *II European Nuclear Physics Conference*, Bucharest, Romania, 17-21 Settembre 2012.

6 Publications

1. P. Gianotti,"Results and perspectives in hadron spectroscopy", Phys. Scripta T150 (2012) 014014.

2. $\overline{\text{P}}$ANDA Collaboration, "Technical Design Report for the: PANDA Straw Tube Tracker ", arXiv:1205.5441.

3. $\overline{\text{P}}$ANDA Collaboration,"Technical Design Report for the: PANDA Micro Vertex Detector", arXiv:1207.6581

References

1. `http://www.fair-center.com/`.

2. `http://www-panda.gsi.de/`.

3. S. Costanza *et al.*, Nucl. Instr. Meth. **A617**, 148-150, 2010.

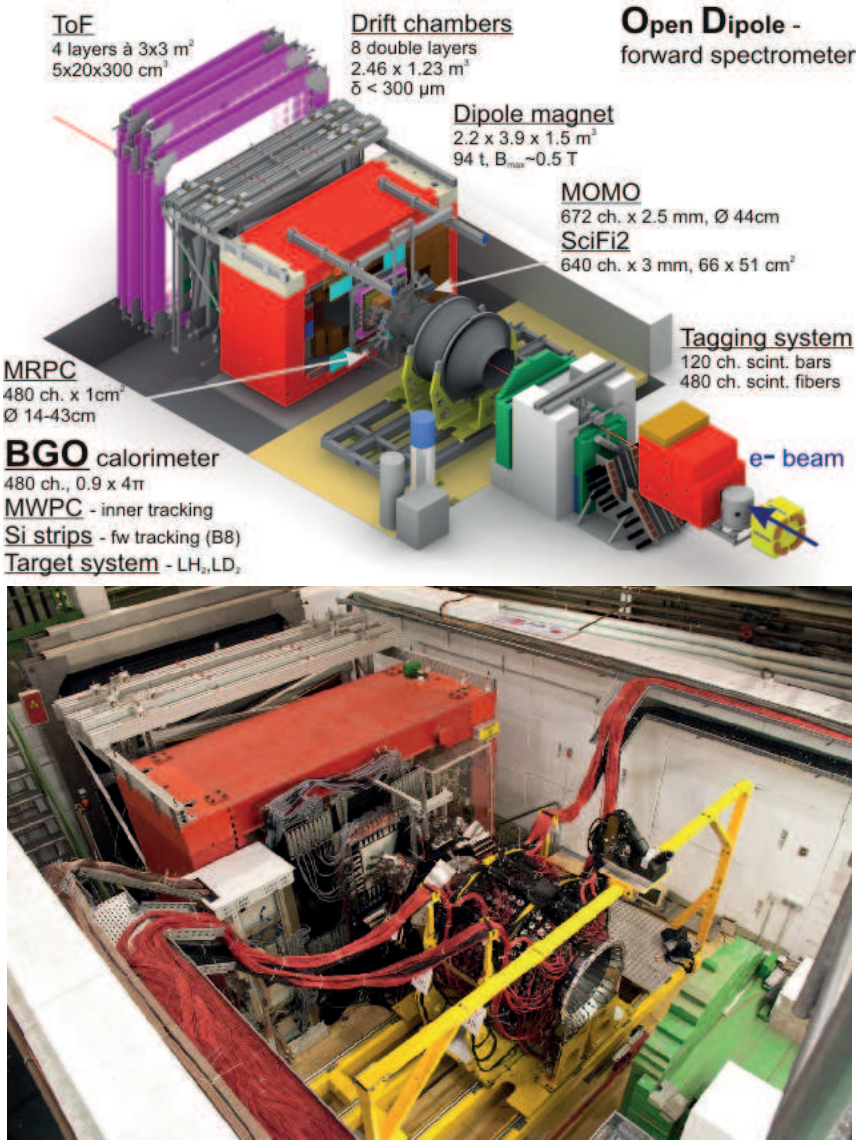

Figure 1: *Top: drawing of the full BGO-OD setup; bottom: the BGO-OD setup in october 2012*

VIP

S. Bartalucci, M. Bazzi (Art. 23), A. Clozza, C. Curceanu (Resp. Naz.),
C. Guaraldo, M. Iliescu (Art. 23), F. Lucibello (Tecn.),
S. Okada (Art. 23), D. Pietreanu (Bors. UE), A. Rizzo (Bors. PhD),
A. Scordo (Ass. Ric), D. Sirghi (Art. 23), F. Sirghi (Bors. UE), O. Vazquez Doce (Bors. UE)

1 The VIP scientific case and the experimental method

The Pauli Exclusion Principle (PEP), which plays a fundamental role in our understanding of many physical and chemical phenomena, from the periodic table of elements, to the electric conductivity in metals and to the degeneracy pressure which makes white dwarfs and neutron stars stable, is a consequence of the spin-statistics connection. Although the principle has been spectacularly confirmed by the huge number and accuracy of its predictions, its foundation lies deep in the structure of quantum field theory and has defied all attempts to produce a simple proof. Given its basic standing in quantum theory, it seems appropriate to carry out precise tests of the PEP validity and, indeed, mainly in the last 15-20 years, several experiments have been performed to search for possible small violations. Moreover, many (if not all) of these experiments are using methods which are not obeying to the so-called Messiah-Greenberg superselection rule. The indistinguishability and the symmetrization (or antisymmetrization) of the wave-function should be checked independently for each particle, and accurate tests were and are being done.

The VIP (VIolation of the Pauli Exclusion Principle) experiment, an international Collaboration among 6 Institutions of 7 countries, has the goal to improve the limit on the probability of the violation of the PEP for electrons, ($P < 1.7 \times 10^{-26}$ established by E. Ramberg e G. A. Snow: *Experimental limit on a small violation of the Pauli principle*, Phys. Lett. **B 238** (1990) 438) by three-four orders of magnitude ($P < 10^{-29 \div -30}$), exploring a region where new theories might allow for a possible PEP violation.

The experimental method consists in the introduction of electrons into a copper strip, by circulating a current, and in the search for X-rays resulting from the forbidden radiative transition that occurs if one of the new electrons is captured by a copper atom and cascades down to the 1s state already filled by two electrons with opposite spins. The energy of this transition would differ from the normal K_α transition by about 300 eV (7.729 keV instead of 8.040 keV) providing an unambiguous signal of the PEP violation. The measurement alternates periods without current in the copper strip, in order to evaluate the X-ray background in conditions where no PEP violating transitions are expected to occur, with periods in which current flows in the conductor, thus providing "fresh" electrons, which might violate PEP. The rather straightforward analysis consists in the evaluation of the statistical significance of the normalized subtraction of the two spectra in the region of interest.

The experiment is being performed at the LNGS underground Laboratories, where the X-ray background, generated by cosmic rays and natural radioactivity, is reduced.

2 The VIP experimental setups

The first VIP setup was realized in 2005, starting from the DEAR setup, reutilizing the CCD (Charge Coupled Devices) X-ray detectors, and consists of a copper cylinder, 4.5 cm in radius, 50 μm thick, 8.8 cm high, surrounded by 16 equally spaced CCDs of type 55.

The CCDs were at a distance of 2.3 cm from the copper cylinder, grouped in units of two chips vertically positioned. The setup was enclosed in a vacuum chamber, and the CCDs cooled to about 165 K by the use of a cryogenic system. The setup was surrounded by layers of copper

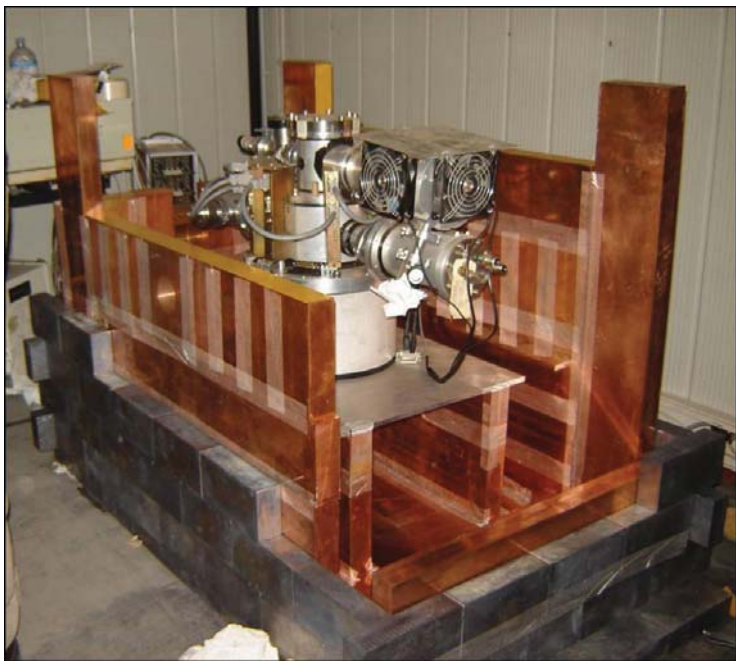

Figure 1: The VIP setup at the LNGS laboratory during installation.

and lead (as seen in the picture) to shield the setup against the residual background present inside the LNGS laboratory, see Fig. 1.

A schematic drawing of the VIP setup is shown in Fig. 2.

The DAQ alternated periods in which a 40 A current was circulated inside the copper target with periods without current, referred as background.

VIP was installed at the LNGS Laboratory in Spring 2006 and was taking data in this configuration until Summer 2010. Since 2011 we are preparing a new version of the setup - see below - in order to gain a factor 100 in the probability of violation.

3 Activities in 2012

3.1 Present VIP limit on PEP violation

Until summer 2010 the VIP experiment was in data taking, alternating periods of "signal" (I=40 A) with periods without signal (I=0 A). Data analyses were performed (energy calibration, sum of spectra, subtraction of background) and the probability of violation of PEP for electrons obtained (upper limit):

$$\frac{\beta^2}{2} < 4.7 \times 10^{-29} \tag{1}$$

We are attempting an interpretation of our results in the framework of quon-theory, which turned out to be a consistent theory of *small* violations of PEP. The basic idea of quon theory is that (anti)commutators, are replaced by weighted sums

$$\frac{1-q}{2}\left[a_i, a_j^+\right]_+ + \frac{1+q}{2}\left[a_i, a_j^+\right]_- = a_i a_j^+ - q a_j^+ a_i = \delta_{i,j} \tag{2}$$

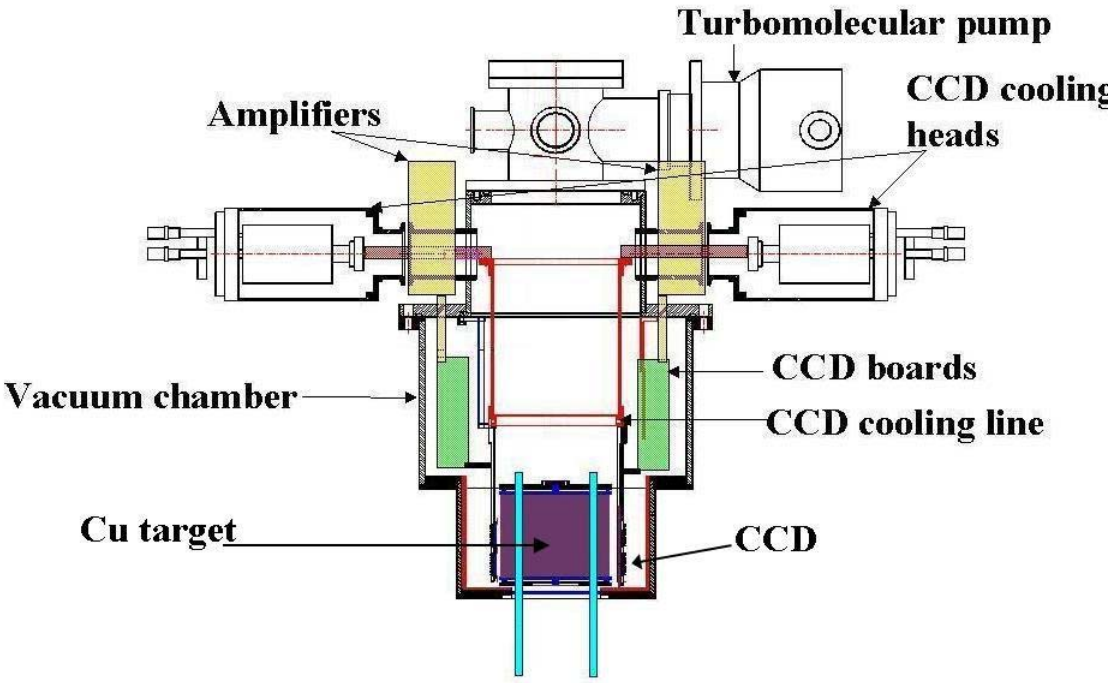

Figure 2: *The VIP setup. All elements af the setup are identified in the figure.*

where $q = -1$ ($q = 1$) gives back the usual fermion (boson) commutators. The statistical mixture in equation (2) also shows that the PEP violation probability is just $(1 + q)/2$ and thus our best experimental bound on q is

$$\frac{1+q}{2} < 4.7 \times 10^{-29} \tag{3}$$

A consistent interpretation of the VIP results can thus be based on quon theory; however here we note that is not easy to devise tests of PEP, because of many conceptual difficulties, presented in our published papers (see list at the end).

3.2 VIP2 - a new high sensitivity experiment

In order to achieve the signal/background increase which will allow a gain of two orders of magnitude for the probability of PEP violation for electrons, we built a new target, a new cryogenic system and use new detectors with timing capability and active veto system. As x-ray detectors we use SDDs which were employed in der SIDDHARTA experiment on kaonic atoms at the DAΦNE electron-positron collider of Laboratori Nazionali di Frascati. SDDs have an even better energy resolution than CCDs but additionally provide timing capability which allow to use anti-coincidence operation with scintillators and therefore active shielding. The VIP2 system will provide:

1. signal increase with a more compact system with higher acceptance and higher current flow in the new copper strip target;

2. background reduction by decreasing the x-ray detector surface, more compact shielding (active veto system and passive), nitrogen filled box for radon radiation reduction.

In the table 1 the numerical values for the improvements in VIP2 are given which will lead to an expected overall improvement of a factor higher than ∼120.

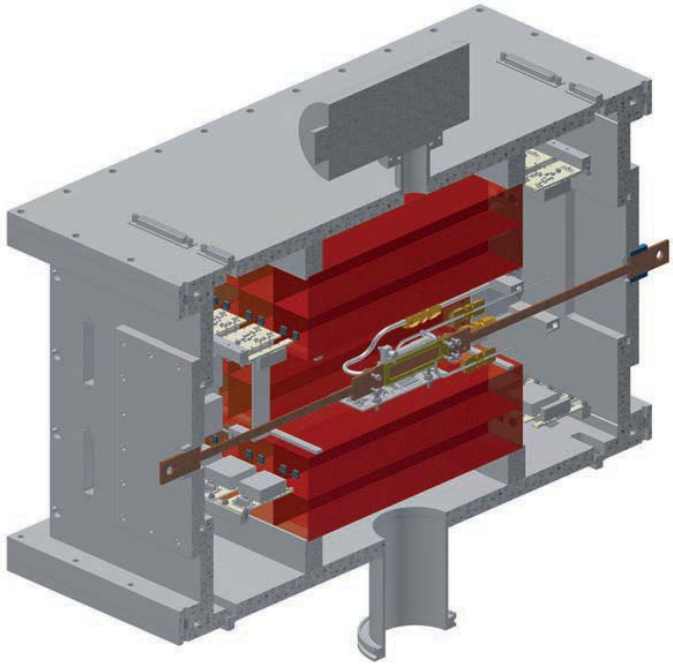

Figure 3: An artist view of the VIP2 experimental setup. In the middle the copper conductor and the x-ray detectors are installed. Plastic scintillators with solid state photodetector readout acting as active sgielding are surrounding the inner part.

Figures 3 shows the main elements for the proposed setup in the VIP2 experiment. The copper strip target is 30 mm long, 10 mm wide and is about 40μm thick, and is installed in the center of the setup. The copper strip is cooled at ∼90K by the use of an external cryogenic system using liquid argon as the cooling medium. The current connection lines made of copper wires with a cross-section area of 1.5 cm^2, allow a current flow of (at least) 100 A.

The current lines exhibit a temperature gradient from inside the vacuum chamber to the outside connectors of about 180 K. Monte Carlo simulations were performed to study the effect of the active shielding in various configurations of the setup and models of the background radiation. The background profiles measured at LNGS were used as input parameters in the simulations. As the veto counters, 2 pieces of 10 cm thick plastic scintillators are found to be optimal. During 2012 various elements of the setup were built and tested. Presently the setup is being assembled in Vienna SMI and Frascati laboratories for the final tests.

4 Activities in 2013

In 2013 we plan to finalize the construction of the VIP upgraded setup and install, debug and test at LNGS and start the data taking. We are, as well, considering to extend the scientific program towards a feasibility study of limits on parameters of the collapse model (as a solution of the measurement problem, put initially forward by Ghirardi, Rimini and Weber) by measurements of X rays spontaneously emitted in the continuous spontaneous localization (CSL) model.

Table 1: List of numerical values of the changes in VIP2 in comparison to the VIP features (given in the brackets)

Changes in VIP2	value VIP2(VIP)	expected gain
acceptance	12%	12
increase current	100A (50A)	2
reduced length	3 cm (8.8 cm)	1/3
total linear factor		8
energy resolution	170 eV(340 eV)	4
reduced active area	6 cm^2(114 cm^2)	20
better shielding and veto		5-10
higher SDD efficiency		1/2
background reduction		200-400
overall implementation		$\sim$120

Acknowledgements

The VIP Collaboration wishes to thank all the LNGS laboratory staff for the precious help and assistance during all phases of preparation, installation and data taking. The support from the HadronPhysics FP6, HadronPhysics2 and HadronPhysics3 FP7 and from EU COST 1006 Action projects is acknowledged.

5 List of Conference Talks by LNF Authors in Year 2012

Include a list of conference talks by LNF authors.

1. A. Rizzo, "A new experimental upper limit on λ paramater", Quantum Malta 2012: Fundamental Problems in Quantum Physics, 24-27 April 2012, La Valletta, Malta.

2. A. Rizzo, "A new experimental upper limit on λ paramater", Open Problems in Quantum Mechanics, 20-22 June 2012, LNF, Frascati, Italy.

3. C. Curceanu, "A glimpse into the Pandora Box of quantum mechanics: the Pauli Exclusion principle violation and the spontaneous collapse models put at test",QFRF6, 11-14 June 2012 Vaxjo, Sweden.

4. C. Curceanu, "A glimpse into the Pandora Box of quantum mechanics: the Pauli Exclusion principle violation and the spontaneous collapse models", Fundamental problems in Quantum Physics, 24-27 April 2012, La Valletta, Malta.

6 Publications

References

1. C. Curceanu (Petrascu) *et al.* (The VIP Collaboration), A glimpse into the Pandora box of the quantum mechanics: The VIP exclusion principle violation and spontaneous collapse models put at test, AIP Conf. Proc., 136-145 (2012).

2. C. Curceanu (Petrascu) *et al.* (The VIP Collaboration), Experimental tests of Quantum Mechanics: from Pauli Exclusion Principle Violation to spontaneous collapse models, Journal of Physics, Conference Series, Vol. 361 (2012).

3. C. Curceanu (Petrascu) *et al.* (The VIP Collaboration), Experimental tests of quantum mechanics: Pauli Exclusion Principle Violation and spontaneous collapse models, AIP Conference Proceedings, 1424, 397-406 (2012).

4. C. Curceanu, J.D. Gillaspy, R.D. Hilborn, Resouce Letter SS-1: The Spin Statistics Connection, American Journal of Physics, Vol. 80, Issue 7, 561-577 (2012).

5. J. Marton *et al.* (The VIP Collaboration), Testing the Pauli Exclusion Principle for Electrons, arXiv:1302.7218 [nucl-ex].

6. S. Donadi *et al.*, Are Collapse Models Testable via Flavor Oscillations?, arXiv:1207.6000 [quant-ph].

7. S. Donadi *et al.*, The effect of spontaneous collapses on neutrino oscillations, arXiv:1207.5997 [quant-ph].

8. C. B. Hiesmayr *et al.*, Revealing Bell's Nonlocality for Unstable Systems in High Energy Physics, Eur.Phys.J. C72 (2012) 1856.

FA51: Fisica Astroparticellare

C. S. Fong (Bors.), E. Nardi (Resp.), E. Peinado (Bors.)

Description of the 2012 activity

i. A comprehensive account of the theory of *leptogenesis* has been presented in ref. [1]. We have explained why leptogenesis is an appealing mechanism for baryogenesis. We have presented a comprehensive review of its motivations and of the basic ingredients, and we have described subclasses of effects, like those of lepton flavours, spectator processes, scatterings, finite temperature corrections, the role of the heavier sterile neutrinos and quantum corrections. We have then addressed leptogenesis in supersymmetric scenarios, as well as some other popular variations of the basic leptogenesis framework.

ii. In ref. [2] we have developed the attempt put forth in ref. [3]to explain the fermion mass hierarchy, starting from the assumption that the Yukawa couplings correspond to vacuum expectation values of a spontaneously broken flavour symmetry. The tree level potential for a scalar multiplet of 'Yukawa fields' Y for one type of quarks admits the promising vacuum configuration $\langle Y\rangle \propto \mathrm{diag}(0,0,1)$ that breaks spontaneously $SU(3)_L \times SU(3)_R$ flavour symmetry. We have investigated whether the vanishing entries could be lifted to nonvanishing values by slightly perturbing the potential, thus providing a mechanism to generate the Yukawa hierarchies. For theories where at the lowest order the only massless states are Nambu-Goldstone bosons we have found, as a general result, that the structure of the tree-level vacuum is perturbatively stable against corrections from scalar loops or higher dimensional operators. We have discussed the reasons for this stability, and we have given an explicit illustration in the case of loop corrections by direct computation of the one-loop effective potential. We have shown that a hierarchical configuration $\langle Y\rangle \propto \mathrm{diag}(\epsilon', \epsilon, 1)$ (with ϵ', $\epsilon \ll 1$) can be generated by enlarging the scalar Yukawa sector, and we have presented a simple model in which spontaneous breaking of the flavour symmetry can account for the fermion mass hierarchies.

iii. In ref. [4] We have considered the see-saw mechanism within a non-supersymmetric SO(10) model. By assuming the SO(10) quark-lepton symmetry, and after imposing suitable conditions that ensure that the right-handed (RH) neutrino masses are at most mildly hierarchical (compact RH spectrum) we obtain a surprisingly predictive scenario. The absolute neutrino mass scale, the Dirac and the two Majorana phases of the neutrino mixing matrix remain determined in terms of the set of already measured low energy observables, modulo a discrete ambiguity in the signs of two neutrino mixing angles and of the Dirac phase. The RH neutrinos mass spectrum is also predicted, as well as the size *and sign* of the leptogenesis CP asymmetries. We have computed the cosmological baryon asymmetry generated through leptogenesis, obtaining the correct sign, and a size compatible with observations.

v. The general theory of leptogenesis, with special attention to its most striking phenomenological consequences, and including all the most recent refinements, constituted the main research topic of the group during the past few years and also during 2012. Nevertheless, the group is also active in other lines of research, among which quite notably is the construction of theoretical models for neutrino masses in GUT theories [5], the phenomenology of lepton flavour violation [6], non-Abelian discrete symmetries as a way to explain the quark and lepton mass matrices [7] and supersymmetric R-parity [8].

References

1. **"Leptogenesis in the Universe,"**
   C. S. Fong, E. Nardi and A. Riotto, Adv.High Energy Phys. **2012** 158303 (2012).
2. **"Yukawa hierarchies from spontaneous breaking of the $SU(3)_L \times SU(3)_R$ flavour symmetry?,"** J. R. Espinosa, C. S. Fong and E. Nardi, arXiv:1211.6428, to appear in JHEP.
3. **"Naturally large Yukawa hierarchies,"** E. Nardi, Phys. Rev. D **84**, 036008 (2011).
4. **"Squeezing out predictions with leptogenesis from SO(10),"**
   F. Buccella, D. Falcone, C. S. Fong, E. Nardi and G. Ricciardi, Phys. Rev. D **86**, 035012 (2012).
5. **"Neutrino masses in $SU(5) \times U(1)_F$ with adjoint flavons,"**
   E. Nardi, D. Restrepo and M. Velasquez, Eur. Phys. J. C **72**, 1941 (2012)
6. **"Lepton flavor violation in minimal flavor violation extensions of the seesaw,"**
   E. Nardi, Nucl. Phys. Proc. Suppl. **225-227** (2012) 236.
7. **"Quark-Lepton Mass Relation in a Realistic A4 Extension of the Standard Model,"** S. F. King, S. Morisi, E. Peinado and J. W. F. Valle, arXiv:1301.7065.
8. **"Flavor origin of R-parity,"** S. Morisi, E. Peinado and A. Vicente, arXiv:1212.4145.

Talks at Conferences

1. *"Topics in Leptogenesis".*
   Enrico Nardi, Invited talk at: *"BeNe 2012 - Behind the Neutrino Mass"*,
   September 17-21, 2012; *"Abdus Salam ICTP"* Trieste, Italy.
   [`http://users.ictp.it/ smr2366/talks/Nardi-Bene2012.pdf`].
2. *" Leptogenesis and neutrino masses,"*
   E. Nardi, Invited talk at: *"PPC 2012 - International workshop on Particle Physics and Cosmology,"*, November 5-9, 2012, KIAS, Seoul, Korea.
   [`http://workshop.kias.re.kr/PPC2012/downloads/Nardi-PPC-2012.pdf`].
3. *"Lepton Flavor Violation in minimal Flavor Violation extensions of the see-saw."*
   Enrico Nardi, Invited talk at NOW 2012: *"Neutrino Oscillation Workshop"*,
   9-16 September 2012, Conca Specchiulla (Otranto, Lecce, Italy).
   [`http://www.ba.infn.it/ now/now2012/web-content/TALKS/Saturday15/parallel1/Nardi-NOW2012.pdf`].
4. *"The effective potential for spontaneous breaking of the flavour symmetry."*
   Chee Sheng Fong, Invited talk at: *"Planck 2012",* May 28 - June 1, Warsaw, Poland.
   [`http://planck12.fuw.edu.pl/talks/fong.pdf`].
5. *"Yukawa hierarchies from spontaneous flavor symmetry breaking."*
   Chee Sheng Fong, Invited talk at: *"2nd KIAS phenomenology workshop",* September 10-14, KIAS, Seoul, KOREA.
   [`http://workshop.kias.re.kr/Pheno2/?download=fong_flavor_ssb.pdf`].

Editorial Work

1. Proceedings of the 3^{nd} Young Researchers Workshop *"Physics Challenges In The LHC Era,"* 16^{th} Frascati Spring School 'Bruno Touschek', Frascati, Italy, May 7 & 10, 2012.
   E. Nardi, Editor.
   [`http://www.lnf.infn.it/sis/frascatiseries/Volume55/volume55.pdf`].
2. Proceedings of *"FLASY12: 2^{nd} workshop on flavor symmetries and consequences in accelerators and cosmology",* 30 Jun - 4 Jul 2012. Dortmund, Germany Eds: E. Peinado *et al.*
   [`http://arxiv.org/abs/arXiv:1210.6239`].

LF21: PHENOMENOLOGY OF ELEMENTARY PARTICLE INTERACTIONS AT COLLIDERS

G. Corcella, V. Del Duca, G. Isidori (Resp.), J. Jones Perez (Post-doc), G. Pancheri (Ass. senior)

1 Summary of the project

The research topics investigated within this project can be divided into two main areas:

- Flavour physics, precision tests and physics beyond the Standard Model (G. Isidori, J. Jones Perez);
- Theoretical and phenomenological aspects of QCD and collider phyiscs (G. Corcella, V. Del Duca, G. Pancheri).

Some of the most significant projects completed in 2012 in these two research areas are listed below.

I. *Flavour physics, precision tests, and physics beyond the Standard Model*

Precise theoretical prediction of BR($B_s \to \mu^+\mu^-$) within the Standard Model and analysis of the implication of the LHCb measurement of CP violation in the charm system. [1, 2, 3]

Analysis of the implications of the discovery of a Higgs boson, with mass around 125 GeV, both in the Standard Model and beyond. [4, 5]

Analysis of the latest LHC data in constraining the structure of the minimal supersymmetric extension of the Standard Model. [6]

Analysis of the possible signatures of new heavy neutral gauge bosons at the LHC in an extended supersymmetric extension of the Standard Model. [9]

II. *Theoretical and phenomenological aspects of QCD and collider phyiscs*

Further progress in the derivation of a general formula to describe the infrared structure of generic scattering amplitudes, within gauge theories, in the high-energy limit. [10]

Refined theoretical predictions for the total and the inelastic cross-sections at the LHC. [12]

2 Main contributions to Conference Proccedings published in 2012

1. L. Magnea, V. Del Duca, C. Duhr, E. Gardi and C. D. White, PoS LL **2012** (2012) 008 [arXiv:1210.6786 [hep-ph]].
2. R. M. Godbole, K. Mohan and G. Pancheri, Frascati Phys. Ser. **54** (2012) 70.
3. G. Pancheri, R. M. Godbole, A. Grau, O. Shekhovtsova and Y. N. Srivastava, Frascati Phys. Ser. **54** (2012) 120.
4. G. Pancheri and Y. Srivastava, Nuovo Cim. C **035N1** (2012) 15.

3 Full list of publications of the year 2012

References

1. A. J. Buras, J. Girrbach, D. Guadagnoli and G. Isidori, Eur. Phys. J. C **72** (2012) 2172 [arXiv:1208.0934 [hep-ph]].
2. G. Isidori and J. F. Kamenik, Phys. Rev. Lett. **109** (2012) 171801 [arXiv:1205.3164 [hep-ph]].
3. G. F. Giudice, G. Isidori and P. Paradisi, JHEP **1204** (2012) 060 [arXiv:1201.6204 [hep-ph]].
4. G. Degrassi, S. Di Vita, J. Elias-Miro, J. R. Espinosa, G. F. Giudice, G. Isidori and A. Strumia, JHEP **1208** (2012) 098 [arXiv:1205.6497 [hep-ph]].
5. G. Blankenburg, J. Ellis and G. Isidori, Phys. Lett. B **712** (2012) 386 [arXiv:1202.5704 [hep-ph]].
6. O. Buchmueller *et al.*, Eur. Phys. J. C **72** (2012) 2243 [arXiv:1207.7315 [hep-ph]].
7. G. Blankenburg, G. Isidori and J. Jones-Perez, Eur. Phys. J. C **72** (2012) 2126 [arXiv:1204.0688 [hep-ph]].
8. G. Isidori and D. M. Straub, Eur. Phys. J. C **72** (2012) 2103 [arXiv:1202.0464 [hep-ph]].
9. G. Corcella and S. Gentile, Nucl. Phys. B **866** (2013) 293 [Erratum-ibid. **2013** (2013) 554] [arXiv:1205.5780 [hep-ph]].
10. V. Del Duca, C. Duhr, E. Gardi, L. Magnea and C. D. White, arXiv:1201.2841 [hep-ph]; Phys. Rev. D **85** (2012) 071104.
11. S. Biondini, O. Panella, G. Pancheri, Y. N. Srivastava and L. Fano, Phys. Rev. D **85** (2012) 095018 [arXiv:1201.3764 [hep-ph]].
12. A. Grau, S. Pacetti, G. Pancheri and Y. N. Srivastava, Phys. Lett. B **714** (2012) 70 [arXiv:1206.1076 [hep-ph]].
13. A. Delgado, G. F. Giudice, G. Isidori, M. Pierini and A. Strumia, arXiv:1212.6847 [hep-ph], to appear in Eur. Phys. J. C
14. O. Gedalia, G. Isidori, F. Maltoni, G. Perez, M. Selvaggi and Y. Soreq, arXiv:1212.4611 [hep-ph], submitted to Phys. Rev. Lett.
15. S. Biondini, O. Panella, G. Pancheri, Y. N. Srivstava and L. Fano, arXiv:1201.3764 [hep-ph].

LF61: Low-dimensional strongly correlated electron systems, spin-Hall effect and nanoscale science and technology

S. Bellucci (Resp. Naz.), M. Benfatto, M. Cini (Ass.), L. Coderoni (Bors.), K. Hatada (Borsista PD), K. Hayakawa (Borsista PD), F. Micciulla (Ass. Ric.), C. Natoli (Ass.), F. Palumbo (Ass.), N. Pugno (Ass.), I. Sacco (Bors.), G. Stefanucci (Ass.)

External collaborating Institutions:

IHEP-Protvino, Russia
Univ. Pavia, Italy
Belorus State Univ. Minsk,
Department of Physics, Yerevan State University, Armenia
Department of Physics, Univ. Roma Tor Vergata, Italy
Institute of Solid State Physics, University of Latvia, Kengaraga Str. 8, 1063 Riga, Latvia
Instituto de Ciencia de Materiales de Aragon, CSIC-Universidad de Zaragoza, 50009 Zaragoza, Spain.
ICB, UMR 5209 Universite' de Bourgogne - CNRS, BP 47870, F-21078 Dijon, France
Institut de Physique de Rennes, UMR UR1-CNRS 6251, Campus de Beaulieu, Universite' de Rennes1, 35042 Rennes-cedex, France

Research Activity

Our theoretical study in collaboration with Riga, Latvia focused on the fundamental properties of various CNT-metal (Me), GNR-Me, and CNT-graphene interconnects. The cluster approach based on the multiple scattering theory as well as effective medium approximation were used to model the dispersion law, electronic density of states (DOS), and conductivity, etc. Multiple scattering problems were solved for nanostructures with radial (quantum dots) and axial (nanowires, nanotubes) symmetry. Interconnect capacitances and impedances have been evaluated in the GHz and THz regimes. Parametrical numerical simulations of conductivity were carried out for zig-zag (m,0), armchair (m,m), and chiral (m,n) CNTs, and the sensitivity of conductivity to the local electronic DOS in CNTs with local impurities (N and B atoms) was demonstrated. CNTs, CNT-Me, and GNR-Me based nanostructures are prospective nanosensor structures [1].

Cluster approach based on the multiple scattering theory formalism, realistic analytical and coherent potentials, as well as the effective medium approximation (EMA-CPA), can be effectively used for modeling of nano-sized systems. This allows us to calculate the dispersion law E(k), the electronic density of states, the conductivity, etc. The multiple scattering problems are stated for radial (e.g., quantum dots) and axial (e.g., nanowires, nanotubes) symmetry approaches. Basic attention is paid now for applications on carbon nanotubes (CNTs) of various morphology which possess the unique physical properties in nanoelectronics, e.g., contacts of CNTs with other conducting elements of a nanocircuit which can be promising candidates for interconnects in a high-speed electronics. The main problems solving for resistance in nanotube junctions with metal particles appear due to the influence of chirality effects in the interconnects of single-wall (SW) and multi-wall (MW) CNTs with the fitting metals (Me = Ni, Cu, Ag, Pd, Pt, Au) for predefined CNT geometry. Using the model of 'effective bonds' developed in the framework of presented approach and Landauer theory, we can predict the resistivity

properties for both SW and MW CNT-Me interconnects. We have also developed the model of the inter-wall interaction inside the MW CNTs, which demonstrates the possible 'radial current' losses [2].

To predict a growth mechanism for carbon nanotubes (CNTs) upon a metal particle as synthesized in the porous membrane block then incorporated in the nanoelectronic device, we have performed a series of large-scale DFT-LCAO calculations using the CRYSTAL-06 code. Carbon adatoms can appear upon the densely-packed Ni(111) catalyst surface due to dissociation of hydrocarbon molecules (e.g., CH4) when applying the CVD method for the nanotube growth. We have started with adsorption properties of carbon atoms. Then, we have simulated the regular C/Ni(111) interface, where adatoms initially form a monolayer which can be disintegrated to nanoflakes gradually transforming into CNT embryos (in the form of semi-fullerenes) and, finally, into the capped CNTs (d C–C ≈ 1.42 Å) with either armchair or zigzag chirality. Periodicity of this system results in models of infinite arrays (bundles) of single-walled (SW) CNTs with a diameter 8.0–8.2 Å and the inter-tube distance 4.2–4.6 Å (depending on chirality). Analyzing the results of calculations on the CNT/Ni interconnect, we have observed a considerable transfer of the electronic charge from the metallic catalyst towards the nanotube (up to ∼1.4 e per contacting C atom) accompanying by substantial redistribution of the electronic density, especially in the case of nanostructured Ni(111) containing nickel nanoclusters. The nanostructured morphology of metal substrate has been found to be the most effective for the growth of CNT bundles [3].

Major attention is paid now to applications of carbon nanotubes (CNTs) and graphene nanoribbons (GNRs) with various morphology which possess unique physical properties in nanoelectronics, e.g., contacts of CNTs or (GNRs) with other conducting elements of a nanocircuit, which can be promising candidates for interconnects in high-speed electronics. The main problems solving for resistance C-Me junctions with metal particles appear due to the influence of chirality effects in the interconnects of single-wall (SW) and multi-wall (MW) CNTs, single-layer (SL) and multi-layer (ML) GNRs with the fitting metals (Me = Ni, Cu, Ag, Pd, Pt, Au) for the predefined carbon system geometry. Using the models of ‘liquid metal’ and ‘effective bonds’ developed in the framework of the presented approach and Landauer theory, we can predict resistivity properties for the considered interconnects. We have also developed the model of the inter-wall interaction inside MW CNTs, which demonstrates possible ‘radial current’ losses. CNT- and GNR- Metal interconnects in FET-type nanodevices provide nanosensoring possibilities for local physical (mechanical), chemical and biochemical influences of external medium. At the same time, due to high concentrations of dangling bonds CNT- and GNR-Metal interconnects as interfaces are also considered as electrically, magnetically and chemically sensitive elements for novel nanosensor devices [4].

Also, double-wall (DW) CNTs consisting of two coaxial single-wall (SW) constituents, possess mechanical, structural and electronic properties which are superior to SW CNTs. DW CNT is also the simplest model of multi-wall (MW) carbon nanotube. In our study, we have simulated DW NTs with not only commensurate (6, 6)@(11, 11) and (10, 0)@(19, 0) morphologies (analogously to those doublewall carbon nanotubes studied so far), but also incommensurate (6, 6)@(19, 0) and (10, 0)@(11, 11) ones, all described by asymmetric P1 rod group. Inter-shell distances in aforementioned nanotubes are changed from 3.37 to 3.54 Å, within the interval of DW CNT stability. Due to essential difference between the translation periods of SW CNTs with (n1, n1) and (n2, 0) chirality indices (their ratio is $1/\sqrt{3}$), we have been able to use the first-principles DFT-LCAO method only for detailed calculations on the first two nanotube configurations mentioned above (using unit cell model), while the semi-empirical self-consistent-charge density-functional tight-binding (SCC-DFTB) method has been applied for calculations of all four DW NT configurations (in the framework of super-cell model

characterized by large translation length unit of incommensurate double-wall nanotube achieving 4.24 nm). Combining both methods for calculations on SW and DW CNTs, we have analyzed their electronic properties (e.g., band structure, density of states as well as electronic charge redistribution) [5].

The process of photon emission by a high-energy electron or positron moving in a bent single crystal with a constant curvature is considered. The relations for differential energy losses of particles and polarization of emitted photons are obtained. Corrections due to multiphoton production are found. The comparison of calculations with existing experimental data is carried out. The process of photoproduction of electron-positron pairs in a bent single crystal is also studied. The differential probabilities of the process taking into account the photon polarization are presented. Equations are obtained which determine the variation of the Stokes parameters of γ quanta, and their solutions are given [6].

The effects of long-range interactions in quantum transport are still largely unexplored, mainly due to the difficulty of devising efficient embedding schemes. In this work we present a substantial progress in the interacting resonant level model by reducing the problem to the solution of Kadanoff-Baym-like equations with a correlated embedding self-energy. The method allows us to deal with short- and long-range interactions and is applicable from the transient to the steady-state regime. Furthermore, memory effects are consistently incorporated and the results are not plagued by negative densities or nonconservation of the electric charge. We employ the method to calculate densities and currents with long-range interactions appropriate to low-dimensional leads, and show the occurrence of a jamming effect, which drastically reduces the screening time and suppresses the zero-bias conductance. None of these effects are captured by short-range model interactions [7].

We investigated the effects of the electron-electron interaction between a molecular junction and the metallic leads in time-dependent quantum transport. We showed that the molecule-lead interaction changes substantially the transient and steady-state transport properties. We first show that the mean-field Hartree-Fock (HF) approximation does not capture the polarization effects responsible for the renormalization of the molecular levels neither in nor out of equilibrium. Furthermore, due to the time-local nature of the HF self-energy, there exists a region in parameter space for which the system does not relax after the switch-on of a bias voltage. These and other artifacts of the HF approximation disappear when including correlations at the second-Born or GW levels. Both these approximations contain polarization diagrams, which correctly account for the screening of the charged molecule. We find that by changing the molecule-lead interaction, the ratio between the screening and relaxation time changes, an effect which must be properly taken into account in any realistic time-dependent simulation. Another important finding is that while in equilibrium the molecule-lead interaction is responsible for a reduction of the highest occupied molecular orbital-lowest unoccupied molecular orbital (HOMO-LUMO) gap and for a substantial redistribution of the spectral weight between the main spectral peaks and the induced satellite spectrum, in the biased system it can have the opposite effect, i.e., it sharpens the spectral peaks and opens the HOMO-LUMO gap [8]

We presented a compact and simplified proof of a generalized Wick theorem to calculate the Green's function of bosonic and fermionic systems in an arbitrary initial state. It was shown that the decomposition of the noninteracting n-particle Green's function is equivalent to solving a boundary problem for the Martin-Schwinger hierarchy; for noncorrelated initial states, a one-line proof of the standard Wick theorem is given. Our result leads to new self-energy diagrams, and an elegant relation with those of the imaginary-time formalism is derived. The theorem is easy to use and can be combined

with any ground-state numerical technique to calculate time-dependent properties [9].

The possibility of finding multistability in the density and current of an interacting nanoscale junction coupled to semi-infinite leads was studied at various levels of approximation. The system is driven out of equilibrium by an external bias and the nonequilibrium properties are determined by real-time propagation using both time-dependent density functional theory (TDDFT) and many-body perturbation theory (MBPT). In TDDFT the exchange-correlation effects are described within a recently proposed adiabatic local density approximation (ALDA). In MBPT the electron-electron interaction is incorporated in a many-body self-energy which is then approximated at the Hartree-Fock (HF), second-Born, and GW level. Assuming the existence of a steady state and solving directly the steady-state equations we find multiple solutions in the HF approximation and within the ALDA. In these cases we investigate whether and how these solutions can be reached through time evolution and how to reversibly switch between them. We further show that for the same cases the inclusion of dynamical correlation effects suppresses bistability [10].

We showed that the energy functional of ensemble density functional theory (DFT) in systems with attractive interactions is a convex function of the fractional particle number N and is given by a series of straight lines joining a subset of ground-state energies. As a consequence the exchange-correlation (XC) potential is not discontinuous for all N. We highlight the importance of this exact result in the ensemble-DFT description of the negative-U Anderson model. In the atomic limit the discontinuity of the XC potential is missing for odd N while for finite hybridizations the discontinuity at even N is broadened. We demonstrate that the inclusion of these properties in any approximate XC potential is crucial to reproduce the characteristic signatures of the charge-Kondo effect in the conductance and charge susceptibility [11].

We proposed a new type of experiment to observe scissors modes in crystals. These experiments are based on the assumption that in systems in which the spin-orbit coupling is much larger than the crystal field, an applied magnetic field should rotate both spin and charge density profile (spin-orbit locking). Rare earth compounds should provide examples of spin-orbit locking, since their 4f electrons have standard values of the crystal field energies one order of magnitude smaller than the spin-orbit coupling. Such standard values, however, have been questioned by a recent experiment suggesting that crystal field and spin-orbit coupling should be comparable in rare earths. Our experiments should also help to settle this issue. [12]

We proposed a comparative and critical assessment of multiple scattering expansions. The so-called multiple scattering series expansion is much used in the description of spectroscopies at higher energies. However, it is plagued with convergence problems when operated at lower energies. We compare this method to related methods that can be found in the literature, relying both on finite and infinite expansions. After discussing the pros and cons of these methods, we establish a simple alternative to multiple scattering series expansion which has a wider and faster range of convergence [13].

We have accomplished Methodological advances in multiple scattering theory (MST) in both wave and Green's function version for the calculation of electronic ground and excited state properties of condensed matter systems with emphasis on core-level photoemission and absorption spectra. We have reviewd Full-Potential MST and have extended it to non-local potentials. Likewise we have reformulated Multichannel MST in terms of the multichannel density matrix whereby strong electron

correlation of atomic multiplet type can be accounted for in both ground and excited states [14].

Cu K-edge extended X-ray absorption fine structure (EXAFS) and Minuit X-ray absorption near-edge structure (MXAN) analyses were combined to evaluate the structure of the copper(II) imidazole complex ion in liquid aqueous solution. Both methods converged to the same square-pyramidal inner coordination sphere [Cu(Im)4Lax]2+ (Lax indeterminate) with four equatorial nitrogen atoms at EXAFS, 2.02 ± 0.01 Å, and MXAN, 1.99 ± 0.03 Å. A short-axial N/O scatterer (Lax) was found at 2.12 ± 0.02 Å (EXAFS) or 2.14 ± 0.06 Å (MXAN). A second but very weak axial Cu–N/O interaction was found at 2.9 ± 0.1 Å (EXAFS) or 3.0 ± 0.1 Å (MXAN). In the MXAN fits, only a square-pyramidal structural model successfully reproduced the doubled maximum of the rising K-edge X-ray absorption spectrum, specifically excluding an octahedral model. Both EXAFS and MXAN also found eight outlying oxygen scatterers at 4.2 ± 0.3 Å that contributed significant intensity over the entire spectral energy range. Two prominent rising K-edge shoulders at 8987.1 and 8990.5 eV were found to reflect multiple scattering from the 3.0 Å axial scatterer and the imidazole rings, respectively. In the MXAN fits, the imidazole rings took in-plane rotationally staggered positions about copper. The combined (EXAFS and MXAN) model for the unconstrained cupric imidazole complex ion in liquid aqueous solution is an axially elongated square-pyramidal core, with a weak nonbonded interaction at the second axial coordination position and a solvation shell of eight nearest-neighbor water molecules [15].

The environment of sulfur in dissolved aqueous L-cysteine has been examined using K-edge x-ray absorption spectroscopy (XAS), extended continuum multiple scattering (ECMS) theory, and density functional theory (DFT). For the first time, bound-state and continuum transitions representing the entire XAS spectrum of L-cysteine sulfur are accurately reproduced by theory. Sulfur K-edge absorption features at 2473.3 eV and 2474.2 eV represent transitions to LUMOs that are mixtures of S–C and S–H σ* orbitals significantly delocalized over the entire L-cysteine molecule. Continuum features at 2479, 2489, and 2530 eV were successfully reproduced using extended continuum theory. The full L-cysteine sulfur K-edge XAS spectrum could not be reproduced without addition of a water-sulfur hydrogen bond. Density functional theory analysis shows that although the Cys(H)S···H–OH hydrogen bond is weak (∼2 kcal) the atomic charge on sulfur is significantly affected by this water. MXAN analysis of hydrogen-bonding structures for L-cysteine and water yielded a best fit model featuring a tandem of two water molecules, 2.9 Å and 5.8 Å from sulfur. The model included a Scys···H–Ow1H hydrogen-bond of 2.19 Å and of 2.16 Å for H2Ow1···H–Ow2H. One hydrogen-bonding water-sulfur interaction alone was insufficient to fully describe the continuum XAS spectrum. However, density functional theoretical results are convincing that the water-sulfur interaction is weak and should be only transient in water solution. The durable water-sulfur hydrogen bond in aqueous L-cysteine reported here therefore represents a break with theoretical studies indicating its absence. Reconciling the apparent disparity between theory and result remains the continuing challenge [16].

Publications by LNF Authors in the Year 2012

[1] Simulation of electromagnetic properties in carbon nanotubes and graphene-based nanostructures, Yuri N. Shunin ; Yuri F. Zhukovskii ; Victor I. Gopeyenko ; Nataly Burlutskaya ; Tamara Lobanova-Shunina ; Stefano Bellucci; J. Nanophoton. 6(1), 061706 (Oct 01, 2012). doi:10.1117/1.JNP.6.061706-

[2] CNT-Metal Interconnects: Electronic Structure Calculations and Resistivity Simulations, Shunin,

Yu. N.; Zhukovskii, Yu. F.; Burlutskaya, N.; Bellucci, S., Journal of Nanoelectronics and Optoelectronics, Volume 7, Number 1, January 2012 , pp. 3-11(9).

[3] CNT Arrays Grown upon Catalytic Nickel Particles as Applied in the Nanoelectronic Devices: Ab Initio Simulation of Growth Mechanism, Yu. F. Zhukovskii, E. A. Kotomin, S. Piskunov, S. Bellucci, Nanodevices and Nanomaterials for Ecological Security, NATO Science for Peace and Security Series B: Physics and Biophysics 2012, pp 101-114.

[4] Simulation of Fundamental Properties of CNT- and GNR-Metal Interconnects for Development of New Nanosensor Systems, Yuri N. Shunin,Yu. F. Zhukovskii, N. Yu. Burlutskaya, V. I. Gopeyenko, S. Bellucci, Nanodevices and Nanomaterials for Ecological Security, NATO Science for Peace and Security Series B: Physics and Biophysics 2012, pp 237-262

[5] Double-Wall Carbon Nanotubes of Different Morphology: Electronic Structure Simulations, Zhukovskii, Yuri F.; Piskunov, Sergei; Bellucci, Stefano, Nanoscience and Nanotechnology Letters, Volume 4, Number 11, November 2012 , pp. 1074-1081(8)

[6] Photon emission and electron-positron photoproduction processes in the planar field of a bent single crystal, S. Bellucci, V.A. Maisheev, Phys. Rev. A 86, 042902 (2012) [15 pages].

[7] Interacting resonant-level model with long-range interactions: Fast screening and suppression of the zero-bias conductance, E. Perfetto, G. Stefanucci, and M. Cini, Phys. Rev. B 85, 165437 (2012) [6 pages].

[8] Image charge dynamics in time-dependent quantum transport, Petri Myöhänen, Riku Tuovinen, Topi Korhonen, Gianluca Stefanucci, and Robert van Leeuwen, Phys. Rev. B 85, 075105 (2012) [18 pages].

[9] Wick theorem for general initial states, R. van Leeuwen and G. Stefanucci, Phys. Rev. B 85, 115119 (2012) [8 pages].

[10] E. Khosravi, A.-M. Uimonen, A. Stan, G. Stefanucci, S. Kurth6, R. van Leeuwen, and E. K. U. Gross, Phys. Rev. B 85, 075103 (2012) [12 pages],

[11] Missing derivative discontinuity of the exchange-correlation energy for attractive interactions: The charge Kondo effect, E. Perfetto and G. Stefanucci, Phys. Rev. B 86, 081409(R) (2012) [5 pages]

[12] Scissors modes and spin-orbit locking in rare earth crystals with uniaxial symmetry, K. Hatada, K. Hayakawa, F. Palumbo, The European Physical Journal B, June 2012, 85:183

[13] A Critical Assessment of Multiple Scattering Expansions, D. Sébilleau, K. Hatada, H. -F. Zhao, C. R. Natoli, e-Journal of Surface Science and Nanotechnology, Vol. 10 (2012) P 599-608

[14] Calogero R. Natoli, Peter Kruger, Keisuke Hatada, Kuniko Hayakawa, Didier Sebilleau, Ondrej Sipr, Multiple scattering theory for non-local and multichannel potentials, 2012 J. Phys.: Condens. Matter 24 365501 (http://iopscience.iop.org/0953-8984/24/36/365501.

[15] The X-ray Absorption Spectroscopic Model of the Copper(II) Imidazole Complex Ion in Liquid

Aqueous Solution: A Strongly Solvated Square Pyramid, Patrick Frank, Maurizio Benfatto, Britt Hedman, and Keith O. Hodgson, Inorg. Chem., 2012, 51 (4), pp 2086–2096, DOI: 10.1021/ic2017819

[16] The x-ray absorption spectroscopy model of solvation about sulfur in aqueous L-cysteine, Ritimukta Sarangi, Patrick Frank, Maurizio Benfatto, Silvia Morante, Velia Minicozzi, Britt Hedman and Keith O. Hodgson, J. Chem. Phys. 137, 205103 (2012); http://dx.doi.org/10.1063/1.4767350 (13 pages)

Phases of strong interactions – Lattice studies (MI11)

M.P. Lombardo, K. Miura (INFN fellow)

Collaborators

G. Aarts, Ch. Allton (Swansea), A. Deuzeman (Bern), S. Kim (Seoul), E. Laermann (Bielefeld), E-M Ilgenfritz (Dubna) M. Muüller–Preussker (Berlin), A. Onishi (Kyoto), E. Pallante (Groningen), O. Philipsen (Frankfurt), S. Ryan (Dublin), D.K. Sinclair (Argonne).

1 Research

We study phases and phase transitions of strong interactions. Our work uses lattice methods and has applications to the phsyics of the Quark Gluon Plasma as well as to model building beyond the standard model based on mechanisms of strong EW breaking. Our research is articulated in several projects – some have produced results published in 2012 and are continuing, some have preliminary results, and some are new.

1. *High temperature phase transition*

Completed project: We have completed the analysis of the transition to the Quark Gluon Plasma, and of the pseudocrtical line for two light flavors using highly improved Wilson Fermions. Results have been presented at Lat2012 and are submitted to PRD.

2. *Quark Gluon Plasma and Bottomonium*

Continuing project: We have studied the thermodynamics Equation of State and the bottomonium spectrum in the LHC working region. Our results for the bottomonium are based on an improved method that we have developed and compare favorably with CMS results. Results have been presented at SEWM2012 (invited opening talk) and at other conferences, and published. We are now investigating in detail the mass systematics, analyzing the different behaviour of charm and bottom, and we are developing alternative tools for the reconstruction of the spectral functions, which are the quanitites directly amenable to a comparision with experimental results.

3. *Dense Matter*

New project: We have begun an investigation of non-homogenous phases at high density by use of QCD–like theories. We have found preliminary intriguing evidences of such phases

4. *Methods for the analysis of dense matter*

Developing project: We are developing a hybrid method for enhanced control on the results on the critical line in the temperature, chemical potential plane. Results have been presented at SEWM2012 and xQCD2012 and a paper is being written.

5. *Conformal and pre-conformal phase of strong interactions*

Continuing project: We have studied the pre-conformal dynamics and the physics of the conformal phase at strong coupling. Two papers have been published and presented as invited talks at several conferences (xQCD, ConfX, SCGT). We are continuing this study – which has received an European PRACE award – along different lines, with the ultimate goal of a complete caracterization of the phases of strong interactions.

6. *Thermmodynamics with two generations of quarks*

New project: by using the newly available high quality zero temperature results we are starting

a study of thermodynamics with the inclusion of Wilson degrees of freedom. We are preparing a new PRACE application to be submitted at the end of March.

2 Main talks and lectures

We have presented the invited plenary review on QCD Thermodynamics at the yearly Lattice Conference(Cairns), and the invited opening talk on Bottomonium physics at Strong Electrowak Matter 2012, as well as several invited topical talks at xQCD2012(Washington D.C.), confX (Munchen), SCGT2012 (Nagoya) and at the Lattice Program at the GGI. MpL has given a 30 hours graduate course on 'QCD at high temperature and density' at the Bielefeld University (ranked first by the student's senate among all the SommerSemeter offering at the Physics Department).

3 Support

We are supported by MIUR (prin09lombardo) and for computation by PRACE, the European Consortium for Computing (MpL PI), as well as under the INFN-CINECA agreement.

4 Service

MpL is a member of the Scientific Board of Ect*, she is serving in the panel for the Ken Wilson Award for excellence in Lattice Field Theory and is the appointed responsible for the agreement between INFN and CMTP. She has served in review panels /refereed for Yale University, ETH Zurich, DFG and Austrian Science Foundation, PhD defence Committee at the Humboldt University Berlin.

References

1. M. P. Lombardo, PoS LATTICE **2012** (2012) 016 [arXiv:1301.7324 [hep-lat]].
2. G. Aarts, C. Allton, A. Kelly, J. -I. Skullerud, S. Kim, T. Harris, S. M. Ryan and M. P. Lombardo *et al.*, arXiv:1212.4368 [hep-lat].
3. K. Miura, arXiv:1210.8013 [hep-lat].
4. F. Burger, M. Kirchner, M. Muller-Preussker, E. -M. Ilgenfritz, M. -P. Lombardo, O. Philipsen, C. Pinke and L. Zeidlewicz, PoS LATTICE **2012** (2012) 068 [arXiv:1212.0982 [hep-lat]].
5. K. Miura and M. P. Lombardo, arXiv:1212.0955 [hep-lat], Nucl. Phys B, in press
6. S. Kim, G. Aarts, C. Allton, M. P. Lombardo, M. B. Oktay, S. M. Ryan, D. K. Sinclair and J. -I. Skullerud, PoS LATTICE **2012** (2012) 086 [arXiv:1210.7586 [hep-lat]].
7. G. Aarts, C. Allton, S. Kim, M. P. Lombardo, M. B. Oktay, S. M. Ryan, D. K. Sinclair and J. -I. Skullerud, arXiv:1210.2903 [hep-lat], JHEP, in press
8. A. Deuzeman, M. P. Lombardo, T. N. da Silva and E. Pallante, arXiv:1209.5720 [hep-lat], Phys. Lett. B, in press
9. G. Aarts, C. Allton, S. Kim, M. P. Lombardo, M. B. Oktay, S. M. Ryan, D. Sinclair and J. -I. Skullerud, AIP Conf. Proc. **1441** (2012) 910.

MI12: Gauge and String Theories

S. Bellucci (Resp.), S. Ferrara (Ass.), S. Krivonos (Osp.), A. Marrani (Bors. PD), A. Shcherbakov (Bors. PD), A. Sutulin (Osp.), B.N. Tiwari (Bors. PD), V. Yeghikyan (Bors. PD), A. Yeranyan (Bors. Fermi Institute)

Research Activity

The string corrections to the Riemann curvature tensor were found to first-order in the string slope parameter. This was done for D = 10, N = 1 supergravity, the presumed low energy limit of string theory. We then used a related constraint and proceed to find a third-order solution [1].

From the perspective of the statistical fluctuation theory, we explored the role of the thermodynamic geometries and vacuum (in)stability properties for the topological Einstein–Yang–Mills black holes. In this paper, from the perspective of the state-space surface and chemical Weinhold surface of higher dimensional gravity, we provide the criteria for the local and global statistical stability of an ensemble of topological Einstein–Yang–Mills black holes in arbitrary spacetime dimensions $D \geq 5$. Finally, as per the formulations of the thermodynamic geometry, we offer a parametric account of the statistical consequences in both the local and global fluctuation regimes of the topological extremal Einstein–Yang–Mills black holes. [2].

We examined the statistical nature of the charged anticharged nonextremal black holes in string theory. From the perspective of the intrinsic Riemannian geometry, the first principle of the statistical mechanics shows that the stability properties of general nonextremal nonlarge charged black brane solutions are divulged from the positivity of the corresponding principle minors of the space-state metric tensor. Under the addition of the Kaluza–Klein monopoles, a novel aspect of the Gaussian fluctuations demonstrates that the canonical fluctuations can be ascertained without any approximation. We offer the state-space geometric implication for the most general nonextremal black brane configurations in string theory. [3]

We presented the scalar moduli stabilization from the perspective of the real intrinsic geometry. In this paper, we describe the physical nature of the vacuum moduli fluctuations of an arbitrary Fayet configuration. For finitely many Abelian scalar fields, we show that the framework of the real intrinsic geometry investigates the mixing between the marginal and threshold vacua. Interestingly, we find that the phenomena of wall crossing and the search of the stable vacuum configurations, pertaining to D-term and F-term scalar moduli, can be accomplished for the Abelian charges. For given vacuum expectation values of the moduli scalars, we provide phenomenological aspects of the vacuum fluctuations and phase transitions in the supersymmetry breaking configurations. [4]

We studied the thermodynamic geometry arising from the free energy for the two- and three-flavor finite temperature hot QCD near the critical temperature. We develop a geometric notion for QCD thermodynamics, relating it with the existing microscopic quantities, e.g. quark-number susceptibility, which appears naturally within an approximately self-consistent resummation of perturbative QCD. We further incorporate thermal fluctuations in the free energy, thus yielding the geometric properties of local and global chemical correlations. These investigations are perturbative in nature. Nevertheless,

one could apply the same line of thought for the geometric realization of underlying quark susceptibilities, either in the fabric of lattice QCD or in that of nonperturbative QCD. [5]

We performed an su(2) Hamiltonian reduction in the bosonic sector of the su(2)-invariant action for two free (4, 4, 0) supermultiplets. As a result, we get the five-dimensional N= 4 supersymmetric mechanics describing the motion of an isospin carrying a particle interacting with a Yang monopole. We provide the Lagrangian and Hamiltonian descriptions of this system. Some possible generalizations of the action to the cases of systems with a more general bosonic action, a four-dimensional system which still includes eight fermionic components and a variant of five-dimensional N= 4 mechanics constructed with the help of the ordinary and twisted N= 4 hypermultiplets were also considered. [6]

We demonstrated the effectiveness of the action-angle variables in the study of superintegrable systems. As an example, we construct the spherical and pseudospherical generalizations of the two-dimensional superintegrable models introduced by Tremblay, Turbiner and Winternitz and by Post and Winternitz. [7]

We study “minimal degree” complete bases of duality- and “horizontal”- invariant homogeneous polynomials in the flux representation of two-centered black hole solutions in two classes of $D = 4$ Einstein supergravity models with symmetric vector multiplets’ scalar manifolds. Both classes exhibit an $SL(2, R)$ “horizontal” symmetry which mixes the two centers. [8]

Understanding the consequences of the E7(7) duality on the UV properties of N=8 supergravity requires unravelling when and how duality-covariant actions can be constructed so as to accommodate duality-invariant counterterms. For nonsupersymmetric Abelian gauge theories exhibiting U(1)-duality, with and without derivative couplings, it was shown that such a covariant construction is always possible. In this paper we describe a similar procedure for the construction of covariant nonlinear deformations of U(1)-duality invariant theories in the presence of rigid N=2 supersymmetry. This is a concrete step towards studying the interplay of duality and extended supersymmetry. [9]

We studied both the large and small U-duality charge orbits of extremal black holes appearing in D=5 and D=4 Maxwell-Einstein supergravity theories with symmetric scalar manifolds. We exploit a formalism based on cubic Jordan algebras and their associated Freudenthal triple systems, in order to derive the minimal charge representatives, their stabilizers and the associated “moduli spaces.” After recalling N=8 maximal supergravity, we consider N=2 and N=4 theories coupled to an arbitrary number of vector multiplets, as well as N=2 magic, STU, ST2 and T3 models. While the STU model may be considered as part of the general N=2 sequence, albeit with an additional triality symmetry, the ST2 and T3 models demand a separate treatment, since their representative Jordan algebras are Euclidean or only admit nonzero elements of rank 3, respectively. Finally, we also consider minimally coupled N=2, matter-coupled N=3, and pure N=5 theories. [10]

We studied properties of $D = 4$ $N \geqslant 2$ extended supergravities (and related compactifications of superstring theory) and their consistent truncation to the phenomenologically interesting models of N=1 supergravity. This involves a detailed classification of the “degenerations” of the duality groups of type E 7, when the corresponding quartic invariant polynomial built from the symplectic irreducible representation of G4 “degenerates” into a perfect square. With regard to cosmological applications, minimal coupling of vectors in consistent truncation to N=1 from higher-dimensional or higher−N theory is non-generic. On the other hand, non-minimal coupling involving vectors coupled to scalars and axions is generic. These features of supergravity, following from the electric-magnetic duality, may

be useful in other applications, like stabilization of moduli, and in studies of non-perturbative black-hole solutions of supergravity/string theory. [11]

We described the systematical construction of the first order formalism for multi-centered black holes with flat three dimensional base-space, within the so-called T 3 model of N = 2, D = 4 ungauged Maxwell-Einstein supergravity. The three possible flow classes (BPS, composite non-BPS and almost BPS) are analyzed in detail, and various solutions, such as single-centered (static or under-rotating) and all known multi-centered black holes, are recovered in this unified framework. We also consider the possibility of obtaining new solutions. The almost BPS class is proved to split into two general sub-classes, corresponding to a positive or negative value of the duality-invariant polynomial for the total charge; the well known almost BPS system is shown to be a particular solution of the second sub-class. [12]

List of Conference Talks

S. Bellucci, On the road to N=2 supersymmetric Born-Infeld theory, Invited Presentation at the 5th Round Table France–Italy–Russia «Frontiers of Mathematical Physics», December 16-18, 2012

Publications by LNF Authors in the Year 2012

[1] STRING CORRECTIONS TO THE RIEMANN CURVATURE TENSOR AND THE THIRD-ORDER SOLUTION, S. BELLUCCI and D. O'REILLY, Mod. Phys. Lett. A 27, 1250122 (2012) [10 pages] DOI: 10.1142/S0217732312501222.

[2] Thermodynamic Geometry and Topological Einstein–Yang–Mills Black Holes, Stefano Bellucci and Bhupendra Nath Tiwari, Entropy 2012, 14(6), 1045-1078; doi:10.3390/e14061045

[3] STATE-SPACE GEOMETRY, NONEXTREMAL BLACK HOLES AND KALUZA–KLEIN MONOPOLES, Stefano Bellucci and Bhupendra Nath Tiwari, Mod. Phys. Lett. A 27, 1250095 (2012) [11 pages] DOI: 10.1142/S0217732312500952.

[4] SCALAR MODULI, WALL CROSSING AND PHENOMENOLOGICAL PREDICTIONS, Stefano Bellucci and Bhupendra Nath Tiwari, Mod. Phys. Lett. A 27, 1250155 (2012) [11 pages] DOI: 10.1142/S0217732312501556.

[5] A GEOMETRIC APPROACH TO CORRELATIONS AND QUARK NUMBER SUSCEPTIBILITIES, Stefano Bellucci, Vinod Chandra and Bhupendra Nath Tiwari, Mod. Phys. Lett. A 27, 1250055 (2012) [6 pages] DOI: 10.1142/S0217732312500551.

[6] SU(2) reductions in N = 4 multidimensional supersymmetric mechanics, S. Bellucci, S. Krivonos, A. Sutulin, Journal of physics. A, Mathematical and theoretical, 2012, vol. 45, no12, [Page(s): 125402.1-125402.12].

[7] Action-angle variables and novel superintegrable systems, T. Hakobyan, O. Lechtenfeld, A. Nersessian, A. Saghatelian, V. Yeghikyan, Physics of Particles and Nuclei, September 2012, Volume

43, Issue 5, pp 577-582.

[8] On invariant structures of black hole charges, Sergio Ferrara, Alessio Marrani, Armen Yeranyan, Journal of High Energy Physics, February 2012, 2012:71

[9] N=2 supersymmetry and U(1)-duality, Johannes Broedel, John Joseph M. Carrasco, Sergio Ferrara, Renata Kallosh, and Radu Roiban, Phys. Rev. D 85, 125036 (2012) [15 pages].

[10] Small orbits, L. Borsten, M. J. Duff, S. Ferrara, A. Marrani, and W. Rubens, Phys. Rev. D 85, 086002 (2012) [27 pages]

[11] Degeneration of groups of type E 7 and minimal coupling in supergravity, Sergio Ferrara, Renata Kallosh, Alessio Marrani, Journal of High Energy Physics, June 2012, 2012:74

[12] Multi-centered black hole flows, A. Yeranyan, Journal of High Energy Physics, August 2012, 2012:158

!CHAOS

A. Stecchi (Resp.)

Not received

γ-RESIST

G. Gatti (Resp.), D. Alesini, P. Antici (Art. 23), M. Ferrario, A. Ghigo, C. Vaccarezza, M. P. Anania (Ass. Ric.), F. Villa (Ass. Ric.)

Participant Institutions:

INFN LNF, INO CNR Pisa , INFN Bologna, Advanced Beam Technology Division JAEA, Kizugawa Kyoto Japan, Physics Department Pisa university.

1. Introduction

The aim of γ-resist is to realize a very compact high flux gamma ray source using a Compton scattering interaction. The novel approach in such experiment is to employ an all-optical setup. In fact, thanks to the latest techniques of electron beam generation/acceleration through laser-plasma excitation with high intensity lasers (10^{19} W/cm^2) [1], it is possible to get electron bunches on the order of tens-hundreds pC charge, with energies up to hundreds MeV in lengths of a few millimeters. Hence, the basic concept of such an arrangement is to split a high power laser, then to use one of the two replicas to drive the plasma interaction and produce the electrons, and the other one counter propagating would be scattered by the incoming electrons, thus being up shifted in frequency. A source like the one depicted has several advantages, compared to larger scale facilities, in terms of cost, compactness. A successful implementation of a scheme like that could be a considerable step ahead, respect to nowadays Bremsstrahlung based sources and comparable in performances just to very high cost, large scale facilities [2,3]. Furthermore, a laser-plasma based γ ray source has the unique feature of supplying very short photon beams (few fs in time), which could be employed in the next future whereas today interest is mainly focused in having a high average photon flux (rather than peak values).

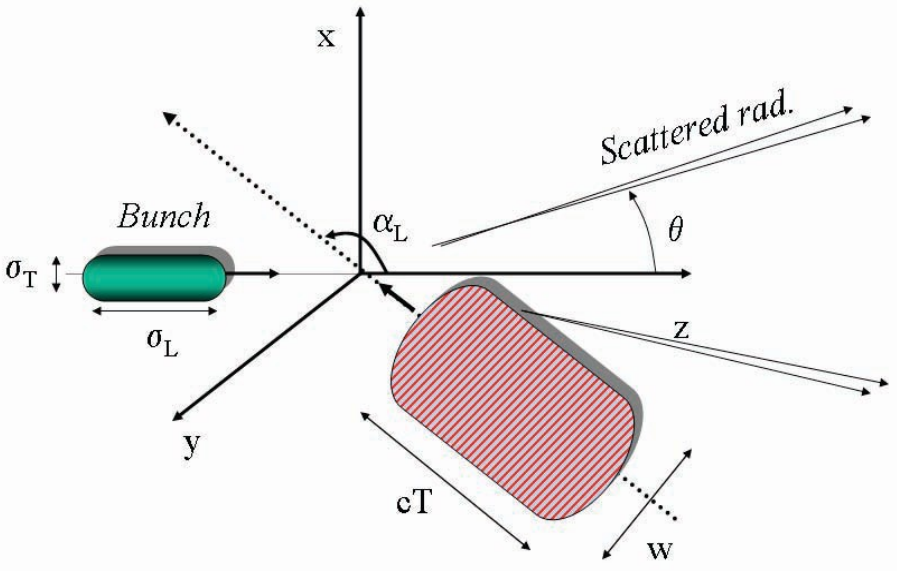

Figure 1 : Pictorial view of a Compton scattering of a laser beam by an electron bea

2. Features of the project and hosting structures

γ-resist, is a 3-years project, started in 2012, strongly based at LNF as the hosting laboratory, though several institutions are collaborating for the success of such a proposal.

Because of the increasing number of activities regarding plasma based acceleration techniques in the SPARCLAB framework at LNF, this shows to be an ideal environment for γ-resist. In particular, experience has been gained in the laser based generation/acceleration of e-beams [4], thanks to the high power laser FLAME (Frascati Laser for Multidisciplinary Experiments). This is a last generation Chirped Pulsed Amplification titanium-sapphire doped sapphire solid state laser, able to supply very short pulses (> 20 fs) with energies up to 5 J and repetition rate up to 10 Hz in the near infrared (800 nm central wavelength), for a maximum power of 250 TW. FLAME laboratory is placed right besides SPARC accelerator hall and it also features a small target area. Here it is possible to host the experiments which foresees the exclusive use of the laser, whereas transfer lines may alternatively deliver the laser pulse in the SPARC hall for the linac/laser based experiments.

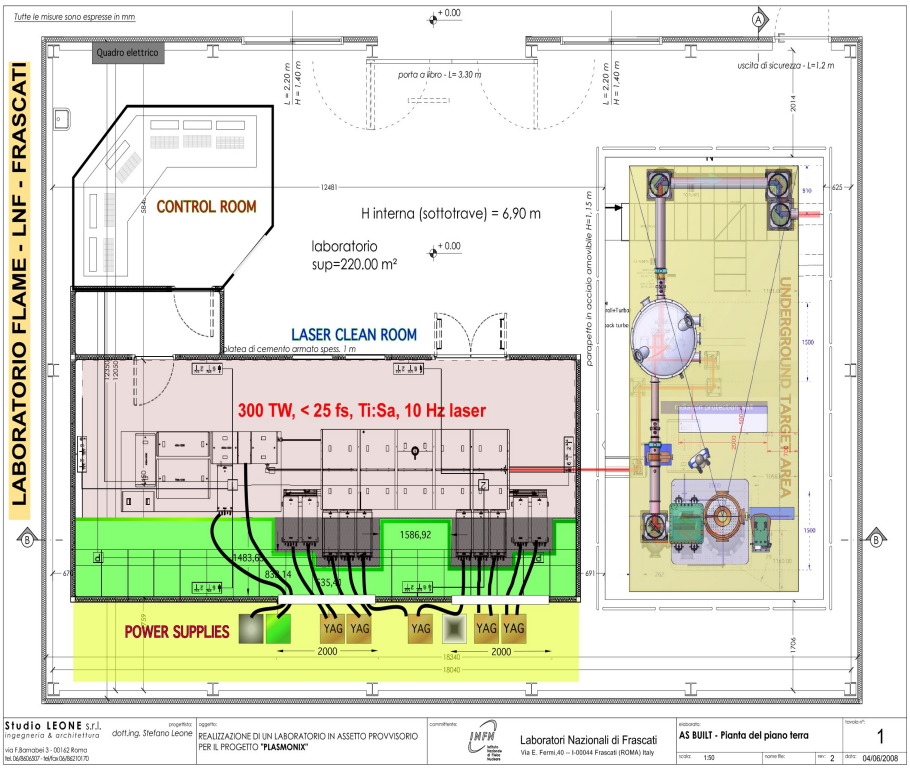

Figure 2 : Upper view of the FLAME laboratory with the target area on the right side

FLAME bunker is already hosting an interaction chamber used for laser plasma interaction whether on gas and on solid target, respectively for electron and for proton/ion generation. In particular, experience has been gained on the optimization of the interaction on gas target aimed to achieve stable, high quality electron beams. The target is given by a nozzle able to deliver a supersonic profile gas jet, whose densities are in the range of 10^{18}-10^{19} cm^{-3} electrons. Mainly nitrogen and helium have been used here so far. The scheme used to generate and accelerate electrons by just the laser in plasma is named self-injection, whereas for other schemes the two stages might be split and controlled by other parameters. γ-resist will use this same interaction chamber. Within the first steps, the aim would be to optimize the interaction in order to get maximum stability, high quality

out of the electrons (low emittance and low energy spread), together with energy tunability. Then a quasi head-on interaction scheme would be taken in account in order to have the higher energy photons out of the scattering with the right synchronization and focal spot. Another important aspect is to study effects like radiation reaction, not directly observed, which should start playing a role, for example in the spectra of the emitted photon, and which computer codes are taking in account in order to model a real outcome of the all-optical Compton [5].

3. Achievements in 2012

The planning of the experiment foresees the completion of the project CDR (conceptual design report), which has been done. A real technical design report together with the first trials of a counterpropagating scheme in the interaction chamber, acquirement of detector for time/spectrally resolving the photon beam, simulations for the outcome of the interactions are foreseen for 2013.

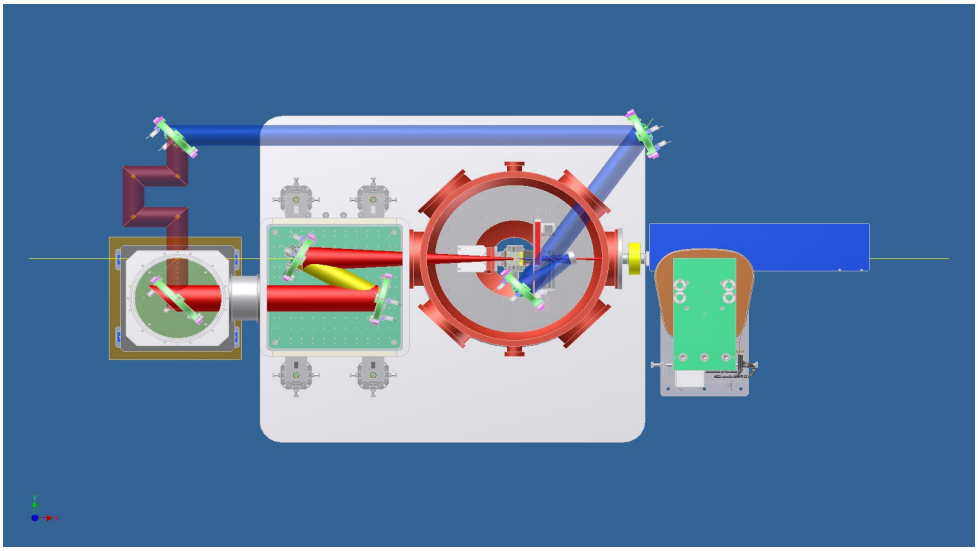

Figure 3 : Upper view of the experimental setup foreseen for the all-optical Compton scheme

References

1. Mangles et al., Nature **431**, 535 (2004); Leemans et al., Nat. Phys. **2**, 696 (2006).

2. Higs http://www.tunl.duke.edu/documents/public/HIGSBeamParameters.pdf

3. ELI NP http://www.eli-np.ro/documents/ELI-NP-WhiteBook.pdf

4. L.A. Gizzi et al., Il Nuovo Cimento C **32**, 433 (2009).

5. A. Di Piazza, K.Z. Hatsagortsyan and C.H. Keitel, Phys. Rev. Lett. **102**, 254802, (2009)

2012 HCPAF GROUP ACTIVITY REPORT

P. Chimenti (art.15), A. Marcelli(P.R.), B. Spataro(D.T.) (resp.)

1 Aim of the experiment

In order to determine the maximum sustainable gradients in normal conducting RF powered particle beam accelerators operating at 11.424 GHz with extremely low probability of RF breakdown, the HCPAF group investigated the possibility of using the Mo coating method. Molybdenum films were grown by RF magnetron sputtering technique on glass and sapphire substrates at room temperature. The sputtering parameters were optimized specifically addressing the growth of oxygen free Mo layers. The characterization of the chemical properties of the coated film has been carried out at Diamond Light Source (UK) with the XANES (X-ray Absorption Near Edge Structure) technique.

2 Introduction

Technological advancements are strongly required to fulfill the demands of new accelerators devices with highest accelerating gradients reliability for the future collider [1)] and [2)]. An intense technological activity is therefore committed to making X-band accelerating structures, using different materials and methods.

In the frame of the collaboration with INFN-LNF/SLAC/KEK concerning breakdown studies about RF high gradient accelerating structures working at 11.424 GHz, an extensive R&D activity concerning molybdenum coatings is also in progress.

Materials with a higher fusion point seem to be good candidates to fabricate the accelerating structures working at 11.424 GHz with a higher accelerating gradient. A sintered Mo bulk brazed RF structure has been realized at LNF and tested at SLAC [3)].

The breakdown rate of the brazed Mo structure is higher than that of copper structures for the same RF parameters. From the investigation of the sintered molybdenum bulk brazed section some technological problems have been detected: the main issue is for sintered molybdenum bulk is the long time for machining the cavity, a maximum of 300 nm surface roughness using tungsten carbide tools, the gas contamination and an uneven loading stress in the brazed region [3)]. For these reasons we are investigating the possibility to grow Mo films on copper.

3 Sputtering technique procedure at the Thin film Laboratory of CNR (Institute of Complex Systems, ISC)

Mo thin films were grown by rf magnetron sputtering technique on different insulating substrates, such as Corning 7059 glass, Al2O3 (0001) and Al2O3(11-20), starting from a high purity (99.995%) Mo target [4)]. The sputtering system is a custom apparatus equipped with a turbo molecular pump backed by a dry scroll pump: the primary pump is used to rough out the chamber to a pressure low enough for use of a secondary turbo molecular pump. The use of a dry mechanical pump instead of an oil sealed mechanical pump avoids the oil back-streaming, thus improving the sputtered films quality, controlling the gas contamination. The apparatus is equipped with four targets (4" in diameters), four gas inlets and two sample holders; the films can be sputtered on cold samples or on hot samples (up to 500C). The sample holders move during the sputtering process at a

Background pressure	2 10^{-7} Torr
Substrate type	Corning glass; sapphire (0001) and (11-20); silicon (001)
Substrate temperature	20 C
Pre-sputtering pressure	4mTorr
Pre-sputtering power	100 W
Pre-sputtering gas	ultra pure Argon (23 sccm)
Sputtering pressure	4mTorr
Sputtering power	60 W (150W)
Sputtering gas	ultra pure Argon (23 sccm)
Film thickness	3000 $\AA$; 6000 $\AA$; 9000 $\AA$.

Table 1: *Mo film optimized sputtering parameters*

variable rate, in order to improve the film uniformity. Before each deposition, the target was pre-sputtered for 30 minutes in order to remove any surface contamination layer, being the sputtered film deposited on the shutter surface. The sputtering process was performed in ultrapure Ar gas atmosphere and the substrates were positioned on a cold sample holder. In order to optimize the sputtering parameters, two different sputtering powers were tested: 60 and 150 W.

A series of preliminary runs was made in order to select the sputtering parameters suitable for low oxygen Mo films. The optimized sputtering parameters are listed in the Table 1. The glass substrates were carefully cleaned before being put inside the chamber in an ultrasonic bath containing an hot aqueous alkaline solution and then were carefully rinsed by ultra-pure deionized water; finally the samples were dried by an Ar flux. Cautions were also used to clean the sapphire substrates which were housed individually and pre-cleaned in a class 10 room provided by the manufacturer. Two different sputtering RF power values, 60 and 150 Watt, were applied, corresponding to two different deposition rates (and obviously deposition time): the Mo films grown on glass were sputtered at 60 Watt, while the Mo films grown on Al2O3 (11-20) and Al2O3 (0001) were sputtered at 150 Watt. At present, preliminary investigations on the Mo films grown on glass reveal that the films have a quite low oxygen content and Mo films grown on sapphire substrates show an oxygen content lower than 5%. The different oxygen content may be due to a possible surface contamination from the glass substrates: although the high quality of the Corning 7059 glass substrates, an oxygen migration from the slide to the Mo film may be induced by the sputtering process, as a consequence of the locally increased temperature of the slide surface. Moreover, the lower Mo sputtering power used for the glass substrates and hence the longer layer deposition time increases the probability of film contamination from the residual gasses.

RBS (Rutherford Back Scattering) measurements were performed on Mo films sputtered on glass and sapphire and compared with simulations of a pure Mo film of equal thickness: the acquired spectra show only a 0.5% O_2 concentration on the films surface assessing the optimization of the sputtering parameters [5]. Structural and electronic properties were estimated by XAS spectroscopy. Data will be discussed in the next section. Moreover, samples resistivity measurements at room temperature as function of the frequency up to 20 GHz have been also completed.

4 Structural and morphological characterization of molybdenum coatings

Different methods are typically used to characterize the properties and the structure of metallic thin films or coatings [6]. To characterize our Mo coatings we used non-conventional methods. The first is an imaging technique with a high spatial resolution recently introduced, that involves

the use of a Focused Ion Beam (FIB) microscope [7)] to obtain morphological and dimensional information, the second is a spectroscopic technique: the X-ray Absorption Spectroscopy (XAS), used to investigate the Mo structure at the local level.

4.1 Focused Ion Beam (FIB) microscope

A FIB microscope can be usefully considered to characterize metallic coatings. This non-conventional microscopy technique now available has imaging and micromachining capabilities at the nm-μm scale, two characteristics extremely important and nowadays widely used in materials science. Actually, in addition to imaging, a FIB can be also used to prepare extremely thin and oriented crystal sections. Thanks to its versatility and spatial resolution, FIB was employed here to visualize with high spatial resolution the coating morphologies and the cross sections of these films, to measure the thickness of the Mo coatings. A typical FIB image of one of the Mo films grown on Al_2O_3 (sample B5) is shown in Fig.1. It refers to a film with a thickness of $\sim$ 615 nm. The Mo coatings investigated are reported in Table 2. The FIB characterization has been performed at the LIME laboratory of the Roma Tre University.

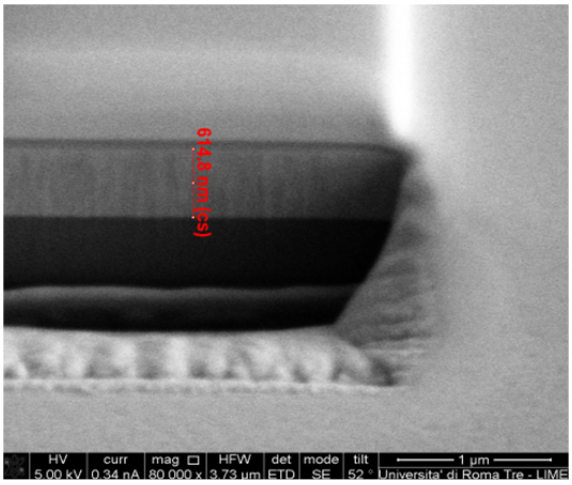

Figure 1: Figure 1 The FIB image of one Mo/Al2O3 coating (sample B5)

5 XAS (X-ray Absorption Spectroscopy)

The XAS (X-ray Absorption Spectroscopy) technique is a well-established method capable to perform a quantitative analysis of local structural properties such as geometry and coordination numbers in ordered and disorder systems such as coatings or interfaces. To characterize the chemical status of Mo atoms in our samples (see Table2), we performed X-ray Absorption Spectroscopy experiments at the Mo K edge. XAS experiments were carried out at B18, the Core XAS beamline of the Diamond Light Source (UK). This synchrotron radiation source operates at the electron energy of 3 GeV with $\sim$250 mA current, in the top-up mode. Data were collected using a double crystal monochromator equipped with two Si(111) crystals and coupled to a Pt coated mirror focusing radiation in a spot of $\sim$200x200 μm. Acquisition of Mo K-edge spectra has been performed in the continuous scan mode using a 9-element Ge detector with XSPRESS-II acquisition electronics in the fluorescence detection mode. Experiments have been performed both at normal incidence and at grazing incidence to enhance the signal associated to thin surface layers, and in different areas of the Mo coatings to probe the homogeneity of the investigated samples

Sample	Mo coatings	Thickness /nm[a]
A1	Mo/ Cu	630
A2	Mo/Cu	1300
B1	Mo/Al_2O_3	70-75
B2	Mo/Al_2O_3	130-140
B3	Mo/Al_2O_3	205-225
B4	Mo/Al_2O_3	310
B5	Mo/Al_2O_3	615
B6	Mo/Al_2O_3	1030

Table 2: Measured thickness of all investigated Mo coatings. a)measured with a Focused Ion Beam (FIB)

6 Results and discussions of XAS (X-ray Absorption Spectroscopy)

In Fig.2 we compared XAS spectra of different Mo coatings with a Mo metallic film. Spectra were normalized by fitting linear polynomials in the pre- and post-edge regions. Looking at the comparison of X-Ray Absorption Near Edge Spectroscopy (XANES) data between Mo coatings and Mo metallic film measured in the transmission geometry we may claim that all coatings have a slightly disordered structure. An observed energy shift comparing with the metallic Mo film indicates that all Mo coatings are negligibly contributed by oxygen. Furthermore, spectra are similar except for the sample with a thickness of 1300 nm, which shows a significant Mo oxide contribution, e.g., MoO_2 and/or MoO_3 [8].

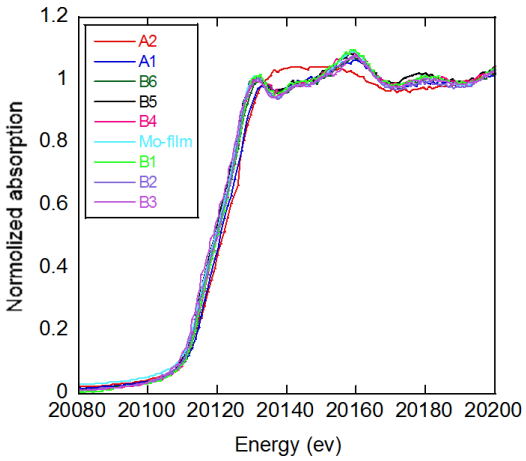

Figure 2: Mo K edge XAS spectra (info in Table 1)

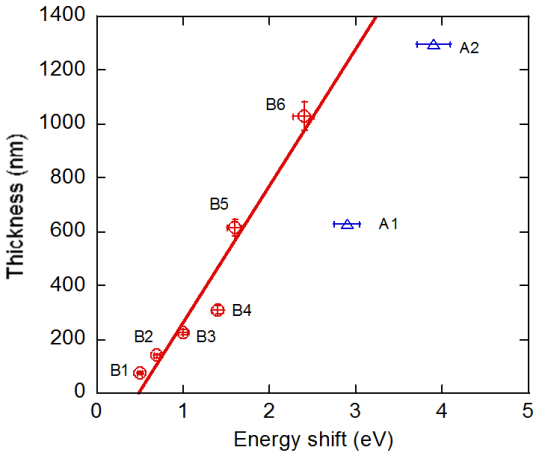

Figure 3: The linear behavior of the edge shift vs. thickness of Mo films on Al_2O_3. Coatings on Cu substrates are well outside the observed linear behavior.

To better analyze XANES spectra, we plot the edge energy shift relative to the metallic Mo film absorption edge versus the thickness of Mo coatings. For all samples the edge has been determined from the normalized absorption at the height corresponding to the value of 0.8. As shown in Fig.3, for samples grown on Al_2O_3 (B1-B6), the position of the edge moves linearly towards higher energies. The mechanism is possibly associated to a shift of the Fermi level increasing the

film thickness, while EXAFS data (not shown here) point out that the Mo-Mo distance of the main contribution decreases with thickness. Samples have not been annealed and for the thinner samples a clear distortion of the unit cell with the presence of a lower distance component occur.

For samples grown on Cu (A1-A2), the XANES spectra are slightly different (in particular for thicker samples) and the measured energy shift position shows that those samples are well outside the trend associated to the samples grown on Al_2O_3. This can be attributed to the expansion of the nest-nearest distance around Mo atoms caused by oxygen contributions [9].

7 Summary and future work

As shown by the experimental results we presented, the sputtering method is really a promising approach to obtain homogeneous Mo coatings increasing the performances of RF cavities working at high frequencies. Structural properties of these sputtered coatings have been determined by a combined analysis of FIB imaging and XAS spectroscopy [10]. We used a FIB microscope to visualize at high spatial resolution the morphology of these films and to accurately measure their thickness. XAS spectra were used to characterize the chemical state of Mo coatings, their local structure and the possible presence of Mo oxides. Data show that all coatings are made by metallic molybdenum with negligible oxygen contributions. The measurements have shown that modifying the thickness of the films both structural and electronics changes occur. While the Mo bcc structure close to the Mo/substrate boundary is naturally deformed, the Fermi level shifts to higher values. This has direct consequences on the transport properties of the coating material [11].

XAS spectroscopy is really a powerful method for coatings characterization not only because allows to identify the oxidation state but also because it may easily probe order/disorder composition in metallic coatings of different thickness. Other experiments have been planned at Diamond and a more detailed analysis of XAS data is in progress.

Because dedicated RF devices with such coatings have to be manufactured and tested at high power, a lot of work is in progress to improve both quality and performances of Mo coatings. A full characterization of conductivity properties and of the behavior under high fields is under way for these systems and will the subject of a forthcoming publication Moreover, to optimize coatings performances on film grown on copper, deposition with other metals, different manufacturing and characterization methods are in progress. This extensive characterization is required to improve the RF breakdown performance and a lot of work is really necessary to identify reliable procedures for the components of the next generation accelerating devices.

References

1. A. Grudiev, S. Calatroni, and W. Wuensh, New local field quantity describing the high gradient limit of accelerating structures, PRST-Accelerators and Beams 12, 102001 (2009).

2. V.A. Dolgashev et al., Status of High Power Tests of Normal Conducting Single-Cell Standing Wave Structures, Proceeding of IPAC 2010, Kyoto, Japan, 2010, pp. 3810-3812 (and references therein).

3. B. Spataro et al., Technological issues and high gradient test results on X Band Molybdenum accelerating structures, NIM-A-657 (2011) 114-121;

4. P. Chimenti, C. Caliendo, B. Spataro, A procedure to abtain a very low Mo films oxygen contamination, SPARC-RF-12/005

5. L. Romano and INFN-LNF collaboration - private comunications - Universita di Catania - Dipartimento di Fisica e Astronomia & MATIS-IMM-CNR Via S. Sofia 64, 05123 Catania, Italy

6. Ohring M 1992, The Materials Science of Thin Films (London: Academic Press Limited)

7. Orloff J, Utlaut M and Swanson L 2003 High Resolution Focused Ion Beams: FIB and its Applications (New York: Kluwer Academic/Plenum Publishers)

8. Ressler T, Wienold J, Jentoft R E and Neisius T, 2002 J. Catal. 210 67-83

9. Rocca F, Kuzmin A, Mustarelli P, Tomasi C and Magistris A, 1999 Solid State Ionics 121 189-192

10. XuYong,B.Spataro,S.Sarti,V.A. Dolgashev, S.Tantawi, A.D.Yeremian, Y.Higashi, M.G. Grimaldi, L.Romano, F.Ruffino, R.Parodi,C.Caliendo,A.Notarigiacomo, G.Cibin and A.Marcelli, Structural and morphological characterization of molybdenum coatings for high gradient accelerating structures, Proceedings 15th International Conference on X-ray Absorption Fine Structure, July 22-28, 2012, Beijing, China

11. S. Bini, B. Spataro, A. Marcelli, S. Sarti, V.A. Dolgashev, S. Tantawi, A.D. Yeremian, Y. Higashi, M.G. Grimaldi, L. Romano, F. Ruffino, R. Parodi, G. Cibin, C. Marrelli, M. Migliorati and C. Caliendo, Molybdenum sputtering film characterization for high gradient accelerating structures, Chinese Physics C (2013) in press [http://arxiv.org/abs/1212.6203]

iFCX: Fast Contrast X-ray imaging

S.B. Dabagov (Resp. Naz.), D. Hampai, G. Cappuccio, A. Esposito, A. Gorghinian,
L. Allocca (Ass.), L. Marchitto (Ass.), S. Alfuso (Ass.),
R.M. Montereali (Osp.), F. Bonfigli (Osp.), E. Pace (Osp.), A. De Sio (Osp.)

Participant Institutions:

Italy: INFN Laboratori Nazionali di Frascati
CNR ENEA, Frascati
CNR Istituto Motori, Napoli

Russia: P.N. Lebedev Physical Institute, Moscow
National Research Nuclear University "MEPhI", Moscow

The iFCX (Fast Contrast X-Ray Imaging) project of a new LNF unit "XLab Frascati" (http://www.lnf.infn.it/xlab/index.html) aims in X-ray high resolution imaging studies based on the use of polycapillary optical elements. The main scope is to design a prototype unit for new imaging technique to investigate low contrast and fast developing processes in the energy range of 5÷30 keV (from soft to hard X-rays). For 2012 we have realized two desktop testing layouts: one for high resolution imaging analysis of static biological samples, while another one - for X-ray imaging of the engine fuel sprays.

1 Introduction

As known, one of the main properties of X-rays is the permeability into the matter that can be exploited for X-Imaging (mainly X-ray microscopy), the technique in a wide use at scientific and industrial centers, at hospitals, etc. The advanced X-ray imaging instrument, known as X-ray computed tomography, is a non-destructive analysis technique to evaluate the inner structure of investigated objects with extremely high spatial resolution . A rapid development of SR laboratories has induced essential improvement in dedicated optical components resulting in strong increment of a spatial resolution, rising up to several tens of nanometers of sample penetration range. Nowadays, X-ray microscopy is a unique tool to complement existing imaging techniques such as light and electron microscopies. The tomographic images are achieved by mathematical reconstruction of sample projections; such projections are represented by the intensity data (matrixes) of transmitted X-rays through the object.

A major number of papers dedicated to high resolution X-ray tomography is principally obtained at SR centers. However, SR procedure requires long time planned experiments, moreover, the SR research is rather expensive and can be performed just at a fixed number of facilities. Obviously, it complicates any SR study. Additionally to various procedure difficulties we have to take into account another factor; typically, any SR probe is characterized by high exposition dose on a studied sample that followed by direct consequence of a rapid degradation of biological samples.

On the contrary, conventional X-ray tubes are worldwide distributed. Optimized combination of X-ray tubes and optical elements, such as, for instance, polycapillary lens, can provide an equipment with intense photon flux probes necessary to realize a proper layout for high resolution X-Imaging. Moreover, a specific design can result in a compact and portable X-ray instrument for "in situ" studies . In this context a prototype of X-ray microscope based on polycapillary semi lens has been designed in our laboratory.

As a result we have shown first results on polycapillary lens ability as an optical device for high resolution tomography. The tomography slices instrumentally obtained (registered by the detector) allowed the image reconstruction by the projection frames realized via the OCTOPUS (inCT Co.) code . Successfully, supported by the AMIRA rendering software

2 Activity in 2012

2.1 X-ray μ-tomography of organic samples

The X-ray tomography test bench is composed of a radiation source, an Oxford Apogee 5000 tube (Cu Kα), with a source spot of about 50×50 μm^2 and power of 50 W, a Photonic Science CCD (FDI 1:1.61) with a pixel resolution of 10.4×10.4 μm^2 and a Newport micrometer positioner $xyz\theta$ (Fig. 1).

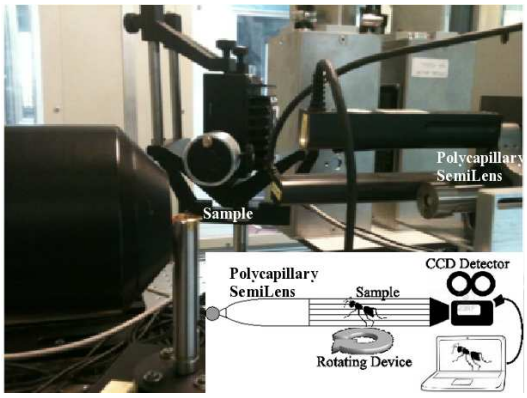

Figure 1: Tomography prototype for biological sample. To obtain a quasi-parallel beam we have used a polycapillary semilens as schematically shown.

To obtain a rather small radiation divergence, which allows getting a very small blurring effect, we have used a polycapillary semilens. Any lens is characterized by a residual divergence responsible for the resolution graduation. If one supposes that the sample dimension ΔX_0 is reproduced at the detector as ΔX, then the effect can be estimated as $|\Delta X_0 - \Delta X_0| \propto l\Delta\theta$, where l is the distance from the sample to the detector. To reach the higher resolution it becomes necessary either to use the optics with the small residual divergence, or to place the sample as close as possible to the detector. Since the used semilens had a residual divergence of 1.5 mrad and the sample was placed about 15 mm from the detector because of the physical dimensions of the stage rotation, the minimum allowed resolution was about 15 μm (comparable with the CCD resolution).

The first 3D image reconstruction we performed on a biological sample, namely, on an ant. The CCD exposure time was 250 ms, enough to avoid the CCD saturation. The sample was positioned on the $xyz\theta$ micro-positioner and step rotated by 0.5 degrees per image, for a total of 720 projection images: the rotation velocity was 0.5 deg/s for a total exposition time of 720 s. To reduce the noise effects a background subtraction has been preformed by the image acquisition software ("Image-Pro Express").

The reconstruction work is separated in two stages: the conversion of the projection images into the slice images (Octopus code) and the rendering process (Amira code). The results of image rendering carried out by highlighting the sample inner parts, central nervous system and mandibular glands (brown areas) are shown in Fig. 2. The X-ray tomography permits a 3-dimensional vision of the ant head and body structure: the biological sample "is seen" through all the planes and it is possible to enter in the investigated body volume and to resolve the projections on a single information plane.

Due to the fact that, an ant exoskeleton has made by hard surface, a second reconstruction was done for a flower bud. Such kind of a sample is perfect to test qualitatively and to obtain quantitatively the information on the prototype of soft-biological matter. In Fig. 3, a 3D reconstruction with a corner cube cut is shown. The onion-geometry of all biological layers is clearly seen.

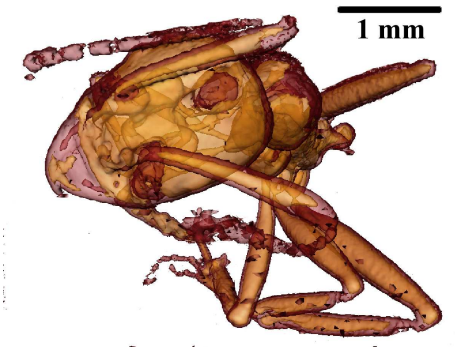

Figure 2: Rendered image of an ant. The brown areas represent the sample inner structure making evident the nervous system as well.

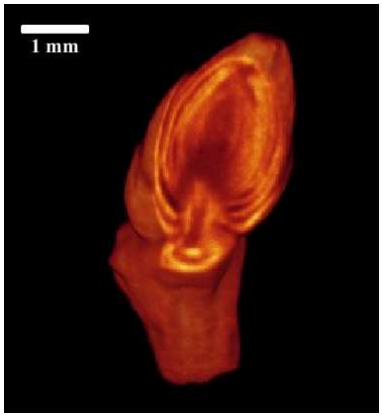

Figure 3: X-ray micro Tomography of a flower bud. The experimental setup is based on polycapillary semilens with 1.4 mrad residual divergence and the power source of 22 W. To obtain this 3D image, 720 images on 360° with an exposition time of 250 ms/image for a total exposition time of 12 minutes were registered and analyzed.

2.2 X-ray μ-tomography of fuel sprays

Additionally to our studies on biological objects, one of the main topics of the project iFCX (gr. V - INFN) is to investigate the fast processes involving low absorption samples. Within this project a few years ago the XLab Frascati LNF has started the collaboration with the Istituto Motori CNR aiming to study the fuel injection processes through the X-Imaging technique.

Attempts to analyze the fuel density distributions inside transient high-density fuel sprays by X-ray based techniques have been carried out in several laboratories around the world. Obviously, SR facilities are mainly adopted for such research due to high SR intensity and its pulsed nature. X-radiation penetrates the dense part of a fuel spray because of its weak interaction with the hydrocarbon chain, and, hence, useful information is provided from the emerging radiation. Time-resolved X-ray both radiography and tomography have been used to elucidate three-dimensional structures both for gasoline and diesel sprays in close-nozzle high-dense optically-impenetrable regions allowing quantitative data on fuel densities, jet structure and morphology, induced shock waves, droplet ruptures, etc. Typically, all these works used of pulsed high-brilliant sources like SR. As known, they overcome the initial limits of X-ray tube sources , and are characterized by continuous in both time and energy radiation spectra, by their monochromaticity, by pulsed time-structure and high time resolution. On the contrary, this sources have, as above said, the intrinsic limitations of high costs, beamlines with dedicated instrumentation, as well as poor duty cycles. The table-top Tomography prototype designed within our collaboration can overcome these

problems, Fig. 4. Evidently, our prototype, revealed rather high ability to perform X-imaging studies, is intended as a preliminary instrument to be advanced in the future.

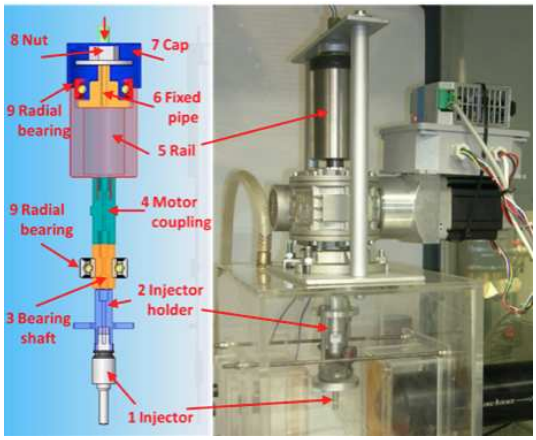

Figure 4: Fuel-tight high-pressure rotating system: schematic sketch on the left and photo on the right: 1 - the injector; 2 - the injector holder; 3 - the bearing shaft; 4 - the motor coupling; 5 - the rail; 6 - the fixed pipe; 7 - the cap; 8 - the nut; 9 - the radial bearing.

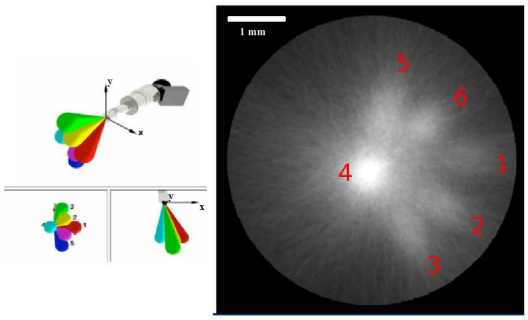

Figure 5: (On the right an axial slice of the GDI 6 jets tomography reconstruction after the Octopus processing is shown, while in the left there are 3D spatial schemes of the GDI injections.

The CCD detector has been synchronized via external trigger with the fuel injection event. Its acquisition time is defined by enabling TTL pulse duration. At this stage the temporal resolution has not been pursued. A time resolution of the system is achievable by reducing the duration of the enabling pulse and synchronizing it at different time from the start of the injection. On the contrary, the signals reduce in intensity, and highest repetition rates are necessary with the unavoidable problems of fuel deposits and fog. The best compromise between the detector intensity and the number of acquisitions should be found. Likewise for the space resolution, slits or spatial windows can be adopted to reduce the focused area of the spray.

Fig. 5 reports an axial tomography slide of a six-hole GDI spray at 12.0 MPa injection pressure and 3.0 ms in duration. The X-radiography of the spray has been carried out with an injector rotation of 360°, step 1° with the images stored and processed off-line.

To realize the setup for GDI injector tomography, a homemade rotating device has been designed and successfully tested at high pressure. The system allows a controlled trip, 360° rotation and 0.1° precision step, of the injector body working at pressures up to 20 MPa. The challenge has been to realize the coupling between the fixed and the rotating parts at high pressure, preventing fuel loss. The device has been designed as an assembly of several components in order to quickly change parts without compromise the system set-up (for the device details see).

Ideal projections for the tomography reconstructions are the images free of noise. In practice, this is never the case due to the statistical nature of the measurements, as repetitions and ensemble averages do not warranty identical conditions at the same spatial and temporal coordinates. However, low noise is present only in measures of static and unanimated objects. On the contrary, sprays are not in this set, but constituted by periodic events of evolving objects (droplets, ligaments, bulks) that changes continuously shape and thermodynamic conditions during their life-time. By this way, it is necessary to find a threshold of number of images to average in order to lose all the informations. As a starting point, at each angle the resulting picture is a

sum of 48 images, 12 bit resolution with the detector acquisition as long as the spray duration. The huge noise on the outline could destroy the sinogram constructions. To minimize the stray signals (caused from the deposition of the drop-let on the Kapton sheets and residual fog) and the injector precession mode during the rotation, acquisition of back-ground images have been carried out per each measurement point. Background subtraction, intensity stretching, low-pass filtering and contrast enhancing have been applied to process the images.

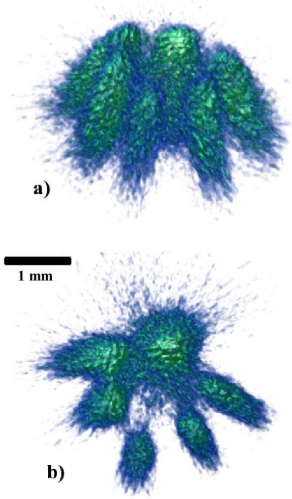

Figure 6: Tomography pictures, in pseudocolors, of the six hole GDI spray.

At this stage, we didn't define both local densities of the fuel and droplet diameter or parcel structures. Due to the geometry of the injector, in Fig. 5, the fourth jet is much intense than the others, even if the fuel density is equal for all jets. In this way , a normalization function for that jet should give us the information of the droplet size and the density.

Figs. 6a and 6b show 3D reconstruction of the axial tomography results of the six-jet spray structure, as obtained from the sinograms. The field of view of the object is limited to the part immediately downstream the nozzle tip, typically a few millimeters. Fig. 6a reports a sight from the top (injector body) while, on the right, a lateral view is shown. Fig. 6b shows clearly the footprint of the spray, viewing positions and propagating directions of the six jets. No interferences of squirts occur at these locations; the fuel delivered from the different holes propagates in an independent way and the profiles appear distinct.

3 Conclusions

During 2012 we prospected polycapillary lenses and the possibility to use them in combination with conventional sources for portable tomography instruments with a resolution about 10 μm with a radiation exposition less than 15 min using a low power X-ray source.

In particular we have shown, as preliminary results, static biological samples, both for axial tomography and for 3D reconstruction. As a second step, we have studied a GDI injector, mounted on a high-pressure rotating device, with a $\Delta\theta < 0.1^\circ$ angular resolution, that explored at 12 MPa injection pressure in a vented pirex chamber. Good reconstructions of the spray structure have been obtained for the six-hole injector with recognition of positions and propagation directions of the six jets. Vision of fuel density and parcel number are possible everywhere inside the spray implying a potential powerful tool to characterize events time-evolving, non-repetitive and at complex fludynamic structure.

MoonLIGHT-ILN

G. Bellettini (Ass.), S. Berardi (AR), G. Bianco (Ass.), A. Boni (Ass. Ric.),
C. Cantone (Ass. Ric.), E. Ciocci (Bors.), S. Dell'Agnello, G. O. Delle Monache,
N. Intaglietta (Tecn.), C. Lops (Ass. Ric.), M. Maiello (Ass. Ric.), R. March (Ass.),
M. Martini (PhD), G. Patrizi (Bors.), L. Salvatori (Bors.), S. Contessa (Ass.),
L. Palandra (Ass), R. Tauraso (Ass.), M. Tibuzzi (Tecn.), R. Vittori (Ass.)

1 Introduction

Lunar Laser Ranging (LLR) experiment, performed since 1969 with retro-reflector arrays deployed by Apollo (Apache Point Observatory Lunar Laser-ranging Operation) 11, 14 and 15, is the only Apollo experiment, designed by a team led by C. O. Alley, D. Currie, P. Bender and Faller et al [4], still taking data today. In the past 40 years, laser ranging (LR) to these arrays has provided most of the definitive tests of the many parameters describing General Relativity (GR) [5, 7]. In addition, the analysis of the LLR data, has greatly enhanced our understanding of the interior structure of the Moon [6, 7, 8, 9]. Initially, the Apollo arrays contributed a negligible portion of the LLR error budget. Nowadays, the ranging accuracy of ground stations has improved by more than two orders of magnitude: the new APOLLO station at Apache Point, USA, is capable of mm-level range measurements [1]; MRLO (Matera Laser Ranging Observatory), at the ASI Space Geodesy Center in Matera, Italy, has re-started LR operations. Now, because of lunar librations, the Apollo arrays dominate the LLR error budget, which is a few cm. The University of Maryland, Principal Investigator for the Apollo arrays, and INFN-LNF are proposing an innovative Corner Cube Retroreflectors (CCRs) array design that will reduce the error contribution of LLR payloads by more than two orders of magnitude, down to tens of microns. This is the goal of the MoonLIGHT-ILN (Moon Laser Instrumentation for General relativity High-Accuracy Tests for the ILN) (International Lunar Network) [2], a technological experiment of INFN and of the SCF (Satellite/lunar laser ranging Characterization Facility), the CCR space test facility at LNF.

2 Science Objectives of MoonLIGHT-ILN

LLR has for decades provided the very best tests of a wide variety of gravitational phenomena, probing the validity of Einstein's theory of GR. The lunar orbit is obviously influenced by the gravity fields of the Earth and Sun, but also is sensitive to the presence of many other solar system bodies. This makes the dynamics of the lunar orbit complex, but the system is relatively pure in that non-gravitational influences (solar radiation pressure, solar wind, drag) are negligible. This makes the Earth-Moon distance an useful tool for testing the nature of gravity, constraining potential deviations from GR [3]. LLR currently provides the best constraints on fig.1.

The equivalence principle states that any mass, independent of composition, will react (accelerate) in precisely the same way when placed in a gravitational field. This is the same as saying that the inertial mass and gravitational mass of any object are precisely the same. The equivalence principle is fundamental to GR, allowing gravity to be treated as an aspect of the geometry of spacetime. In general, scalar additions to GR – motivated by string theories or quantum gravity – produce a violation of the equivalence principle and also lead to secular changes in the fundamental constants. Scalar fields are also frequently invoked to account for the apparent acceleration of the expansion of the universe. Thus tests of the equivalence principle are a vital part of understanding the interface between gravity and quantum mechanics, and in probing our cosmological fate.

The equivalence principle comes in two flavors. The WEP (Weak Equivalence Principle)

Gravity Science Measurement	Timescale	LLR Measurement Accuracy		
		Current (cm)	1 mm	0.1 mm
Weak Equivalence Principle (WEP)	Few years	$\lvert\Delta a/a\rvert<1.3\times10^{-13}$	10^{-14}	10^{-15}
Strong Equivalence Principle (SEP)	Few years	$\lvert\eta\rvert<4.4\times10^{-4}$	3×10^{-5}	3×10^{-6}
Time Variation of Gravitational Constant	~5 years	$\lvert\dot{G}/G\rvert<9\times10^{-13}\mathrm{yr}^{-1}$	5×10^{-14}	5×10^{-15}
Inverse Square Law (ISL)	~10 years	$\lvert\alpha\rvert<3\times10^{-11}$	10^{-12}	10^{-13}
Parameterized Post-Newtonian (PPN) β	Few years	$\lvert\beta-1\rvert<1.1\times10^{-4}$	10^{-5}	10^{-6}

Figure 1: The expected improvements on the GR measurements with MoonLIGHT are shown in table, together with their measurement time scale.

relates to the composition of an object, in effect probing electromagnetic, strong nuclear and weak nuclear energy contributions. The SEP (Strong Equivalence Principle) extends to include gravity itself. The Earth-Moon system allows a test of the SEP in a way that laboratory tests cannot, in that the contribution of gravitational self-energy to the total mass-energy budget is 5×10^{-10} for the earth, but only 10×10^{-27} for typical laboratory masses. LLR allows us to ask the questions: "Do the Earth and Moon fall at the same rate toward the sun? Does the gravitational self-energy of the Earth fall toward the Sun at the same rate as the less gravity-burdened Moon? Does gravity pull on gravity in the same way it pulls on ordinary matter?". The Earth-Moon system is currently the best laboratory for answering these questions. If the SEP were to utterly fail – that is, gravitational self-energy failed to gravitate – the Moon's orbit would be shifted by 13 meters. Current LLR constrains this shift to be less than 5 mm, constituting a 4×10^{-4} constraint on violation of the SEP.

LLR can also constrain new theoretical paradigms. An example is an idea to account for the apparent acceleration of the universe by allowing gravitons to leak off of our 4-dimensional spacetime "brane" into another bulk dimension, thus weakening gravity over cosmological scales. Though small, such a process would have an impact on the lunar orbit, causing it to precess by effectively invalidating the $1/r^2$ force law of gravity. LLR needs to see a factor of 15 improvement to reach this level of sensitivity to new physics.

Furthermore much of our knowledge of the interior of the Moon is the product of LLR [8, 9, 10, 11], often in collaboration with other modalities of observation. These physical attributes of the lunar interior include Love number of the crust, the existence of a liquid core, the Q of the Moon, the physical and free librations of the Moon and other aspects of lunar science.

3 2nd Generation of Lunar Laser Ranging

The general concept of the second generation of LLR is to consider a number (notionally eight) large single CCRs. Each of these will have a return that, with a single photoelectron detection system such as current APOLLO system located at the Apache Point Observatory, can be used to determine the range to the limit determined by the librational effects of the current arrays and the laser pulse length. By using single CCRs, the return is unaffected by the libration. That is, there is no increased spread of the FWHM (Full Width at Half Maximum) due to the CCR and the librational effects. We plan to use eight such single reflectors spread over tens of meters. The return from each of the CCRs will be registered separately and can be identified by comparison

with the nominal lunar orbit and earth rotational parameters. This is shown schematically in Fig.2.

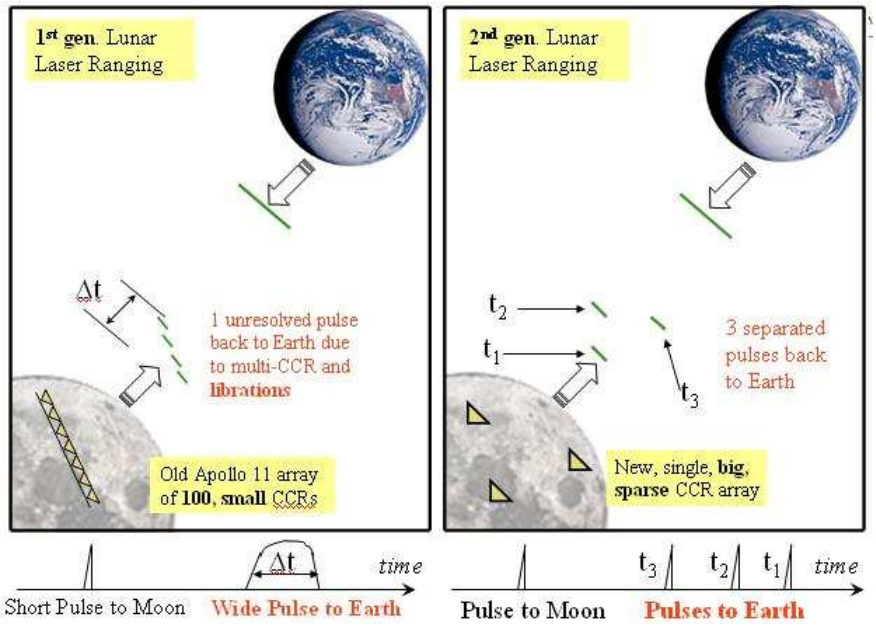

Figure 2: *Concept of the 2nd generation of Lunar Laser Ranging*

4 The New Maryland/Frascati Payload

We currently envision the use of 100 mm CCRs composed of T19 SupraSil I. This is the same material used in LLRA (Lunar Laser Ranging Array) 20^{th} and both LAGEOS satellites. This will be mounted in an aluminum holder that is thermally shielded from the Moon surface, in order to maintain a relatively constant temperature through the lunar day and night. It is also isolated from the CCR, by two co-axial "gold cans", so the CCR receives relatively little thermal input due to the high temperature of the lunar day and the low temperature of the lunar night. The mounting of the CCR inside the housing is shown in Fig.3. KEL-F could be used for this mounting (its used in LAGEOS) due to its good insulating, low out-gassing and non-hygroscopic properties.

5 Technical challenges of the MoonLIGHT CCR

The primary technical objectives of the LLRRA-21 (Lunar Laser Retro Reflector Array) are to provide adequate laser return to Earth ground stations and to be stable over long term, decades, with respect to the center of mass of the Moon. The major technical/engineering challenges that follow from the technical objective are then:

- Fabricate a large CCR with adequate homogeneity and that meet the required tolerances, mentioned in the previous section.
- Thermal control to reduce thermal gradients inside the CCR to acceptable levels. Thermal gradients produce index of refraction gradients, which cause beam spread and low return.

Figure 3: Views of current design of the MoonLIGHT/LLRRA21 CCR: (a) fully assembled; (b) exploded view with its internal mounting elements and outer aluminum housing.

- Emplacement goal of long-term stability of $10\mu m$ with respect to the Center of Mass of the Moon.

The large diameter of the CCR introduces a great challenge in its fabrication, the availability of such material of the required homogeneity, the fabrication and polishing procedures and the measurement methods. The angle between the three back reflecting faces, which govern the shape of the pattern, have a more challenging tolerance of ± 0.2 arcsec; this is more restrictive by a factor of 2.5 than the current state of the art for SLR (Satellite Laser Ranging) CCR fabrication. The material choice is primarily driven by three requirements:

- extremely uniform index of refraction (very good homogeneity)
- resistance to darkening by cosmic radiation
- low solar radiation absorption

To satisfy these requirements, this CCR has been fabricated with SupraSil 1. For the next generation of CCRs, LLRRA-21, we plan to use SupraSil 311 which has even better homogeneity.

The optical performance of the CCR is determined by its Far Field Diffraction Pattern (FFDP), which represents the intensity of the laser beam reflected back to the ground by the CCR. Figure 4 is a simulation of the FFDP of the LLRRA-21 (performed with the software CodeV) according to its dimensions and angle specifications; at the correct velocity aberration the intensity (calculated in optical cross section) should have a value which guarantees that enough photons come back to the ground station. Optical cross section is an intrinsic characteristic of CCRs or LRAs, and it is defined as follows:

$$\sigma_{CCR} = I_{CCR/MIRR}\,(\theta_x, \theta y)\, 4\pi \left(\frac{A_{CCR}}{\lambda}\right)^2 \tag{1}$$

Where $I_{CCR/MIRR}$ is the intensity of the FFDP of the CCR, at a certain point of the (θx, θy) plane, referred to a perfect mirror of the same aperture as the CCR, λ is the laser wavelength and A_{CCR} is the area of the aperture of the CCR. One of the most critical challenges of this new

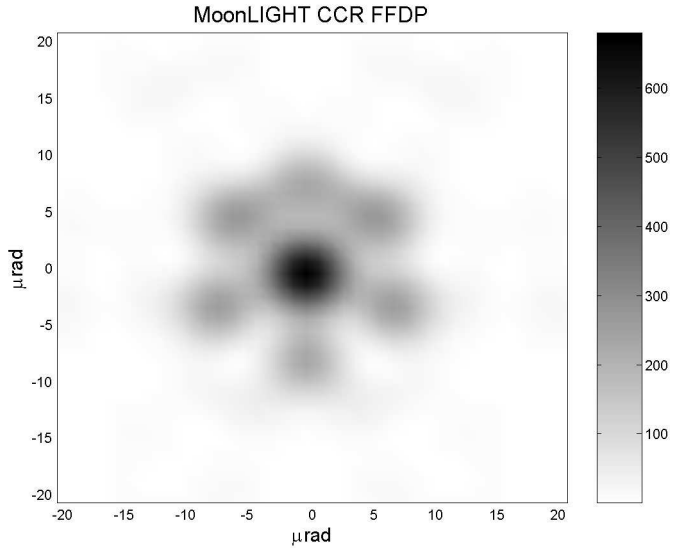

Figure 4: *FFDP of LLRRA-21 under its design specification of offset angles (0.0" 0.0" 0.0"). Grid is in angular dimensions (μrad)*

model is the issue of the thermal gradient. Since the index of refraction of the fused silica depends upon temperature, a thermal gradient inside the CCR will cause the index of refraction to vary within the CCR and thus modifying the FFDP. In Figure 6, is represented the average intensity over the velocity aberration for the LLRRA-21 at Standard Temperature and Pressure (STP). At the velocity aberration for the Moon, $\sim 4\mu rad$, we will test thermal perturbations and, if needed, developed an optimized design to control the drop of FFDP intensity to an acceptable level. For this reason we need to understand in detail how the external factors heat the CCR and in what magnitude, either on the Moon or on a satellite. This is accomplished using dedicated programs developed in parallel at LNF and UMD (University of Maryland). To perform these simulations we use Thermal Desktop, a software package of C&R Technologies of Boulder CO. Then using softwares IDL and CodeV we translate these thermal gradients into the effects on the FFDP of the CCR. There are three primary sources of heat that cause thermal gradients; here we briefly describe their effect:

- *Absorption of solar radiation within the CCR*: during a lunar day, the solar radiation enters the CCR and portions of this energy are absorbed by the fused silica. Since the different wavelengths in the solar radiation are absorbed with different intensity, according to fused silica absorptivity characteristic, the heat is deposited in different parts of the CCR.

- *Heat flux flowing through the mechanical mounting tabs*: if the CCR is at a temperature that is different than the housing temperature there will be a flux of heat passing into (or out of) the CCR through the holding tabs. Conductivity of the mounting rings should be reduced.

- *Radiation exchange between the CCR and the surrounding pocket*: in the case of the Apollo LRAs, the back surfaces of the CCRs view the aluminum that makes up the housing, machined with a relative high emissivity/absorptivity. If the temperatures of the CCR and the aluminum are different there is a radiation exchange of thermal energy, which in turn causes a flux in the CCR as the heat exits out of the front face to cold space. In the Apollo array this

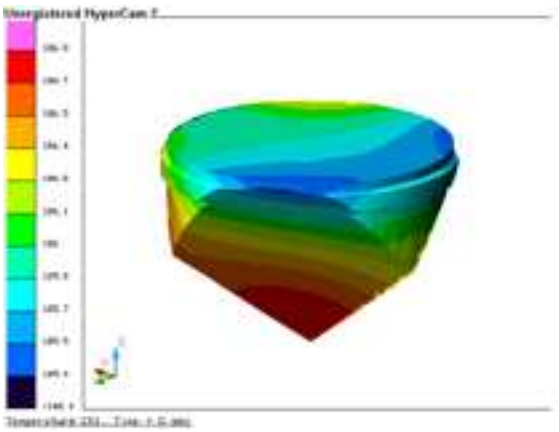

Figure 5: *Typical distribution of temperature inside the CCR for a given set of conditions.*

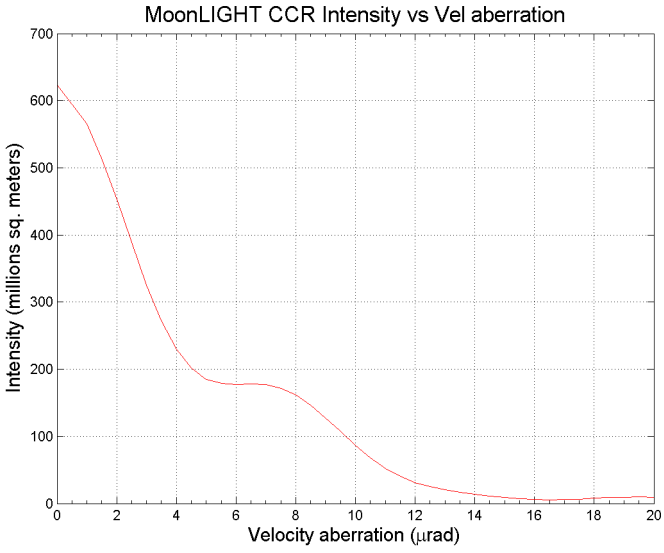

Figure 6: *Average intensity over velocity aberration of an unperturbed MoonLIGHT CCR*

is not been a serious issue, but the bigger dimensions of the LLRRA-21 complicate things, and we need to reduce this effect. Thus we enclose the CCR into two thermal shields, with a very low emissivity (2%), that should prevent this radiative heat flow.

Thermal simulations performed on the current configuration show that currently the variation of the ΔT between the front face and the tip of the CCR is within 1K. We are still proceeding to optimize this further, both with optical design procedures and with thermal stabilization of the overall housing.

As mentioned earlier, to achieve the desired accuracy in the LLR, a long term stability is needed with respect the center of mass of the Moon; to attain this we must understand and simulate the temperature distribution in the regolith (and its motion), the effects of a thermal blanket that will be spread about the CCR and the effects of heat conduction in the INVAR supporting rod. A locking depth is chosen such that the thermal motion effects are small ($\sim 1m$). The placement of the thermal blanket further reduces thermal effects and also reduces the effects of conduction in the supporting rod.

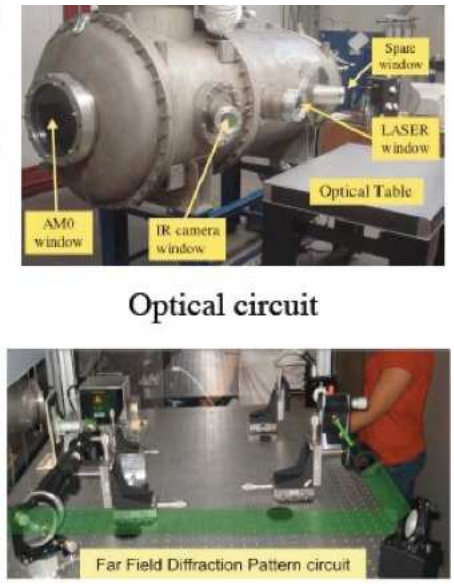

Figure 7: *SCF cryostat and optical table.*

6 Thermal-optical-vacuum SCF-Tests in Frascati

SCF, fig.: 7, at LNF/INFN in Frascati, Italy, is a cryostat where we are able to reproduce the space environment: cold (77 K with Liquid Nitrogen), vacuum, and the Sun spectra. The SCF includes a Sun simulator (www.ts-space.co.uk), that provides a 40 cm diameter beam with close spectral match to the AM0 standard of 1 Sun in space ($1366.1 W/m^2$), with an uniformity better than $\pm 5 W/m^2$ over an area of 35 cm diameter. Next to the cryostat we have an optical table, where we can reproduce the laser path from Earth to the Moon, and back, studying the FFDP coming back from the CCR to the laser station, useful to understand how good is the optical behavior of the CCR. The SCF-Test (Dell'Agnello et al. 2011) is a new test procedure to characterize and model the detailed thermal behavior (fig.: 8 and 9) and the optical performance of laser retroreflectors in space for industrial and scientific application, never before been performed. We perform a SCF-

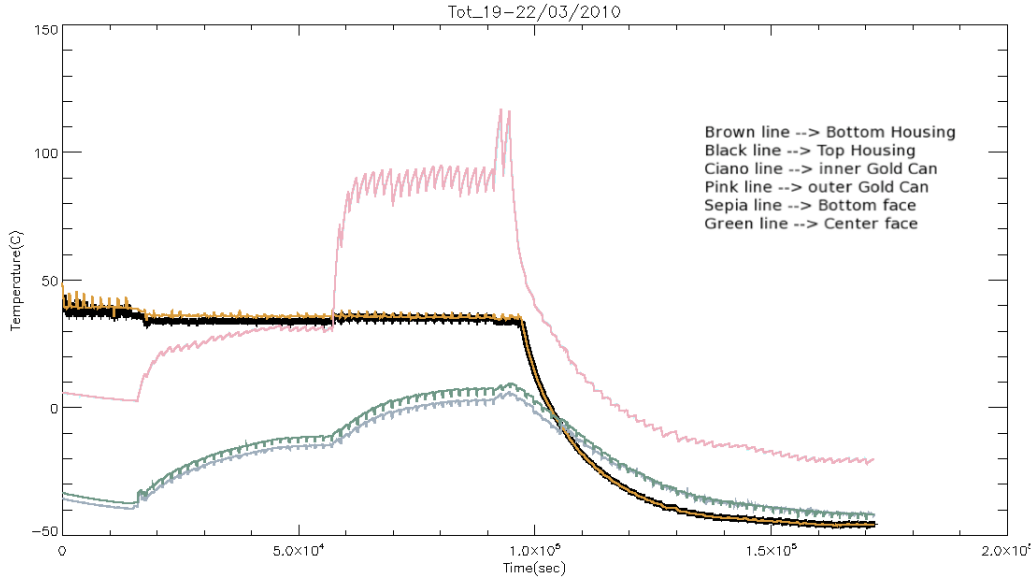

Figure 8: MoonLIGHT/LLRRA-21 flight CCR temperature variations of various housing parts and of CCR (19-22/March/2010).

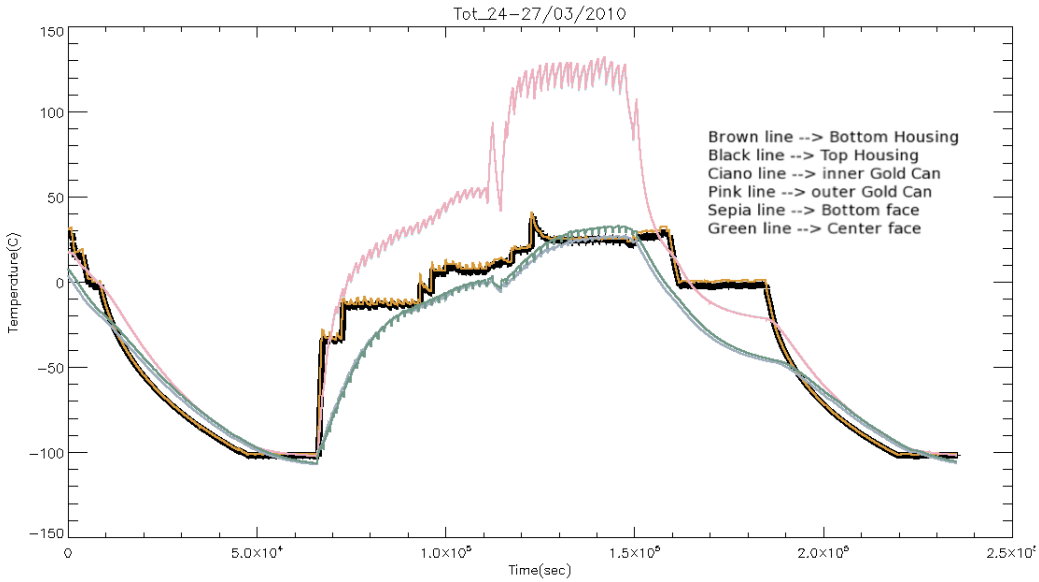

Figure 9: MoonLIGHT/LLRRA-21 flight CCR temperature variations of various housing parts and of CCR (24-27/March/2010).

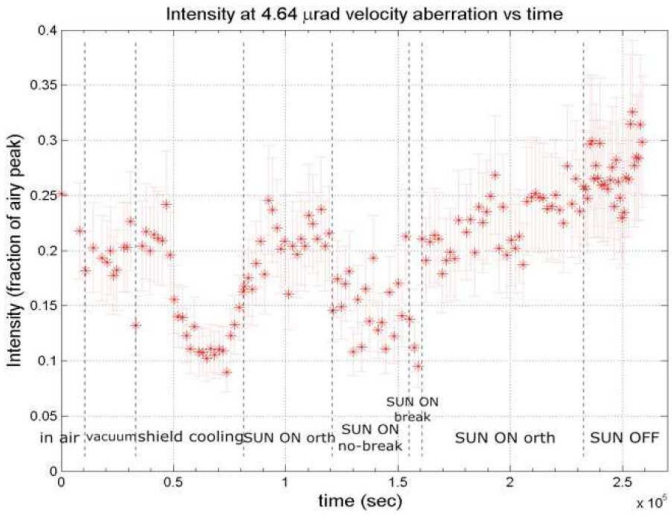

Figure 10: MoonLIGHT/LLRRA-21 flight CCR FFDP intensity variation at Moon velocity aberrations (2V/c) during tests (time subdivision refers to the fig.: 8).

Test on the MoonLIGHT CCR to evaluate thermal and optical performances in space environment. About thermal measurements we use both an infrared (IR) camera and temperature probes, which give a real time measurements of all components of the CCR and its housing. In particular we look at the temperature difference from the front face to the tip, studying how the FFDP changes during the different thermal phases. This is the best representative of the thermal distortion of the return beam to the Earth. Various configurations and designs of the CCR and the housing have been and are being tested in the SCF Facility. In fig.: 10 and 11 is shown the MoonLIGHT/LLRRA-21 flight CCR FFDP intensity variation at Moon velocity aberrations (2V/c) during key points of the SCF-Test: (1) in air, (2) in vacuum, (3) during chambers shields cooling, (4) Sun on orthogonal to the CCRs face with the housing temperature controlled at $T = 310K$, (5) Sun on at 30° of inclination (no break-through), (6) Sun on at $-30°$ of inclination (break-through), (7) Sun on orthogonal with the housing temperature left floating. From this graph we can deduce that the intensity decreases during no orthogonal lighting of the CCR, in particular when the Sun enters in the housing cavity during the break-through phase. This effect is due to a strong increase of the "Tip-Face thermal gradient during these two phases of the test. When the housing temperature is left floating, the intensity slightly increases because the "Tip-Face" gradient is reducing.

7 Analysis of lunar laser ranging data

In order to analyze LLR data we used the PEP (Planetary Ephemeris Program) software, developed by the CfA, by I. Shapiro et al. starting from 1970s. PEP was designed not only to generate ephemerides of the planets and Moon, but also to compare model with observations (Reasenberg et al., 1979; Chandler et al., 1996; Battat et al., 2007). One of the early uses of this software was the first measurement of the geodetic precession of the Moon (Shapiro et al., 1988). PEP asserts that the solar system barycenter frame is an inertial frame. Thus far, there is no evidence to suggest otherwise. Where the solar system barycenter frame non-inertial, then one would expect to see residuals between observations and calculations (the OC residuals) due to unmodeled coriolis-type

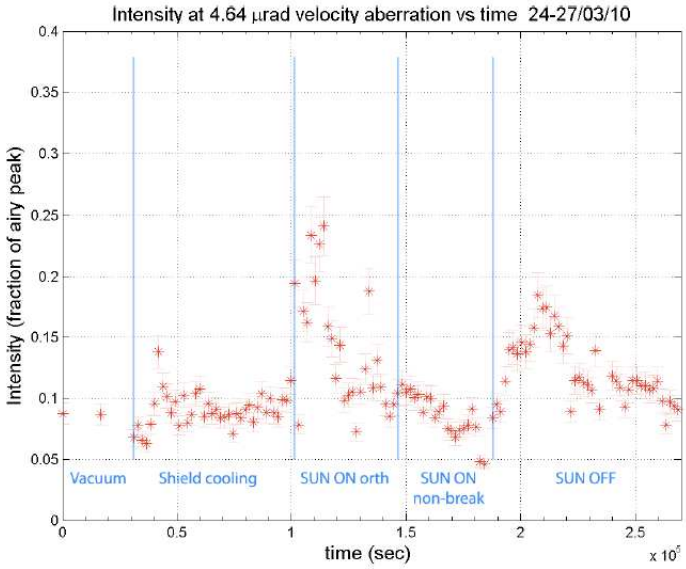

Figure 11: MoonLIGHT/LLRRA-21 flight CCR FFDP intensity variation at Moon velocity aberrations (2V/c) during tests (time subdivision refers to the fig.: 9).

forces. Although the forces are calculated in the solar system barycenter frame, PEP reports the positions and velocities of the solar system bodies with respect to the Sun center of mass (Solar System Barycenter, SSB). The heliocentric coordinates of the solar system barycenter are also computed. Nevertheless, the physics is performed in the (inertial) SSB frame; the heliocentric coordinates are derived quantities. The PEP software has enabled constraints on deviations from standard GR physics. For example, it can be used to estimate PPN (Parametrized Post Newtonian) parameters β and γ; relative deviation from the geodetic precession, K_{GP} and the time variation of the gravitational constant, $\frac{\dot{G}}{G}$. The spacetime torsion equations of motion March et al. (2011a,b) can be included in PEP and constrained with all LLR data, including the newest APOLLO data (at the present the published constraints on spacetime torsion are calculated using LLR data from other stations). The APOLLO station (Battat et al., 2009; Murphy et al., 2000, 2002) is located at the Apache Point Observatory in southern New Mexico and utilizes a 3.5 m telescope. Compared to MLRS, the 3.5 m telescope of APOLLO has a factor of 20 greater light-collecting area. The greater return rate of APOLLO allows us to study systematic effects improving statistical error. The main goal of APOLLO is to push LLR into the millimeter range precision, this will improve the determination of fundamental physics parameters of about few order of magnitude (see Table 1). We have performed a preliminary analysis of LLR data from three different stations: McDonald Observatory in Texas, Grasse in France and APOLLO in New Mexico. The latter station provides the best quality data since 2006. On March 25, 2010, the Matera Laser Ranging Observatory in Italy (MLRO, led by G. Bianco) recorded LLR echos from the array of Apollo 15.
The histograms in Fig.11 show photon-by-photon data and are used to form a single LLR normal point of the Apollo 15 array taken by the APOLLO station (led by T.W. Murphy) on November 19, 2007. A normal point contains several information e.g. date of observation, atmospheric conditions, as well as time of flight, data quality and CCR arrays.
The APOLLO instrumental accuracy (in terms of laser, detector, timing electronics, etc) shown by the fiducial returns in Fig. 11 is a root mean square contribution of 120 ps (18 mm). From a

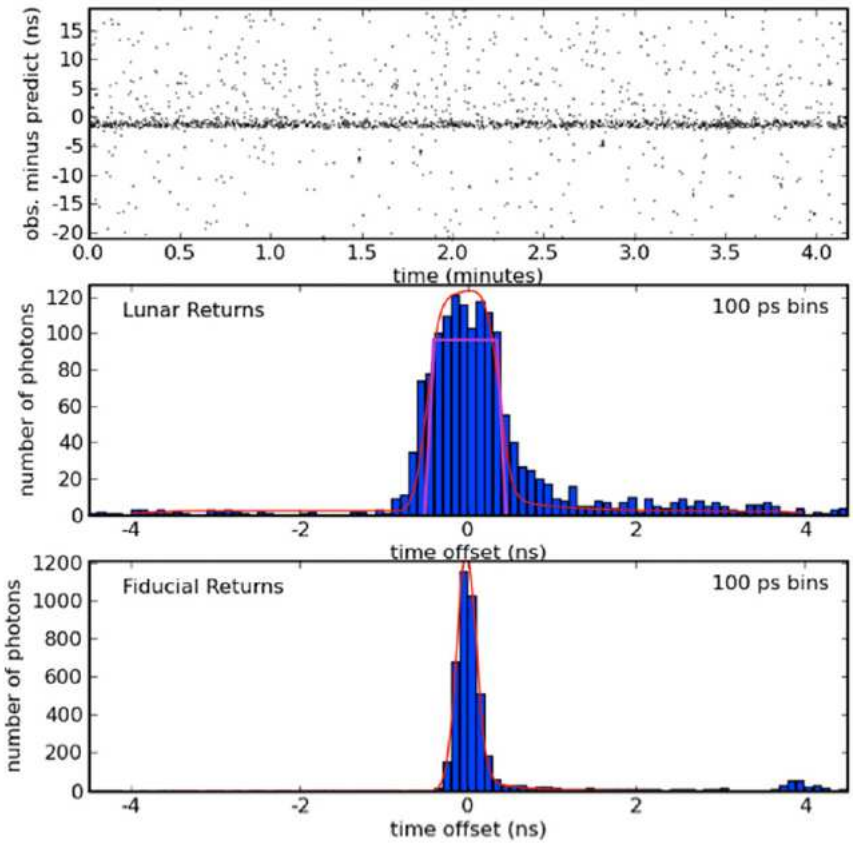

Figure 12: Example run of Apollo 15. In the plot, the top panel shows a 40 ns window of observed round trip time minus the predicted range. Background noise and detector dark current appear as scattered dots, while the lunar return is in the middle. The middle panel shows a histogram of the lunar returns, while the bottom panel shows the local fiducial CCR return, fitted by the red Gaussian. The Lunar return is additionally spread by the tilted reflector array modeled by the superimposed magenta trapezoidal shape

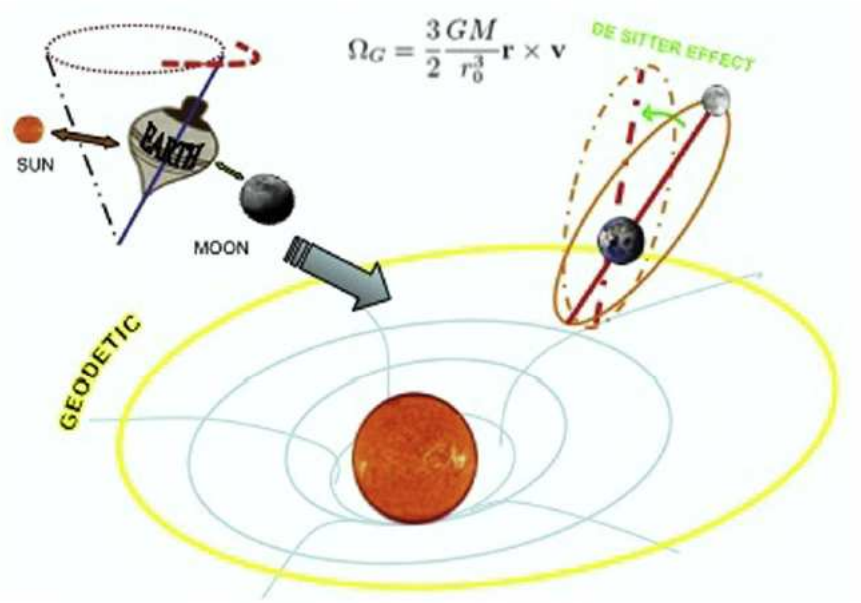

Figure 13: KGP is the relative deviation of geodetic precession from the GR value.

comparison between the middle and the last plot we can see how the tilt in the arrays affects the accuracy of the ranging measurements. The model parameter estimates are refined by minimizing the residual differences, in a weighted least-squares sense, between observations (O) and model predictions (C, stands for Computation), OC. Observed is round-trip time of flight. Computed is modeled by the PEP software.

8 Determination of the geodetic precession

With PEP software we have measured relative deviation from the GR value (deviation from zero) of the geodetic precession (the Sitter effect in Fig. 12), expressed by the K_{GP} parameter. We have used all the data available to us from Apollo CCR arrays: Apollo 11, Apollo 14 and Apollo 15. Results are reported in two tables, one until 2003, acquired with data by the old ILRS (International Laser Ranging Service) stations (Table 2) and one with data from 2007 to 2009 acquired by the new APOLLO station (Table 3). Results described in the tables are obtained fixing the parameters to their GR values:

$$\beta = \gamma = 1, \frac{\dot{G}}{G} = 0 \tag{2}$$

Using APOLLO LLR data, the estimated value is slightly larger than for the old stations (see Table 3). Nominal errors returned by the fit are significantly smaller than the value of K_{GP}, and smaller than the best published values. Therefore, we want to use the data to understand and estimate independently the size of the error budget. As a systematic check of the stability of the K_{GP} estimate, we have also performed a fit using every single old station. The results are shown in Table 4. These preliminary measurements are to be compared with the best result published by JPL (Jet Propulsion Laboratory) (Williams et al., 2004) ($K_{GP} = (-1.9 \pm 6.4)10^{-3}$), obtained using a completely different software package, developed over the last 40 years. On the contrary,

Table 2
Estimates of geodetic precession, K_{GP}, with the dataset from MLRS, MLR2 and CERGA stations.

Parameter	GR initial value	Final value
K_{GP}	0	0.009

Table 3
Estimates of geodetic precession, K_{GP}, with the new dataset from APOLLO station.

Parameter	GR initial value	Final value
K_{GP}	0	−0.0096

Table 4
Estimates of geodetic precession, K_{GP} using every single old station.

Station	K_{GP}
CERGA	−0.016
MAUI	0.0060
MLR2	0.0095
TEXL	−0.044

after the original 2% K_{GP} measurement by CfA (Center for Astrophysics) in 1988, the use of PEP for LLR has been resumed only since a few years, and it is still undergoing the necessary modernization and optimization.

9 Conclusions

We have created a unique facility and a new industry-standard laboratory test to validate the thermal and optical behavior of CCR in space. The experimental apparatus and the test procedures are described in great detail in Dell'Agnello et al. (2011) and ETRUSCO (2011). The MoonLIGHT experiment is the result of a collaboration between two teams: LLRRA21 and the INFN-LNF. With Moon- LIGHT we are exploring improvements in both instrumentation and the modeling of CCR. For the SCF-Test, we can conclude that the intensity of the FFDP decreases during no orthogonal lighting of the CCR, in particular when the Sun enters in the housing cavity during the test. We have obtained a measurement of geodetic precession that is consistent with the prediction of GR with a competitive uncertainty. This is an interesting and promising preliminary study.

10 Acknowledgements

We would like to acknowledge University of Maryland via the NASA LSSO (Lunar Science Sortie Opportunities) program (Contract NNX07AV62G) to investigate Lunar Science for the NASA Manned Lunar Surface Science and the LUNAR consortium (http://lunar.colorado.edu), headquartered at the University of Colorado, which is funded by the NASA Lunar Science Institute (via Cooperative Agreement NNA09DB30A) to investigate concepts for astrophysical observatories on the Moon. A special thank to Prof. Douglas Currie for his great support and the helpful discussions. Special thanks to the Italian Space Agency (ASI) for the support during the 2007 Lunar Study, the MAGIA (Misura Accurata di G mediate Interferometria Atomica) Phase A study. In particular we thank S. Espinasse, formerly at ASI, now at ESA, for encouraging the applications of our work for the ILN and ESA first lunar lander.

References

1. Murphy T., Battat J., et al., *"The Apache Point Observatory Lunar Laser-Ranging Operation (APOLLO): two years of Millimeter-Precision Measurements of the Earth-Moon Range"*, PASP 121, 29 (2009).

2. D.G.Currie, S. Dell'Agnello, *"A Lunar Laser Ranging Retroreflector Array for the 21st Century"*, AMOS 2009.

3. J.G.Williams, S.G.Turyshev, D.H.Boggs, *"Progress in Lunar Laser Ranging Test of Relativistic Gravity"*, Phys.Rev.Lett.93:261101,2004.

4. Bender P. L., et al, *"The Lunar Laser Ranging Experiment"*, Science, Volume 182, Issue 4109, pp. 229-238, 1973.

5. Williams J. G., Turyshev S. G., Boggs D. H., Ratcliff J. T., *"Lunar Laser Ranging Science: Gravitational Physics and Lunar Interior and Geodesy"*, 35th COSPAR Scientific Assembly, July 18-24, 2004.

6. Williams J. G., Boggs D. H., Ratcliff J. T., *"A larger lunar core?"*, 40th Lunar and Planetary Science Conference, March 23-27, 2009.

7. Williams J. G., Turyshev S. G., Boggs D. H., *"Lunar Laser Ranging Test of the Equivalence Principle with the Earth and Moon"*, International Journal of Modern Physics D, Volume 18, 1129-1175, 2009.

8. Rambaux N., Williams J. G., Boggs D. H., *"A Dynamically Active Moon-Lunar Free Librations and Excitation Mechanisms"*, 39th Lunar and Planetary Science Conference, March 10-14, 2008.

9. Williams J. G., Boggs D. H., Ratcliff J. T., *"Lunar Tides, Fluid Core and Core/Mantle Boundary"*, 39th Lunar and Planetary Science Conference, March 10-14, 2008.

10. Nordtvedt K., *"Lunar Laser Ranging: a comprehensive probe of post-Newtonian gravity"*, Gravitation: from the Hubble length to the Planck length, edited by Ciufolini I., Coccia E., Gorini V., Peron R., Vittorio N., ISBN 07503 0948, published by Institute of Physics Publishing, the Institute of Physics, London, 2005, p.97.

11. Murphy T. W., Adelberger E. G., Strasburg J. D., Stubbs C. W., Nordtvedt K., *"Testing Gravity via Next Generation Lunar Laser-Ranging"*, Nuclear Physics B Proceedings Supplements, Volume 134, 155-162.

12. Nordtvedt K., *"Testing the Equivalence Principle with laser ranging to the Moon"*, Adv. in Space Research, Volume 32, Issue 7, 1311-1320.

13. Dvali G., Gruzinov A., Zaldarriaga M., *"The Accelerated Universe and the Moon"*, Physical Review D, Vol. 68, Issue 2, id. 024012.

14. Currie D. G., et al., *"A Lunar Laser Ranging Retro-Reflector Array for NASA's Manned Landings, the International Lunar Network, and the Proposed ASI Lunar Mission MAGIA"*, 16th International Workshop on Laser Ranging Instrumentation, October 13-17, 2008.

15. Prete F., *"Contact structural analysis of the MoonLIGHT Laser Retro-reflector Assembly with ANSYS"*, Bachelor thesis (unpublished), Dipartimento di Meccanica e Aeronautica, University of Rome "La Sapienza".

16. Minghiglioni A., *"Modal analysis of the MoonLIGHT Laser Retro-reflector Assembly with ANSYS"*, Bachelor thesis (unpublished), Dipartimento di Meccanica e Aeronautica, University of Rome "La Sapienza".

17. `http://ilrs.nasa.gov/docs/retroreflectorspecification070416.pdf`

18. Pearlman M. R., Degnan J. J., Bosworth J. M., *"The International Laser Ranging Service"*, Adv. in Space Research, Vol. 30, No. 2, 135-143, 2002.

19. Urschl C., Beutler G., Gutner W., Hugentobler U., Schaer S., *"Contribution of SLR tracking data to GNSS orbit determination"*, Adv. in Space Research, 39(10), 1515-1523, 2007.

20. Urschl C., Beutler G., Gutner W., Hugentobler U., Ploner M., *"Orbit determination for GIOVE-A using SLR tracking data"*, ILRS Workshop, 2006.

21. `http://ilrs.nasa.gov/docs/ILRSRetroreflectorStandards200812.pdf`

22. Neubert R., Neubert J., Munder J., Grunwaldt L., *"Proposed Single Open Reflector for the GALILEO Mission"*, International Technical Laser Workshop on SLR Tracking of GNSS Constellations, 2009.

MUEXC

M. Cestelli Guidi (Art. 23), G. Della Ventura (Ass.), D. Di Gioacchino (Resp.),
A. Marcelli, A. Mottana (Ass.), E. Pace (Ass.),
A. Puri (Ass.), N. Saini (Ass.), F. Tabacchioni (Tecn.)

1 *MUEXC* project

MUEXC is a project based on the PRESS-MAG-O apparatus designed to perform experiments on materials under extreme conditions of pressure, magnetic field in a wide temperature range from room temperature down to 4K. It has been designed for fundamental researches and for technological applications of the interest of the Institute. The project is based on a large collaboration between the LNF, the INFN Unit of Florence, the High-pressure Raman group and the Spectroscopy group of the Department of Physics of the *Sapienza* University, the Department of Geological Science of the Roma Tre University and the Department of Physics of the University of Camerino.

In 2012 the main activities of the *MUEXC* collaboration can be summarized as follows:

a) *Maintenance of the cryostat*: after the evaluation of the damage to the PRESS-MAG-O system due to mishandling of the internal transport staff in the LNF, have been carried out the repairs to the cryostat and superconducting magnet. Before the end of the year begins the reassembling of the system to make possible vacuum tests and later operations at low temperature.

b) *Operation on PRESS-MAG-O insert*: we proceeded in the final commissioning of the PRESS-MAG-O insert.

2 Maintenance of the cryostat

The cryostat has been repaired to the DG-Technology company that has realized the system. Moreover, operation, reliability and safety of the superconducting magnet have been tested by the manufacturer of the magnet: the AMI Inc. in USA, where it has been control the superconducting switch of the magnet and it has been energized with currents up to 100A (corresponding to a maximum value of 7 Tesla). Regarding the cryostat, before the end of the year begins the reassembling of the system to make possible vacuum tests and later operations at low temperature.

3 Operation on the PRESS-MAG-O insert

We proceeded also the final commissioning of the PRESS-MAG-O insert. The heart of the system is a SQUID gradiometer designed and manufactured to operate inside the Diamond Anvil Cell (DAC) with a SQUID amplifier placed on the bottom of the insert. Several measurements have been performed to test the gradiometer operation at 4.2 K with a superconducting sample (a YBCO sample of dimension $\sim$0.16 mm^3) loaded in the DAC cell. To remove noises due to the interferences of RF signals we shielded the SQUID signals with a box made by ferrite RF filters and capacitors (see fig.1 left).

Different measurements have been performed to set the procedure and the suitable experimental set-up for ac susceptibility multi harmonic experiments using the instrumental chain formed by a Sinusoidal Pulse Amplifier and an AC Current Amplifier to control the magnetic field excitation and the SQUID-gradiometer, the Lock-In amplifier to measure the magnetic signal of the superconducting coils sets inside the DAC cell. The procedure optimizes: **1)** The functionality of the SQUID maximizing the response with a signal test generated by the SQUID system. At first

we use a sinusoidal test signal of 6mV at 107Hz corresponding to ∼12 mGauss that give a pick-up signal of 15 flux quanta (see fig. 1, rigth panel). **2)** The ac exciting magnetic field starting with an amplitude of 12.8 mV corresponding to 25.6 mGauss at 107 Hz frequency to test the linear response of the SQUID. **3)** The Lock-In amplifier has measured the signals of the first and third harmonics of the SQUID that pick-ups the superconducting gradiometer at 4.2 K, 107Hz and 25.6 mGauss. We carried out also measurements at different values of the frequency (17-1070 Hz) and of the ac magnetic fields (10 mGauss-10 Gauss) always at 4.2 K. The SQUID-gradiometer showed a high sensitivity working at magnetic fields excitation of the order of mGauss. For magnetic fields greather then 1 Gauss attenuators have to be inserted to probe the magnetic response with the Lock-In amplifier.

Figure 1: *(left) The RF filter box of the SQUID connector; (right) SQUID test performed at* $4.2K$ *with an a.c. magnetic field of* $0.012G$ *at* $107Hz$. 15*fluxons quanta have been measured*

4 Experimental activity

In additions to the commissioning of the PRESS-MAG-O instruments, we continued in the LAMPS-LNF laboratory to perform experiments on highly correlated materials. In this context, we contributed with our magnetic susceptibility measurements to publish an important research within an international collaboration between the *Laboratori Nazionali di Frascati* of the INFN, the London Centre for Nanotechnology (LCN), the Rome International Center for Materials Science RICMASS, and the *Sapienza* University on the Proceedings of the National Academy of Sciences (USA).The breakthrough we discussed in this contribution is that the competition between networks drive these materials to an optimum inhomogeneity made of a complex scale free distribution similar to the competition between two networks of social relations. We show that is the organization of two types of defects in the La_2CuO_{4-y}, that determines the superconductivity at high temperature in a ceramic superconductor. The first defects are the additional oxygen atoms that are introduced in a simple parent oxide of copper to induce superconductivity, while the second network is made of deviations of atoms from where they would have been in the parent material (see Fig. 2 Right). At Frascati we measured the components of the multi-harmonic ac susceptibility that probes the different phases superconducting controlled by thermal processes (see fig. 2 Left). This results has been also presented as a NEWS on the INFN webpage on October 8, 2012.

We also continued flux dynamic studies on 1111 and 11 iron-based superconductors such as $NdFeAsO_{0.86}F_{0.14}$ and iron chalcogenide superconductors. AC multi-harmonic susceptibility measurements have been performed and the analisys have been performed in the glass-weak pinning scenario. In particular, the comparison of the third harmonic components vs. temperature under a magnetic field returned information on pinning strength and dimensionality. We showed that in some HTS systems, although in the presence of large thermal fluctuations, an increase of the

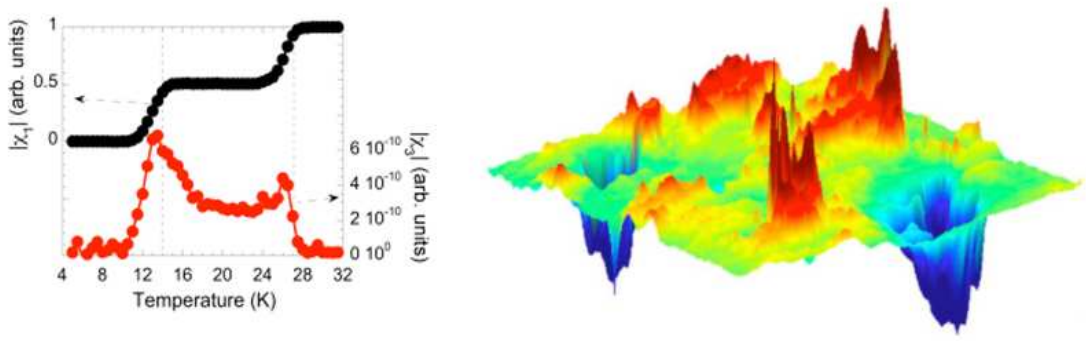

Figure 2: *Right: the first harmonic (real part),* χ_1'*, and the modulus of the ac susceptibility third harmonic,* χ_3*, of the underdoped* $La_2CuO_{4.06}$ *showing two transitions at* $14K$ *and* $\sim 27K$*. Left: the three dimensional color plot imaging the position dependence of the Q3-LLD superstructure intensity I(Q3)/*I_0 *(values>*0*) and of the Q2-Oi superstructure intensity I(Q2)/*I_0 *(values<*0*) (from PNAS 109, (39) (2012) pp. 15685-15690)*

pinning amplitude is observed. The phenomenon is particularly evident in the 1111 Fe-based superconductor systems where a spacer layer among superconducting planes exists (see fig.3).

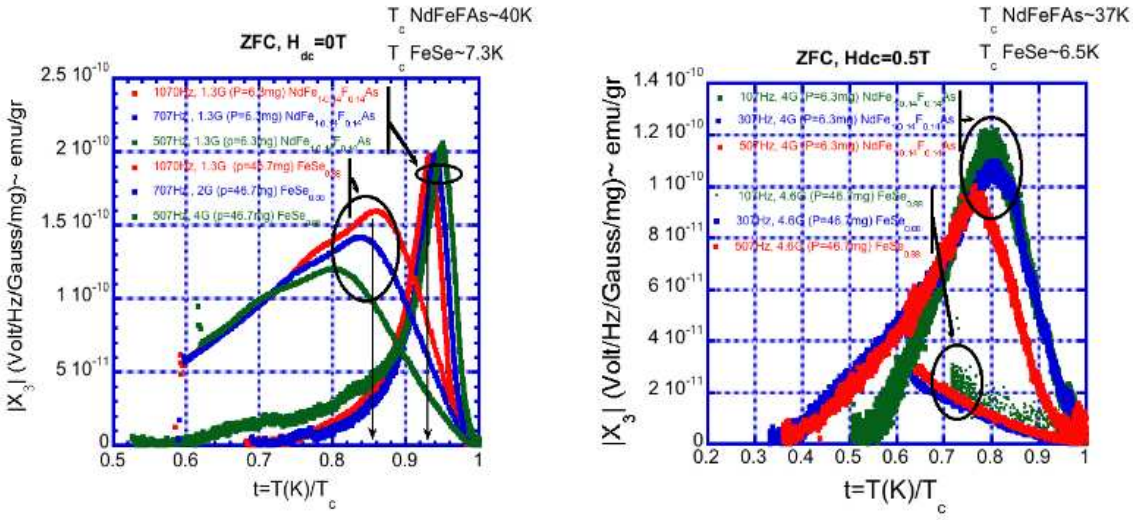

Figure 3: *Comparison of the* χ_3 *module vs. reduced temperature t at different frequencies for* $NdFeAsO_{0.86}F_{0.14}$ *and* $FeSe_{0.88}$*, Left:* H_{dc}=$0\,T$ *, Right:* H_{dc}=$0.5\,T$*. The black arrows pointing the t axes indicating the different t values for two samples*

5 International collaboration

In 2012 within the Executive Programme of Scientific and Technological Cooperation between Italian Republic and the Republic of India for the years 2012 2014 was funded by the Italian Minister of Foreign Affair a bilateral project to the INFN-LNF. From the Italian side is coordinated by A. Marcelli and the cooperation is established with the Institute of Plasma Research (IPR) in Gandhinagar coordinated by C. Balubramanian. The project is dedicated to the investigation of local structure and magnetism of Co nano-structures. In 2012 we hosted Indian researchers and started the experimental activities in the LAMPS-LNF laboratory. Some preliminary experimental data are shown in Fig. 4

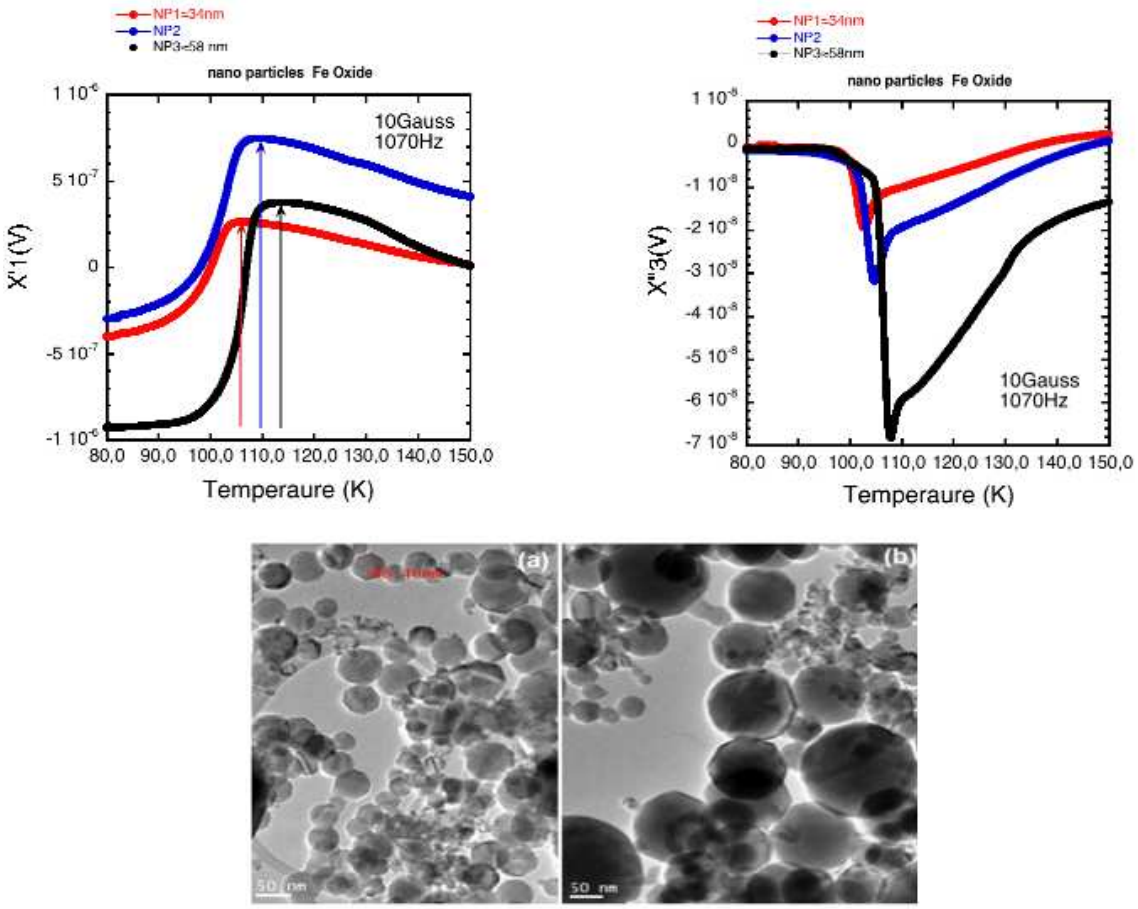

Figure 4: *Up: AC susceptibility first harmonic real part, χ'_1, and third harmonic imaginary part, $\chi"_3$, vs. temperature for different Fe-oxide nano-particles. Down: TEM micrographs of the nano-particle samples dimension. (a) and (b) are respectively samples prepared under conditions 32 Ampere (d∼34nm) and 65 Ampere (d∼58nm)*

.

6 Thesis and PhD

At the laboratory, "LAMPS" in INFN-LNF (Frascati) were carried out the following theses:

1) Dr. Alessandro Puri PhD XXIV Materials Science Universit Sapienza Rome, title: Experiments on strongly correlated materials under extreme conditions, 2009/2012.
Supervisors: Dr. D. Di Gioacchino, Dr. A. Marcelli , Prof. Naurang Saini.
After obtaining the doctorate, dr. A. Puri is doing a two-year contract at the Faculty of Sciences Radboud University in European Magnetic Field Laboratory - EMFL Project-High Field Magnet Laboratory - Nijmegen (Netherlands).

2) Buerhan Shalamu, Degree thesis in the Structure of Matter, University of Camerino, title: Vortex dynamics in the HTSC iron pnictide $SmFeAsO_{0.85}F_{0.15}$, 2012/2013
Supervisors: Dr. D. Di Gioacchino, Dr. A. Marcelli , Prof. Roberto Gunnella.

3) Kamili Yimamu, Degree thesis in the Structure of Matter, University of Camerino,title: Characterization of carbon based resistive patterns on synthetic diamond plates for microdevice design, 2011/2012
Supervisors: Dr. A. Marcelli, Dr. D. Di Gioacchino, Prof. Roberto Gunnella.

7 Oral contribution

1) D. Di Gioacchino, "Flux dynamics in Iron-based superconductors" *Applied Superconductivity Conference 2012, 7-12 October 2012 Portland, (Oregon)*
2) A. Puri, "Evidence of 3D 2D transition in the magneto flux dynamic of $NdFeAsO_{1-0.14}F_{0.14}$" *SuperFOx-2012, First Conference on Superconductivity and Functional Oxides, Como (Italy), 19-22 June 2012*

8 Acknowledgements

We thank the technical staff of the DAΦNE-Light laboratory of the LNF for their continuous and invaluable technical support. A special thank is due to Fabio Tabacchioni.

References

1. D. Di Gioacchino A. Puri, A. Marcelli, N.L. Saini, *Flux dynamics in Iron-Based Superconductors* , IEEE Transaction on Applied Superconductivity, in press

2. D. Di Gioacchino A. Marcelli, A. Puri, A. Iadecola, N.L. Saini, A. Bianconi Influence of the extra layer on the transport properties of $NdFeAsO_{0.86}F_{0.14}$ and $FeSe_{0.88}$ superconductors from magneto dynamic analysis J. Supercond. Nov. Magn. (2012) 25 (5) , pp. 1289-1292

3. Poccia, N., Ricci, A., Campi, G., Fratini, M., Puri, A., Di Gioacchino, D., Marcelli, A., Bianconi, A. *Optimum inhomogeneity of local lattice distortions in* La_2CuO_{4+y} , Proceedings of the National Academy of Sciences of the United States of America 109 (39) (2012) pp. 15685-15690)

NESCOFI@BTF
NEutron Spectrometry in COmplex FIelds @ Beam Test Facility

R. Bedogni (Resp., Art. 23), D. Bortot (Ass.), B. Buonomo, M. Chiti (Tech.), B. De Giorgi (Tech.), A. Esposito, A. Gentile (Tech.), J. M. Gomez-Ros (Ass.), G. Mazzitelli, M.V. Introini (Ass.), A. Pola (Ass.), L. Quintieri (Art. 23)

In collaboration with:
Politecnico di Milano and INFN-Milan
CIEMAT-Madrid, Spain

1 Introduction and motivation

NESCOFI@BTF started in 2011 with the aim of developing innovative neutron sensitive instruments for the spectrometric and dosimetric characterization of neutron fields, intentionally produced or present as parasitic effects, in particle accelerators used in industry, research and medical fields. Neutron spectra in these fields range from thermal (10^{-8} MeV) to tens or hundreds MeV, thus spanning over more than 10 decades in energy. Only the multisphere spectrometer (or Bonner Sphere spectrometer) is able to simultaneously determine all energy components over such a large energy interval. The main disadvantage of this spectrometer is the need to sequentially expose a considerable number (usually more than 10) of detector+moderator configurations, thus leading to time-consuming irradiation sessions. The idea behind NESCOFI is to provide real-time spectrometers able to simultaneously provide all energy components in a single irradiation. These could be employed for:

1. Monitoring the neutron fields in terms of energy-integrated neutron flux and spectral neutron flux in energy intervals of interest.

2. Active real-time control of possible deviations from nominal field properties and of possible modifications induced by materials introduced in the radiation field (samples, waste elements, materials to be tested).

The final users of the NESCOFI products will be a variety of facilities interested to monitor not only the intensity of a neutron beam, but also -and simultaneously- its energy and/or direction distribution (chip-irradiation, material science neutron beam-lines, reference neutron fields, research and cancer therapy facilities).

The basic idea behind the project is to exploit the moderation of neutrons in hydrogenated materials, as extensively done in Bonner Sphere spectrometers, but new designs and computational methods have been introduced. Particularly, instead of estimating the neutron energy distribution by exposing different detector+moderator configurations, this project aims at a single moderator embedding several "direct reading" thermal neutron detectors at different positions. The energy or angle distribution of the neutron field will be obtained using unfolding algorithms relying on the device response matrix and on the reading of the different detectors. This "unfolding" problem has a number of analogies with the spectrum reconstruction with Bonner Sphere spectrometers, for which a special code called FRUIT (FRascati Unfolding Interactive Tools) was developed at LNF. The NESCOFI project planned to be completed in three years (2011-2013), organized as follows:

2011

1. optimization (via Monte Carlo simulation) of the spectrometer geometry and development of a prototype working with passive detectors
2. establishment of a reference neutron field for testing purposes, namely the photo-neutron beam from the n@BTF facility at the LNF.

2012

Development of suitable "direct reading" (or active) thermal neutron detectors to be embedded in the final spectrometers

2013

Establishment and calibration of the final spectrometers

2 Achievements of the first year (2011)

See 2011 Annual report

3 Achievements of the second year (2012)

3.1 Cylindrical spectrometer (CYSP): final design and response matrix

The CYSP (cylindrical spectrometer) is the target instrument for workplaces where a directional spectrometry must be performed. Typical cases are the fast neutron irradiation beam-lines used at spallation facilities like ISIS, SNS and (in future) ESS. Key elements of the CYSP are:

- Length and diameter suited for the energy interval of interest (thermal up to GeV);
- A Cd-lined collimator to define the direction of interest;
- The distribution of the thermal neutron detectors (TNDs) along the cylindrical axis should be adequate to maximise the spectrometric performance with a reduced self-perturbation effects;
- A high-Z radiator to allow detecting neutron above 20 MeV, placed at the adequate depth.

An extensive simulation campaign was performed with the Monte Carlo code MCNPX. This allowed studying the variation of the CYSP response matrix as the mentioned parameters varied. Fig. 1 reports the sketch of one among the studied configurations.

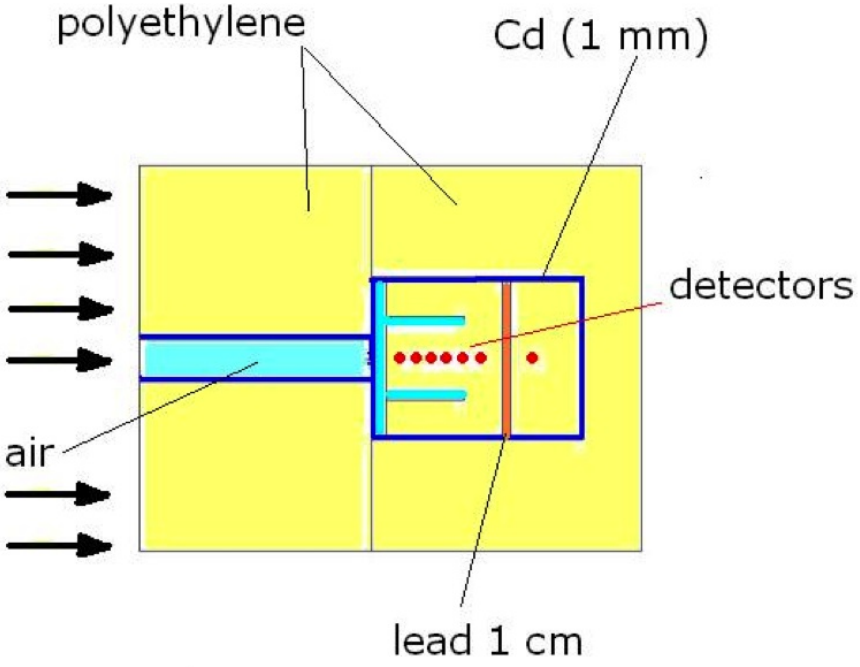

Fig. 1: The CYSP design.

Figure 2 shows a typical response matrix. The signal of every detector is reported, per unit incident fluence, as a function of the monochromatic neutron energy. Detector "0" is located on the CYSP front face and only detects thermal neutron present in the external field. Detectors "1" to "8" are located at increasing depth along the cylindrical axis. Detectors "6" to

"8" are "below lead", thus their response shows a "threshold" at approx 1 MeV. The detectors located near the lead filter (above and below) respond to high-E neutrons because secondary neutrons from (n,xn) reactions are also emitted at large angles. The spectrometric capability of the device is determined by the variation in the response observed when the position and the energy vary.

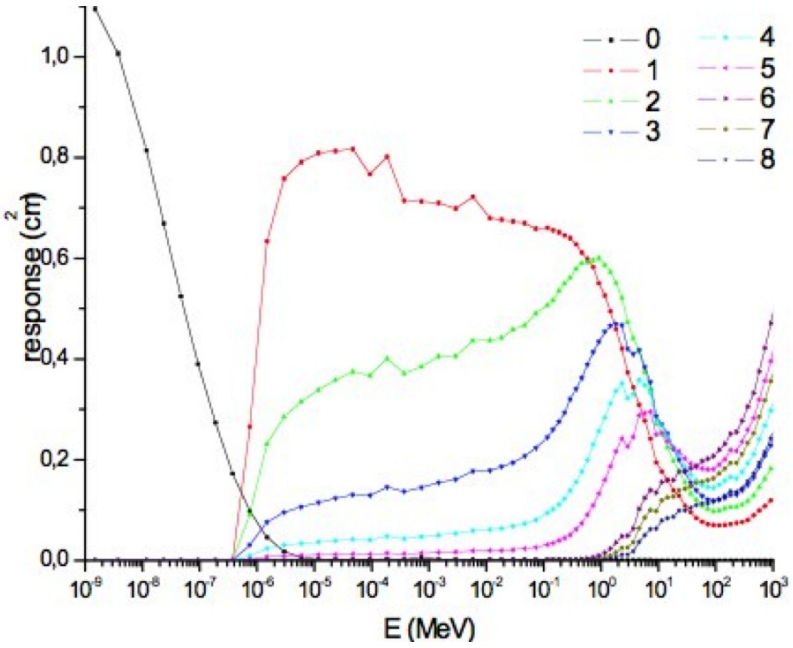

Fig. 2: Typical response matrix of the CYSP.

The directionality of the response was studied by simulating a realistic scenario where the CSYP is located in an irradiation room (see Fig. 3) where a neutron beam at different energies, emerging from a collimated source, reaches the CYSP front face. Two simulations have been launched for a given CYSP geometry:

- one with realistic walls, such to produce significant room scatter in any direction;
- another without walls, in order to have neutrons only in the desired measurement direction, i.e. the CYSP axis.

For every CYSP geometry the (wall absent / wall present) ratio was reported as a function of the detector position and of the irradiation energy (see Fig. 4 for $E = 10$ MeV).

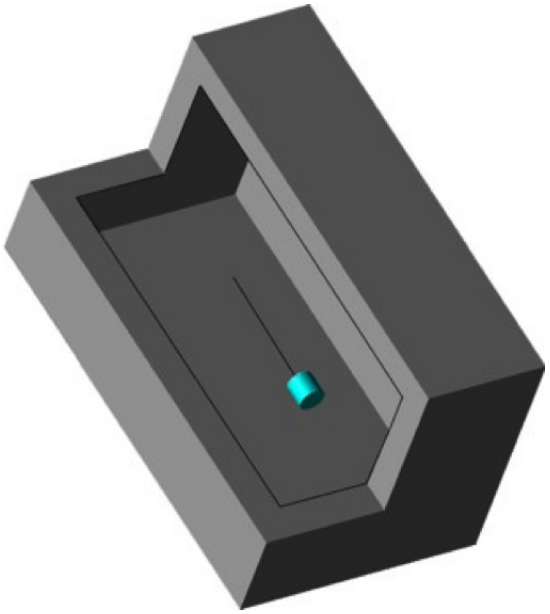

Fig. 3: Geometric set up for studying the directional response of the CYSP.

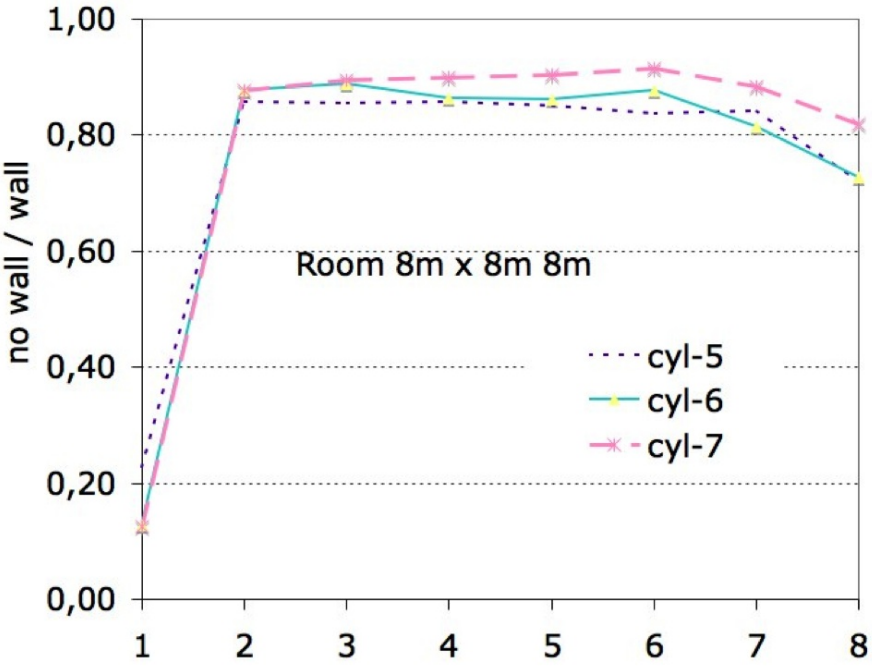

Fig. 4: Directional response study.

The simulation campaigns above described allowed reaching a compromise configuration (see Figure 5) showing good spectrometric capability and optimal directionality. The prototype is currently under construction.

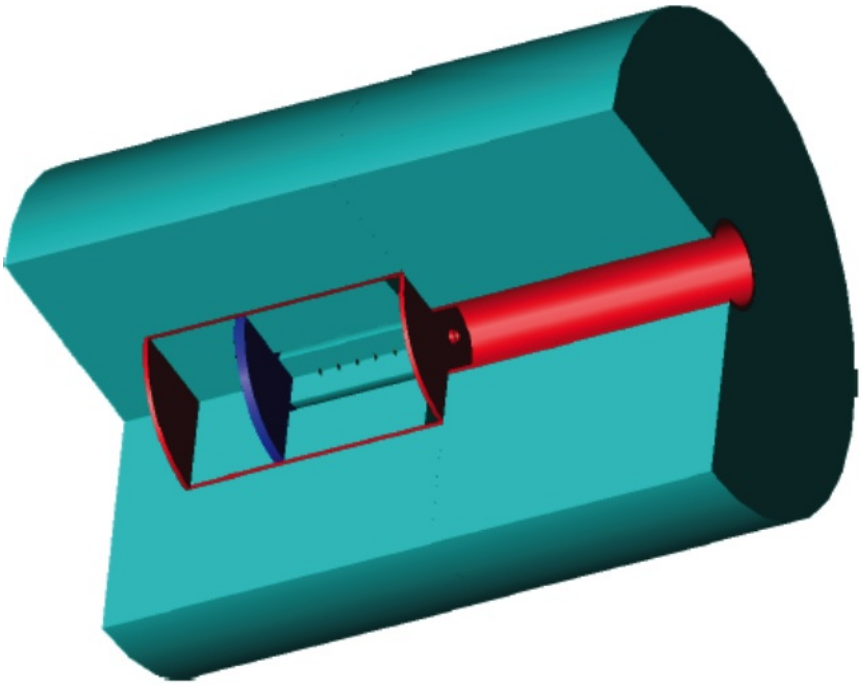

Fig. 5: Solid model of the CYSP.

3.2 Active detectors: state of art

Both CYSP and SP^2 spectrometers in their final versions will embed a number of active thermal neutron detectors (ATND), 31 in the SP^2 and 8 in the CYSP. The target dimension for the single ATND is approximately 1 cm^2 area and $1 - 2$ mm thickness. Several options have been analyzed, including diamond detectors, gas detectors and silicon-based semiconductors. A multi-criteria analysis was done, considering the cost, the sensitivity and the level of miniaturization as key parameters. The final choice was 1 cm^2 silicon-based elements made sensitive to thermal neutrons with an in-house physical-chemical process. Silicon detectors are cheap but are known to be prone to radiation damage. Thus the decision was to firstly produce spectrometers for low-medium flux range using silicon detectors (up to approx. 10^6 $cm^{-2}s^{-1}$ continuous for ten years in the measurement point).

3.3 Spectrometric chain

For every detector a spectrometric chain (charge preamplifier + amplifier) is needed. Because many detectors must be simultaneously acquired, dedicated 8-detector boards were developed. This choice is a factor 50 less expensive than purchasing commercial systems. The electronic performance of the NESCOFI board was evaluated and compared with that of common commercial systems (ORTEC and SILENA). No significant differences were observed (See Fig. 6)

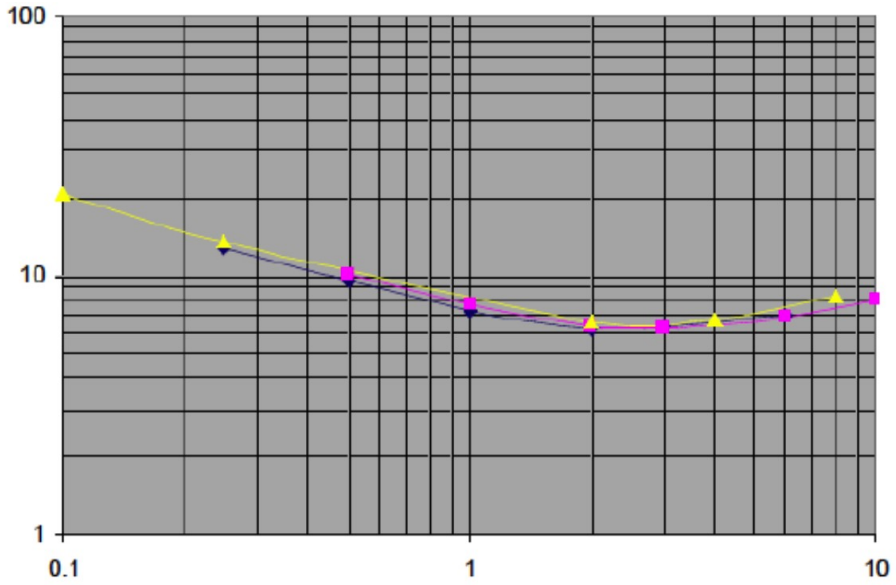

Fig. 6: NOISE FWHM in keV as a function of the shaping time (us): the NESCOFI board (yellow) compared with ORTEC (pink) and SILENA (blue) systems. Vbias=12.2 V, test pulse amplitude = 2.5 mV, injection capacitor = 4.91 pF.

3.4 Thermal neutron sensitisation

Silicon detectors are made sensitive to thermal neutrons with the deposition of an adequate converter. Two types of converters, called C1 and C2, have been evaluated. The sensitivity of the final detector can be tuned over more than a factor 10 by varying the deposit thickness and mixture. The sensitization process is reproducible within 8% (in terms of variability of the response of a batch of detectors deposited with the same nominal converter thickness). The deposition process is quality assured by exposing the final detector to a standardized thermal neutron field obtained with a 1 Ci $^{241}Am - Be$ source

and a moderating assembly (see Fig. 7). The reference spectrum is shown in figure 8. This test also serves as calibration procedure.

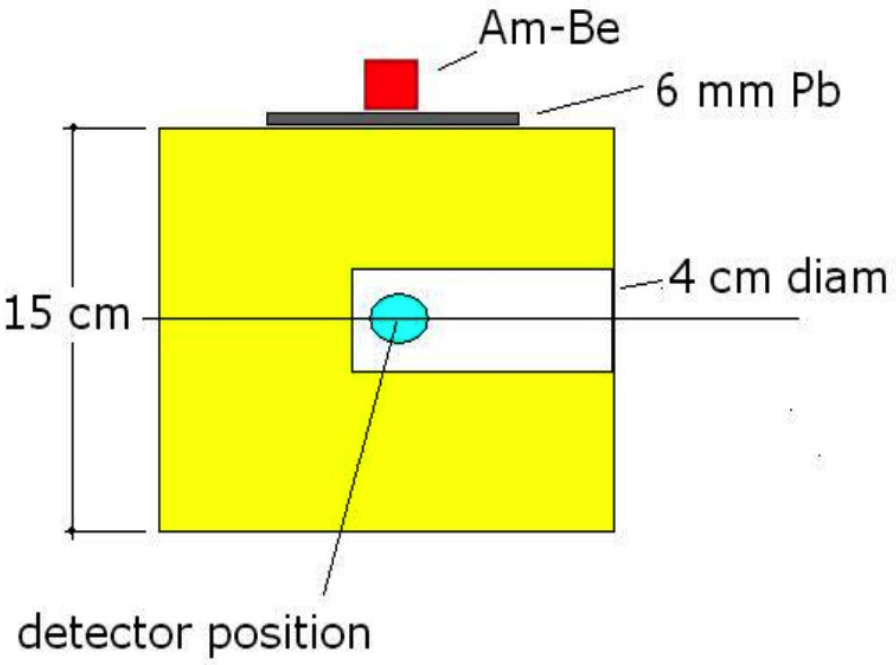

Fig. 7: Assembly for detector testing and calibration.

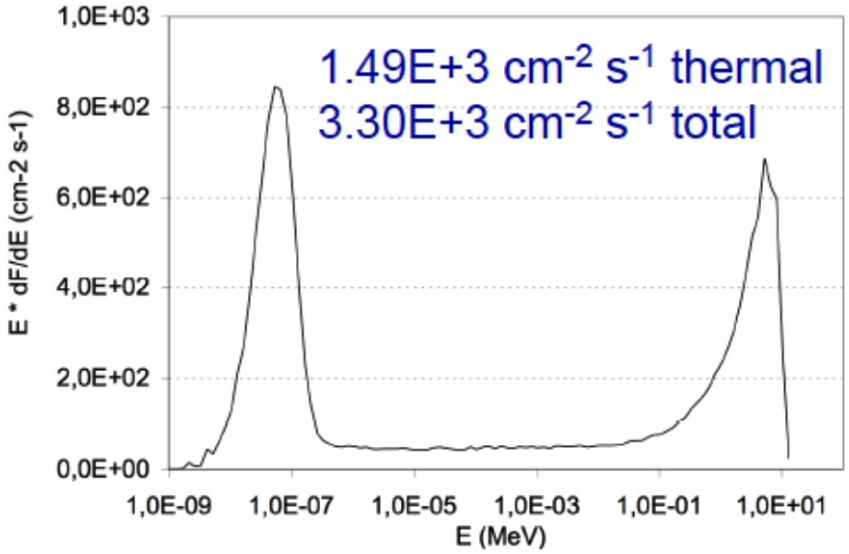

Fig. 8: Neutron spectrum and integrated flux at the reference point of the calibration field.

3.5 Performance of converter C1

To assess the performance of converter C1, a set of detectors were covered with different thicknesses and exposed to the same thermal neutron fluence using the test facility described in 3.4. The typical spectrum of energy deposited in silicon is reported in Figure 9. The label "bare" denotes the uncovered detector. The signal due to thermal neutrons is obtained by subtracting the "bare" spectrum from the "covered" spectrum. Unfortunately the thermal neutron peak (at approx. 80 mV) basically coincides with the maximum of the continuous energy distribution of the secondary electrons, thus requiring exposing a pair of detectors (bare and covered) to accurately determine the thermal neutron component. In other words, the ATND produced with converter C1 is sensitive to photons. Due to this disadvantage, further studies were undertaken to design another converter (C2) with considerably lower photon sensitivity (see 3.6).

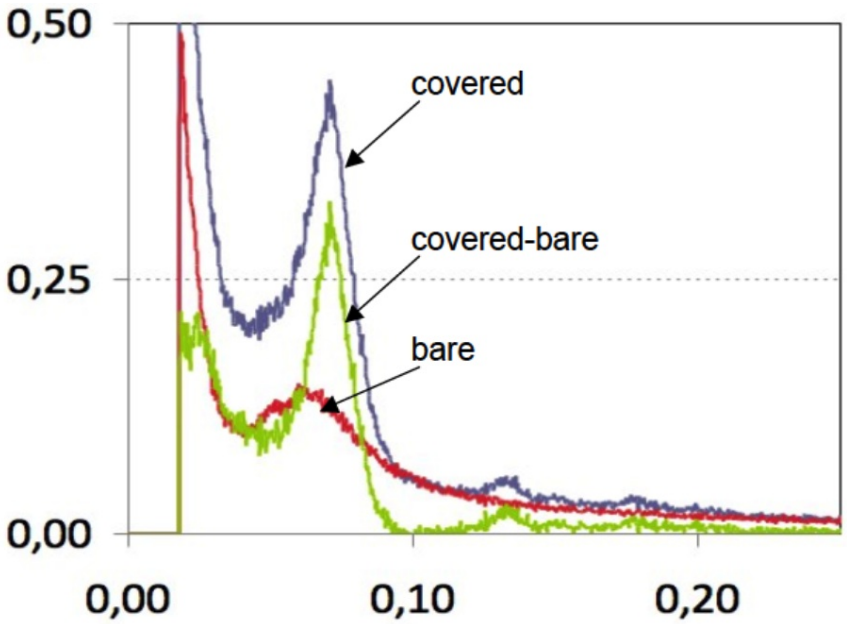

Fig. 9: Typical spectrum of energy deposited in silicon using converter C1. The label "bare" denotes the uncovered detector. X axis is pulse height (V) and Y axis is number of pulses (a.u.).

Characteristics of converter C1 are:

- Different detector thicknesses are easy to fabricate and well controllable;

- Optimal sensitivity obtained: 0.02 counts per unit thermal fluence (cm^2);
- Fabrication reproducibility 8%;
- Radiation damage: absent for integrated thermal neutron fluence up to 510^{10} $cm^{-2}s^{-1}$ (measured at the NPL thermal pile).
- A double exposure (bare and covered) is needed to determine the thermal neutron component of the field.

ATNDs obtained with converter C1 have been arranged in a "CYSP-like" assembly (see Figure 10) to perform simultaneous acquisition with the NESCOFI-developed 8-channel boards. Irradiation tests with reference monochromatic neutron beams of 0.565 MeV and 5 MeV were performed at NPL (Teddington, UK).

Fig. 10: On the left: moderating cylinder embedding seven ATNDs simultaneously acquired. On the right: shadow-cone used for room-scatter subtraction purposes at the NPL reference monochromatic neutron beam facility.

The spectrometric capability of such a moderating assembly is demonstrated by Figure 11, where the count profile (count rate in ATND as a function of the position along the cylindrical axis) is shown for both irradiation energies. Detector positions varies from 1 to 7, where 1 is the shallowest position and 7 the deepest one (See Figure 12).

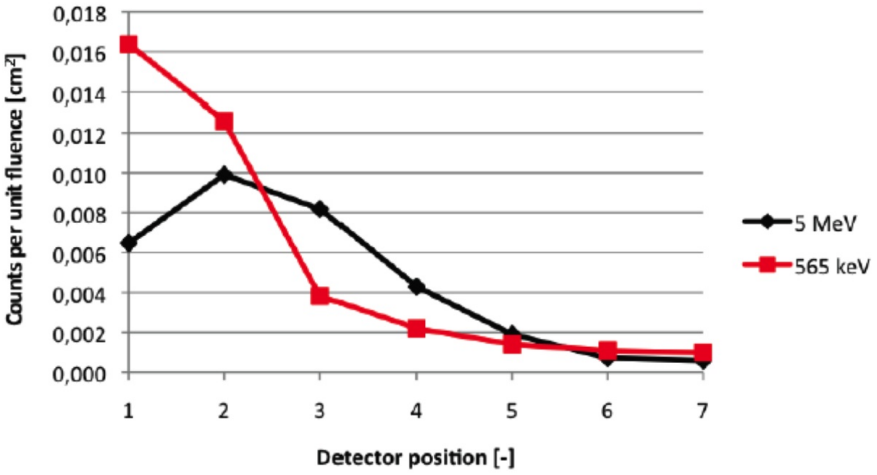

Fig. 11: Count profile (count rate in ATND as a function of the position along the cylindrical axis) for 0.565 and 5 MeV monochromatic beams.

Fig. 12: Cross section of the testing cylinder (50 cm length, 40 cm diameter). Position 1 is the shallowest one, whilst position 7 is the deepest one.

3.6 Performance of converter C2

Converter C2 was developed with the special aim of reducing the photon sensitivity without compromising the thermal neutron sensitivity. Different thicknesses were fabricated and tested in the facility described in 3.4. The results in terms of thermal neutron sensitivity as a function of the thickness are reported in Table 1, where RT denotes the so called "reference thickness".

Thickness (in unit of RT)	Response (cm^2)
0.17	0.003
0.25	0.007
0.32	0.013
0.50	0.016
0.87	0.017
1.00	0.026

Table 1: Thermal neutron sensitivity as a function of the thickness of converter C2.

As shown in Figure 13, the use of converter C2 does not require to expose a double detector because the photon-induced signal falls well below the spectral region of interest for thermal neutrons.

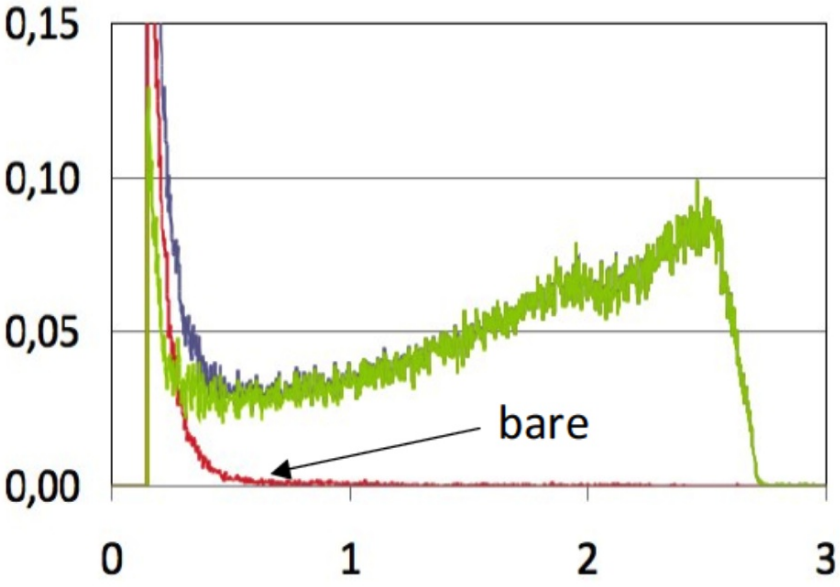

Fig. 13: Typical spectrum of energy deposited in silicon using converter C2. The label "bare" denotes the uncovered detector. The Blue spectrum is the "covered" detector. The green spectrum is the "covered" - "bare" spectrum. X axis is pulse height (V) and Y axis is number of pulses (a.u.).

Characteristics of converter C2 are:

- Different detector thicknesses are easy to fabricate and well control-

lable;

- Optimal sensitivity obtained: 0.026 counts per unit thermal fluence (cm^2);
- Fabrication reproducibility $< 10\%$;
- Radiation damage observed for integrated thermal neutron fluence $3 \cdot 10^{12}$ cm^{-2} (measured at TRIGA reactor, ENEA Casaccia).
- A single exposure is sufficient to determine the thermal neutron component of the field.

3.7 Testing new detectors a standard Bonner spheres spectrometer

The ATNDs obtained with converters C1 and C2 were further tested against a well-established detector, the ^{6}LiI(Eu) scintillator, at the center of a set of Bonner spheres. The test was performed at TSL Uppsala, where a wide neutron spectrum is produced by bombarding a Be target with 30 MeV protons. Figure 14 reports the count profile obtained for the three configurations (LiI(Eu), C1 and C2). This profile is defined as the count rate per unit proton current as a function of the sphere diameter. Ideally, the ratio LiI(Eu)/C1 and LiI(Eu)/C2 should remain constant as the sphere diameter varies. Actually this was experimentally confirmed within $\pm$ 5%.

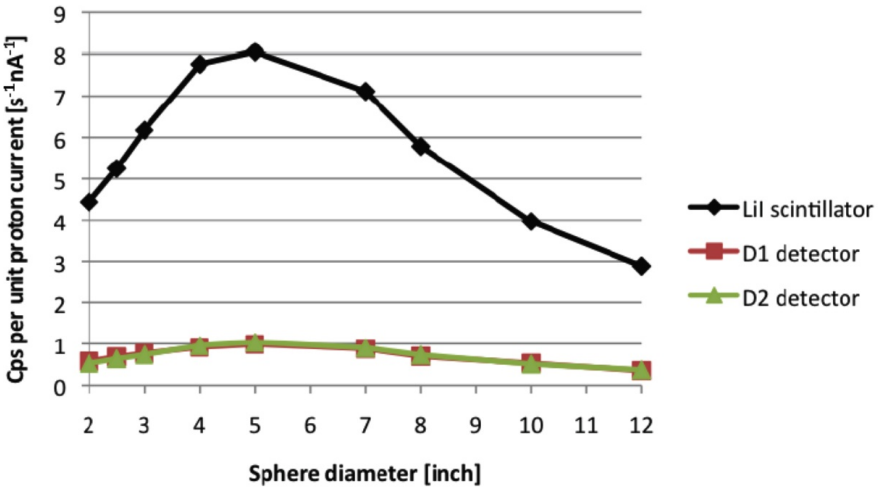

Fig. 14: Count profile obtained for the three configurations (LiI(Eu), C1 and C2) in the TSL experiment.

3.8 Testing new detectors in the medical field

Thermal neutron fluence measurements using converter C2 were performed inside an anthropomorphic phantom undergoing a 15 MV radiotherapy treatment at the Ospedale S. Camillo (Roma) (Figure 15). The thermal fluence at selected points representing special organs were known via Monte Carlo simulations and previous measurements with passive techniques (TLD pairs).

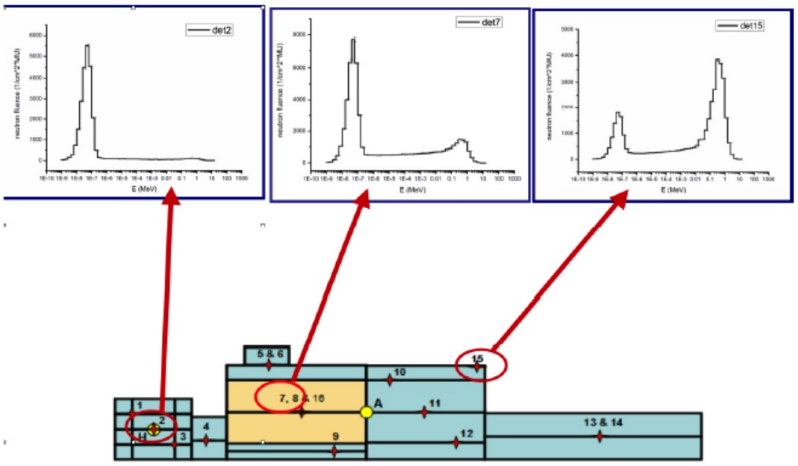

Fig. 15: Sketch of the phantom and location of the measurement positions. Neutron spectra in given positions are reported.

The test consisted in exposing the ATND (C2 converter) in the positions representing lung, abdomen and skin. A head treatment (10 Gy at isocenter) was delivered. Table 2 reports the thermal fluence measured with the ATND as compared with the TLD results. Uncertainties are 10 %.

Organ	ATND fluence (x10^4 cm^{-2}MU^{-1})	TLD fluence (x10^4 cm^{-2}MU^{-1})
lung	2.0	2.3
abdomen	0.1	0.1
skin	0.9	0.7

4 Publications 2012

R. Bedogni, K. Amgarou, C. Domingo, S. Russo, G.A.P. Cirrone, M. Pelliccioni, A. Esposito, A. Pola, M.V. Introini. Experimental characterization of the neutron spectra generated by a 62 AMeV carbon beam on a PMMA

phantom by means of extended range Bonner sphere spectrometers. NIM A 681 (2012) 110-115.

R. Bedogni, C. Domingo, M. J. Garcia Fuste, M. de-San-Pedro, A. Esposito, A. Gentile, L. Tana, F. d'Errico, R. Ciolini, A. Di Fulvio. Calibration of neutron sensitive devices in the neutron field produced in the treatment room of a medical LINAC. Radiation Measurements (2012), doi:10.1016/j.radmeas.2012.04.009.

J. M. Gomez-Ros, R. Bedogni, M. Moraleda, A. Esposito, A. Pola, M.V. Introini, G. Mazzitelli, L. Quintieri, B. Buonomo. Designing an extended energy range single-sphere multi-detector neutron spectrometer. Nucl. Instr. Meth. A 677 (2012) 4-9.

R. Bedogni, J. M. Gomez-Ros, A. Esposito, A. Gentile, M. Chiti, L. Palacios-Perez, M. Angelone, L. Tana. Workplace testing of the new single sphere neutron spectrometer based on Dysprosium activation foils (Dy-SSS). NIM A 684 (2012) 105-108.

R. Bedogni, A. Esposito Experimental study for improving the angle dependence of the response of PADC-based personal neutron dosemeters. Radiation Measurements (2012), http://dx.doi.org/10.1016/j.radmeas.2012.10.005

F. Sànchez-Doblado; C. Domingo; F. Gòmez; B. Sànchez-Nieto; J.L. Muñiz; M.J. Garcìa-Fusté; M.R. Expòsito, R. Barquero; G. Hartmann; J.A. Terròn; J. Pena; R. Méndez; F. Gutiérrez; F.X. Guerre; J. Rosellò; L. Nùñez; L.Brualla-Gonzàlez; F. Manchado; A. Lorente; E. Gallego; R. Capote; D. Planes; J.I. Lagares; X. Gonzàlez-Soto; F. Sansaloni; R. Colmenares; K. Amgarou; E. Morales; R. Bedogni; J.P. Cano; F. Fernàndez.Estimation of neutron-equivalent dose in organs of patients undergoing radiotherapy by the use of a novel online digital detector. Phys. Med. Biol.57,pp. 6167-6191.2012.

S. Agosteo; R. Bedogni; M. Caresana; N. Charitonidis; M. Chiti; A. Esposito; M. Ferrarini; C. Severino; M. Silari.Characterization of Extended Range Bonner Sphere Spctrometers in the CERF high-energy broad neutron field at CERN.Nucl. Instr. Meth. A.694,pp. 55 - 68.2012

L. Quintieri; R. Bedogni; B. Buonomo; A. Esposito; M. De Giorgi; G. Mazzitelli; P. Valente; J. M. Gomez-Ros. Photoneutron source by high energy electrons on high Z target: comparison between Monte Carlo codes and experimental data.Fusion Science and Technology.61,pp. 314 - 321.2012.

5 Collaboration and external funds

EU FP7 Erinda Program: 2.5 k€(instrument shipment) + 35 beam hours at TSL for project PAC 3/9 - 2012
CIEMAT Madrid 35,000 equiv-hours CPU time on EULER cluster
CRISP (INFN-LNF): 12 k€(neutron converters, trips exp. campaigns)
Politecnico di Milano 6 k€(trips at experimental campaigns) + support for electronics design and testing
Ospedale San Camillo: usage of 15 MV electron LINAC
LNF support: Beam-time (one week) at n@BTF
2 man per month at mechanical workshop
Guest-house: 30 man per night
Experiments for detector fabrication and characterization performed at FISMEL laboratories.

6 Project meetings

16 May 2012: NESCOFI@BTF 2012 Mid-Year Meeting & International Review Panel Meeting. INFN-LNF.

7 International Review Panel

Prof. Carles Domingo, Profesor Titular of the Universitat Autonoma de Barcelona, UAB Head of the Neutron Measurement group of the UAB `carles.domingo@uab.cat`

Prof. Francisco Sanchez Doblado, Profesor Catedratico of the Universidad de Sevilla, Head of the Physiology Department. `paco@us.es`

8 website

`http://www.lnf.infn.it/acceleratori/public/nescofi/`

9 Bibliography

Alevra, A. V. and Thomas, D. J. Neutron spectrometry in mixed fields: multisphere spectrometers. Radiat. Prot. Dosim. 107(1-3), 37-72 (2003).

Bedogni, R., Domingo, C., Esposito, A., Fernandez, F., 2007. FRUIT: an operational tool for multisphere neutron spectrometry in workplaces. Nucl. Instr. Meth. A 580, 1301–1309.

Bedogni, R., Pelliccioni, M., Esposito, A., 2010. A parametric model to describe neutron spectra around high-energy electron accelerators and its application in neutron spectrometry with Bonner Spheres. Nucl. Instr. Meth. A 615, 78-82.

R. Bedogni, L. Quintieri, B. Buonomo, A. Esposito, G. Mazzitelli, L. Foggetta, J.M. Gomez-Ros, Nucl. Instr. Meth. A 659 (2011) 373-377.

Bedogni, R., Domingo, C., Esposito, A., Fernandez, F., 2007. FRUIT: an operational tool for multisphere neutron spectrometry in workplaces. Nucl. Instr. Meth. A 580, 1301 1309.

Bedogni, R., Pelliccioni, M., Esposito, A., 2010. A parametric model to describe neutron spectra around high-energy electron accelerators and its application in neutron spectrometry with Bonner Spheres. Nucl. Instr. Meth. A 615, 78-82.

Amgarou K, Bedogni R, Domingo C, Esposito A, Gentile A, Carinci G, Russo S, Measurement of the neutron fields produced by a 62 MeV proton beam on a PMMA phantom using extended range Bonner sphere spectrometers. NUCL INSTRUM METH A, 654-1, (2011)

Bedogni R, Esposito A, Gentile A, Angelone M, Pillon M. Comparing active and passive Bonner Sphere Spectrometers in the 2.5 MeV quasi monoenergetic neutron field of the ENEA Frascati Neutron Generator (FNG). RADIAT MEAS, 46-12, (2011)

Angelone M, Batistoni P, Bedogni R, Chiti M, Gentile A, Esposito A, Pillon M, Villari R. Mixed n-gamma fields dosimetry at low doses by means of different solid state dosimeters. RADIAT MEAS, 46-12, (2011).

Angelone M, Pillon M, Prestopino G, Marinelli M, Milani E, Verona C, Verona-Rinati G, Aielli G, Cardarelli R, Santonico R, Bedogni R, Esposito A. Thermal and fast neutron dosimetry using artificial single crystal diamond detectors. RADIAT MEAS, 46-12, (2011).

Gomez-Ros JM, Bedogni R, Palermo I, Esposito A, Delgado A, Angelone M, Pillon M. Design and validation of a photon insensitive multidetector neutron spectrometer based on Dysprosium activation foils. RADIAT MEAS, 46-12, (2011).

J. M. Gomez-Ros, R. Bedogni, M. Moraleda, A. Esposito, A. Pola, M.V. Introini, G. Mazzitelli, L. Quintieri, B. Buonomo. Designing an extended energy range single-sphere multi-detector neutron spectrometer. Nucl. Instr. Meth. A 677 (2012) 4-9.

NIO2BEAM

F. Murtas (Resp.)

Not received

OPTICAL DIFFRACTION RADIATION INTERFERENCE

E. Chiadroni (Resp.), L. Cacciotti (Tecn.), M. Castellano (ass.), G. Gatti (Ric.) R. Sorchetti (Tecn.)

Participant Institutions:
Italy: INFN LNF, Roma 2-Tor Vergata; University of Roma Tor Vergata.
Germany: DESY (Hamburg)

1 Introduction

Fourth generation light sources, e.g. Free-Electron Lasers (FEL), and future linac colliders demand high brightness, high repetition rate electron beams. The control and measurement of beam parameters, in particular transverse emittance, along the accelerator is one of the fundamental diagnostic required for such facilities. Conventional diagnostic methods, based on the interaction of the electron beam with intercepting measurement devices, might not be suitable due to the high charge density, high energy characteristic of such beams. Diffraction radiation (DR) diagnostic is based on the observation of the DR angular distribution emitted by an electron beam passing through an aperture in a metallic foil. DR is produced by the interaction of the electromagnetic field of an electron beam with the screen surface. Since the beam goes through the aperture, DR-based diagnostics is suitable for measuring the properties of such beams in a non-intercepting, non-perturbing way.

2 ODRI experiment

The aim of the experiment, set up at FLASH (DESY), is studying the angular distribution of incoherent optical DR (ODR) which gives information on both transverse beam size and angular divergence, to allow a single shot emittance measurement provided the beam has its waist on the DR screen. Some limitations of ODR diagnostic [1)] can be overcome by mounting a shielding mask normally to the beam and in front of the DR screen. Since the two slits have different apertures (1 mm the mask and 0.5 mm the DR screen), the amplitudes of the two sources are different both in intensity and in angular distribution, resulting in an advantageous interference effect. We call it ODRI, i.e. Optical Diffraction Radiation Interference, produced by the interference between forward ODR emitted on the shielding mask and backward ODR from the DR target [2)]. The main benefits are given by the reduction of synchrotron radiation background, the increase of the sensitivity of the angular distribution on the beam size, and the possibility to distinguish effects caused by beam size and offset [3)] within the slit.

3 Achievements in 2012

The planning for the ODRI experiment scheduled in February 2012 during accelerator studies concerned the following two items:

- the measurement of the ODRI angular distribution from both round beams and beams with different aspect ratio, i.e. flat beam typical for colliders, which means different angular divergences;
- the achievement of a totally non intercepting quadrupole scan, therefore the first ever measurement of the normalized transverse emittance by means of ODRI angular distribution.

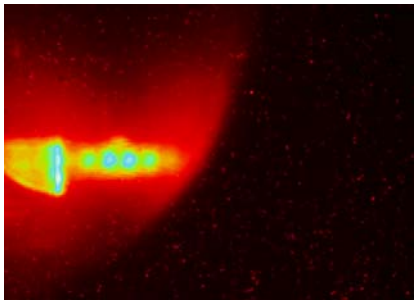

Figure 1: *ODRI angular distribution produced by 1 bunch of 200 pC at 800 nm. The large background is visible all around the signal.*

During the first 12-hour shift, the beam has been successfully transported up to the bypass, into the ODRI experimental station. achieving transverse beam dimension below 50 μm RMS in both planes. This starting point was needed to check the alignment of the optical system with the Optical Transition Radiation (OTR). All these tests have been performed at 1 Hz, to avoid any interruption caused by the radioprotection system.

The beginning of the second 12-hour shift has been characterized by a large signal background, being an indication of coherent emission as result of micro-bunching instability enhanced by the bypass dispersive line [5].

Indeed, beyond the huge background (1), we observed saturation of the OTR beam image even at very low charge, *i.e.* less than 100 pC. The main contribution seemed due to coherent synchrotron radiation coming from upstream with respect to the DR screen.

At the beginning of the third 12-hours shift, we decreased the laser iris in order to preserve the charge density at the cathode, according to the last measurements in January 2011. After that we found a much smoother transport up to the ODRI station, we did not have any strong evidence of coherent emission anymore. This configuration allowed us to tune the beam in order to have small spot size at the DR target. The minimum spot size measured was 50 μm in both directions. We tuned better also the light optics system looking at a clean ODRI angular distribution image. The goal of the shift was the quadrupole scan emittance measurement performed with both OTR beam imaging and ODRI angular distribution measurement.

The emittance has been measured at two observation wavelengths, 800 nm and 500 nm, by means of the quadrupole scan technique, using the last quadrupole before the DR target. Two quadrupole scans have been performed to compare and validate our result. We report here only the the case at 800 nm observation wavelength.

The first quadrupole scan was intercepting, by OTR imaging of a single electron bunch, the second one, fully non-intercepting, looking at the ODRI angular distribution, produced by a 2s integration of 20 bunches traveling through the slits at 10 Hz. The higher number of bunches was needed to increase the signal to noise ratio.

From the standard quadrupole scan we measured a normalized vertical emittance as low as 3.6 (0.4) mm mrad, in very good agreement with the normalized vertical emittance retrieved through the measured ODRI angular distributions, *i.e.* 3.7 (0.8) mm mrad. Data and fit are shown in 2 (black, squares and solid line, for ODRI angular distribution and red, circles and solid line, from OTR imaging).

The forward tracking of the beam optical function (Twiss parameters) allowed to estimate both vertical RMS beam size and divergence at the ODRI target, *i.e.* $\sigma_y = 73$ μm and $\sigma_y^{'} = 31$ μrad. These values are in very good agreement with those retrieved from the fit of the measured ODRI angular distribution. An is shown in Fig.3.

Due to a residual coherent emission, we did not succeed to try the transport of the flat beam. Therefore, we collected some statistics and ODRI angular distribution data with round beam at different wavelengths (between 500 nm and 800 nm) and for both polarization, *i.e.* vertical and

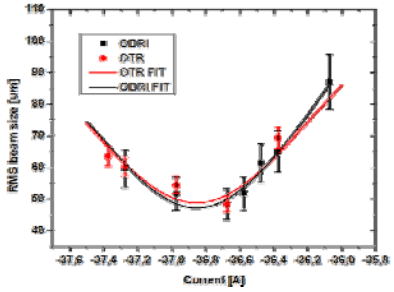

Figure 2: *RMS vertical beam size measured, at the ODRI station, by both OTR imaging (red circles) and ODRI angular distribution (black squares), as function of the current of the upstream quadrupole. The red and black solid curves result from the chi-square fit. The retrieved normalized vertical emittance from the intercepting, OTR-based, measurement is 3.6 (0.4) mm mrad, in very good agreement with the one obtained through the fully non-invasive ODRI-based measurement, i.e. 3.7 (0.8).*

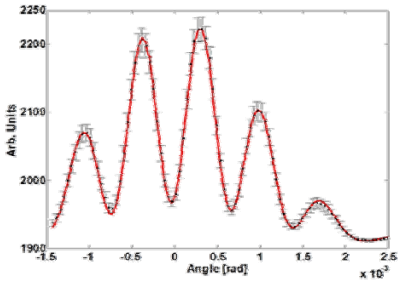

Figure 3: *Example of a profile of the measured ODRI angular distribution. Superimposed the fit calculated by Minuit. The cut on the left of the angular distribution is due to some stray light that falls into the CCD camera.*

horizontal.

In Summer 2012, the bypass line has been dismounted to allow the upgrade to FLASH2. The ODRI diagnostics station has been requested to be mounted at FLASH2 on the main line after the variable gap undulator, where optimized electron beam transport is foreseen.

In addition to the operation of ODRI as standard diagnostics, further experiments are foreseen to study the contribution and the effects of coherent emission due to microbunching within the electron beam. These tasks will concern the activity in the following 3-years project, named as ODRI2D, starting in 2013.

4 Publications during the 3-years project

- M. Castellano, E. Chiadroni, A. Cianchi, "Phase Control Effects in Optical Diffraction Radiation from a Slit", Nucl. Instr. and Methods in Physics Research A **614**, 163 - 168 (2010).
- A. Cianchi *et al.*, "Nonintercepting electron beam size monitor using optical diffraction radiation interference", Phys. Rev. Special Topics - Accel. and Beams **14**, Issue 10, 102803 (2011).
- E. Chiadroni, M. Castellano, A. Cianchi, K. Honkavaara, G. Kube, "Effects of transverse electron beam size on transition radiation angular distribution", Nucl. Instr. and Methods in Physics Research A **673**, 56 - 63 (2012).
- V. Shpakov, S. Dabagov, M. Castellano, A. Cianchi, K. Honkavaara, G. Kube, E. Chiadroni,

"Far- and near-field approximation for diffraction radiation", Nucl. Instr. and Methods in Physics Research B (accepted for publication), 2013.

5 Acknowledgment

Authors wish to thank colleagues collaborating from participant institutions: L. Catani, A. Cianchi (INFN Roma 2-Tor Vergata) and V. Balandin, N. Golubeva, K. Honkavaara, G. Kube (DESY). In addition we would like to acknowledge S. Dabagov and V. Shpakov (collaborating PhD student from Moscow University) for important theoretical contributions.

References

1. E. Chiadroni *et al.*, Nucl. Instr. and Meth. in Phys. Res. B **266**, 37893796 (2008).
2. E. Chiadroni, M. Castellano, A. Cianchi, K. Honkavaara, G. Kube, TUOA02, in: Proc. of DIPAC 2009, Basel, Switzerland.
3. A. Cianchi *et al.*, "Nonintercepting electron beam size monitor using optical diffraction radiation interference", Phys. Rev. Special Topics - Accel. and Beams **14**, Issue 10, 102803 (2011).
4. A. Cianchi *et al.*, Proc. of the RREPS Conference, London, UK (2011).
5. E. Chiadroni, M. Castellano, A. Cianchi, K. Honkavaara, G. Kube, "Effects of transverse electron beam size on transition radiation angular distribution", Nucl. Instr. and Meth. in Phys. Res. A 673, 56 - 63 (2012).

SPACEWEATHER

M.A.Franceschi, T. Napolitano, M.Ricci (Resp.), B.Spataro

Participant Institutions:

ITALY: INFN Bologna, LNF, Napoli, Perugia and Roma 2-Tor Vergata; ASI (Italian Space Agency);
RUSSIA: MePhi, IBMP, Roscosmos
CHINA:CNSA (Chinese Space Agency), CEA (Chinese Earthquake Administration)

1 Introduction

The SPACEWEATHER experimental program is devoted to the exploration - through dedicated space missions - of three main research fields:

1. Interaction between terrestrial geophysical events and Earth radiation belts.
2. Physics of the space environment in Earth orbits.
3. Biomedical effects of space radiation on human body.

These tasks will be achieved by:

1. The study of the correlation between seismic events and perturbation of the Van Allen belts.
2. Monitoring of the radioactive environment and of the nuclear abundances inside and outside the ISS (International Space Station).
3. Measurements of passive shielding to reduce the dose on astronauts.
4. Study of the "light flashes" phenomenon observed by astronauts in space.

This program is a continuation and an extension of the activities carried out for the experiments SIEYE1 and SIEYE2 on board the Russian Space Station MIR in the years 1995-2002 and for the experiment SIEYE3/ALTEINO on board the International Space Station (ISS), still running [1] [2] [3].

2 The Experimental Program

In 2011, the SPACEWEATHER experiment received the approval for the development and the realization of a series of detectors (mini-magnetic spectrometer, electric field detector, magnetic field detector, low frequency e.m. wave detector), under the acronym CSES (Chinese Seismo-Electromagnetic Satellite), to study the fast variations of the fluxes of protons and electrons trapped in the radiation belts due to pertrbations caused by seismic events. In the Sections of Roma Tor Vergata and in the LNF an executive project to set up the sensors for the measurement of the electric field and of the first level data acquisition system has been carried out. Laboratory tests are in progress. The Section of Perugia is developing the design of the magnetic spectrometer and is carrying out laboratory tests as well. The mechanics of the experiment is being designed in Bologna. Roma Tor Vergata is also in charge of the general system of data acquisition, storage and telemetry of the italian portion of the experiment. Agreements between the Space Agencies ASI and CSNA have started and are in progress. In Fig.1, a sketch of the CSES Satellite and the Payload instruments is shown.

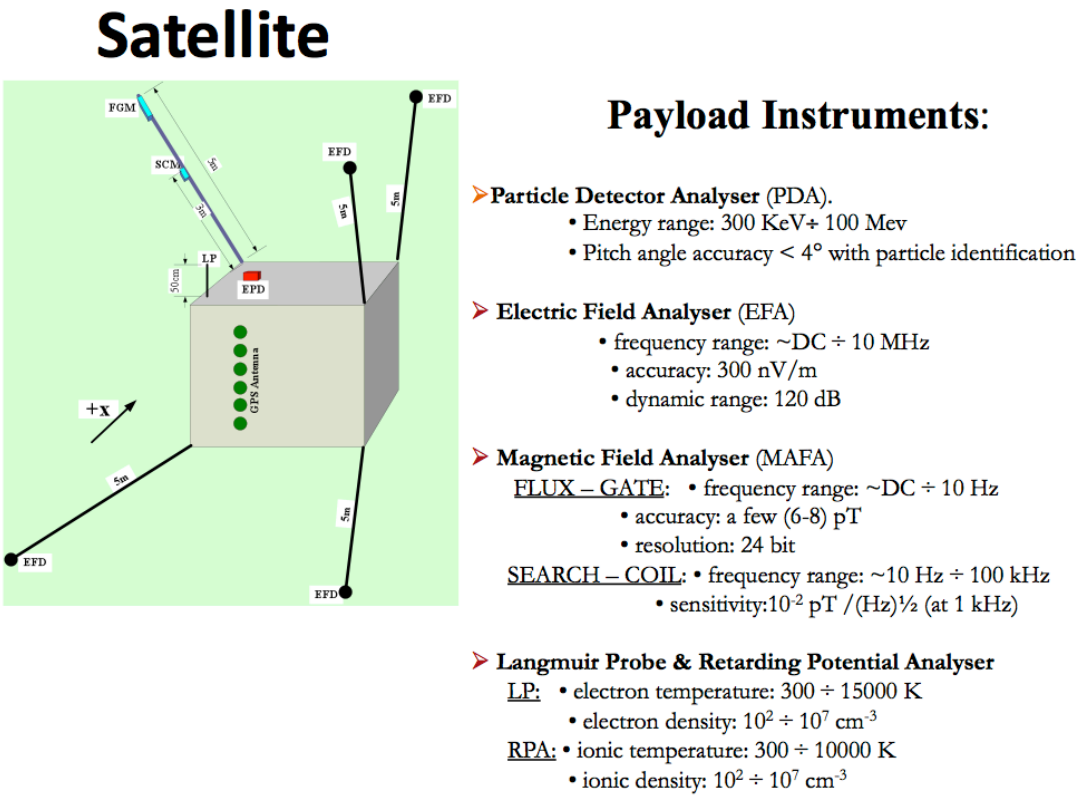

Figure 1: Sketch of the CSES Satellite with the Payload Instruments.

The task of the SI-RAD-ALTCRISS experiment (approved by ESA and ASI in Phase A) was to develop a detector to be placed on the external part of the ISS. The detector will be used to monitor cosmic rays and radiation environment in Low Earth Orbit. Long term (Solar modulation) and short term (coronal mass ejections, orbit dependence) effects on the particle flux will be monitored as well as the dose absorbed by the astronauts. In addition, data will be compared with measurements taken inside the ISS with ALTEA [4], ALTEINO and LAZIO/SIRAD [5] detectors to validate radiation transport and dose estimation codes. At the same time, the investigation, with a more sophisticated instrument, of the "Light Flashes" phenomenon [6], will be conducted to improve and refine the results obtained with the previous SIEYE experiments.

The preparation of the next SI-RAD extended mission is advancing towards the completion and test of the full flight instrument consisting of a 16-plane tower of double-sided silicon detectors (8x8 cm^2 area) equipped with trigger and anticoincidence counters, as shown in Fig.2. The total weight is about 15 kg and the total power consumption should not exceed 30 W. The hardware set-up is accomplished through three steps by the construction of a laboratory prototype model, an engineering model and the final flight, space qualified model.

The activity has been mainly focused on the development of the following systems of the engineering model:

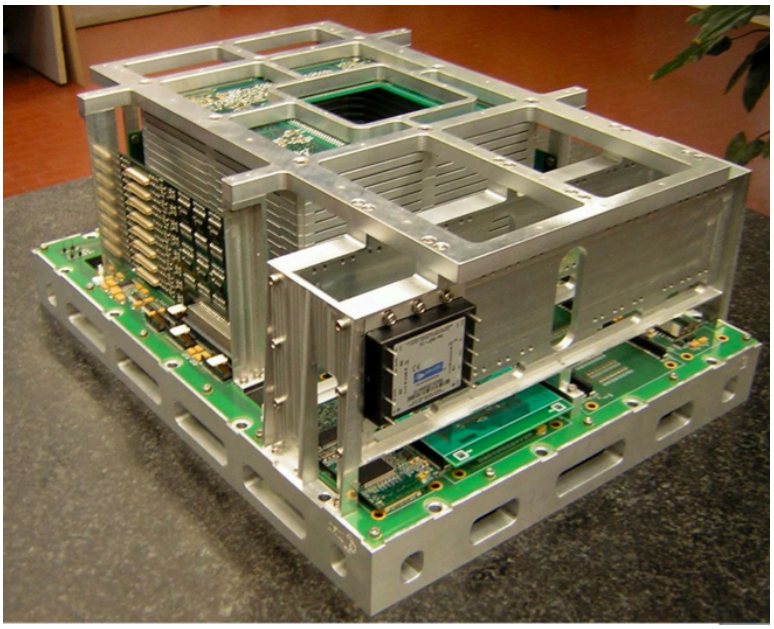

Figure 2: The SI-RAD detector.

- Trigger system.
- Development of Silicon Photomultiplier (SI-PM) technology for space applications and test of different SI-PM configurations.
- Completion and test of a highly integrated silicon board (16 cm x 16 cm).
- Production and test of a low-power, low-mass Digital Processing Unit (DPU).

For the year 2013, the planned activity includes the completion of the engineering unit and the set-up of the flight configuration equipped with autotrigger capabilities for heavy nuclei and a trigger for crossing protons and nuclei. The interface with the ISS Space Station will be realized with an intermediate CPU to manage the telecommands from ground and the download of the data. Beam tests at the LNF-BTF, GSI/Darmstadt and other facilities are also planned together with the continuation of the R&D on the SI-PM technology.

3 Activity of the LNF group

The LNF group has taken the responsibility of the design, construction and test of the mechanical structures and interfaces of the three models of the SI-RAD detector also contributing to the integration of the mechanical support for the DAQ. This activity is carried out with the support and the participation of the LNF Service for Design and Mechanical Costructions (SPCM). The activity in 2012 has been mainly devoted to the completion of the mechanical support of the engineering model and to the interfaces of the front-end and DAQ with the detector, ready to be tested on beams. These systems are being developed for the final space-qualified flight configuration. The LNF group participates as well in the beam test activities at the above mentioned facilities having the responsibility of the beam trigger counters and of the general arrangement and set-up.

Finally, the LNF is actively participating in the definition studies and first executive designs of CSES prototypes of the sensors for the measurement of the electric field and for the DAQ of the experiment.

4 Selection of recent publications

1. L. Di Fino *et al.*, "Heavy-Ion anisotropy measured by ALTEA in the International Space Station", Radiat. Res. **176**, 397 (2011).
2. M. Larosa *et al.*, "Ion rates in the International Space Station during the December 2006 Solar Particle Event", J. Phys. G. Nucl. Part.. **38**, 095102 (2011).
3. V. Zaconte *et al.*, "The radiation environment in the ISS-USLab measured by ALTEA", Adv. Sp. Res. **46**, 797 (2010).
4. V. Zaconte *et al.*, "High Energy Radiation fluences in the ISS-USLab: ion discrimination and particle abundances", Rad. Meas. **45**, 168 (2010).

References

1. V.Bidoli *et al.*,"In-flight performances of SilEye-2 Experiment and cosmic ray abundances inside space station MIR"; Journal of Physics G: Nuclear and Particle Physics **27**, 2051(2001).
2. M.Casolino *et al.*,"The Sileye/3-Alteino experiment on board the International Space Station"; Nucl.Phys. **113B**, 88 (2002).
3. V.Bidoli *et al.*, "Dual origin of light flashes in space", Nature **422**, 680 (2003).
4. L.Narici *et al.*,"ALTEA: Anomalous long term effects in astronauts. A probe on the influence of cosmic radiation and microgravity on the central nervous system during long flights", Adv. Space Res. **31**, 141 (2003).
5. F.Altamura *et al.*,"Preliminary results from the LAZIO-Sirad experiment on board the International Space Station", Proc. XXIX ICRC, Pune (2005), SH35 p.101.
6. G. Horneck, "Radiobiological experiments in space: a review", Nucl. Tracks Radiat. Meas., **20**, 185 (1992).

TPS

V. Patera (Resp.)

Not received

BY-NanoERA

(Institutional Development of Applied Nanoelectromagnetics: Belarus in ERA Widening)

S.Bellucci (Resp. INFN), R. Baldini (Tecn.), L. Coderoni (Bors.), G. Giannini (Ass. Ric.), F. Micciulla (Ass. Ric.), I. Sacco (Bors.)

External collaborating Institutions:

Institute of Nuclear Problems of Belarusian State University,
Institut fuer Festkoerperphysik, Technische Universitaet Berlin,
Central Laboratory of Physico-Chemical Mechanics, Bulgarian Academy of Sciences, Sofia,
Institute of Electronic Structure and Laser (IESL), Heraklion, Crete,
Belarusian Institute of System Analysis and Information Support of Scientific Technical Sphere,
Science & Technology Park “Metolit” at Belarusian National Technical University.

We participate as a partner (the INFN unit) to the Coordination and support actions of the FP7-INCO-2010-6. BY-NanoERA has a duration of 36 months and started its activities on 1st January 2011. The consortium binds together four Universities, two Research Organizations and an industry (Science & Technology Park).

Project objectives:

The main objectives of the project BY-NanoERA are to prove necessity and promising capability of nanoelectromagnetics in the core objective of FP7 Theme 4 'Nanosciences,Nanotechnologies, Materials and new Production Technologies – NMP' and to develop a concept of nanoelectromagnetics as a perspective direction in NMP. We also wish to establish network with research centers in Member States or Associated Countries in the field of applied nanoelectromagnetics aimed with the progress in solving concrete scientific problems and submission of joint research projects, as well as to organize a set of workshops and seminars on nanoelectromagnetics.

Publications by LNF Authors in the Year 2012

Paddubskaya, D. Bychanok, A. Plyushch, P. Kuzhir, A. Nemilentsau, S. Maksimenko, S. Bellucci, L. Coderoni, F. Micciulla, I. Sacco, G. Rinaldi, Epoxy Resin/SWCNT Shielding Paint for Super-High-Frequency Range, J. Nanoelectronics and Optoelectronics, 7(1), 81-86 (2012).

Pliushch A., Paddubskaya A., Kuzhir P., Maksimenko S., Coderoni L., Micciulla, F., Sacco I., Bellucci S., Nanocarbon modified epoxy resin and microwaves, Fullerenes, Nanotubes, and Carbon Nanostructures, 20 (4-7), 496-501, 2012, DOI: 10.1080/1536383X.2012.655666.

J. Macutkevic, D. Seliuta, G. Valusis, R. Adomavicius, P. Kuzhir, A. Paddubskaya, M. Shuba, S. Maksimenko, L. Coderoni, F. Micciulla, I. Sacco and S. Bellucci, Terahertz time domain spectroscopy

of epoxy resin composite with various carbon inclusions, Chemical Physics, Vol. 404, pp 129-135, 24 August 2012, DOI: 10.1016/J.CHEMPHYS.2012.02.002.

P. Kuzhir, A. Paddubskaya, M. Shuba, S. Maksimenko, A. Celzard, V. Fierro, G. Amaral-Labat, A. Pizzi, J. Macutkevic, G. Valusis, J. Banys, S. Bistarelli, M. Mastrucci, F. Micciulla, I. Sacco, S. Bellucci, Electromagnetic shielding efficiency in Ka-band: carbon foam versus epoxy/CNT composites, Journal of Nanophotonics, 6(1), 061715(18) 2012 DOI: 10.1117/1.JNP.6.061715.

P. Kuzhir, A. Paddubskaya, M. Shuba, S. Maksimenko, A. Celzard, V. Fierro, G. Amaral-Labat, A. Pizzi, J. Macutkevic, G. Valusis, J. Banys, S. Bistarelli, M. Mastrucci, F. Micciulla, I. Sacco, S. Bellucci, Electromagnetic shielding efficiency in Ka-band: carbon foam versus epoxy/CNT composites, Journal of Nanophotonics, 6(1), 061715(18) 2012 DOI: 10.1117/1.JNP.6.061715.

P. Kuzhir, A. Paddubskaya, M. Shuba, S. Maksimenko, A. Celzard, V. Fierro, G. Amaral-Labat, A. Pizzi, J. Macutkevic, G. Valusis, J. Banys, S. Bistarelli, M. Mastrucci, F. Micciulla, I. Sacco, S. Bellucci, Electromagnetic shielding efficiency in Ka-band: carbon foam versus epoxy/CNT composites, Journal of Nanophotonics, 6(1), 061715(18) 2012 DOI: 10.1117/1.JNP.6.061715.

List of Conference Talks by LNF Authors in the Year 2012

S. Bellucci, P.P. Kuzhir, S.A. Maksimenko, K.N. Lapko, V.A. Lomonosov, O.A. Ivashkevich, A.I. Lesnikovich, P.V. Sedyshev, V.N. Shvetsov, A.S. Kurilin, L. Sartinska, P. Silenko, G. Frolov, Yu. Solonin, New Materials for Neutron Shielding Based on Boron Enriched Unfired Phosphate Ceramics, International Conference Functional Materials and Nanotechnologies FMNT – 2012, Institute of Solid State Physics, University of Latvia, Riga, Latvia, April 17 - 20, 2012, Book of abstract , ww.fmnt.lu.lv

Kuzhir, P.P.; Maksimenko, S. A.; Paddubskaya, A. G.; Celzard, A.; Fierro, V.; Basso, M.-C.; Pizzi, A.; Macutkevic, J.; Valusis, G.; Ivanov, M.; Banys, J.; Bellucci,S., Highly porous conducting carbon foams for electromagnetic applications, International Symposium on Electromagnetic Compatibility EMC EUROPE 2012, September 17-21, 2012, Rome, Italy, http://www.emceurope2012.it/

P. Kuzhir, A. Paddubskaya, S. Maksimenko, A. Celzard, V. Fierro, G. Amaral-Labat, A. Pizzi, J. Macutkevic, G. Valusis, M. Ivanov, J. Banys, S. Bellucci, Highly porous conducting carbon foams for electromagnetic applications , ID: 162, International symposium EMC Europe 2012, Rome, Italy, 17-21 September, 2012

S. Bellucci, I. Sacco, F. Micciulla, P. Kuzhir, A. Paddubskaya, S. Maksimenko, A. Celzard, V. Fierro, Microwave probing of composites based on exfoliated graphite and nanocarbons, International workshop Nanoscience and nanotechnology 2012, NN2012, Frascati Italy October 1-4, 2012

DENSE

Development and Electromagnetic Characterization of Nano Structured Carbon Based Polymer CompositEs

S. Bellucci (Resp. INFN), R. Baldini (Tecn.), L. Coderoni (Bors.), G. Giannini (Ass. Ric.), F. Micciulla (Ass. Ric.), I. Sacco (Bors.)

External collaborating Institutions: Univ. Roma La Sapienza, Università degli Studi di SALERNO, Università degli Studi di PALERMO.

We participate as a partner (the INFN unit) to the PROGRAMMA DI RICERCA SCIENTIFICA DI RILEVANTE INTERESSE NAZIONALE (PRIN) of the Italian MINISTERO DELL'ISTRUZIONE DELL'UNIVERSITà E DELLA RICERCA DIREZIONE GENERALE DELLA RICERCA. DENSE has a duration of 36 months and started its activities on 1st January 2010. The consortium binds together three Universities (with four different Departments) and one Research Organization.

Project objectives:

The main objectives of the project DENSE are the realization and characterization of new multifunctional polymeric nanocomposites employing as nanofillers graphene and multiphase systems clay/Carbon Nanotubes (CNTs). Such nanocomposites, based on thermosetting (epoxy) resin are intended for industrial
applications, such as aeronautics, automotive, electronics, where remarkable thermal and mechanical properties and, at the same time, tailored and controlled electromagnetic (EM) performances are required. The design and realization of such nanocomposites will be performed from the tailoring of the electromagnetic performances.
In fact, although several interesting results had been obtained in the realization of new and improved nanocomposites, the researchers are still far from obtaining a precise control of the desired nanostructure and thus optimize the materials performances. To reach such a goal it is required to act on both the choice of the most appropriate nanofillers and the fabrication techniques. The present research proposal pursues both aspects, by deepening the knowledge of the basic chemical and physical mechanisms and enhancing the technological competences required for the production of nanocomposites based on graphene and multiphase clay/CNTs.
These nanocomposites are potentially very interesting for different industrial applications but, up to now, have not been intensively and accurately investigated.
An and extensive structural and morphological analysis will be carried out on nanofillers and nanocomposites in order to provide detailed information on nanostructures. These data will be correlated with the information obtained from an accurate characterization at both micro and macro scale concerning EM
properties (at low and high frequency), thermal and mechanical characteristics in order to improve the physical and numerical models adopted in materials analysis and design.
A further effort is aimed at the global optimization of the base materials properties (nanofillers and polymer) and parameters of the production process able to lead to the desired EM performances of the nanocomposites. Robust optimization techniques will be employed to overcome the drawbacks of the currently adopted approaches consisting in the choice of the best solution for each step of the production process parameters (local optimization) which generally may not lead to the

global optimum. The main objectives are pursued by a multidisciplinary research team composed by five Research Units which develop complementary and integrated research lines.

Relevant results achieved:

The activity carried out by INFN-LNF has concerned the mechanical and electrical characterization of nanocomposite materials, which were made using an epoxy resin (EPIKOTE 828) as matrix, loaded with different types of fillers such as carbon nanotubes, carbon black and graphite. Work has concerned the study of mechanical and electrical properties, carried out on epossidic nanostructured materials. The effects of concentration and dispersion's degree of carbon nanotubes (Cnts in short) on the tensile strength and electrical conductivity of the nanocomposites were studied. In order to realize these materials we used an epoxy resin (EPIKOTE 828) as matrix, which is a liquid of medium-low viscosity at room temperature and it is hardened by the curing reaction with polyamines. The curing agent, called A1 (specific gravity 1.02g/cm3 and viscosity 0.21Pa•s at 25ºC) is obtained from a common TEPA (tetraethylenepentamine) by reaction with formaldehyde (CH2O).This resin is loaded with different percentages of conductive nanofillers such as Cnts, synthesized with the arc discharge method. To check the efficiency of the coating, graphite and carbon black were taken as referencing fillers, on which both mechanical and electrical tests were carried out.
From a mechanical standpoint the analysis showed that:
- The mechanical properties of the matrix are not improved by fillers because they are short fibers (or amorphous).
- At equal concentrations, composites loaded with CNTs are substantially better than the ones loaded with carbon black and graphite.
From the electrical standpoint the analysis showed that:
- The electrical conductivity increases, with the increasing concentration of Cnts. This is probably because they are distributed randomly in such a way as to create a preferential path for current flow inside the matrix.
- At equal concentrations, composites loaded with Cnts have greater electrical conductivity than the ones loaded with carbon black and graphite.
In a second step, since the Cnts have showed values of electrical conductivity higher than the other fillers, we decided to compare them with commercial Swnts and Mwnts, synthesized with the CVD technique (Chemical Vapor Deposition). On the nanocomposites obtained using these fillers, electrical measurements and measurements of epsilon' and epsilon" in microwave range were carried out.
As regards DC electrical measurements, for low percentage Cnts loadings the obtained results seem to indicate that the method of synthesis by arc discharge yields better results than the growth of nanotubes with CVD technique. In this regard the samples were subjected to TEM and SEM micrographies, and the images showed how the Cnts of INFN (arc discharge) have less defects than commercial ones (CVD). Regarding higher concentration of fillers one can see that the values of resistivity of the matrix with INFN-Cnts and the one with Mwnts are comparable with each other, while the value of resistivity of the matrix with Swnts is approximately three orders of magnitude lower. Therefore, increasing the amount of nanotubes, a mechanism of percolation is activated, in which an interconnected network is formed (so we are beyond the percolation threshold).
Finally, as regards the measurements in microwave range, it was found that commercial Mwnts are more effective than Swnts for the realization of DC conductive composites. At the same time, using the same epoxy/Cnts composites in Ka-band (26-37 GHz), the results have shown that in 26-27 GHz both fillers have almost the same efficiency, although Swnts show slightly better results.

Publications by LNF Authors in the Year 2011

S. Bellucci, F. Micciulla, I. Sacco, L. Coderoni and G. Rinaldi, Electrical Properties and Electromagnetic Shielding Effectiveness of Carbon Based Epoxy Nanocomposites, Nanodevices and Nanomaterials for Ecological Security, NATO Science for Peace and Security Series B: Physics and Biophysics, 2012, Part 1, 115-123, DOI: 10.1007/978-94-007-4119-5_10.

A. Pliushch, A. Paddubskaya, P. Kuzhir, S. Maksimenko, L. Coderoni, F. Micciulla, I. Sacco, S. Bellucci, Nanocarbon Modified Epoxy Resin and Microwaves, Fullerenes, Nanotubes and Carbon Nanostructures, Volume 20, Issue 4-7, 2012, pages 496-501

J. Macutkevic, D. Seliuta, G. Valusis, R. Adomavicius, P. Kuzhir, A. Paddubskaya, M. Shuba, S. Maksimenko, L. Coderoni, F. Micciulla, I. Sacco, S. Bellucci, Terahertz time domain spectroscopy of epoxy resin composite with various carbon inclusions, Chemical Physics, Volume 404, 24 August 2012, Pages 129–135

Paddubskaya, A.; Bychanok, D.; Plyushch, A.; Kuzhir, P.; Nemilentsau, A.; Maksimenko, S.; Bellucci, S.; Coderoni, L.; Micciulla, F.; Sacco, I.; Rinaldi, G.; Macutkevic, J.; Seliuta, D.; Valusis, G.; Banys, J., Epoxy Resin/SWCNT Shielding Paint for Super-High-Frequency Range, Journal of Nanoelectronics and Optoelectronics, Volume 7, Number 1, January 2012 , pp. 81-86(6)

List of Conference Talks by LNF Authors in the Year 2011

S. Bellucci, “Epoxy-Nano-Carbon Coating for Shielding in Wide Frequency Range”, FM&NT 2012, April 17 – 20, Riga, LATVIA.

F. Micciulla, "New nanocomposites fillers obtained via Self-propagating High-Temperature Synthesis (SHS) method", 7th International Conference on NANOSTRUCTURED POLYMERS AND NANOCOMPOSITES April 24 – 27 Praga, Czech Republic

S. Bellucci, "Microwave probing of graphitic materials – filled composites", GRANADA'12, Graphene Nanoscience:
from Dirac Physics to Applications 9-13 September 2012, Granada, Spain.

S. Bellucci, "Atomistic simulations of defect containing tubular nanostructures", Fundamental and Applied NanoElectroMagnetics (FANEM), Belarusian State University, Minsk, Belarus, May 22-25, 2012

S. Bellucci, “Microwave probing of composites based on exfoliated graphite and nanocarbons”, Nanoscience & Nanotechnology 2012, Laboratori Nazionali di Frascati 1-4 October 2012.

DAΦNE

The DAΦNE Team

D. Alesini, M.E. Biagini, S. Bini (Ass.), M. Boscolo, B. Buonomo, G. O. Delle Monache, T. Demma (Art. 23), E. Di Pasquale (Art. 23), G. Di Pirro, A. Drago, L. Foggetta (Art. 23), O. Frasciello (Bors.), A. Gallo, A. Ghigo, S. Guiducci, C. Ligi, F. Marcellini, G. Mazzitelli, C. Milardi (Resp.), L. Pellegrino, R. Ricci, U. Rotundo, C. Sanelli, M. Serio, F. Sgamma, A. Stecchi, A. Stella, S. Tomassini, M. Zobov

The DAΦNE Technical Staff

G. Baldini, P. Baldini, A. Battisti, A. Beatrici, M. Belli, B. Bolli, L. Cacciotti, G. Ceccarelli, R. Ceccarelli, A. Cecchinelli, S. Ceravolo, P. Chimenti (Ass.), P. Ciuffetti, R. Clementi, O. Coiro, S. De Biase, M. De Giorgi, T. Di Domenico (Bors.), R. Di Raddo, G. Ermini, M.R. Ferrazza, G. Fontana, U. Frasacco, C. Fusco, F. Galletti, E. Gaspari, M. Giabbai, O. Giacinti, E. Grossi, F. Iungo, V. Lollo, M. Marchetti, C. Marini, S. Martelli (Art. 15), M. Martinelli, A. Mazzenga, C. Mencarelli, M. Monteduro, M. Paris, E. Passarelli, S. Pella, D. Pellegrini, G. Piermarini, S. Quaglia, M. Rondinelli, L.A. Rossi (Art. 15), M. Sardone, M. Scampati, G. Sensolini, R. Sorchetti, A. Sorgi, M. Sperati, A. Sprecacenere, S. Strabioli (Art. 15), R. Tonus, T. Tranquilli, M. Troiani, V. Valtriani, R. Zarlenga, A. Zolla

DAΦNE is an electron-positron Φ *meson factory* operating at Frascati since 1997. Factories are storage ring colliders designed to work at the energies of the meson resonances, where the production cross section peaks, to deliver a high rate of events to high resolution experiments.

The factory luminosity (the number of events per unit time produced by the reaction under investigation divided by its cross section weighted by the acceptance of the detector) is very high, about two orders of magnitudes larger than that obtained at the same energy in colliders of the previous generation. One of the key-points to get a substantial luminosity increase is the use of separated vacuum chambers for the two beams merging only in the interaction regions (IRs). When sharing the same ring the two N-bunch trains cross in $2N$ points and the maximum luminosity is limited by the electromagnetic beam-beam interaction. The unwanted effects of this interaction can be reduced with a very strong focussing (called "low-β") at the interaction point (IP), obtained by means of quadrupole doublets or triplets. However these magnetic structures take up much space and excite chromatic aberrations which must be corrected elsewhere in the ring.

This limitation does not hold for the double ring option, consisting in two separate rings crossing at two low-β points. The number of bunches that can be stored in such a collider is limited only by the geometry of the IR's.

DAΦNE is an accelerator complex consisting of a double-ring collider, a linear accelerator (LINAC), an intermediate damping ring to make injection easier and faster and 180 m of transfer lines connecting these machines. The beam accelerated by the Linac can also be switched into a laboratory called "Beam Test Facility (BTF)", for dedicated experiments and calibration of detectors. Three synchrotron radiation lines, two from bending dipoles and the other from the wiggler are routinely operated by the DAΦNE-LIGHT group in a parasitic mode, providing photons from the infrared to soft x-rays.

1 Injection System

In a low energy electron-positron collider, such as DAΦNE, the lifetime of the stored current is mainly limited by the Touschek effect, namely the particle loss due to the scattering of the particles inside the bunches. In the present typical operating conditions the Touschek lifetime is below 1000 s. It is therefore necessary to have a powerful injection system, capable of refilling the beam without dumping the already stored one. In addition, flexibility of operation requires that any bunch pattern can be stored among the 120 available buckets. The injection system of DAΦNE is therefore designed to deliver a large rate of particles in a single bunch at the working energy of the collider. It consists of a linear accelerator with a total accelerating voltage of 800 MV. In the positron mode, electrons are accelerated to $\approx$ 250 MeV before hitting a tungsten target (called positron converter) where positrons are generated by bremsstrahlung and pair production with an efficiency of $\approx$ 1%. The positrons exit from the target with an energy of few MeV and are then accelerated by the second section of the LINAC to their final energy of $\approx$ 0.51 GeV. The positrons are then driven along a transfer line and injected into a small storage ring, called Accumulator, at frequency of 50 Hz. Up to 15 positron pulses are stacked into a single bucket of the Accumulator, then injection stops and the bunch damps down to its equilibrium beam size and energy spread, which are much smaller than the LINAC ones. Damping takes $\approx$ 0.1 s and then the beam is extracted from the Accumulator and injected into the positron main ring at an overall repetition rate of 2 Hz. A powerful and flexible timing system allows the storage of any desired bunch pattern in the collider. In the electron mode, a magnetic chicane deviates the particle trajectory around the positron converter and electrons are directly accelerated to 0.51 GeV and injected into the Accumulator in the opposite direction with respect to positron operation. They are then extracted like in the positron case and injected into the electron main ring through the second transfer line.

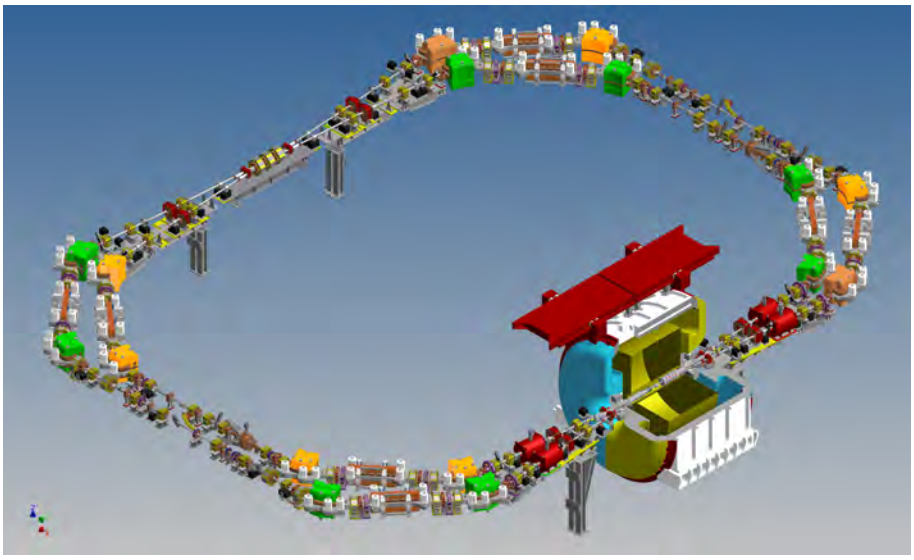

Figure 1: *The DAΦNE Main Rings in the present crab-waist scheme for the KLOE-2 run.*

The Accumulator ring has been introduced in the accelerator complex to increase the injection efficiency, especially for the positrons that are produced by the LINAC at 50 Hz rate in 10 ns pulses with a charge of $\approx$ 0.5 nC. Since the design charge of the main ring at the maximum luminosity is $\approx$ 1.5 μC and the longitudinal acceptance of the main rings is only 2 ns, the number of 50 Hz pulses necessary to fill the ring is of the order of 10^4. In order to avoid saturation it is

therefore necessary that at each injection pulse a fraction smaller than 10^{-4} of the already stored beam is lost, and this is not easy to achieve. The Accumulator instead works with a lower frequency RF cavity and therefore with a larger longitudinal acceptance. In this way the full charge coming from the LINAC can be stored in a single RF bucket. In a complete injection cycle, that has a duration of 500 ms, up to 15 LINAC pulses can be stored in a single Accumulator RF bucket, and after being damped to the ring equilibrium emittances and energy spread, the whole stacked charge can be stored into a single RF bucket of the main ring. In this way the nominal single bunch charge can be stored with only one pulse from the Accumulator, reducing to 120 the number of injection pulses (at 2 Hz) into each main ring. As an additional benefit, the transverse beam size and energy spread of the beam coming from the Accumulator are at least one order of magnitude smaller than those of the LINAC beam, and this strongly reduces the aperture requirements of the main ring and, as a consequence, the overall cost of the collider.

2 Main Rings

In the DAΦNE collider the two beam trajectories cross at the interaction point (IP) with an horizontal angle that has been recently increased from ≈ 25 mrad to ≈ 50 mrad. A positron bunch leaving the IP after crossing an electron one will reach the following electron bunch at a distance of half the longitudinal separation between bunches from the IP.

Due to the horizontal angle between the trajectories of the two beams, the distance in the horizontal direction between the two bunches is equal to the horizontal angle times half the longitudinal distance between the bunches in each beam. The beam-beam interaction can be harmful to the beam stability even if the distance in the horizontal direction between bunches of opposite charge is of the order of few bunch widths at points where the β function is high and this sets a lower limit on the bunch longitudinal separation and therefore on the number of bunches which can be stored in the collider. However, the so called *crab waist collision scheme* (CW) recently implemented in the machine alleviates this problem, as it will be exhaustively explained in the following of this report.

By design the minimum bunch separation at DAΦNE has been set to ≈ 80 cm, and the maximum number of bunches that can be stored in each ring is 120. This number determines the frequency of the radiofrequency cavity which restore at each turn the energy lost in synchrotron radiation, which must be 120 times the ring revolution frequency. The luminosity of the collider can therefore be up to 120 times larger than that obtainable in a single ring with the same size and optical functions. Crossing at an angle could in principle be a limitation to the maximum single bunch luminosity. In order to make the beam-beam interaction less sensitive to this parameter and similar to the case of single ring colliders where the bunches cross head-on, the shape of the bunches at the IP is made very flat (typical ranges of r.m.s. sizes are $15 \div 30$ mm in the longitudinal direction, $0.2 \div 1.5$ mm in the horizontal and $2.5 \div 10$ μm in the vertical one). The double ring scheme with many bunches has also some relevant challenges: the total current in the ring reaches extremely high values (5 A in the DAΦNE design, $\approx$ 1.4 A in the DAΦNE operation so far) and the high power emitted as synchrotron radiation needs to be absorbed by a complicated structure of vacuum chambers and pumping systems in order to reach the very low residual gas pressure levels necessary to avoid beam loss. In addition, the number of possible oscillation modes of the beam increases with the number of bunches, calling for sophisticated bunch-to-bunch feedback systems.

The double annular structure of the DAΦNE collider as it is now after the recent modifications to implement the crab waist scheme (described in the following sections) with KLOE is shown schematically in Fig. 1. Both rings lay in the same horizontal plane and each one consists of a

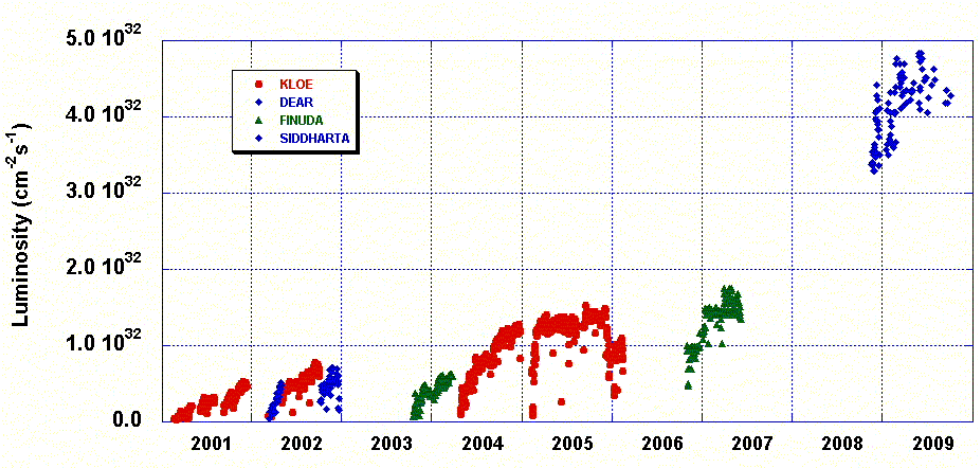

Figure 2: *Peak luminosity at DAΦNE.*

long external arc and a short internal one. Starting from the IP the two beams share the same vacuum chamber while traveling in a common permanent magnet defocusing quadrupole (QD) which, due to the beam off-axis trajectory increases the deflection of the two beam trajectories to ≈ 75 mrad. Shortly after the QD, the common vacuum chamber splits in two separated ones connected to the vacuum chambers of the long and short arcs. Two individual permanent magnet quadrupoles (QFs) are placed just after the chamber separation. Together with the previous QD they constitute the low-β doublets focusing the beams in the IP. The long and short arcs consist of two "almost achromatic" sections (deflecting the beam by ≈ 85.4 degrees in the short arc and ≈ 94.6 degrees in the long one) similar to those frequently used in synchrotron radiation sources, with a long straight section in between. Each section includes two dipoles, three quadrupoles, two sextupoles and a wiggler. This structure is used for the first time in an electron-positron collider and it has been designed to let DAΦNE deal with high current beams.

The amount of synchrotron radiation power emitted in the wigglers is the same as in the bending magnets and the wigglers can be used to change the transverse size of the beams. The increase of emitted power doubles the damping rates for betatron and synchrotron oscillations, thus making the beam dynamics more stable, while the possibility of changing the beam sizes makes the beam-beam interaction parameters more flexible.

The straight section in the long arc houses the kickers used to store into the rings the bunches coming from the injection system, while in the short straight arc there are the radiofrequency cavity and the equipment for the feedback systems which are used to damp longitudinal and transverse instabilities. The vacuum chambers of the arcs have been designed to stand the nominal level of radiation power emitted by the beams (up to 50 KW per ring). They consist of 10 m long aluminum structures built in a single piece: its cross section exhibits a central region around the beam and two external ones, called the antechambers, connected to the central one by means of a narrow slot. In this way the synchrotron radiation hits the vacuum chamber walls far from the beam and the desorbed gas particles can be easily pumped away. The chambers contain water cooled copper absorbers placed where the radiation flux is maximum: each absorber has a sputter ion pump below and a titanium sublimation pump above. The Main Rings have undergone many readjustments during the years to optimize the collider performances while operating for different detectors.

In principle the rings could host two experiments in parallel, but only one at a time has been

operated so far. Three detectors, KLOE, DEAR and FINUDA, have taken data until 2007 and logged a total integrated luminosity of ≈ 4.4 fb^{-1} with a peak luminosity of $\approx 1.6 \cdot 10^{32}$ cm^{-2} s^{-1} and a maximum daily integrated luminosity of ≈ 10 pb^{-1}.

KLOE has been in place on the first IP from 1999 to 2006, while DEAR and FINUDA have alternatively run on the second one. The detectors of KLOE and FINUDA are surrounded by large superconducting solenoid magnets for the momentum analysis of the decay particles and their magnetic fields represent a strong perturbation on the beam dynamics. This perturbation tends to induce an effect called "beam coupling", consisting in the transfer of the betatron oscillations from the horizontal plane to the vertical one. If the coupling is not properly corrected, it would give a significant increase of the vertical beam size and a corresponding reduction of luminosity. For this reason two superconducting anti-solenoid magnets are placed on both sides of the detector with half its field integral and opposite sign, in this way the overall field integral in the IR vanishes.

The rotation of the beam transverse plane is compensated by rotating the quadrupoles in the low-β section. In the case of KLOE the low-β at the IP was originally designed with two quadrupole triplets built with permanent magnets, to provide high field quality and to left room to the detector. The structure of the FINUDA IR is quite similar to the KLOE one. Since its superconducting solenoid magnet has half the length (but twice the field) of the KLOE one, the low-β focusing at the IP was obtained by means of two permanent magnet quadrupole doublets inside the detector and completed with two other conventional doublets outside.

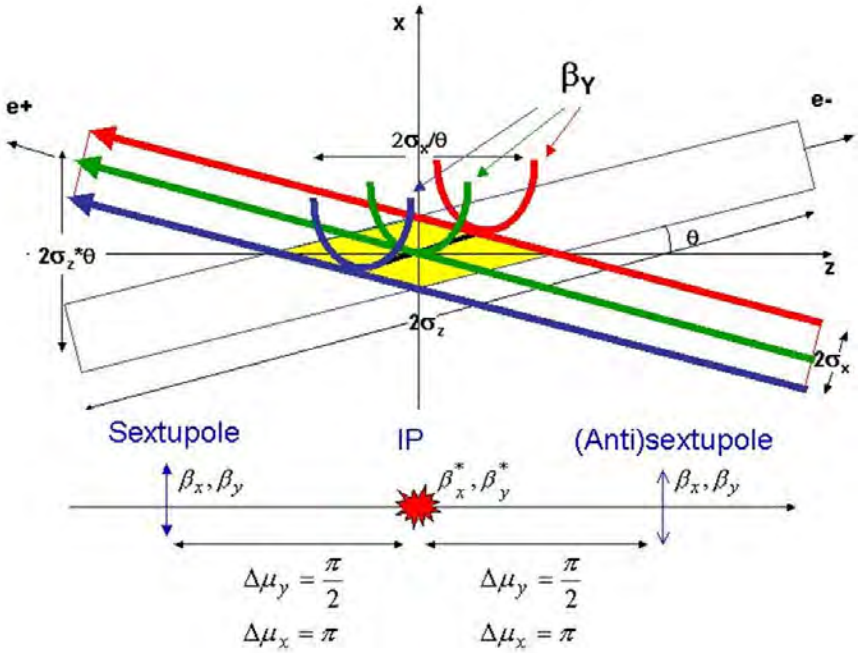

Figure 3: *Crab waist scheme*

The DEAR experiment, which was installed on the IR opposite to KLOE, took data during the years 2002-2003. It does not need magnetic field and therefore only conventional quadrupoles were used for the low-β. FINUDA rolled-in at DEAR's place in the second half of 2003 and took data until spring 2004. It was then removed from IP2 in order to run the KLOE experiment with only one low-β section at IP1, and rolled-in back in 2006 for a second data taking run ended in June 2007. After that the detector has been rolled-out again, and presently there are no detectors

installed in IR2. The two chambers are vertically separated so that the two beams do not suffer from parasitic interactions in the whole IR2. A summary of the peak luminosity during these runs is shown in Fig. 2.

3 The large Piwinski angle and crab waist collision scheme at DAΦNE

In standard high luminosity colliders the key requirements to increase the luminosity are: very small vertical beta function β_y at the IP, high beam intensity I, the small vertical emittance ϵ_y and large horizontal beam size σ_x and horizontal emittance ϵ_x required to minimize beam-beam effects. The minimum value of β_y is set by the bunch length to avoid the detrimental effect on the luminosity caused by the hour-glass effect. It is very difficult to shorten the bunch in a high current ring without exciting instabilities. Moreover, high current implies high beam power losses, beam instabilities and a remarkable enhancement of the wall-plug power. In the CW scheme of beam-beam collisions a substantial luminosity increase can be achieved without bunch length reduction and with moderate beam currents. For collisions under a crossing angle θ the luminosity L and the horizontal ξ_x and vertical ξ_y tune shifts scale as:

$$L \propto \frac{N\xi_y}{\beta_y} \propto \frac{1}{\sqrt{\beta_y}} \tag{1}$$

$$\xi_y \propto \frac{N\sqrt{\beta_y}}{\sigma_z\theta}; \tag{2}$$

$$\xi_x \propto \frac{N}{(\sigma_z\theta)^2} \tag{3}$$

The Piwinski angle ϕ is a collision parameter defined as:

$$\phi = \frac{\sigma_z}{\sigma_x}\tan\left(\frac{\theta}{2}\right) \approx \frac{\sigma_z}{\sigma_x}\frac{\theta}{2} \tag{4}$$

with N being the number of particles per bunch. Here we consider the case of flat beams, small horizontal crossing angle $\theta << 1$ and large Piwinski angle $\phi >> 1$. In the large Piwinski angle and Crab Waist scheme described here, the Piwinski angle is increased by decreasing the horizontal beam size and increasing the crossing angle. In such a case, if it were possible to increase N proportionally to $\sigma_z\theta$, the vertical tune shift ξ_y would remain constant, while the luminosity would grow proportionally to $\sigma_z\theta$. Moreover, the horizontal tune shift ξ_x would drop like $1/\sigma_z\theta$. However, the most important effect is that the overlap area of the colliding bunches is reduced, as it is proportional to σ_x/θ (see Fig. 3). Then, the vertical beta function β_y can be made comparable to the overlap area size (i.e. much smaller than the bunch length):

$$\beta_y \approx \sigma_x/\theta << \sigma_z \tag{5}$$

We get several advantages in this case:

- Small spot size at the IP, i.e. higher luminosity L.
- Reduction of the vertical tune shift ξ_y with synchrotron oscillation amplitude.
- Suppression of synchrobetatron resonances.

Table 1: DAΦNE Beam parameters for KLOE (2006) and SIDDHARTA (2008-2009)

PARAMETERS	KLOE Run	SIDDHARTA Run
L [cm^{-2}s^{-1}]	$1.5 \cdot 10^{32}$	$4.5 \cdot 10^{32}$
N_{part}/bunch	$2.65 \cdot 10^{10}$	$2.65 \cdot 10^{10}$
I_{bunch} [mA]	13	13
ϵ_x [10^{-9} m $\cdot$ rad]	340	260
ϵ_y [10^{-9} m $\cdot$ rad]	1.5	1
σ_x [μm]	760	200
σ_y [μm]	5.4	3.5
σ_z [mm]	25	17
β_x^* [m]	1.7	0.25
β_y^* [mm]	17	9
θ [mrad]	2×12.5	2×25

There are also additional advantages in such a collision scheme: there is no need to decrease the bunch length to increase the luminosity as proposed in standard upgrade plans for B- and Φ-factories. This will certainly help solving the problems of HOM heating, coherent synchrotron radiation of short bunches, excessive power consumption etc. Moreover, parasitic collisions (PC) become negligible since with higher crossing angle and smaller horizontal beam size the beam separation at the PC is large in terms of σ_x.

However, large Piwinski angle itself introduces new beam-beam resonances which may strongly limit the maximum achievable tune shifts. At this point the crab waist transformation enters the game boosting the luminosity, mainly because of the suppression of betatron (and synchro-betatron) resonances arising (in collisions without CW) through the vertical motion modulation by the horizontal oscillations. The CW vertical beta function rotation is provided by sextupole magnets placed on both sides of the IP in phase with the IP in the horizontal plane and at $\pi/2$ in the vertical one (see Fig. 3).

For comparison, the parameters used during the last DAΦNE run with the KLOE detector (2005-2006) are shown in Table 1. As discussed above, in order to realize the CW scheme in DAΦNE, the Piwinski angle ϕ should be increased and the beam collision area reduced: this is achieved by increasing the crossing angle θ by a factor 2 and reducing the horizontal beam size σ_x. In this scheme the horizontal emittance ϵ_x is reduced by a factor 1.5, and the horizontal beta function β_x lowered from 1.5 to 0.2 m. Since the beam collision length decreases proportionally to σ_x/θ, the vertical beta function β_y can be also reduced by a factor 3, from 1.8 cm to 0.6 cm. All other parameters are similar to those already achieved at DAΦNE.

4 Hardware upgrades for the Crab Waist test at DAΦNE with the SIDDHARTA run

DAΦNE has been upgraded to allow the CW collision scheme test with the SIDDHARTA run during the summer shutdown of 2007.

The major upgrades on the machine are summarized as:

- new IR1 geometry for the CW test;
- new IR2 geometry with two completely separated vacuum chambers with half moon profile;
- new shielded bellows;

- the four e^+ e^- transverse feedbacks have been upgraded;
- solenoid windings in the two long IRs sections of the e^+ ring;
- new calorimeter for luminosity measurement and tuning;
- new longitudinal position of the two IRs horizontal collimators;
- new injection kickers.

The need of a new IR geometry is essentially due to have a very small β_y (9 mm) and a large crossing angle (25 mrad per beam). Splitter magnets installed in the original design have been removed thanks to the large crossing angle in the CW scheme. Defocusing and focusing quadrupoles (QD, QF) on both sides of the IP have been placed to obtain the required low-β structure. Further trajectory separation is provided by two small dipole correctors upstream and downstream the quadrupole doublets, while other three quadrupoles are used to match the betatron functions in the arcs.

The low-β section quadrupoles near the IP are of permanent magnet (PM) type. The QDs are located near the IP where the beams share a common vacuum chamber, while the QFs are positioned where the chambers are splitted and each one acts on a single beam. Therefore a total of two QDs and four QFs is required to get the two doublets around IP1. Four corrector dipoles provide a deflection of 9.5 mrad to match the inlet and outlet arc chamber flanges.

CW sextupoles are placed at ~ 9.3 m far from the IP1. Bending dipoles facing the IRs have been rotated and their field adjusted according to requirements. They have been powered with independent supplies to match these requirements.

For the SIDDHARTA experiment a new aluminium alloy (AL6082T6) chamber with two thin windows (0.3 mm 0.02 thickness) in the top and bottom sides has been designed and built.

Electromagnetic simulations have shown the presence of trapped modes which add resonant contributions to the beam coupling impedance in the Y-chamber junctions, the regions where the two separate ring pipes merge in the common vacuum chamber near the IP. In the worst possible scenario, that occurs when a beam spectrum line at a frequency equal to a multiple to the bunch repetition rate is in full coupling, the joule loss does not exceed 200 W. To keep this effect under control the Y-chambers have been equipped with cooling pipes.

This additional cooling circuit allows to remove the beam induced HOM heating and, if necessary, to reduce it by detuning the mode frequencies with respect to the dangerous beam spectrum lines.

A new design of the central IR2 beam pipe has been implemented, the two vacuum chambers are completely separated and their cross section has an half moon profile.

The main Bhabha monitor consists of a 4-modules sandwich calorimeter, made of lead and scintillator. Four modules of calorimeters surround the final permanent quadrupole magnets, located at a distance of 32.5 cm on both sides of the IR, as shown in Fig. **??**. They cover an acceptance of $18 \div 27$ degrees in polar angle, and are segmented in azimuthal angle in five sectors, 30 degrees wide.

Two gamma monitor detectors are located 170 cm away from the IR, collecting the photons radiated by electron or positron beam. The detectors are now made of four PbW04 crystals (squared section of 30×30 mm^2 and 110 mm high) assembled together along z, in order to have a 30 mm face towards the photon beam, and a total depth of 120 mm corresponding to about 13 X_0. Thanks to the high rate, those detectors are mainly used as a fast feedback for the optimization of machine luminosity versus background, since the relative contribution of background is changing with the machine conditions. A total systematic uncertainty on the luminosity measurement of 11% can be estimated.

Table 2: DAΦNE luminosity performances with the CW scheme and low-β parameters compared to the KLOE and FUNUDA runs. SIDDHARTA data taking does not profit of the fast injection rate system, that would increase $L_{\int logged}$.

	SIDDHARTA March 08 ÷ Nov 09	KLOE May 04 ÷ Nov 05	FINUDA Nov 06 ÷ Jun 07
L_{peak} [cm^{-2}s^{-1}]	4.5	1.5	1.6
$L^{MAX}_{\int day}$ [pb^{-1}]	15.24	9.8	9.4
$L^{MAX}_{\int hour}$ [pb^{-1}]	1.033	0.44	0.5
$I^{-\ MAX}_{coll}$ [A]	1.4	1.4	1.5
$I^{+\ MAX}_{coll}$ [A]	1	1.2	1.1
$n_{bunches}$	105	111	106
$L_{\int logged}$ [fb^{-1}]	2.9	2.0	0.966
β^*_x [m]	0.25	1.5	2.0
β^*_y [m]	0.009	0.018	0.019
ϵ_x [10^{-6} m·rad]	0.25	0.34	0.34
ξ_y	0.0443	0.025	0.029

5 Luminosity achievements during the SIDDHARTA run

The commissioning of the upgraded machine started in November 2007. At the end of the year the ring vacuum was almost recovered, the beams were stored in the upgraded rings, all the sub-systems went quickly to regime operation.

The first collisions in the CW scheme have been obtained in February 2008, with the first experimental confirmation of the potentiality of the new configuration in terms of specific luminosity growth and reduction of the beam-beam detrimental effects.

DAΦNE luminosity as a function of the colliding bunches compared to past runs is reported in Fig. 4. Blue and red dots refer to the two KLOE runs, with the initial triplet low-β IR quadrupoles and with the new IR doublet, respectively. Yellow dots refer to the FINUDA run; in green is the luminosity with the CW scheme. The gain provided by the new IR gets higher with the products of the currents and the difference with respect to collisions with the crab sextupoles off can reach 50%. During 2009 the peak luminosity has been progressively improved by tuning the collider and increasing the beam currents; the maximum value achieved is $\approx 4.5 \cdot 10^{32}$ cm^{-2}s^{-1} measured in several runs with good luminosity to background ratio. The present peak luminosity is close to the nominal one predicted by numerical simulations. The highest single bunch luminosity achieved is $\approx 5 \cdot 10^{30}$ cm^{-2}s^{-1} measured with 20 bunches in collisions instead of the usual 105. The single bunch specific luminosity, defined as the single bunch luminosity divided by the product of the single bunch currents, at low currents exceed by 4 times the best value measured during the past DAΦNE runs (present values are red and blue dots in Fig. 5). It gradually decreases with colliding beam currents, as can be seen in Fig. 5. This reduction can be only partially explained by the growing beam size blow up due to the beam-beam interaction. Another factor comes from the fact that in the large Piwinski angle regime the luminosity decreases with the bunch length, which in turn is affected by the ring coupling impedance. The impact of the Crab-Waist sextupoles can be recognized comparing runs taken with CW sextupoles on and off (Fig. 5). At low current the

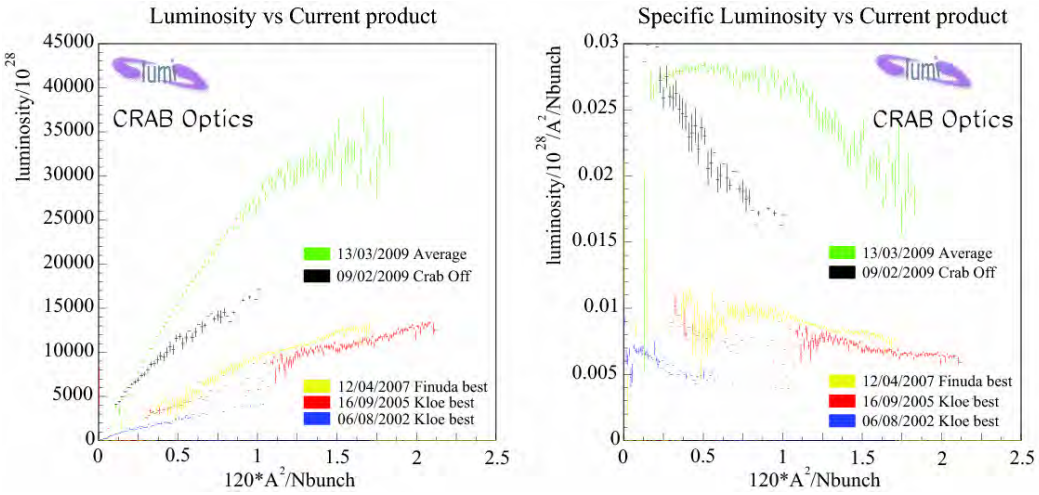

Figure 4: *Comparison of the upgraded DAΦNE perfomance (green) with respect to the results during previuos KLOE (blue, red) and FINUDA runs (yellow).*

luminosity is the same in the two cases and higher than the one measured with the original collision scheme. As the product of the stored currents exceed 0.3 A, the luminosity with CW sextupoles off becomes lower and a corresponding transverse beam size blow up and beam lifetime reduction are observed as a consequence of the uncompensated beam-beam resonances. The convolved vertical beam size at the IP in collision has been measured by means of a beam-beam scan technique. The measured Σy of 5.6 μm is compatible with the value obtained by using the coupling value ($k = 0.7\%$) as measured at the Synchrotron Light Monitor (SLM), being the single vertical beam size at the IP1 of the order of 4 μm.

Fig. 6 reports another proof of the crab sextupoles effectiveness, where the positrons transverse beam profile measured at the synchrotron light monitor with crab sextupoles OFF (left plot) and with crab sextupoles ON (right plot) is shown. The measurement refers to collision in a strong-weak regime (1 A electrons beam current against 0.1 A of positrons beam current): it is evident that the transverse beam size is smaller and its shape remains Gaussian during collision with the sextupoles ON.

The crab waist sextupoles proved to be of great importance for the collider luminosity increase, since much lower luminosity is achieved with crab sextupoles off, with a larger blow up and a sharp lifetime reduction is observed for single bunch currents greater than 8-10 mA. This is in agreement with beam-beam simulations taking into account the DAΦNE nonlinear lattice. The results achieved at DAΦNE have pushed several accelerator teams to study and consider the implementation of this scheme on their machines. Besides, the physics and the accelerator communities are discussing a new project of a Super B-factory with luminosity as high as 10^{36} cm^{-2}s^{-1}, i.e. by about two orders of magnitude higher with respect to that achieved at the existing B-factories at SLAC and KEK.

6 Hardware modifications for the KLOE-2 run

During 2009 the new interaction region design for KLOE has been completed and several components of the new hardware have been acquired. In beginning 2010 the KLOE detector has been

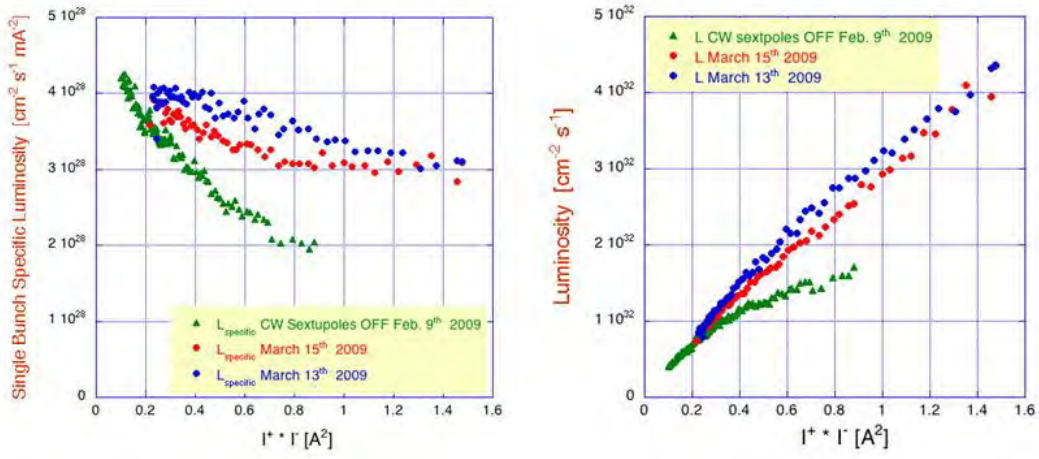

Figure 5: *Single bunch specific luminosity (left) and luminosity (right) versus the product of the colliding currents for two of the best run and for the crab waist sextupoles off.*

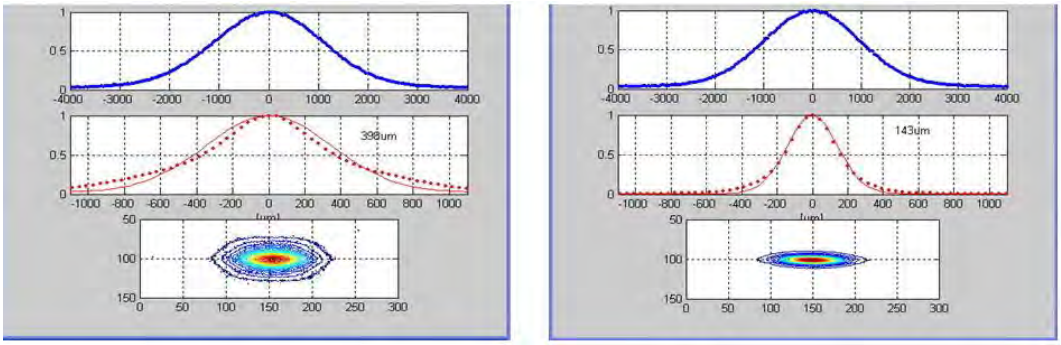

Figure 6: *Transverse positron beam profile as measured at SLM with crab sextupoles off (left) and crab sextupoles on (right) for beams in collisions (103 bunches).*

rolled in on IR1.

The new IR magnetic layout, sketched in Fig. 7, has been designed in order to maximize the beam stay clear letting the beam trajectory pass as much as possible through the center of the magnetic elements. The field integral introduced by the solenoidal detector is almost cancelled by means of two anti-solenoids, installed symmetrically with respect to the IP in each ring, which provide compensation also for off-energy particles. Due to the larger crossing angle, the vertical displacement of the beam in the IR is about an order of magnitude larger than in the last KLOE run. To keep the beam vertical trajectory within reasonable values, two permanent magnet dipoles (PMD) have been added just after the first permanent magnet horizontally focusing quadrupole, inside the detector magnetic field, in each one of the four IR branches (see Fig. 7). The PMDs are based on a modular design in view of a possible KLOE-2 run at a lower solenoidal field. Since the two beams are vertically deflected in opposite directions by the KLOE solenoid, they provide a horizontal magnetic field directed towards the center of the ring in the positron ring and towards the outside in the electron one. Four new skew quadrupoles have been added on the IR, just outside the KLOE magnet, to provide fine tuning for the coupling compensation.

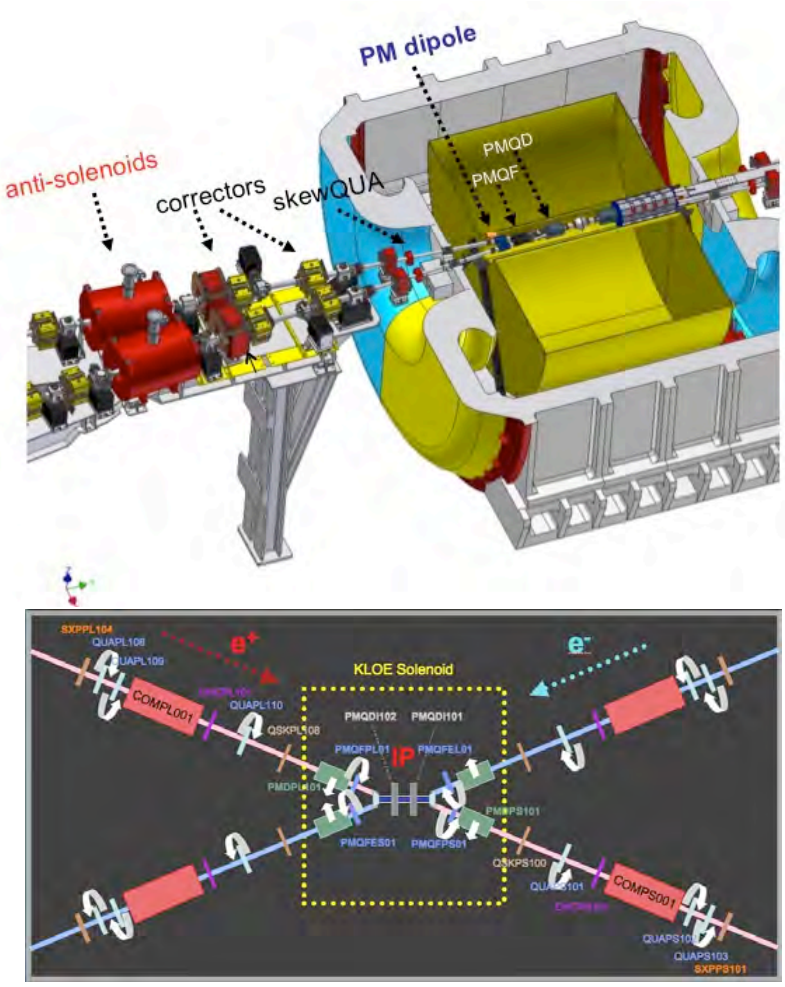

Figure 7: *(Top) The KLOE-2 detector and the new DAΦNE Interaction Region 1. (Bottom) Schematic drawing of the DAΦNE Interaction Region 1 magnetic layout.*

The shimmed plates added on the wiggler poles in 2004 have been removed and the poles displaced alternately in the horizontal direction by ±8 mm with respect to the wiggler axis in order to keep the beam trajectory as much as possible centered with respect to the pole axes. Due to the reduction of the gap and of the overall length of the magnetic circuit, this new configuration allows to reach, at a current of 450 A, a magnetic field still higher than that achieved at 550 A in the previous configuration with shimmed plates inserted. A further improvement has been obtained by powering in series all the 7 poles of the wigglers, while before each couple of terminal poles was powered independently. This has been obtained by short-circuiting one out of the five windings in the terminal poles coils and correcting the field integral in each wiggler below 1 Gm by tuning the end pole clamps aperture. In this way eight power supplies are no more necessary and the cycling procedure at startup is much more reliable. All the DAΦNE wigglers have been removed, modified and measured.

New stripline electrodes have been designed and inserted in the wiggler and dipole vacuum chambers of the positron ring. These electrodes, powered by DC voltages, counteract the parasitic

electron cloud formation, which helps in increasing the positron beam current threshold.

The exhausted LINAC gun cathode has been replaced with a new one.

The modifications on the machine for the KLOE-2 run have been completed at the beginning of May. At the end of June the KLOE magnet has been partially warmed-up to allow the installation of the anti-solenoids cryogenic transfer lines. Since then, and up to mid November, several problems at the cryogenic plant and its ancillary systems occurred, preventing the KLOE solenoid energization. In September a magnetic setup without the KLOE magnet, but using the anti-solenoids, has been found to allow the DAΦNE beam conditioning. Up to about 1 A of positrons has been stored in the main ring with this optics, while the electron current was limited to ≈ 0.1 A due to ion trapping. On November 16th, the KLOE magnet was cooled and energized and beam conditioning in the nominal configuration was started with currents around 0.8 A stored at the same time in both rings, with half circumference filled in each one to avoid beam-beam interactions.

The first phase of the main ring commissioning has been done with the KLOE detector off. The lack of focusing from the solenoid has a strong impact on the ring optics, which had to be deeply modified. In November all the six DAΦNE bunch-by-bunch feedback systems have been upgraded to new software and hardware versions. The two (electron and positron) longitudinal feedbacks have been completely replaced with new ones, with the goal to have more compact systems with updated hardware components and new software programs compatible with the currently used operating system. These efforts are motivated also by reaching lower noise in detecting and better performance in damping the beam longitudinal oscillations. The vertical feedback systems have been equipped with 12-bit AD and DA converters in place of the 8-bit old units to reduce the quantization noise impact in the system gain. The positron ring horizontal feedback power has been doubled (1 kW now) providing about 40% increase in the kick strength. Furthermore, the horizontal feedback kicker has been replaced with a device with a double length stripline and reduced plate separation, providing larger shunt impedance at the low frequency typical of the positron horizontal unstable modes. The kicker has been also moved in a position with a higher horizontal β value.

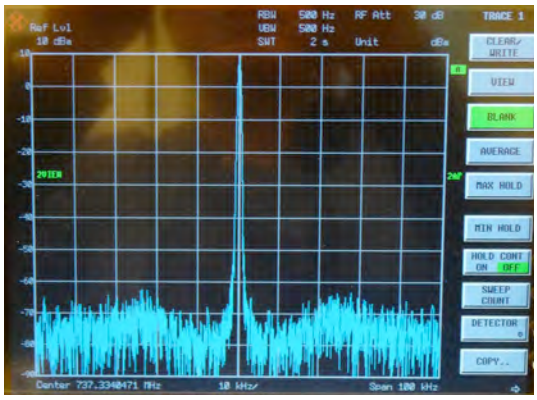

Figure 8: *Beam spectrum snapshot.*

7 DAΦNE commissioning for the KLOE-2 run

DAΦNE upgrade for the KLOE-2 run has been completed in July 2010. KLOE cool-down started on the second half of April 2010, however several problems involving the cryo-plant prevented to

energize the detector till October 25^{th}.
From November 2010 until June 2011 there have been several faults involving:

- injection septum of the positron ring;
- linac gun cathode and D modulator of the injection system;
- cooling system of the KLOE magnet power supply;
- vertical orbit oscillation in both rings.

These faults slowed down the commissioning and caused two major unscheduled shut-down periods. On January 11^{th} the 34 degrees injection septum of the positron ring got permanently damaged due to a water leakage together with a fault in the alarm system. Since no spare part was available it has been impossible to store the positron beam for three months. However, the accident had a positive drawback: the new septum coil has been optimized by reducing the coil gap and changing the geometrical dimension of the conductor, thus achieving a 50% reduction in the wall plug power with respect to the original device.
The cooling system of the KLOE magnet power supply experienced a faulty behaviour (from February 20^{th} to March 30^{th}), which has been linked, eventually, to the internal oxidation of the cooling circuit, that has been fixed in two weeks.

The Linac had several problems concerning the D modulator system, essential for positron production and the gun cathode, which required several replacements till to run out of spare parts by mid-May. This circumstance forced the last, and more relevant, unscheduled shut-down four months long.

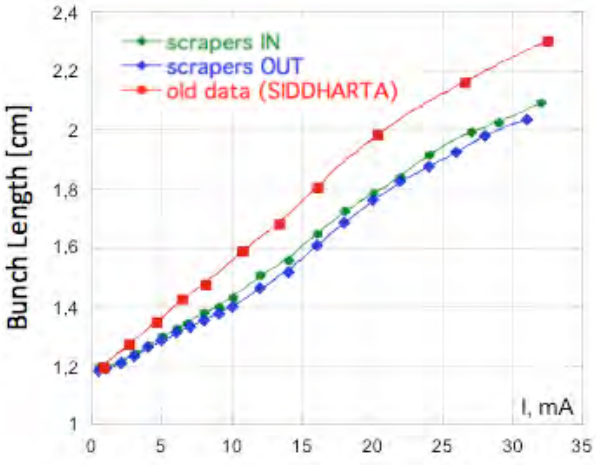

Figure 9: *Bunch length measurements in the electron ring.*

Suspending the DAΦNE activity gave a useful opportunity to start an extensive program of maintenance and consolidation involving almost all the collider subsystems.
It is the case of the test and replacement activities involving several Linac components such as: radio frequency loads in the gun area, modulators with their high power units, buncher phase shifter, diagnostic tools and cathode test station.
Concerning magnetic elements: all the four 34 degrees septa have been replaced and four correctors in the IR replaced with devices having better field quality.

About mechanics and layout many vibration measurements have been done in the Interaction Region area to sort out the source of the vertical oscillation observed, on both beams. Measurement analysis indicated how to consolidate the Interaction Region supports halving the vertical oscillation.

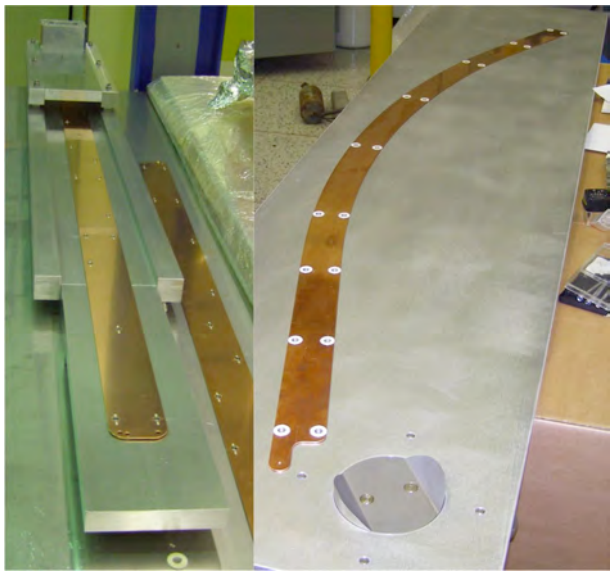

Figure 10: *Pictures of the electrodes inserted in the chambers of the dipole (on the right) and in the wiggler (left picture).*

Alignment has been revised in several sections of the main rings relying on beam measurement analysis.
The cryogenic plant has been maintained with a standard cleaning procedure.
Concerning controls: the fluid plant low-level interface has been upgraded and front-end controls for several class of elements have been ported to new more performing processors.
A lot has been done to reduce and optimize the demand for electric power. In fact the electric power necessary to run DAΦNE is $\approx 3.34\ MW$ now, which is $\approx 2.56\ MW$ lower than during the last KLOE run with a consequent reduction of $\approx 2.0\ Meuros$ on the electric bill due for a 200 days long run.

Although the collider uptime has been very limited, especially for the positron ring, some relevant work has been done to test the upgraded systems and to tune the Main Rings optics.

As for all circular colliders, the DAΦNE beam longitudinal dynamics is very much affected by the Low Level Radio-Frequency (LLRF) control. In particular, the dynamics of the beam barycentre motion (the coupled bunch zero-mode) is very sensitive to the large RF cavity detuning required to compensate the reactive beam loading, which is particularly huge at DAΦNE where the operating conditions are characterized by relatively low accelerating gradients ($\approx$ 200 kV) e large stored currents (up to 2 A). For this reason a fully analog RF feedback loop has been added to the LLRF system and commissioned on both e^+ and e^- rings, resulting in a drastic limitation of the synchrotron zero-mode coherent frequency shift that have affected the operation of the collider in the past. The measured beam spectrum around the RF 2^{nd} harmonics is shown in Fig. 8, where the sidebands of the longitudinal barycentre motion appear much lower and broader compared to what we observed in the past before the feedback implementation. The efficiency of the RF system

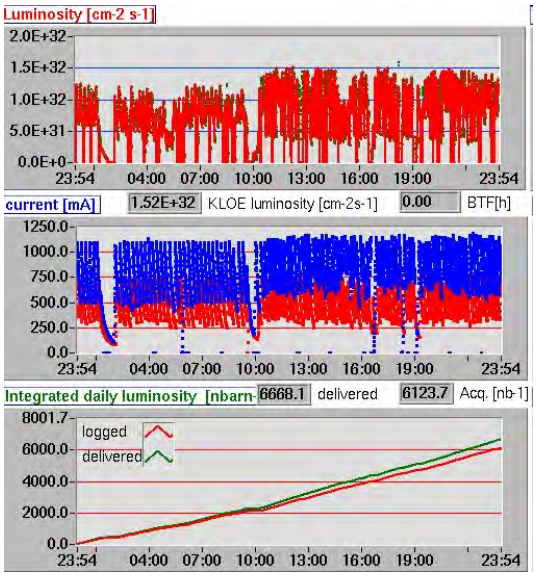

Figure 11: *(Top) Luminosity, (Middle) beam currents, (Low) Integrated luminosity for the best day, Dec.* 17^{th} *2011.*

has been also increased since no extra cavity detuning is necessary with direct RF feedback in operation. The RF systems of both rings are now operating reliably in the new configuration.

The ring impedance has been estimated relying on bunch length measurements as a function of bunch current. Numerical fits based on potential well as well as microwave regime converge to a ring coupling impedance of 0.3Ω; it was 0.4Ω during the previous run (see Fig. 9).

One of the main limitations in the maximum stored current of the positron ring has been identified in previous runs, in a horizontal instability due to the electron cloud effect. To mitigate such instability, metallic -copper- electrodes have been inserted in all dipoles and wigglers chambers of the machine and have been connected to external dc voltage generators in order to absorb the photo-electrons. With a dc voltage of about 200 V applied to each electrode we expect a reduction of such density by two orders of magnitude that will contribute to reduce substantially the source of the instability. The pictures of the electrodes inserted in the dipole and wiggler chambers are shown in Fig. 10.

The dipole electrodes have a length of 1.4 or 1.6 m depending on the considered arc (short or long), while the wiggler ones are 1.4 m long. They have 50 mm width, 1.5 mm thickness and their distance from the chamber is about 0.5 mm. This distance is guaranteed by special ceramic supports made in SHAPAL and distributed along the electrodes. This ceramic material is also thermo-conducting in order to partially dissipate the power released by the beam to the electrode through the vacuum chamber. Moreover, the supports have been designed to minimize their beam coupling impedance as well as to sustain the strip. First experimental measurements on the electrodes effectiveness in mitigating the electron cloud effects in the positron beam are very encouraging.

The new configuration of the wiggler magnets, based on shifted poles has proved to be effective in reducing the non-linear terms in the magnetic field (B) . The field quality has been tested by measuring the beam tune shift induced by a horizontal closed orbit bump at the wiggler place. This bump, including the two dipoles adjacent to the wiggler, slightly changes the ring energy: this effect has been carefully compensated tuning the frequency of the RF cavity. The orbit position at the wiggler centre has been obtained by averaging the readout from two beam position monitors

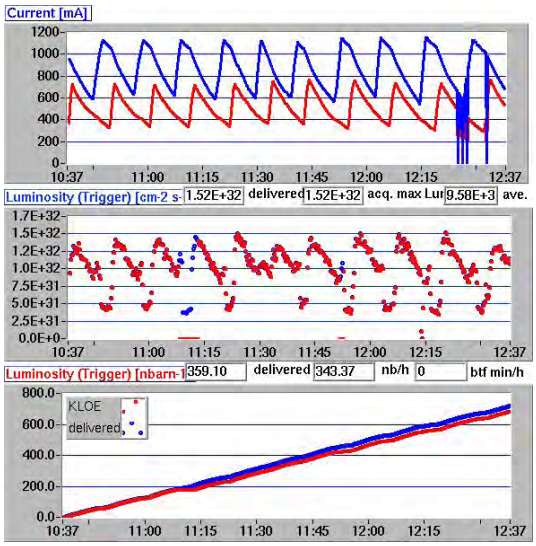

Figure 12: *Best two hours for KLOE-2 run.*

(BPM) placed at the magnet end side. For large values of the bump the BPMs non-linearity have been taken into account and properly corrected. The measured horizontal and vertical tune shifts exhibit a clear linear behaviour.

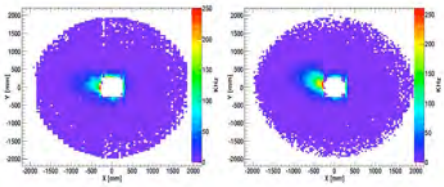

Figure 13: *Transverse profile of the backward EmC rates. Left and right plots are data and MC, respectively.*

The lattice for the KLOE-2 run with the crab-waist scheme has been optimized and matched to the real beams, relying on optics measurements (beta functions, dispersion, chromaticity, coupling, betatron tunes). The lowest value of the betatron coupling that has been measured is as small as 0.14% with a $\sigma_y = 75\mu m$ at the syncrotron light monitor. The vertical beam-beam luminosity scan showed that vertical orbit oscillation does not affect beam size at the IP, $\sigma_y = 3\mu m$ has been measured at IP. The new configuration of the wiggler magnets, based on shifted poles has proved to be effective in reducing the non-linear terms in the magnetic field. Luminosity is still not at nominal value due to different reasons, however beam-beam is not a limiting factor, and crab-waist sextupoles work well, as expected.

The luminosity has been optimized by storing 100 bunches in collision at low current. The single bunch specific luminosity at low currents is of the order of about $\approx 4.5 \cdot 28$ cm^{-2} s^{-1}, the same as the one measured during the crab-waist test without the detector solenoid. The DAΦNE performances at the end of December 2011 reproduced the best ones obtained during the previous KLOE run. In fact, up to now the maximum peak luminosity is $1.52 \cdot 10^{32}$ cm^{-2} s^{-1}, obtained on December 17^{th} 2011, with $I^- = 0.93$ A and $I^+ = 0.719$ A stored in 100 bunches. This value can

be compared to the same luminosity $1.53 \cdot 10^{32}$ cm^{-2} s^{-1} with $I^- = 1.4$ A and $I^+ = 1.2$ A with 111 bunches, achieved during the KLOE run in 2005. The same day (December 17^{th}) has been also the best day in terms of daily integrated luminosity (see Fig. 11).

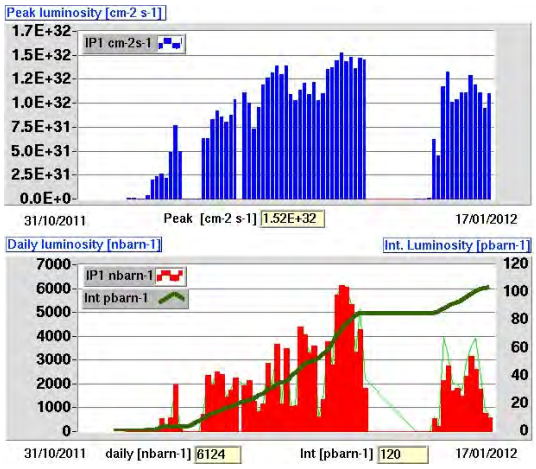

Figure 14: *Summary of current and luminosity during year 2011.*

The plot with the highest luminosity per hour is shown in Fig. 12. The best hourly integrated luminosity is 0.359 pb^{-1}, which might provide 8.62 pb^{-1} per day.

However, an efficient data taking requires not only high luminosity but also background rates induced in the detector as low as possible.

The two collimators mostly effective are the one upstream the IR and the one just after the old IP2, as predicted also by numerical simulations. The beam stay clear at these two collimators has been reduced to intercept Touschek scattered particles that would be lost at the IR. They proved to be very much effective in reducing background showers. However, after careful orbit optimization and collimator tuning, an additional lead shielding 1 cm thick has been added around the inner layer (QCAL) of the KLOE-2 detector to prevent background contamination in the physics events without reducing the detector acceptance. A full Monte Carlo (MC) simulation that allows a direct comparison between the expected and measured background rates at the KLOE electromagnetic calorimeter (EmC) has been developed in the new KLOE-2 configuration. The data/MC background rates are in agreement within a factor of two in the different regions of the KLOE EmC and the main features of the shapes are well reproduced (see Fig. 13). A good agreement for the Touschek lifetime is found between measured and calculated lifetime with scrapers inserted at the experimental set. On the contrary, the comparison without scrapers shows a disagreement of about a factor 1.9, which might be explained by a misalignment of the on-energy beam orbit that induced beam scraping in the IP2 section. This allows us to expect some margins of optimization, especially by correcting orbit and dynamic aperture.

The summary of current and luminosity during year 2011 is shown in Fig. 14. In order to push the collider performances in terms of luminosity, multibunches and high current operation must be consolidated and improved by tuning the working points in the two rings, the coupling at the IP for the two beams, the non-linear beam dynamics and, last but not least, beam-beam interaction. Background has been improved especially at high current and mainly for the positron ring. Dedicated studies may help to optimize the collimator configuration and to understand the possibility to introduce additional shieldings between the beam pipe and the detector.

8 DAΦNE setup and data taking tests with the KLOE-2 detector

DAΦNE activity in year 2012 has been aimed at completing the machine commissioning and at starting the detector data taking. However the machine operation has been seriously slowed down by several technical problems and faults that outlined a clear need for planning a radical consolidation program involving the whole accelerator complex.

On mid January a sudden rise, more than 90 ℃, occurred in the temperature of the beam pipe inside the detector, which was compatible with the lack of electrical continuity in the bellows of the section common for the two beams. It occurred close by the low-β defocusing quadrupole installed at the incoming side of the electron beam. In order to avoid a rather long machine shut-down, an attempt has be done to fix the problem by pushing the two halves of the IR from outside the detector, thus achieving a considerable reduction of the temperature variation in the range $25 \div 55$ ℃. This excursion, albeit reduced, has been causing sudden and unpredictable variation in the vertical tune and non-reproducibility in the betatron function measurements. In fact the low-β QDs are permanent magnet made by a SmCo alloy and experience a rather relevant variation in the gradient with the temperature of the order of ~ 0.0004 m^{-2} ℃$^{-1}$.

Many faults affected the cooling system causing also water leakages in the wiggler magnets of the electron ring, which, in turn, required several not simple soldering interventions to fix holes and to replace two end poles coils.

In the first months of the year in spite of the considerable downtime several encouraging results have been obtained in terms of luminosity. The maximum values achieved for peak, hourly and daily integrated luminosity have been: $L_{peak} = 1.53 \times 10^{32}$ (with colliding currents $I^- = 840$ mA and $I^+ = 810$ mA stored in 100 bunches), $L_{\int 1hour} = 0.350$ pb^{-1} and $L_{\int day} = 7$ pb^{-1}. The specific luminosity, at low current, exceeded by more than a factor of 2 the best value measured during the KLOE run in 2005 (see Fig. 15).

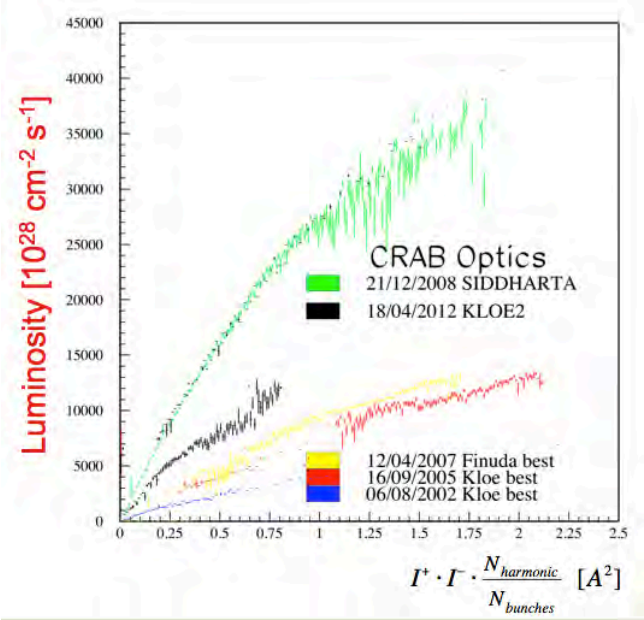

Figure 15: *Luminosity versus the product of the colliding currents normalized to the number of colliding bunches. Data refer to runs acquired before (bottom) and after (top) implementing the Crab-Waist scheme.*

DAΦNE is the first collider operating routinely with long electrodes, for e-cloud mitigation, installed in all dipole and wigglers vacuum chambers. These electrodes not only permitted a more stable operation with the positron beam, but have also allowed unique measurements such as e-cloud instabilities growth rate, transverse beam size variation, and tune shifts along the bunch train, demonstrating their effectiveness in mitigating the e-cloud induced effects. All measurements have been done with positive voltage polarity. The power supplies connected to the electrodes absorb electrons from the cloud. Betatron tune measurements taken by a spectrum analyzer have shown an average tune shift, especially in the horizontal plane, when switching off the electrodes. For this reasons a more sophisticated analysis has been done using the front-end data of the bunch-by-bunch feedbacks, which can measure the tune-shift for each bunch in the train [1)]. The results are presented in Fig. 16.

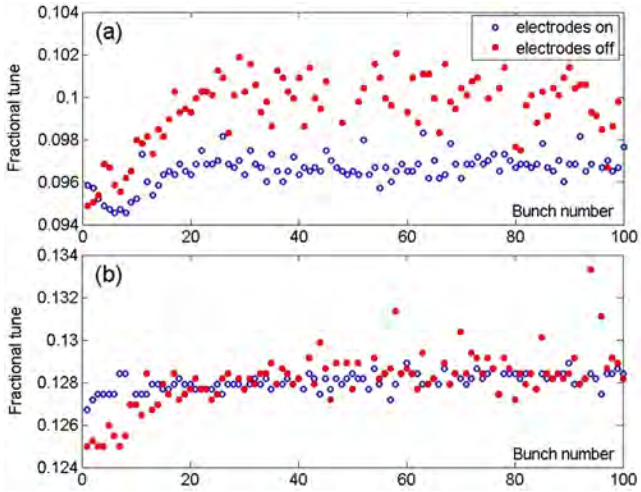

Figure 16: *Bunch by bunch measurements of horizontal (a) and vertical (b) fractional tunes for a positron current of the order of* $\sim$ *500 mA.*

When the electrodes are off horizontal tunes show a typical modulation along the train induced by the e-cloud density variation. The measured values increase progressively and reach a steady state regime after $\sim$ 20 bunches. The head-tail tune spread is about $0.006 - 0.008$. Switching the electrodes on the tune shift reduces by a factor of 2-3, but still the tune spread is not completely cancelled. This is likely due to the fact that the electrodes in the wigglers cover only 67% of the total magnet length. On the contrary the vertical tune spread is notably smaller and the electrodes almost completely cancel it.

A clear effect due to the single bunch e-cloud instability has been detected measuring the vertical beam size at the synchrotron light monitor by gradually turning off the electrodes. The observed beam size increases from about 110 μm with electrodes on, to more than 145 μm with the electrodes off. The e-cloud plasma can interact with RF waves transmitted in the vacuum chamber changing the phase velocity of the waves. The e-cloud changes the electromagnetic properties of vacuum, which can induce a shift of the resonant frequencies modes trapped in the chamber. In principle, from these shifts it is possible to evaluate the e-cloud density. Resonant TE-like modes are trapped in the DAΦNE arcs and can be excited through button pickups. A first measurement of these resonant modes has been done at DAΦNE for several beam currents with the electrodes on and off [2)]. A preliminary analysis of the data has given the following results: (a) all modes have a positive frequency shift with the positron beam current and it is between 100 and 400 kHz

depending on the modes taken into account; (b) switching on the electrodes the frequency shift can be partially cancelled for almost all modes; (c) the quality factor of the modes decreases with positron current.

The power supplies connected to the electrodes absorb cloud electrons. The current delivered by the generator has been measured as a function of the generator voltage for different beam currents. The result is given in Fig. 17.

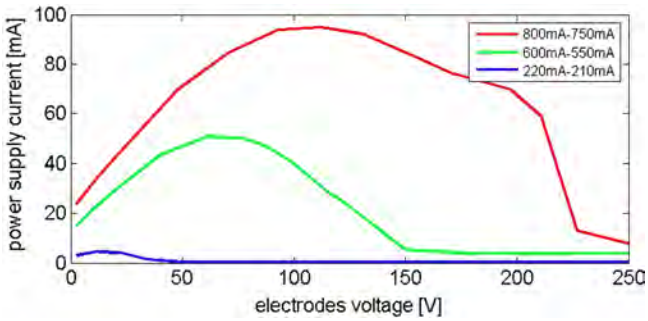

Figure 17: *Current supplied by the DC generator as a function of the applied voltage and beam current; the e-cloud is completely adsorbed when* $I = 0$.

Relying on numerical predictions, confirmed by measurement, it was evident that, in order to store positron beam currents higher than 1 A, voltages of the order of 250 V (presently available) are no longer adequate to completely absorb and suppress the e-cloud in DAΦNE.

Since the effectiveness of the e-cloud suppression does not depend on the voltage polarity it is preferable using negative voltages in order to avoid damages, caused by electron bombardment of the electrodes, and power supply overcurrent.

On July a medium intensity earthquake caused a relevant misalignment in the IR vanishing large part of the achievements obtained during the previous part of the commissioning: luminosity reduced dramatically and, in the positron ring, even beam injection was problematic. These circumstances forced an anticipated summer shutdown which has been exploited to undertake several activities. The detector end-caps have been opened to measure and restore the nominal position of the low-β elements. The electromagnetic quadrupoles in the IR have been checked too.

An endoscopic inspection of the low-β vacuum chamber confirmed the presence of broken bellows at the place where the temperature rise had been observed. However that component has not been replaced because the operation required the disassembly of the whole IR. An additional air-flow based cooling system has been installed in the IR to stabilize the temperature level. The functionality of the low-level system supervisor, based on old components no longer in production, has been restored by using part from another broken equipment.

Concerning the experimental detector, a half cylinder pure carbon target has been inserted inside the detector drift chamber to study the kaon-nuclei interaction process by using the KLOE-2 apparatus. This study, in fact, can lead to interesting scientific results by acquiring a rather modest data sample of the order of ~ 100 pb^{-1}, for this reason it was quite compatible with the preliminary tests needed before the main KLOE-2 data taking.

DAΦNE operation restarted on mid September. The optics of the two rings has been refined as well as the alignment of electromagnetic quadrupoles in the IR and the Crab-Waist sestupoles by using beam based alignment techniques.

In less than three months performances in terms of peak luminosity have been recovered, $L_{peak} = 1.44\times10^{32}$ m^{-2} s^{-1}, while hourly and daily integrated luminosity had even some improvements achieving the values: $L_{\int 1hour} = 0.415$ pb^{-1} (Fig. 18) and $L_{\int day}$ 8 pb^{-1} respectively

(Fig. 19).

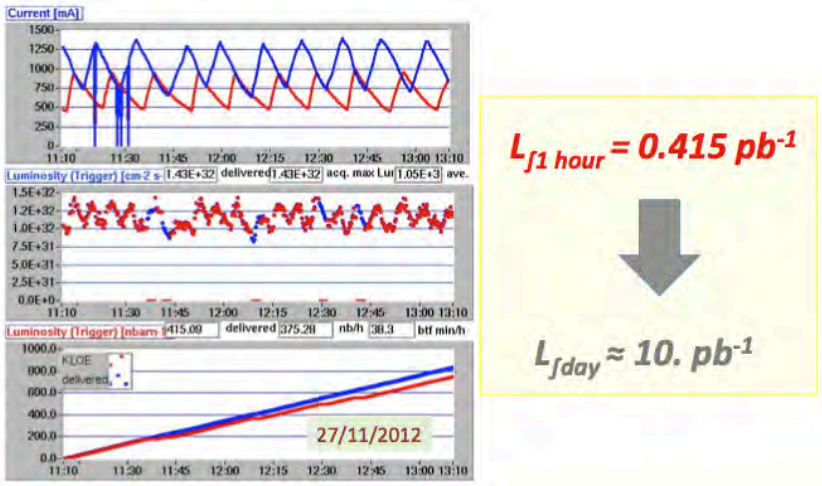

Figure 18: *Best hourly integrated luminosity.*

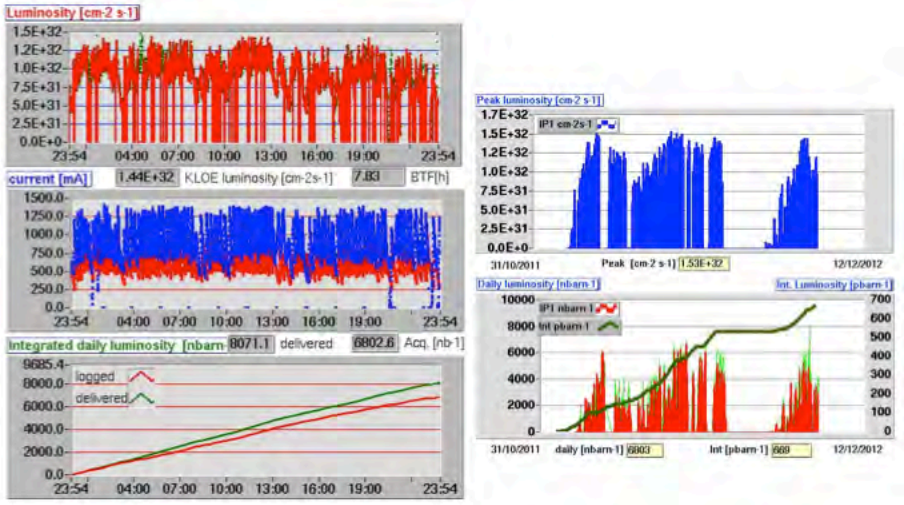

Figure 19: *Best daily run (left), peak luminosity (right top), daily integrated luminosity (right bottom).*

By the end of the year two important tests have been done concerning the effectiveness of the Crab-Waist sextupoles in presence of a strong solenoidal field introduced by the detector, and the maximum achievable luminosity putting 10 bunches in collision.

All the tests concerning the Crab-Waist sestupoles have been done in collision. A clear increase in the transverse vertical dimension of the electron beam, σ_y^-, has been observed as the Crab-Waist sextupoles strength is reduced in the corresponding ring, see Fig. 20; at the same time σ_y^+ decreases as a consequence of the reduced beam-beam kick.

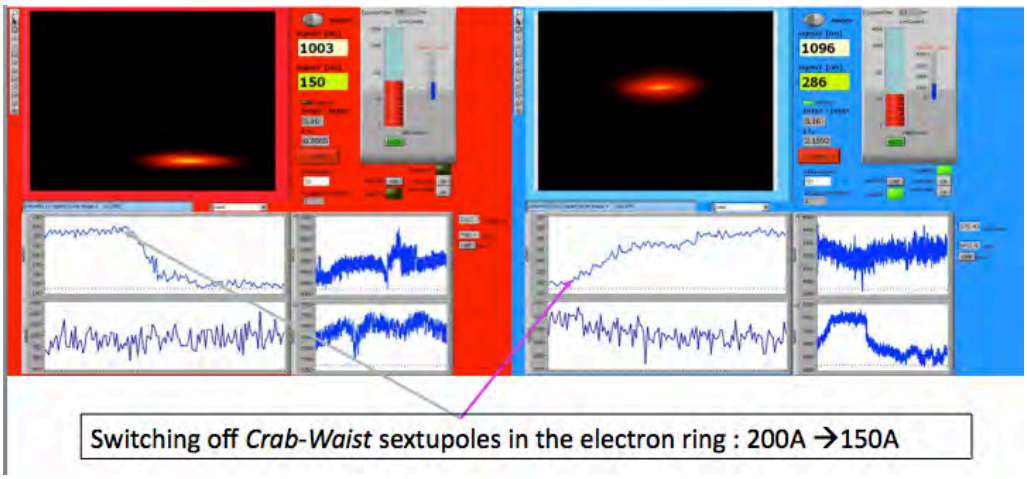

Figure 20: *Vertical beam dimension of the colliding beams as Crab-Waist sextupoles are switched off in the electron ring.*

A consistent behavior is observed when the Crab-Waist sextupoles are progressively turned off in both rings, see Fig. 21. In this case the transverse vertical beam dimensions become larger for both beams.

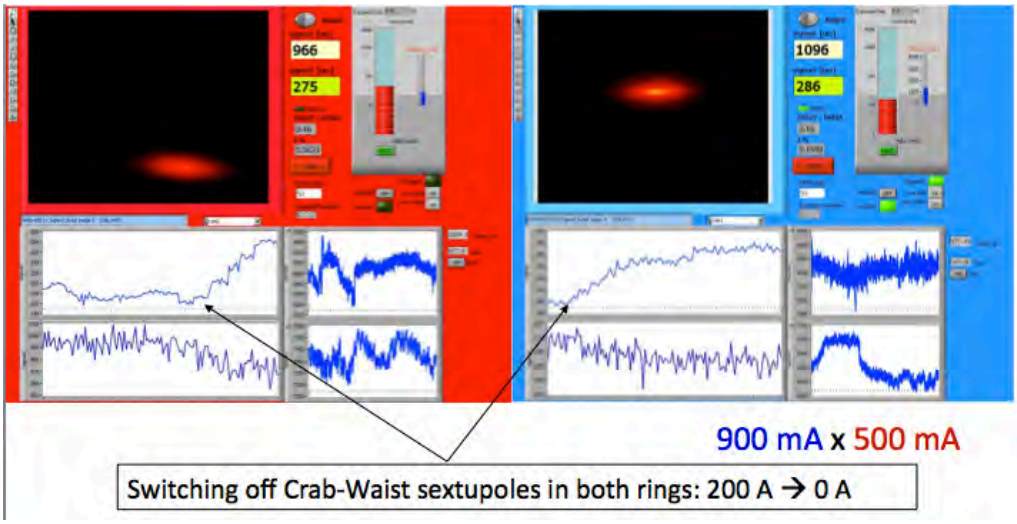

Figure 21: *Vertical beam dimension of the colliding beams as Crab-Waist sextupoles are switched off in both rings.*

Data from the machine γ-monitor and from the detector, see Fig. 22, point out an evident reduction in the luminosity when the Crab-Waist sextupoles are off. These observations all together give a clear evidence about the Crab-Waist sextupoles capability in keeping under control the coupling resonances due to collision with large horizontal crossing angle even in presence of a large detector having a strong solenoidal field.

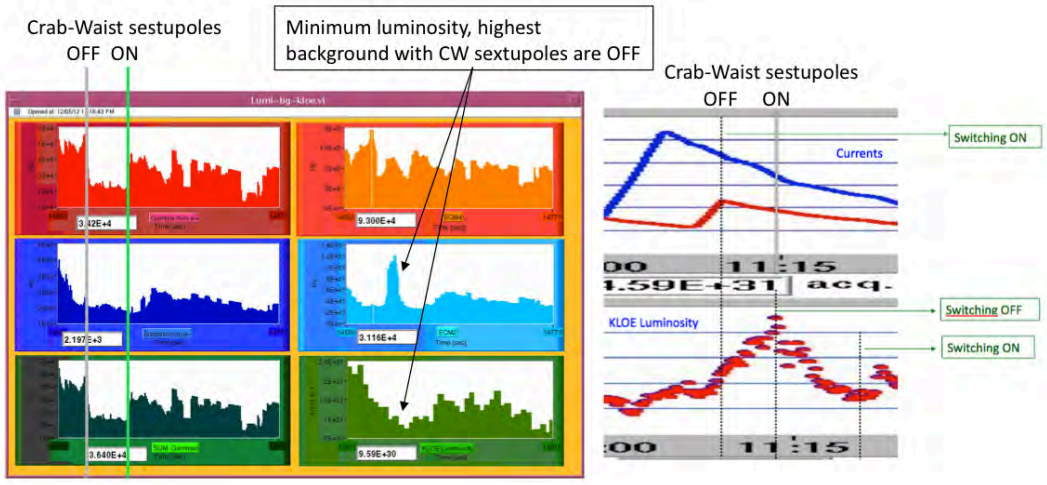

Figure 22: *luminosity evolution as measured from the DAΦNE γ-monitor (left) and from the KLOE detector (right), while switching on the Crab-Waist sestupoles in both rings.*

Collisions with 10 consecutive bunches permit to measure the maximum achievable luminosity independently from the effects introduced by multi-bunch operations. The maximum value obtained by now in this configuration with the KLOE-2 optics has been 2.19×10^{31} cm^{-2} s^{-1}, which devises the possibility to achieve a peak luminosity of the order of $\sim 2.5 \times 10^{32}$ cm^{-2} s^{-1} by optimizing 110 bunches operations. This test has been also relevant in showing that the present limit in the measured peak luminosity does not depend on the beam-beam or on the Crab-Waist collision scheme.

By beginning of November, contextually with the machine studies, the data taking activity has started. This phase has been quite relevant to optimize the collider background, to improve adiabatically the collisions as well as to deliver to the KLOE-2 detector the 100 pb^{-1} integrated luminosity required for the experiment with the carbon target.

Consolidation Plan

The DAΦNE accelerator complex has been working for more than 15 years. Recent operation experience has clearly shown that an extraordinary consolidation effort is required in order to provide a 80% uptime in the next years and secure a reliable data taking for the KLOE-2 experiment. A brainstorming on DAΦNE refurbishment started on past spring, stemming from a detailed analysis of the fault occurrences and a critical revision of all the subsystems containing old or out of production parts.

A list of mandatory items has been defined and the relative costs have been evaluated. The more relevant items are:

- Revamping of the low level control system.
- Control system upgrade.
- New power supplies for the skew correctors.

- Improved diagnostic in the accelerator complex.
- Power supplies for e-cloud suppression replaced with devices providing higher voltage.
- New kicker for the transverse feedback in the electron ring.
- Improved design for the vacuum chamber of the low-β section and the relative support.

The consolidation plan has been endorsed and funded by the INFN management. This revamping program will be implemented during the six months long shut starting on January 2013, which has been planned to complete the KLOE-2 detector upgrade.

9 Publications

1. A. Drago, D. Alesini, T. Demma, A. Gallo, S. Guiducci, C. Milardi, P. Raimondi, M. Zobov (INFN-LNF), "Mitigation and control of instabilities in DAΦNE positron ring", Beam Instrumentation Workshop 2012, Apr 2012.
2. T. Demma, A. Drago, A. Gallo, S. Guiducci, C. Milardi, P. Raimondi, M. Zobov, D. Alesini (INFN-LNF), S. De Santis (LBL, Berkeley), "Experimental measurements of e-cloud mitigation using clearing electrodes in the DAΦNE collider", IPAC-2012 Conf. Proc. C1205201 (2012) 1107-1109

DAFNE-BTF

B. Buonomo, L. Foggetta (Art. 23), O. Frasciello (Bors.), G. Mazzitelli, L. Quintieri (Art. 23), P. Valente (Resp.)

During year 2012 a number of improvements of the BTF facility have been implemented:

BTF electron beam: a full beam transport study was performed. A new setup for the LINAC pulse was prepared, triggered by the requirement of the AMY experiment of a very short beam: 1.5 and 10 ns are now selectable as BTF electron beam pulse durations. 3 ns pulses will also be possible with a small modification of the Linac gun driving signal. The shape of the "long" pulse is approximately flat, while the shorter pulses have a distribution rather triangular in shape, i.e. with a peak of particles followed by a falling edge with lower intensity.

BTF facililty improvements and upgrades

A number of improvements and modifications were performed in order to have better services and easier user experience with the BTF beam(s):

- **Gas system**: the gas lines in the BTF area have been upgraded and fully tested. Now four different gas lines are fully operational: low pressure hydrocarbons, high pressure hydrocarbons, two lines for CO_2/Ar/N/He and similar gases.
- **Vacuum system**: the pumping system has been improved and now we are able to get a stable value of (average) $2\ 10^{-9}$ mbar on all the sections of the BTF vacuum pipes. Now there are no more vacuum breaks, an important improvement, since it reduces the amount of multiple scattering and energy loss due to small sections in air (and the presence of corresponding entrance/exit windows). A new straight section has been designed, realized and installed. Now a vacuum can be produced in the straight section separable from the rest of the pipe with a manual valve. This allows the speed-up of user operations during installation of experimental setup in vacuum. The pipe is equipped with a KF flange for pre-vacuum operations, an independent pressure gauge, a ionic pump, a YAG flag with its remote controlled pneumatic movement, a Basler CCD camera with its own black-box. A new passive protection system for the thin vacuum exit window of the bent line has been designed in order to house the wall current monitor (WCM) detector as well as protecting the ceramic pipe and the Berillium window with a removable polycarbonate window spacer.
- **General services and safety**: the main air ducts of the experimental hall have been sanitized. This improves the air quality and allows to reduce the problems related to the outgassing of BTF vacuum, as well as improving safety levels. The safety rules have been updated in accordance with Radiation Safety guidelines in the BTF experimental hall and in the control room for high-intensity operations. A dedicated neutron and gamma monitor has been installed in the BTF area.

- **Detector and DAQ improvements (related to the AIDA project)**:
    - **GEM trackers**. A dedicated run has been done to determine the future operative modes of the GEM and we started and completed the tests in July. These were comforting on the GEM operative status and the instrument seems appropriate to the specific experimental beam diagnostics in the three axes. More tests will be needed for integration with the BTF data acquisition. To have a glance to the !CHAOS framework, we study for future development of the control of GEM virtual machine through the use of responder CAN bus over Ethernet. We start to develop an engineered support frame (gas, electronics and remote position control) for the GEM structure, toward a runtime beam diagnostics on demand.
    - For the DAQ topics we have resolved problems related to the data format, improving time correction routine check on the existing DAQ. Moreover, user-friendly BTF environmental sensors have been implemented. New sensors for the radioactive background in BTF control room (Berthold manufacture) have been implemented.
    - Related to the !CHAOS project: a CU is now operational on the installed environmental sensors from four months in a synchronous fetching development of CU. A new prototype of oscilloscope users with mode of fetching and synchronous control. We start to think about future definition of software coupling mode between DAQ and users.

BTF user access

During 2012 the BTF has been running for 316 days, hosting many different experimental groups. Beam was delivered quite successfully to all the users, with an excellent degree of satisfaction.

A list of experiments running at the BTF during year 2012, to which 6 weeks of maintenance/dedicated runs for BTF use should be added (used for diagnostics improvements and developments and for characterization of background, improvement of the beam characteristics, etc.):

- VIRHIS (3 runs)
- K2HET (KLOE2 high-energy taggers calorimeters)
- SuperB-DCH (prototype of the SuperB drift chamber)
- SuperB-LSO (LSO calorimeters prototype)
- QCAL-CCAL (KLOE2 small angle calorimeters, 2 runs)
- Siddharta/Amadeus
- VIPIX (Silicon pixel detector test)
- JLAB12-Genova (PbWO calorimeter and hodoscope for CLAS12)
- AMY (one month in total, including the complex setup of anechoic chamber, complex experiment for detection of GHz radiation from electron beam) [1,2,3]
- K2-IT (KLOE2 GEM inner tracker)
- NRCA (neutrons)

- JLAB12-RICH
- ATLAS-Muon-upgrade (2 runs, micro-megas detectors)
- ANSI (positron channeling)
- K2-CCALT
- MAMBO (low energy scan of calorimeter)
- Gamma-neutron (neutrons/gamma background)
- UA9-quartz fibers

BTF neutron source
A pulsed neutron source has been realized at the BTF sending full energy (510 MeV) electrons on an optimized Tungsten target. Neutrons with an energy spectrum that spans over more than 9 decades of energy (from few meV up to hundred of MeV) are produced, even if most of them have energy around 1 MeV. This source may be suitable for calibrating neutron sensitive devices with response in the MeV region, as well as it could be efectively used for material and nuclear science investigations. Neutron and photon rates and their spectra have been measured along well designed extraction lines, by using a Bonner Sphere Spectrometer (BSS). The tests and measurements performed in the framework of the n@BTF project in year 2011 for the development of the neutron source were analysed and the main results were also published [1,2].
Additional measurements of the gamma field were performed and data analysis is under way in order to estimate the neutron/gamma ratio at different positions and distances from the optimized target.

A list of publications of experimental groups running their test-beams at the BTF can be found in the Reference section [R-1 to R-4]

Publications

[1] L. Quintieri *et al.*, *A Photoneutron source at the DAFNE Beam Test Facility of the INFN National Laboratories in Frascati: design and first experimental results*, Physics Procedia **26**, 249-260 (2012).

[2] J.M. Gòmez-Ros *et al.*, *Designing an extended energy range single-sphere multi-detector neutron spectrometer*, Nucl. Instrum. Meth. **A677**, 4-9 (2012).

[3] M. Bassan *et al.*, *Measurement of the thermal expansion coefficient of the Al5056 alloy in the 0.3<T<2 K temperature range*, arXiv:1212.0368 (2012).

[4] L. Catani *et al.*, *Introducing a new paradigm for accelerators and large experimental apparatus control systems*, Physical Review Special Topics – Accelerators and Beams **15** (11), 112804 (2012).

[5] P.W. Cattaneo *et al.*, *On-ground calibration of AGILE-GRID with a photon beam: results and lessons for the future*, SPIE Astronomical Telescopes+ Instrumentation, 84434D-84434D-12 (2012).

[6] P.W. Cattaneo *et al.*, *Characterization of a tagged gamma-ray beam line at the DAFNE Beam Test Facility*, Nucl. Instrum. Meth. **A674**, 55-66 (2012).

[7] B. Buonomo *et al.*, *Remote test bench equipped with service movable platform in two axis: Manual instruction and warnings* (2012).

References

[R-1] J. Alvarez-Muñiz *et al., The Air Microwave Yield (AMY) experiment to measure the GHz emission from air shower plasmas*, Journal of Physics, Conference series, ECRS 2012 Conference, in press.

[R-2] J. Alvarez-Muñiz *et al., Air Microwave Yield (AMY): An experiment for measuring the GHz emission from air shower plasma*, Nuovo Cimento, Year 2013 - Issue 1 - January-February.

[R-3] G. Eigen *et al.*, *A LYSO calorimeter for the SuperB factory*, Nucl. Instrum. Meth. **A** (in press).

[R-4] M. Bazzi *et al.*, *Experimental tests of the trigger prototype for the AMADEUS experiment based on Sci-Fi read by MPPC*, Nucl. Instrum. Meth. A671, 125-128 (2012).

DAΦNE-Light Laboratory and Activity

A. Balerna (Resp.), P. Calvani (Ass.), M. Cestelli Guidi (Art. 23), R. Cimino, A. De Sio (Osp.), R. Flammini (Ass.), L. Gambicorti (Osp.), A. Grilli (Tecn.), R. Larciprete (Ass.), A. Nucara (Ass.), E. Pace (Ass.), M. Pietropaoli (Tecn.), A. Raco (Tecn.), V. Sciarra (Tecn.), V. Tullio (Tecn.), G. Viviani (Tecn.).

1 Summary

The scientific activity at the DAΦNE-Light laboratory, in 2012, was mainly performed using conventional sources. Due to the not continuous DAΦNE operation, synchrotron radiation was mainly used for check tests. The experimental teams that got access to the DAΦNE-Light laboratory were from Italian Universities and research Institutions, and some of them also from EU countries within the INFN-FAI framework. The experimental activities, performed in 2012, were also dedicated to some upgrades of the beamlines with new instrumentations, the test of the clean-room laboratory for biological sample preparation and also to the completion of the construction of the two new XUV beamlines that will hopefully be commissioned in 2013.

2 Activity

2.1 SINBAD - IR beamline

The experimental activity on the SINBAD IR beamline mainly concerns micro imaging and FTIR (Fourier transform InfraRed) spectroscopy in different research areas, including material science and THz applications, biology, radiobiology, live cell imaging, cultural heritage and geophysics. All these studies are made possible by the imaging capabilities of the IR microscope coupled to the synchrotron source. Due to the problems of DAΦNE, during the last year, researches on the IR beamline were carried out mainly using conventional sources. The institutions involved were mainly Italian teams, due to the late beginning of the EU user access project CALIPSO, that will probably start in 2013. Some of the international collaborations were financed by INFN-FAI fundings. During 2012 the Attenuated Total Reflection (ATR) microscope objective designed to image live biological cells (Fig. 1), partially funded by the Vth INFN scientific Commission, has been realized and first tests are ongoing.

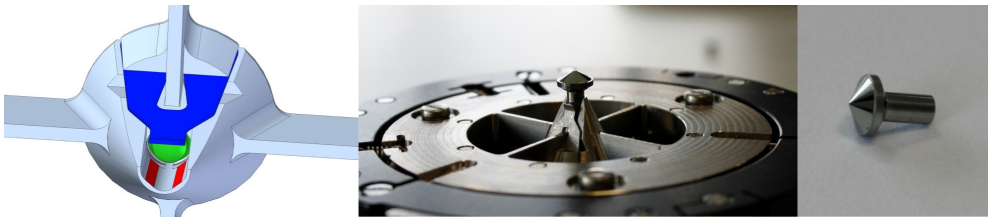

Figure 1: Design and realization of the dedicated ATR objective with a removable Germanium crystal tip.

A powerful 24 V conventional infrared source has been installed on the Vertex interferometer to provide high IR flux on samples when synchrotron radiation is not available. The source has been tested and provides 40% more signal than the standard 12 V globar source, allowing FTIR imaging analysis with improved signal-to-noise ratio and reduced acquisition times. Taking into account the

very interesting results achieved in researches related to astrophysics (radiobiology and dosimetry) and medical applications (cystic fibrosis) different projects have been submitted for funding. Some of the scientific results obtained at the SINBAD IR beamline are here summarized:

1. *The Degradation Process of Lead Chromate in paintings by Vincent van Gogh studied by means of spectro-microscopic methods.*

   C. Miliani, CNR-ISTM - Perugia

   Previous investigations about the darkening of chrome yellow pigments in Vincent van Gogh paintings revealed that this form of alteration is attributable to a reduction of the original Cr(VI) to Cr(III) and that the presence of sulfur-containing compounds plays a key role during this process. In the present work we show how both the chemical composition and the crystalline structure of lead chromate-based pigments influence their stability. For this purpose, artificially aged oil model samples made with in-house synthesized powders of $PbCrO_4$ and $PbCr_{1-x}S_xO_4$ were artificially aged and characterized. Analyses employing UV-visible diffuse reflectance and Fourier Transform infrared (FTIR) spectroscopy were performed on (un)aged model samples in order to obtain additional information on the physicochemical changes induced by the aging treatment (Fig. 2).

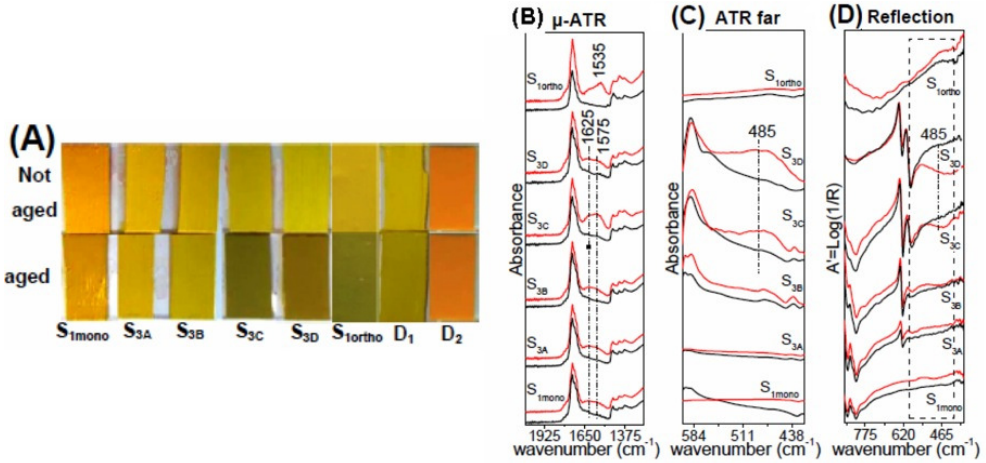

Figure 2: (A) Aged samples, after exposure to UV-A visible light, of paint models containing different amount of sulfate; (B) micro-ATR mid; (C) macro -ATR far; (D) Reflection

These results are a part of a very extended study on yellow paintings of Van Gogh made in collaboration with CNR-ISTM and the ESRF and SOLEIL synchrotron radiation facilities. The results were published on Analytical Chemistry (ACS Publications) and have been cited in many web articles like: http://www.repubblica.it/speciali/arte/recensioni/2013/01/18/news/allarme_i_led_oscurano_il_giallo_di_van_gogh-50792854/ and http://cultura.panorama.it/arte-idee/van-gogh-gialli.

2. *A crystal-chemical study of cordierite, synthesis and stability at variable H_2O and CO_2 concentration: geological and technological applications.*

   F. Radica et al., University of Roma Tre - Dipartimento di Geologia

   Cordierite is a unique case of a microporous mineral stable under geological conditions spanning from the amphibolite facies to UHT metamorphism to crustal anatexis. The interesting

feature of this mineral is its ability to trap different amounts of H_2O and CO_2 as a function of pressure and temperature; the crystal chemical study of cordierite is thus important for both petrological and technological applications. The experimental introduction of volatile components in the structural channels of cordierite has been studied by various authors; they pointed out, particularly for CO_2, the difficulty in reaching the sample saturation and homogeneity, a condition which is crucial for the accurate determination of the volatile content in the specimen. The experimental protocol for this study was developed using a natural, optically transparent, Mg-cordierite as starting material, and silver carbonate as CO_2 source. The experimental apparatus consisted of a non end-load piston-cylinder press housed at INGV (Rome). The reason for this choice is strategic because this apparatus covers a range of pressures and temperatures compatible with those of the lower crust and upper mantle.

The experimental products were analyzed by FTIR spectroscopy, a powerful technique that allows quantifying very low CO_2 concentrations. When using novel bidimensional detectors (FPA detector at INFN-LNF), this technique is also able to provide the distribution of the target molecule, thus allowing to get insight for its diffusion across the specimen. The preliminary experiments so far covered the pressure range from 200 to 700 MPa and temperature range from 700°C to 900°C, with running time up to 48 hours. FPA images showed that carbon dioxide is preferentially distributed along the crystal edges and cracks; in detail concentration along the cracks can be up to five times higher than in the crystal edges (Fig. 3), suggesting that (1) the diffusion of CO_2 across the cordierite matrix is relatively slow under the used experimental conditions; experiments for longer duration time are thus required to address this issue. (2) knowledge of the non-homogeneous composition of the sample is a pre-requisite to get accurate micro-analytical data.

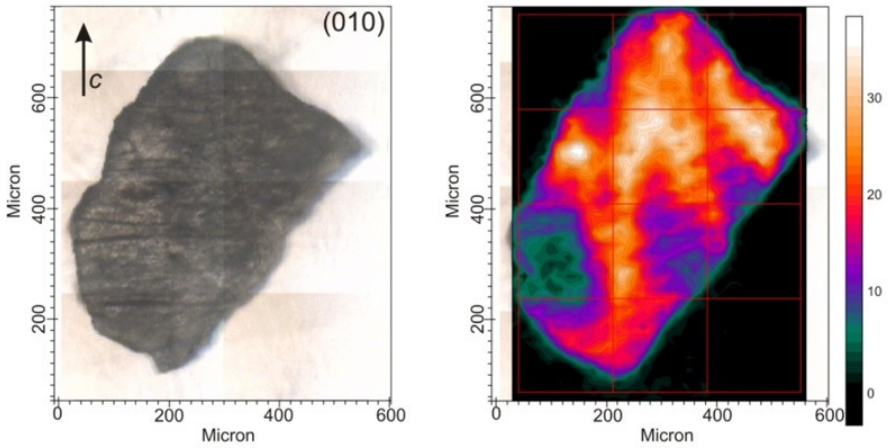

Figure 3: Visible (left) and infrared image (right) of the CO_2 distribution of a 90 μm thick cordierite slab (CRD_PR35) treated at 700 MPa and 800°C for 15 hours. The chromatic intensity is proportional to the CO_2 concentration, intensity units in the right picture are arbitrary.

3. *Fourier transform InfraRed micro-spectroscopy (micro-FTIR): a useful method to evaluate the effects of CFTR modulators in cells.*

   G. Bellisola, University of Verona

   Translational research on cystic fibrosis (CF) aims at developing diagnostic tools to iden-

tify CFTR (Cystic Fibrosis Transmembrane conductance Regulator) mutants, at increasing knowledge on the pathophysiology of CFTR protein and at developing therapeutic molecules targeting the corresponding defective CFTR protein responsible for multi-organ alterations in CF people. Recently, research efforts have been awarded with the first drug approved by US FDA for the therapy of underlying CFTR defect. In this contest, the availability of both new validated CFTR biomarkers and of corresponding biomarker assessment techniques has become a research priority. Actual methods to measure CFTR biomarkers suffer from some limitations. For instance, the results of sweat chloride sometimes can be affected by concomitant diseases or therapies and sweat test cannot be applied to test drugs in *ex vivo* CF cell systems. The *in vivo* measurements of trans-epithelial nasal potential difference (NPD) or the *ex vivo* intestinal current measurements (ICM) reference bioassays result uncomfortable, scarcely practicable and are not widely available to perform multiple assessments as usually required in clinical trials. Methods such as the measurements of trans-membrane potentials in single cells by patch-clamp and/or by trans-membrane potential-sensitive fluorescent $DiSBAC_2(3)$ probe are time consuming and have high variability. Therefore, CF research still focuses on the development of more reliable and comfortable methods necessary to monitor changes induced by drugs targeting CFTR protein/activity, respectively.

The biomolecular and structural composition of a cell as well as biochemical changes induced by drug treatment in the samples can be studied by Fourier transform InfraRed (FTIR) spectroscopy and microscopy (micro-FTIR). This non destructive, high sensitive and reproducible spectroscopic technique allows to obtain in a few seconds an IR spectrum reflecting qualitative and quantitative information on different molecules and their interactions in the sample. Therefore, an IR spectrum can be a useful biomarker to identify and compare the responses of CFTR defective cells to drug molecules. This global information can be acquired at the different levels of spatial resolution in samples without the use of specific probes and with minimal sample manipulation. In association with unsupervised multivariate data treatment methods subtle differences induced by drugs can be objectively identified in the corresponding dataset.

2.2 DXR1 - Soft X-ray Beamline

The DAΦNE soft X-ray beamline, DXR-1, is mainly dedicated to soft X-ray absorption spectroscopy. The X-ray source of this beamline is one of the 6-poles equivalent planar wiggler devices installed on the DAΦNE electron ring (0.51 GeV) for the vertical beam compaction. The 6 wiggler poles and the high storage ring current (higher then 1 Ampere) give a useful X-ray flux for measurements well beyond ten times the critical energy. The useful soft X-ray energy range is 900 eV - 3000eV where the lower limit is given by the Beryl crystals used in the double-crystal monochromator and the higher limit is given by the wiggler working conditions. Some check tests were performed on all the elements of the beamline because after the long 2011 DAΦNE shut down a first beamline realignment was performed at the end of 2011 and ended in 2012 when the beam condition became more stable. In order to control the new working conditions also some XANES measurements were performed in october 2012 in the presence of good and stable beam conditions (Fig. 4).

Some recent experimental results achieved on data taken some years ago were presented in 2012 at the Symposium on Synchrotron Radiation in Natural Science held in Krakow (Poland):

1. *Valence of constituents of selected rare earth silicides -XANES and LAPW numerical study.*
   Pavel ZAJDEL - University of Silesia, Institute of Physics, Katowice, Poland

   The inter-metallic rare earth (RE) silicides call a lot of attention due to their uranium based members, frustrated geometry and interesting magnetism. Although the electronic structure

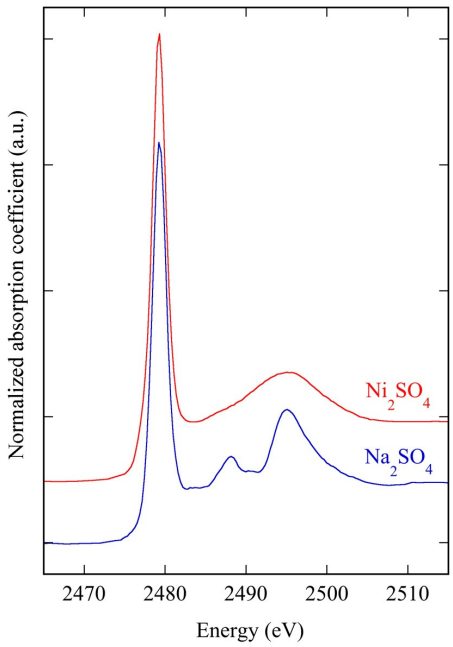

Figure 4: Normalized XANES spectra of Ni_2SO_4 and Na_2SO_4 reference compounds.

and magnetism are primarily determined by the rare earth and the RE-Pd/Rh hybridization it is interesting to verify the role of silicon as ″passive″ spacer. The investigation of the chemical environment and electronic structure of Si and Pd using X-Ray Absorption Fine Structure related to two different families of samples is reported. The XAS experiments were performed at the DAΦNE-Light Laboratory of the Laboratori Nazionali di Frascati. Data were collected at room temperature, in the transmission mode. Two families of silicides were chosen for the study. The similarities and differences caused by different rare earth in the same matrix for RE_2PdSi_3 series, where RE=Ce, Nd, Td, Dy, Ho, Er are shown. The compounds crystallize in an AlB_2-type structure (space group P6/mmm). The RE ions occupy the Al-equivalent positions, while nonmagnetic Pd and Si atoms should be statistically distributed on B sites.

2.3 DXR2 -UV branch Line

The synchrotron radiation (SR) photon beam from a wiggler installed on the DAΦNE storage ring is split by a grazing incidence Au-coated mirror (θ_i = 40 mrad, cut-off energy about 800 eV), in order to provide the X-ray and UV beamlines. The reflected UV radiation travels through the UV beamline and ends in a 63 mm diameter MgF_2 window. The UV-VIS beamline operates on an extended spectral range from 120 nm to 650 nm, spectral regions commonly referred to as Visible, UV-A, UV-B and UV-C. There are three experimental stations: one operates in the VUV (UV-B and UV-C) region between 120 nm and 200 nm (monochromatic radiation), the second covers the range 200-650 nm (VIS, UV-A, UV-B) with monochromatic radiation and the third covers the same spectral range but in white light or broadband typically for experiments of irradiation or aging. The same spectral range can be also covered by conventional light sources like gas discharge lamps that have emission spectra not continuous as synchrotron radiation, but have particularly

intense emission lines (see Fig. 5).

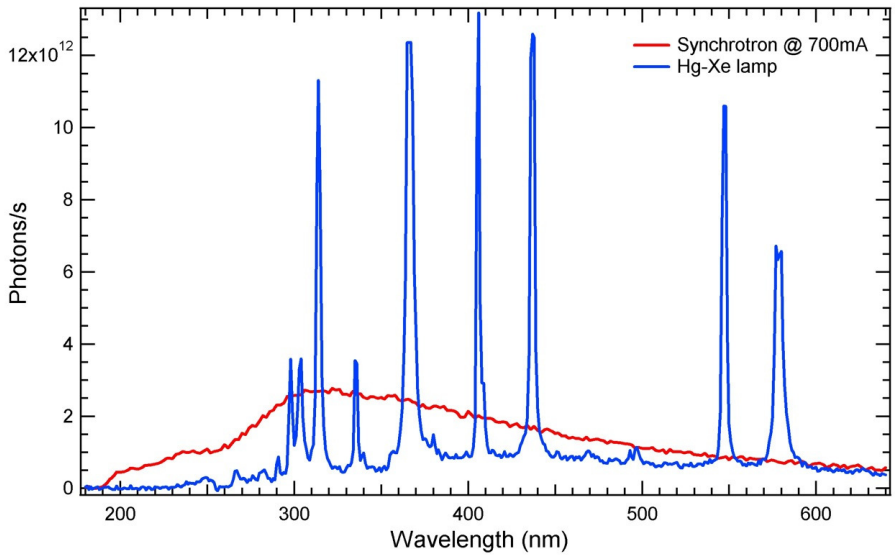

Figure 5: Emission spectrum of the Hamamatsu 500 W Hg-Xe lamp compared to the synchrotron radiation spectrum in the UV-VIS range measured with a 700 mA electron current circulating in the storage ring.

The three stations can also be used in test operations and calibration of components of optical systems even of large size, of photon detectors having standard sizes and of thin layers or multilayers. It is possible to carry out measurements of reflectivity, transmissivity and absorption of thin layers. This beamline is particularly suitable for experiments of photochemistry and photobiology related to the characterization of inorganic and organic materials, the alteration of organic molecules and inorganic complexes as an effect of irradiation experiments and aging. The UV region of this beamline has been used for photochemistry experiments to study molecules of astrobiological interest. Also bacteria, which were tested on board in the International Space Station, showing no evidence of radiation damaging, were exposed to UV radiation in order to investigate the effects on such radiation resistant systems. The interest of this research is to find, if it exists, the effective dose that can induce a damage, i.e., the surviving threshold. This experiment is still going on, exploring a wide range of photon doses and exploiting the synchrotron radiation beam intensity in order to simulate prolonged exposures or life conditions on other space environments, like Mars. This kind of experiments was also performed in combination with the use of the SINBAD IR beamline to monitor in real time the UV irradiation effects. An on-going project for a photochemical facility at the DAΦNE-L laboratory combines the UV and the IR beamlines. Such a facility takes advantage from the capabilities of the two synchrotron radiation beam-lines: the first one, operating in the visible-UV range, is used as a strong excitation and irradiation light-source in which both intensity and spectral range can be selected to fulfill the experiment requirements while the infrared beamline provides FTIR micro-spectroscopy and imaging. An optical fiber allows the UV irradiation of samples directly into the FTIR interferometer or microscope. Fast photochemical reactions can be analyzed in real time, letting unveil inter-phases not normally observable by analyzing the reagents and products of the reaction itself. Complex unstable systems can be irradiated and analyzed without changing the sample condition (morphology, humidity etc.). The accessible

wavelength region for the photochemical experiments is 180-400 nm. Two optical configurations are available: the first makes use of the synchrotron radiation (SR) white beam while the second brings monochromatic SR on the sample. A different setup was conceived to UV irradiate samples of micrometric size in the IR microscope. This arrangement allows real-time imaging or microanalysis of processes occurring under UV irradiation. In this case, UV irradiation can not be vertical: the fiber optics is arranged laterally with an angle of about 20° producing a non-uniform elliptical spot. However, the size of the spotlight and the related non-uniform photon flux on the sample can be easily estimated. After some preliminary tests, we realized that the optical coupling at the vacuum feedthrough on the interferometer is very critical. The position of the two fibers inside the feed-through is not fixed: even very small mismatching may cause a decrease of the already small throughput. We decided to put another couple of sapphire spherical lenses in between the two fibers in order to collect the radiation even if the two fibers are not perfectly aligned. The optical transmission improved from roughly 10% up to 72%, providing the spectrum reported in Fig. 5. The photon flux at the main lines of the UV lamp is of the order of 10^{11} photons/s/nm in the spotlight, while the SR integrated flux from 200 nm to 400 nm is of the order of 10^{14} photons/s/nm in the spotlight. In order to fully assess the methodology and the optical system tests using the Hg-Xe lamp as UV source and nucleobases as samples were made. Pure nucleobases, as adenine, uracil, pyrimidine and cytosine, and the same nucleaobases in presence of inorganic mineral matrices, were irradiated using the UV white beam and real-time FTIR analysis, making use of the diffused reflectance technique, was used to monitor their degradation. A 500 W Hg-Xe lamp was optically coupled to a 10-m UV-grade optical fiber illuminating the organic sample. IR radiation was sent on the sample inside the FTIR interferometer of the SINBAD beamline and the diffused/reflected beam was collected by means of the Praying Mantis optical tool. The FTIR spectra of the nucleobases were acquired every 10 minutes during the two-hour exposition to UV light. The IR spectra from Uracil are shown in Fig. 6 as an example.

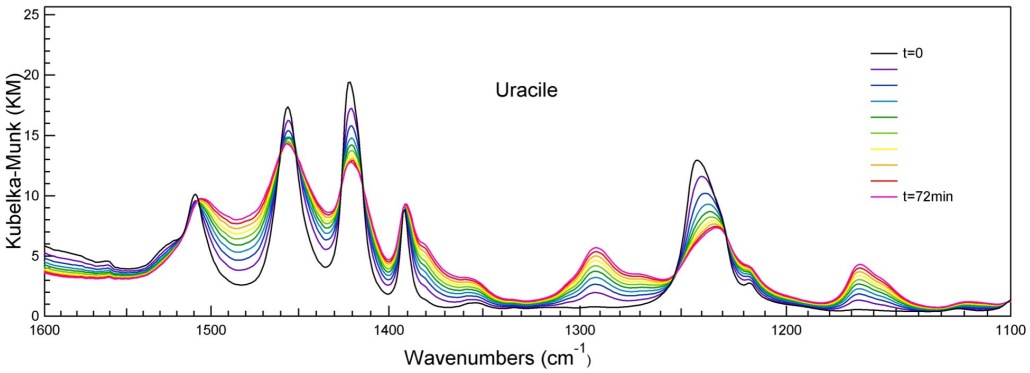

Figure 6: FTIR spectra of the degradation process of uracil molecule after UV irradiation.

The interaction between electromagnetic radiation and bio-molecules in heterogeneous environments is a prebiotically relevant process. Minerals may have a pivotal role in the prebiotic evolution of complex chemical systems, mediating the effects of electromagnetic radiation, influencing the photostability of bio-molecules, catalyzing important chemical reactions and/or protecting molecules against degradation. In particular, nucleobases are relevant bio-molecules to investigate both in the prebiotic context, because they are coding components of nucleic acids, and from the standpoint of the survival of biological systems in space conditions. Experimental results confirmed the high intrinsic photostability of such molecules, because a rather low probability of interaction

between UV radiation and nucleobases was estimated, and furthermore indicate that cytosine and hypoxanthine have a greater photostability compared to adenine and uracil, both pure and adsorbed onto magnesium oxide and forsterite.

2.4 New XUV beamlines

In 2012, the new XUV laboratory has continued its construction, based both on the detailed plans approved by the SRL Committee and on available resources. Aim of this laboratory is to host two bending magnet beamlines covering the photon energy range from 30 eV to 1000 eV. One beamline will cover the low energy part of this interval (30-200 eV) and is called LEB (Low Energy Beamline), the other will cover the energy range from 60 eV to 1000 eV and is called HEB (High Energy Beamline). Both beam lines are in UHV and directly connected to the vacuum of the main DAΦNE ring. All the safety protocol and control systems are ready and tested. Since the beginning of the year, the two beam lines were ready to start commissioning with synchrotron light. The commissioning did not even start in 2012 because stable and continuous DAΦNE working conditions are clearly required. The complex procedures of commissioning of the two XUV beamlines will start as soon as the necessary beam conditions will become available. Meanwhile, the two *state of the art* end stations, whose construction was nearly completely funded without using resources from the DAΦNE-L laboratory were implemented and successfully used. Both experimental set-up have been equipped with commercial laboratory sources (X-ray lamp and He-discharge lamps), electron sources and all the needed tools to perform not only detailed tests on their functionality but also experiments. The tests of the experimental chambers were also used to perform experiments on SEY (Secondary Electron Yield) reduction versus electron bombardment, surface conditions and carbon deposition, which are the objectives of the IMCA-NTA Project (see this annual report for a detailed description of this activity) and were done in collaboration with R. Larciprete (ISC-CNR) and R. Flammini (IMIP-CNR), who are associated to that project. During 2012, a state of the art micro-Raman station was set up. This was done in order to enrich the available techniques and experimental apparata offered by the DAΦNE-L laboratory to its users community. Such ancillary equipment has been founded combining DAΦNE-L and IMCA-NTA economic resources. The XPLORA micro-Raman Instrument from Jobin-Yvon was installed in the laboratory as shown in Fig. 7.

Figure 7: The new micro-Raman instrument XPLORA from Horiba Jobin-Yvon installed in 2012.

Already some test experiments have been done to commission the instrument and see its potentialities. An example is given in Fig.8 where the Raman spectra measured on C film grown at room temperature on polycrystalline copper by magneton sputtering, before and after thermal annealing at 800 °C are shown.

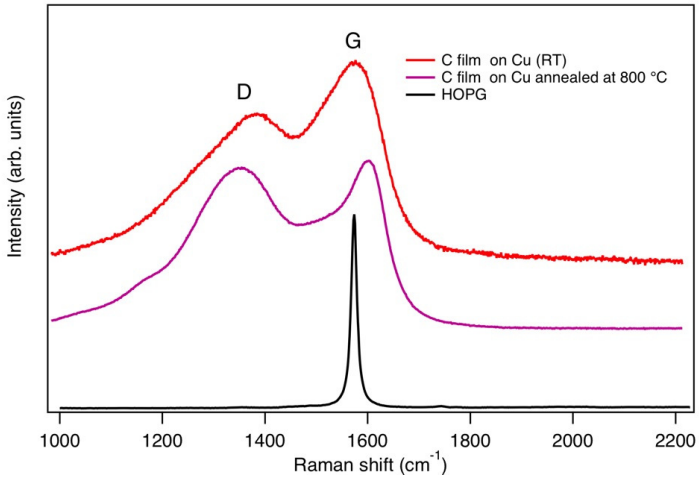

Figure 8: Raman spectra measured on C film deposited at RT by magnetron sputtering, before and after the thermal annealing at 800 °C. For comparison the bottom curve shows the Raman spectrum of HOPG.

For comparison the Raman spectrum of highly oriented polycrystalline graphite (HOPG) is also reported. The C film spectra show the D (disordered) and G (ordered or graphitic) bands at 1380 and at about 1580 cm^{-1} typical of carbonaceous materials. The D band is absent in the HOPG spectrum. The thermal annealing reduces the width of the D and G bands indicating a higher degree of ordering of the C network.

3 List of Conference Talks

1. E. Pace ″Innovative photochemical facility at DAΦNE-Light synchrotron source″, SRI2012: 11th International Conference on Synchrotron Radiation Instrumentation , Lione (FR), July 9-13, 2012.

2. M. Cestelli-Guidi, ″In vivo skin leptin modulation after 14 MeV neutron irradiation: a molecular and FT-IR spectroscopic study″, ISSBB - Italian Society for Space Biomedicine and Biotechnology - Brindisi 25-27 October 2012.

4 List of other contributions to Conferences

1. P. Zajdel (oral presentation), A. Kisiel, A. Szytula, P. Starowicz, J. Goraus, J. Konior, A. Banas, A. Balerna, G. Cinque and A. Grilli ″Valence of constituents of selected rare earth silicides -XANES and LAPW numerical study.″, ISSRNS 2012 11th International School and Simposium on Synchrotron Radiation in Natural Science, Krakow, Poland May 20-25, 2012.

5 Publications

1. P. Savchyn, I. Karbovnyk, V. Vistovskyy, A. Voloshinovskii, V. Pankratov, M. Cestelli Guidi,C. Mirri, O. Myahkota, A. Riabtseva, N. Mitina, A. Zaichenko, and A. I. Popov, ″Vibrational properties of $LaPO_4$ nanoparticles in mid- and far-infrared domain″, J. Appl. Phys. **112**, 124309 (2012)

2. M. Cestelli Guidi, C. Mirri, E. Fratini, V. Licursi, R. Negri, A. Marcelli and R. Amendola, ″In vivo skin leptin modulation after 14 MeV neutron irradiation: a molecular and FT-IR spectroscopic study″, Anal Bioanal Chem **404**, 1317 (2012)

3. S. Lupi, A. Nucara, A. Perucchi, M. Cestelli Guidi, E. Chiadroni, M. Ferrario, M. Ortolani, L. Baldassarre, D. Nicoletti, C. Mirri, F. M. Vitucci, P. Di Pietro, U. Schade and P. Calvani, ″A survey of the Italian research in solid state physics by infrared spectroscopy with electron-beam sources″, J. of Phys.: Conf. Series **359**, 012001 (2012)

4. L. Monico, K. H. Janssens, C. Miliani, G. Van der Snickt, B. G. Brunetti, M. Cestelli Guidi, M. Radepont, and M. Cotte, ″The Degradation Process of Lead Chromate in paintings by Vincent van Gogh studied by means of spectromicroscopic methods″, Anal. Chem. doi: 10.1021/ac3021592 Publication Date (Web): October 10, 2012

5. M. Cestelli Guidi, S. Yao, D. Sali, C. Sabine, A. Marcelli and C. Petibois ″Experimental ATR device for real-time FTIR imaging of living cells using brilliant synchrotron radiation sources″, Biotechnol. Adv. (2012), doi:10.1016/j.biotechadv.2011.11.009

6 Other pubblications

1. A. Mottana, A. Gorghinian, M. Cestelli-Guidi, A. Marcelli, ″Esame gemmologico qualitativo integrato con misure quantitative in microspettroscopia di fluorescenza dei raggi X, e in s pettroscopia vibrazionale dei raggi infrarossi, identificazione delle pietre preziose e dei leganti.″, Splendore Marciano, M. L. Sebasatiani and P. Crisostomi, ISBN 978-88-95047-14-0, Edizioni Nova Charta, 2012.

GILDA - GENERAL PURPOSE ITALIAN BEAMLINE FOR DIFFRACTION AND ABSORPTION - AT ESRF.

A. Balerna, A. Grilli (Tecn.), S. Mobilio (Resp.), A. Raco (Tecn.),
V. Sciarra (Tecn.), V. Tullio (Tecn.)

1 Introduction

GILDA (General Purpose Italian BeamLine for Diffraction and Absorption), is the Italian CRG beamline, built to provide the Italian scientific community with an easy access to the European Synchrotron Radiation Facility to perform experiments with a high energy and brilliance X-ray photon beam. GILDA is operative since autumn 1994. Today GILDA is funded by the Italian public research Institutes: Consiglio Nazionale delle Ricerche (CNR) and Istituto Nazionale di Fisica Nucleare (INFN). Experimental stations for X-ray Absorption Spectroscopy, Anomalous X-ray Scattering and X-ray Diffraction (XRD) are present on the GILDA beamline.
The LNF group is involved in the technical maintenance and update of the beamline, with particular emphasis to the electronic and software controls of all the instrumentation.

2 Technical activity on the GILDA beamline during 2012

During 2012 the main implementations on the instrumentation were:

1. the installation and commissioning of a new hardware for controlling the vacuum operations in the EXAFS hutch. The new hardware is compliant with ESRF software; it consists in WAGO boxes linked to the control computer via ethernet and bearing modules for the remote control of pumping and venting of the experimental chambers, refill and pumping of the Ionization Chambers.

2. The installation of ICEPAPS hardware and SPEC software for the control of the stepping motors. Almost all motors are now controlled by the standard ESRF environment (SPEC) and can be used in automatic programs either under SPEC or Labview. The new system has permitted the development of automatic routines for the beamline alignment so at present the configuration change of mirrors (Pd/Pt/NoMirrors) can be realized in a couple of hours instead of a whole day in the past years.
   Now only the stepping motors of the monochromator are still controlled by the old VME-based system; this is mainly due to the considerable complexity of this device.

3. Implementation od the data acquisition under SPEC. The data acquisition programme permitted to access codes available at ESRF for data collection, like the XIA device server for the fluorescence detectors, and for data treatment that highly enlarged the experimental capabilities of GILDA. The possibility of collecting elemental maps on surfaces directly comes from this.

4. A new cryostat for the collection of XAS data on liquid samples down to 80K was built and installed on the beamline. The new cryostat cools the sample by a flux of cold gas: in this way no vacuum environment around the sample is needed. Working conditions have been determined: the new cryostat is compatible with both transmission and fluorescence data collection, can stand for about 20hrs of continuous operation before refilling and the samples are cooled down in about 30 minutes.

3 Beamtime use during 2012 and scientific outcomes

The beamline operation was deeply affected by the extremely reduced staff. It was possible to accept and perform only a limited number of easy experiments in XAS hutch.
After the long shutdown of ESRF, in order to restart with all the instruments correctly working, run 2012-I was totally dedicated to beamline commissioning. During the other runs 7 ESRF experiments have been carried out for a total number of 101 shifts delivered out of 124 requested by ESRF.

The remainder 372 shifts available were dedicated to beamline commissioning/test-with-expert-users.
During 2012, 32 paper were published in International journal with referee, the main topics being material science, catalysis, nanoparticles and cultural heritage. The following studies are to be mentioned:

1. *Bimetallic Gold −Palladium vapour derived catalysts: The role of structural features on their catalytic activity*
   A procedure to synthesize new AuPd bimetallic catalysts using Au and Pd vapours as reagents (metal vapour synthesis, MVS) is reported. The simultaneous co-condensation of Au and Pd vapours with acetone vapour affords AuPd/acetone-solvated metal atoms which have been used to deposit AuPd bimetallic nanoparticles on c-alumina and titanium oxide supports. Transmission electron microscopy (TEM) analysis determined the nanoparticles dimensions (d_m = 2.22.4 nm) and size distribution while the X-ray absorption spectroscopy (XAS) analysis showed the presence of small bimetallic AuPd nanoparticles with a large amount of AuPd bonds. The bimetallic co-condensed systems, tested in the selective oxidation of benzyl alcohol with molecular oxygen both in toluene solvent and in solvent-free conditions, showed higher catalytic activity and selectivity than the corresponding monometallic systems as well as of the analogous systems obtained by separate evaporation of the two metals.

2. *Silver Nanoparticles Stabilized with Thiols: A Close Look at the Local Chemistry and Chemical Structure*
   The local atomic structure and chemical nature of newly synthesized silver nanoparticles (AgNPs) functionalized with the organic thiol allylmercaptane (AM) have been probed combining synchrotron radiation-based techniques: Xray photoelectron spectroscopy (XPS) and X-ray absorption fine structure spectroscopy (XAFS). Complementary information about the chemical and electronic structure is obtained combining XAFS and XPS data. These results coherently suggest a core shell morphology of the NPs resulting in metallic Ag cores surrounded by Ag_2S-like phase. The external layer of AM molecules is grafted to the NPs surface through Ag-S chemical bonds. NP size and composition were found as a function of the chemical synthetic route (i.e., Ag/AM molar ratio). It was observed that by increasing the Ag/AM ratio, larger AgNPs were obtained. It was found that a higher Ag/AM molar ratio leads to an increasing of the Ag_2S layer thickness, while the external AM layer remains unvaried. TEM analysis showed well-separated and dispersed nanoparticles, and ED pattern allowed one to identify two different phases of single crystal corresponding to the presence of Ag face-center-cubic single-crystal symmetry, together with weak diffraction spots in agreement with Ag_2S cubic symmetry.

3. *Interaction of Cisplatin with Human Superoxide Dismutase*
   cis-Diamminedichloroplatinum (II) (cisplatin) is a chemotherapeutic drug that has been used to treat various types of cancer since the 1960s. In this paper, the interaction of cisplatin with human superoxide dismutase (hSOD1) has been investigated. Cys6 and Cys111 residues of hSOD1 have been claimed to be involved in the aggregation of demetalated hSOD1, which

may be associated with a neurodegenerative disease known as amyotrophic lateral sclerosis (ALS), the causes of which have yet to be understood. Here, the crystal structure of the cisplatin bound apo hSOD1 determined from XRD data (ID14-4 beamline) shows that cisplatin binds covalently the sulfur atom of Cys111. It also binds to Cu2-Zn2 and Zn2-Zn2 forms of hSOD1. The EXAFS data (beamline GILDA) of the cisplatin-bound apo hSOD1 indicates the same donor sets and equal coordination geometry for the Pt(II) ion in solution as in the crystal structure. Thus, also in solution cisplatin binds to a sulfur containing residue of hSOD1. Moreover, results of laboratory tests show that cisplatin inhibits aggregation of demetalated oxidized hSOD1 and it is further able to dissolve already formed hSOD1 aggregates in vitro and in cell, without affecting the hSOD1 enzymatic activity. From this work, cisplatin appears as a promising compound for the design of ALS disease treatments.

4. *Discoloration of the smalt pigment: experimental studies and ab-initio calculation*
Smalt is a deep blue pigment based on potassium silicate glass doped with Cobalt(II) ions. This revealed to be a fragile pigment as it tends to discolorate with time giving a grayish hue. In this contribution, fragments of a deteriorated painting (Il battesimo di Ges, Luca Signorelli, XV century) were analyzed via colorimetric, morphologic and structural analyses. A set of artificially aged smalt samples was produced and revealed to be identical, from a colorimetric point of view, to the original fragments. All specimens showed a depletion of K in the pigment grain when observed at the Scanning Electron Microscope. The K loss, presumably due to humidity, causes an acidification of the glass with consequences on the Co environment. X-ray Absorption Spectroscopy revealed a gradual shift from tetrahedrally coordinated Co in blue samples to a mix of tetrahedral and octahedral (30(providing a pink coloration of the matrix) provides a qualitative structural explanation for the discoloration. However, theoretical simulations of the optical absorption spectra of the various Co complexes by Time Dependent Density Functional Theory (TD-DFT) showed that octahedral complexes have a too low absorption to induce discoloration with only 30structures resulting from a partial protonation of the Co ligands provide at the same time high coordination and high optical absorption cross section and these are the correct complexes that cause the pigment deterioration.

5. *Development of a software package for EXAFS data analysis*
ESTRA and FitEXA are two programs for processing X-ray absorption spectroscopy data, extraction of extended X-ray absorption fine structure (EXAFS) signal, and EXAFS data analysis via least square refinement procedure (shell fitting). ESTRA and FitEXA propose useful options such as the analysis of the noise on the raw v(k) data and a high flexibility in the choice of the model distribution function: harmonic, anharmonic (cumulants) and hard sphere models. The minimization routines underneath the FitEXA code allow ample choice/control of the non-linear minimization procedure and check of the correlation among the parameters.

6. *Elemental mapping of surfaces*
By using a moderate microbeam (in our case 200μm*200 μm) it is now possible to collect at GILDA elemental maps of large surfaces (particularly useful in the case of natural stones or ceramic decorations) for which extreme microbeams (<5μm) are not suited. Tests have been carried out on ceramic samples; at each point illuminated by the beam a complete fluorescence spectrum is collected and successively images are retrieved by integrating suitable Region of Interest (ROI). This technique permits to characterize a sample before carrying out XAS spectra in selected points. It is also possible to realize maps of valence-state or local symmetry by using the change of shape of the XANES when an element changes its valence or the local symmetry (tetrahedral-octahedral). The same sample was investigated

by collecting the maps at particular energies, one far from the edge and the other on the top of the pre-edge peak of tetra-coordinated Fe^{3+} and taking the ratio. This succesfull experiment demonstrates how GILDA is effective in surface mapping on large surfaces and how additional information other then the simple elemental distribution can be obtained by using the tunable energy from the source.

4 2013 - GILDA Forseen Activity

During 2013 both the user facility operations and technical activities will be strongly influenced by the actual lack of personnel working on the beamline. For the user community the same criteria of 2012 will be adopted i.e. delivery of user mode only to ESRF experiments, operation with the sole Si(311) crystal, no experiments involving complex/dangerous sample environment and no diffraction experiment. In case of re-establishment of the correct staff level these procedures will be of course reviewed. The main foreseen activities for 2013 are:

1. Development of a new crystal mounting for an easy access to the high energy range (E>30 KeV) This will be realized by substituting the first Si(311) crystal with a couple of Si(311) and Si(755) in order to extend the energy interval to 30-90 keV. The intervention does not involve the delicate change of the second (curved) crystal as actually is. In this way a wide energy range (5.5-90 keV) will be available without needing further interventions inside the monochromator. The crystals have already been cut and will be mounted in the monochromator at the next machine startup.

2. Development of a data treatment software for reducing the effect of Bragg peaks present in the measurement performed the cold-chamber cryostat During exp. SC-3507 data at the Cu-K edge were affected by the presence of Bragg Peaks due to the frozen solution. Test will be carried out in order to develop a suitable data treatment procedure (fit of the raw fluorescence data, treatment of the dead time corrections) capable to reduce this effect.

5 Publications

1. C. Evangelisti *et al.*,"Bimetallic GoldPalladium vapour derived catalysts: The role of structural features on their catalytic activity", J. of Catalysis **286**, 224-236 (2012).

2. C. Batocchio *et al.*, "Silver Nanoparticles Stabilized with Thiols: A Close Look at the Local Chemistry and Chemical Structure", J. Phys. Chem C **116**, 19571 (2012).

3. C. Meneghini, F. Bardelli and S. Mobilio, "ESTRA-FitEXA: A software package for EXAFS data analysis", Nuclear Instrument and Methods B**285**, 153 (2012).

6 List of Conference Talks

1. A. Balerna ″EXAFS and XANES structural characterization of bimetallic AuPd vapor derived catalysts″, XAFS15: 15th International Conference for X-ray Absorption Fine Structure , Beijing (China), July 22-28, 2012.

NTA-CLIC

A. Ghigo (Resp.)

Not received

NTA ILC

D. Alesini, M. E. Biagini, S. Bini, R. Boni, R. Cimino, A. Clozza, A. Gallo, A. Ghigo,
S. Guiducci (Resp.), F. Marcellini, A. Stecchi

1 Introduction

The INFN has contributed to the GDE (Global Design Effort) for the International Linear Collider (ILC) since the beginning in 2005 with a qualified participation to the project design and R&D. In 2012 INFN has provided an important contribution to the completion of the Technical Design Report (TDR) [1]. This activity is fully integrated at the international level with INFN responsibilities in the GDE on Main Linac (Milano-LASA) and the responsibility of the Damping Rings (DR) area system at LNF.

2 Year 2012 Activities

In 2012 the GDE activity has been dedicated to the preparation of the Technical Design Report. LNF has chaired the write-up of the Damping Rings section of the TDR. The LNF effort has been dedicated to the coordination of the DR working group and to the technical sections on the radio frequency system and on the bunch-by-bunch feedback systems.

The R&D activity focussed on the mitigation of the electron cloud instability has achieved an important success with the test of electron clearing electrodes at DAΦNE [2, 3]. The electron cloud instability is one of the main issues for the performance of the ILC positron damping ring [4]. In order to mitigate such instability, special electrodes have been inserted in all dipole and wiggler magnets of the DAΦNE positron ring. It has been the first installation all over the world of this type; long metallic electrodes have been installed in all arcs of the collider positron ring and are currently used during the machine operation in collision. Experimental measurements have shown an impressive effectiveness of these devices in mitigating the e-cloud impact on the positron beam dynamics.

In the framework of the GDE, LNF has also contributed to the International Accelerator School for Linear Colliders [5]

The LNF accelerator Division is also involved in a Low Emittance Rings Collaboration, started from the ILC and CLIC working group on damping rings, with the scope to bring together scientific communities of synchrotron light sources, storage rings, damping rings and lepton colliders in order to communicate, identify and promote research work on common topics affecting the design of low emittance lepton rings. This collaboration will continue with the Low Emittance Rings Network within the FP7 European Project EuCARD-2, starting on May 1st 2013.

3 Publications and Talks

1. ILC Global Design Effort and World Wide Study, "International Linear Collider Technical Design Report‘", to be published.
2. D. Alesini, A. Drago, A. Gallo, S. Guiducci, C. Milardi, M. Zobov, S. De Santis, T. Demma, P. Raimondi, "Experimental Measurements of e-cloud Mitigation Using Clearing Electrodes in the DAΦNE Collider", p. 1107, Proc. of IPAC2012, New Orleans, Louisiana, USA, (2012)

3. D. Alesini, A. Drago, A. Gallo, S. Guiducci, C. Milardi, A. Stella, M. Zobov, S. De Santis, T. Demma, P. Raimondi, "DAΦNE Operation with Electron-Cloud-Clearing Electrodes", Physics Review Letters, to be published

4. J.A. Crittenden, J.V. Conway, G. Dugan, M.A. Palmer, D. L. Rubin, L.E. Boon, K.C. Harkay, M.A. Furman, S. Guiducci, M.T.F. Pivi, L. Wang, "Investigation into Electron Cloud Effects in the ILC Damping Ring Design", p. 1963, Proc. of IPAC2012, New Orleans, Louisiana, USA, (2012)

5. S. Guiducci, "Accelerator physics Lecture A3 Damping rings and ring colliders", presented at the Seventh International Accelerator School for Linear Colliders, 27 November 8 December 2012, Indore, India, (2012)

NTA - IMCA (Innovative Materials and Coatings for Accelerator)

A. Balerna, R. Cimino (Resp.), T. Demma (art. 23), S. Guiducci, C. Milardi,
C. Vaccarezza, M. Zobov (INFN-LNF)
R. Larciprete (CNR-ISC),
R. Flammini (CNR-IMIP),

The IMCA experiment was started in 2010 in order to develop new materials and coatings with stable and low enough SEY (Secondary Electron Yield) to guarantee full operation of present and future accelerator machines. This issue, in fact, is crucial in controlling Electron Cloud formation and in reducing its effects, that are well known to be a potential bottle-neck to the performances obtainable from particles accelerators. Frascati has a long-standing experience in qualifying materials in terms of surface parameters of interest to e-cloud issues. We are routinely measuring SEY, its dependence from electron energy, temperature and scrubbing dose. We are now able to characterize "in situ" the surface chemical composition and eventual modifications occurring during electron or photon irradiation by using XPS with conventional X-ray source and we are ready to exploit for this purpose the synchrotron radiation beamlines in construction at DAΦNE [1]. Our experimental measurements of the relevant parameters can be also confidently compared to simulations, performed by running the EC codes, in order to elucidate the final consequences on machine performances. Such a combined characterization effort is also suggesting ways to produce low SEY materials coatings. This issue is particularly important in view of the foreseen LHC luminosity upgrades and ILC- Damping ring studies, where e-cloud issues are expected to be present.

The previous experimental and theoretical results obtained with the "Nuvola" experiment during the past years, are the scientific base of this project [2, 3]. Indeed during these years in the Surface Laboratory in Frascati, we measured SEY reduction versus dose (the number of impinging electrons per unit area on sample surfaces). This process is usually called "Scrubbing". We now can correlate the SEY reduction obtained by electron bombardment with the surface chemical composition by using X-ray photoemission spectroscopy, confirming that the electron bombardment results in the graphitization of the carbon impurities on the copper surface [2]. Such characterizations have suggested also ways to produce low SEY materials, which are still under study. We have two running setups: both are now routinely working. They both operate in UHV conditions being steadily in a vacuum better than 1×10^{-10} Torr after bake-out. Both are based on a UHV μ-metal chamber, with less than 5 mG residual magnetic field at the sample position. Both are equipped with an Omicron LEED; an electron gun to measure SEY; a Faraday cup to characterize beam currents and beam profiles and both can produce samples with different growing technique inserting them in the measuring system without breaking the vacuum.

One system is designed to deposit thin films and analyze their SEY in connection with XPS at room or higher temperature. This is done by using an Omicron electron analyzer (which is the main contribution to the collaboration from R. Larciprete institute) and an X-Ray and a UV Lamps to acquire photoemission spectra and to obtain chemical information on the studied surface. The other system is optimized to perform SEY experiment at cryogenic temperature (down to 8 K) and in connection to angle resolved VUV photoemission studies. For this reason has been equipped over the years with an OMICRON AR65 angle resolving analyzer and a monochromatic VUV source.

In 2012, in collaboration with the major laboratories which are playing an international leading role on the study and characterization of e-cloud effects, we have addressed a series of issues studying

different materials. Such activity not only is promoting our Material Science Laboratory in Frascati as one of the most advanced Laboratory in this field, but also provided a quite comprehensive understanding on the physical phenomena governing the SEY and its variations during the various surface modifications.
Some of the most relevant scientific 2012 results are here reported.

1. In close collaboration with CERN, we studied the chemical origin of the scrubbing process of Cu surface representative of LCH beam screen and its dependence on the energy of the primary electrons. We observe a lower efficiency in reducing the SEY when the energy of the scrubbing electrons is less than 20 eV. This may have an impact on the scrubbing strategies for LHC. Also, we finally understand the chemical modification occurring at the surface during electron bombardment. SEY reduction can be assigned to the formation of graphitic carbon on the surface and low energy electrons seem not to be able to promote such graphitization as the higher energy electrons do. Those results have been published on Physical Review Letters [4] and Physical Review ST-AB [5] and presented in different conferences [6]. The XPS data are shown together with the SEY data for the case studied and partial or more complete graphitization is shown by C 1s core level shift towards lower binding energies and corresponds to a systematic reduction of the measured SEY.

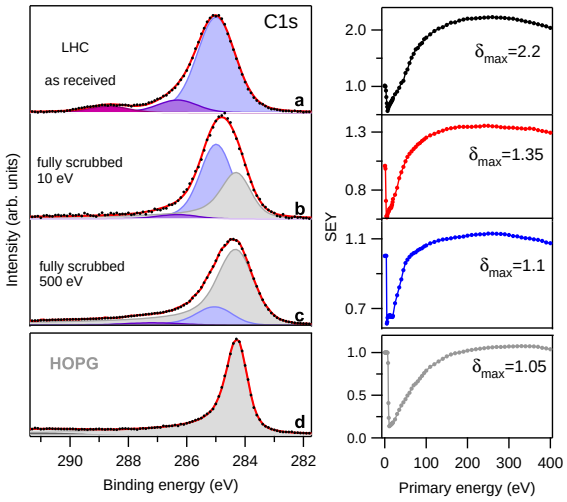

Figure 1: C1s XPS spectra and SEY curves measured on the LHC Cu sample: a) "as received" ; b) after a dose of 3×10^{-2} Cmm^{-2} at 10 eV; c) after a dose of 3×10^{-2} Cmm^{-2} at 500 eV; d) on a freshly cleaved HOPG surface [4].

2. In collaboration with the DAΦNE accelerator division and the DESY vacuum group running PETRA III, we have studied the SEY and the chemical variations of Al samples representative of the two accelerators. PETRA III is a positron ring for very low emittance Synchrotron Radiation and its actual performances seems to be affected by ECE (Electron Cloud Effects). Our study confirms the high SEY value of the Al and that its reduction during scrubbing can vary even due to subtle differences in the experimental conditions. The combined SEY and XPS analysis identify in the extremely high reactivity of Al to oxygen the main cause of

variability. Due to this reactivity, C does not undergo the graphitization process, as it does on other surfaces, suggesting that Al is not suitable for the construction of accelerators with potential ECE [7, 8].

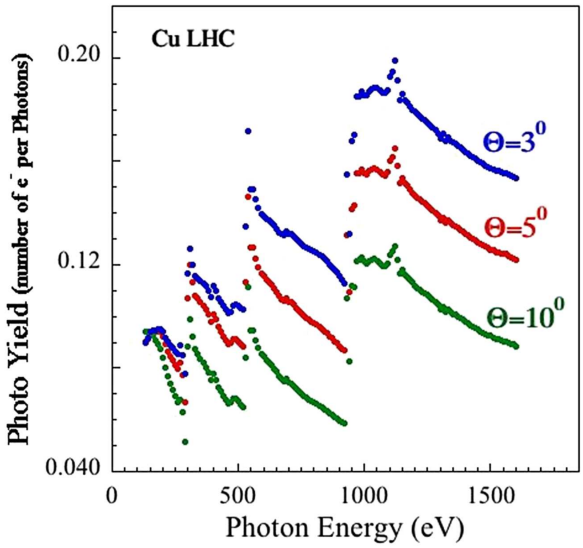

Figure 2: C1s XPS spectra and SEY curves measured on the LHC Cu sample: a) "as received" ; b) after a dose of 3×10^{-2} Cmm^{-2} at 10 eV; c) after a dose of 3×10^{-2} Cmm^{-2} at 500 eV; d) on a freshly cleaved HOPG surface. [9]

3. In collaboration with F. Schäfers from the optic group at BESSYII we pursue an extensive work to study in details reflectivity and Photoelectric Yield (PY, ie. the number of electrons produced per incident photon) [9]. Those parameters are essential ingredients to be used in the simulation codes of electron cloud related instabilities and have been rarely studied with the required precision and parameter space. It has been shown that the mere existence of a certain electron density in the accelerator is able to detrimentally affect the beam quality by the so called single beam instabilities. The electron density present in a vacuum chamber, even in the absence of resonant phenomena, is indeed due to the number of photoelectrons produced to their actual geometrical location. Such essential parameters (especially for LHC consolidation and upgrade) has to be carefully simulated, controlled and careful material choice is needed for its mitigation. One example of this research line is shown in fig.2, where Cu PY has been measured as function of photon energy at different incidence angles.

Last but not least, R. Cimino and F. Zimmermann chaired the fifth electron-cloud workshop ECLOUD12. More than 60 physicists and engineers from around the world gathered at La Biodola, Elba, on 5-8 June, to discuss the state of the art and review recent electron-cloud experience. Fig.2 shows the group photo of the event. ECLOUD12 was jointly organized and co-sponsored by INFN-Frascati, INFN-Pisa, CERN, EuCARD-AccNet and the Low Emittance Ring (LER) study at CERN. R. Cimino was chairing also the local organizing committee, being heavily involved in the organization of this workshop. It was very successful and gave the correct visibility to INFN. A brief report on this workshop can be found in the September issue of the CERN Courrier and the proceedings, edited by R.Cimino, G. Rumolo

and F. Zimmermann will be published as CERN yellow book in 2013. [11].

Figure 3: Group Picture of the 5th International workshop on Electron cloud (ECLOUD-12) [11] chaired by R. Cimino and F. Zimmermann; (Courtesy of: V. Tullio).

Conference Talks

- R. Larciprete: The chemical origin of SEY at technical surfaces presented at Ecloud-12, Isola Elba, 2012.
- F. Schäfers: Soft X-Ray Reflectivity: from Quasi Perfect mirrors to Accelerator Walls" presented at Ecloud-12, Isola Elba, 2012.
- R. Flammini: "XPS and SEY Measurements Upon Scrubbing at Different Electron Kinetic Energies: the Case of TiN' presented at Ecloud-12, Isola Elba, 2012.
- R. Cimino: "ECLOUD12 concluding remarks", presented at Ecloud-12, Isola Elba, 2012.
- R. Cimino: "Material Science for next generation Accelerator Vacuum systems", LAL 12-12-2012.

References

1. LNF Annual Report. This and previous issues.
2. R. Cimino et al., "Experimental efforts at LNF to reduce secondary electron yield in particle accelerators", proceedings of ECLOUD10, 2010.
3. R. Cimino et al., "Can Low-Energy Electrons Affect High-Energy Physics Accelerators?" Phys. Rev. Lett. 93, 14801 (2004).
4. R. Cimino et al., Nature of the Decrease of the Secondary-Electron Yield by Electron Bombardment and its Energy Dependence Phys. Rev. Lett. 109 (2012) 064801
5. R. Larciprete et al. : "Secondary electron yield of Cu technical surfaces: dependence on electron irradiation Phys. Rev. ST-AT, 16 (2013) 011002.

6. R. Larciprete et al., The chemical origin of SEY at technical surfaces Proc. ECloud-12, Isola Elba, 2012.

7. D.R. Grosso et al.: "SEY of Al Samples from the Dipole Chamber of PETRA III at DESY", proceedings of IPAC11.

8. D. R. Grosso et al. :Effect of the surface processing on the secondary electron yield of Al samples" submitted to Phys. Rev. ST-AT.

9. F. Schäfers and R. Cimino, Soft X-Ray Reflectivity: from Quasi Perfect mirrors to Accelerator Walls Proc. ECloud-12, Isola Elba, 2012.

10. R. Cimino, G. Rumolo and F. Zimmermann editors: Proceedings of the:"International Workshop on Electron-Cloud Effects (ECLOUD '12)". To be published as CERN Report No. CERN-2013.

11. R. Cimino, and F. Zimmermann "ECLOUD12 sheds light on electron clouds" CERN Courier September, 2012.

THE *SuperB* ACCELERATOR PROJECT

M.E. Biagini (resp.), R. Boni, M. Boscolo, A. Chiarucci, A. Clozza, A. Drago,
A. Esposito, M Ferrario, A. Gallo, S. Guiducci, C. Ligi, S.M. Liuzzo, G. Mazzitelli, R. Ricci,
C. Sanelli, M. Serio, A. Stella, S. Tomassini

1 Introduction

The scientific success of heavy quark factories (PEP-II at SLAC and KEKB at KEK) in probing new physics scenarios at still unexplored energies through the enormous sensitivity to rare decays deliverable by large luminosity machines and the increasing R&D activity related to future linear electron nano-beam machines that could be better developed through the construction of a nano-beam based machine were the motivations to promote the project of a high luminosity B-factory, called *SuperB*. A number of steps, from the completion of a Conceptual Design Report, issued in 2007, signed by 320 physicists belonging to 85 institutions from 16 countries and successfully evaluated by an international committe to the launch of the Technical Design Report effort, were performed together with a constant parallel development of the users scientific community. In 2010 progress reports with updates from Detector, Accelerator and Physics were published.

The Italian financial support was given within the "flagship project financial plan" at the end of 2010 and endorsed by CIPE, the inter-ministerial body for main infrastructures, in Spring 2011. The governance of the project, following the model of main research European infrastructures, was based on a Consortium, constituted in this case according to the Italian law, funded in a large share by public funds, but able to include memberships and contributions from international partners. The accelerator Consortium was named after Nicola Cabibbo for his pioneering work in weak interactions and for opening what today is called flavor physics. The Consortium founders were the INFN and the University of Rome Tor Vergata whose campus was chose by a bilateral agreement to host the infrastructure. The consortium statute also foresees regular costing review with the first not later than a year from constitution on October 7 2011.

2 Year 2012 activity

In 2012 the activity by the *SuperB* collaboration has been focused on producing a costing document for the Finance Committee of the Nicola Cabibbo Laboratory, which was appointed by the Italian Minister of Research and University to make an evaluation of the final cost of the project.

A small group of physicists and engineers from INFN-LNF, INFN-Genova and INFN-LNS (Catania), under the supervision of Ing. C. Sanelli, has spent several months to evaluate the cost of each single accelerator component, based on the latest design (2011). The possibility to drive a SASE X-ray FEL using the 6 GeV electron linac foreseen by the *SuperB* project, working in parasitic mode with respect to the collider operation, has been also considered and a preliminary design study has been delivered. Some modification of the *SuperB* linac layout resulted to be necessary in order to produce the high brightness beam required for this specific application thus producing an additional cost with respect to baseline *SuperB* linac design. In addition a 100 m long undulator chain has to be considered together with a suitable downstream experimental hall. The Committee declared that this is a scientifically and economically attractive option.

A Work Breakdown Structure (WBS) has been built which describes:

- the cost for each component of the *SuperB* accelerator complex at Tot Vergata;
- the cost of civil infrastructures;
- the cost of personnel, spare equipment and contingency.

A planning with personnel and project timeline was also provided. The cost estimate was carried out by the leaders of the accelerator and technical systems: Main Rings, Radio Frequency, Diagnostics and instrumentation, Feedbacks, Vacuum, Injection system (including: Sources, Linacs, Damping Ring, Transfer Lines), XFEL option, Power supplies, Normal conducting magnets, Supraconducting magnets and solenoids, HVAC and fluids, Cryogenics, Electrotechnics, Mechanics, Controls, Civil engineering, Safety, Radioprotection.

The Total Project Cost is the sum of many different items:

- Accelerator cost
- Area preparation cost
- Civil Engineering cost
- PEP-II components re-utilization cost
- Personnel cost
- Contingency
- Spare parts

The first three items, Accelerator, Area preparation and Civil Engineering costs have been evaluated according to the WBS, where different parts or components of the accelerators, related buildings and their infrastructures have been individually identified. An extremely detailed WBS normally does not exceed 8 digits. In the *SuperB* case we got generally 6 digits, this can be considered equivalent to a confidence level of about 90-95%. Single components of a system or plant have been identified, their quantities have been defined and, once the cost of the single unit has been evaluated, the system or plant cost has been determined. The unit cost of a single component has been determined in three different ways. In the first, the responsible of the related activity has contacted one or more companies to quote an updated price. In some cases only one firm gave the quotation, but where more quotations were available, the more convenient one has been considered. This was true for the commercially available components and systems. In the second way, for those parts of the accelerators not commercially available, the quotation has been derived from previous similar realization. This is the case for custom vacuum chambers or diagnostics components: their cost has been derived from the experience gained by the recent construction of the Pavia hadro-therapy accelerator CNAO. A third way is the analytic approach where, based on the working group expertise, the cost is reconstructed form basic row material costs. A special case has been made for magnets, in particular for the main rings, whose cost has also been evaluated in two different ways. The two method gave small differences of the order of few per cent. The same independent groups evaluated and excluded on economic and functionality considerations the option of reusing PEP-II magnets.

The committee in its final report has underlined the high quality of the work that was presented. In the following is a short summary of the conclusions:

"The project team presented a comprehensive and detailed cost estimate for the project. The WBS approach of assessing the cost is systematic and carried out at a level sufficient to assure

more than 90% completeness. We found the cost estimate to be broadly credible. We believe that the scale of the cost is roughly correct, and is sufficiently sound to enable decisions to be taken on funding for the project. The committee wishes to underline the high quality of the work that was presented, especially considering the very limited manpower and resources allocated to a project of this size. The committee feels that we are facing a very critical point of the project and decisions have to be taken quickly on the funding and on the support to the project by national laboratories. Without that, the technical advance of international competitors will increase, putting in serious danger the scientific case of *SuperB*."

The Committee report was presented to the Minister of Research and Education in December 2012. The budget already allocated for the Flagship Project *SuperB* was not sufficient to guarantee the needed resources.

However it was suggested that a downscaling of the accelerator to a smaller size and lower energy should be pursued in order to estimate if its cost could be covered by the available budget.

It has been then decided that the *SuperB* team, with the technical personnel hired by the Cabibbo Laboratory, will be involved in 2013 in the design of a smaller collider, working in the Tau/Charm energy range, which could meet all the requirements and also be compatible with the Flagship Project already approved, since it was planned that the *SuperB* collider could be operated at the Tau/Charm energy for high precision rare measurements, as for example the Lepton Flavor Violation.

3 Publications in 2012

1. M.E. Biagini, " Overview of B-Factories ", Invited talk at the 3rd International Particle Accelerator Conference IPAC 2012, New Orleans, USA, May 2012.

2. S.M. Liuzzo, M.E. Biagini, P. Raimondi et al, "Tests of low emittance tuning techniques at SLS and DAΦNE", Proceedings of 3rd International Particle Accelerator Conference IPAC 2012, New Orleans, USA, May 2012.

3. S.M. Liuzzo, M.E. Biagini (INFN/LNF), Y. Papaphilippou (CERN) , T. Demma (LAL) ,P. Raimondi (ESRF), "Frequency map analysis for *SuperB*", Proceedings of 3rd International Particle Accelerator Conference IPAC 2012, New Orleans, USA, May 2012.

4. S. Guiducci, A. Bacci, M. E. Biagini, R. Boni, M. Boscolo et al., "Baseline design of the *SuperB* factory injection system ", Proceedings of 3rd International Particle Accelerator Conference IPAC 2012, New Orleans, USA, May 2012.

5. D. Alesini et al., "A possible hard X-Ray FEL with the SuperB 6 GeV Electron Linac, INFN-12-14/LNF, 2012.

6. M. Ferrario, on behalf of the XFEL@SuperB collaboration, "Additional cost estimate for the XFEL option", June 2012.

SPARC_LAB
Sources for Plasma Accelerators and Radiation Compton with Lasers and Beams

M. Ferrario (Resp. Naz.), D. Alesini, M. P. Anania (Ass. Ric.), F. Anelli (Art. 15), M. Bellaveglia (Art. 23), R. Boni (Ass.), L. Cacciotti (Tecn.), M. Castellano (Ass.), E. Chiadroni, P. Chimenti (Art. 15), D. Di Giovenale (Art. 23) G. Di Pirro, A. Drago, A. Gallo, C. Gatti, G. Gatti, A. Ghigo, V. Lollo (Tecn.), M. Migliorati (Ass.), A. Mostacci (Ass.), E. Pace, L. Palumbo (Ass.), L. A. Rossi (Art. 23), R. Sorchetti (Tecn.), B. Spataro, S. Strabioli, (Art. 15), C. Vaccarezza, F. Villa (Ass. Ric.).

Participant institutions: other INFN sections (Mi, RM1, RM2, Bo, Pi, Fe, Le, Fi, Na, LNS, Ba, Ca, Ts), ENEA-Frascati, CNR-INO-Pisa

1 Introduction

A new facility named SPARC_LAB (Sources for Plasma Accelerators and Radiation Compton with Lasers and Beams) has been recently launched at the INFN National Laboratories in Frascati, merging the potentialities of the former projects SPARC [1] and PLASMONX [2]. Ten years ago in fact, a robust R&D program on ultra-brilliant electron beam photoinjector and on FEL physics, the SPARC project, a collaboration among INFN, ENEA and CNR, was approved by the Italian Ministry of Research and located at the INFN National Laboratories in Frascati.

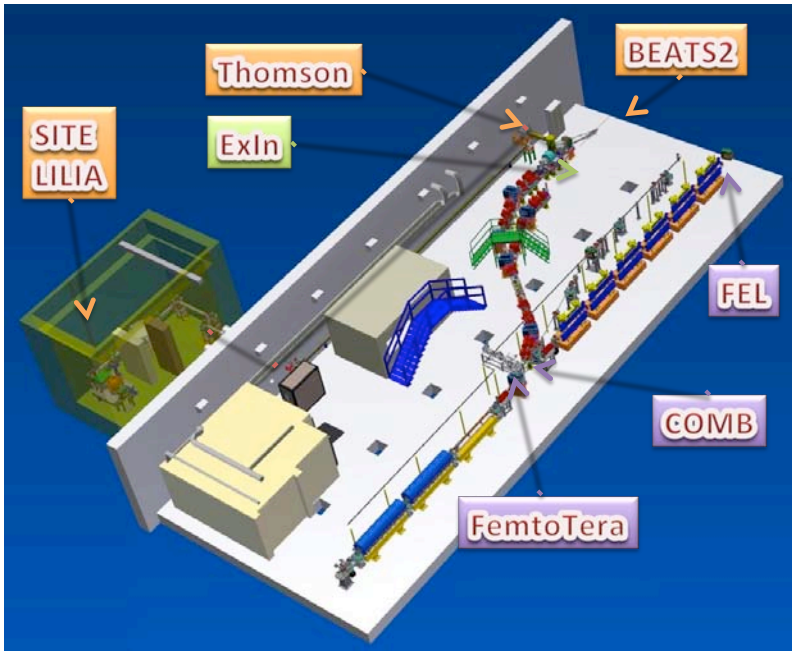

Figure 1.1: Layout of the SPARC_LAB facility with the experiments

The test facility is now operating, hosting a 150 MeV high brightness electron beam injector [3], able to operate also in the velocity bunching configuration [4], which feeds a 12 meters long undulator (*FEL experiment*). Observations of FEL radiation in the SASE [5], Seeded [6] and HHG [7] modes have been performed from 500 nm down to 40 nm wevelength. A parallel beam line is used to test new diagnostics tools, like Electro Optical Sampling. A narrow band THz radiation source [8] (*experiment TERASPARC*) is now located at exit of the linac. In parallel to that, INFN decided to host a 200 TW laser that will be linked to the linac and devoted to explore laser-matter interaction, in particular with regard to laser-plasma acceleration of protons (*experiment LILIA*) and electrons [9] in the self injection mode (*experiment SITE*) and external injection mode (*experiment EXIN*). The facility will be also used for particle driven plasma acceleration experiments [10], (*COMB experiment*). A Thomson back-scattering experiment coupling the electron bunch to the high-power laser to generate coherent monochromatic X-ray radiation is also in the commissioning phase (*experiment THOMSON*). An upgrade of the linac energy is also foreseen by the end of 2013 by installing two new high gradient C-band structures developed at LNF in the framework of the ELI_NP collaboration [18]. In Figure 1.1 the layout of the facility is shown.

The SPARC_LAB high power laser system, named FLAME, has been recently fully commissioned. FLAME is based upon a Ti:Sa, chirped pulse amplification (CPA) laser able to deliver up to 220 TW laser pulses, 25 fs long, with a 10 Hz repetition rate at a fundamental wavelength of 800 nm, see Figure 1.2.

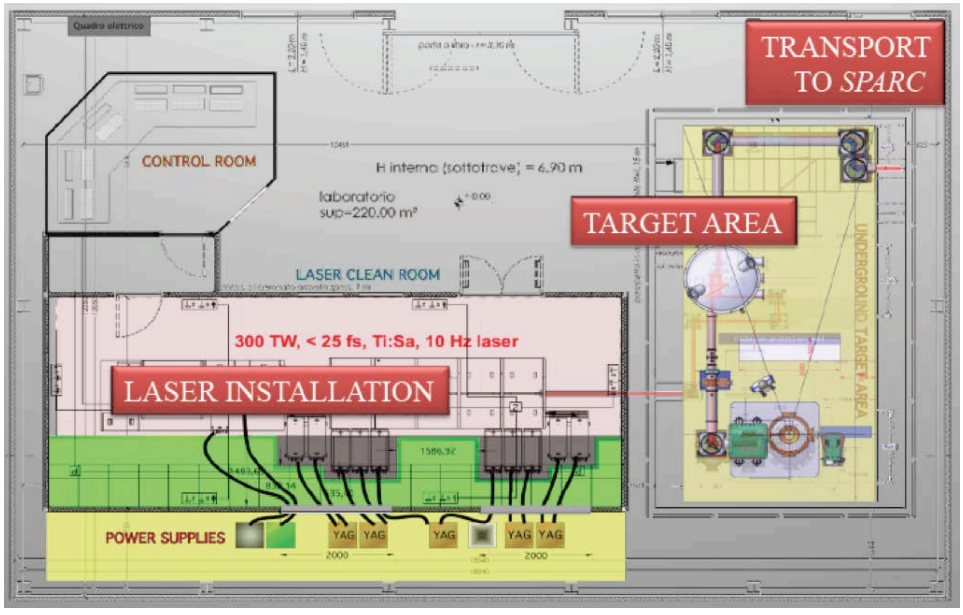

Figure 1.2: Layout of the FLAME laser with the target area for self-injection plasma acceleration experiments.

The system features a high contrast ratio (>10^{10}) and has a fully remotely controlled operation mode. It includes a front-end with pulse contrast enhancement, bandwidth control and regenerative amplifier and yields pulses with 0.7 mJ in 80 nm bandwidth. These pulses are then further amplified by the first amplifier up to 25 mJ while the second amplifier brings the energy up to the 600 mJ. The third

cryogenic amplifier is based on a 50 mm Ti:Sa crystal pumped by 10 frequency doubled Nd:YAG laser pulses, reaching an energy up to 20 J at 532 nm. The extraction energy is as high as 35%, leading to a final energy in the stretched pulses in excess of 7 J. The pulse is then compressed to a minimum pulse duration below 30 fs. Once compressed, the pulse is transported under vacuum to the target area via remotely controlled beam steering mirrors. In the typical experimental conditions of laser wakefield acceleration in self-injection configuration, the laser pulse is focused at peak intensities exceeding 10^{18} W/cm^2 which, with our ASE contrast, gives a precursor laser intensity on target below 10^9 W/cm^2. In the case of interaction with gases with pressures ranging from 1 to 10 bar, this laser intensity is below the plasma formation threshold for laser pulses of sub-nanosecond duration which is the typical duration of ASE pulses. Therefore we can reasonably assume that in the case of interaction with gases, no premature plasma formation occurs and the CPA pulse can be focused directly in the gas.

Among the different uses of FLAME, the scientific program includes self-injection and external injection [19] experiments and the realisation of an X-ray source based on the Thomson backscattering process. To this purpose, a careful characterization of FLAME performances, with particular reference to the transverse beam quality was carried out during the commissioning. The measured Strehl ratio is greater than 50% up to pulse energies of approximately 6J. For energies between 6 and 7 J, the phase front distortion increases leading to a reduction of the Strehl ratio to a minimum value of 35%. Our measurements show that the phase front pattern remains very stable from shot to shot at a given pulse energy. This makes the phase front correction with adaptive optics (planned for installation by the end of 2012) a reliable and complete solution to achieve a high quality focal spot.

We describe hereafter in more details the status and the achievements of the SPARC_LAB experiments during the year 2012.

References

[1] D. Alesini et al., Nucl. Instr. and Meth. A 507, 345 (2003).
[2] D. Giulietti et al., Proc. of PAC 2005, Knoxville, Tennessee, USA.
[3] M. Ferrario et al., Phys. Rev. Lett. 99, 234801,(2007)
[4] M. Ferrario et al., Phys. Rev. Lett. 104, 054801 (2010)
[5] L. Giannessi et al., Phys. Rev. Lett. 106, 144801 (2011).
[6] M. Labat et al., , Phys. Rev. Lett. 107, 224801 (2011).
[7] L. Giannessi et al., Phys. Rev. Lett. 108, 164801 (2012).
[8] E. Chiadroni et al., Journal of Physics: Conference Series 357 (2012) 012034.
[9] L. A. Gizzi et al., Europ. Phys. Journal - Special Topics 175, 3 (2009).
[10] M. Ferrario et al., Nucl. Inst. and Meth. A, V. 637, 1, May 2011, S43-S46
[11] P. Oliva et al., Nucl. Instrum. Meth. A 615 93-99, (2010)
[12] A. Bacci et al, Nucl. Instrum. Meth. A 608 S90-S93, (2009)
[13] U. Bottigli, et al., Il Nuovo Cimento, 29C , N.2 , 2006.
[14] A. Mostacci et al., TUPPD055, these proceedings.
[15] P. Muggli, Proc. of PAC 2009, Vancouver, Canada
[16] A. Bacci et al, Proc. of FEL Conf. 2011, Shanghai, China.
[17] P. Tomassini, private communication.
[18] C. Vaccarezza, TUOBB01, proceedings of IPAC 2012.

[19] A. R. Rossi, WEEPPB002, proceedings of IPAC 2012.

2 SITE experiment

M. P. Anania (Ass. Ric.), L. Cacciotti (Tecn.), D. Di Giovenale (Art. 23) G. Di Pirro, A. Drago, A. Gallo, C. Gatti, G. Gatti, V. Lollo (Tecn.), F. Villa (Ass. Ric.).

Participant institutions: other INFN sections (Mi, RM1, RM2, Bo, Pi,), CNR-INO-Pisa (L.A. Gizzi, Resp. Naz)

The control of ultra-high gradient laser-plasma acceleration [1] is being pursued worldwide and advanced schemes [2] are being proposed for the future staged configurations. Meanwhile, existing laser-plasma accelerating scheme are being considered for the development of all-optical radiation sources. In view of this perspective [3], experimental runs dedicated to laser-plasma acceleration experiment with self- injection (NTA_SITE) [4] have been performed at FLAME based on previous pilot experiments [5]. The first run was carried out during the early commissioning stage in 2010 at relatively low laser power (≈10 TW), and showed successful generation of mono-energetic, high energy electron bunches with a moderate to high degree of collimation down to the 6 mrad level [6]. These results were also described in the previous issues of the LNF report with an overview of the experimental set up. A second experiment at higher laser power (≈100 TW) was carried out in July 2012 and enabled us to further explore the experimental configurations [6, 7]. Here we present some preliminary highlights of the results of the observed acceleration process.

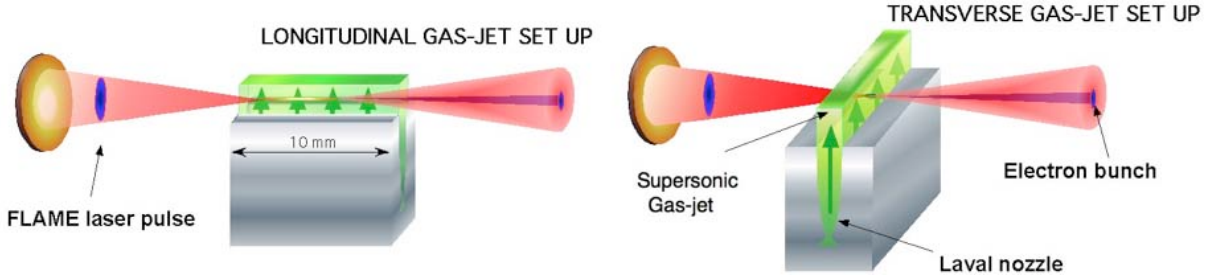

Figure 2.1: Schematic layout of the laser-gas-jet interaction for the production of energetic electron bunches in the self-injection configuration used in the SITE experiment at LNF. We used two different gas-jet length of 10 mm (longitudinal propagation) and 1.2 mm or 4 mm (transverse propagation).

The second SITE run was focused on a more systematic study of the acceleration process for different gas type, gas density using both the transverse and lon- gitudinal gas-jet configurations of Figure 2.1. We used nitrogen or helium with a back pressure ranging from 1 to 17 bar, corresponding to a maximum gas density approximately in the range from 5×10^{18} and 2×10^{19} atoms/cm^3 and a maximum laser-intensity on target of 2×10^{19} W/cm^2 . A total of 3000 shots with e-bunch production was recorded and data were taken with an optical imaging system and Lanex screen placed at 475 mm from the gas-jet to measure both the electron bunch transverse size and, with the insertion of the 50 mm long magnetic dipole at 132.5 mm from the gas-jet, the energy spectrum. In addition, a shadowgraph of the interaction region was taken to measure the longitudinal extent and the transverse

size of the interaction region. The imaging system was set to view the interaction region in the vertical direction, i.e. along the axis perpendicular to the laser polarization plane to image out the Thomson scattered radiation. The plot of Figure 2.2 shows the typical Thomson image obtained from measurements with the longitudinal gas-jet configuration.

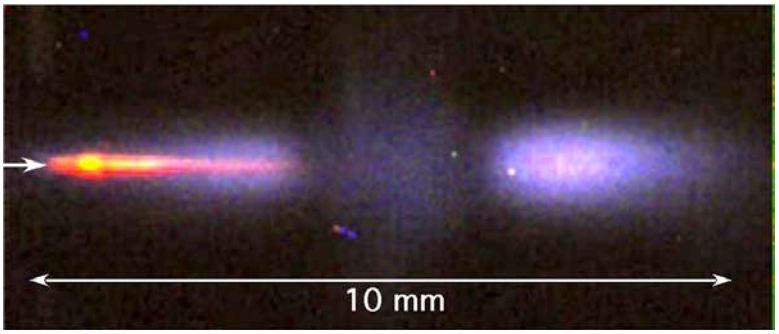

Figure 2.2: Images of the Thomson emission from propagation of the laser pulse in a Nitrogen gas-jet at 10 bar valve pressure. The laser propagates from left to right. Also visible in the image is the plasma self-emission.

As shown by the arrow, the laser propagates from left to right showing a clear Thomson emission (red-yellow in the color figure) in the first 3.2 mm (FWHM) of the propagation. Taking into account the laser beam parameters, we expect a depth of focus of approximately ± 260 μm. Therefore, according to the image of Figure 2.2, laser propagation occurs over a propagation length which is several times the depth of focus. The propagation length was found to be dependent on the gas density and pressure, ranging from approximately 1.3 mm (FWHM) for 70% Nitrogen gas mixture (air) at 1 bar pressure to less than 2 mm (FWHM) for Helium at 15 bar pressure. These results indicate that propagation length increases at higher electron density where stronger refraction effects may occur on the propagation of the laser pulse in the plasma. At this stage we can anticipate possible contribution of self-focusing effects to the observed behavior of the laser pulse. Detailed numerical simulations are in progress [8] for a confirmation of this result.

Information about the accelerated electron bunches was obtained by using the LANEX scintillating screen to measure both the angular divergence and the energy spectrum. The image of Figure 2.3 (left) shows the typical image of a single electron bunch obtained from optimized acceleration in Nitrogen. According to this image, the single bunch exhibits a divergence of approximately 1 mrad FWHM, a value significantly smaller than that measured during the first 2010 SITE run and among the smallest values measured in similar experiments worldwide. The image of Figure 2.3 (right) shows instead the same image integrated over 30 laser shots which gives a overall cone of emission of approximately 10 mrad HWHM. The latter measurement gives an indication of the shot-to-shot pointing stability of the electron bunch. As for the origin of this fluctuation, it is unlikely to be affected by the laser pointing stability which was measured to be within the μrad range. The oscillation of the electron bunch inside the accelerating structure [9] is instead being explored as a possible explanation of the observed limit to the bunch pointing stability.

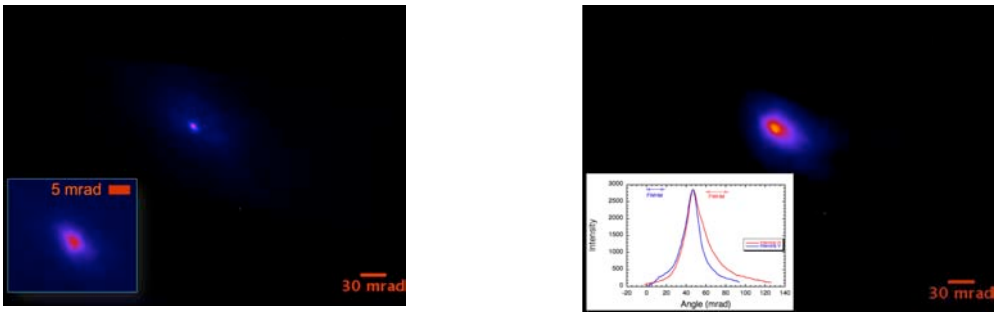

Figure 2.3: Left: Image the scintillating LANEX screen at 47 cm downstream the interaction point showing the bunch transverse size of approximately 0.5 mm and a corresponding bunch divergence of 1 mrad. Right: integrated image of the electron bunch over 30 laser shots showing a total pointing stability of approximately 10 mrad. The bottom-left plot shows the lineout of the image across the vertical and horizontal directions.

Finally, information about the energy of the electron bunch was obtained by inserting the permanent magnet dipole down-stream from the laser focal position. Although analysis of electron spectra is still in progress, at this stage we can anticipate that the measured energy was typically in the range between 50 and 200 MeV, with occasional higher energy events up to the upper limit of the working range of our spectrometer (1GeV). The image of Figure 2.4 shows a typical spectrum of acceleration in Nitrogen in the same conditions of Figure 2.3. The white dot in the centre of the image indicates the average undeflected (no magnet) landing position of electrons.

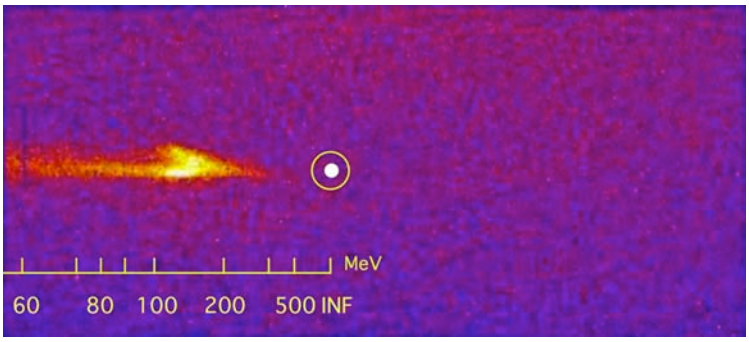

Figure 2.4: Raw spectrum of a typical electron bunch accelerated from a Ni- trogen gas-jet. The spectrum shows a main component above 100 MeV and a low energy tail extending down to 60 MeV. The white dot indicates the landing position of undeflected electron.

In the presence of the magnet, electrons will be deflected on the l.h.s. of the screen according to the dispersion curve of the spectrometer. According to this image, the spectrum shows a main component around 150 MeV and a low energy tail extending down to 60 MeV. This general behavior was quite reproducible from shot to shot and accurate deconvolution of all the spectra is currently in progress to take into account instrumental broadening. These results are being investigated via numerical simulations and the actual acceleration regime operating in our experimental conditions is being identified.

Experimental results obtained during the 2012 self-injection run at FLAME show effective acceleration of highly collimated, high energy electrons up to 1 GeV, with moderate reproducibility and good pointing stability around the 200 MeV energy, a first step for the proposed all-optical radiation source at FLAME.

Acknowledgements

The work was carried out in collaboration with the High Field Photonics Unit (MD.P03.034) and X-ray Photonics (MD.P03.006.006) at INO-CNR partially funded by CNR through the ELI-Italy project and by the MIUR-FIRB SPARX respectively. We acknowledge the CINECA Grant N. HP10CZX6QK2012 for the availability of high performance computing resources and the INFN APE project for the availability of the QUonG cluster.

References

[1] J. Faure et al., Letters to Nature **431**, 541 (2004)
[2] W. P. Leemans *et al.*, Nat. Phys. **2**, 696 (2006).
[3] L.A.Gizzi et al., Nuclear Instr. Methods, B, 2013, in press
[4] L.A.Gizzi *et al.*, Il Nuovo Cimento C **32**, 433 (2009).
[5] L.A.Gizzi, in *Charged and Neutral Particles Channeling Phenomena*, *The Science and Culture Series*, edited by W. S. Publishing (2010).
[6] T. Levato *et al.*, in *Laser-Plasma Acceleration*, International School of Physics "Enrico Fermi", edited by F.Ferroni and L.A.Gizzi (IOS Press, 2011), Vol. CLXXIX.
[7] L.A.Gizzi, Technical report, INFN and CNR-INO (unpublished).
[8] F. Rossi *et al.*, AIP Conference Proceedings **1507**, 184 (2012).
[9] K. T. Phuoc *et al.*, Phys. Rev. Lett. **97**, 225002 (2006). [44]

3 LILIA experiment

M.P. Anania (Ass. Ric.), L. Cacciotti (Tecn.), D. Di Giovenale (Art. 23) G. Di Pirro, A. Drago, G. Gatti, R. Sorchetti (Tecn.), F. Villa (Ass. Ric.).

Participant institutions: other INFN sections (Mi (C. De Martinis (Resp. Naz) , RM1, RM2, Bo, Pi, LNS), CNR-INO-Pisa

NTA-LILIA is an experiment of light ions acceleration trough laser interaction with thin metal targets to be done at the FLAME facility, which is now running in Frascati. LILIA, in particular, is finalized to study, design and verify a scheme which foreseen the production, the characterization and the transport of a proton beam toward a stage of post acceleration (high frequency compact linacs). Now the maximum operating laser intensity is limited to 10^{19} W/cm^2 due to the lack of a parabola with a focal length shorter that the current used. In this configuration, according to the interaction theory by short pulse laser and to performed numerical simulations, we expect a proton beam with maximum energy of a few MeV and a number of proton/shot up to 10^{10}-10^{12}.

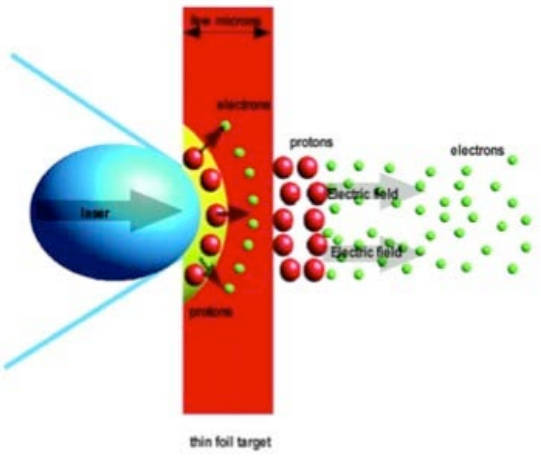

Figure 3.1 Schematic representation of the proton acceleartion experiment

In the majority of experiments for proton accelerations, the regime occurring is the so called TNSA (Target Normal Sheath Acceleration). The laser pulse heats the electrons and ionizes the medium. Next the electrons diffuse around the target building an intense electric field. This field accelerates the free protons present on the target surfaces, both in the forward direction (from the rear side) and in the backward direction (from the front surface).

The FLAME facility has been fully operational in the middle of 2012 for the first test experiments of electron Laser Wakefield Acceleration (LWFA). At the end of October 2012 it was possible to install the components for the proton acceleration experiment (LILIA).

As of now the maximum laser intensity is limited to 10^{19} W/cm^2 due to the lack of a parabola with focal length shorter than the present one. In this configuration, according to performed numerical simulations, we expect a proton beam with maximum energy of few MeV (10 MeV is as of now the maximum energy allowed by the local authorities for the place where the experiment will be located) and total intensities up to 10^{10}-10^{12} protons/shot. Although these values are modest compared to the present state of art, nevertheless their scientific relevance is very important due to the fact that we will have, with a reasonable effort, a real laser driven source that will play the role of a test facility as far as emission process control and repeatability and post acceleration studies will be involved. In LILIA phase I we plan to perform a parametric study of the correlation of the maximum TNSA accelerated proton energy, with respect to the following parameters:

- Laser pulse intensity (in the range $10^{18} – 5\ 10^{19}$ W/cm^2)
- Laser pulse energy (in the range 0.1-5 J)
- Laser pulse length (in the range 25 fs- 1ps)
- Metallic target thickness (in the range 1-100 μ).

In such a frame we would like to deeply investigate the experimental scale rules within the possibilities offered by the FLAME facility. Moreover, this will provide the opportunity to get experience in the development of diagnostic techniques and in target optimization. The possibility to produce a real proton beam able to be driven for significant distances (50-75 cm) away from the interaction point and which will act as a source for further accelerating structures will be also investigated.

When FLAME phase II performances will be available (Short focal length OA Parabola: waist≈2.5μ, $I \approx 10^{21} W/cm^2$, we might select a bunch at E = 30 MeV with a narrow spread ΔE and still have a reasonable number of protons (10^7 ~ 10^8). This opens a very interesting perspective for applications such as hadrontherapy in connection with a post-acceleration stage in order to reach energies up and beyond 100 MeV. Indeed if a sufficient current intensity can be reached at 30 MeV with a narrow spread ΔE/E ~ 1% and a good beam quality after transport, energy selection and collimation, the protons bunch might be post-accelerated after injection in a high field linac (Figure 3.2), as the one developed for the INFN ACLIP project (suitable for medical applications)

The LILIA experiment has been designed to be housed in the interaction chamber available at the exit of the laser compressor in the FLAME bunker. The layout of the first phase of the experiment is shown in Figure 3.2 and 3.3 and it foresees:

- a special designed optical breadboard, with standard metric holes format, to allow the definition of a common reference plane level and the assembly of components within the chamber;
- a multi shot target holder able to be remotely moved in x-y-z directions and rotated along the z-axis with respect to the laser beam. This will allow a very accurate positioning of the targets with respect to the laser beam and the possibility to perform multi shot experiments without having to open the vent of the chamber to replace the already used targets. The target holder has been designed for the use of aluminium foils (pure up to 99.0%) with thickness as low as *1 μm*and the possibility to provide up to 30 usable shots. The position accuracy of the targets with respect to the laser beam is of the order of *20 μm* for the translation stages and of 0.1 degrees for the rotation stage. The alignment of the targets with respect to the power laser beam will be accomplished using alignment lasers and devoted optical windows in the chamber;
- a remotely movable multi-detector holder able to house 8 stacks of radio-chromic detectors to be used close (*50 mm*) to the interaction point. A fixed lead foil (*3 mm* thick) is used to avoid the damage of stacks adjacent to the one of interest for a specific laser shot;
- the availability of multiple detectors copes with the possibility to perform multiple experiments on different targets in a very short time, minimizing the fluctuations in the laser beam characteristics;
- a more accurate analysis of the energy distribution of the produced ions will be carried out at a fixed emission angle with a Thomson parabola (TP) spectrometer with its related detectors. A *150 mm* diameter vacuum movable window in the interaction chamber at an angle of 120 degree with respect to the laser beam will allow the positioning of the TP.

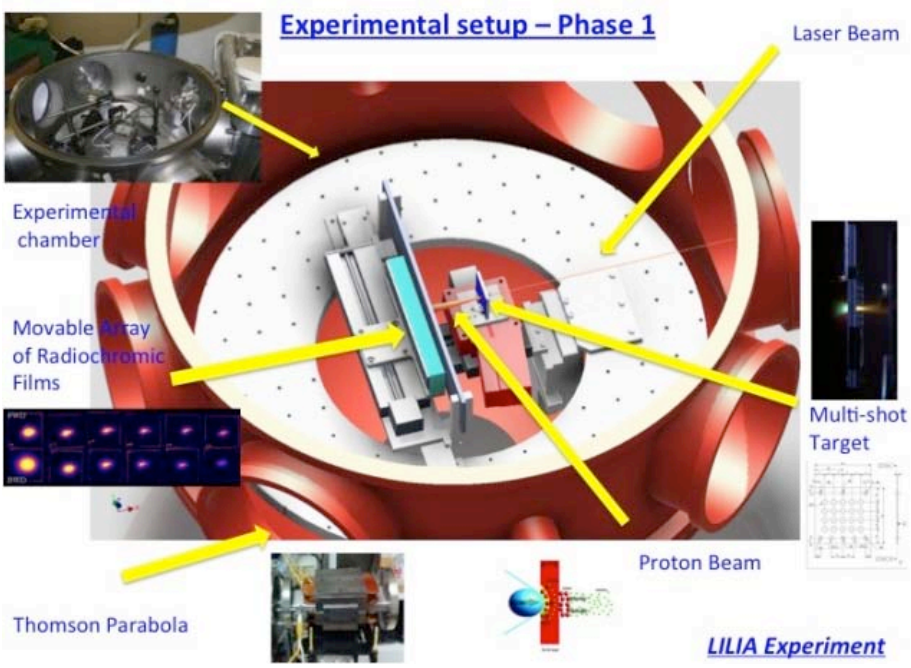

Figure 3.2 Sketch of the LILIA mechanical setup

During autumn 2012 the mechanical set up has been installed and aligned in the interaction chamber. The FLAME beam has been focused on the target and preliminary test have been carried out during two shifts in October and December 2012. During these tests we were limited for technical problems in the laser power that was of the order of 2 joules. Nevertheless we have obtained the first experimental evidence of proton acceleration.

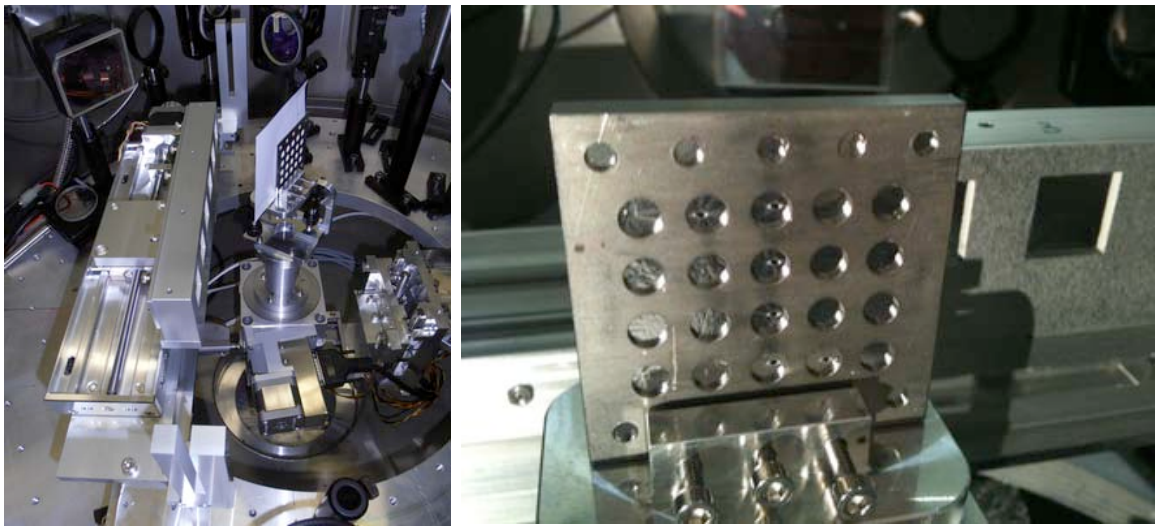

Figure 3.3 The remotely movable radio-chromic detectors and the multi-shot target holder

Behind the multi-shot target two different detectors are placed: an a EBT3 radio-chromic film by Gafchromic films or a CR-39 plastic polymer. The Figures 3.4 and 3.5 show the first pictures of the EBT3 and CR-39 impressed by protons emitted from a 3 μm Al target with a 1.5 Joule laser shot.

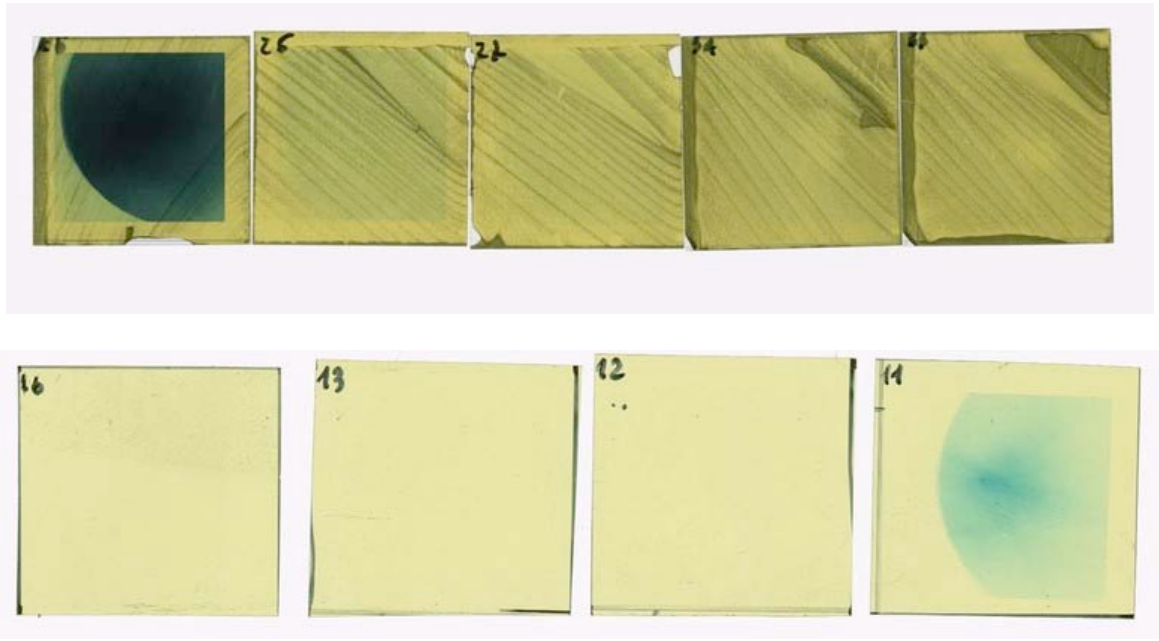

Figure 3.4 Impressed EBT3 radio-chromic films

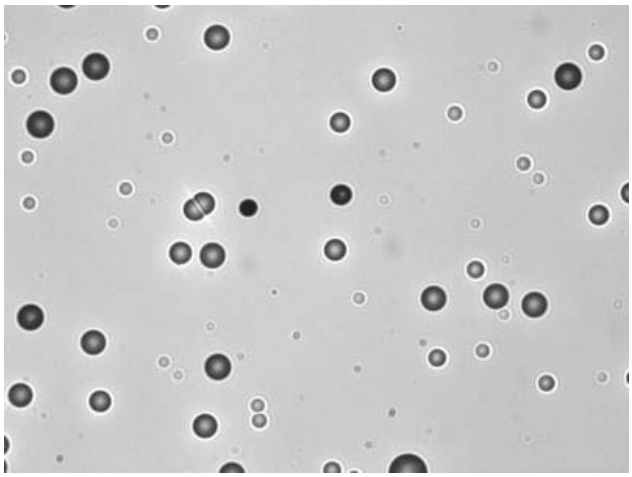

Figure 3.5 Impressed CR39 film

The radio-chromic detector was shielded by a 6 μm thick aluminium foil in order to protect it by the light emission during the laser interaction.

By the obtained results we can derive a lower limit for the maximum energy of the emitted protons of at least 1.6 *MeV*. A detailed analysis of the acquired data is now underway.

References

[1] A. Bacci, D. Batani, G.P. Cirrone, C. De Martinis, D. Delle Side, A. Fazzi, D. Giove, D. Giulietti, L. Gizzi, L. Labate, T. Levato, P. Londrillo, M. Maggiore, L. Martina, V. Nassisi, M. Passoni, A. Sgattoni, L. Serafini, S. Sinigardi, G. Turchetti, L. Velardi, "Laser induced proton acceleration at the FLAME facility in Frascati: LILIA experiment", Atti del II Workshop Plasmi, Sorgenti Biofisica ed Applicazioni, Lecce, 26 Ottobre 2010, Edizione Coordinamento SIBA, ISBN 978-88-8305-087-9 (print version), (2011)

[2] M. Ferrario et al. "Recent Results at the SPARC_LAB Facility" Proceedings of IPAC2012, New Orleans, Louisiana, USA

[3] L.Serafini, A.Rossi, A.Bacci, M.Ferrario, P.Tommasini, C.De Martinis, "Status of the Project PLASMONX and the experiment LILIA" Proceedings COULOMB'11:Optical Acceleration of Ions and Perspectives for Biomedicine. November 4-5 2011 –Bologna – in press

[4] V. Nassisi, D. Delle Side, L. Velardi, G. Buccolieri, F. Paladini, D. Giove, C. DeMartinis, A.Fazzi. High voltage pulse of short duration to feed solenoids for intense ion beam transport. IIIWorkshop Plasmi, Sorgenti, Biofisica ed Applicazioni, Lecce 19 Ottobre 2012

[5] G.Turchetti, S.Sinigardi, P.Londrillo, F.Rossi, D.Giove, C.De Martinis, "Transport and energy selection of laser generated protons for postacceleration with a compact linac " accepted for publication as a Regular Article in Physical Review Special Topics- Accelerators and Beams.

4 THOMSON experiment

C. Vaccarezza (Resp. Naz.), M.P. Anania (Ass. Ric.), M. Bellaveglia (Art. 23), M. Cestelli Guidi (Art. 23) , D. Di Giovenale (Art. 23) G. Di Pirro, A. Drago, M. Ferrario, A. Gallo, G. Gatti, A. Ghigo, A. Marcelli, E. Pace, L. Palumbo (Ass.), F. Villa (Ass. Ric.).

Participant institutions: other INFN sections (Mi, RM1, RM2, Ba, Ca, Pi, Ts, Fe, Le, Fi, Na, LNS), ENEA-Frascati

In the 2012 the SL-Thomson project has seen the completion of the procurement of the hardware foreseen for the interaction region. The Thomson source installation will be completed by February 2013 and the electron beam line commissioning will take place in March, while the photon beam transport optimization will be addressed in April 2013 and the collisions are expected soon after.
The SL-Thomson project foresees the realization of a monochromatic source of ultra-fast X-ray pulses by Thomson back-scattering (TS): the key points of this configuration are the flexibility and the potential compactness with respect to conventional synchrotron sources.
The TS source driven by the SPARC photoinjector high-quality electron beam will be able to work in the high-flux- moderate-monochromaticity-mode(HFM2), in the moderate-flux- monochromatic-mode (MFM) and in the short-and-monochromatic-mode (SM).

The first experiment to take place will be BEATS2 [1] with the source operating at high flux.

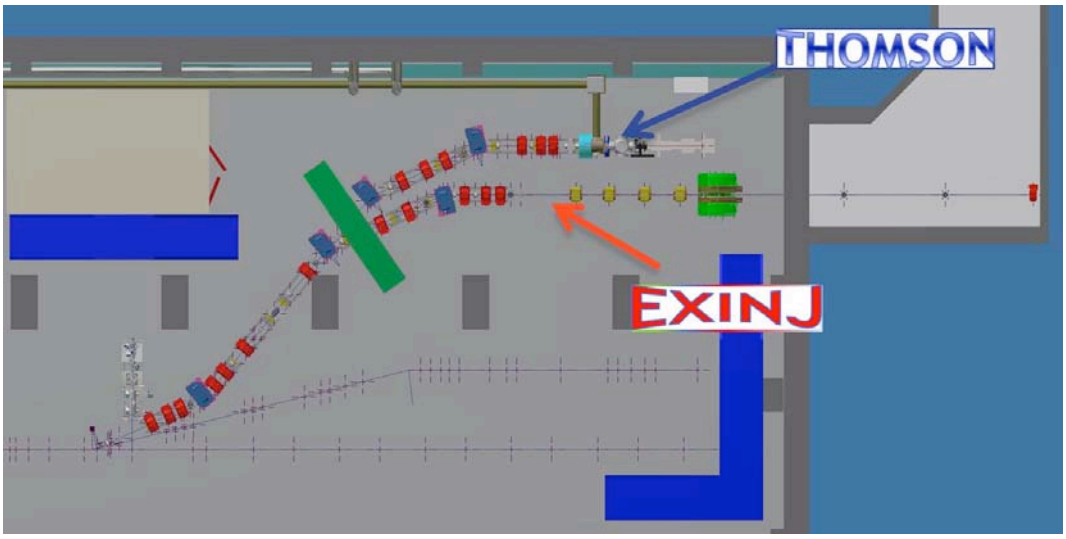

Figure 4.1 CAD drawing of the Thomson and Exinj electron beam transfer lines layout.

The installation of the electron and photon beam lines up to the Thomson Interaction Point has been almost completed in 2011, while in 2012 the interaction chamber setup has been finalized and procured together with the 1.2 T solenoid magnet for the final focusing at low energy.
The electron beamline brings the electron beam from the photoinjector to the interaction point where the laser pulse coming from the FLAME laser system arrives through a dedicated photon beamline. In this configuration the electron beam energy can range from 28 MeV up to 150 MeV, and the electron beam transport is meant to preserve the high brightness at the linac exit and to ensure a very tight focusing and a longitudinal phase space optimization for the whole energy span.
The electron beam parameter list for the two interaction points are reported in Table 1. In Figure 4.1 the machine layout is shown, where the electron transfer line departs from a three way vacuum chamber inside the first dipole downstream the RF deflector that is used for the six-dimensional phase space analysis of the SPARC beam.

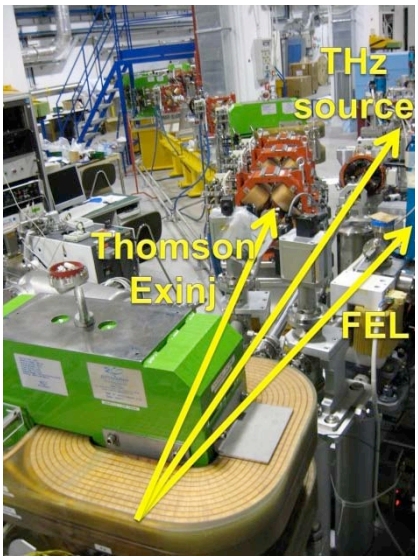

Figure 4.2 Three-way branch for the FEL, THZ and Thomson-Exinj beamlines.

This dipole is also part of the chicane foreseen for the seeding configuration of the SPARC FEL undulator (straight direction downstream the photoinjector) and of the 14° degrees dogleg that brings the electron beam up to the SPARC Therahertz source, see Figure 4.2

Table 1 Electron beam parameters at the Thomson source interaction point

Parameter	Value
Bunch charge (nC)	**0.2 ÷ 1.0**
Energy (MeV)	28 ÷150
Length (ps)	15 ÷ 20
$\varepsilon_{n\ xy}$ (mm mrad)	1 ÷ 5
Energy spread (%)	0.1 ÷ 0.2
Spot size at interaction point rms (mm)	05 ÷ 20

The electron beamline consists in a 30 m double dogleg ending in a two branch beam delivery line that provides two separate interaction regions: the outer one from the photoinjector is dedicated to the Thomson Source. The total beam deflection is about six meters from the photoinjector and undulator axes. A total of six rectangular dipoles and 19 quadrupoles have been installed in 2011 to drive the electron beam up to the two IPs.
From the magnetic measurements results all the dipoles show a relative magnetic length deviation of about 0.1 %, while at the nominal current the deviation from the Tosca 3D code evaluation is around 1% within a good field region of ±10 mm in both x and y directions.
In place of the foreseen dumping dipole, not yet delivered, an existing dipole will be used to dump the electron beam inside the well off in the floor of the hall; this will limit at the beginning the beam energy up to 90 MeV for the Thomson experiment. The well off aperture is able to host the two electron trajectories: the 14° nominal one from the designed dipole and the 25° trajectory from the temporary solution see Figure 4.3.

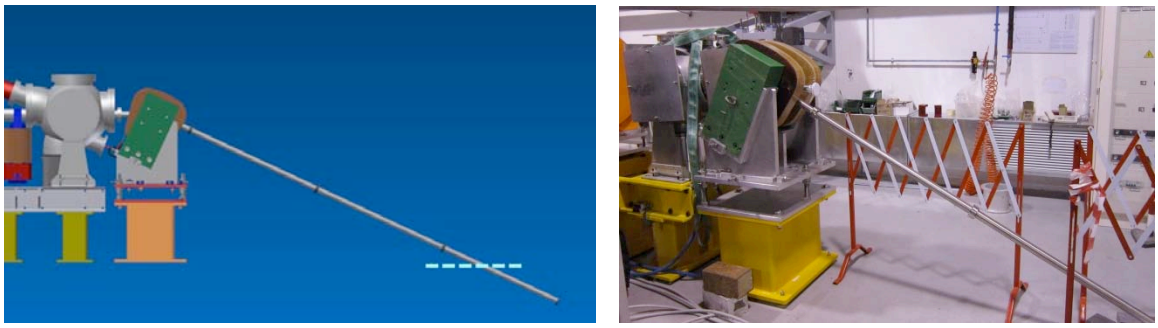

Figure 4.3: Temporary dumper solution realized with an existing dipole mounted downstream the parabolic mirror location, while the nominal position of the ad hoc designed dipole is downstream the short interaction tee vacumm chamber.

Nine over a total of thirteen Beam Position Monitors (BPM) have been installed for the first phase of the Thomson beamline commissioning; together with three high resolution beam imaging setup they will provide the necessary beam diagnostic for the orbit correction and beam phase space measurements. Each BPM device is equipped with a readout electronics based on the Libera four single pass processors from Instrumentation Technology .

The Thomson Interaction vacuum chamber has been delivered at the end of 2012, see Figure 4.4, the setup consists in two mirror stations that will determine the in & out trajectory of the photon beam (red path in the figure), plus an interaction chamber in the middle that also hosts the diagnostic for both the electron and photon beams. After the first phase of the commissioning devoted to the tuning of the electron beam, the foreseen parabolic mirror will be installed downstream the interaction point on a movable support table remotely controlled. The mirror will be able to focus the photon beam at the IP down to a 10 μm spot size.

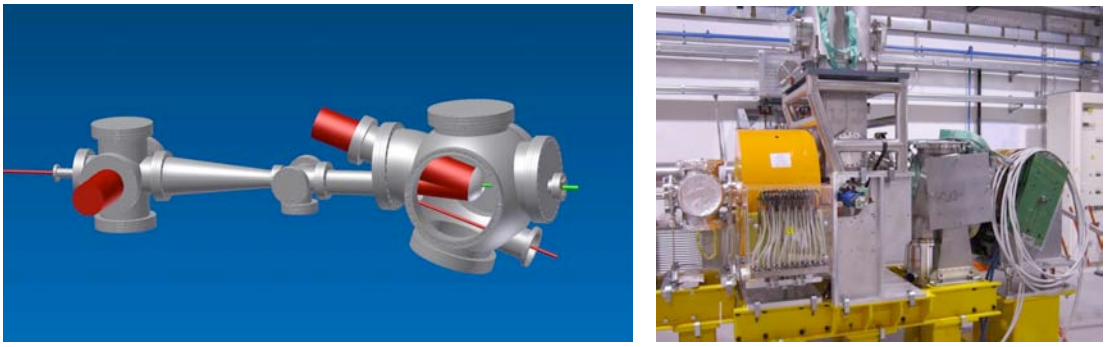

Figure 4.4: The Thomson IP vacuum chamber setup: lefte the CAD drawing of the system with the path of the laserright the interaction chamber as mounted in the beamline.

The actual Thomson interaction chamber is the central tee-vacuum chamber where a double screen movement is mounted to get the imaging of the electron and photon beam at the IP, Figure 4.5. The double screen setup consists in an OTR plus a YAG screen with two mirrors oriented in such a way to recoil the image of the two beams coming from the opposite directions.

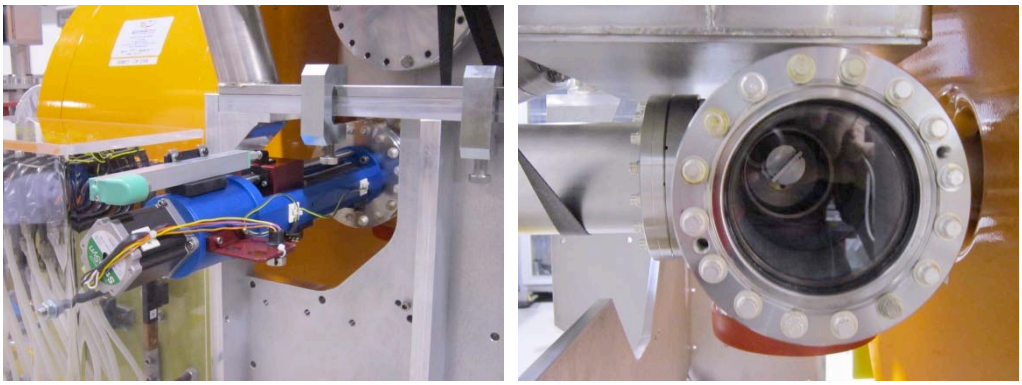

Figure 4.5: The Thomson IP electron-photon diagnostic system

The laser beam transfer line from FLAME to the Thomson interaction region is composed by a series of high reflectivity mirrors inserted in a vacuum pipe 50 m long. The mirrors, 8 inches diameter, are supported by motorized gimbal mounts in order to assure the alignment up to to the off-axis parabola that focuses the laser pulse on the electron beam, see Figure 4.6.
At the entrance of the photon beam line in the SPARC bunker a concrete wall has been realized in order to stop any radiation draft from the FLAME area towards the SPARC bunker, and to allow people entering in the SPARC hall during the FLAME laser operation and viceversa. The vacuum of the photon beam line is a the level of 10^{-6} *Torr* and suitable for the transport of the compressed laser

pulse ~10 *fs* length as needed for the plasma acceleration experiment. In Table 2 the laser pulse parameters are reported as foreseen for the Thomson Source application.

Table 2 Laser beam parameter list

Parameter	Value
Wavelength (nm)	800
Compressed pulse energy(J)	5
Pulse duration/bandwidth (ps/nm)	3÷12(80)
Rep.Rate (Hz)	10
Prepulses contrast	$>10^6$
Contrast ratio at 1 ns before (ASE)	$>10^8$
Contrast ratioat 1–100 ps before	$>10^6$
Contrast ratio of replica	$>10^5$
Beam quality M^2	↕1.5
Energy stability (%)	10
Pointing stability (μm)	< 2
Synchronization with SPARC clock (ps)	<1

The Thomson scattering experiment needs an extremely precise synchronization between electron bunch and laser pulse. The relative time of arrival jitter of the two beams is fundamental to obtain a repeatable and efficient interaction. The electrons and photons have to be synchronized with a relative jitter < 500 *fs*. This can be obtained with a standard electrical distribution of the reference signal, already present at SPARC. Anyway an optical distribution is preferable to obtain precise time of arrival measurement resolution (equal or less than 5 *fs*) and to obtain better synchronization between the two beams. This can be achieved by means of an optical cross-correlation between short laser pulses (100÷200 *fs*). In particular the electrical (or optical) master oscillator in our project will serve two laser oscillator clients: SPARC photo injector for the production of electrons and FLAME laser for the production of the high intensity pulse for the Thomson interaction.

The RF system phase will be also locked to the master oscillator using low noise phase detection; and the phase feedback loops will be implemented too. They can be divided in two general types: slow (bandwidth <10 Hz) and fast (10 Hz to some MHz bandwidth). The formers are used typically to compensate slow drifts caused by thermal elongation of cables and are implemented by means of high resolution stepper motors. The others are designed to compensate the high frequency noise suffered by the systems that is normally due to mechanical vibrations or electrical noise in the RF circuits or power amplifiers (klystron tubes and driver amplifiers).

In 2012 the activity of the BEATS2 [2] group has been joined to the SL-Thomson Source due to the synergy between the first phase of the experiment devoted to the calibration of the detector systems and the collision phase of the source commissioning devoted to the characterization of the X-ray radiation.

In the first months of the 2012 the calibration of the diode-scintillator systems has been performed with quasi-monochromatic x-ray beam in the range 16-24 keV at the Larix laboratories, Ferrara University; at the same time the response of such a system has been studied for x-ray energies >500keV, together with an imaging system for the same energy range. From summer to the end of 2012 the procurement of this high energy radiation diagnostic system has been carried on together with the first measurements of background activity in the SPARC LAB bunker during the machine runs.

According to the SPARC-LAB approved schedule for 2013 the commissioning of the Thomson source is foreseen to start in March 2013 with the following steps:

Figure 4.6: SL-Thomson laser transfer lines inside the SPARC bunker (left). Motorized mirror vacuum chamber (right).

a) Phase 1: electron beam line commissioning that foresees a 200 pC beam at the energy of 80 MeV and 30 MeV that will be focused at the IP by means of the final quadrupole triplet only.
b) Phase 2: Photon beam line commissioning at high power with synchronization system tuning for first collisions and characterization of the first obtained radiation.
c) Phase 3: electron beam focusing at 30 MeV by means of the 1.2 Tesla solenoid to get the tight focusing of the beam with charge Q=0.3 ÷ 1 nC .
d) Beats2 experiment tuning and data taking.

Publications in 2012

- C. Vaccarezza, "Thomson_radiation_source\& applications", Joined IZEST - Helmholtz Beamlines Workshop, GSI - Darmstadt - Germany, April 23-25, 2012
- Paolo Cardarelli *et al*, "Energy distribution measurement of narrow-band ultrashort x-ray beams via K-edge filters subtraction", Appl. Phys. 112, 074908 (2012), DOI:10.1063/1.47
- "Characterization of a "PIN diode-scintillator" detector for the measurement of pulsed x-ray beam flux in the range 16-24 keV", Bachelor Thesis: F. Forlani. Supervisors: Prof. M. Gambaccini, P Cardarelli. Università diFerrara, March 2012

References

[1] P. Oliva et al., Nucl. Instr. Meth. A 615 93-99, (2010)
[2] http://www.ba.infn.it/beats/

5 EXIN experiment

M.P. Anania (Ass. Ric.), E. Chiadroni (Ric.), D. Di Giovenale (Art. 23), G. Di Pirro (Resp.), M. Ferrario, A. Gallo, G. Gatti, A. Ghigo, E. Pace, C. Ronsivalle (Ass.), S. Tomassini,C. Vaccarezza, F. Villa (Ass. Ric.)

Participant institutions: other INFN sections (Mi (L. Serafini -Resp. Naz.), RM1, RM2, Pi, Na,), CNR-INO-Pisa

The external injection experiment at SPARC LAB aims at combining the high accelerating gradient characteristic of plasma-based accelerators with the production of high quality, stable and reproducible beams, typical of conventional RF linear accelerators. In terms of electron beam parameters, the target beam, after acceleration, possesses a low normalized emittance (a few mm mrad), short time duration (a few tens of fs) and an energy spread of less than 1%. Such high quality electron bunches can actually enable a variety of applications of plasma accelerators, such as front-end injectors for conventional accelerators and drivers for compact, short-pulse radiation sources.

Plasma accelerators are based on the excitation of large amplitude waves (or wakes) in a plasma; they can be driven by laser pulses [1] (LaserWakeField Acceleration , LWFA) or by particle bunches [2] (PlasmaWakeField Acceleration, PWFA). The driver first displaces plasma electrons while propagating in the plasma; the subsequent oscillation of the plasma creates a plasma wave (a wake) following the driver. The accelerating field of the wake depends on the unperturbed plasma density and can reach a value of several GV/m, up to 1 TV/m in some regimes.

The route to external injection experiment can be logically divided into two parts. The first one concerns the generation and acceleration of proper high brightness electron beam up to the injector end. The second part consists in the design, realization and commissioning of the transport lines down to the interaction chamber with the plasma wave and the subsequent diagnostic stations. The electrons and high power laser pulse transport lines installations are underway, while the engeneering of the interaction chamber is ongoing.

The main goal of the experiment is to produce in a stable and reproducible way a beam with a charge of few tens of pC, an energy up to 1 GeV with a spread less than 1% and a normalized emittance of few mm-mrad. High accuracy and precision diagnostic tools are compulsory for both transverse and longitudinal characterization of the electron beam; preferably non intercepting and single shot diagnostics, whenever available, should provide the required resolution of few tens of fs bunch length and few microns transverse beam size.

At SPARC LAB a wide energy range spectrometer will provide means of measuring the beam energy and its spread. The emittance constitutes a much harder parameter to measure: a possible candidate is the quadrupole scan technique, tough, if the beam energy spread is relatively large, the results could be unreliable due to chromatic effects [3]. As for the longitudinal diagnostics, we will insert an RF deflector downstream the plasma interaction chamber. Finally, a device to measure the betatron radiation and the coherent transition radiation is foreseen, to gain knowledge on many parameters of the accelerating process [4].

The high brightness beam needed to feed the plasma wave must be short compared to the plasma wavelength λp ($\lambda p > (30 - 40)\sigma z$), in order to prevent an excessive correlated energy spread after plasma interaction, since we plan to operate the plasma accelerator in a linear to mildly non-linear regime. This choice comes from the need to prevent the possibility of self-injecting spurious charge, which can happen in the bubble regime. To ease the task, the plasma wavelengths should be in excess of 100 μm, meaning plasma densities up to 10^{17} cm^{-3}. The expected accelerating fields can then be estimated to be of the order of few tens of GV/m. To meet the desired energy it is then necessary to guide the driving laser pulse over a length which is much greater then its natural one. There are two main strategies for achieving guiding: either by transverse tapering of the plasma density (n_0 / r^2) or by using a capillary as an optical waveguide [5]. Transverse tapering, though harder to properly manage, has the advantage of preventing any laser energy leakage from the plasma channel, allowing a longer acceleration; on the contrary, the capillary waveguide is easier to operate but, due to losses at the dielectric boundaries, allows acceleration lengths up to 6 - 8 cm (assuming a glass capillary) and severely constrains the laser spot-size w_0 and focus position [6]. We will employ both techniques, at least for the first part of the external injection experiment.

Preliminary simulations, have benn berformed using the code QFLUID2, a cylindrical code that uses fluid approximation and QSA for plasma currents [7]. Since the needed input bunch length is very demanding, a first set of simulation using ELEGANT [8] has been run in order to asses its feasibility. A 0.5-1 nC, 5 ps long bunch has been simulated from SPARC photo-cathode to interaction chamber. During the transport it has been compressed by velocity bunching and/or magnetic compression and longitudinally tailored by a slit collimator, after dispersion by means of the SPARC RF deflector. The produced beams had a length down to 7 μm, a charge in the range of 5-20 pC and emittance under 1 mm − mrad. Even if the length requirements were not met yet, such beams have been injected and accelerated in the capillary using QFLUID2. The transverse and longitudinal phase spaces of the accelerated beam are shown in figure 5.1 while figure 5.2 reports a slice analysis. The beam parameters are summarized in Table 1.

Charge	5 pC
Energy	570 MeV
$\Delta\gamma/\gamma$	2.70%
ε_n	1.4 mm-mrad

Table 1: Beam parameters for capillary laser guiding

The plasma density is 10^{17} cm^{-3}, the acceleration length is 8 cm and the capillary inner diameter is 100 μm. It is clear how the input bunch excessive length prevented to reach the desired performance in energy spread and final energy. These working conditions should be considered intermediate, easier steps toward the target parameters reported before that will be met when shorter bunches will be available.

In order to reach the required bunch length, numerical studies are underway foreseeing to directly produce a short, low charge bunch from the photo-cathode, which will be then compressed by velocity

bunching and, if needed, magnetic compression and a collimator. With such beams it seems to be possible achieving the desired beam energy and quality.

For preventing a huge normalized emittance dilution after the bunch leaves the plasma [9], a proper matching at plasma entrance end exit must be enforced [10]. This can be done by focussing the laser inside the plasma and by guiding its defocusing after acceleration.

Another problem arises when trying to increase the bunch charge: since the focusing forces inside the plasma waves are very intense, the beam transverse equilibrium size is small and the bunch density can become comparable to the plasma's. When this happens the electron beam becomes the driver of another plasma wave, loosing energy to the plasma instead of gaining it.

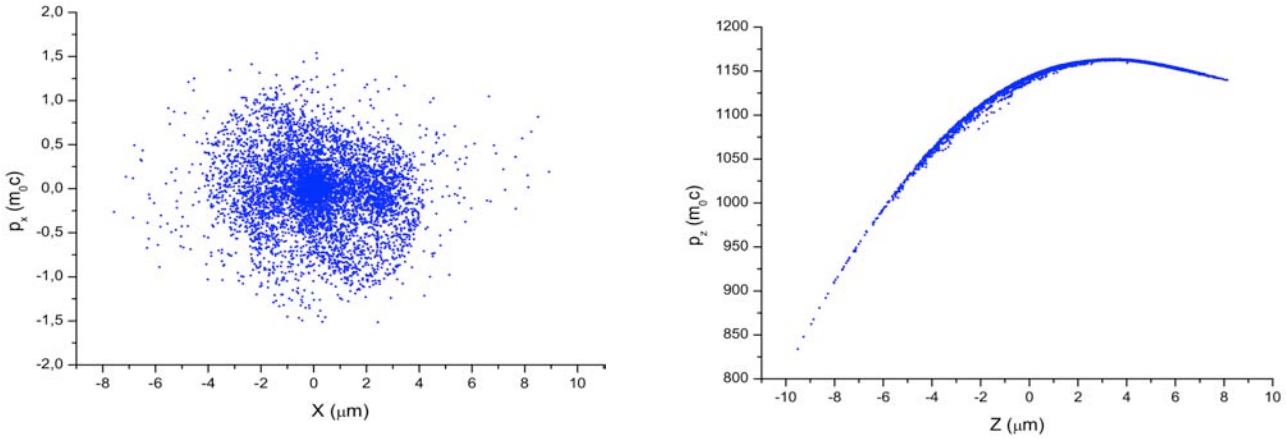

Figure 5.1: Phase spaces of the accelerated beam.

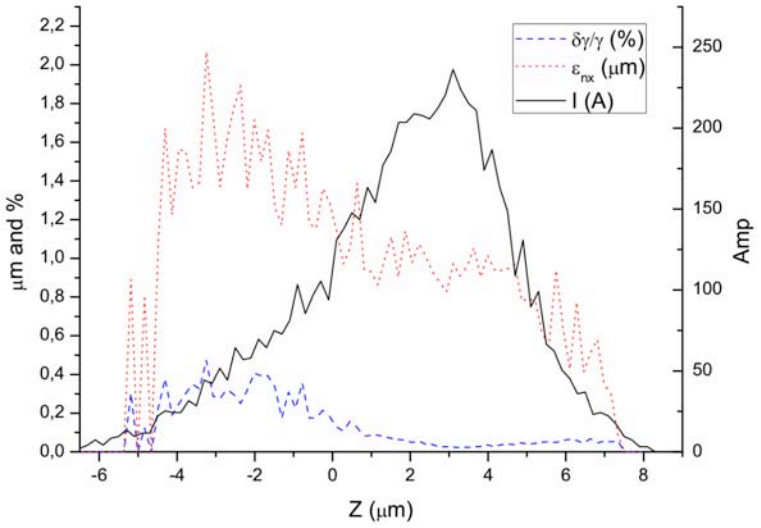

Figure 5.2: Slice analysis of the accelerated beam.

Publications in 2012

- A.R. Rossi, Plasma Acceleration Experiment at SPARC_LAB with External Injection, International Particle Accelerator Conference, poster session, New Orleans, USA.
- Mostacci et al., Phys. Rev. Spec. Top. Acc. & Beams **15**, 082802 (2012).
- M. Migliorati et al., Phys. Rev. Spec. Top. Acc. & Beams **16**, 011302 (2013).
- P. Antici et al., J. App. Phys. **112**, 044902 (2012).
- Cianchi et al., NIM A, in press.

References

[1] E. Esarey, C.B. Schroeder and W.P. Leemans, Rev. Mod. Phys. **81**, 1229 (2009).
[2] P. Muggli et al, in Proc. of 2011 Particle Acc. Conf., New York, NY, USA, TUOBN3.
[3] A. Mostacci et al., Phys. Rev. Spec. Top. Acc. & Beams **15**, 082802 (2012).
[4] S. Corde et al., Plasma Phys. Control. Fusion **54**, 124023 (2012).
[5] F. Wojda et al., Phys. Rev. E **80**, 066403 (2009).
[6] N. Cross et al., Phys. Rev. E **65**, 026405 (2002).
[7] See the presentation by P. Tomassini available at http://agenda.infn.it/getFile.py/access?resId=0&materialId=slides&confId=3444.
[8] M. Borland, in *Proceedings of the* 6th *International Computational Accelerator Physics Conference*, Phys. Rev. Spec. Top. Acc. Beams **4**, 070701 (2001).
[9] M. Migliorati et al., Phys. Rev. Spec. Top. Acc. & Beams **16**, 011302 (2013).
[10] M. Ferrario in *Proceedings Of The International School Of Physics, Enrico Fermi, Course CLXXIX - "Laser-Plasma Acceleration"*, (2011).
[11] P. Antici et al., J. App. Phys. **112**, 044902 (2012).
[12] A. Cianchi et al., NIM A, in press.

6 COMB experiment

M. Ferrario (Resp. Naz.), D. Alesini, M.P. Anania (Ass. Ric.), F. Anelli (Art. 15), M. Bellaveglia (Art. 23), L. Cacciotti (Tecn.), M. Castellano (Ass.), E. Chiadroni, D. Di Giovenale (Art. 23) G. Di Pirro, G. Gatti, A. Ghigo, M. Migliorati (Ass.), A. Mostacci (Ass.), E. Pace, R. Sorchetti, F. Villa (Ass. Ric.).

Participant institutions: other INFN sections (Mi, RM1, RM2, Bo, Pi, Na), CNR-INO-Pisa

In laser COMB operating mode the SPARC photocathode is illuminated by a comb-like laser pulse to extract a train of electron bunches which are injected into the same RF bucket of the gun. The SPARC laser system, based on a Ti:Sa oscillator has been upgraded for this specific application. The technique used relies on a α-cut beta barium borate (α-BBO) birefringent crystal, where the input pulse is decomposed in two orthogonally polarized pulses with a time separation proportional to the crystal length. In the first accelerating structure operating in the VB mode, i.e. injecting the bunch train near the zero crossing of the RF wave, the bunch train is compressed by the longitudinal focusing effect of the RF wave and with a proper choice of injection phase is possible to keep under control both the intra-bunch distance as well as the single bunch length. This method preserves all the extracted charge and it is different from other passive tecniques [1], where the train is produced by using a mask that

stops a significant fraction of the charge. Up to four electron beam pulses shorter than 300 fs and separated by less than 1 ps have been characterized and a narrowing THz spectrum produced by the bunch train has been measured [2]. In addition two electron beam pulses have been injected in the undulator and a characteristic interference spectrum produced by the FEL interaction in this new configuration has been observed, confirming that both pulses have been correctly matched to the undulator and were both lasing [3]. Coherent excitation of plasma waves in plasma accelerators [1] can be also performed with this technique. Preliminary simulations [4] shown that a train of 3 electron drive bunches, each of them 25 mm long, with 200 pC at 150 MeV and 1 mm rms normalized emittance, could accelerate up to 250 MeV a 20 pC, 10 mm long witness bunch, injected at the same initial energy in a 10 cm long plasma of wavelength 383 mm. As shown in figure 6.1 the drive bunches will loose energy to excite the plasma accelerating field up to 1 GV/m in favour of the witness bunch. Simulations show also that the witness bunch can preserve a high quality with a final energy spread less than 1 % and 1.6 mm rms normalized emittance. A test experiment is foreseen at SPARC_LAB, aiming to produce a high quality plasma accelerated beam able to drive a FEL in the SASE mode.

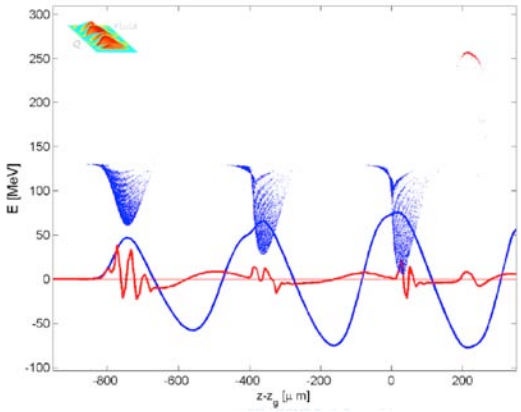

Figure 6.1: Longitudinal phase space of the COMB beam at the end of the acceleration process. The accelerating field is also plotted in arbitrary units.

A specific tool able to make precise measurements of the temporal profile of extremely short electron bunches is needed for a detailed understanding of the bunch length and, in the framework of SPARC_LAB, it has been identified in the Electro-Optical Sampling (EOS). Single-shot electro-optic (EO) detection techniques are ideally suited for this purpose since they are nondestructive and can be carried out concurrently during regular operation of the PWFA experiments. An important aspect is that they permit correlation studies between the measured time profile of the injected electron bunches and the properties of the accelerated ones.

When a relativistic picosecond duration bunch passes within a few millimeters of an electro-optic crystal (like ZnTe and GaP), its transient electric field is equivalent to a half-cycle THz pulse impinging on the crystal. The temporal profile of this equivalent half-cycle THz pulse provides a faithful image of the longitudinal charge distribution inside the electron bunch if the electrons are

highly relativistic. The transient electric field induces birefringence in the electro-optic crystal. As the electric field propagates through the crystal, the birefringent properties of the crystal also propagate (see figure 6.2). This birefringence can be probed by a copropagating optical laser pulse being, in our case, the SPARC_LAB photocathode's laser, i.e., a titanium- sapphire (Ti:Sa) laser (100 fs pulse duration) with a wavelength of 800 nm.

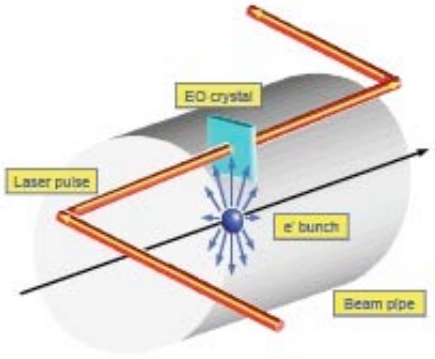

Figure 6.2: EOS working principle

The use of the same photocathode's laser enable us to have

- a simplified setup apparatus, since an independent laser system isn't necessary;
- always a synchronized laser with the electron beam;
- high laser's pulse energy available and low repetition rate (10 Hz); as a consequence, to image the laser beam, an intensified CCD (ICCD) isn't necessary and a commonly used CCD is sufficient.

The laser is sent from the SPARC_LAB Laser Room to the EOS Station through a transfer line (figure 6.3) consisting of 12 columns (height 2.2m), a laser pipe black anodized both internally and externally and two lenses (7.5m focuses) realizing a relay optics with 1:1 image ratio.

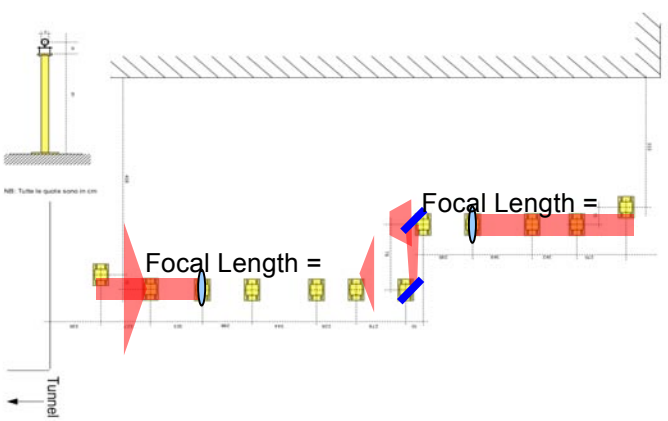

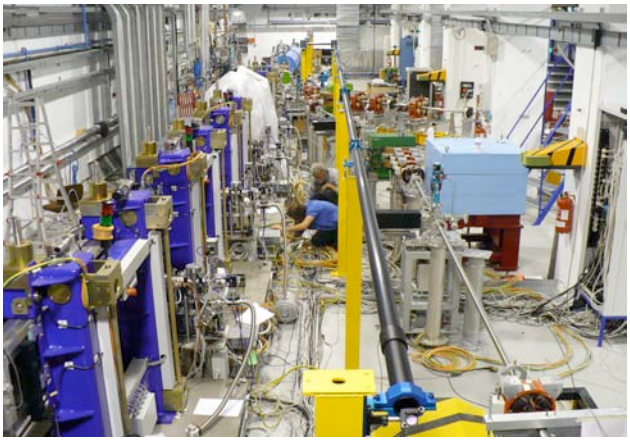

Figure 6.3: laser transfer line from the SPARC_LAB gun to the EOS Station

The EOS vacuum chamber has been realized and installed during 2012. The technical layout and the installation are reported in figure 6.4. The chamber is equipped with 3 axes: one for the electro-optic crystals and the beam targets (YAG, OTR) and two for the CCD Camera Autofocus.

Figure 6.5 shows the optical setup on the EOS station. Before passing in the nonlinear crystals, the laser is polarized and delayed (respect to the electron beam) through a motorized delay line. After the crystals it passes through another polarizer rotated by 90° respect to the first one. In such a way only the portion of the laser affected by the induced birefringence emerges from the second polarizer, and it can be measured by a CCD camera.

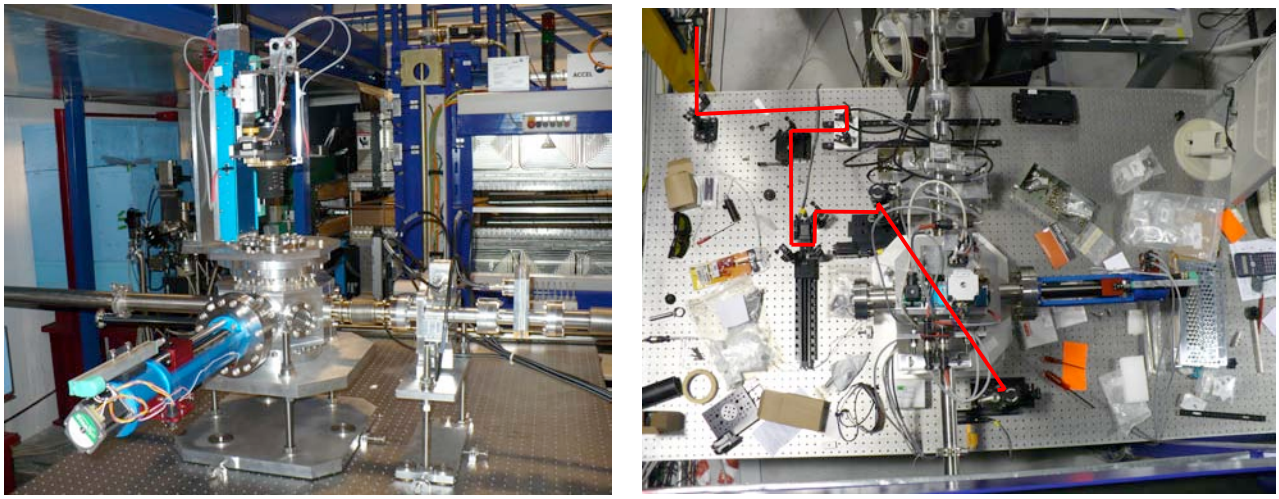

Figure 6.4: EOS chamber installed (left); EOS optical setup (right).

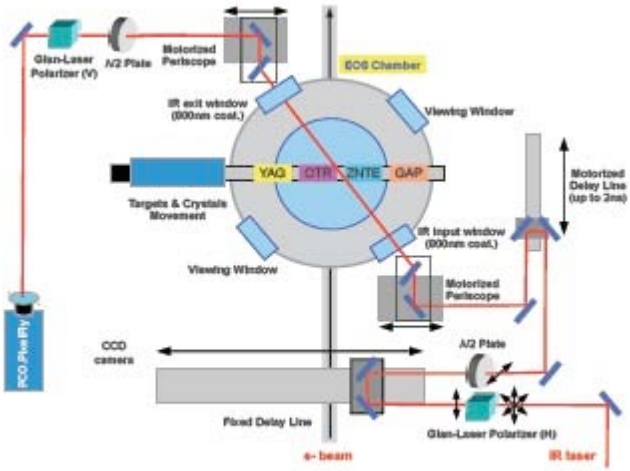

Figure 6.5: EOS optical detection scheme

During the last year the following goals have been achieved:

- realization, installation and test of the laser transfer line (32 meters long) from the SPARC_LAB photocathode to the EOS station;
- installation of the EOS Chamber with the nonlinear crystals (ZnTe and GaP);
- optical setup realized on the EOS station;

Now the experiment is ready to start with the measurements, that will be started from March.

References

[1] P. Muggli, Proc. of PAC 2009, Vancouver, Canada
[2] E. Chiadroni et al., Journal of Physics: Conference Series 357 (2012) 012034.
[3] A. Bacci et al, Proc. of FEL Conf. 2011, Shanghai, China.
[4] P. Tomassini, private communication.

7 TERASPARC experiment

P. Calvani (Resp., Ass.), M. Bellaveglia (Art. 23), M. Boscolo, M. Castellano (Ass.), M. Cestelli Guidi (Art. 23), E. Chiadroni, G. Di Pirro, M. Ferrario, G. Gatti, A. Nucara (Ass.), L. Palumbo (Ass.), R. Sorchetti (Tecn.), C. Vaccarezza

Participant institutions: other INFN sections (RM1, RM2, LNS, To)

The motivation for developing a linac-based THz source at SPARC stays in the ever growing interest of filling the so-called THz gap with high peak power radiation for both scientific and technological applications and longitudinal diagnostics issues. The THz radiation peak power expected at SPARC, and confirmed by measurements is in the order of 100 MW, corresponding energy per pulse is of the order of tens of μJ 1), 2) that is well above standard table top THz sources. Applications of this kind of source concern mainly time domain THz spectroscopy and frequency domain measurements on novel materials 3). Beyond these applications, coherent THz radiation is also used as longitudinal electron beam diagnostics to reconstruct the beam charge distribution 4). In addition, taking advantage from electron beam manipulation techniques, high power, narrow-band THz radiation can be also generated at SPARC 5, 6). This provides a unique chance to realize, with the SPARC THz source, THz-pump/THz-probe spectroscopy, a technique practically unexplored up to now.

The TERASPARC project, is a 3-years project, started in 2010, which aims at the generation, development and characterization of THz radiation produced by the SPARC photo-injector 7). TERASPARC is the result of a collaboration between LNF, INFN-Roma1, LNS, INFN-Torino, INFN-Roma2 and University of Roma Tor Vergata.

The source is Coherent Transition Radiation (CTR) from an aluminum coated silicon screen. CTR radiators are placed in the vacuum pipe, at 45° with respect to the electron beam direction (Figure 7.1), both at the end of the by-pass line and downstream from the third accelerating sections. The latter THz station holds also Diffraction Radiation (DR) screens with different slit apertures, i.e. 3 mm and 5 mm. Both TR and DR are extracted at 90° with respect to the beam axis through a z-cut quartz window and then collected by a 90° off-axis parabolic mirror. The parallel beam is then reflected down to a flat mirror at 45° which reflects radiation horizontally.

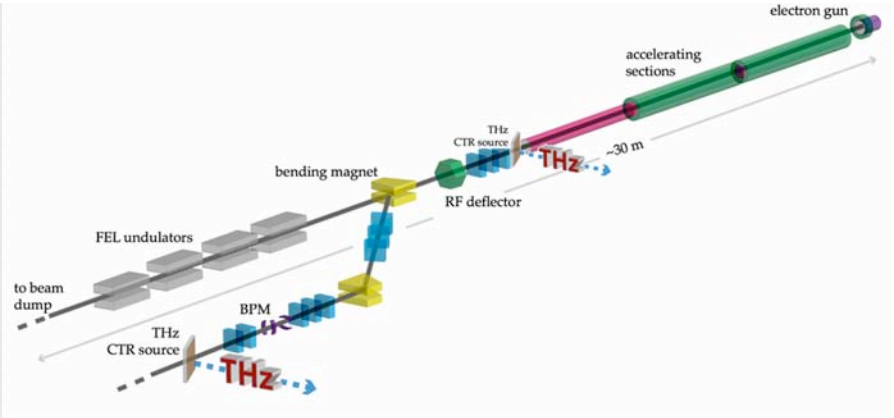

Figure 7.1: Layout of the SPARC accelerator, with the two THz sources placed at the linac exit and at the end of the by-pass line.

Two schemes are foreseen for the detection of both CTR and CDR spectra: one for interferometer measurements and one for integrated CTR/CDR measurements with the possibility of selecting custom band pass filters in the THz range 8).

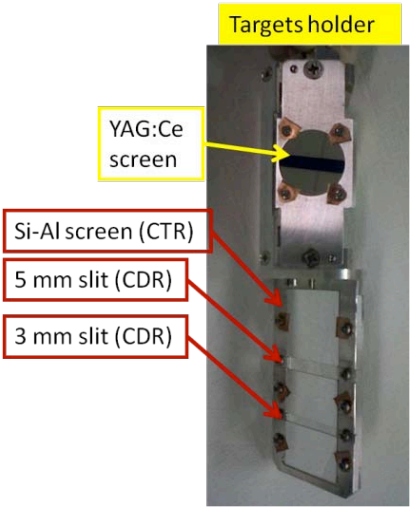

Figure 7.2: New targets holder, placed at the linac exit, for beam imaging (YAG:Ce screen) and both CTR and CDR generation.

Coherent radiation, both from the whole target (TR) and from part of it (DR), is emitted by both an ultra-short high-brightness electron beam and a longitudinally modulated one 6). In the former case high peak power broadband THz radiation is generated, while the latter, using a train of sub-ps electron bunches, is suitable for the production of narrow spectral bandwidth and tunable THz radiation. The technique used at SPARC to manipulate such electron beam relies on low energy RF compression, i.e. the velocity bunching technique 9) and on the use of properly shaped trains of UV laser pulses hitting the photo-cathode, i.e. laser comb beam schemes 10).

The activity in 2012 has been dedicated to the installation and commissioning of the new THz station downstream from the third accelerating section, hosting both CTR and CDR radiators.

The successful commissioning of the new THz station allowed us to compare the two sources under ultra-short single bunch operation, 300 pC bunch charge, 160 fs pulse duration, 120 MeV electron beam energy. The CTR energy per pulse, measured by means of a Golay cell detector in the spectral range between 150 GHz and 5 THz, is as high as 18 μJ (Figure 7.3), corresponding to electric and magnetic fields in the order of few MV/cm and sub-T, respectively. Figure 7.3 also shows the energy per pulse in case of CDR from both a 3 mm and 5 mm slit aperture, being in the order of few μJ.

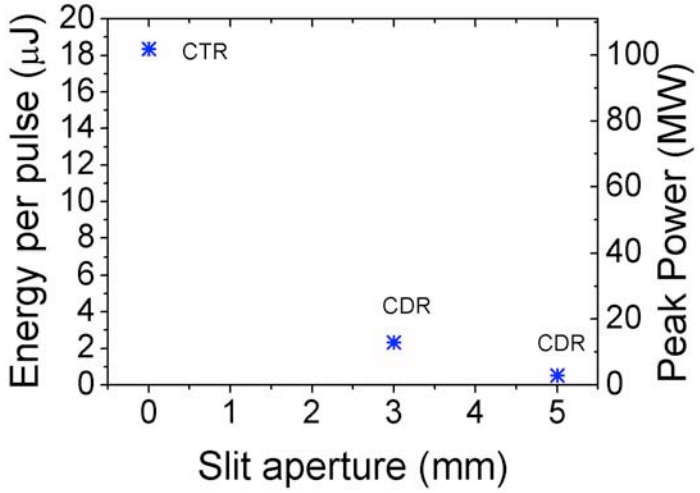

Figure 7.3: Measured CTR energy per pulse compared to that in case of CDR from both 3 mm and 5 mm slit aperture. Measurements are performed by means of a Golay cell detector in the spectral range from 150 GHz to 5 THz.

In addition, the CTR-based THz source has been used as diagnostic tool for the reconstruction of the electron beam longitudinal profile along the accelerator under different compression regimes. Indeed, the frequency analysis of the CTR autocorrelation function allows the reconstruction of the longitudinal temporal profile of the electron beam for different compression factors as obtained through the velocity bunching technique. An example of the retrieved results, for a 120 MeV and 300 pC electron beam, is shown in Figure 7.4, demonstrating the use of THz radiation also as a valid tool for the diagnosis of ultra-short electron bunches.

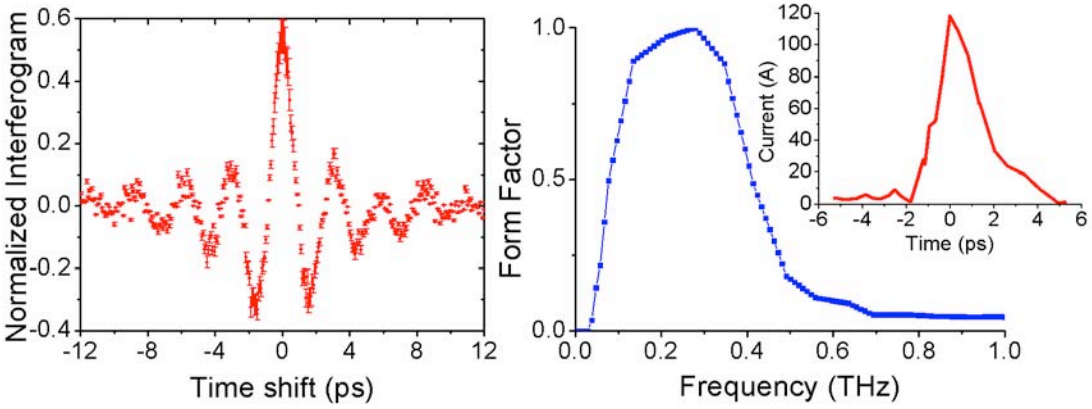

Figure 7.4: (Left) CTR autocorrelation function as measured through a Martin-Puplett interferometer. (Middle) Bunch form factor and, (right) the retrieved longitudinal bunch profile, providing a RMS bunch length of 1.4(0.10) ps.

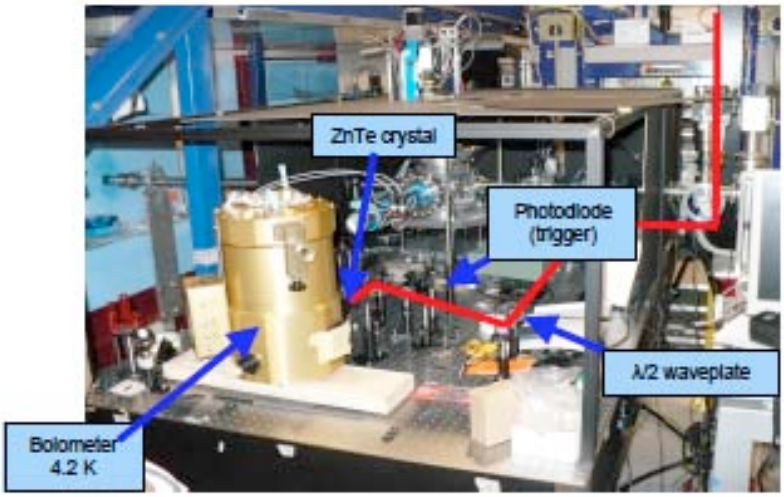

Figure 7.5: Experimental apparatus.

The latest achievement of 2012 regards the characterization of Electro-Optical (EO) crystals, being preparatory for the generation of THz radiation through Optical Rectifications and for the development of Electro-Optical Sampling (EOS) techniques, able to image the temporal profile of a transient THz pulse. Optical Rectification has been used in this preliminary experiment to characterize the ZnTe crystal axes orientation. Indeed, OR is a technique utilizing ultrafast laser pulses to generate broadband electromagnetic pulses in free space. The OR uses electro-optic crystals (like ZnTe) as a rectification medium and depending on the optical fluence the rectification is a second- order (difference frequency generation) or a higher-order nonlinear optical process. The THz amplitude depends on the laser's incident polarization angle. The experimental apparatus is shown in Figure 7.5. A titanium-sapphire (Ti:Sa) laser, 100 fs pulse duration, at a 800 nm wavelength, 52 μJ energy is split at the beginning into

a trigger beam (2μJ) sent to a photodiode and a pump beam (50 μJ). This one passes a half-wavelength wave-plate in order to change its polarization and then it is focalized with a lens on the 1 mm thick ZnTe crystal. Between the ZnTe crystal and the detector (a bolometer operating at 4.2 K) a Silicon screen is used to block the laser pulse, allowing only the so produced THz to be detected by the bolometer. The THz amplitude has been measured as function of the polarization angle of the laser as shown in Figure 7.6. This result allows to determine the [-1,1,0] axis of the crystal along which the laser's polarization needs to be directed to probe the birefringence change in future EOS experiments.

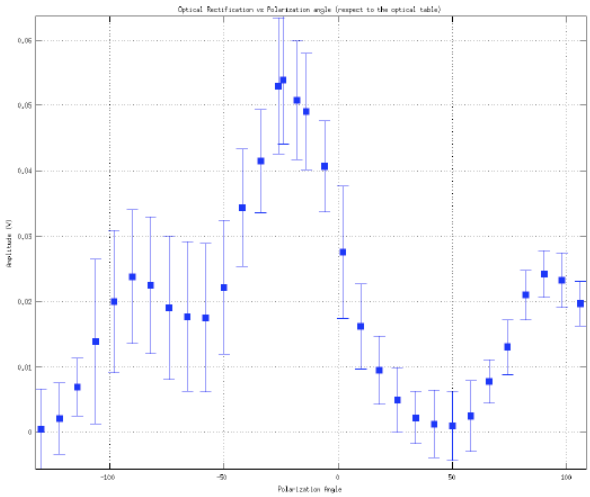

Figure 7.6: THz amplitude (in V) as function of the polarization angle (in deg).

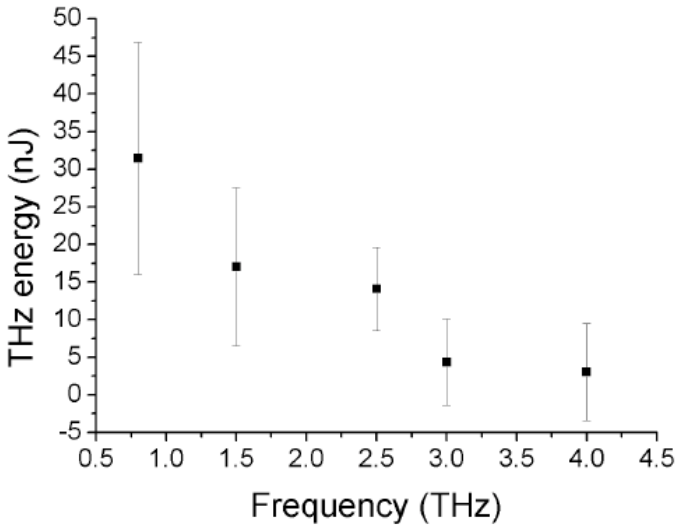

Figure 7.7: Measured THz radiation spectrum. The estimated energy takes into account the filters transmission (25%) and the bolometer responsivity (2.4*105 V/W).

Once defined the axis, the THz generation by optical rectification has been characterized as function of custom band-pass filters 8), the emission extending up to 4 THz. The corresponding THz energy has been retrieved assuming a 25% transmission for the band pass filters and a bolometer responsivity of 240 kV/W, see Fig 7.7

Publications in 2012

- E. Chiadroni, *The THz Beamlines at SPARC LAB*, Invited seminar at Karlsruhe Institut of Technology - ANKA (2012), Karlsruhe, Germany.
- E. Chiadroni, *Characterization of the THz radiation source at SPARC_LAB*, Oral contribution at the Workshop on Terahertz Sources for Time Resolved Studies of Matter, July 30-31, 2012, Argonne National Laboratory, Argonne, IL, USA.
- E. Chiadroni et al., J. Phys.: Conf. Ser. **357**, 012034 (2012).
- S. Lupi et al., J. Phys.: Conf. Ser. **359**, 012001 (2012).
- E. Chiadroni et al., J. Phys.: Conf. Ser. **359**, 012018 (2012).

Acknowledgment

Authors wish to thank colleagues collaborating from participant institutions:

- INFN Roma 1-La Sapienza: O. Limaj, S. Lupi
- University of Rome La Sapienza, SBAI: L. Palumbo, A. Mostacci
- INFN Roma 2-Tor Vergata: L. Catani, A. Cianchi, B. Marchetti, S. Tazzari
- INFN LNS: A. Rovelli
- INFN Torino: R. Gerbaldo, G. Ghigo, L. Gozzellino, E. Mezzetti, B. Minetti

References

[1] E. Chiadroni et al., Proc. of IPAC 2010, TUOARA03, Kyoto (2010).

[2] E. Chiadroni et al., "The SPARC linear accelerator based terahertz source", Appl. Phys. Lett. (in press) doi:10.1063/1.4794014.

[3] M.S. Sherwin et al., Opportunities in THz Science, Report of a DOE-NSF-NIH Workshop (2004).

[4] E. Chiadroni, "Bunch Length Characterization at the TTF VUV-FEL", TESLA-FEL 2006-09 (2006).

[5] A. Mostacci et al., Proc. of IPAC 2011, THYB01, San Sebastian (2011).

[6] E. Chiadroni et al., Rev. Sc. Inst. **84**, 022703 (2013).

[7] D. Alesini et al., Nucl. Instrum. and Meth. in Phys. Res. A 507, 345 (2003).

[8] N. I. Landy, 1-4244-1449-0/07/$25.00 c 2007 IEEE (2007); P. Carelli et al., unpublished (arXiv:0907.3620v2).

[9] M. Ferrario et al., Physical Review Letters 104, 054801 (2010).

[10] M. Ferrario et al., Nucl. Instrum. and Meth. in Phys. Res. A **637**, S43–S46 (2011).

8 POSSO experiment

S. Dabagov (Resp. Naz.), E. Chiadroni, G. Di Pirro, M. Ferrario, C. Vaccarezza

Recently we have started with a new project POSSO on studying the features of moderate-energies (0.1-1 GeV) electron beam channeling in various crystals [1]. The project aims in creating for a SPARC_LAB group both knowledge and experience for applying orientational behaviours of charged particles passage through the crystals to shape the beams (beam bending, collimation) as well as to generate a powerful x-ray and γ-radiation source (coherent bremsstrahlung, channeling radiation, parametric x-ray radiation) [2], see figure 8.1 and 8.2. One of the most interesting channeling-based application is a technique originated on its optimized combination with conventional methods for positron sources; electron channeling, namely channeling radiation by ultrarelativistic electrons (> 1 GeV) in crystals, is rather promising for getting high brilliant positron beams for the future e-/e+ colliders.

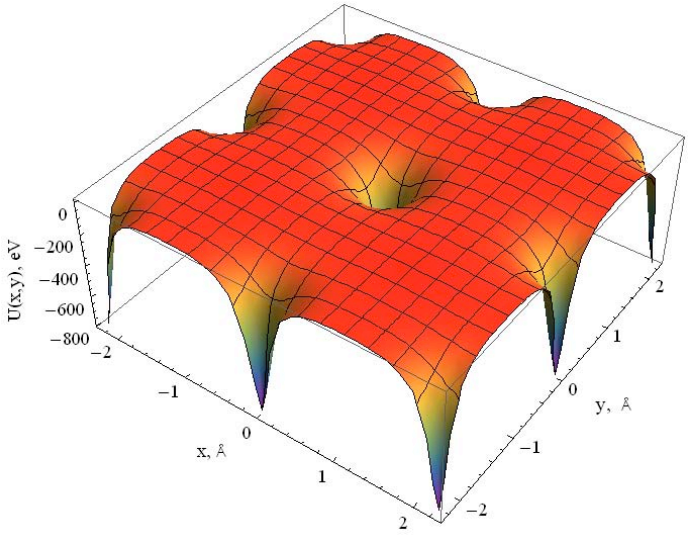

Figure 8.1: The averaged potential energy of electron interaction with W <100> crystallographic axis within the Doyle-Turner approximation. Due to extremely high gradiant of the potential well 102-103 GeV/m we can expect high flux of channeling radiation [2] .

Within the project we have performed theoretical studies that finalized in new computer codes for planar and axial channeling of relativistic electrons in various types of the crystals, detailed analysis of orientation features of electron scattering at axial channeling in very thin (submicron) monocrystals (studies on mirror reflection of the beam), detailed analysis of electron dechanneling and rechanneling at planar case based on solution of Fokker-Plank equations, getting the radiation power behind the crystals at the channeling orientations for various emittance parameters of the beam before the crystal, and electron beam simulations by the GEANT4-based codes for the optimization of experimental layout.

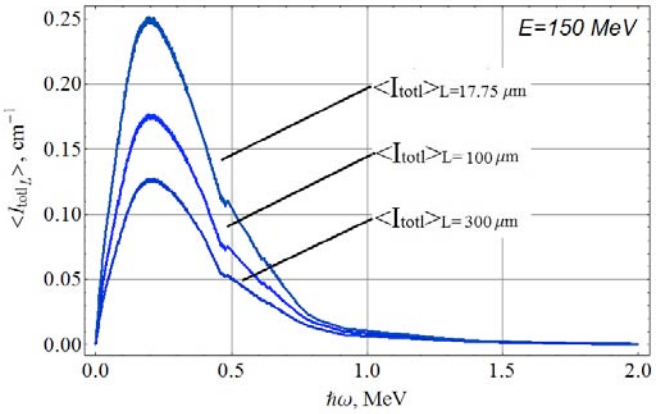

Figure 8.2: Total radiation yield of channeling radiation by single electron per unit of a Si (110) crystal length for 3 various crystal thicknesses. In final design the thickness should be optimized.

With the increase of electron energy the radiation loss due to the beam channeling becomes essential; for instance, for the electron energy change from 150 MeV to 200 MeV the radiation intensity in Si (110) increases two times, while for 800 MeV electrons the radiation flux becomes one order higher. Keeping in mind that the depth of a Si (110) potential well (~20 eV) is much less deeper than the one for a W <100> (~800 eV), we can expect extremely high channeling radiation flux in W to be emitted witin the cone of $1/\gamma \sim 10\text{-}3$ [2].

Additionally, together with the SPARC_LAB team we have evaluated various possible solutions for a new beam line dedicated to channeling studies, and, finally, have chosen the layout to be constructed as a continuation of the dogleg piece of the THz beamline.

References

[1] S.B. Dabagov, N.K. Zhevago, La Rivista del Nuovo Cimento 31 (9), 491 (2008).
[2] S.B. Dabagov et al. IJMPh A 22 (23) 4280 (2007).

Communication and Outreach

R. Centioni (Resp.), M. Scudieri (Art. 15), E. Santinelli (Bors.)

SIDS - Scientific Information and Documentation Service

From many years, the LNF has been interested in and active in communication in the area of scientific education. Throughout the year they provide basic education in physics by means of a vast outreach program for the general public, teachers and students.

The aims of the program are various: "open the laboratories" inviting general public to be part of INFN "scientific world"; to "stimulate" the curiosity on scientific issues; to offer a more complete view of the scientific institutions operating in the area; to transfer scientific knowledge, methodology and technologies of the research; to inform people about the latest developments in physics; to enable people to acquire the knowledge and understanding of INFN research activities.

Most of the activities are organized inside LNF, such as Visits, Scientific Week, Open Days, Physics Lessons, Meetings with authors of scientific books, Concerts.

Special events are dedicated to schools: the Incontri di Fisica - a course for high school teachers and Stages for high school students.

Other activities are organized outside the LNF such as Seminars at school or at the public libraries, European Researchers Night.

These activities are made possible by the enthusiastic involvement of INFN-LNF people: graduate students, postdocs, researchers, engineers and technicians.

1) **Visits** www.lnf.infn.it/edu/visite to LNF are a well established tradition. They consist of a brief historical presentation of the Laboratories and their activities on site and abroad and of a guided tour to the open air museum and to the experimental areas.

The visits are organized for high school students (age: 17-19) and for primary and secondary schools (age: 10-14, Quasar Project). In this last case a special program is foreseen that includes a first meeting with the students at their school to introduce the world of research and some basic concepts of modern physics followed by the visit to the LNF in small groups.

The visits are requested not only by Italian schools, but also by other countries: Denmark, Austria, Czech Republic, Belgium, Germany, Romania, France, Greece, Japan, India, Taiwan, USA.

During 2012 about 5000 people visited the LNF.

(Scientific Coordinator: D. Babusci and B. Sciascia for the Quasar Project)

2) **Scientific weeks and Open Days** www.lnf.infn.it/edu/settimana/ are organized at LNF in collaboration with the other Research Centres located in the Frascati area, Public Institutions, Cultural Associations, International non-government organizations.

This type of event provides guided tours, conferences, public lectures, scientific videos. Most of the LNF employees are in action to present their research centre, answer questions and care for their guests.

Open Day LNF April 2, 2012

(Care of SIDS-Ufficio Comunicazione ed Educazione Scientifica).

Open Day 2012 (INFN-LNF Photo)

3) **Lessons of Physics** www.lnf.infn.it/media/ are held by world leading scientists in various field of the science. Students and teachers are invited to attend the lessons which are video-recorded. Slides and videos are available on the LNF website to be utilized even for lessons at school.
(Care of O. Ciaffoni, G. Di Giovanni and SIDS-Ufficio Comunicazione ed Educazione Scientifica)

4) **Seminars** www.lnf.infn.it/edu/seminaridivulgativi/ Upon request, LNF researchers give lessons to high school students and general public. A special program is performed together with public Libraries, especially with Frascati one Library. The arguments deal with science and society or they take inspirations from scientific or fiction books and theatre.

- *Teoria della Relatività*, C. Curceanu e A. Clozza, March 16th, 2012, Lic. G. da Catino Poggio Mirteto (RI).
- *La realtà quantistica*, D. Babusci, April 19th, 2012, AIF Sezione Romana;
- *Big Bang, particelle, acceleratori... Dall'importanza della ricerca fondamentale alle opportunità di comunicazione scientifica*, G. Mazzitelli, May 7th, 2012, Lic. Sc. Sulpicio, Veroli (FR);
- *Tracce dall'universo oscuro*, M. Pietroni, October 18th, 2012, LNF Frascati;
- *Energia e sostenibilità*, G. Mazzitelli, October 23th, 2012, Lic. Sc. B. Touschek, Grottaferrata (RM);

- *Fisica delle particelle elementari e il Bosone di Higgs: l'ultima frontiera della fisica moderna*. Collegamento in videoconferenza con il Prof. J. Ellis dal CERN, P. Di Nezza, November 16th, 2012, Lic. Sc. E. Majorana, Isernia;
- *Le costanti fondamentali della natura e la fisica moderna*, E. Nardi, November 17th, 2012, ISIS Malignani, Udine;
- *Alla scoperta dell'universo con LHC*, A. de Rujula, December 7th, 2012 LNF Frascati;
- Presentazione del libro *Psicosi 2012*, Matteo Martini, November 28th, 2012, Lic. Sc. B. Touschek, Grottaferrata (RM);
- *Armonia celeste: dal jazz della meccanica quantistica al rock sulle corde dell'universo*, C. Curceanu, December 19th, 2012, Lic. Sc. B. Touschek, Grottaferrata (RM).

5) **Incontro con l'Autore** www.lnf.infn.it/edu/ica/ LNF organize meeting with authors who present their scientific book to the general public, students, teachers.
Il fisico che visse due volte: i giorni straordinari di Lev Landau genio sovietico, Fabio Toscano intervistato da V. Napolano (Ufficio Comunicazione INFN), October 12th, 2012, LNF Frascati.

6) **European Researchers' Night** http://www.frascatiscienza.it/ organized by FrascatiScienza. The SIDS is involved organizing guided tours at LNF.
This event is also performed in other European cities to promote the activities of the main research centres at international level. During all day and night are organized: experiments held by the researchers, games for children, visits to major Italian and European research laboratories, science shows, scientific coffees, and so on. These initiatives enable dialogue with researchers and help people to discover science through entertainment.
LNF September 28th, 2012.

Among the activities organized inside LNF two particular events are performed in the education program: Incontri di Fisica and Stages.

7) **Incontri di Fisica** www.lnf.infn.it/edu/incontri/ is organized since 2001. The event is a three-days course for high school teachers and people involved in scientific research dissemination. About 200 from all over Italy, attend this event each year. The goal is to stimulate teachers' professional training and provide an occasion for interactive and hands-on contact with the latest developments in physics.
The program consists of plenary lessons, presentation of INFN-LNF activities, visits to LNF experimental area and discussion. The peculiarity of this course is the second day entirely dedicated to the special participation in working groups (8 hours laboratory).
The working groups concern INFN research topics (nuclear and subnuclear physics, astroparticle physics and technology). They are conducted by INFN researchers, engineers and technicians and they are held in the various experimental LNF laboratories.
Each working group consists of a theoretical lesson, hands-on activity or data analysis of a real experiment. In this way, teachers have a direct contact with researchers and they can use typical experimental instrumentation employed in contemporary physics.
The lessons are given by speakers from INFN or from other Institutions such as Universities, or other Laboratories like CERN. They concern arguments on physics or other scientific matters, application of physics and more general topics.
If we only think that each teacher is in contact with about 120-130 students and their families, Incontri di Fisica represents an important occasion for dissemination of physics.
Moreover, by informing them on cutting-edge science, it is possible to introduce modern and contemporary physics in school programs. Teachers can stay in contact with INFN researchers also after the course.

The evaluation of the course is performed by a questionnaire. The analysis is very useful for the study of future programs.
Teachers, authorized by the Minister of Education, receive a certificate of participation.
All the programs are published on LNF web site (lessons, video, photo).
LNF October 10th -12th, 2012.
(Organizing Committee: D. Babusci, R. Centioni, C. Curceanu (Chair), P. Di Nezza, U. Dosselli, R. Fabrianesi (AIF), C. Gatti, G. Venanzoni – Secretariat: E. Santinelli, M. Scudieri)

8) **Stages for students** www.lnf.infn.it/edu/stagelnf have been organized since 2000 for high school students (age 18-19). Students are selected by their teachers on the basis of their curriculum but especially on the basis of their interest and motivation.
Tutors are INFN staff: researchers, engineers and technicians. They prepare the program with the following goals:
- to offer a special experience in an important research Institute;
- to transfer scientific knowledge, methodology and high level research technology;
- to present INFN-LNF experimental activities;
- to promote the teaching of modern and contemporary physics;
- to contact schools from all over Italy and abroad;
- for student orientation (university or career).

In a direct contact with their tutors (1 tutor / 2 students), students are involved in theoretical lessons and practical operations. They acquire knowledge and understanding of INFN research activities in an interactive modality. Curiosity, investigation, hands-on learning, working in a team are the key words of this experience.
During their stay at LNF, students are like staff members, working from 8 a.m. to 4 p.m. and they participate in the social events (e.g. lunch at the LNF canteen). At their arrival students receive educational material and general information about INFN-LNF and they visit the experimental area.

Various types of stages in different periods of the year are organized.

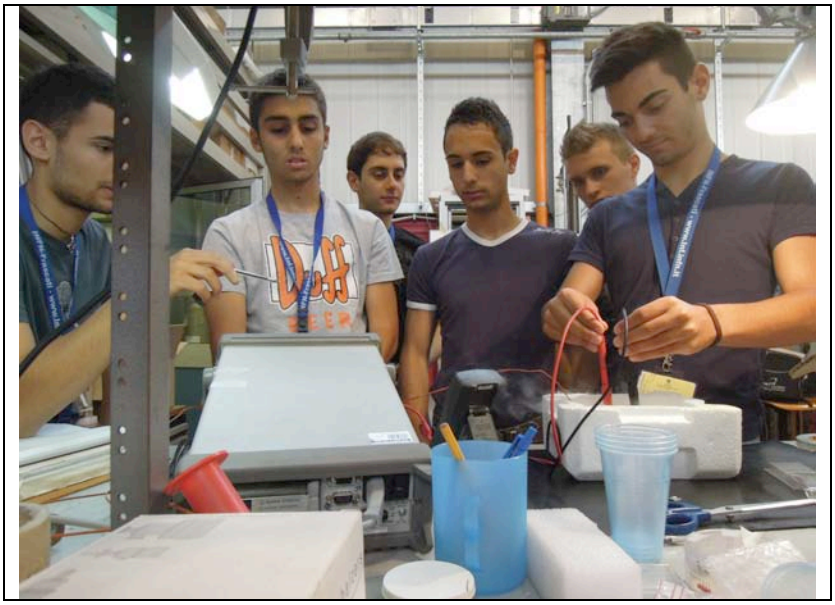
Stages Estivi e Residenziali 2012 (INFN-LNF Photo)

- The Stage Masterclass is organized on behalf of IPPOG Masterclasses International Project. It lasts 4 full days, usually during February. Students, in a unique group of 34, follow lessons on modern physics and analyze data from ALICE experiment at CERN.
LNF January 30th, February 2nd, 2012

(Scientific Coordinators: F. Bossi, D. Domenici (Resp), P. Di Nezza)

- The International Masterclass is open for 40 students in last year(s) of high school/college coming from all European countries. It si organized in lecture on Modern Physics and its applications in Society, and in activities to be performed in laboratories, The participants have, as well, the opportunity to visit the main experiments and accelerating facilites of the LNF. The official language is English. LNF, LNF January 30th, February 2nd, 2012
(Scientific Coordinator: C. Curceanu);

- The Summer Stages are organized in June, at the end of the school year, and last 10 days.
Summer Stages – 125 students - LNF June 11th -22nd, 2012.
(Scientific Coordinator: C. Bloise)

The theoretical plenary lessons are scheduled during the morning. Then, divided in small groups, the students participate in various experimental activities.
At the end of the stages, students make a report of their experience. This report is presented in the LNF main auditorium during a cerimony in the presence of families, teachers and other students.
Each student receive a certificate of participation and evaluate the experience of stages by filling out a questionnaire.

Tutors consider the experience of Stage very positively. They think it can also be replicated in other INFN laboratories or Research Centres.
The project phase of the stage program is very important. Tutors take into account that students belong to various schools so their preparation may not be the same. They give particular importance to the use of a scientific/technical language appropriate to the educational preparation of students. Since the scientific language is very peculiar, tutors recommend that the concepts not included in school programs are explained.
Surely, it is extremely important to keep in contact with school teachers, in order to better understand the preparation of students. Moreover tutors take particular care of the experimental activities which represent the real different pedagogical approaches to the scientific studies.

The Stages are a very special occasion for the students. They can work and study in a big research centre and meet students from other schools. Particularly fascinating is the use of sophisticated instrumentation certainly not available in school laboratories.
The stages offer the opportunity of learn about physics but also computing and electronics and to be oriented for the university choice or career.
The interaction with the scientists is very stimulating as well as the knowledge of their work and their life. Meeting researchers of different ages, nationalities and experience, the students can understand better the role of the researcher, too often simply considered only as a person who works into a laboratory, far from the real world. Students are curious to ask questions about scientists' experiences and their reasons for becoming a physicist, their hobbies and passions.

Teachers note that at the end of the stage students are well oriented in a work environment different from a school one, having had the opportunity to integrate their knowledge on scientific matters. They say that students learn that the research is an enthusiastic adventure made by passion and study realized by working in team on the solution of problems. Concerning science and scientists students appreciate: the importance of the scientific collaboration, being passionate and tenacious to achieve the goals, the effort needed in the study, curiosity, and the importance of making sacrifices.
Each school, participating in the LNF Stage program, includes it into their own Annual Training Project. This also means that schools often organize an event during which students make a report on the stage experience to their classmates and parents. From this point of view, Stages become a special initiative of diffusion of the scientific culture with a big impact on: families, other students, teachers.

Regarding the university choice students who participate in the LNF stages are oriented to scientific studies in particular Engineering and Physics.

The participation in the stage program has increased over these last 10 years: since 2000, 1235 students attended the stages. In the year 2000, LNF hosted 12 students from only one local school while in the year 2012, 206 students from 72 different schools all over Italy came to Frascati.

Tab. 1

Year	Students	Females	Males	School	INFN Tutors
2000	12	1	11	1	7
2001	14	3	11	1	14
2002	57	15	42	8	50
2003	56	11	45	14	22
2004	114	34	80	21	25
2005	154	42	112	29	56
2006	161	48	113	46	58
2007	163	45	118	51	55
2008	161	47	114	51	63
2009	177	40	137	54	67
2010	166	36	130	60	60
2011	184	61	184	60	70
2012	206	59	147	72	59

The LNF monitor the success of the various initiatives proposed mostly through questionnaires (each one specific of the event type) and also keep track of the "history" using dedicated databases by which it is possible to perform simple statistical analysis. The questionnaires are a valid instrument to know students' evaluation of the stages: general organization, lessons contents and exposition by the tutors, working groups, their personal considerations about the modality and the opportunity of the stages and their idea concerning university or career choice.

9) **Web page**

On the LNF web site are reported all the events organized: tutors lessons, videos, photos, reports that, together with the educational material and the general information about the LNF research activities, allow general public and schools to the knowledge of modern physics and to INFN-LNF research so to bridge the gap from science and society.

Tab. 2 - Number of participants to LNF events during 2012

EVENTS 2010	**PARTICIPANTS**
Visits	5000
Scientific Week and Open Days	550
Seminars (at LNF and outside)	1935
European Researchers' Night	1450
Incontri di Fisica for high school teachers	213
Stages for high school students	206

Aknowledgments
Thanks to LNF Director and the Heads of Accelerator, Research and Technical Divisions.
Special thanks to all LNF Tutors and Services staff.

CONFERENCES, WORKSHOPS and MEETINGS

International conferences, workshops and meetings hosted and/or organized by LNF:

1. *XI Workshop on Resistive Plate Chambers and Related Detectors (RPC2012)* LNF, 5-10 February 2012.
2. *ALICE HLT Physics Workshop*, LNF 9-11 February 2012.
3. *ALICE Physics Week 2012-LNF*, LNF 15-20 March, 2012.
4. *3rd SuperB Collaboration Meeting* LNF 19-23 March, 2012.
5. *Radiative Corrections and Generators for Low Energy Hadronic Cross Section and Luminosity* LNF 16-17 April, 2012.
6. *Management of radioactive waste: from transmutation to bioremediation*, LNF 16-23 April, 2012.
7. *Commissione Scientifica Nazionale II*, LNF 16-18 April, 2012.
8. *XVI Frascati Spring School "Bruno Touschek"*, LNF 7-11 May, 2008.
9. *Frontier objects in Astrophysics and Particle Physics*, Vulcano 28 May - 2 June, 2012.
10. *ECLOUD'12*, LNF 5-8 June, 2012.
11. *Open Problems in Quantum Mechanics - QF2012*, LNF 20-22 June 2012.
12. *New Trends in Algebraic Quantum Field Theory*, LNF 12-14 September, 2012.
13. *MC-PAD*, LNF 19-22 September, 2012.
14. *Channeling 2012*, Alghero 23-28 September, 2008.
15. *Nanoscience and Nanotechnology 2012*, LNF 1-4 October, 2012.
16. *r-ECFA*, LNF 5 October, 2012.
17. *Dark Forces at Accelerators - Dark 2012*, LNF 16-19 October, 2012.
18. *International Technical Laser Workshop 2012 (ITLW-12)*, LNF 5-9 November 2012.
19. *2nd Joint HiLumi LHC-LARP Annual Meeting*, LNF 14-16 November, 2012.
20. *Bruno Touschek Memorial Lectures 2012* LNF 7 December, 2012.
21. *6th SuperB Collaboration Meeting* LNF 11-14 December, 2012.
22. *JLab12 e gli altri esperimenti: punti di incontro e prospettive future*, LNF 18-19 December, 2012.

FRASCATI PUBLICATIONS

Available at www.lnf.infn.it

Frascati Physics Series

Volume LIII – Special Issue
Les Rencontres de Physique de la Valle dAoste - Results and Perspectives in Particle Physics
Ed. M. Greco
La Thuile, Aosta Valley, February 27 March 5, 2011
ISBN 978-88-7438-068-8

Volume LIV
LC11 Workshop: understanding QCD at linear colliders in searching for old and new physics
Villazzano (TN), 12-16 September 2011
ISBN: 978-88-86409-60-5

Volume LV
Third Young Researchers Workshop Physics Challenges in the LHC Era 2012
Ed. E. Nardi
Frascati, May 7th and May 10th, 2012
ISBN 978-88-86409-59-9

Volume LVI
DARK2012 Dark Forces at Accelerators0
Ed. F. Bossi i
Frascati, October 16th and 19th 2012
ISBN 978-88-86409-62-9

Frascati Physics Series - Italian Collection
Collana: Scienza Aperta Vol. III (2012) - ComunicareFisica2010 Atti 3 Convegno "Comunicare Fisica e altre Scienze"
Ed.: Franco L. Fabbri, Piero Patter
Frascati 12-16 aprile 2010
ISBN – 978-88-86409612

LNF Frascati Reports

INFN-12-01/GE
M. Conte , Relativistic tests

INFN-12-02/LNF
V. Shpakov et al., Diffraction radiation of electron bunches for one- and two-slit systems

INFN-12-03/MI
F. Broggi, Tools and facilities of the Milan section of the INFN n

INFN-12-04/MI
G. Manfreda et al., MATPRO Upgraded version 2012: a computer library of material property at cryogenic temperature

INFN-12-05/LNF
M. Pallotta, Cesros summability vs Diracs delta

INFN-12-06/LNF
A. Balla et al., Noise lower limit calculation for SuperB DCH Cluster Counting front-end electronics

INFN-12-07/LNF
L. Iafolla et al., TDC e sistema di acquisizione per il rivelatore HET di KLOE-2: Manuale utente

INFN-12-08/LNF
L. Iafolla et al., Report on the development of the DisOpto board for the HET taggers of KLOE2

INFN-12-09/LNF
L. Iafolla et al., Studio di fattibilit di un TDC tollerante alle radiazioni per la camera a deriva di SuperB

INFN-12-10/LNF
C. Lo Surdo, Fondamenti Matematici della Fisica Macroscopica (un percorso geometrico), Parte I

INFN-12-11/GE
M. Sanguineti et al., A study on sparking events in the data analysis of the ANTARES detector

INFN-12-12/LNF
C. Lo Surdo, Fondamenti Matematici della Fisica Macroscopica (un percorso geometrico), Parte II

INFN-12-13/LNF
Q. Hou et al., Phase contrast imaging opportunities at DAFNE

INFN-12-14/LNF
D. Alesini et al., A possible hard X-Ray FEL with the SuperB 6 GeV Electron Linac

INFN-12-15/PG
A. Balla et al., Test system for the General Interface Boards

INFN-12-17(T)/LNF
S. Colafranceschi, A STUDY OF MATERIALS USED FOR MUON CHAMBERS AT THE CMS EXPERIMENT AT THE LHC: INTERACTION WITH GAS, NEW MATERIALS AND NEW TECHNOLOGIES FOR DETECTOR UPGRADE

INFN-12-19/LNF
C. Lo Surdo, Fondamenti Matematici Della Fisica Macroscopica(un percorso geometrico), Parte III

INFN-12-20/TO
D. Berzano, SSH AUTHENTICATION USING GRID CREDENTIALS

INFN-12-21/PD
M. Michelotto et al., SERVER PER NODI DI CALCOLO

INFN-12-22/PG
A. Codino, Progresso e Pregiudizi nella Fisica dei Raggi Cosmici sino al 2006

INFN-12-23/LNF
A. Calcaterra et al., Measuring Propagation Speed of Coulomb Fields

INFN-12-24/LNF
S. Guiducci et al., Beam dynamics studies and design of the LINAC-LER transfer line for the electron Injector of SuperB

INFN-12-25/CNAF
A. Mazza et al., OTTIMIZZAZIONE ENERGETICA OTTENIBILE DALLAMPLIAMENTO DEI PARAMETRI TERMOIGROMETRICI ALLINTERNO DEL CENTRO DI CALCOLO TIER 1

INFN Reports

INFN / CCR_11 / 1
D. Fabiani, E. Mazzoni Interventi su KERNEL e Microcode per Adeguare il Processore AMD 8356 REV. B2 allAmbiente GRID

INFN / TC_11 / 1
V. Variale, Charge Breeding Simulations in a Hollow Gun Ebis

INFN / CCR_11 / 2
M. Canaparo, C. Galli, E. Ronchieri, C. Vistoli, A Data Environment for Software Development Process

INFN / TC_11 / 2
S. Aiola, P. La Rocca, O. Parasole, F. RiggiPreliminary Tests of a Scintillator-Based Mini-Station for Extensive Air Showers Measurements

INFN / TC_11 / 3
C. Strizzolo et al., Riprogettazione del Sito WEB della Sezione di Trieste dell'INFN in Base ad Alcuni Principi del Design Centrato sull'Utente

INFN / TC_11 / 4
S. Aiello et al., The Measurement of Late-Pulses and After-Pulses in the Large Area Hamamatsu R7081 Photomultiplier with Improved Quantum-Efficiency Photocathode

INFN / TC_11 / 5
K. Gracheva, M. Anghinolfi,V. Kulikovskiy, E. Shirokov, Y. Yakovenko, Down Going Muon Rate Monitoring in the Antares Detector

INFN / TC_11 / 6
M. Conte, The Spin Contribution to the Synchrotron Light

INFN / TC_11 / 7
F. Astuti et al., Calibrating the Photosensors for the DCAL Extension of the Alice Electromagnetic Calorimeter: An Activity Report

INFN / TC_11 / 8
G. Alampi, G. Cotto, P. Mereu, D. Gamba, The Fancy Table, a 5-axis silicon detector beam test bench

INFN / TC_11 / 9
M. Conte, Electrostatic Storage Ring

LNF GENERAL SEMINARS

LNF Seminars Committee: M. Boscolo (Resp.), T. Spadaro, A. Paoloni, A. Fantoni, S. Bellucci, S. Dell'Agnello, D. Babusci, U. Dosselli, M. Legramante (secr.)

In addition to the general seminars program, we initiated a *LNF mini-workshop series* with the idea of encourage a deeper discussion on a focused topic. In total, seven mini-workshops have been organized covering different research areas, from space physics to high energy physics, as well as applied physics. Typically, they are organized as one-afternoon session workshops.

1 LNF Mini-workshop series list:

Figure 1: *Poster of the 2nd LNF mini-workshop series.*

1. **Geodetic and time measurements for the CNGS (January 26th)**

   (a) Augusto Mazzone (DICEA - Area di Geodesia e Geomatica, Univ. Roma): "CERN-LNGS distance computation for the OPERA project",

   (b) Adrian Jaggi (Astronomical Institute of the University of Bern): "Global Navigation Satellite Systems for Positioning and Time Transfer ",

   (c) Thomas Schildknecht (Astronomical Institute of the University of Bern): "Time Transfer".

2. **Space Exploration (March 8th)** (see poster in Fig. 1)

   (a) Roberto Vittori (ESA-HSO-U and INFN-LNF): "Highlights of Endeavor's final flight and outlook on the Space Shuttle Program"

Figure 2: *Poster of the 3rd LNF mini-workshop series.*

(b) M. Spagnulo (ASI, Office of Presidency):
"ASI Perspectives on space exploration from Long Term Strategic Plan"

(c) David Smith (MIT):
"Highlights of planetary laser ranging and altimetry: Mars (Mars Global Surveyor), Moon (Lunar Reconnaissance Orbiter), Mercury (MESSENGER) and beyond"

3. **Higgs Search at LHC (March 28th)**

Overview:

At present, Higgs search at the LHC is the real hot topic in particle physics. Tremendous effort is being carried on these years to push analyses of LHC data to the sensitivity needed for an unambiguous Higgs identification.The goal of this mini workshop is to give a fresh and deep insight from the people with hands on the matter: those with leading roles in the analyses, who will underline pros and cons of each experimental signature, discuss in depth factors limiting the sensitivity, and present reliable perspectives on future developments, hopefully towards a discovery of uttermost importance. Latest analyses results and hot topics on this interesting issue will be covered (see poster in Fig. 2).

Programme:

(a) Vittorio del Duca (INFN-LNF):
"Introduction"

(b) Stefano Rosati(INFN-RM1):
"Search of the Standard Model Higgs Boson in the $ZZ^* \to 4l$ decay channel at the LHC

(c) Roberto di Nardo (INFN-LNF):
"Search of the Standard Model Higgs Boson in the $H \to WW^* \to l\nu l\nu$ in the decay channel at LHC"

(d) Daniele del Re (Univ. Roma La Sapienza and INFN-RM1):
"Search for a Higgs boson in the $H \to \gamma\gamma$ channel at the LHC"

(e) Simone Gennai (INFN-MIB and CERN):
"Search for a Higgs boson in the $H \to \tau\tau$ in production processes in association with jets at the LHC"

Figure 3: *Poster of the 4th LNF mini-workshop series.*

4. **CNAO Primo Centro Italiano di Adroterapia Oncologica con Ioni (April 12th)**

Overview:

Verrà presentato il Centro Nazionale di Adroterapia Oncologica (CNAO) di Pavia, un centro di avanguardia per la cura dei tumori: é, infatti, il secondo in Europa e uno dei pochi al mondo dove saranno eseguiti trattamenti sia con protoni che con ioni carbonio. La struttura é unica in Italia (poster in Fig. 3).

Programme:

(a) Sandro Rossi (CNAO, Pavia):
"Introduzione"

(b) Claudio Sanelli INFN-LNF):
"L'INFN e il CNAO"

(c) Caterina Biscari (INFN-LNF):
"Commissioning e operazione del CNAO"

(d) Maria Rosaria Fiore (CNAO, Pavia):
"Adroterapia: prospettive cliniche"

5. **Monte Carlo Generators at LHC (May 16th)**

(a) Michael Seymour (University if Manchester) :
"Monte Carlo event generators for the LHC"

(b) Biagio di Micco (CERN) :
"Event generators for the Higgs boson searches at the LHC"

6. **Jet Phenomenology at the LHC (June 27th)**

   (a) Mrinal Dasgupta (University if Manchester):
   "QCD and jet physics"

   (b) Paolo Francavilla (CERN):
   "Jet Physics in ATLAS"

   (c) Paolo Bartalini (National Taiwan University):
   "Underlying event and multiple parton interactions studies at CMS-How soft QCD can prepare the ground for the interpretation of some rare SM backgrounds to searches"

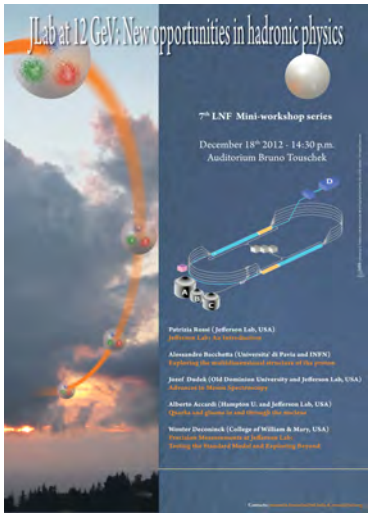

Figure 4: *Poster of the 7th LNF mini-workshop series*

7. **JLab at 12 GeV: New opportunities in hadronic physics (December 18th)**

   Overview:

   Jefferson Lab is a fundamental research laboratory located in Newport News (Virginia-USA). Its primary mission is to explore the fundamental nature of confined states of quarks and gluons, including the nucleons that comprise the mass of the visible universe. It consists of a high-intensity electron accelerator based on continuous wave superconducting radio frequency technology and a sophisticated array of particle detectors. The design features and excellent performance of the accelerator made it possible to plan an upgrade in energy from 6 to 12 GeV without substantially altering the construction scheme of the accelerator. The program includes the construction of major new experimental facilities for the existing three halls, A, B, C and the construction of the new experimental hall D. The project will be completed by the year 2013 and the commissioning of the experimental halls will be extended until the end of 2015. An overview of the 12 GeV experimental program will be presented. It includes: the study of the nucleon "tomography" through the study of generalized parton distribution functions (GPDS) and transverse momentum dependent parton distribution functions (TMDs), the study of exotics and hybrid mesons to explore the nature of the quarks confinement, precision test of the Standard Model through parity-violating electron scattering experiments (see poster in Fig. 4).

Programme:

(a) Patrizia Rossi (Jefferson Lab)"
"Introduction"

(b) Alessandro Bacchetta (Università di Pavia and INFN):
"Exploring the multidimensional structure of the proton"

(c) Josej Dudek (Old Dominion University and Jefferson Lab):
"Advances in Meson Spectroscopy"

(d) Alberto Accardi (Hampton University and Jefferson Lab):
"Quarks and gluons in and through the nucleus"

(e) Wouter Deconinck (College of William and Mary):
"Precision measuremens at Jefferson Lab: Testing the Standard Model and Exploring Beyond"

2 List of the LNF General Seminars in 2012:

1. Paride Paradisi (CERN):
"Direct CP violation in charm and flavor mixing beyond the SM", February 23rd.

2. Barbara Sciascia (LNF):
"First evidence for CP violation in charm decays at LHCb. A short presentation", February 23rd.

3. Nunzio Motta (Queensland University of Technology):
"Conducting polymers and carbon nanostructures for solar energy ", March 1st.

4. Gaia Lanfranchi (INFN-LNF):
"Highlights from Moriond 2012", March 14th.

5. Pierre Bonnal (CERN):
"Planning an accelerator project to ease its follow-up", March 21st.

6. Benoit Daudin (CERN):
"EVM tools at CERN", March 21st.

7. Luisella Lari (CERN) :
"Scheduling the LHC accelerator installation works: an overview of what was done", March 21st.

8. Giacomo Briani (Centre de Spectromtrie Nuclaire et de Spectromtrie de Masse CNRS/IN2P3 - Universit Paris Sud) :
"Ultracarbonaceous antarctic micrometeorites: a new window on the solar system origin", March 30th.

9. Beatrix Hiesmayr (Masaryk Univ., Institute for Theoretical Physics and Astrophysics, Czech Rebublic):
"Testing Foundational Issues at DAPHNE" , April 5th.

10. J. R. Lloyd (Manchester Univ.) :
"Harnessing microbial processes for the bioremediation of radioactive waste", April 23rd.

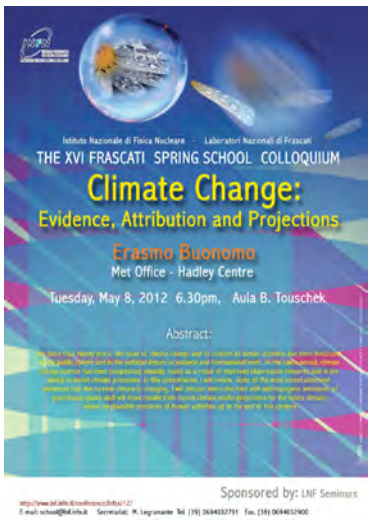

Figure 5: *Poster of the LNF Spring School Colloquium*

11. Erasmo Buonomo (Hadely Centre for Climate Changes):
"Climate Changes", May 8th (see poster in Fig. 5).

12. M. Muhlleitner (Karlsruhe, Inst. Technology):
"Electroweak symmetry breaking and the LHC", May 9th.

13. Gilad Perez (CERN and Weizmann Institute of Science) :
"The flavour physics at the LHC era , I, II", May 10th-11th.

14. Rodolfo Bonifacio (University of Strathclyde) :
" Quantum effects in Compton Back-scattering", May 17th.

15. Patrik Frank (SLAC) :
"Do we know the Temperature of Earth?", May 31st.

16. Nicolae-Victor Zamfir National Institute for Physics and Nuclear Engineering (IFIN-HH), Bucharest, Romania):
"ELI-NP Peoject", June 6th.

17. Victor Malka (CNRS):
" Laser Plasma Accelerators", June 6th.

18. Victor Malka (CNRS):
"Ultra-bright X ray sources with Laser Plasma Accelerators", June 8th.

19. Claude Duhr (ETH Zurich) :
"From Hopf algebras to Feynman Integrals", June 26th.

20. Gabor Somogyi (Hungarian Academy of Sciences):
"Higher-Order QCD Calculations via local subtraction", June 27th.

21. Mauro Mezzetto (INFN-PD):
"Prospettive future per esperimenti di neutrini short e long baseline", July 2nd.

22. Delia Hasch(INFN-LNF) : "Highlights from ICHEP2012", July 19th.

23. David Hertzog (University of Washington):
"Next-Generation Muon g-2", September 3rd.

24. Andrei Linde (Stanford University):
"Inflation in String theory and Supergravity", September 18th.

25. Pantaleo Raimondi (ESRF):
"The Upgrade Project for ESRF", October 15th.

26. Massimo Giovannozzi (CERN):
"Dynamic aperture studies for LHC and its upgrade", October 18th.

27. Rui de Oliveira (CERN):
"Gem, Micromegas and thick GEM production at CERN", October 25th.

28. Piergiorgio Picozza (Università di Roma2 and INFN-RM2) :
"Studying Cosmic Rays with Space Experiments", October 29th.

29. Francesco Vissani (INFN-LNGS):
"Progress and Prospects in Neutrino Astronomy", November 22nd.

30. Rob Bernstein (FNAL) :
" A Search for Charged Lepton Flavor Violation in Muon-Electron Conversion with a Sensitivity $< 10^{-16}$ ", December 4th.

31. Paride Paradisi (CERN) :
"Flavor Physics in the LHC era", December 6th.

32. Orfeu Bertolami Neto (Porto University):
"Phenomelogical and Theoretical Aspects of Modified Theories of Gravity with Non-Minimal Coupling between Curvature and Matter", December 7th.

All these seminars have been organized by the LNF Seminars Committee; we funded most of them, the rest have been co-funded with different budget.

The General Services and Technical Division

M. Arpaia, F. Angeloni (Art. 15), G. Bernardi, G. Bisogni, F. Bocale, M. Campoli, P. Caponera*, B. Casagrande*,A. Cassarà, A. Ceccarelli*, P. Celli, O. Cerafogli, A. Chiarucci, A. Clozza, V. Crisanti, A. De Paolis, A. Donkerlo, G. Ferretti, M.A. Franceschi, C. Fusco, M. Giorgi, E. Iacuessa, L. Iannotti, M. Marchetti, U. Martini, M. Matteo (borsista), S.G.A. Monacelli, M. Monteduro, L. Musella*, T. Napolitano, P. Panattoni, E. Passarelli, L. Pellegrino*, R. Ricci, A. Riondino, M. Rondinelli, M. Rossi*, U. Rotundo, M. Ruggeri, C. Sanelli (Head, Tech. Div.), F. Sanelli, A. Saputi*, A. Sorgi, A. Tacchi, A. Tiburzi*, R. Tonus, R. Valtriani

** have left the Division (retirement or transfer)*

1 Introduction

The main task of the Technical Division is the facility management of the Frascati Laboratories but, at the same time, the Division must guarantee all the necessary support to research and accelerator activities, mainly in the field of mechanics, electrical systems and HVAC systems. The Division can also supply technical and scientific support in the fields of vacuum and diagnostics systems, magnets and power electronics for accelerating machines.

During 2012, the Division collaborated, supported and gave consultancies with many INFN activities, such as: AMADEUS, BES III, CCR, CED TIER2, CNAO, CUORE, DAFNE, ETRUSCO2, ICARUS, JEM-EUSO, KAONNIS, KLOE2, LHCb, MOONLIGHT, NA62, PLASMON-X, SIDDHARTA, SPACEWEATHER, SPARC-LAB, SUPER B, TPS, VIP2. In addition, the Division supplied technical assistance to the INFN Headquarters in Rome and prepared all the infrastructures necessary for the operation of the new LNF canteen, as described below.

2 General Services Dept.

The General Services Dept. of the LNF deals with the organization and management of the general operational activities of the LNF and the Central Administration of the INFN, such as:

1. ENEA Canteen + Bar/Canteen LNF
2. Cleaning Service
3. Guards Service
4. Gardening Service
5. Porterage
6. Purchase of new furniture and reuse of discarded furniture
7. Child care center
8. Buses
9. Coffee breaks and lunches
10. Deratization and pest control
11. Purchase of hygienic materials and rental of no-dust carpets
12. Purchase and cleaning of work clothes
13. Drink water dispensers rental
14. Microbiological analyses of LNF bar food & equipment
15. Lease, insurances, maintenance and documentation of LNF vehicles
16. Emission of badges for staff & guests of LNF & AC and several other INFN structures
17. Liaising with the City of Frascati for licenses, authorizations and taxes
18. Liaising with the ENEA Frascati Center.

In addition to routine activities, the Service has dealt with public tender procedures such as:

- Management of LNF bar and canteen;
- Transport facilities for personnel (ENEA coaches, LNF shuttles);
- Purchase of equipment and furniture for the new Canteen of LNF.

In 2012, the porterage service was required for several heavy jobs: the dismantling and removal of about 10 temporary office buildings used by the SPARC Group, transfer of the SIDS Group (Research Division) to another building, collaboration with the Communication Office of the Rome Head Quarters for transport and stocking of exhibition material, emptying of 3 apartments necessary to the renovation of the roof of the external guest house Villa Laura, emptying of the ground floor of the Computing Building in preparation of the renovation works on its AC plants, disposal of discarded electronic equipment.

Collaboration with the Research Groups in the organization of meetings and conferences – coffee breaks, lunches, conference room preparation, participants transport (*Summer Internships, Spring School, Researchers' Night, Channeling 2012, SuperB, Incontri di Fisica, NN2012, HiLumi, BRML etc.*).

Procedures for the separate collection of rubbish as per Frascati municipality by-law have been instituted.

The extraordinary weather conditions in February with exceptionally heavy snow fall, which forced the LNF to close activities, put a heavy demand on facility management services.

The General Services Dept. of the LNF consists of two persons: the Dept. Head and one collaborator. Retirement of the Head is due at January 1st, of 2013.

The budget managed by the Dept. in 2012 was about € 293.000.

3 Central Stores and Purchasing Dept.

The Central Stores and Purchasing Dept. supervises the purchasing and stocking of goods of the Central Stores as well as those of the Metal Stores, and incoming and outgoing articles; development and extension of the stocked articles.

Moreover, the Dept. carries out market researches upon request of the users for the extension and upgrade of the collection of stocked goods, and maintains quality standards of stocked articles, and performs maintenance and updating of web pages, including the online General Catalogue database for the general users.

During the 2012 accounting period the Central Stores and Purchasing Dept. has transferred a total amount of € 200.000,00 for stock materials replenishment as follows:

- € 48.500,00 on Cap. 130110 (standard consumables),
- € 151.500,00 on Cap. 130120 (research consumables).

Furthermore, the Dept. has spent approx. € 84.500,00 for its ordinary activities, including mail handling services and management of small services such as the fork lift and small office equipment.

4 Building Management Dept.

In the course of the year, the porter lodge and entrance gate have been transferred to the new entrance area after fencing and landscaping in the area of the new entrance to the LNF and the adjoining service buildings has been completed.

The tender regarding the renovation of the roof of the Villa Laura guest house has been awarded and the related works are under way.

The executive project for the connection of the LNF sewage system to the communal sewage system, which runs under Via E. Fermi, has been completed. The tender for the works will be started as soon as the INFN will authorize the related public tender.

The executive project for the renovation of the roof of the ADONE guest house has been completed, and the contract has been awarded. The related works are under way.

Twelve prefab offices have been purchased and positioned in the area destined to new LNF research activities.

During the year, routine maintenance and repairs as well as extraordinary maintenance has been executed on the LNF buildings in order to preserve the value of the LNF assets. Other repair and maintenance works involving modifications, adaptations and renovations on LNF buildings have been carried out upon requests of the various LNF experimental groups.

The budget managed by the Dept. in 2012 was almost €300.000.

5 Mechanical Design and Construction Dept.

The Mechanics Design and Construction Dept. (SPCM) consists of five Units: Mechanical Design, Carpentry and Soldering, Machine Shop, Metrology and Alignment, Material Store.

During 2012, the SPCM personnel lost some staff units due to retirements, with no subsequent hiring of new resources; Metrology and Material Store in particular suffered lack of personnel and only for the latter internal resources have been found in SPCM; Metrology instead had to stop its activities in June.

The SPCM performs the following tasks:

- Mechanical design of experimental apparatuses and detectors, using CAD/CAE software and FEM analysis;
- Construction of prototypes and structures with the support of various soldering techniques and numeric control machine tools;
- Production of high precision mechanical components, relying on manual and numeric control machine tools equipped with CAM control;
- High precision dimensional check, material strength test, large structures and apparatus optical alignment;
- Acquisition and storing of mechanical components, tooling, metallic and plastic materials of workshop common use.

During the year, the SPCM has supplied support to several experimental activities, playing a role of direct responsibility in the design, production, construction or installation: CUORE at LNGS (engineering coordination and integration of the whole experimental apparatus), JEM-EUSO to be installed aboard the International Space Station (photo detector module and focal surface mechanics), SPACEWEATHER to be placed aboard a space satellite (structural design, optimization and analysis).

Many other activities were supported as well, though with no direct involvement in terms of responsibility: ATLAS, ETRUSCO2, JLAB12, KAONNIS, KLOE2, MAMBO, NA62, NESCOFI@BTF, NTA-SL-EXIN, UA9, VIP2 were supported in terms of mechanical design, construction, or dimensional checks and functional tests.

In conclusion, some 40 short-term actions were taken by the SPCM personnel to support experimental activities, in case of unplanned interventions or urgent repairs.

The budget managed by the Dept. in 2012 was about €63.000.

CUORE: Suspension test @LNGS

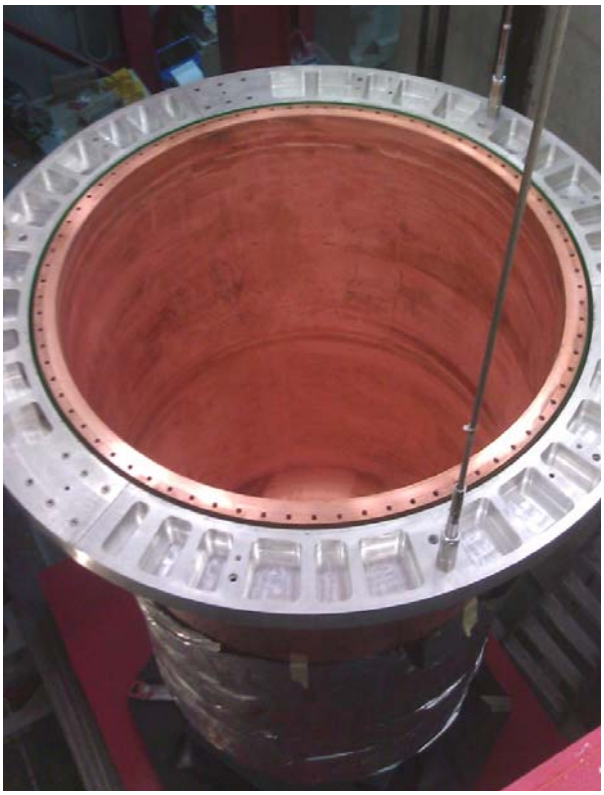

CUORE: installation of cryostat Outer Vacuum Vessel @LNGS

6 Heating, Ventilation and Air Conditioning Dept.

The Dept. is in charge of the operation and maintenance of the auxiliary plants, such as water cooling plants, water treatment facilities, compressed air and other gases production and distribution systems, HVAC plants for accelerators and experimental halls.

As of the end of 2012, the Dept. is also in charge of the HVAC Building Management (civil plants).

The procurements for new installations, from technical specifications definition to the follow-up of tender procedures, construction, commissioning, start-up, performance tests and standard operations, constitute part of the work scope of the Dept.

In 2012, the Dept. has provided support to DAFNE, KLOE, BTF, SPARC, FLAME, DAFNE-LUCE, MUEXC and the LNF Data Center.

During the year, the works for the upgrade of the Frascati Data Center air conditioning system started. The tender for the revamping of the SPARC supervisory and control system for Cooling and HVAC plants was awarded and the related works started. The Dept. also collaborated with the Electrical Installation Dept. in the tender for revamping of the PLCs system for the management of the Fluid Plants related to the DAFNE accelerator complex.

The budget managed by the Dept. in 2012 was about € 383.500,00.

7 Electrical Installations Dept.

The Dept. manages the LNF electrical installations from the high voltage power supply to end users and the lighting. The150 kV main station and the eight secondary cabins are operated by staff, who also cover emergency calls and fault fixing. Routine safety and functional maintenance activities are usually performed by external operators under the Dept.'s supervision.

Maintenance involves several skilled scheduled activities on electric switchboards, transformers, medium voltage devices, safety lighting, UPS, emergency generating sets and electrical devices of the DAFNE and SPARC cooling systems, but also small repairs or changes requested by users.

The Department also supplies technical support to the INFN Rome Headquarters offices' installations.

During the year, the renovation of the old electrical installation supervisor and control system of the electric distribution network started. The HV main station and the eight secondary cabins are now under control of new PLCs and a new control system. Several new, cheap and efficient energy analysers have been installed in key points of the lab enabling a better knowledge of power demand so as to optimize energy saving activities.

The renovation and resizing of the outdoor lighting system is almost completed, resulting in a 40% power demand reduction.

The preliminary design and the costing of SuperB and ELI-NP electrical installation have been studied.

The VoIP upgrade of the telephone switchboard has been technically developed in cooperation with the LNF Computing Service, the work will be completed next year.

Several HV & MV maintenance activities have been performed contemporary to the general power cut required by Enel during the winter holidays.

The Dept. was also involved in the definition of the energy supplier contract with contacts with public utility companies and central INFN offices. A total of 31,7 GWh were registered by LNF in 2012, with a cost of 5,7 M€. The average energy cost was of about 0,18 €/kWh.

The budget managed by the Dept. was about €253.000.

8 Other technical-scientific support activities

A lot of work was done on the INFN flag-project Super B in collaboration with the Consortium Laboratorio Nicola Cabibbo. Over the summer, many graduates were selected through selection procedures, who were engaged by the Consortium mainly at the end of the year. From the technical point of view, the Departments of the Technical Division contributed to the preliminary design and the costing evaluation of the project. The following technical areas were covered: conventional magnets, vacuum systems, electric plant and distribution, fire systems and conventional safeties systems, and finally the interface with the Tor Vergata University deputed firm on civil engineering and the general coordination of the full WBS (Work Breakdown Structure). More in particular, a preliminary design of the vacuum system of the SuperB machine complex has been carried out going in detail with LINAC, Transfer Lines, Damping Ring and Main Rings vacuum system.

The technical support activity for AMADEUS & SIDDHARTA also continued: the activities related to the realization of the new setup for the upgrade of SIDDHARTA - SIDDHARTA-2 - are currently in progress. Regarding AMADEUS, in August a carbon target has been inserted inside

the KLOE detector to enable the study of kaon-nuclei interaction using the KLOE detector capabilities. The activities related to VIP experiment proceeded with the realization of an aluminium box that will enclose the experimental setup keeping it under vacuum. Moreover, some other activities related to the VIP experimental area, located in Laboratori Nazionali del Gran Sasso, have been carried out.

Last but not least, a member of Division Staff has tutored a bachelor student in the elaboration of his thesis, titled *Deposizione film sottile di TiN su Allumina sinterizzata per ridurne l'emissione secondaria*. The student subsequently obtained his bachelor's degree with honours.

The Division Staff personnel also supported the Division Head with regard to civil engineering projects executed by specialized firms.

Two particular tenders have been dealt with by Division Staff: one for the refurbishment on the premises of the new LNF Canteen, awarded on 30/05/2011, and concluded on 04/04/2012, and another for the supply of furniture and utensils for the new LNF Canteen, awarded on 13/09/2011, and concluded on 01/08/2012 with final commissioning.

Unfortunately, a third tender for the selection of the catering firm for the new canteen dealt with by the General Services Dept. was stopped due to the "Spending Review" Law, which imposed the diminution of the value of the meals to be dispensed, changing hereby the essential terms of the tender. A new tender was called which will be concluded in 2013.

9 Some Statistics

During 2012, a total number of 581 registered requests reached the Technical and General Services Division, either through the General Users Form or through an automatic mail system for conference support requests. Not included in this number are the scheduled maintenance activities on the research and general facilities of the LNF, the mail requests for illumination repairs and those for change of tenocodes, or the 6 jobs executed by the Electrical Systems Dept. on request of the INFN Head Quarters in Rome.

The following departments were involved in the requests:

DEPT.	**%**	**Q.TY**
PIPING SYSTEMS	4%	23
HVAC	5%	29
ELECTRICAL SYSTEMS	7%	40
TELEPHONE SYSTEMS	12%	67
BUILDING MANAGEMENT	17%	100
SPCM	22%	126
GENERAL SERVICES	34%	196
TOTAL TD 2012	**100%**	**581**

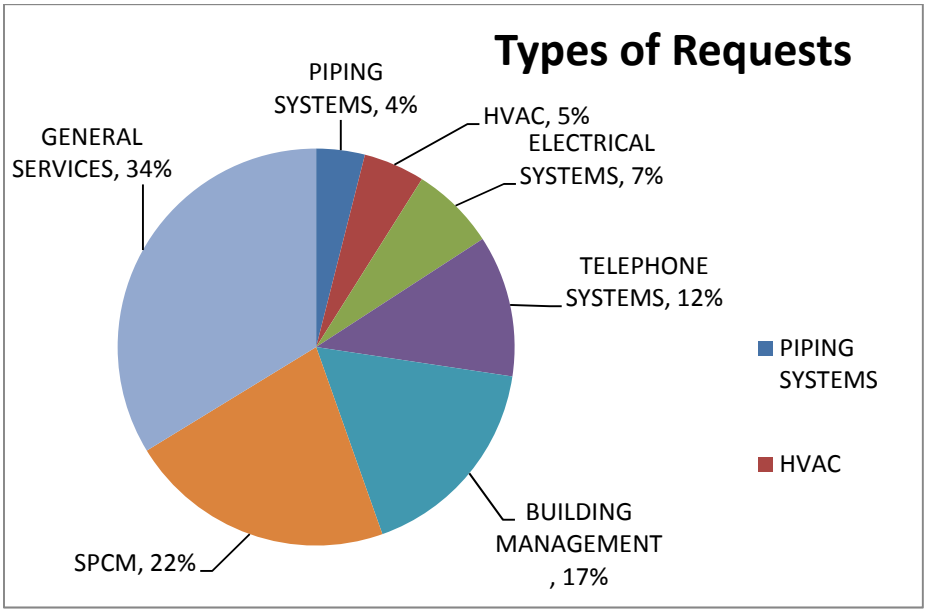

Compared to the previous year, 2011, the amount of requests handled by the Division has diminished by about 10% (581 in 2012, against 640 in 2011), but the Division staff has suffered a loss of 6 units due to retirement, 3 due to relocation within the LNF, and 2 for other reasons, for a total of 11 out of 49, i.e. more than one fifth of the work force. Two more people will be retired at the beginning of the next year.

More than half of all requests (55%) were from the Research Division, second and third requesters were the Accelerator (17%) and the Technical (12%) Divisions:

ORIGIN OF JOB REQUESTS	**%**	**Q.TY**
Research Division	55,08%	320
Accelerator Division	17,04%	99
Technical and General Services Division	12,05%	70
Directorate Offices	6,37%	30
Central Administration	3,61%	21
LNF Administration Dept.	2,24%	13
Human Resources Dept.	1,38%	8
Safety and Protection Dept.	0,86%	5
Radiation Protection and Medical Services Dept.	0,69%	1
SPARC-lab	0,69%	4
TOTAL TD	100%	**581**

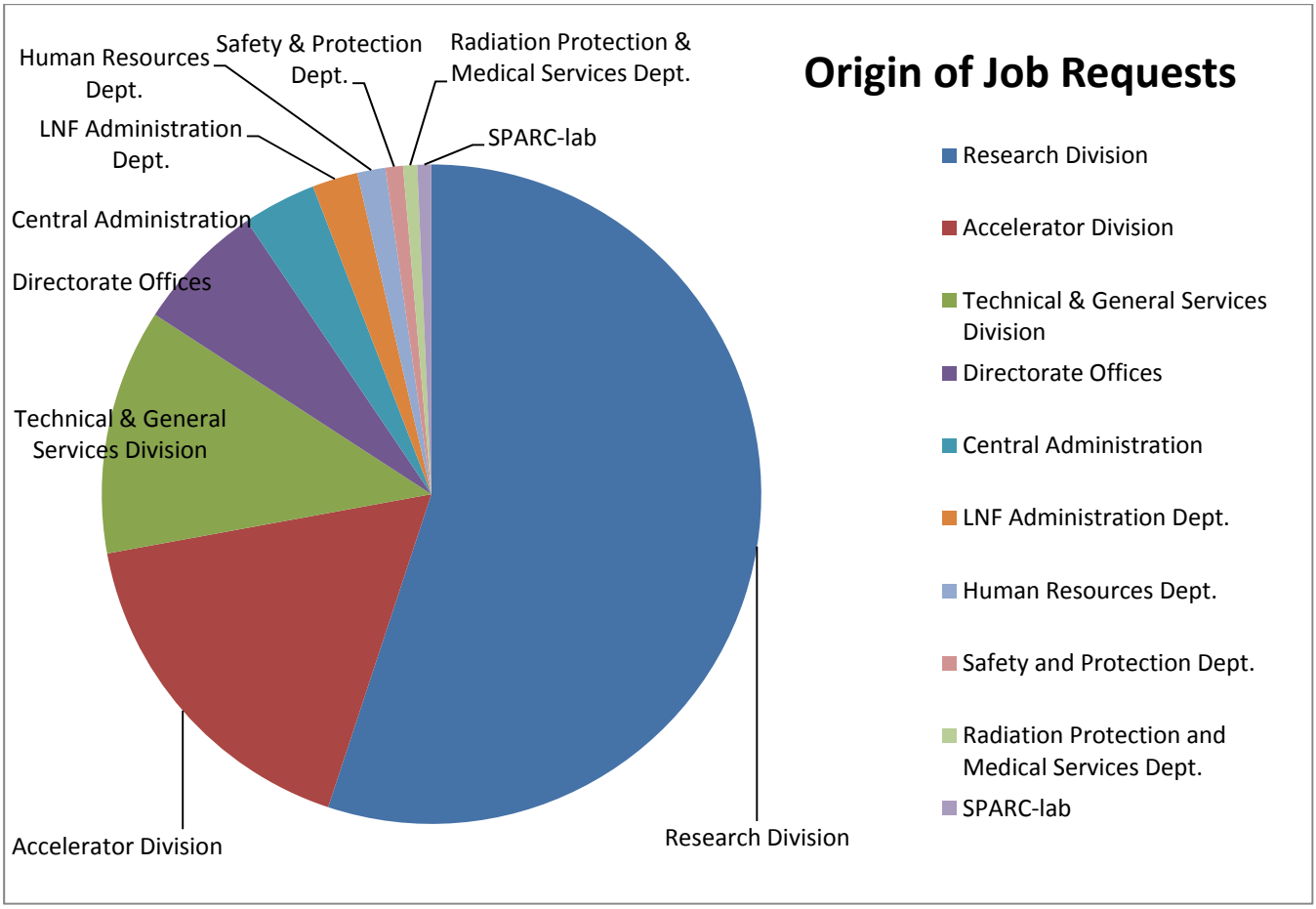

The average time of job completion was 39 days. However, since job completion often depends on external factors, one should not interpret the below graphic as an indication of efficiency. And again, scheduled maintenance on research and general facilities has not been included in the statistics.

AVERAGE TIME OF JOB COMPLETION	
DEPT.	**DAYS**
SPCM	17
Telephone Systems	28
General Services	36
Electrical Systems	44
Building Management	52
HVAC	87
Piping Systems	105
Overall	**39**

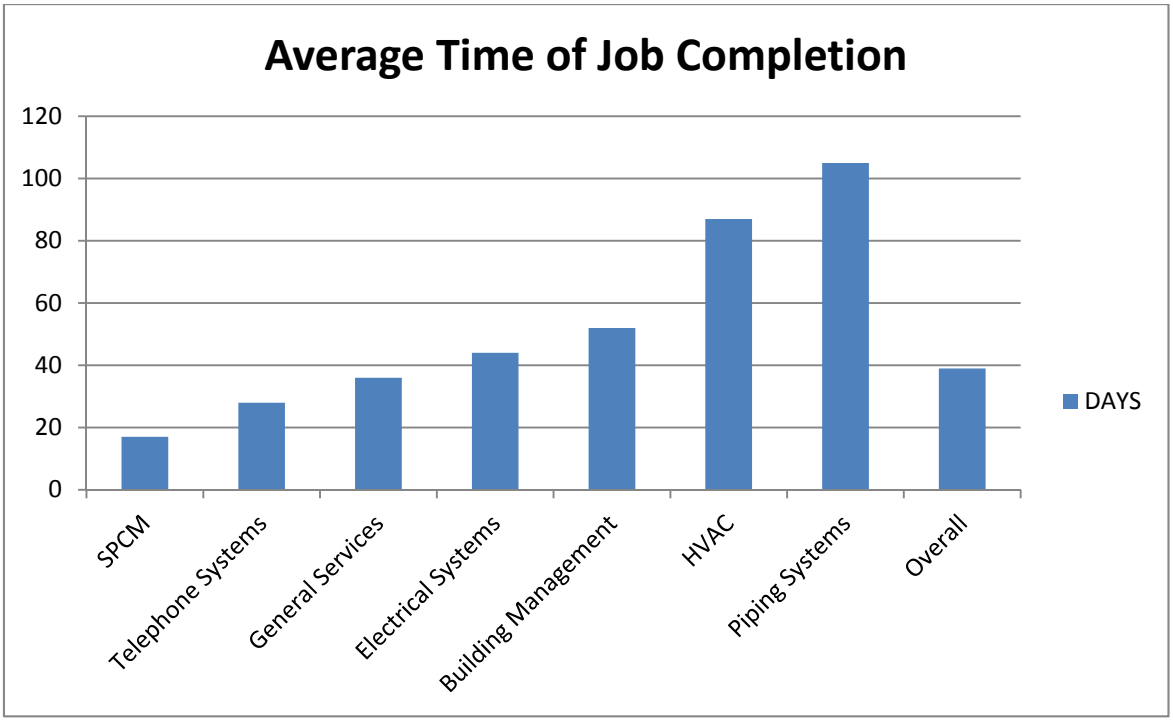
Average Time of Job Completion
120
100
80
60
40
20
0
SPCM
Telephone Systems
General Services
Electrical Systems
Building Management
HVAC
Piping Systems
Overall
DAYS